Physics of Atomic Nuclei, Vol. 63, No. 2, 2000, pp. 145–150. Translated from Yadernaya Fizika, Vol. 63, No. 2, 2000, pp. 197–203.

NUCLEI
Experiment

Observation of an Anomaly in the Angular Distribution of Cumulative Hadrons near the Backward Direction

L. S. Vorobiev, V. B. Gavrilov, Yu. G. Grishuk, P. V. Degtyarenko, Yu. V. Efremenko, B. V. Zagreev, M. V. Kossov, S. V. Kuleshov, G. A. Leksin, N. A. Pivnyuk, V. S. Serov, A. V. Smirnitsky, B. B. Shvartsman, and S. M. Shuvalov

Institute of Theoretical and Experimental Physics, Bol'shaya Cheremushkinskaya ul. 25, Moscow, 117259 Russia

Received January 21, 1999

Abstract—The angular distributions of secondary pions, protons, and deuterons originating from π^-Pb interactions at an incident-pion momentum of 5 GeV/*c* was determined in a new run of measurements relying on track reconstruction. While showing a decrease over a large angular interval with increasing emission angle, the yield of cumulative particles of each species was found to be anomalously large near the backward direction. *© 2000 MAIK "Nauka/Interperiodica".*

1. INTRODUCTION

In hadron–nucleus collisions, the yield of cumulative particles as a function of the laboratory emission angle θ was originally measured in [1, 2]. While slowly decreasing with increasing θ on a broad angular scale, this yield was found to be irregular at the largest values of θ and, in particular, to be enhanced near θ = 180°. Moreover, the observation of dips near 170° in the θ distributions of secondary protons, deuterons, pions, and tritons from deuteron–nucleus collisions at 8.9 GeV/*c* was claimed in [1]. Later on, this result was disproved by the same group in [3], but, from the data presented there for the yields of secondary 500-MeV/*c* protons emitted in collisions of primary 8.9-GeV/*c* protons with Pb nuclei, it follows that there are some irregularities in the behavior of the relevant cross sections in the angular range 150°–180°; in particular, an enhancement was observed near 180°.

Still later, our group performed measurements of the angular distributions of cumulative particles originating from the reactions

$$p(\pi^-) + A(\mathrm{C}, \mathrm{Pb}) \longrightarrow h(p, d, \pi) + X$$

induced by 4.5- and 7.5-GeV/*c* protons and by 1.5-, 3.0-, and 5.0-GeV/*c* pions [4]. Irregularities in the range of laboratory emission angles between 170° and 180° were observed under various conditions—in particular, at a projectile-proton momentum of 4.5 GeV/*c* and at a projectile-pion momentum of 5.0 GeV/*c*, in which cases the angular distributions of secondaries showed 2°-wide dips at θ = 172°, the position of the dips being independent of the type and energy of detected secondaries.

That the dip at θ = 172° was unusually narrow and that other large-θ irregularities, including some evidence for the presence of a maximum in the angular range 160°–170°, were established at the limit of the statistical accuracy of the measurements prompted us to conduct the above experiment anew. For projectiles, we chose 5-GeV/*c* negative pions in order to reproduce experimental conditions under which the dip at θ = 172° showed up previously [4] in the most spectacular way. In addition, the angular interval scanned in detail was extended here to become 161°–178°. In the new experiment, special attention was given to the geometric reconstruction of the tracks of projectiles and of ejectiles traveling in the backward direction and to the on-line monitoring of the local efficiency of the tracking system.

2. DESCRIPTION OF THE DETECTOR

The layout of the apparatus is illustrated in Fig. 1*a*. Beam particles were detected by counters S1, S2, and S3. Pulses generated by the scintillation counters S1 and S2 and corrected for geometric effects by a dedicated compensating circuit of the counters provided a zero point for time-of-flight measurements. For incident particles that should trigger the detector, the beam spot was effectively restricted by the self-quenched streamer counter S3 of transverse area 36×36 mm^2. Triggering by beam particles that failed to interact in a target T was prohibited by the downstream counter S4, which operated in anticoincidence with S1 and S2. The track of a beam particle upstream of the target was reconstructed by using signals from two-coordinate wire chambers WC1–WC7, which had a fiducial area of 200×200 mm^2 each and a wire pitch of 2 mm and which operated in the limited-streamer mode. We employed a lead target T of thickness $d = 1$ g/cm^2 oriented orthogonal to the beam axis. Secondaries emitted in the backward hemisphere traversed the wire chambers WC5–WC7 and were recorded by a nonmagnetic

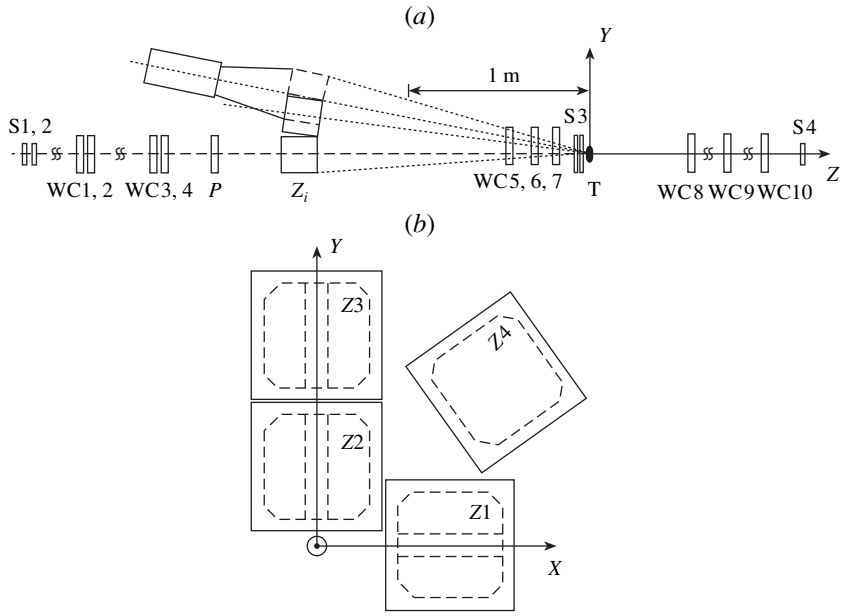

Fig. 1. Layout of the detector. The notation used in this figure is explained in the main body of the text.

hadron spectrometer (NHS) [5] formed by a system of counters (referred to as *Z* counters) measuring the hadron time of flight and ionization losses in a thick scintillator. The configuration of *Z* counters in the plane orthogonal to the beam axis is shown in Fig. 1*b*.

The beam was focused in the region of the *Z* counters rather than on the target, whereby spurious actuations by beam-halo particles hitting the *Z* counters were suppressed; this also increased effectively the beam spot on the target. That the beam spot on the target was relatively large (about 5 cm in diameter) resulted in the averaging of local fluctuations of coordinate-chamber efficiencies, since secondaries with a given value of θ traversed different areas of the wire chambers. The dead time of the data-acquisition system was negligibly small because of a relatively low intensity of the incident beam (10^5 particles per second). The defocusing of the beam also contributed to reducing the dead time of the wire chambers to some 1%. For a beam-position monitor *P*, we used a two-coordinate wire chamber that operated in the proportional mode.

In order to detect hadrons traveling backward toward the counters *Z*1–*Z*4 of the nonmagnetic spectrometer, the wire chambers WC5–WC7 were displaced from the beam axis, as is shown in Fig. 1*a*. That the counters subtended overlapping areas of the emission angle allowed us to monitor the efficiencies of the wire chambers and to estimate the systematic experimental errors arising from the inefficiencies of the wire chambers and *Z* counters. The detector was triggered by coincident actuations of the beam counters S1–S3 and of at least one *Z* counter. Backward-going secondaries were identified by the time of flight between the target and the hit *Z* counter and by the energy deposition in the 20-cm-thick scintillator of the counter, and their emission angles were reconstructed in the wire chambers with a mean precision of 0.3°. Secondaries traveling at small angles in the forward hemisphere were detected by the downstream wire chambers WC8–WC10 in coincidence with the backward-going secondaries detected by the upstream chambers WC5–WC7. These downstream chambers also allowed us to identify the tracks of extra beam particles that had not interacted in the target.

3. DATA PROCESSING

For a physical analysis, we selected those events that featured a beam particle and a backward-going secondary that satisfied the following conditions: the former was detected in at least eight of the 14 wire planes of the chambers WC1–WC7 and hit the target, while the latter was detected in at least four planes of the chambers WC5–WC7 and actuated a *Z* counter. Events that featured extra beam tracks—there were about 10% such events—were rejected. (The only beam track in an event was reconstructed with the aid of seven two-coordinate chambers WC1–WC7.) Likewise, an event was dropped if at least one of the points where the (single) beam particle intersected a wire-chamber plane fell beyond four standard deviations from the fitted track.

The position of a collision vertex was determined as the intersection of a fitted beam track and the thin target. By using the coordinates of a hit in the wire chambers WC5–WC7 beyond the beam track, the tangent of the angle between the radius vector from the collision vertex in the target to the point of the hit in question and the beam-track direction could be estimated in each

projection. If two hits in different wire planes corresponded to compatible tangent values in the same projection (compatible angles indicating that the hit points form a straight line with the projected collision vertex), these hits were thought to be due to a backward-going secondary. If such candidates for a backward-going particle were found in the orthogonal planes of wires and if the track reconstructed on the basis of the above hits intersected an actuated *Z* counter, the corresponding event was included in a further analysis.

The above procedure for an interaction-point determination followed by a reconstruction of the track of a backward-going secondary proved to be more viable than the alternative strategy of reconstructing a beam-particle track and the track of a backward-going secondary and then matching these tracks with a common vertex required to lie within the target. The point is that, in practice, the latter procedure was extremely time-consuming because, in that case, it was necessary to sample a large number of true and spurious tracks reconstructed on the basis of hits in two of the three wire planes for each projection, the situation being impaired by fluctuations in the coordinate chambers. In contrast to this, a determination of the collision vertex in the adopted approach immediately singled out a relatively narrow corridor between the collision vertex and an actuated *Z* counter, and it was this corridor where we considered the hits of a backward-going secondary in the planes of the chambers WC 5–WC 7. For approximately 10% of all backward-going secondaries, the reconstruction of the tracks was more difficult because some or all hits of the two nearby tracks of backward-going particles coalesced with the result that one of the projections of such tracks could not be separated from that of the beam track. (In particular, this is true for secondaries hitting the counters *Z*1, *Z*2, and *Z*3—see Fig. 1*b*.) Despite this overlap of track projections, a primary track could still be reliably reconstructed with the aid of upstream wire chambers WC1–WC4, in which case its fitted projection in the counters WC5–WC7 was used as that of the secondary track. This approximation, however, might distort the angular distribution of secondaries. In our analysis, we therefore rejected tracks that intersected those areas of the *Z* counters that could coincide with a beam track in each projection (these areas are illustrated in Fig. 1*b*). Thereby, the acceptance to backward-going hadrons was slightly reduced, but their angular distribution remained unaffected.

For a backward-going secondary, the track fitted in the way described above was then used to determine the point where this secondary hit a *Z* counter [owing to an accurate determination of the collision vertex—by four to seven wire planes in each projection (see above)—such a reconstruction of the intersection point in space was more accurate than that which could be performed by using only the hits of backward-going particles]. The position of this intersection point was required for rejecting those secondaries that had hit the edge region of the *Z* counter, where they could be misidentified because of pulse-height distortions caused by a nonuniform collection of scintillation light. The 2-cm-wide border areas and the corner areas of the counters were disregarded in our analysis (see Fig. 1*b*).

The adopted experimental procedure involved specific systematic uncertainties that varied with emission angle. In particular, our tracking system could not distinguish between interactions occurring in the target and in ambient air if a secondary had been emitted at an angle close to 180°. The longitudinal position of the collision vertex was estimated with the uncertainty

$$dz = \frac{k dx}{|\tan\theta|}\sqrt{\chi^2/\mathrm{NDF}},$$

where $k \approx 3$ is a numerical factor dependent on the arrangement of the tracking planes with respect to the target, $dx = 0.6$ mm is the precision to which coordinates were measured in the wire chambers, θ is the angle of secondary-particle emission, and the $\sqrt{\chi^2/\mathrm{NDF}} \leq 2$ value per degree of freedom for the reconstruction of a backward track was required to be less than four in our analysis. Because of the uncertainty in the position of the interaction vertex, collisions in the ambient air were partly accepted in addition to collisions in the target proper. By way of example, we indicate that the uncertainty in question is 4 cm for $\theta = 175°$ and 1 cm for $\theta = 160°$. Since the target thickness effectively increases by 0.0052 g/cm^2 in the former case and by 0.0014 g/cm^2 in the latter case, the systematic uncertainty arising from this effect is within 1%. There is yet another systematic uncertainty, that which springs from multiple scattering of secondaries in the lead target. For secondary pions, protons, and deuterons with energies in the ranges covered by our experiment, it proved to be within 0.3%.

It should also be noted that our data were corrected for the geometric inefficiency of the apparatus.

4. RESULTS OF THE MEASUREMENTS

In order to test the geometric efficiency of the detector, the distributions in the azimuthal angle of backward-going secondaries, φ, were individually investigated in different θ intervals subtended by *Z* counters, but no φ dependence of the yield of secondaries was revealed in this way within our statistical accuracy.

Actually measured in our experiments were the angular distributions of cumulative protons, deuterons, and pions that were emitted from collisions of 5-GeV/*c* negative pions with Pb nuclei and which had kinetic energies in the ranges 60–240, 14–320, and 45–350 MeV, respectively. As in [4], the yield of protons was separately studied in three subranges of proton energy: 60–80, 80–110, and 110–240 MeV.

The measured θ distributions of cumulative protons, deuterons, and pions are illustrated in Fig. 2, where different symbols correspond to different *Z* counters used

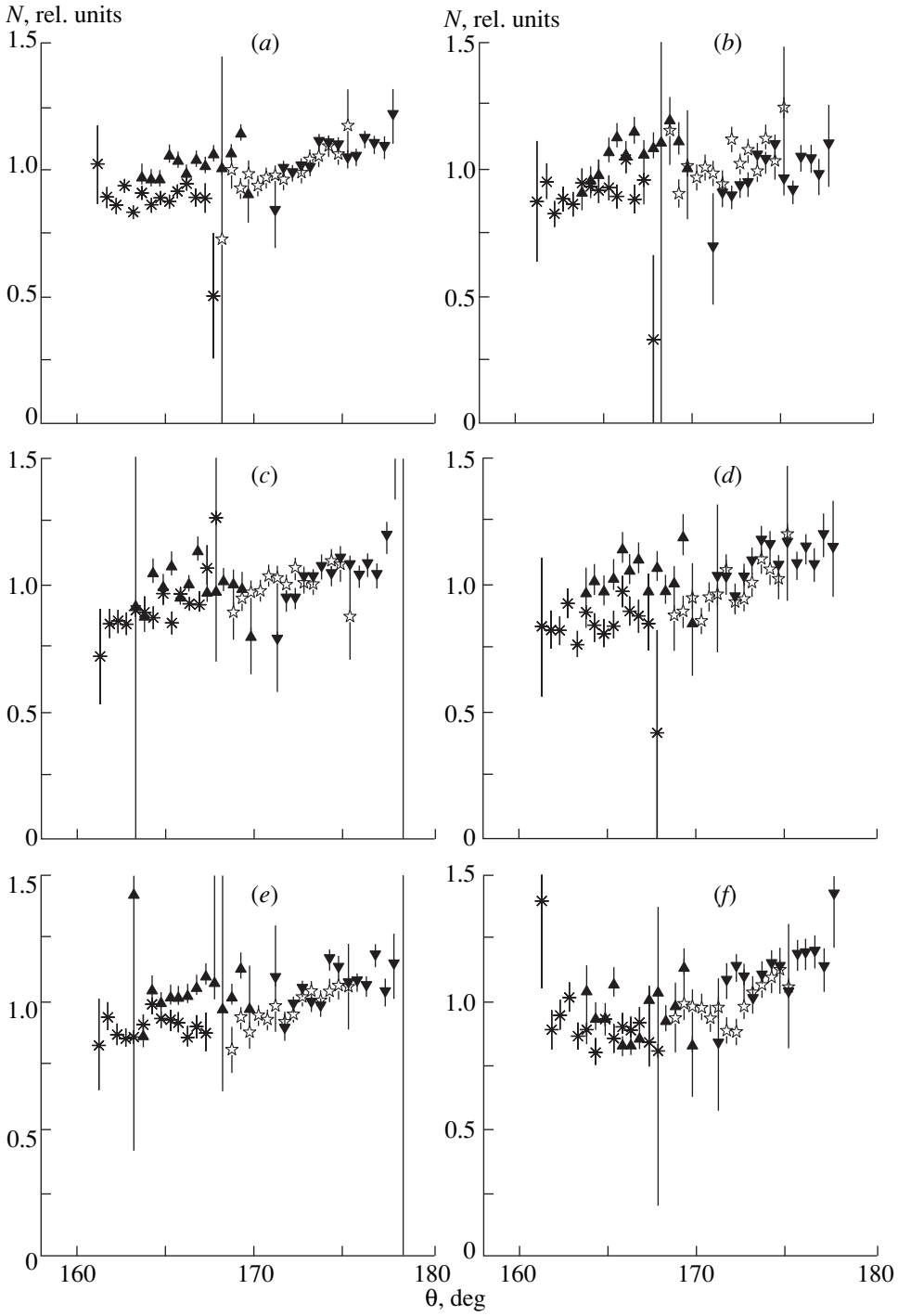

Fig. 2. Angular distributions of various cumulative hadrons from the interactions of 5-GeV/*c* π^- mesons with Pb nuclei: (*a*, *b*, *d*, *f*) data for protons with energies of 60–240, 60–80, 80–110, and 110–240 MeV/*c*, respectively; (*c*) data for deuterons with energies of 14–320 MeV/*c*; and (*e*) data for charged pions with energies of 45–350 MeV/*c*. The normalization is arbitrary. Experimental results obtained with different *Z* counters are represented by different symbols.

to analyze secondary hadrons. That the θ ranges subtended by different *Z* counters partly overlap provided an independent estimate of the systematic uncertainty. On the whole, the data are self-consistent, but we can see that, for a given *Z* counter, the measurement tends to underestimate the yield of cumulative particles in the boundary regions of θ. In view of this, data points that correspond the lowest and highest values of θ for each *Z* counter and which show large statistical errors were disregarded in averaging the θ distributions over all relevant *Z* counters. That independent estimates of the yield for a given value of θ are compatible within sta-

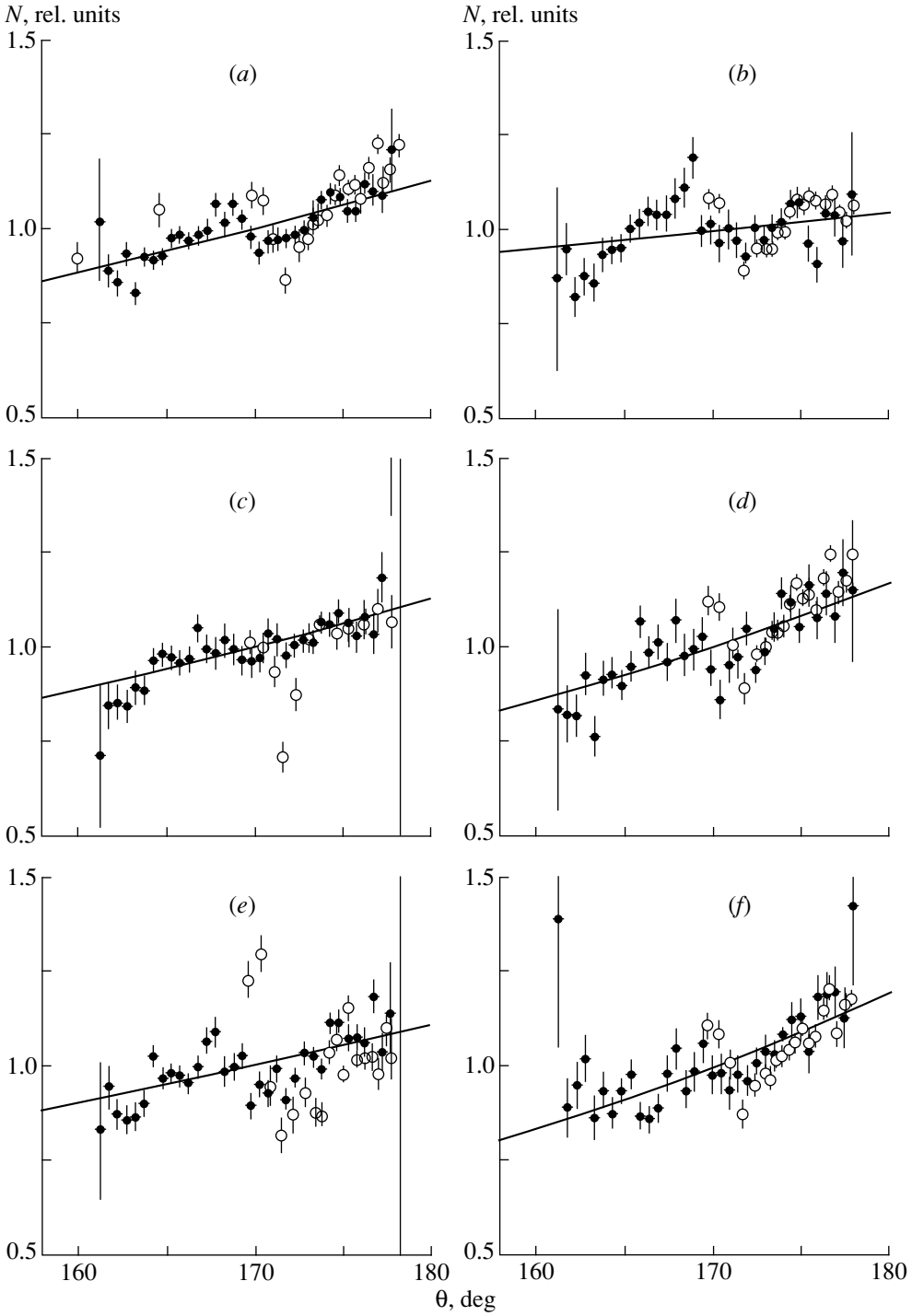

Fig. 3. As in Fig. 2, but on the basis of data averaged over overlapping *Z* counters (closed circles). Open circles show the results from [4] for the corresponding particle species and energy ranges. The normalization is arbitrary. Straight lines represent fits to the exponential form (1).

tistical errors suggests that, in the measurements being discussed, the systematic uncertainties do not exceed statistical ones.

The θ distributions averaged over overlapping *Z* counters are shown in Figs. 3*a*, 3*c*, and 3*e* for secondary protons, deuterons, and pions, respectively. The θ distributions of protons in the aforementioned three subintervals of proton energies are illustrated in Figs. 3*b*, 3*d*, and 3*f*. Qualitatively, all θ distributions in Fig. 3 follow the same pattern; in particular, each of these shows an increase toward θ = 180°. Fitting these distributions

Fits of θ distributions for various cumulative hadrons (see Fig. 3) to the exponential form (1)

Hadron (energy range in MeV)	b, 10^{-2}	χ^2/NDF
Proton (60–240)	1.207 ± 0.046	1.99
Deuteron (14–320)	1.204 ± 0.064	1.03
Pion (45–350)	1.034 ± 0.057	2.55
Proton (60–80)	0.475 ± 0.074	1.95
Proton (80–110)	1.569 ± 0.082	1.56
Proton (110–240)	1.810 ± 0.081	1.27

to the exponential form

$$N = Ae^{b\theta}, \quad (1)$$

we obtain the values of the slope parameter b that are listed in the table.

On a broader angular scale, the yield of cumulative particles decreases with increasing θ. For cumulative protons, the yield as a function of θ and of the kinetic energy T is given by [6]

$$f = A\exp\left[-\frac{T}{T_0}(1-\beta\cos\theta)\right],$$

where T_0 is the slope parameter of the proton energy spectrum and β is the parameter of the angular distribution, its numerical value being close to 0.5. According to the extrapolation of this parametrization to the angular range 161°–178°, which is studied here, the yield of cumulative protons should be virtually constant there. This prediction is at odds with the results of our measurements: from the table, we can see that the parameter b in (1) is always positive far beyond the experimental uncertainties—that is, the yield definitely increases toward the largest values of θ.

For the fits of the θ distributions to the form (1)—the results are represented by solid curves in Fig. 3—the χ^2 values per degree of freedom are quoted in the last column of the table. It can be seen that, although $\chi^2/\mathrm{NDF} \le 2$, the approximation in question is not quite satisfactory: Fig. 3 shows evidence for some local irregularities in the θ distributions of cumulative hadrons. For the sake of comparison, data from [4] are also shown in Fig. 3. We can see that the angular distributions obtained in [4] are not fully consistent with the present data. In particular, we no longer observe the narrow dip at θ = 172° reported in [4]. (In the present study, the region of the dip was probed by a specially deployed Z counter subtending the θ range 169°–175° (see Fig. 2*a*). Likewise, there is no agreement between the results of the two measurements in the region θ ≤ 171°, although the existence of a local maximum near 170° is supported by the new data as well. The discrepancy between the two measurements becomes nonexistent if we assume that the systematic uncertainties in [4], where no special attention was given to them, actually exceeded two quoted statistical errors.

5. DISCUSSION OF THE RESULTS

We have demonstrated that, over the range of laboratory angles θ between 160° and 180°, the yield of cumulative hadrons increases anomalously with increasing θ. We have already discussed this phenomenon in [4]. We still adhere to the arguments adduced there. Let us try to clarify them in the context of similar effects in various collisions. It is natural to invoke, first of all, data on elastic backward scattering of hadrons on light nuclei, since cumulative particles traveling in the backward hemisphere in the laboratory frame and having the maximum possible momentum value for a given cumulative number may result from quasielastic scattering on few-nucleon clusters inside the nucleus. It is encouraging to learn that the cross section for elastic scattering does indeed increase toward the scattering angle of 180°.

Likewise, the cross sections for elastic ion–ion collisions at tens of MeV per nucleon show various irregularities in the region of backward scattering. In the review article [7], where these irregularities are compiled and analyzed from various points of view, the enhancement at θ = 180° is tentatively attributed to the exchange of a constituent subsystem between the colliding ions. A constituent nucleon is exchanged in backward *pd* scattering. The cross section for backward $\pi^+ p \longrightarrow p\pi^+$ scattering proceeding via baryon exchange is also enhanced at θ = 180°. We can hypothesize that an analogous effect in the inelastic pion–nucleus scattering studied here is due to the exchange of a multiparticle system. That the collisions under investigation are inelastic renders the enhancement at θ = 180° less pronounced, but the effect remains very distinct.

ACKNOWLEDGMENTS

This work was supported in part by the State Program for Fundamental Nuclear Physics (project no. 11202-98).

REFERENCES

1. V. S. Stavinskiĭ, Fiz. Élem. Chastits At. Yadra **10**, 949 (1979) [Sov. J. Part. Nucl. **10**, 373 (1979)].
2. Yu. D. Bayukov *et al.*, Preprint No. 90, ITEP (1988).
3. A. M. Baldin *et al.*, Preprint No. R1-83-432, JINR (1983).
4. L. S. Vorobiev *et al.*, Yad. Fiz. **44**, 1396 (1986) [Sov. J. Nucl. Phys. **44**, 908 (1986)].
5. Yu. D. Bayukov *et al.*, Prib. Tekh. Éksp., No. 3, 25 (1982).
6. Yu. D. Bayukov *et al.*, Yad. Fiz. **42**, 185 (1985) [Sov. J. Nucl. Phys. **42**, 116 (1985)].
7. K. A. Gridnev and A. A. Ogloblin, Fiz. Élem. Chastits At. Yadra **6**, 393 (1975) [Sov. J. Part. Nucl. **6**, 158 (1975)].

Translated by A. Asratyan

Physics of Atomic Nuclei, Vol. 63, No. 2, 2000, pp. 151–155. Translated from Yadernaya Fizika, Vol. 63, No. 2, 2000, pp. 204–208.

NUCLEI
Experiment

Production of Light Nuclei in the Reactions of Protons with Separated Tin Isotopes

A. S. Danagulyan, J. Adam[1), 2)], A. R. Balabekyan[1), *], V. G. Kalinnikov[1)], V. I. Stegaĭlov[1)], V. K. Rodionov[1)], V. I. Fominikh[1)], and J. Frana[2)]

Yerevan State University, Yerevan, 375049 Armenia

Received October 15, 1998; in final form, January 29, 1999

Abstract—The cross sections for the production of ^{7}Be, ^{22}Na, ^{24}Na, ^{28}Mg, ^{38}S, ^{38}Cl, and ^{39}Cl nuclei from ^{112}Sn, ^{118}Sn, ^{120}Sn, and ^{124}Sn targets irradiated with 0.6-, 1.0-, and 8.1-GeV protons were measured by the method of induced activity. In analyzing resulting data, it was established that the above nuclei are produced in the fragmentation process and that the reaction cross section is a power-law function of the mass and charge numbers of fragmentation products. A strong dependence of the reaction cross section on the nucleonic composition of the targets and of the products is observed. The measured cross sections, together with data available in the literature, are discussed within various assumptions. *© 2000 MAIK "Nauka/Interperiodica".*

1. INTRODUCTION

Since the discovery of the fragmentation process, a great number of articles on the subject have been published [1]. Despite this, there is yet no unified theoretical framework that would describe a vast body of experimental data, explaining not only the mechanism of fragment production but also some fine effects associated with the nucleonic composition of target nuclei and of fragments. The last problem has also attracted much attention [2–5]. New theoretical approaches and various models developed in the last decade [6–8] have given impetus to new complicated experiments aimed at recording fragments over a full solid angle of 4π [9–11]. Those experiments usually used targets of natural composition. Some of them studied the prompt thermal breakup of nuclei into light and medium-mass ($3 \le Z \le 20$) fragments that was induced by energetic protons. Others pursued dynamical effects like the compression and the rotation of nuclear matter that are caused by the effect of high-energy heavy ions and which eventually result in nuclear decay. In addition to investigations relying on a direct detection of fragments, experiments are still being performed that record radioactive products of nuclear reactions induced by high-energy particles [12, 13]. The objective of the present study is to determine experimentally the cross sections for the production of light nuclei as functions of proton-beam energy. These measurements, performed by the method of induced activity, are aimed at deducing information about the mechanism of their production and at investigating fine effects pertinent to fragments of separated tin isotopes.

2. EXPERIMENTAL PROCEDURE AND EXPERIMENTAL RESULTS

The target used consisted of four metal foils containing tin isotopes ^{112}Sn, ^{118}Sn, ^{120}Sn, and ^{124}Sn enriched to 92.6, 98.7, 99.6, and 95.9%, respectively. The foil thicknesses listed in the same order were 390, 61, 70, and 72.7 mg/cm^2. The target was irradiated at the phasotron of the Laboratory of Nuclear Problems and at the synchrophasotron of the Laboratory of High-Energy Physics (JINR, Dubna). Two runs of duration 27 and 5 min were performed in a 660-MeV proton beam from the phasotron, the beam intensities being 1.36×10^{16} and 1.19×10^{16} protons per hour, respectively. In the experiments at the synchrophasotron, we also conducted two runs in which the target was exposed to a 1.0-GeV proton beam for 1 h and to a 8.1-GeV proton beam for 0.6 h. In that case, the beam intensities were 4.97×10^{12} and 2.27×10^{13} protons per hour, respectively. The beam was monitored by using the reaction ^{27}Al(p, $3pn$)^{24}Na, whose cross sections are known at the energy values used (10.7, 10.1, and 8.1 mb). The activities induced in the targets were measured with Ge(Li) and HpGe detectors upon a lapse of some time after the exposures. In order to separate long-lived reaction products, the measurements were repeated regularly within a year. In the measurements, the distances between the source and the detector were chosen to be 160, 26, 15, and 8 cm in order to ensure that the source was pointlike and that electronics operated under conditions of an optimum load. A preliminary treatment of measured γ spectra was performed with the aid of special software. We were able to sepa-

[1)] Joint Institute for Nuclear Research, Dubna, Moscow oblast, 141980 Russia.
[2)] Nuclear Physics Institute, Academy of Sciences of Czech Republic, CZ-250 68 Řež, Czech Republic.
* e-mail: anahit@nusun2.jinr.dubna.su

Table 1. Cross sections σ (mb) for the production of light nuclei from tin isotopes irradiated with 0.66-, 1.0-, and 8.1-GeV protons

Product nucleus	Cross-section type	^{112}Sn			^{118}Sn			
		0.66 GeV	8.1 GeV	Calc. [18]	0.66 GeV	1.0 GeV	8.1 GeV	Calc. [18]
^{7}Be	I	2.10 ± 0.20	23.50 ± 2.00	111.03	0.92 ± 0.10	–	20.90 ± 2.00	82.80
^{22}Na	C	0.16 ± 0.02	6.60 ± 1.20	13.25	0.20 ± 0.02	–	3.80 ± 0.40	10.40
^{24}Na	C	0.12 ± 0.02	4.00 ± 0.20	5.16	0.09 ± 0.01	0.50 ± 0.05	5.10 ± 0.04	5.8
^{28}Mg	C	–	0.58 ± 0.14	0.09	–	–	0.98 ± 0.15	0.14
^{38}S	C	–	–	–	–	–	0.22 ± 0.08	–
^{38}Cl	I	–	–	0.35	–	–	0.80 ± 0.10	0.6
^{39}Cl	C	–	–	0.09	–	–	0.53 ± 0.05	0.14

Product nucleus	Cross-section type	^{120}Sn		^{124}Sn		
		8.1 GeV	Calc. [18]	0.66 GeV	8.1 GeV	Calc. [18]
^{7}Be	I	16.50 ± 1.00	74.16	0.54 ± 0.06	13.00 ± 2.00	65.14
^{22}Na	C	2.40 ± 0.30	9.2	0.20 ± 0.03	2.50 ± 0.25	7.60
^{24}Na	C	5.10 ± 0.20	6.0	0.09 ± 0.01	5.30 ± 0.20	6.65
^{28}Mg	C	1.06 ± 0.12	0.20	–	1.34 ± 0.10	0.51
^{38}S	C	0.17 ± 0.07	–	–	0.40 ± 0.15	–
^{38}Cl	I	1.36 ± 0.15	0.91	–	1.35 ± 0.15	0.76
^{39}Cl	C	0.63 ± 0.10	0.3	–	0.85 ± 0.20	0.42

rate light product nuclei and to determine the cross sections for their production by using characteristic γ lines and by taking into account the half-lives of these nuclei. The resulting cross-section values are displayed in Table 1, along with the types of the cross sections for product nuclei (I and C label, respectively, the independent and cumulative cross sections). The quoted errors in the cross sections are purely statistical.

3. DISCUSSION OF THE EXPERIMENTAL RESULTS

The cross sections for the production of seven residual nuclei from all targets studied here are given in Table 1 for various energies of the proton beam. We can see that, with increasing energy of the incident particle, the cross sections for ^{7}Be, ^{22}Na, and ^{24}Na production grow substantially (by more than one order of magnitude), which is peculiar to the fragmentation mechanism [1]. We did not record ^{28}Mg, ^{38}S, ^{38}Cl, and ^{39}Cl isotopes at proton energies of 0.66 and 1.0 GeV; therefore, it was impossible to estimate the energy dependence for these isotopes. At 8.1 GeV, short-lived isotopes ^{38}Cl and ^{39}Cl from the ^{112}Sn target were not recorded because, for this target, the γ spectrum was measured only upon a lapse of a few hours after the exposure (to avoid the overload of the detector). The γ lines of ^{38}S were not observed in the γ spectrum of the irradiated ^{112}Sn target because of a small production cross section (a nucleus with a high neutron excess). For a ^{118}Sn target, Fig. 1 shows the cross sections versus the fragment mass numbers. The curve represents a fit to the form $\sigma(A_f) = aA_f^{-\tau}$, the fitted parameters being $a = 1334$ and $\tau = 2.10 \pm 0.06$. The dependence on the charge number was fitted to the similar form $\sigma(Z_f) \sim Z_f^{-2.47}$. In [8, 14, 15], the power-law dependence of the cross section for fragment production on Z_f and A_f was associated with the "liquid–gas" phase transition occurring as soon as hot nuclear matter formed in the target nucleus irradiated with high-energy particles attains a critical temperature. A mechanism of production of medium-mass fragments due to the condensation of strongly heated nucleon gas was proposed in [14, 15], where the analysis was based on the theory of condensation near the critical point [16]. By analogy with a Van der Waals gas, the production cross section of fragments is a power-law function of their masses A_f and charges Z_f; that is,

$$\sigma(A_f) \sim A_f^{-\tau},$$

where the exponent τ lies between 2 and 3 and where $\sigma(A_f)$ [or $\sigma(Z_f)$] are the total isobaric (or isotopic) cross sections. In the present experiment, we performed measurements only for those radioactive isotopes whose contributions of the total cross sections are small. Nevertheless, a power-law dependence was observed for radioactive fragments, with a τ value being close to that obtained in other studies (for example, in [17]) where

fragments produced under the effect of protons with energies of 2.7–7.5 GeV were recorded directly by means of the ΔE–E_1–E_2 procedure. It is interesting to note that, here, we obtained different values of τ, from 1.55 to 2.1 for different tin targets. Therefore, we can assume that, at a proton energy of 8.1 GeV, the fragments being studied were produced, with a nonnegligible probability, in the multifragmentation process as well (prompt nuclear breakup).

The cross sections for fragment production from all targets irradiated in our experiment with 8.1-GeV protons were calculated on the basis of the model proposed by Bondorf, Botvina, *et al.* [18]. The results are listed in Table 1. From a comparison of the calculated and experimental cross-section values, we can see that there is satisfactory agreement for the medium-mass fragments ^{24}Na and ^{38}Cl and that the values calculated for the light fragment ^{7}Be exceed the experimental values by a factor of 5. On the contrary, the values calculated for the neutron-rich nuclei ^{28}Mg and ^{39}Cl are a few times as small as the experimental values. It seems that excessively high values were taken in [18] for the excitation energies (E^*) of the intermediate nucleus produced upon the completion of the cascade; as a result, the number of light fragments was overestimated. In addition, no account was taken there of some fine details associated with the isotopic effect. Despite all this, the calculations demonstrate a correct tendency toward a decrease in the cross sections for ^{7}Be and ^{22}Na and toward an increase in them for the rest of the nuclei in passing from ^{112}Sn to ^{124}Sn.

By using our data and data available from the literature, we will now consider the cross sections for the production of the fragments being studied as functions of the target mass number A_t. This dependence is known to change strongly with the initial-proton energy [1] and to remain constant in the fragmentation region (E_p > 8–10 GeV). Therefore, we employed the data obtained at proton energies above 8 GeV [19–22]. The cross sections σ for the production of the neutron-rich fragments ^{24}Na and ^{28}Mg versus A_t are shown in Fig. 3 along with the third projection of the target isospin, T_{3t}/A_t (the ratio $3T_{3t}/A_t$ is plotted there to make the presentation clearer). We can see that the displayed dependences are similar in shape, which suggests a correlation between the cross sections and the ratio T_{3t}/A_t, so that there are grounds to assume that σ depends on the target isospin T_t. A similar fine structure is observed for the fragment nuclei ^{7}Be and ^{22}Na. For neutron-rich residual nuclei, there is also a general tendency toward an increase in the cross sections with increasing A_t (see Fig. 2). For the neutron-deficit nucleus ^{7}Be and for ^{22}Na, where the number of neutrons is equal to the number of protons (T_{3t} = 0), the cross section decreases as we go over from the target nucleus ^{112}Sn to the target nucleus ^{124}Sn (see Table 1).

In addition, Fig. 2 shows the photoyield for ^{24}Na as a function of A_t. These data, obtained in measurements

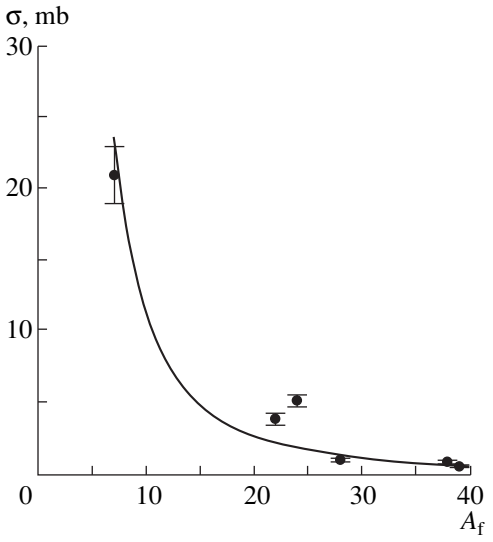

Fig. 1. Cross sections versus the mass number of the fragments for the ^{118}Sn target. The curve represents a fit to the form $\sigma(A_f) = aA_f^{-\tau}$, where the fitted parameter values are a = 1334 and τ = 2.1.

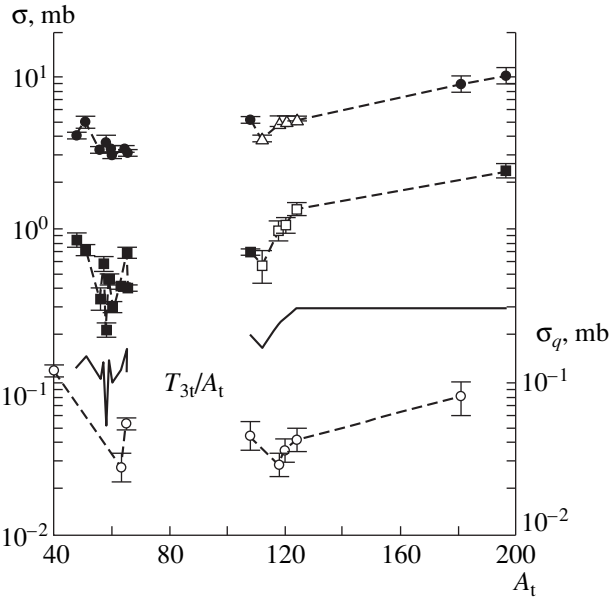

Fig. 2. Cross sections for the production of the neutron-rich fragments (●, △) ^{24}Na and (■, □) ^{28}Mg versus the mass number A_t of the targets (closed symbols represent the data from [19–21], while open symbols show our data). Open circles for ^{24}Na show data on the photonuclear reactions from [23, 24] (right scale). The solid curve depicts $3T_{3t}/A_t$ as a function of A_t.

where the endpoint energy of the bremsstrahlung spectrum was $E_{\gamma max}$ = 4.5 GeV [23, 24], also show a structure somewhat different, however, from that discussed immediately above. It seems that this dissimilarity is due to the absence of data for some targets. The above

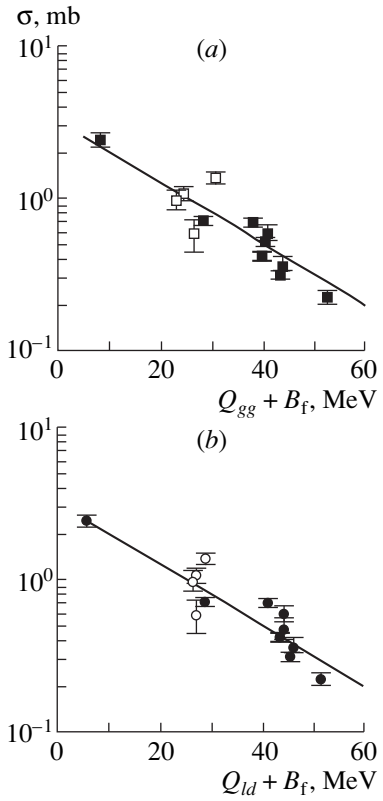

Fig. 3. Cross section for ^{28}Mg production versus (*a*) $Q_{gg} + B_f$ and (*b*) $Q_{ld} + B_f$: (closed symbols) experimental data from [19–21] and (open symbols) our data. The curve represents a fit to the form $\sigma = a\exp[-(Q_f + B_f)/T]$.

suggests that the isotopic effect is independent of the type of the initial particle.

In order to study the mechanism of fragment production, we considered the dependence of the cross sections for their production on the sum of the fragment-separation energy and the effective Coulomb barrier, $Q_f + B_f$. In this study, the fragment-separation energy was determined by two methods: (i) by using the experimental values of $Q_{gg} = M(A_f, Z_f) + M(A_{res}, Z_{res}) - M(A_t, Z_t)$, where the masses of the fragments, of the residual nuclei, and of the targets were taken from [25], and (ii) by using the expression $Q_{ld} = M_{ld}(A_f, Z_f) + M_{ld}(A_{res}, Z_{res}) - M_{ld}(A_t, Z_t)$ from the liquid-drop model. In the latter case, the binding energy is calculated by the formula [5]

$$E_{bind} = \varepsilon_{is}A + \varepsilon_{iv}T_3^2A^{-1} - 0.71Z^2A^{-1/3},$$

where $\varepsilon_{is} = 15.68(1 - 1.184A^{-1/3})$, $\varepsilon_{iv} = -112.4(1 - 1.184A^{1/3})$, and $T_3 = (N - Z)/2$; the effective Coulomb barrier is $B_f = 0.55Z_fZ_{res}e^2/(R_f + R_{res})$, $R = r_0A^{1/3}$; and $r_0 = 1.44 \times 10^{-13}$ cm.

By using data from the literature for the fragments ^{7}Be, ^{22}Na, ^{24}Na, and ^{28}Mg in the target-mass region between 48 and 197, we have studied the dependence of the cross sections on $Q_f + B_f$ for $E_p > 8$ GeV. Figure 3 shows the cross section as a function of (*a*) $Q_{gg} + B_f$ and (*b*) $Q_{ld} + B_f$ for ^{28}Mg. It can be seen that the dependence of the cross section on $Q_{ld} + B_f$ is nearly exponential. Similar dependences are observed for ^{7}Be, ^{22}Na, and ^{24}Na isotopes (for ^{7}Be, the parameter *a* is taken in the form A_t^a), but the scatter of experimental points is greater here than for ^{28}Mg. By fitting experimental data to the form $\sigma = a\exp[-(Q_f + B_f)/T]$, we were able to evaluate the parameters *a* and *T*. The results are presented in Table 2 (the parameter *T* is related to the temperature of the system decaying into fragments). From the table, we can see that none of the *T* values falls below 20 MeV; that is, these values exceed the expected temperatures of the system formed upon the completion of the cascade caused by target irradiation with protons of energies not lower than 8 GeV. It should be noted that the values of *T* obtained in proton–nucleus ([26], E_p = 1 GeV) and photonuclear ([27], $E_{\gamma max}$ = 4.5 GeV) reactions leading to ^{7}Be production are thought to be high by the authors of [26, 27]. As can be seen from Table 2, better agreement with experimental data for the ^{7}Be, ^{22}Na, and ^{24}Na fragments is obtained when the separation energy is calculated within the liquid-drop model. This means that the cross sections are not sensitive to fluctuations of the separation energy that are due to shell effects in the nuclear binding energy. In Fig. 3, we can see the scatter of data, which reflects the dependence of the reaction cross sections on the nucleonic composition of the target and of the fragments (see also Table 1). In an attempt at taking into account the effect of isospins [5] on the reaction probability, we added a term of the $T_{3f}T_{3t}$ type to the

Table 2. Values of the parameters *a* and *T*

Product nucleus	$Q_{ld} + B_f$			$Q_{gg} + B_f$		
	a	*T*, MeV	χ^2/NDF	*a*	*T*, MeV	χ^2/NDF
^{7}Be	0.93 ± 0.05	20.90 ± 3.03	61.13/13	0.69 ± 0.03	59.83 ± 15.40	81.80/14
^{22}Na	14.14 ± 6.53	19.98 ± 4.79	58.45/12	3.25 ± 0.53	86.88 ± 33.30	72.69/12
^{24}Na	15.65 ± 1.25	25.24 ± 1.58	74.60/16	9.64 ± 0.66	40.42 ± 3.46	144.10/15
^{28}Mg	3.17 ± 0.39	21.54 ± 1.41	99.13/11	3.48 ± 0.28	19.30 ± 0.80	165.50/16

exponential form of σ, but this led to unsatisfactory results.

ACKNOWLEDGMENTS

We are indebted to V.M. Tsupko-Sitnikov, V.S. Pronskikh, A.N. Priemyshev, and L.G. Martirosyan for their participation in the measurements of the γ spectra and to G.S. Aĭvazyan and L.G. Martirosyan for their assistance in data processing. Thanks are also due to the technical staff of the phasotron and synchrophasotron for providing good beam parameters during the target exposures. A.S. Danagulyan is grateful to the Directorate of the Laboratory of Nuclear Problems and of JINR for providing the possibility of performing the experiment at JINR.

The work of A.S. Danagulyan was supported financially by the Ministry for Science and Higher Education of the Republic of Armenia.

REFERENCES

1. V. S. Barashenkov and V. D. Toneev, *Interactions of High-Energy Particles and Nuclei with Nuclei* (Atomizdat, Moscow, 1972).
2. V. I. Bogatin *et al.*, Yad. Fiz. **19**, 32 (1974) [Sov. J. Nucl. Phys. **19**, 16 (1974)]; **17**, 9 (1973) [**17**, 4 (1973)].
3. V. I. Bogatin *et al.*, Nucl. Phys. A **260**, 446 (1976).
4. Yu. P. Yakovlev, Fiz. Élem. Chastits At. Yadra **14**, 1285 (1983) [Sov. J. Part. Nucl. **14**, 541 (1983)].
5. Yu. P. Yakovlev, Yad. Fiz. **46**, 459 (1987) [Sov. J. Nucl. Phys. **46**, 244 (1987)].
6. D. H. E. Gross, Rep. Prog. Phys. **53**, 605 (1990).
7. D. Morretto and G. J. Wozniak, Annu. Rev. Nucl. Part. Sci. **43**, 37 (1993).
8. J. P. Bondorf, A. S. Botvina, A. S. Iljinov, *et al.*, Phys. Rep. **257**, 133 (1995).
9. V. Lips, R. Barth, S. P. Avdeyev, *et al.*, Phys. Rev. Lett. **72**, 1604 (1994).
10. L. Pienkowski *et al.*, Phys. Lett. B **336**, 147 (1994).
11. A. Schüttauf, W. D. Kunze, *et al.*, Nucl. Phys. A **607**, 457 (1996).
12. R. Wölfle and S. M. Qaim, Radiochim. Acta **50**, 185 (1990); B. Dittrich, U. Herpers, *et al.*, Radiochim. Acta **50**, 11 (1990).
13. D. W. Bardayan *et al.*, Phys. Rev. C **55**, 820 (1997).
14. A. S. Hirsch, *et al.*, Phys. Rev. C **29**, 508 (1984).
15. A. D. Panagiotou, M. W. Curtin, and D. K. Scott, Phys. Rev. C **31**, 55 (1985).
16. M. E. Fisher, Am. J. Phys. **3**, 255 (1967).
17. V. V. Avdeĭchikov *et al.*, Yad. Fiz. **48**, 1736 (1988) [Sov. J. Nucl. Phys. **48**, 1043 (1988)].
18. A. S. Botvina *et al.*, Nucl. Phys. A **584**, 737 (1995).
19. M. Noguchi *et al.*, Phys. Rev. C **38**, 1811 (1988); T. Asano *et al.*, Phys. Rev. C **28**, 1718 (1983); T. Tominaka *et al.*, Nucl. Phys. A **414**, 385 (1984).
20. N. T. Porile, G. D. Cole, C. R. Rudy, *et al.*, Phys. Rev. C **19**, 2288 (1979).
21. G. M. Raisleck *et al.*, Phys. Rev. C **12**, 527 (1975).
22. S. Katcoff *et al.*, Phys. Rev. Lett. **30**, 1221 (1973).
23. A. A. Arakelyan *et al.*, Yad. Fiz. **41**, 833 (1985) [Sov. J. Nucl. Phys. **41**, 533 (1985)]; **52**, 319 (1990) [**52**, 202 (1990)].
24. K. A. Amroyan *et al.*, Preprint No. 1193(70)-89, YERPHI (Yerevan Physics Inst., 1989).
25. G. Audi and A. H. Wapstra, Nucl. Phys. A **565**, 22 (1993).
26. L. Kh. Batist *et al.*, Preprint No. 861, LNPI (Leningrad Nuclear Physics Inst., 1983).
27. A. A. Arakelyan *et al.*, in *Abstracts of Papers presented at 39th Workshop on Nuclear Spectroscopy and Nuclear Structure, Tashkent, 1989*, p. 319.

Translated by E. Kozlovskiĭ

Physics of Atomic Nuclei, Vol. 63, No. 2, 2000, pp. 156–160. From Yadernaya Fizika, Vol. 63, No. 2, 2000, pp. 209–213.

NUCLEI
Experiment

Self-Similar Properties of Collisions between Light Nuclei*)

V. V. Glagolev, J. Hlaváčová[1)], G. Martinská[2)], J. Urbán[2)], and M. Vytykáčová[2)]

Joint Institute for Nuclear Research, Dubna, Moscow oblast, 141980 Russia

Received November 17, 1998

Abstract—A new way of representing data on the fragmentation of nuclei is suggested. The self-similar behavior of these processes, that is dictated by their kinematics, is demonstrated. The convenience of working in accelerated nuclei is emphasized, particularly for the determination of the binding energy of a wide class of nuclear fragments. © *2000 MAIK "Nauka/Interperiodica".*

1. INTRODUCTION

Recently, fairly large samples of experimental data on the interactions of light nuclei (d, ^{3}He, ^{4}He) with protons have been accumulated under the full solid angle conditions of the JINR LHE 1-m bubble chamber. Various fragmentation reactions, including both mesonless and pion containing channels, have been reliably identified [1].

It is now possible to compare the characteristics of the reactions at different energies and with different fragment masses. One of the classical data representation, the Chew–Low plot [2], has usually been used for $2 \longrightarrow 3$ processes and for multiparticle processes. The authors of this work, entitled "Unstable Particles as Targets in Scattering Experiments," used a plot of the type M^2 versus $|t|$ to analyze the $\pi\pi$ and nn scatterings.

However, in the case of nuclear collisions, the masses of the produced fragments A' may considerably differ from that of the initial nucleus A. The comparison of the reactions in terms of the Chew–Low plots become inappropriate, at least for the great differences in the four-momentum transfers, which lead to a "dispersion" of events containing different fragments. This can be seen in Fig. 1, where the Chew–Low plot for two reaction channels of ^{4}Hep collisions at 2.15A GeV/c, containing ^{3}H and ^{2}H fragments, is shown.

2. A NEW WAY OF FRAGMENTATION-DATA REPRESENTATION

Without affecting the generality of the proposed way of the fragmentation data representation, let us examine the simple case of the proton–nucleus interaction: $p + A \longrightarrow A' + X$.

The use of the relative four-velocity squared $b_{AA'}$, introduced by Baldin [3],

$$b_{AA'} = -\left(\frac{P_A}{M_A} - \frac{P_{A'}}{M_{A'}}\right)^2\Bigg|_{\mathbf{p}_A = 0} = 2\left(\frac{E_{A'}}{M_{A'}} - 1\right), \qquad (1)$$

instead of $|t|$, is the basic difference between the Chew–Low plot and the proposed way. Here and from now on, P stands for the four-momentum.

This variable seems to be the most suitable for the processes in relativistic nuclear physics and is widely used.

The second difference lies in the normalization of the missing mass squared MM^2 to the studied fragment A'.

In the notation of the diagram (Fig. 2), M can be interpreted as a product of the interaction of the incoming proton with an off-mass-shell part of the nucleus A, denoted R (recoil).

The treatments followed from here are more convenient in the A-nucleus rest frame, though all the quantities used are invariant. In accordance with the above mentioned, we introduce indices: A—for the initial nucleus; A'—for its fragment (spectator); R—for the

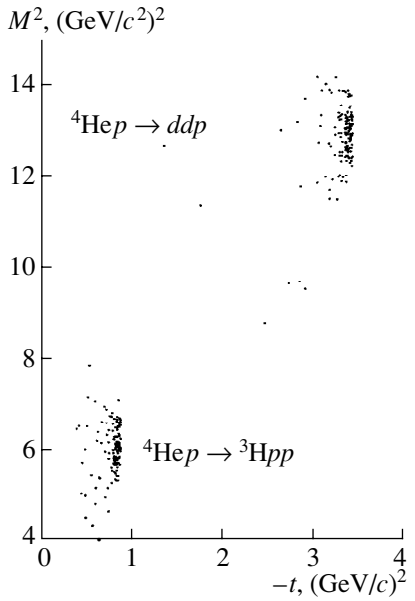

Fig. 1. The Chew–Low plot of the reaction ^{4}Hep at 2.15A GeV/c with deuteron and tritium fragments.

* This article was submitted by the authors in English.
[1)] Technical University Košice, Slovak Republic.
[2)] University of P.J. Šafarik, Košice, Slovak Republic.

rest of the initial nucleus; p—for the incoming proton (projectile).

Then, assuming $\mathbf{p}_{A'} = -\mathbf{p}_R$ and all the off-mass-shellness being on M_R, one can write

$$\begin{aligned} M_A &= E_R + E_{A'}, \\ M_R^2 &= E_R^2 - \mathbf{p}_{A'}^2 = M_A^2 - 2M_A E_{A'} + M_{A'}^2. \end{aligned} \tag{2}$$

In this case, the square of the total energy in the upper vertex of the diagram Fig. 2 or, similarly, the missing mass squared MM^2 without the fragment A' can be expressed as

$$MM^2 = [M_p^2 + M_R^2 + 2E_p E_R] + 2\mathbf{p}_{A'} \cdot \mathbf{p}_p. \tag{3}$$

The expression in the squared brackets is the total cms energy squared for the collision of the incoming particle (proton) with a part of the nucleus A excluding the fragment A' (i.e., with off-mass-shell R).

From here follows the way to use the quantity S', expressed in the recoiled on-mass-shell "R" rest frame as

$$S' = (P_p + P_{\text{“}R\text{”}})^2 = M_p^2 + M_{\text{“}R\text{”}}^2 + 2E_p M_{\text{“}R\text{”}}$$

for normalization purposes.

From (2) and (3) comes

$$\begin{aligned} \frac{MM^2}{S'} &= \frac{M_A^2 - 2M_A E_{A'} + M_{A'}^2 + M_p^2 + 2(M_A - E_{A'})E_p}{S'} \\ &+ \frac{2\mathbf{p}_p \cdot \mathbf{p}_{A'}}{S'} \end{aligned} \tag{4}$$

or

$$\frac{MM^2}{S'} = \frac{(P_p + P_A - P_{A'})^2}{S'}, \tag{5}$$

which is the same.

Experimental data are proposed to present MM^2/S' versus $b_{AA'}$ in the form of a plot.

From (4) one can easily get an expression for the contour line of the plot:

$$\begin{aligned} \frac{MM^2}{S'} &= \frac{(M_A - M_{A'})^2 + 2E_p(M_A - M_{A'}) + M_p^2}{S'} \\ &- \frac{M_{A'}(M_A + E_p)}{S'} b_{AA'} \pm \frac{2M_{A'}|\mathbf{p}_p|\sqrt{b_{AA'} + b_{AA'}^2/4}}{S'}, \end{aligned} \tag{6}$$

for which the lower bound is given by

$$M_X^2/S',$$

where M_X is the sum of masses in the upper vertex of the diagram in Fig. 2.

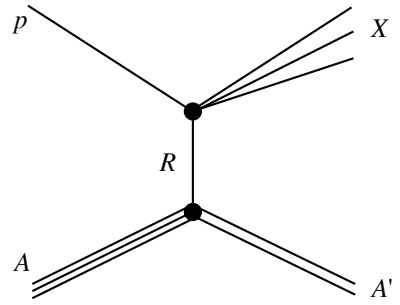

Fig. 2. Schematical representation of the fragmentation process.

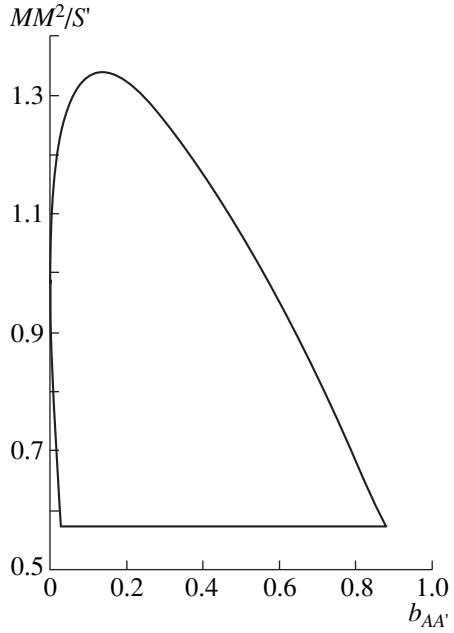

Fig. 3. The contours of the MM^2/S' versus $b_{AA'}$ plots for the reaction $^4\text{He}p \longrightarrow {}^3\text{H}pp$ at 2.15A GeV/c.

As an example, in Fig. 3 the full contour line for the $^4\text{He}p \longrightarrow {}^3\text{H}pp$ at 2.15A GeV/c is shown.

We demonstrate the use of the introduced representation on the fragmentation process, characterized by small values of $b_{AA'} \ll 1$ [4]. Examples of the contour lines in the fragmentation region for the discussed reaction are displayed in Fig. 4 at several incoming proton momenta from 2 to 500 GeV/c. In addition to the contours, the figure also shows the central lines, corresponding to the two first terms of equation (6).

In this region, one can see the characteristic behavior of the limiting curve width. The width Γ is defined as the distance between the lower and upper branches of the graph at a given value of $b_{AA'}$. From expression (6), for the width at small $b_{AA'}$, we get

$$\Gamma = \frac{4M_{A'}|\mathbf{p}_p|\sqrt{b_{AA'} + b_{AA'}^2/4}}{S'}.$$

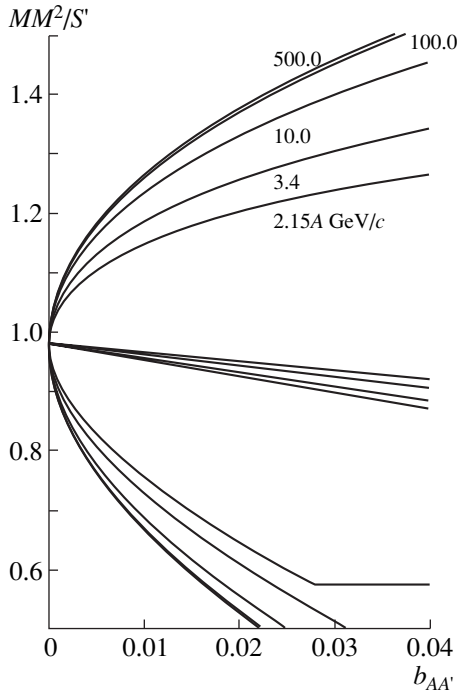

Fig. 4. Limiting contours for the ^{4}He$p \longrightarrow {}^3$Hpp in the fragmentation region at different incoming proton momenta.

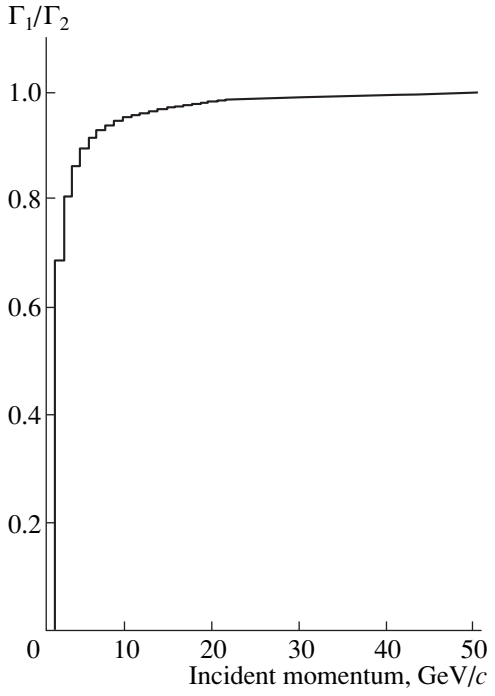

Fig. 5. The ratio of the widths at a given momentum to that at a doubled one in the fragmentation region.

The ratio of the widths at two energies for a given type of reaction (fixed A and A') does not depend on $b_{AA'}$ and with increasing energy tends to 1.

This can be explicitly seen in Fig. 5, where the ratio of the widths at a given incoming momentum, on the x axis, to that at a doubled one is shown. In this way, the self-similar behavior of the fragmentation process has been demonstrated.

We would like to emphasize an additional feature of the plot, suitable for supplementary use. At $b_{AA'} = 0$, the branches of the contour lines meet at

$$\frac{MM^2}{S'} = 1 - 2\epsilon\frac{(M_{\text{“}R\text{”}} + E_p)}{S'} + \frac{\epsilon^2}{S'}, \qquad (7)$$

where ϵ is the binding energy of the fragment A' in the parent nucleus A.

For the special case of quasi NN scattering, this expression, with an accuracy of 10^{-4}, turns out to be

$$\frac{MM^2}{S'} \simeq 1 - \frac{\epsilon}{M_p},$$

which allows us to determine the binding energy of different fragments, including the unstable ones.

The proposed method is predestined for accelerated nuclei and high-precision spectrometers because reliable fragment identification and high precision momentum measurements in the region of small value $b_{AA'}$ [5] are inevitable.

3. EXPERIMENTAL RESULTS

During the years by the use of the JINR 1-m HBC, exposed to beams of relativistic nuclei, great samples of experimental data have been collected for the interaction of light nuclei (d, ^{3}He, ^{4}He) with photons [1]. These data will be used in the following analysis.

Figures 6*a* and 6*b* display the ^{4}He$p \longrightarrow {}^3$Hpp reaction data and the contour lines at two values of proton momenta (2.15 and 3.4A GeV/c). The “middle” line

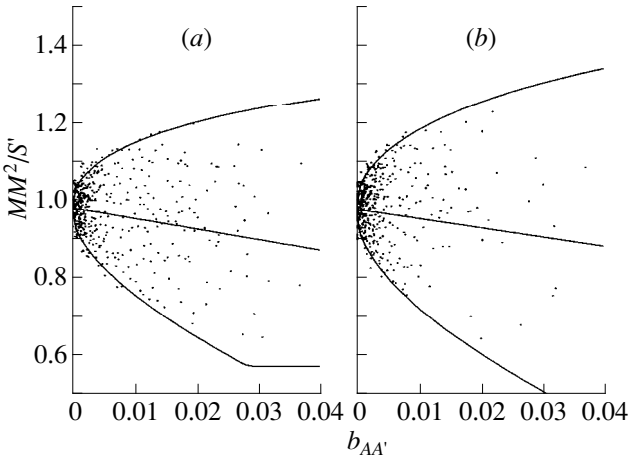

Fig. 6. MM^2/S' versus $b_{AA'}$ plot for the ^{4}He$p \longrightarrow {}^3$Hpp reaction at (*a*) 2.15A GeV/c and (*b*) 3.4A GeV/c.

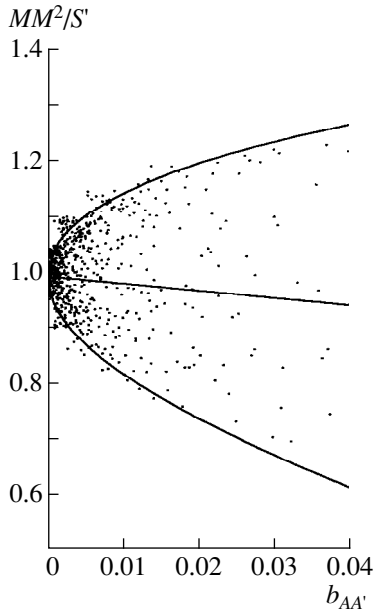

Fig. 7. The same plot as previously (Fig. 6) for the ^{3}He$p \longrightarrow dpp$ reaction at 4.5A GeV/c.

corresponds to A'-fragment production at 90° to the A-nucleus rest frame, i.e., $\mathbf{p}_0 \cdot \mathbf{p}_{A'} = 0$.

The given experimental points, as can be seen, are mainly inside the corresponding contour lines. The points outside are connected with the errors of measurement. The events with a triton fragment are predominantly concentrated in the area of small $b_{AA'}$ (<0.04), as has been predicted by [4]. For example, in Fig. 6*a*, only two events have $b_{AA'} > 0.04$ out of 2.808.

A similar situation can also be seen for the ^{3}He$p \longrightarrow dpp$ reaction at 4.5A GeV/c, for which the plot is shown in Fig. 7.

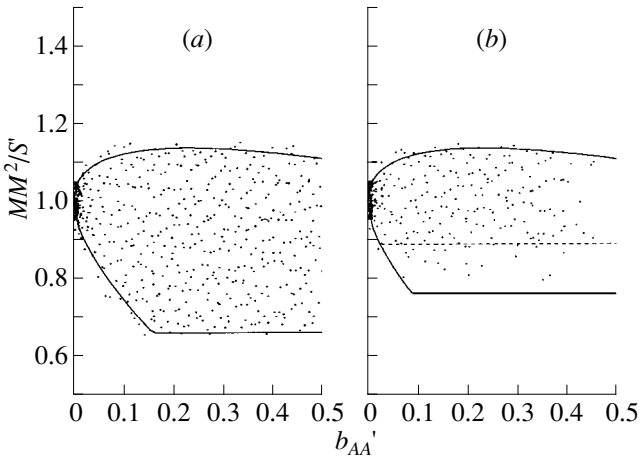

Fig. 8. Plots for the (*a*) $dp \longrightarrow ppn$ and (*b*) $dp \longrightarrow ppp\pi^-$ processes at 1.67A GeV/c.

The natural lower limit for the proposed plot contour is given by the threshold value of the ratio M_X^2/S'. This can be demonstrated in the examples of $dp \longrightarrow ppn$ and $dp \longrightarrow ppp\pi^-$ reactions at 1.67A GeV/c in Figs. 8*a* and 8*b*. Here, the lower horizontal bounds of the contours correspond, respectively, to the sum of masses of two nucleons and to that of the two nucleons and a pion. The dashed line in Fig. 8*b* corresponds to the boundary of Δ production (1.24 GeV/c^2) in the upper vertex of the diagram in Fig. 2. In the $dp \longrightarrow ppp\pi^-$ reaction, the density of the experimental values above the dashed line argues for the predominance of the pion production mechanism via Δ isobar and its consecutive decay.

Because the studied reactions are of quasinucleon type, we try to use the expression

$$\frac{MM^2}{S'} \simeq 1 - \frac{\epsilon}{M_p}, \tag{8}$$

proposed in [6], to determine the fragment binding energy ε in the parent nucleus. As an example, the plot of the ^{4}He$p \longrightarrow {}^3$Hepn reaction at small $b_{AA'}$ is examined. Figure 9*a* shows these data in the region of $b_{AA'} < 5 \times 10^{-4}$.

Projecting the experimental data onto the y axis (Fig. 9*b*) and fitting the Gaussian to the obtained MM^2/S' distribution, one estimates the mean value $\langle MM^2/S' \rangle = -0.9780 \pm 0.0013$.

Hence, using expression (8), we obtain for the binding energy of ^{3}He in ^{4}He $\epsilon = 20.6 \pm 1.3$ MeV/c^2, being in good agreement with the value $\epsilon_t = 20.57$ MeV/c^2, evaluated from the known masses of ^{4}He, ^{3}He, and n.

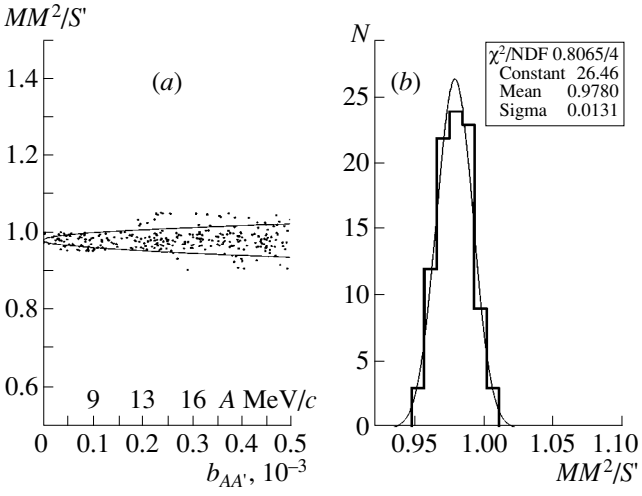

Fig. 9. (*a*) The plot for the ^{4}He$p \longrightarrow {}^3$Hepn reaction at 2.15A GeV/c in the $b_{AA'} < 5 \times 10^{-4}$ region, the upper scale on the x axis is for the fragment momentum per nucleon in the parent nucleus rest frame; (*b*) MM^2/S' distribution for $b_{AA'} < 2 \times 10^{-4}$ (^{3}He momenta with respect to the ^{4}He rest frame below 13A MeV/c).

Using the exact expression

$$\frac{MM^2}{S'} = 1 - 2\epsilon\frac{(M_p + E_p)}{S'} + \frac{\epsilon^2}{S'}, \quad (9)$$

one obtains $\epsilon = 20.7 \pm 1.3$ MeV/c^2.

In addition to the $b_{AA'}$ scale (Fig. 9*a*), the momentum scale with respect to the *A*-nucleus rest frame is also present, from which it can be seen that, due to small values of the fragment momenta, the proposed method of binding energy determination cannot be applied to the fragmentation of the nuclei at rest (target). To work in the beams of accelerated nuclei with precise measurements of the fast fragments' momenta in the region of $b_{AA'} \longrightarrow 0$ seems to be inevitable.

4. CONCLUSION

A new way of fragmentation data representation is introduced. With its aid, the self-similar behavior of the light-nucleus-fragmentation processes at small $b_{AA'}$ is shown.

Different aspects of the proposed plot application to the light-nucleus-fragmentation reactions have been shown. It can be seen, as is expected, that the fragmentation mainly occurs at small values of the relative four-momentum squared $b_{AA'}$. The plot occupancy at different energies lies within the computed contours, and, in this way, it supports the reaction self-similar behavior at small $b_{AA'}$, i.e., in the fragmentation region.

The use of this data representation for the pion containing fragmentation reactions allows us to reveal the mechanisms of the quasinucleon interactions. The determination of the fragment nucleus binding energy in the parent nucleus has been demonstrated on the example of the ^{4}He$p \longrightarrow {}^3$Hepn reaction.

The advantage of working in the beams of accelerated nuclei with the use of wide-aperture spectrometers has been shown, which also reduces the distortions at the study of fragmentation processes.

ACKNOWLEDGMENTS

This work was partly supported by the Grant Agency for Science at the Ministry of Education of the Slovak Republic.

REFERENCES

1. V. V. Glagolev, Nucl. Phys. B (Proc. Suppl.) **36**, 509 (1994).
2. G. F. Chew and F. E. Low, Phys. Rev. **113**, 1640 (1959).
3. A. M. Baldin, Nucl. Phys. A **447**, 203 (1985).
4. A. M. Baldin and L. A. Didenko, *Lecture for the Young Scientist: Preprint of JINR*, Dubna, 1987, no. R1-87-912.
5. M. Vytykáčová *et al.*, JINR Rapid Commun. (Dubna), No. 3[89]-98, 37 (1998).
6. V. V. Glagolev, G. Martinská, and J. Urbán, JINR Rapid Commun. (Dubna), No. 3[89]-98, 31 (1998).

Physics of Atomic Nuclei, Vol. 63, No. 2, 2000, pp. 161–169. Translated from Yadernaya Fizika, Vol. 63, No. 2, 2000, pp. 214–222.

NUCLEI
Theory

Manifestation of Pairing Effects in the Cross Section for ^{238}Pu Fission Induced by Neutrons

V. M. Maslov

Institute of Physicochemical Problems of Radiation, Minsk-Sosny, 220109 Belarus

Received June 26, 1998; in final form, April 1, 1999

Abstract—The cross section for ^{238}Pu fission induced by neutrons with energies between 1 keV and about 5 MeV is described within the statistical model. It is shown that the stepwise structure observed above the fission threshold (at incident-neutron energies of $E > 1$ MeV) is due to the step in the level density of the fissile ^{239}Pu nucleus at deformations corresponding to the inner fission barrier. In turn, the step in the level density of the odd nucleus ^{239}Pu is associated with the excitation of internal single- and three-quasiparticle states. The level density is described with allowance for collective, pairing, and shell effects. © *2000 MAIK "Nauka/Interperiodica".*

1. INTRODUCTION

Manifestations of pairing effects in the fission process is understood rather fully. Pairing effects in even–even fissile nuclei were revealed in the angular anisotropy of fission fragments rather long ago. A stepwise structure in the parameter K_0^2 determining the angular anisotropy of fission fragments was interpreted as a consequence of the threshold excitation of few-quasiparticle states at saddle-point deformations of fissile nuclei [1]. A manifestation of the stepwise structure that arises in the level density because of pairing at equilibrium deformations was discovered by studying statistical spectra in the radiative decays of even–even rare-earth nuclei [2–4]. One more manifestation of pairing in even–even nuclei was found in the cross section for the neutron-induced fission of ^{235}U nuclei. A simulation of the excitation of few-quasiparticle states in the level density of the fissile nucleus ^{236}U made it possible to describe the threshold structure observed in the cross section for ^{235}U fission induced by neutrons with an energy of about 1 MeV [5–7]. Irregularities of the same origin can also be observed in the cross section for the neutron-induced fission of nuclei where the parities of constituent neutrons and protons differ from those in the cases considered above [8]. By way of example, we indicate that, for even–even Cm target nuclei, resonance-like irregularities were found at above-barrier neutron energies. However, an analysis of the cross sections for the fission of Cm isotopes is complicated considerably by systematic distinctions between experimental data of different authors, to say nothing about the paucity of the entire body of such data. In the present article, the analysis of cross sections will therefore be restricted to the case of the ^{238}Pu nucleus, whose fission has been studied in sufficient detail. The measured cross section for ^{238}Pu fission induced by neutrons whose initial kinetic energies exceed substantially the fission threshold ($E \geq 1$ MeV) shows a stepwise structure of width about 1 MeV. This structure can be reproduced both within the statistical theory of nuclear reactions and within the model of a two-humped fission barrier. We assume that a decisive role is played here by the density of internal quasiparticle states of the fissile even–odd nucleus ^{239}Pu, although the level density in the residual nucleus ^{238}Pu is also of importance. Previously, it was analyzed in studying the cross section for the reaction ^{239}Pu(n, $2n$) [9]. The threshold structure that was observed in the cross section for the reaction ^{239}Pu(n, $2n$) was interpreted as the result of a threshold excitation of two-quasiparticle states in the residual even–even nucleus ^{238}Pu. In describing the fission reaction ^{235}U(n, f), a key role is played by the level density in the fissile nucleus ^{236}U at deformations corresponding to the outer saddle point of the two-humped fission barrier. The structure of the fission barrier in ^{236}U is such that the inner barrier is substantially lower than the outer one. But in the case of the reaction ^{238}Pu(n, f), the inner fission barrier is higher; therefore, the level density corresponding to saddle-point deformations plays a dominant role there. In all probability, the aforementioned structure in the cross section for ^{238}Pu fission induced by neutrons is one of the few manifestations of pairing in odd nuclei. In the following, we will briefly discuss relevant experimental data and the model used to describe them. The result of the calculations based on this model and regularities revealed in the behavior of the level density will also be considered.

2. STATISTICAL MODEL

The level density in a fissile nucleus and the parameters of the fission barrier are key elements of the sta-

1063-7788/00/6302-0161$20.00

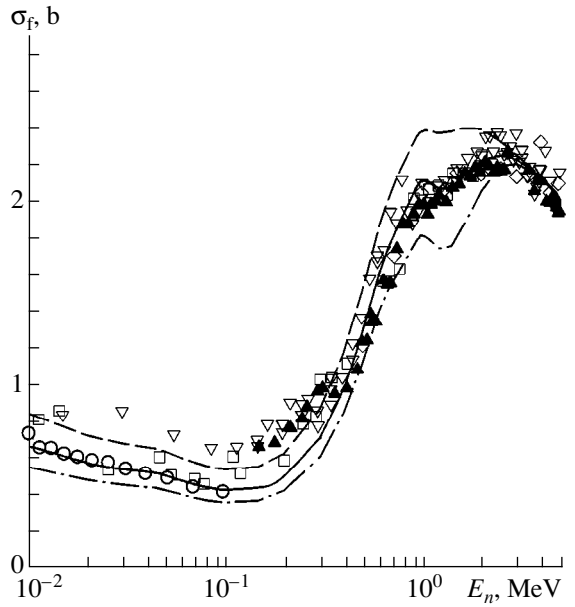

Fig. 1. Cross sections for the neutron-induced fission of ^{238}Pu. The solid curve corresponds to the approximation used for the level density in the fissile nucleus ^{239}Pu and in the residual nucleus ^{238}Pu. The dashed and the dash-dotted curve illustrate the dependence of the fission cross section on the density of single-quasiparticle levels in the ^{239}Pu nucleus (δ_3 = 1.05 and 1.45 MeV, respectively). Points represent experimental data from (○) [11], (▽) [12], (◇) [13], (□) [14], and (▲) [15].

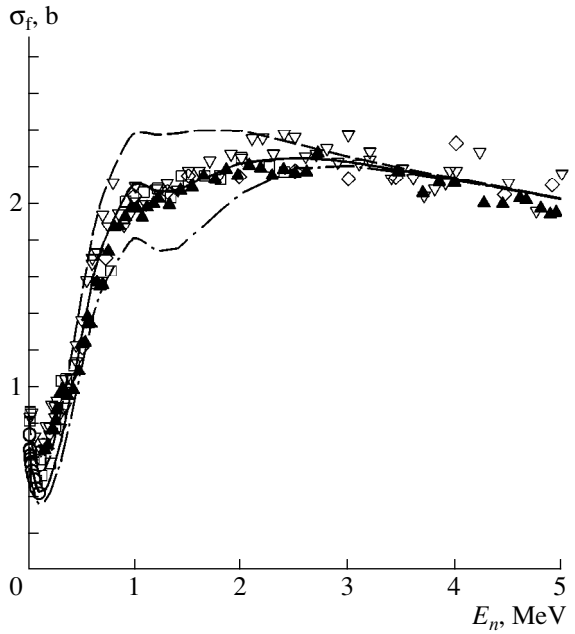

Fig. 2. As in Fig. 1, but on a linear energy scale.

tistical theory of the neutron-induced fission of actinide nuclei. An important point is that the level-density parameters are related to the parameters of fission barrier [10]. A consistent description of the measured cross section for ^{238}Pu fission in the interval between deep-subbarrier excitation energies and the excitation energies of the compound nucleus ^{239}Pu that correspond to the first plateau would give sufficient ground to believe that the expression used for the level density and the parametrization chosen for the fission barrier are quite reliable.

The cross section for ^{238}Pu fission has been investigated experimentally in sufficient detail. Data from [11] on the cross section for the ^{238}Pu fission induced by neutrons with energies less than 100 keV correspond to the deep-subbarrier region of excitation energies. Data from [12] cover the interval of incident-neutron energies from 0.1 eV to about 10 MeV. Unfortunately, data from those two studies are somewhat different in the energy interval where they overlap. The energy dependences of the cross section that follow from these data are different, the results from [11] falling systematically short of those from [12] (see Figs. 1 and 2). Data obtained in [13] and rescaled to the up-to-date values of reference cross sections comply with those from [11] at neutron energies less than 100 keV. For neutron energies in excess of 1 MeV, data from [12] agree with those from [13, 14] within the errors of those experiments. A stepwise structure at incident-neutron energies above 1 MeV is the most spectacular feature of the cross sections measured in [11–13]; a similar structure was also observed in recent measurements of Fursov *et al.* [15]. Another characteristic feature of the experimental cross sections for neutron-induced fission is their sharp dropout for neutron energies in excess of 2.5 MeV. Taking the above into account, we can conclude that the basic features of the energy dependence of the cross section for ^{238}Pu fission induced by neutrons have been revealed quite reliably. In Figs. 1 and 2, relevant experimental data are presented, respectively, on a logarithmic and on a linear scale of the neutron energy.

Of the aforementioned features of the observed cross sections for the neutron-induced fission of ^{238}Pu, either can be reproduced within the statistical theory of nuclear reactions. The cross section for fission induced by neutrons of energy E is given by

$$\sigma_{nf}(E) = \frac{\pi\lambda^2}{2(2I_0+1)} \times \sum_{ljJ\pi}(2J+1)T_{lj}^{J^\pi}(E)P_{\rm f}^{J^\pi}(E)S_{\rm nf}^{ljJ^\pi}. \quad (1)$$

For the input channel ($ljJ\pi$), the neutron penetrabilities $T_{lj}^{J^\pi}(E)$ were calculated by the coupled-channel method. In this calculation, we took into account the direct excitation of the first four levels in the rotational band of the ground state [16], $J = I_0 + j$ (I_0 is the target-nucleus spin, and $j = l + s$, l and s being, respectively, the neutron orbital angular momentum and spin). The factor $S_{\rm nf}^{ljJ^\pi}$ takes into account the Porter–Thomas fluctuations of the neutron, fission, and radiative widths. For the com-

pound nucleus with excitation energy $U = E + B$ (B is the neutron binding energy), a spin J, and a parity π, the fission probability $P_f^{J^\pi}(E)$ is given by

$$P_f^{J^\pi}(E) = \frac{T_f^{J^\pi}(U)}{T_f^{J^\pi}(U) + T_n^{J^\pi}(U) + T_\gamma^{J^\pi}(U)}. \quad (2)$$

The quantities $T_f^{J^\pi}(U)$, $T_n^{J^\pi}(U)$, and $T_\gamma^{J^\pi}(U)$ are the penetrabilities of the fission, neutron, and radiative channels of compound-nucleus decay. At excitation energies higher than the fission threshold, fission and neutron emission appear to be the main competing decay channel. We will assume that the stepwise structure in the observed cross section for the fission process ^{238}Pu(n, f) is associated with the properties of the level density in the even–odd fissile nucleus ^{239}Pu and in the even–even residual nucleus ^{238}Pu. At incident-neutron energies below $E_d \sim 1.14$ MeV, in which case only collective levels of ^{238}Pu that occur within the pairing gap are excited in inelastic neutron scattering on a target nucleus, the fission cross section was calculated with allowance for Porter–Thomas fluctuations of the neutron and fission widths. For the fission widths, the effective number of degrees of freedom that is needed for calculating the factor $S_{nf}^{ljJ^\pi}$ was determined at deformations associated with the inner hump as $\nu_f^{J^\pi} = T_f^{J^\pi}/T_{f\max}^{JK^\pi}$, where $T_{f\max}^{JK^\pi}$ is the maximal penetrability corresponding to the JK^π collective state (K is the projection of the spin J onto the symmetry axis of the nucleus) at the outer barrier. At neutron energies greater than E_d, in which case the continuum levels of ^{238}Pu are excited in inelastic scattering, the correction for width fluctuations was taken into account within the approximation introduced by Tepel *et al.* [17].

2.1. Fission Penetrability and Spectrum of Transition States

Let us consider the model of a two-hump fission barrier. Under the assumption of a successive two-step propagation through the inner and outer humps of the fission barrier, its penetrability $T_f^{J^\pi}$ can be represented in the form [18, 19]

$$T_f^{J^\pi}(U) = \frac{T_{fA}^{J^\pi}(U)T_{fB}^{J^\pi}(U)}{T_{fA}^{J^\pi}(U) + T_{fB}^{J^\pi}(U)}. \quad (3)$$

Equation (3) represents a rough estimate, but it can be used to analyze the cross section for ^{238}Pu fission induced by neutrons with energies E in excess of 1 keV, in which case resonances that are due to the two-humped structure of the fission barrier do not manifest themselves any longer in the observed cross section. In view of the high fissility of the ^{239}Pu nucleus, the disregard of photon and neutron emission in the second well in deriving equation (3) is legitimate for subbarrier neutron energies and for lower energies as well. We also note that the maximal neutron energy at which intermediate resonances manifest themselves in the observed cross section for the fission process ^{238}Pu(n, f) as an anomalously large value of the fission width is 284.5 eV [16].

The fission penetrability $T_{fi}^{J^\pi}(U)$ is determined by the spectrum of discrete transition states, ε^{JK^π}, and by the level density $\rho_{fi}(\varepsilon, J^\pi)$ in the inner and outer humps ($i = A$ and B, respectively) of the fissile nucleus. Specifically, we have

$$T_{fi}^{J^\pi}(U) = \sum_{K=-J}^{J} T_{fi}^{JK^\pi}(\varepsilon^{JK^\pi}, U) + \int_0^U \frac{\rho_{fi}(\varepsilon, J^\pi)d\varepsilon}{1 + \exp(2\pi(E_{fi} + \varepsilon - U)/\hbar\omega_i)}, \quad (4)$$

where the first term corresponds to the contribution of low-lying collective states ε^{JK^π}, the second represents the contribution of continuum levels at saddle-point deformations, and ε is the internal-excitation energy of the fissile nucleus with a spin J and a parity π. The penetrabilities $T_{fi}^{JK^\pi}(\varepsilon^{JK^\pi}, U)$ were calculated with the aid of the Hill–Wheeler relation [20]. The first term on the right-hand side of equation (4)—it is associated with discrete transition states (Bohr fission channel)—and the total level density $\rho_{fi}(\varepsilon, J^\pi)$ in the fissile nucleus are dependent on the symmetry of the nuclear shape at saddle-point deformations. According to the calculations by the shell-correction method that were performed by Howard and Moller [22], a nonaxial configuration corresponds to higher inner hump of the fissile nucleus ^{239}Pu. The same calculations reveal that the fissile nucleus ^{239}Pu retains an axisymmetric configuration at the outer barrier, but it becomes soft with respect to mass-asymmetric deformations. A strong interplay of the fission-barrier height calculated by the shell-correction method and the saddle-point deformation is an important circumstance. The heights of the inner and outer barriers, E_{fi}; their curvatures; and the parameters of the level density for the deformations of the inner and outer humps are parameters of the problem investigated here.

Below, we demonstrate that single-quasiparticle neutron states of the even–odd fissile nucleus ^{239}Pu that occur below the threshold for the excitation of three-quasiparticle states determine the energy dependence of the calculated cross section for ^{238}Pu fission induced by neutrons with energies less than some 1.5 MeV.

Table 1. Bandheads in the spectra of transition states of the fissile nucleus ^{239}Pu

K^π	E_{K^π}, MeV	K^π	E_{K^π}, MeV
Inner hump		Outer hump	
$1/2^+$	0.0	$1/2^+$	0.0
$5/2^+$	0.08	$1/2^-$	0.0
$1/2^-$	0.05	$3/2^+$	0.08
$3/2^-$	0.01	$3/2^-$	0.08
		$5/2^+$	0.01
		$5/2^-$	0.01

Three-quasiparticle states are excited at higher neutron energies. For each single-quasiparticle state ε^{JK^π}, we constructed a rotational band, with a rotational parameter being dependent on the nuclear deformation at the saddle point. The resulting diagrams of levels represent the spectra of discrete transition states for axisymmetric saddle-point configurations. For the single-quasiparticle states predicted by Bolsterli *et al.* [23], discrete transition states were constructed for excitation energies up to 100 keV (see Table 1). At higher energies, the continuum of excitations was described by simulating level densities. The dependence of the discrete spectra of transition states, as well as the dependence of the density of transition states, on the symmetry of the inner and outer saddle-point configurations of the fissile nucleus ^{239}Pu will be taken into account in the following way. We will assume that, at the inner saddle point, $(2J + 1)$ states correspond to each state with a spin J [21]. Positive- and negative-parity bands, $K^\pi = 1/2^\pm$, $3/2^\pm$, $5/2^\pm$, …, at the outer saddle point are assumed to be degenerate because of mass-asymmetric deformations. Having determined the spectra of transitions states in this way (see Table 1), we can then address the problem of assessing the fission-barrier parameters.

2.2. Neutron Channel

For neutron scattering, the penetrability factor is given by

$$T_n^{J^\pi}(U) = \sum_{l'j'q'} T_{l'j'}^{J^\pi}(E - E_{q'}) + \sum_{l'j'I'} \int_0^{U-E_d} T_{l'j'}^{J^\pi}(E')\rho(U - E', I'^\pi)dE', \quad (5)$$

where the first term on the right-hand side corresponds to the excitation of collective levels $E_{q'}$ occurring within the pairing gap ($E_{q'} < E_d$), while $\rho(U - E', I'^\pi)$ is the level density in the residual nucleus. In the calculations of the n + ^{238}Pu system, we used the deformed optical potential from [16]. The quadrupole- and hexadecapole-deformation parameters, β_2 and β_4, respectively, which affect the behavior of the reaction cross section at neutron energies below 1 MeV, were determined from a fit to the experimental value of the *s*-neutron strength function S_0. In the output channel of inelastic scattering, the neutron penetrabilities $T_{l'j'}^{J^\pi}$ were calculated with the aid of the deformed potential from [16] as well, but the coupling of the levels of the residual nucleus ^{238}Pu was disregarded in this case.

2.3. Level Density

In the model of a two-humped fission barrier, the competition between the neutron-fission and neutron-emission processes is determined primarily by the level densities of the fissile nucleus for the inner and outer saddle points and by the level density of the residual nucleus at equilibrium deformations. The contribution to the level density $\rho(U, J^\pi)$ from quasiparticle and collective states can be represented in a factorized form [24]. We will rely on the phenomenological model that was proposed in [25] and which takes consistently into account shell and collective effects, as well as pairing interactions of the correlation type. The corresponding expression for the level density has the form

$$\rho(U, J^\pi) = K_{\text{rot}}(U, J)K_{\text{vib}}(U)\rho_{\text{qp}}(U, J^\pi), \quad (6)$$

where $\rho_{\text{qp}}(U, J^\pi)$ is the density of the quasiparticle levels, while $K_{\text{rot}}(U, J)$ and $K_{\text{vib}}(U)$ are factors describing, respectively, the rotational and the vibrational enhancement of the level density. Equation (6) is valid in the adiabatic approximation, in which case the contributions of internal and of collective states to the total level density can be factorized.

The actinide nucleus ^{238}Pu at equilibrium deformations and the actinide nucleus ^{239}Pu at deformations of the inner saddle point are axisymmetric. In this case, the coefficient of the rotational enhancement of the level density can be represented as

$$K_{\text{rot}}^{\text{sym}}(U) = \sum_{K=-J}^{J} \exp(-K^2/K_0^2) \approx \sigma_\perp^2 = F_\perp t, \quad (7)$$

$$K_0^2 = (\sigma_\parallel^{-2} - \sigma_\perp^{-2})^{-1}, \quad (8)$$

where $\sigma_\perp$ and $\sigma_\parallel$ are parameters of the angular distribution, while t is a thermodynamic temperature. At high excitation energies $U > U_{\text{cr}}$, in which case pairing is destroyed, the moment of inertia $F_\perp$ (orthogonal to the symmetry axis of the nucleus) was set to the moment inertia of the rigid body $F_\perp^{\text{rig}}$,

$$F_\perp^{\text{rig}} = (2/5)m_0 r_0^2 A^{5/3}(1 + \epsilon/3), \quad (9)$$

where $r_0 = 1.24$ fm, m_0 is the nucleon mass, and ϵ is the quadrupole-deformation parameter. At zero value of

Table 2. Parameters of the level density for the fissile nucleus ^{239}Pu and for the residual nucleus ^{238}Pu

	δW, MeV	Δ, MeV	ϵ	$F_0/\hbar^2$, MeV
Inner hump	2.5	$\Delta_0 + \delta$	0.6	100
Outer hump	0.6	$\Delta_0 + \delta$	0.8	200
Neutron channel	–2.439	Δ_0	0.24	73

Note: The value of $\delta = 0.06$ MeV was determined from a fit to the cross section for the fission process in the plateau region.

the thermodynamic temperature t, the moment of inertia $F_\perp$ was set to the experimental value F_0; at intermediate temperatures, the values of $F_\perp$ were calculated by means of a linear interpolation [25].

The mass asymmetry at the deformations of the outer saddle point doubles the rotational-enhancement factor $K_{\rm rot}(U, J)$ given by (7). For deformations, the rotational enhancement factor can be represented as

$$K_{\rm rot}^{\rm asym}(U) \approx 2\sqrt{2\pi}\sigma_\perp^2\sigma_\parallel. \qquad (10)$$

The density of quasiparticle levels, $\rho_{\rm qp}(U, J^\pi)$, is given by

$$\rho_{\rm qp}(U, J^\pi) = \frac{(2J+1)\omega_{qp}(U)}{4\sqrt{2\pi}\sigma_\perp^2\sigma_\parallel}\exp\left[-\frac{J(J+1)}{2\sigma_\perp^2}\right], \qquad (11)$$

where $\omega_{\rm qp}(U)$ is the density of the internal quasiparticle states.

The shell dependence of the level-density parameter $a(U)$ is determined by the relation [25]

$$a(U) = \begin{cases}\tilde{a}(1 + \delta W f(U - E_{\rm cond})), & U > U_{\rm cr}\\ a(U_{\rm cr}) = a_{\rm cr}, & U \le U_{\rm cr}.\end{cases} \qquad (12)$$

Here, $U_{\rm cr} = 0.47a_{\rm cr}\Delta^2 - m\Delta$, where $m = 0, 1, 2$ for even–even, odd, and odd–odd nuclei, respectively; $f(x) = 1 - \exp(-0.064x)$ is a dimensionless function determining the damping of the shell effect on the level density with increasing excitation energy; $\tilde{a}$ and $a_{\rm cr}$ are the values of the parameter $a(U)$ at, respectively, high excitation energies and the critical value of the excitation energy $U = U_{\rm cr}$; and the condensation energy is given by $E_{\rm cond} = 0.152a_{\rm cr}\Delta^2 - m\Delta$, Δ being a correlation function that is equal to $12/\sqrt{A}$ for ground-state deformations. The shell correction δW, the correlation function Δ, the quadrupole deformation ϵ, and the moment inertia at zero temperature ($F_0/\hbar^2$), which appear, as parameters, in the level density for the inner and outer saddle points and for equilibrium deformations, are presented in Table 2. The values of the shell corrections at the inner and outer humps, $\delta W_f^{A(B)}$, were borrowed from [26]. The shell correction in the ground state has the form $\delta W = M^{\rm expt} - M^{\rm MS}$, where $M^{\rm MS}$ is the liquid-drop nuclear mass calculated with the Myers–Swiatecki parameters [27], while $M^{\rm expt}$ is the experimental value of the nuclear mass. The values of $\tilde{a}$ and $a_{\rm cr}$ in the level-density parameter $a(U)$ were determined from a fit to the observed density of neutron resonances. We assume that the value of the parameter $a(U)$ at high excitation energies ($\tilde{a}$) is independent of nuclear deformation taking, in particular, the same value at saddle-point and equilibrium deformations. It should be noted that the shell correction proved to be negative at equilibrium deformations [27] and positive at saddle deformations [26]; as a result, the values used for the parameter $a(U)$ at low excitation energies are also quite different.

Let us now consider the basic element of our model—the density of internal quasiparticle states, $\omega_{\rm qp}(U)$. In the Boltzmann gas model, it is determined as the sum of the partial densities of n-quasiparticle states, $\omega_{n\rm qp}(U)$. We have

$$\omega_{\rm qp}(U) = \sum_n \omega_{nqp}(U) = \sum_n \frac{g^n(U - U_n)^{n-1}}{((n/2)!)^2(n-1)!}, \qquad (13)$$

where $g = 6a_{\rm cr}/\pi^2$ is the density of single-particle states at the Fermi surface, while n is the number of the quasiparticles. The partial densities of n-quasiparticle states, $\omega_{n\rm qp}(U)$, depend greatly on the thresholds for the excitation of n-quasiparticle configurations, U_n, with $n = 1, 3, \ldots$ for A-odd nuclei and $n = 2, 4, \ldots$ for even–even nuclei. In [28], U_n was estimated as

$$U_n = \begin{cases}E_{\rm cond}(3.23n/n_{\rm cr} - 1.57n^2/n_{\rm cr}^2), & n < 0.446n_{\rm cr}\\ E_{\rm cond}(1 + 0.627n^2/n_{\rm cr}^2), & n \ge 0.446n_{\rm cr},\end{cases} \qquad (14)$$

where $n_{\rm cr} = 12/\pi^2(\ln 2)gt_{\rm cr}$, with the critical temperature $t_{\rm cr}$ being $t_{\rm cr} = 0.571\Delta$. This estimate of U_n takes into account the energy dependence of the correlation function $\Delta(U)$ and the correction to the excitation energy for the effect of the Pauli exclusion principle. The above estimate also depends substantially on the value of the shell correction. The angular-distribution parameter $\sigma_\parallel^2$ can be represented as

$$\sigma_\parallel^2 = \sum_n \langle m^2\rangle \omega_{n\rm qp}(U)/\sum_n \omega_{nqp}(U), \qquad (15)$$

where $\langle m^2\rangle = 0.24A^{2/3}$ is the mean square of the projection of the angular momentum of single-particle states onto the symmetry axis. From equation (8), it follows that, at saddle-point deformations, we have $K_0^2 \approx \sigma_\parallel^2$;

obviously, the parameter K_0^2, which determines the angular distribution of fission fragments, is much less sensitive to the energy dependence of the density of few-quasiparticle states, $\omega_{n\mathrm{qp}}(U)$, than the fission cross section.

2.3.1. Level density in ^{239}Pu

In an odd nucleus, the effect of an unpaired particle on pairing can be taken into account, in the first approximation, via a shift of excitation energy. For the fissile nucleus ^{239}Pu, the level density can be calculated with the aid of equations (6)–(15) if we define the effective excitation energy as $\mathcal{U} = U + \Delta$, where Δ is the correlation function for saddle-point deformations (see Table 2). At low excitation energies, the level density depends strongly on the number of excited quasiparticles. In the case of the even–odd nucleus ^{239}Pu, the partial contributions of n-quasiparticle states, $\omega_{n\mathrm{qp}}(U)$, to the total level density $\omega_{\mathrm{qp}}(U)$ generates a stepwise structure at energies below the threshold for the excitation of three-quasiparticle states. This is because the excitation of few-quasiparticle states weakens pairing; in the case of actinides, only the excitation of states featuring a minimal number of quasiparticles leads to the emergence of a structure in the level density. If this minimal number of excited quasiparticles is $n = 1$, the density of internal excited states, $\omega(U)$, is proportional to g—that is, $\omega(U)$ does not depend explicitly on excitation energy in the Boltzmann gas model. The density of single-quasiparticle states determines a stepwise dependence of the cross section for the fission process induced by incident neutrons with energies near $E_3 = U_3 + E_{fA} - B \sim 1.5$ MeV, where B is the neutron binding energy, while E_{fA} is the height of the higher inner hump of the fission barrier. The energy E_3 corresponds to the threshold for the excitation of three-quasiparticle states at deformations of the inner fission barrier; the internal density of these states is $\omega_3(U) \sim g^3U^2$. The excitation of three-quasiparticle states can result in a further growth of the fission cross section. By fitting the fission cross section, we can obtain an empirical estimate for the density of internal few-quasiparticle states: $\bar{\omega}_1 \sim 3\omega_1$ and $\bar{\omega}_3 \sim 2\omega_3$. It should be borne in mind that this estimate of the level density at low excitation energies depends on the parameters of the fission barrier; however, the resulting empirical coefficients are rather large. In all probability, the approximation of the level density in a realistic nucleus within the Boltzmann gas model reproduces the level density at low excitation energies only qualitatively. At higher energies, the parameter of the density of single-particle states must be normalized to the level density in the model featuring an indefinite number of quasiparticles [25].

In the following, we will approximate the level density in a somewhat differ manner.

Instead of using the equations for the Boltzmann gas model to simulate the density of internal excitations, we will reproduce the stepwise structure of the level density at low excitation energies by means of the empirical parameters introduced in the constant-temperature model [26]. The level density in an axisymmetric nucleus,

$$\rho(U) = K_{\mathrm{rot}}(U, J)K_{\mathrm{vib}}(U, J)\frac{\omega_{\mathrm{qp}}(U)}{\sqrt{2\pi}\sigma_{\|}}, \qquad (16)$$

can be calculated equations by means of equations (6)–(15). At the same time, this level density can be estimated on the basis of the constant-temperature model by using the relation

$$\rho(U) = T_{\mathrm{f}}^{-1}\exp((U - U_0)/T_{\mathrm{f}}), \qquad (17)$$

where $U_0 \approx -m\Delta$, with m being 0, 1, and 2 for even, odd, and odd–odd nuclei, respectively. The nuclear temperature T_{f} and the shift of the excitation energy U_0 are determined by requiring that, at the excitation energy of $U_{\mathrm{c}} = 2.4$ MeV, the constant-temperature model be matched smoothly with the superfluid-nucleus model featuring an indefinite number of quasiparticles [25]. At higher excitation energies, the continuous spectrum of transition states is described on the basis of the model proposed in [25]. Further, we take into account the effect of nonaxial and mass asymmetries (see above). In the case of an even–odd nucleus, the level density $\rho(U)$ at excitation energies less than the threshold for the excitation of three-quasiparticle states depends only slightly on the excitation energy since the density of the internal single-quasiparticle states is constant ($\omega_1 \sim g$). For $U < U_3$, the level density can be calculated as

$$\begin{aligned}\rho(U) &= T_{\mathrm{f}}^{-1}(1 + 2(U - 0.5U_3))\\ &\times \exp((U_3 + \Delta_{\mathrm{f}} - U_0 - \delta_3)/T_{\mathrm{f}})\\ &\approx T_{\mathrm{f}}^{-1}\exp((\Delta_{\mathrm{f}} - U_0)/T_{\mathrm{f}}).\end{aligned} \qquad (18)$$

By using equation (18), we can reproduce the measured cross section. We assume that the fission cross section is determined primarily by the parameters of the inner fission barrier. In the even–odd fissile ^{239}Pu nucleus, single- and three-quasiparticle states determine the energy dependence of the fission cross section at incident-neutron energies not greater than 2.5 MeV (see Figs. 1 and 2). For excitation energies that are higher than the threshold for the excitation of three-quasiparticle states, but which are lower than the threshold for the excitation of five-quasiparticle states, the level density was somewhat increased in relation to the estimate on the basis of the constant-temperature model:

$$\rho(U) = T_{\mathrm{f}}^{-1}\exp((U - U_0 + \delta_5)/T_{\mathrm{f}}). \qquad (19)$$

Here, the parameter $\delta_5 = 0.145$ MeV was determined from a fit to the fission cross section at energies not less than 2.5 MeV. For the fissile nucleus ^{239}Pu, the level

density at the inner hump of the fission barrier is shown in Fig. 3, nonaxial deformations being taken into account in these results. The level density calculated on the basis of equations (18) and (19) is contrasted against the results of the level-density approximations within the constant-temperature model [equation (17)] and within the renormalized Boltzmann gas model. The arrows on the horizontal axis in Fig. 3 indicate the thresholds for the excitation of an odd number of quasiparticles at deformations of the inner hump of the fission barrier.

2.3.2. Level density in ^{238}Pu

For even–even nuclei, the partial contributions $\omega_{nqp}(U)$ of the n-quasiparticle states to the total density of states, $\omega_{qp}(U)$, lead to the emergence of a stepwise structure only for $n = 2$ and 4 configurations (see Fig. 4). The arrows on the horizontal axis in Fig. 4 correspond to the thresholds for the excitation of n-quasiparticle configurations with an even number of quasiparticles at equilibrium deformations. The density of internal states in the residual nucleus ^{238}Pu, $\omega_2(U)$, can be represented in the form $\omega_2(U) = g^2(U - U_2)$, which modifies the approximation of the Boltzmann gas model. Below the threshold for the excitation of four-quasiparticle configurations, $\omega_2(U)$ is modified by using the Woods–Saxon form:

$$\omega_2(U) = g^2(U_4 - U_2 - 0.35) \times \times (1 + \exp((U_2 - U + 0.1)/0.1))^{-1}. \quad (20)$$

This estimate of the density of two-quasiparticle configurations, $\omega_2(U)$, was obtained in interpreting the near-threshold stepwise structure in the cross section for the reaction ^{239}Pu(n, $2n$) [10].

Here, we will calculate the level density by analogy with the determination of the level density in ^{239}Pu (see above). At excitation energies that are higher than the pairing gap, but which are lower than the threshold for the excitation of four-quasiparticle configurations, the level density is determined as

$$\rho(U) = \rho(U_4 - \delta_4)/(1 + \exp(U_2 - U + \delta_a)/\delta_s), \quad (21)$$

where $\delta_4 \sim 0.5(U_4 - U_2)$. The density of the internal two-quasiparticle internal states in the even–even nucleus ^{238}Pu affects the calculated cross section for ^{238}Pu fission induced by incident neutrons with energies above 1.2 MeV. The parameter values of $\delta_4 = 0.25$ MeV and $\delta_a = \delta_s = 0.1$ MeV were obtained from a fit to the fission cross section. The level density calculated by means of equations (18) and (19) is compared with that obtained within the constant-temperature model [equation (17)] and within the Boltzmann gas model. The present estimate and the estimate within the Boltzmann gas model are very close at high excitation energies; they begin to deviate at energies less than 5 MeV.

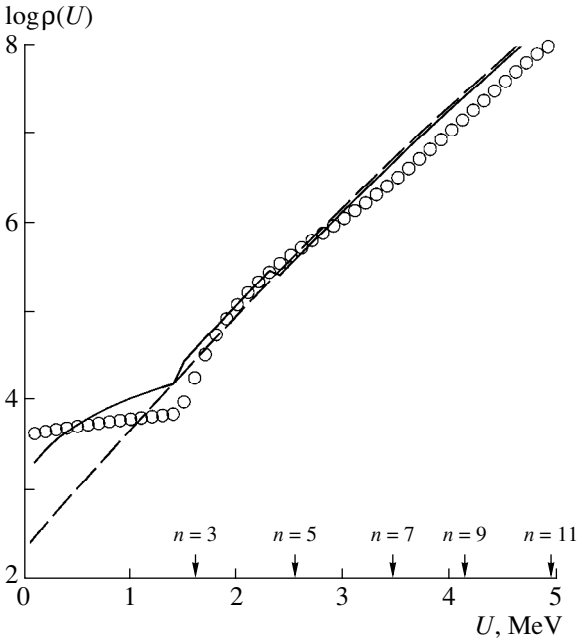

Fig. 3. Density of the levels of the fissile nucleus ^{239}Pu within the inner hump of the fission barrier: (solid curve) results corresponding to the approximation used here for the level density, (dashed curve) results within the constant-temperature model, and (points) results corresponding to the approximation of the density of quasiparticle states within the Boltzmann gas model.

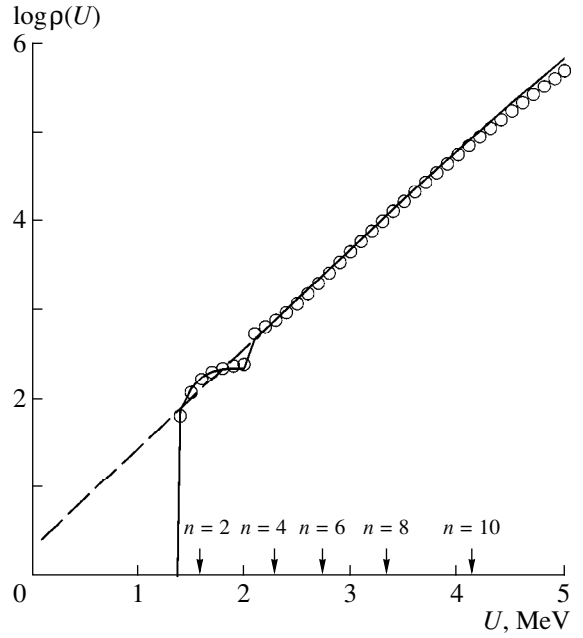

Fig. 4. Level density in the ^{238}Pu nucleus at an equilibrium deformation. The notation is identical to that in Fig. 3.

Only collective levels are taken into account at excitation energies below the threshold U_2 for neutron-pair dissociation [29]. At excitation energies that are higher than the threshold for four-quasiparticle states, U_4, but which are lower than the energy $U_c = 3.6$ MeV at which

matching is performed, a continuous level density is calculated within the constant-temperature model at the parameter values of U_0 = –0.0002 MeV and T = 0.38454 MeV, which make it possible to describe the increasing sum of low-lying levels. For higher excitation energies, we used the phenomenological model from [25]. For the ^{238}Pu nucleus, the level-density parameter was obtained by using the systematics from [30] for actinides from Th to Cf.

2.4. Calculation of the Fission Cross Section within the Statistical Model

In Fig. 1, deep-subthreshold data on the fission cross section that were obtained in [11] with a spectrometer relying on information about the moderation time in lead are compared with the data from [12–15], where electrostatic accelerators were used. The dashed and dash-dotted curves in Figs. 1 and 2 demonstrate the sensitivity of the calculated cross section to the level density in the fissile nucleus ^{239}Pu for internal-excitation energies $U < U_3$. As a matter of fact, the dashed and dash-dotted curves were calculated for the parameter values of, respectively, δ_3 = 1.05 and 1.45 MeV in equation (18), while the solid curve was obtained with the parameter value of δ_3 = 1.25 MeV. It should be noted that the computed fission cross section depends only slightly on the density of single-quasiparticle states for incident-neutron energies below 1 MeV as well. At the same time, the fission cross section depends rather strongly on the barrier parameters (see Table 3); this makes it possible to estimate their computational uncertainties at δE_{fA} = 0.05 MeV, δE_{fB} = 0.1 MeV, and $\delta\hbar\omega_B$ = 0.03 MeV, the uncertainty in the curvature of the inner fission barrier being rather great ($\delta\hbar\omega_A > 0.4$ MeV). Our estimates of the level-density and fission-barrier parameters are in accord with experimental data on the cross section for neutron-induced fission (see Figs. 1 and 2). At incident-neutron energies in excess of 2.5 MeV, the fission cross section can be reproduced by enhancing the correlation function for the deformed nucleus as $\Delta_f = \Delta_0 + \delta$ (see Fig. 2). The enhancement δ depends on the relationship between the values that the level-density parameter $a(U)$ takes at the saddle-point and at the equilibrium deformation; in turn, this relationship is governed by the relationship between the shell corrections that is used in the calculations ($\delta W_f^{A(B)} - \delta W_n$). It can be hoped that the value that was obtained here for the parameter $\delta = \Delta_f - \Delta_0$ corresponds to the total difference of pairing and shell properties between the equilibrium and strongly deformed states.

3. CONCLUSION

A simple simulation of few-quasiparticle effects in the density of internal states of the fissile nucleus ^{239}Pu and of the residual nucleus ^{238}Pu makes it possible to reproduce the above-threshold stepwise structure in the observed cross section for the fission process ^{238}Pu(n, f). This irregularity is due primarily to the excitation of three-quasiparticle states in the fissile nucleus ^{239}Pu. Estimates obtained for the fission thresholds and for the excitation of three-quasiparticle states comply with the measured cross section for fission both above and below the fission threshold. Similar above-threshold structures have been observed in the cross sections for the neutron-induced fission of other even–even isotopes of uranium, plutonium, and curium. The proposed method for simulating the density of internal states at equilibrium and saddle-point deformations can be used to analyze those irregularities. Both stepwise (in the case of uranium and plutonium nuclei) and quasiresonance (in the case of curium nuclei) above-threshold structures in the fission cross sections can be interpreted within this approach. An inevitable complication of a simulation of the level density in relation to that within the back-shifted Fermi gas model, which is still widely used, seems justified, but the resulting description remains rather rough. In any case, this is a further step toward consistently simulating the energy dependence of the fission cross section and extracting the values of the level-density and fission-barrier parameters. The estimates that were obtained in this study for the level density in odd and even nuclei can be useful in microscopically simulating the level density at low excitations.

ACKNOWLEDGMENTS

This work was supported by the International Center for Science and Technology (Moscow, Russia), project no. V-03, and by the International Atomic Energy Agency (Vienna, Austria), research contract no. 8832/RB.

REFERENCES

1. D. L. Shpak, Yu. B. Ostapenko, and G. N. Smirenkin, Yad. Fiz. **13**, 950 (1971) [Sov. J. Nucl. Phys. **13**, 547 (1971)].
2. T. Dossing, T. I. Khoo, T. Lauritsen, *et al.*, Phys. Rev. Lett. **75**, 1276 (1995).
3. S. T. Boneva, V. A. Khitrov, Yu. P. Popov, *et al.*, in *Proceedings of IV International Seminar on Interaction of Neutrons with Nuclei* (JINR, Dubna, 1996), no. E3-96-336, p. 183.
4. T. S. Tveter, L. Bergholt, M. Guttormsen, *et al.*, Phys. Rev. Lett. **77**, 2404 (1996).
5. A. V. Ignatyuk and V. M. Maslov, Yad. Fiz. **54**, 647 (1991) [Sov. J. Nucl. Phys. **54**, 392 (1991)].
6. A. V. Ignatyuk and V. M. Maslov, in *Proceedings of International Conference on Nuclear Data for Science and Technology, Julich, 1991* (Springer-Verlag, Berlin, 1992), p. 153.
7. A. V. Ignatyuk and V. M. Maslov, in *Proceedings of International Symposium on Nuclear Data Evaluation Methodology, Brookhaven, 1992* (World Sci., Singapore, 1993), p. 440.

8. V. M. Maslov, in *Proceedings of International Conference on Nuclear Data for Science and Technology Trieste, 1997* (IPS, Bologna, 1997), p. 1320.
9. V. M. Maslov, Z. Phys. A **347**, 211 (1994).
10. V. Maslov and Y. Kikuchi, Nucl. Sci. Eng. **124**, 492 (1996).
11. B. Alam, R. C. Block, R. E. Slovacek, *et al.*, Nucl. Sci. Eng. **99**, 267 (1988).
12. C. Budtz-Jorgensen, H.-H. Knitter, and D. L. Smith, in *Proceedings of International Conference on Nuclear Data for Science and Technology, Antwerpen, 1982* (Reidel Publ. Co, Antwerpen, 1983), p. 206.
13. S. B. Ermagambetov and G. N. Smirenkin, Pis'ma Zh. Éksp. Teor. Fiz. **9**, 510 (1969) [JETP Lett. **9**, 309 (1969)].
14. S. B. Ermagambetov and G. N. Smirenkin, At. Energ. **25**, 1364 (1969).
15. B. I. Fursov, V. N. Polynov, B. F. Samylin, *et al.*, in *Proceedings of International Conference on Nuclear Data for Science and Technology, Trieste, 1997* (IPS, Bologna, 1997), p. 488.
16. V. M. Maslov, E. Sh. Sukhovitskij, Yu. V. Porodzinskij, *et al.*, INDC(BLR)-009, IAEA, Vienna (1997).
17. J. W. Tepel, H. M. Hoffman, and H. A. Weidenmuller, Phys. Lett. B **49**, 1 (1974).
18. V. M. Strutinsky, Nucl. Phys. A **95**, 420 (1967).
19. S. Bjornholm and V. M. Strutinsky, Nucl. Phys. A **136**, 1 (1969).
20. D. L. Hill and J. A. Wheeler, Phys. Rev. **89**, 1102 (1953).
21. A. Bohr and B. R. Mottelson, *Nuclear Structure*, Vol. 2: *Nuclear Deformations* (Benjamin, New York, 1975).
22. W. M. Howard and P. Moller, At. Data Nucl. Data Tables **25**, 219 (1980).
23. M. Bolsterli, E. O. Fiset, J. R. Nix, *et al.*, Phys. Rev. C **5**, 1050 (1972).
24. S. Bjornholm, A. Bohr, and B. R. Mottelson, in *Proceedings of Symposium on Physics and Chemistry of Fission, Rochester, 1973* (Vienna: IAEA, 1974), Vol. 1, p. 367.
25. A. V. Ignatyuk, K. K. Istekov, and G. N. Smirenkin, Yad. Fiz. **29**, 875 (1979) [Sov. J. Nucl. Phys. **29**, 450 (1979)].
26. S. Bjornholm and J. E. Lynn, Rev. Mod. Phys. **52**, 725 (1980).
27. W. O. Myers and W. J. Swiatecki, Ark. Fys. **36**, 243 (1967).
28. C. Fu, Nucl. Sci. Eng. **86**, 344 (1984).
29. C. M. Lederer, *Table of Isotopes*, 7th ed. (1978).
30. Yu. V. Porodzinskij, E. Sh. Sukhovitskij, and V. M. Maslov, in *Proceedings of International Conference on Nuclear Data for Science and Technology, Trieste, 1997* (IPS, Bologna, 1997), p. 937.

Translated by A. Isaakyan

Physics of Atomic Nuclei, Vol. 63, No. 2, 2000, pp. 170–178. Translated from Yadernaya Fizika, Vol. 63, No. 2, 2000, pp. 223–231.

NUCLEI
Theory

One-Nucleon Spectroscopic Factors and Momentum Distributions of Nucleons in the ^{6}Li and ^{9}Be Nuclei within Three-Body Models

M. A. Zhusupov*, K. A. Zhusupova, and E. T. Ibraeva

Institute for Experimental and Theoretical Physics, Kazakh State University, ul. Timiryazeva 46, Almaty, 480121 Republic of Kazakhstan

Received August 31, 1998; in final form, November 23, 1998

Abstract—Within the three-body $\alpha 2N$ and $2\alpha N$ models of the ^{6}Li and ^{9}Be nuclei, respectively, the spectroscopic factors and the momentum distributions of nucleons are computed for the cases where residual nuclei can be formed both in the ground and in excited states. The impact of model parameters on the values of one-nucleon features is discussed. The results of the calculations performed in the present study are compared with available experimental data. *© 2000 MAIK "Nauka/Interperiodica".*

1. INTRODUCTION

One-nucleon characteristics like spectroscopic factors S, reduced widths θ^2, partial widths Γ, and momentum distributions of nucleons play an important role in studying nuclear reactions where one nucleon is attached to or detached from a target nucleus. These include direct nuclear reactions of nucleon stripping or pickup, elastic or inelastic nucleon scattering on nuclei, and resonance processes where the excitation of high-lying levels of a compound nucleus is followed by their decay through the nucleon channel. Available experimental data that could be used to determine the above features involve significant ambiguities; moreover, these data, obtained in different experiments and under different conditions, have not yet been systematized. In view of this, model calculations of one-nucleon features are required for developing the theory of the above-type nuclear processes further and for planning target-oriented experiments.

In recent years, the dynamical $\alpha 2N$ and $2\alpha N$ models of, respectively, $A = 6$ and 9 nuclei have been widely used to calculate the features of various nuclear processes [1–3]. It turned out that the $\alpha 2N$ model reproduces well all static characteristics of the ^{6}Li nucleus (with the exception of its relatively small quadrupole moment) and describes successfully two-body photodisintegration in the τt channel [4], photo- and electrodisintegration in the αd channel [5, 6], and elastic and inelastic hadron scattering [7]. Within the same model, the electromagnetic form factors and the spectroscopic S factor for deuteron and triton separation are faithfully reproduced, provided that antisymmetrization has been performed [8].

Similar calculations of the features of $A = 9$ nuclei were successfully performed on the basis of the three-body $2\alpha N$ model [2, 3, 9]. Of particular interest in this case is the possibility of studying the role of $\alpha\alpha$ interaction. It is well known that the constituent-nucleon structure of alpha particles can be taken into account in terms of the wave functions of relative motion in two ways. In the first model version, the Fermi statistics of nucleons is simulated by using the l-dependent Ali–Bodmer potential, which features repulsion at small distances. In the second model version, the deep $\alpha\alpha$ potential of attraction due to Buck [10] is employed for the same purpose. The latter has a Gaussian form and involves states forbidden by the Pauli exclusion principle. The quality of fits to phase shifts shows virtually no changes in going over from one model to the other [3]. On the whole, a description of the energy spectra and of some other characteristics of the ^{9}Be nucleus is somewhat better in the model employing a narrow l-dependent potential with the Ali–Bodmer repulsion than in the model relying on a deep attractive potential involving forbidden states [3, 9].

The nucleon channels of the decay of the aforementioned nuclei were also studied within three-body models. Of particular interest in this connection is the ^{9}Be nucleus because, for the ^{8}Be nucleus, which is formed following the neutron emission from ^{9}Be, there exist wave functions established reliably within the potential $\alpha\alpha$ cluster model [13]. In the case of proton separation from the ground-state ^{6}Li nucleus, we consider the cases where a ^{5}He nucleus is produced either in the ground state or in a highly excited state. In the first case, the calculation relies on the wave function of the ground-state ^{5}He nucleus treated as that which has the $\alpha + n$ configuration. In the second case, the wave function is set to that in the potential $d + t$ cluster model.

* e-mail: zhus@ietp.alma-ata.su

A somewhat different method for calculating the S factors in the channel $^6\mathrm{Li} \longrightarrow {}^5\mathrm{Li} + n$ was used by Ryzhikh *et al.* [14], who expanded the wave function of the multicluster dynamical model in terms of wave functions of the multiparticle shell model (abbreviated as MSM in the table). That approach permits fully taking advantage of the well-developed mathematical formalism of the shell model, but it leads to very cumbersome calculations because a great number of wave-function components appear in shell-model expansions. The method that we will follow here admits a straightforward extension of its computational scheme to the cases where both ground and excited nuclear states may appear in initial and final states. As to the method of shell-model expansions, its implementation presents serious difficulties for transitions featuring excited nuclear states and for nuclei from the middle of the $1p$ shell, including the ^{9}Be nucleus, whose ground-state wave function does not involve a dominant S wave component, which is present in the case of the ^{6}Li nucleus. In the wave function of the ground-state ^{9}Be nucleus, there are three components characterized by a nonzero orbital angular momentum each [2], whence it follows that its shell-model expansion will feature a great number of components.

In contrast to shell-model functions, wave functions calculated within three-body cluster models for the $^5\mathrm{He} + p$ and $^8\mathrm{Be} + n$ channels and represented as superpositions of Gaussian forms show a correct asymptotic behavior, a circumstance that is of importance in calculating momentum distributions. That currently available experimental values of spectroscopic factors as determined on the basis of different data sets show wide variations, especially for the ^{9}Be nucleus, adds importance to a theoretical calculation of these factors, which was first performed within the three-body model.

Some of the results presented here were obtained in [11, 12, 15]. Here, however, we give a full account of the mathematical formalism of the theory and, what is the most important of all, calculate anew the momentum distributions of nucleons. The point is that, for the target nucleus ^{6}Li, there are now reliable experimental data on the momentum distributions of protons from the (e, ep) reaction leading to ^{5}He formation both in the ground state and in excited states [16]. In [11, 12], the momentum distributions in question were computed in the plane-wave approximation. The results obtained in this way comply with experimental data up to momentum values of a few tens of MeV/c, exceeding them at higher momenta. These discrepancies are due to the effect of distortions in the final state. In order to take correctly into account these distortions, it is necessary to know the p^5He and n^8Be interaction potentials. Because of the instability of the $A = 5$ and $A = 8$ nuclei, these potentials cannot be found, however, from phase-shift analyses, which are usually used in such cases. For this reason, we take into account the above distortions within the strong-absorption method, introducing, for this purpose, cutoff radii R_0 in the integrals that are calculated for momentum distributions in the plane-wave approximation. Previously, this method for taking into account distortions was successfully used to compute the features of quasielastic cluster knockout in reactions of the (p, pd) type [17].

Spectroscopic factors for neutron separation from the ^{9}Be nucleus in the transitions leading to the formation of the ground and the first excited state of the ^{8}Be nucleus

Model, experiment	State of the ^{8}Be nucleus	
	$J^\pi = 0^+$	$J^\pi = 2^+$
$2\alpha N$:		
version (I)	0.36	0.28
version (II)	0.20	0.24
version (III)	0.30	0.24
MSM [27]:		
version (I) [28]	0.58	0.73
version (II) [29]	0.37	0.71
version (III) [30]	0.58	–
Experiment:		
(pd) E_p = 50 MeV [31]	0.55	0.36
(dt) E_d = 18 MeV [32]	0.23	0.20

2. SPECTROSCOPIC FACTORS AND MOMENTUM DISTRIBUTIONS OF PROTONS IN THE ^{6}Li NUCLEUS

For the ground state of the ^{6}Li nucleus, we used the αnp wave function obtained by using a potential featuring even–odd splitting of phase shifts for αn interaction, $V_{\alpha N}$ [2, 18], and the soft-core Reid potential V_{NN} for nucleon–nucleon interaction [19]. In the wave function of the ground-state ^{6}Li nucleus, we take into account only two dominant configurations, that where $\lambda = l = L = 0$ and $S = 1$ (S wave) and that where $\lambda = 2$, $l = 0$, $L = 2$, and $S = 1$ (D wave). The ^{6}Li wave function can then be represented in the form

$$\Psi_{i,f}^{(\lambda l)} = \Psi_S^{(00)} + \Psi_D^{(20)}, \tag{1}$$

where

$$\Psi_S^{(00)} = \frac{1}{4\pi}\sum_{ij} C_{ij}^{(00)} \exp(-\alpha_i r^2 - \beta_j R_{\alpha d}^2)\Phi_\alpha(\mathbf{r}_\mu)\chi_{1M}, \tag{2}$$

$$\Psi_D^{(20)} = \sum_{M_L M_S} \langle 2M_L 1M_S | 1M_J\rangle \times Y_{2M_L}(\mathbf{r}) Y_{00}(\mathbf{R}_{\alpha d})\Phi_\alpha(\mathbf{r}_\mu)\chi_{1M_S} r^2 \times \sum_{ij} C_{ij}^{(20)} \exp(-\alpha_i r^2 - \beta_j R_{\alpha d}^2). \tag{3}$$

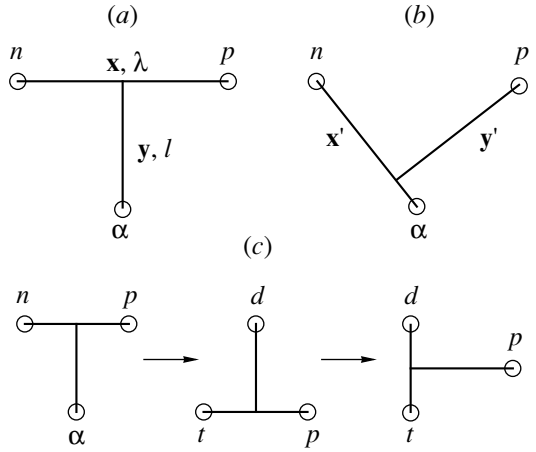

Fig. 1. (*a*) Jacobi coordinates *x* and *y* for the ^{6}Li nucleus in the $\alpha 2N$ model; (*b*) Jacobi coordinates *x*' and *y*' used in calculating the proton spectroscopic factors for the transition to the ground state of the ^{5}He nucleus; and (*c*) diagram representing the transformation of the Jacobi coordinates in the ^{6}Li nucleus for the transition to the first excited state of the ^{5}He nucleus.

According to Kukulin *et al.* [1], the *S* wave makes a dominant contribution to the ground state of the ^{6}Li nucleus (a contribution that exceeds 90%), whereas the *D* wave appears to be a small correction ranging between 3 and 7%, its specific value being dependent on the choice of interaction potential.

In experiments at NIKHEF [16], the spectroscopic factors and the momentum distributions of protons were determined quite accurately both for transitions to the ground state of the ^{5}He nucleus and for transitions to its highly excited states. For the ground state of the ^{6}Li nucleus, we have calculated the proton features for the formation of the $J^\pi = 3/2^-$, $T = 1/2$ ground state of the ^{5}He nucleus and for the formation of its excited state at $E = 16.75$ MeV with spin–parity $J^\pi = 3/2^+$ and isospin $T = 1/2$. Within the shell model, the former arises upon the separation of a valence $1p$ nucleon from the $(1s)^4(1p)^2$ ground state of the ^{6}Li nucleus, while the latter results from the separation of an *s* nucleon entering into the composition of the α-cluster core. In our model, the $P_{3/2^-}$ resonance in the αn system at $E_n = 1.15$ MeV ($E_{\text{c.m.}} = 0.9$ MeV) was associated with the ground state of the ^{5}He nucleus. This resonance was computed in an attractive αn interaction potential having a Gaussian form and involving a state forbidden in the *s* wave and even–odd splitting of levels [18].

Of particular interest is proton separation from a ^{6}Li nucleus in the reaction resulting in the excitation of a highly excited state of the ^{5}He nucleus. In our model, this state is considered as a near-threshold $L = 0$, $S = 3/2$ resonance of *dt* scattering at $E_d = 0.07$ MeV. This level determines the cross section for the reaction $t(d, n)\alpha$, which plays the main role in thermonuclear fusion, and the properties of the mesic molecule $dt\mu$ [20]. In order to calculate the wave function of this state, we employed the attractive potential from [21], which involves forbidden states and which faithfully reproduces the low-energy $l = 0, 1, 2$ quartet phase shifts in the $d\tau$ system. Only the Coulomb component of the $d\tau$ potential was changed for the *dt* system being considered. In [22], it was assumed that the above "thermonuclear" resonance may have a three-body structure of the (^{3}H + *n* + *p*) type. We have calculated the nucleon features by using the wave functions of this model.

In order to obtain the proton features, we took the overlap of the ^{6}Li wave function (2) and the ^{5}He wave function in the αn model [18]. As before, the latter was expanded in the Gaussian basis as

$$\Psi^{\tilde{J}\tilde{M}_J} = \sum_n D_n x' \exp(-\gamma_n x'^2) \times \sum_{\tilde{m}_l \tilde{m}_s} \left(1\tilde{m}_l \frac{1}{2}\tilde{m}_s \middle| \tilde{J}\tilde{M}_J\right) Y_{\tilde{l}\tilde{m}_l}(\mathbf{x}') \chi_{\frac{1}{2}\tilde{m}_s}. \quad (4)$$

In order to deduce spectroscopic features, it is necessary to go over to a new set of Jacobi coordinates *x* and *y* in the wave function of the ground-state ^{6}Li nucleus (see Fig. 1*a*). This transition can be accomplished with the aid of the matrix

$$\hat{A} = \begin{pmatrix} a_{11} & a_{12} \\ a_{21} & a_{22} \end{pmatrix}, \quad (5)$$

where $a_{11} = -4/5$, $a_{12} = -1$, $a_{21} = 3/5$, and $a_{22} = -1/2$. The radial component of the wave function (4) then takes the form

$$\Phi_{\lambda l}(x, y) = \sum_{ij\lambda_1 l_1 j_1 j_2} C_{ij}^{\lambda l} B_{\lambda l j_1 j_2}^{L\lambda_1 l_1}(x') (x')^{\lambda_1 + l_1} (y')^{\lambda - \lambda_1 + l - l_1} \times \exp[-\mu_{ij}(x')^2 - \nu_{ij}(y')^2 - \rho_{ij}(x'y')], \quad (6)$$

where

$$\mu_{ij} = \alpha_i a_{11}^2 + \beta_j a_{21}^2, \; \nu_{ij} = \alpha_i a_{12}^2 + \beta_j a_{22}^2, \; \rho_{ij} = 2\alpha_i a_{11} a_{12} + 2\beta_j a_{21} a_{22}.$$

In order to eliminate the crossed term in the exponent, we make one more coordinate transformation:

$$\mathbf{x}' = \mathbf{x}'' + a_{jm}\mathbf{y}'', \quad \mathbf{y}' = \mathbf{y}''. \quad (7)$$

The eventual form of the coordinate transformation is

$$\begin{pmatrix} \mathbf{x} \\ \mathbf{y} \end{pmatrix} = \hat{Q}\begin{pmatrix} \mathbf{x}'' \\ \mathbf{y}'' \end{pmatrix} = \begin{pmatrix} Q_{11} & Q_{12} \\ Q_{21} & Q_{22} \end{pmatrix}\begin{pmatrix} \mathbf{x}'' \\ \mathbf{y}'' \end{pmatrix} = \hat{A}\begin{pmatrix} 1 & a_{ijn} \\ 0 & 1 \end{pmatrix}\begin{pmatrix} \mathbf{x}'' \\ \mathbf{y}'' \end{pmatrix}, \quad (8)$$

where $a_{ijn} = -\rho_{ij}/2\mu_{ijn}$ and $\mu_{ijn} = \mu_{ij} + \gamma_n$.

The transformation coefficients in (6) can be expressed in terms of the elements of the matrix Q as

$$B^{L\lambda_1 l_1}_{\lambda j j_1 j_2} = (-1)^{\lambda + l} Q_{11}^{\lambda_1} Q_{12}^{\lambda - \lambda_1} Q_{21}^{l_1} Q_{22}^{l - l_1} \times \begin{pmatrix} \lambda_1 & l_1 & j_1 \\ 0 & 0 & 0 \end{pmatrix} \begin{pmatrix} \lambda - \lambda_1 & l - l_1 & j_2 \\ 0 & 0 & 0 \end{pmatrix} \times \left(\frac{[\lambda]![l]![\lambda][l][\lambda_1][\lambda - \lambda_1][l - l_1][j_1][j_2]}{[\lambda_1]![l_1]![\lambda - \lambda_1]![l - l_1]!} \right)^{1/2}, \quad (9)$$

where $[\lambda] = 2\lambda + 1$.

The $J^\pi = 3/2^+$ excited state is slightly above the dt threshold [23]. This state is of paramount importance for the thermonuclear-fusion reaction $d + t \longrightarrow n + \alpha$. The cross section for this reaction is enhanced by both initial- and final-state resonances. It is assumed that the $(3/2)^+$ resonance is due to a weak coupling between the $d + t$ and $n + \alpha$ channels via a tensor interaction. In the $d + t$ channel, the $(3/2)^+$ level has a spin of $S_1 = 3/2$ and an orbital angular momentum of $L_1 = 0$; in the $n + \alpha$ channel, the spin of the resonance is $S_2 = 1/2$, while its orbital angular momentum is $L_2 = 2$. It is interesting to note that, in single-channel calculations, no L_2 resonance arises in the $n + \alpha$ system [18]. A calculation within the algebraic version of the resonating-group method [24] revealed that the resonance in question appears only upon taking into account the coupling of the $n + \alpha$ and $d + t$ channels. Nonetheless, the estimates presented in [24] demonstrate that the $(3/2)^+$ resonance is formed owing primarily to the $d + t$ channel: the wave-function amplitude in this channel is three orders of magnitude greater than that in the $n + \alpha$ channel. In order to calculate the wave function of the $(3/2)^+$ state, we therefore used a dt potential that involves forbidden states and which was obtained from the $d\tau$ potential from [21] by changing only the Coulomb term. This potential makes it possible to reproduce fairly well low-energy $d\tau$ phase shifts and the cross section for radiative-capture reaction $d + {}^3\mathrm{He} \longrightarrow {}^5\mathrm{Li} + \gamma$ [21].

In calculating the spectroscopic features for the transition to the aforementioned excited state of the ^{5}He nucleus, we also employ an expansion in a Gaussian basis:

$$\Psi^{\tilde{J}\tilde{M}_J} = \varphi_t \varphi_d \chi^{\tilde{M}_J}_{\frac{3}{2}} \sum_n D_n Y_{00}(\hat{\rho}) \exp(-\gamma_n \rho^2). \quad (10)$$

For the d, t, and α-particle clusters, we use here wave functions that are represented as sums of Gaussian forms and which faithfully reproduce root-mean-square radii and binding energies [25]. In order to compute the spectroscopic factor, the relevant coordinates are transformed according to the scheme presented in Fig. 1*b*. The resulting p^5He wave function of the ground-state ^{6}Li nucleus has the form

$$\Psi_{p^5\mathrm{He}}(\mathbf{y}'') = \sum_{LS\lambda l \lambda_1 l_1 j_1 j_2} (-1)^{j_2} \frac{3}{\sqrt{2}} B^{L\lambda_1 l_1}_{\lambda j j_1 j_2} \times \Gamma\left(\frac{\lambda_1 + l_1 + j_3 + 3}{2} \right) ([L][S][\tilde{J}])^{1/2} (y'')^{z_1} \times \sum_{\tilde{j} = |j_1 + j_2 - 1|^{\tilde{m}_j}} [\tilde{j}]^{1/2} W(1 - j_1 j_1 \tilde{j} L : 1 j_2) Y_{\tilde{j}\tilde{m}_j}(\mathbf{y}'') \times \begin{pmatrix} j_2 & 1 - j_1 & \tilde{j} \\ 0 & 0 & 0 \end{pmatrix} \sum_{m m_l k} [k]^{1/2} \left(\tilde{j} \tilde{m}_j \frac{1}{2} m | k - m_k \right) \times \left(\frac{3}{2} \tilde{M}_J k - m_k | 1 M_J \right) \chi_{\frac{1}{2}m} \begin{Bmatrix} 1 & L & A \\ 3/2 & 1 & 1/2 \\ k & \tilde{j} & 1/2 \end{Bmatrix} \times \sum_{ijn} C_{ij} D_n a_{ijn}^{1 - \lambda_1} \tilde{\mu}_{ijn}^{-(\lambda_1 + l_1 + j + 3)} \exp(-W_{ijn} y''^2), \quad (11)$$

where $W_{ijn} = \nu_{ij} - \rho_{ij}^2/4\tilde{\mu}_{ijn}$ and $z_1 = \lambda - \lambda_1 + l - l_1 + 1 - j_1$.

The proton spectroscopic factor was computed by the formula

$$S^J = \int |\Psi_{p^5\mathrm{He}}(\mathbf{y}'')|^2 d\mathbf{y}'' = \sum_{LS\lambda l} \sum_{\lambda_1 l_1 \lambda_1' l_1' j_1 j_2 j_1' j_2'} (-1)^{j_2 + j_2'} \frac{q}{2^2} B^{L\lambda_1 l_1 Q}_{\lambda j j_1 j_2} B^{L\lambda_1' l_1' Q}_{\lambda j j_1' j_2'} \times \Gamma(z_2)\Gamma(z_2')\Gamma(z_3)([L][S][\tilde{J}])[J]^{-1} \times \sum_{\tilde{j}} [\tilde{j}] W(1 - j_1 j_1 \tilde{j} L : 1 j_2) \begin{pmatrix} j_2 & 1 - j_1 & \tilde{j} \\ 0 & 0 & 0 \end{pmatrix} \times \begin{pmatrix} j_2' & 1 - j' & \tilde{j} \\ 0 & 0 & 0 \end{pmatrix} \sum_{k m_k \tilde{m} \tilde{m}' M_j M_j'} [k] \left(\frac{3}{2} M_j k - m_k | 1 M_j \right) \times \left(\frac{3}{2} \tilde{M}' J k - m_k | 1 M_j' \right) \begin{Bmatrix} 1 & L & A \\ 3/2 & 1 & 1/2 \\ k & \tilde{j} & 1/2 \end{Bmatrix}^2 \times \sum_{ijn i' j' n'} \frac{C_{ij} C_{i'j'} D_n D_{n'}}{\tilde{\mu}_{ijn}^{z_1} \tilde{\mu}_{i'j'n'}^{z_1'} (W_{ijn} + W_{i'j'n'})^{z_2}}, \quad (12)$$

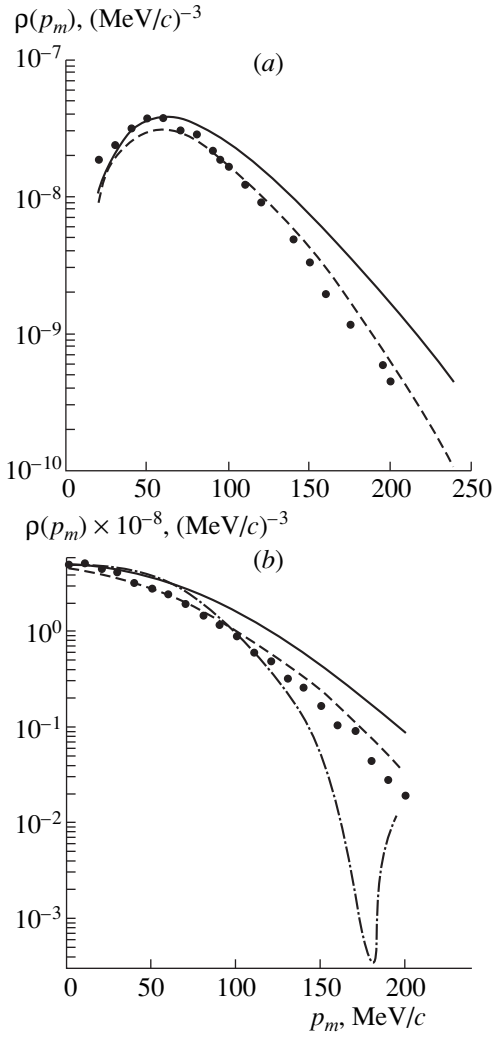

Fig. 2. Momentum distributions of protons in the ground-state ^{6}Li nucleus for the transition to (*a*) the ground and (*b*) a highly excited state of the ^{5}He nucleus: (solid curves) plane-wave results (R_0 = 0), (dashed curves) results obtained with allowance for distortions (R_0 = 2.5 fm), and (dash-dotted curve) results of the calculation within the *tnp* model. Experimental data were borrowed from [16].

where $z_2 = (\lambda_1 + l_1 + j_1 + 3)/2$ and $z_3 = 2\lambda - \lambda_1 - \lambda_1' + 2l - l_1 - l_1' - j_1 - j_1' + 3$.

The momentum distribution is given by

$$\rho = \frac{1}{(2\pi)^3}\left|\int \Psi_{p^5\mathrm{He}}(\mathbf{y}'')\exp(-i\mathbf{p}_m\cdot\mathbf{y}'')d\mathbf{y}''\right|^2$$

$$= \frac{1}{(2\pi)^3}\left|4\pi^{3/2}\sum_{LS\lambda l\lambda_1 l_1 j_1 j_2}(-1)^{j_2}\frac{3}{\sqrt{2}}B^{L\lambda_1 l_1 Q}_{\lambda j j_1 j_2}\right.$$

$$\times\Gamma(z_1)([L][S][\tilde{J}]^{1/2})\sum_{\tilde{j}\tilde{m}_j}[\tilde{j}]^{1/2}W(1-j_1 j_1\tilde{j}L:1j_2)$$

$$\times\begin{pmatrix} j_2 & 1-j_1 & \tilde{j}\\ 0 & 0 & 0\end{pmatrix}\sum_{mm_l k}[k]^{1/2}\left(\tilde{j}\tilde{m}_j\frac{1}{2}m|k-m_k\right) \qquad (13)$$

$$\times\left(\frac{3}{2}\tilde{M}_J k-m_k|1M_J\right)\chi_{\frac{1}{2}m}\begin{Bmatrix} 1 & L & A\\ 3/2 & 1 & 1/2\\ k & \tilde{j} & 1/2\end{Bmatrix}$$

$$\times\sum_{ijn}C_{ij}D_n a_{ijn}^{1-\lambda_1}\tilde{\mu}_{ijn}^{-z_1}(-i)^{\tilde{j}}Y^+_{\tilde{j}\tilde{m}_j}(\mathbf{p}_m)\frac{1}{\sqrt{2p_m}}$$

$$\times\left.\int y^{z_4}J_{\tilde{j}+1/2}(p_m y)\exp(-W_{ijn}y^2)dy\right|,$$

where $z_4 = z_1 + 5/2$.

The calculation performed here for the ^{5}He + *p* spectroscopic factor on the basis of the $\alpha 2N$ model yielded the value of S = 0.63, which is slightly below the experimental value obtained from an investigation of the relevant (*e*, *ep*) reaction ($S = 0.79 \pm 0.10$) [16]. Here, the main contribution (which saturates more than 90% of the total value) comes from the *S*-wave component of the three-body wave function of the ^{6}Li nucleus. In the case where a shell-model function of the type $R_{1p}(r)$ was taken for the ^{5}He wave function, we obtained the value of S = 0.59. Our calculation on the basis of the multiparticle shell model yielded the value of S = 0.71, which agrees with experimental data within errors. A calculation with Lanen three-body wave functions resulted in S = 0.89 [16].

For the transition to the $J^\pi = 3/2^+$ excited state of the ^{5}He nucleus, the spectroscopic factor that we have calculated here for proton separation is S = 0.34, which complies with the experimental value of $S = 0.30 \pm 0.04$ [16]. The Lanen three-body wave functions lead to the value of S = 0.35. [16]. That the result obtained for this level in [22] on the basis of the three-body *tnp* model (S = 0.03) deviates strongly from the above values indicates that this model is inappropriate. Our calculation revealed that, in this case, the radial wave function in the *dt* channel has an oscillatory R_{0S} character; that is, it has no nodes. At the same time, a correct wave functions must have an R_{2S} shell-model character; that is, it must have one internal node. Thus, it turns out that, in the *tnp* model, the total wave function has the form of an oscillatory $(0s)^5$ wave function, but this is forbidden by the Pauli exclusion principle because the 0*s* shell cannot feature more than four nucleons. If a nucleon is separated in this case from the $(0s)^4(1p)^2$ ground state of the ^{6}Li nucleus with the result that the aforementioned $(0s)^5$ configuration, which features no quanta, is formed, the emitted nucleon must carry two excitation quanta, so that the wave function of relative motion in the channel $^6\mathrm{Li} \longrightarrow {}^5\mathrm{He} + p$ must have a 2*S* character, developing one internal node. As usual, a node of the wave function in coordinate space leads to

a node in the momentum-representation wave function (see Fig. 2*b*). Thus, it seems that the authors of the *tnp* model [22] erroneously associated the forbidden-state wave function featuring no internal excitation quanta with the highly excited $J^\pi = 3/2^+$ state of the ^{5}He nucleus.

The results that we obtained for the momentum distribution of protons in the ^{6}Li ground state by using three-body wave functions are displayed, along with experimental data [16], in Fig. 2*a* for the transitions to the ground state of the ^{5}He nucleus and in Fig. 2*b* for the transitions to the aforementioned highly excited state of this nuclear species. As might have been expected, the plane-wave calculation (solid curves) faithfully reproduces the shape of the experimental curve at comparatively low momentum values of 70–80 MeV/*c*. A discrepancy at higher momenta, which correspond to small distances, highlights the importance of distortion effects (and above all, of particle absorption) in the interior of the nucleus being considered. In order to take correctly into account these effects, it is necessary to know the interaction potential in the p^5He channel. Since ^{5}He nuclei cannot be used for a target because of their instability, a conventional method of potential reconstruction on the basis of phase shifts is inapplicable here; therefore, we invoked a different method for taking distortions into account, that which relies on the strong-absorption model, where the interior of a nucleus is singled out by introducing cutoff radii R_0 in integrals that determine momentum distributions. Physically, this procedure takes into account particle absorption in the interior of a nucleus; previously, this recipe for treating distortions proved viable in the calculation of the quasielastic knockout of clusters [17]. Numerically, the cutoff radius, which appears to be a parameter here, is close to the channel radius.

In Fig. 2, dashed curves represent the results that we obtained by calculating, with allowance for distortions, the momentum distributions of protons in the ground-state ^{6}Li nucleus for the transition to the $J^\pi = 3/2^-$ ground state of ^{5}He (Fig. 2*a*) and for the transition to its $J^\pi = 3/2^+$ excited state (Fig. 2*b*). We can see that, for either channel, the agreement between theoretical and experimental results is much better at $R_0 = 2.5$ fm than at $R_0 = 0$—that is, the effects of absorption in the interior of the nucleus are adequately reproduced by introducing a cutoff radius. The shape of the momentum distributions in Fig. 2*b* provides an additional argument against the use of the wave function that the *tnp* model produces for the above highly excited state of ^{5}He (dash-dotted curve) and which was presented in [22].

3. SPECTROSCOPIC FACTORS AND MOMENTUM DISTRIBUTIONS OF NEUTRONS IN THE ^{9}Be NUCLEUS

In calculating the nucleon features of the ^{9}Be nucleus, we used three versions of the $2\alpha N$ model with the following pair interaction potentials $V_{\alpha\alpha}$ and $V_{\alpha N}$ [2, 3]: (i) a potential $V_{\alpha N}$ featuring even–odd splitting of phase shifts and a deep potential $V_{\alpha\alpha}$ having the Buck form and involving forbidden states, (ii) the Sack–Biedenharn–Breit (SBB) potential $V_{\alpha N}$ [26] and the Buck potential $V_{\alpha\alpha}$, and (iii) the same potential $V_{\alpha N}$ as in version (i) and the Ali–Bodmer potential $V_{\alpha\alpha}$.

In the three-body model, the wave function of the $J^\pi = 3/2^-$ ground state of the ^{9}Be nucleus features three-dominant components with approximately identical weights [2]:

$$\Psi^{\frac{3}{2}M_J}(\mathbf{r},\mathbf{R}) = \Psi^{\lambda lL}_{011}(\mathbf{r},\mathbf{R}) + \Psi^{\lambda lL}_{211}(\mathbf{r},\mathbf{R}) + \Psi^{\lambda lL}_{212}(\mathbf{r},\mathbf{R}). \quad (14)$$

Here, **r** and **R** are coordinates that describe, respectively, the relative motion of two alpha particles and the relative motion of the neutron and the center of mass of two alpha particles in the ^{9}Be nucleus; λ and l are the corresponding orbital angular momenta; and L is the total orbital angular momentum of the nucleus. The wave-function components from (14) can be represented as

$$\Psi_{011} = \sum_{M_L M_S}\left(1M_L\frac{1}{2}M_S\middle|\frac{3}{2}M_J\right) \times (001m|1M_L)Y_{00}(\mathbf{r})Y_{1m}(\mathbf{R})\chi_{\frac{1}{2}M_S} \times \sum_{ij} C^{00}_{ij} R\exp(-\alpha_i r^2 - \beta_j R^2), \quad (15)$$

$$\Psi_{211} = \sum_{M_L M_S}\left(1M_L\frac{1}{2}M_S\middle|\frac{3}{2}M_J\right) \times (2\mu 1m|1M_L)Y_{2\mu}(\hat{\mathbf{r}})Y_{1m}(\hat{\mathbf{R}})\chi_{\frac{1}{2}M_S} \times \sum_{ij} C^{21}_{kp} r^2 R\exp(-\alpha_k r^2 - \beta_p R^2), \quad (16)$$

$$\Psi_{212} = \sum_{M_L M_S}\left(2M_L\frac{1}{2}M_S\middle|\frac{3}{2}M_J\right) \times (2\mu 1m|1M_L)Y_{2\mu}(\hat{\mathbf{r}})Y_{1m}(\hat{\mathbf{R}})\chi_{\frac{1}{2}M_S} \times \sum_{ij} C^{21}_{qt} r^2 R\exp(-\alpha_q r^2 - \beta_t R^2). \quad (17)$$

The neutron features of the ^{9}Be nucleus can be calculated quite straightforwardly because additional coordinate transformations, similar to those that are necessary for the ^{6}Li nucleus, are not required in this case. We will take the wave function of the ^{9}Be nucleus

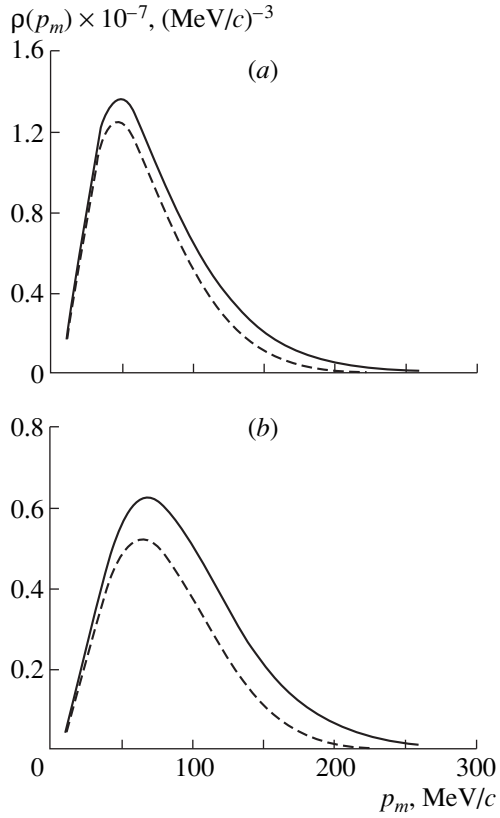

Fig. 3. Momentum distributions of neutrons in the ground-state ^{9}Be nucleus for the transition to (*a*) the ground and (*b*) an excited state of the ^{8}Be nucleus: (solid curves) plane-wave results ($R_0 = 0$) and (dashed curves) results obtained with allowance for distortions ($R_0 = 2.5$ fm). The wave functions of the ^{9}Be nucleus were computed within version (iii) of the three-body model (in this version, the Ali–Bodmer potential is used to simulate αα interaction).

in the form (14). In order to obtain the neutron features, we evaluated the overlap integrals of the wave function of the ^{9}Be nucleus with the wave functions of the ^{8}Be nucleus in the ground and the first excited state. The wave functions of the ^{8}Be nucleus were calculated on the basis of the two-body αα model proposed in [13]. In this calculation, we made use of the Woods–Saxon potential. The wave function of the ^{8}Be nucleus was represented in the form

$$\Psi_{^8\mathrm{Be}}(\mathbf{x}) = \varphi_{\alpha_1}\varphi_{\alpha_2}R_l(x)Y_{lm}(\mathbf{x}), \qquad (18)$$

and the radial component $R_l(x)$ was determined by expanding it in a Gaussian basis as

$$R_l(x) = \sum_{n=1}^{N} C_n N_n x^l \exp(-\alpha_n x^2). \qquad (19)$$

The values found for C_n and α_n by means of a variational procedure are presented in [13]. In calculating the nucleon features, we considered not only the ^{8}Be wave function within the αα model but also shell-model wave functions, whose radial components appear to be R_{4S} and R_{4D} for, respectively, the ground and the first excited state of the ^{8}Be nucleus.

In the ^{8}Be + *n* channel, the wave function of relative motion in the ^{9}Be nucleus has the form

$$\Psi^J_{n^8\mathrm{Be}}(\mathbf{y}) = \int \Psi_{^9\mathrm{Be}}(\mathbf{x},\mathbf{y})\Psi^J_{^8\mathrm{Be}}(\mathbf{x})d\mathbf{x}. \qquad (20)$$

The neutron spectroscopic factor is defined by the conventional expression

$$S^J = \int \left|\Psi_{n^8\mathrm{Be}}(\mathbf{y})\right|^2 d\mathbf{y}. \qquad (21)$$

For the transition to the ground state of the ^{8}Be nucleus, the overlap integral in (20) is determined by the contribution of the first component in the wave function of the ^{9}Be nucleus [see equations (14) and (15)]:

$$\Psi^{0^+}_{n^8\mathrm{Be}}(\mathbf{y}) = \sum_{M_S m}\left(1m\frac{1}{2}M_S\middle|\frac{3}{2}M_J\right)Y^*_{1m}(\mathbf{y})\chi^+_{\frac{1}{2}M_S}N^{l=0} \times \frac{\sqrt{\pi}}{4}\sum_n C^0_n N_{n0}\sum_{ij}\frac{C^{01}_{ij}}{\alpha^{3/2}_{in}}y\exp(-\beta_j y^2). \qquad (22)$$

For the transition to the first excited state of the ^{8}Be nucleus, this overlap integral receives contributions from the remaining two components, those for which $\lambda = 2$ [equations (14), (16), and (17)].

For all cases considered here, we have also calculated the momentum distribution of neutrons, which appears to be the Fourier transform of the wave function of relative motion:

$$\rho = \frac{1}{(2\pi)^3}\left|\int \Psi_{n^8\mathrm{Be}}(\mathbf{y}'')\exp(-i\mathbf{p}_m\mathbf{y}'')d\mathbf{y}''\right|^2. \qquad (23)$$

Upon substituting the wave function (22) of relative motion in the ^{9}Be nucleus and performing integration with respect to the relevant coordinate, we find that, for the transition to the ground state, the distribution in question is given by

$$\rho^{0^+}(p_m) = \frac{p_m^2}{2^9}\left|N^{l=0}\sum_n C^0_n N_{n0}\sum_{ij}\frac{C^{01}_{ij}}{\alpha^{3/2}_{in}\beta^{5/2}_j}\exp\left(-\frac{p_m^2}{4\beta_j}\right)\right|^2. \qquad (24)$$

For the transition to the 2^+ excited state of the ^{8}Be nucleus, the corresponding expressions are somewhat more cumbersome, but they are derived in a similar way.

The results of our calculations are displayed in the table and in Fig. 3. Of particular interest is the relationship between the spectroscopic-factor values for the transitions to the ground and the first excited state of the ^{8}Be nucleus. In accord with a major part of experimental data, the calculations that employ the parity-split αN potential to determine the spectrum of the ^{9}Be nucleus lead to neutron spectroscopic factors that are slightly greater for the transition to the ground state than for the

transition to the first excited state [versions (i) and (iii)]. A different situation arises in version (ii), where the calculation relies on the SBB potential: in this case, the spectroscopic factor for the transition to the excited state is 1.2 times as great as that for the transition to the ground state. This distinction is still greater when the wave functions obtained on the basis of the multiparticle shell model [27] are used for both nuclei.

The relationship between the spectroscopic factors for the transitions to the ground and the first excited state of the ^{8}Be nucleus is determined exclusively by the form of the αN potential used in the three-body model; it undergoes no changes upon going over to the shell-model wave functions for the daughter nucleus [11]. As can be seen from the table, the spectroscopic factors for transitions from the ground state of the ^{9}Be nucleus are only weakly sensitive to the form of the $\alpha\alpha$ interaction potential.

The above procedure for computing one-nucleon features within the three-body cluster model can be extended easily to the case where excited states of the ^{9}Be nucleus are involved. We have calculated the spectroscopic factor for the transition from the ^{9}Be $(1/2)^+$, 1/2 level at $E = 2.78$ MeV to the ground state of the ^{8}Be nucleus. We have performed our calculations for two versions. In the first, we have employed the parity-split αN potential and the Buck $\alpha\alpha$ potential. In the second, we have taken the same αN potential and the Ali–Bodmer $\alpha\alpha$ potential. In contrast to the purely attractive Buck potential, which is independent of the orbital angular momentum l, the Ali–Bodmer potential involves repulsion at small distances. In the first and in the second version, we have obtained $S_n = 0.65$ and 0.54, respectively, the latter result being fully in accord with the experimental value of $S_n = 0.48 \pm 0.06$.

Thus, we have demonstrated that the one-nucleon characteristics of the ^{9}Be nucleus can be obtained within the three-body potential $2\alpha N$ model. The spectroscopic factors and the parameters of the momentum distributions of neutrons in the ground-state ^{9}Be nucleus for the transitions to the ground and the first excited state of ^{8}Be have been analyzed for stability to the choice of models for the nuclei in question. Here, we revealed the highest sensitivity to the form of the αn potential. The spectroscopic factors computed within the three-body model proved to be much less than their shell-model counterparts. The relationship between the spectroscopic factors for the transitions to the ground and the first excited state of ^{8}Be changes markedly when we go over from the cluster model to the shell model [28–30], the values within the former being consistent with experimental data [31, 32].

In Fig. 3, the momentum distributions of neutrons in the ground state of the ^{9}Be nucleus are presented for the transitions to (Fig. 3*a*) the ground and (Fig. 3*b*) the first excited state of the ^{8}Be nucleus. As a matter of fact, we computed these momentum distributions with all known model wave functions of the ^{9}Be nucleus (see [11]), but, because of the absence of relevant experimental data, we present here only the results obtained within version (iii), which relies on the Ali–Bodmer $\alpha\alpha$ potential featuring repulsion at small distances. As was established in [3, 9], it is this model version that provides the best description of the static features of the ^{9}Be nucleus. As can be seen from Fig. 3, the introduction of the cutoff radius equal to $R_0 = 2.5$ fm changes substantially the shape of momentum distributions, suppressing the high-momentum section of the spectrum from a momentum of 50 MeV/c.

4. CONCLUSION

Within the three-body models of the ^{6}Li and ^{9}Be nuclei, we have calculated the one-nucleon spectroscopic factors and momentum distributions for transitions to the ground and excited states of residual nuclei. It has been shown that, for proton separation from a ^{6}Li nucleus in the reaction resulting in the formation of a ^{5}He nucleus in the ground state, the three-body model of the ^{6}Li nucleus makes it possible to reproduce the experimental spectroscopic-factor value extracted from electron data coming from NIKHEF. We would like to note that a fit to this experimental value can also be obtained on the basis of the multiparticle shell model. As to the $(3/2)^+$ excited state of the ^{5}He nucleus, the three-body model faithfully reproduces the experimental value of the spectroscopic factor for the transition to this level as well.

By and large, the spectroscopic factors that we have calculated for the ^{6}Li nucleus are in satisfactory agreement with experimental data. If, however, the wave function in the three-body *tnp* model is used for the above excited state of the ^{5}He nucleus, the calculated values of the proton spectroscopic factor ($S = 0.03$) fall considerably short of the experimental value. Both the spectroscopic factors and the momentum distributions as calculated on the basis of the three-body *tnp* model deviate strongly from the corresponding experimental results, invalidating the wave function that was presented in [22] for the above excited state and which is based on this model.

For the case of the ^{9}Be nucleus, we have demonstrated that, in its ground state, the calculated spectroscopic factors and the parameters of the momentum distributions of neutrons for the transitions to the ground and the first excited state of the ^{8}Be nucleus are sensitive to the choice of model for the nuclei in question, the dependence of the above features on the form of the αn potential being especially sharp. It has been shown that, in contrast to what is obtained in the multiparticle shell model, the calculations within the potential cluster model lead to a correct relationship between the spectroscopic factors for the transitions to the ground and the first excited state of the ^{8}Be nucleus. Thus, it seems that, of the spectroscopic factors considered here within the shell model, those for neutron separation from the ground state of the ^{9}Be nucleus in the

reactions leading to the formation of the ground and the first excited state of the ^{8}Be nucleus exhaust the cases in which the multiparticle shell model yields incorrect results.

It has also been revealed that the momentum distributions computed here within the three-body model can be fitted to experimental data only upon taking into account final-state distortions. This can be done by introducing a cutoff radius, which simulates the absorption of proton waves in the interior of the nucleus being considered.

REFERENCES

1. V. I. Kukulin, V. M. Krasnopolsky, V. T. Voronchev, *et al.*, Nucl. Phys. A **417**, 128 (1984); **453**, 365 (1986).
2. V. T. Voronchev, V. I. Kukulin, V. N. Pomerantsev, *et al.*, Yad. Fiz. **57**, 1964 (1994) [Phys. At. Nucl. **57**, 1890 (1994)]; Izv. Akad. Nauk, Ser. Fiz. **57** (5), 170 (1993).
3. V. T. Voronchev, V. I. Kukulin, *et al.*, Few-Body Syst. **18**, 191 (1995).
4. N. A. Burkova and M. A. Zhusupov, Izv. Akad. Nauk SSSR, Ser. Fiz. **51**, 182 (1987).
5. N. A. Burkova, M. A. Zhusupov, *et al.*, Phys. Lett. B **248**, 15 (1990).
6. M. A. Zhusupov and E. T. Ibraeva, Izv. Akad. Nauk, Ser. Fiz. **56** (1), 166 (1992).
7. M. A. Zhusupov *et al.*, Yad. Fiz. **57**, 2013 (1994) [Phys. At. Nucl. **57**, 1937 (1994)].
8. G. G. Ryzhikh and Yu. M. Tchuvil'sky, Izv. Akad. Nauk SSSR, Ser. Fiz. **54**, 2276 (1990); Izv. Akad. Nauk, Ser. Fiz. **56** (1), 112 (1992).
9. M. A. Zhusupov *et al.*, Izv. Akad. Nauk, Ser. Fiz. **60** (11), 123 (1996).
10. B. Buck, H. Friedrich, and C. Wheatley, Nucl. Phys. A **275**, 246 (1977).
11. M. A. Zhusupov *et al.*, Izv. Akad. Nauk, Ser. Fiz. **58** (5), 55 (1994).
12. M. A. Zhusupov *et al.*, Izv. Akad. Nauk, Ser. Fiz. **59** (1), 80 (1995).
13. S. B. Dubovichenko and M. A. Zhusupov, Izv. Akad. Nauk Kaz. SSR, Ser. Fiz., No. 4, 44 (1983).
14. G. G. Ryzhikh, Yu. M. Tchuvil'sky, A. E. Shkol'nikov, *et al.*, Izv. Akad. Nauk, Ser. Fiz. **60** (11), 94 (1996).
15. M. A. Zhusupov *et al.*, in *Abstracts of Papers Presented at the 48th International Workshop on Nuclear Spectroscopy and Nuclear Structure, Obninsk, 1997* (St. Petersburg, 1997), p. 125; Izv. Akad. Nauk, Ser. Fiz. **62**, 985 (1998).
16. J. B. Lanen *et al.*, Phys. Rev. Lett. **62**, 2925 (1989); **63**, 2793 (1989).
17. M. A. Zhusupov and Yu. N. Uzikov, Fiz. Élem. Chastits At. Yadra **18**, 323 (1987) [Sov. J. Part. Nucl. **18**, 136 (1987)].
18. S. B. Dubovichenko and M. A. Zhusupov, in *Strongly Interacting Quantum Systems* (Atomizdat, Kalinin, 1987), p. 85.
19. R. Reid, Ann. Phys. (N.Y.) **50**, 411 (1968).
20. S. S. Gershtein, Yu. V. Petrov, and L. I. Ponomarev, Usp. Fiz. Nauk **160** (8), 1 (1990).
21. V. G. Neudatchin, A. A. Sakharuk, and Yu. F. Smirnov, Fiz. Élem. Chastits At. Yadra **23**, 479 (1992) [Sov. J. Part. Nucl. **23**, 210 (1992)].
22. V. T. Voronchev, V. I. Kukulin, *et al.*, Yad. Fiz. **37**, 271 (1983) [Sov. J. Nucl. Phys. **37**, 161 (1983)].
23. F. Ajzenberg-Selove, Nucl. Phys. A **490**, 1 (1988).
24. V. S. Vasilevsky, N. F. Gutich, and I. P. Okhrimenko, Yad. Fiz. **46**, 757 (1987) [Sov. J. Nucl. Phys. **46**, 427 (1987)].
25. S. B. Dubovichenko and M. A. Zhusupov, Izv. Akad. Nauk Kaz. SSR, Ser. Fiz.-Mat., No. 4, 64 (1987).
26. S. Sack, L. C. Biedenharn, and G. Breit, Phys. Rev. **93**, 321 (1954).
27. A. N. Boyarkina, *The Structure of Light Nuclei* (Mosk. Gos. Univ., 1973).
28. S. Cohen and D. Kurath, Nucl. Phys. A **101**, 17 (1967).
29. V. V. Balaschov, A. N. Boyarkina, and I. Rotter, Nucl. Phys. **59**, 417 (1964).
30. F. C. Barker, Nucl. Phys. **83**, 418 (1966).
31. N. A. Zaika *et al.*, Yad. Fiz. **39**, 1081 (1984) [Sov. J. Nucl. Phys. **39**, 682 (1984)].
32. S. A. Goncharov *et al.*, Czech. J. Phys. B **38**, 12 (1988).

Translated by A. Isaakyan

Physics of Atomic Nuclei, Vol. 63, No. 2, 2000, pp. 179–190. Translated from Yadernaya Fizika, Vol. 63, No. 2, 2000, pp. 232–243.

NUCLEI
Theory

Multichannel Features of the Continuous Spectrum of ^{6}He

G. F. Filippov* and S. V. Mokhov[1)]

Bogolyubov Institute for Theoretical Physics, National Academy of Sciences of Ukraine, Metrologicheskaya ul. 14b, Kiev, 252143 Ukraine

Received October 14, 1998; in final form, February 18, 1999

Abstract—It is shown that the continuous spectrum of the ^{6}He nucleus immediately above the threshold for its breakup into an alpha particle and two neutrons has some features that are not peculiar to the continuous spectrum of binary systems. This spectrum has an infinite degeneracy multiplicity; hence, there exist an infinite number of decay channels even if we fix the angular momentum and the parity of a channel. In states characterized by a fixed value of the grand orbital, the potential energy of the ^{6}He nucleus decreases with increasing hyperradius in inverse proportion to its cube. This circumstance is reflected in the behavior of the *S*-matrix elements for $3 \longrightarrow 3$ scattering at low above-threshold energies. Because of the effect of the Pauli exclusion principle, the grand orbital generally ceases to be an appropriate quantum number for classifying decay channels, and the resulting conventional situation requires invoking superpositions of states corresponding to different values of the grand orbital. Within the method of three-cluster hyperharmonics and the approximation of an asymptotic potential, we calculate the eigenphases of the scattering matrix and reveal regularities in the behavior of these phases as functions of energy. © *2000 MAIK "Nauka/Interperiodica".*

1. INTRODUCTION

In [1] and later in [2], it was shown that the method of three-cluster hyperspherical functions provides an adequate approximation for describing the ^{6}He bound state that is dominated by the hyperharmonic characterized by the grand-orbital value of $K = 2$ and which features no more than a 5% admixture of the $K = 0$ hyperharmonic. In [2], the character of the asymptotic behavior of the hyperharmonics is discussed, and arguments are adduced that explain why hyperspherical functions are useful in studying the continuous spectrum of three-cluster systems as well.

In [1], the method of hyperharmonics was used in coordinate space, and the effect of the Pauli exclusion principle was simulated by a nucleon–nucleon repulsive potential introduced in an ad hoc manner. In [2], the wave equation was considered in the representation of a three-body harmonic oscillator. This simplified substantially both the procedure for removing forbidden states and the analysis of the asymptotic behavior of the wave function at large intercluster distances.

Later on, it turned out, however, that actual calculations of the continuous spectrum of three-cluster systems by the method of *K* harmonics require a dedicated analysis of some problems arising in such calculations. First, we have to deal with basis states allowed by the Pauli exclusion principle that represent linear superpositions of different hyperharmonics or hyperharmonics that are characterized by the same value of the grand orbital, but which differ by the values of additional quantum numbers. There was no such question when hyperharmonics in the space of dimension $3(A - 1)$ were used to describe *A*-nucleon systems. Second, the complexity of the structure of allowed states results in that not only the matrix elements of the potential-energy operator, which couple orthogonal allowed states differing in grand-orbital content and in number of oscillator quanta, but also matrix elements of the kinetic-energy operator, which decrease slowly at infinity, take nonzero values. In calculating the *S*-matrix elements for relevant scattering processes, the grand-orbital content of the basis functions of various channels through which a three-cluster nucleus may decay must therefore be rearranged with allowance for slowly decreasing nondiagonal matrix elements of the kinetic-energy operator. Finally, there is a third point requiring a dedicated consideration. The continuous spectrum of three-cluster systems is degenerate. Since infinitely many decay channels open up immediately above the threshold for three-body breakup, the multiplicity of this degeneracy is infinite. For practical reasons, we have to restrict our consideration, however, to a finite number of degenerate states, but it is then necessary to establish the dependence of scattering data, which are determined by the *S* matrix, on the number of the channels used. All the above requires a thorough investigation of the problem of continuous spectra of three cluster systems.

This article is organized as follows. In Section 2, we describe a method for constructing states allowed by the Pauli exclusion principle and list, for the ^{6}He nucleus in the 0^+ state, those branches of allowed basis states that are characterized by the minimum possible values of the grand orbital. If the grand orbital *K* is not

* e-mail: gfilippov@gluk.ape.org

[1)] Department of Physics, Taras Shevchenko Kiev University, ul. Glushkova 6, Kiev, 252022 Ukraine.

greater than 4 ($K_a = 4$), there are three such branches. In Section 3, we consider the generating matrix elements of the Hamiltonian of the system, their projections onto states characterized by specific values of the quantum numbers, and a calculation of the Hamiltonian matrix elements between allowed states. In Sections 4 and 5, we investigate the asymptotic behavior of the matrix elements of the potential at large values of the hyperradial quantum number and derive equations for the coefficients in the expansions of the eigenstates of the system in terms of the allowed basis states in the approximation of an asymptotic potential. We also consider there some questions associated with multichannel scattering. In Section 6, we describe our numerical calculations and discuss the results that they produce.

2. CONSTRUCTING ALLOWED STATES

In constructing the stationary states of ^{6}He, we will make use of the harmonic-oscillator basis obtained as a Slater determinant formed by generating orbitals of the six-nucleon system [3]. States characterized by fixed quantum numbers arise from an expansion of this determinant in powers of the generator parameters of the generating orbitals. We restrict ourselves to a basis corresponding to zero value of the total orbital angular momentum. This restriction simplifies calculations, but it is of no crucial importance in the approach used here. Basis functions corresponding to other values of the orbital angular momentum (say, those for 2^+ states) can also be constructed within the developed scheme, but the projection algorithm in this case becomes somewhat more involved.

With each nucleon of the system, we associate the Bloch–Brink orbital [4]

$$\varphi_i(\mathbf{R}_{(i)}, \mathbf{r}, \sigma, \tau) = \frac{1}{\pi^{3/4}} \times \exp\left(-\frac{r^2}{2} + \sqrt{2}\mathbf{r}\cdot\mathbf{R}_{(i)} - \frac{R_{(i)}^2}{2}\right)\xi_i(\sigma,\tau) = \phi_i\xi_i(\sigma,\tau), \quad (1)$$

where ϕ_i is the space orbital for one nucleon, $\mathbf{R}_{(i)}$ is the vector generator parameter, $\xi_i(\sigma, \tau)$ is the nucleon spin–isospin component of the nucleon wave function, and $\mathbf{r}$ is the nucleon radius vector in configuration space. We set the oscillator radius to $r_0 = 1$. For the ^{6}He nucleus, we must take into account the following spin–isospin states:

$$\xi_1 = p\uparrow, \quad \xi_2 = p\downarrow, \quad \xi_3 = n\uparrow,$$
$$\xi_4 = n\downarrow, \quad \xi_5 = n\uparrow, \quad \xi_6 = n\downarrow.$$

The vector generator parameters for the orbitals in (1) are independent variables of entire analytic functions defined in the linear Fock–Bargmann space [5].

We are interested in the motion of nucleons in their c.m. frame; therefore, it is expedient to go over from the nucleon radius vectors to the c.m. vector and the Jacobi vectors determining the arrangement of nucleons with respect to one another. The ^{6}He nucleus involves a subsystem, an alpha cluster, whose breakup energy is considerably higher than the energy of ^{6}He breakup into an alpha particle and two neutrons. Taking into account this circumstance, we introduce, instead of the radius vectors of the first four nucleons, the radius vector of the center of mass of the alpha cluster and three vectors associated with the polarization of the alpha cluster, $\mathbf{e}_1$, $\mathbf{e}_2$, and $\mathbf{e}_3$. The generator vectors in the Fock–Bargmann space transform in a similar way. In the approximation of an unpolarized alpha cluster, the generator parameters that are responsible for the excitation of this cluster are set to zero. Thus, the motion of the nucleons forming the alpha cluster can be described by a single generator parameter, and either remaining neutrons must be consider as separate cluster:

$$\mathbf{R}_{(i)} = \mathbf{R}_\alpha, \quad i = \overline{1,4}, \quad \mathbf{R}_{(5)} = \mathbf{R}_1, \quad \mathbf{R}_{(6)} = \mathbf{R}_2. \quad (2)$$

The normalized generator Jacobi vectors characterizing the relative positions of the clusters and the radius vector of the center of mass of the system are expressed in terms of the cluster radius vectors as

$$\mathbf{a} = \frac{2}{\sqrt{3}}\left(\mathbf{R}_\alpha - \frac{1}{2}(\mathbf{R}_1 + \mathbf{R}_2)\right),$$

$$\mathbf{b} = \frac{1}{\sqrt{2}}(\mathbf{R}_1 - \mathbf{R}_2),$$

$$\mathbf{R} = \frac{1}{\sqrt{6}}(4\mathbf{R}_\alpha + \mathbf{R}_1 + \mathbf{R}_2).$$

In the following, the vectors **a** and **b** defined in this way will be referred to as those that form the main Jacobi tree. Similarly, the vectors **p**, **q**, and $\mathbf{R}_{\text{c.m.}}$ in configuration space are defined in terms of the vectors $\mathbf{r}_\alpha$, $\mathbf{r}_5$, and $\mathbf{r}_6$. There are two more ways to define generator Jacobi vectors; in those cases, one of these vectors is aligned with the vector connecting the alpha cluster and one of the two neutron clusters. The corresponding Jacobi tree is related to the main tree by the orthogonal transformation

$$\mathbf{a}' = -\sqrt{\frac{2}{5}}\mathbf{a} - \sqrt{\frac{3}{5}}\mathbf{b}, \quad \mathbf{b}' = -\sqrt{\frac{3}{5}}\mathbf{a} + \sqrt{\frac{2}{5}}\mathbf{b}. \quad (3)$$

Since the set of the nucleons forming the ^{6}He nucleus is a system of identical particles that may occur in various spatial and spin–isospin states, its total wave function must be antisymmetrized in all pairs of the particles. Hence, the generating function for the basis of allowed antisymmetric states is introduced as the Slater determinant

$$\Phi(\{\mathbf{r}_i, \sigma_i, \tau_i\}) = \det\{\varphi_i(j)\}, \quad (4)$$

where $(j) = (\mathbf{r}_j, \sigma_j, \tau_j)$ are the coordinates of the jth nucleon. The determinant in (4) is proportional to the

expression that is obtained by applying the antisymmetrization operator to the function

$$\Phi_0 = \prod_{i=1}^{6}\phi_i(i)$$

$$= \frac{1}{\pi^{3/4}}\exp\left(-\frac{R_{\text{c.m.}}^2}{2} + \sqrt{2}\mathbf{R}_{\text{c.m.}}\cdot\mathbf{R} - \frac{R^2}{2}\right)$$

$$\times\frac{1}{\pi^{3/2}}\exp\left(-\frac{p^2+q^2}{2} + \sqrt{2}(\mathbf{p}\cdot\mathbf{a} + \mathbf{q}\cdot\mathbf{b}) - \frac{a^2+b^2}{2}\right) \quad (5)$$

$$\times\Phi_{\alpha 0}(\mathbf{e}_1, \mathbf{e}_2, \mathbf{e}_3),$$

multiplied by a spin–isospin factor. The expression in (5) involves the alpha-particle wave function $\Phi_{\alpha 0}$. In the approximation being considered, this wave function has the form

$$\Phi_{\alpha 0} = \frac{1}{\pi^{9/4}}\exp\left(-\frac{e_1^2+e_2^2+e_3^2}{2}\right).$$

In expression (5), the part that describes the relative motion of the clusters, that is,

$$\Phi_0^c = \frac{1}{\pi^{3/2}}$$

$$\times\exp\left(-\frac{p^2+q^2}{2} + \sqrt{2}(\mathbf{p}\cdot\mathbf{a} + \mathbf{q}\cdot\mathbf{b}) - \frac{a^2+b^2}{2}\right)$$

$$= \sum_{\nu=0}^{\infty}\sum_{l_1=0}^{\infty}\sum_{l_2=0}^{\infty}\sum_{K=l_1+l_2}^{\infty}\sum_{L=|l_1-l_2|}^{l_1+l_2}\sum_{M=-L}^{L}\Psi^*_{\nu KLMl_1l_2}(\mathbf{p},\mathbf{q}) \quad (6)$$

$$\times\psi_{\nu KLMl_1l_2}(\mathbf{a},\mathbf{b}),$$

represents the kernel of the integral transformation from the eigenfunctions of the three-particle harmonic oscillator in the c.m. frame, $\Psi^*_{\nu KLMl_1l_2}(\mathbf{p},\mathbf{q})$, to the basis functions $\psi_{\nu KLMl_1l_2}(\mathbf{a},\mathbf{b})$ defined in the Fock–Bargmann space. If the configuration-space basis functions taken without their spin–isospin components are given by

$$\Psi_{\nu KLMl_1l_2}(\mathbf{p},\mathbf{q}) = R_{\nu K}(r)\Phi_K^{LMl_1l_2}(\gamma_r, \Omega_p, \Omega_q),$$

$$p = r\cos\gamma_r, \quad q = r\sin\gamma_r,$$

$$R_{\nu K}(r) = (-1)^\nu\sqrt{\frac{2\nu!}{(\nu+K+2)!}}r^K L_\nu^{K+2}(r^2)e^{-r^2/2},$$

$$\Phi_K^{LMl_1l_2}(\gamma_r, \Omega_p, \Omega_q) = N_K^{l_1l_2}\cos^{l_1}\gamma_r\sin^{l_2}\gamma_r$$

$$\times P_m^{l_2+1/2,\,l_1+1/2}(\cos 2\gamma_r)\mathcal{Y}_{l_1l_2}^{LM}(\Omega_p,\Omega_q),$$

$$N_K^{l_1l_2} = \sqrt{\frac{2m!(K+2)(m+l_1+l_2+1)!}{\Gamma(m+l_1+3/2)\Gamma(m+l_2+3/2)}},$$

$$m = (K-l_1-l_2)/2,$$

$$\mathcal{Y}_{l_1l_2}^{LM}(\Omega_p,\Omega_q)$$

$$= \sum_{m_1+m_2=M} C_{l_1m_1l_2m_2}^{LM}Y_{l_1m_1}(\theta_p,\varphi_p)Y_{l_2m_2}(\theta_q,\varphi_q),$$

the same functions in Fock–Bargmann space can be written as

$$\psi_{\nu KLMl_1l_2}(\mathbf{a},\mathbf{b}) = N_{\nu K}\rho^{2\nu+K}\Phi_K^{LMl_1l_2}(\gamma,\Omega_1,\Omega_2),$$

$$a = \rho\cos\gamma, \quad b = \rho\sin\gamma,$$

$$N_{\nu K} = \frac{1}{2^\nu}\sqrt{\frac{(K+2)!}{(\nu+K+2)!\nu!}}N_{0K},$$

$$N_{0K} = \frac{(2\pi)^{3/2}}{2^{K/2+1}\sqrt{(K+2)!}}.$$

So far, it has not been clear whether the Fock–Bargmann representation is advantageous in relation to the conventional coordinate representation. Upon applying the antisymmetrization operator, however, the picture is clarified—the basis functions in Fock–Bargmann space prove to be much simpler that the basis functions in coordinate space. We can see that, in the former, the antisymmetrization reduces to a linear transformation of the two Jacobi vectors **a** and **b**, while, in the latter, it is performed via an orthogonal transformation relating the five vectors **p**, **q**, $\mathbf{e}_1$, $\mathbf{e}_2$, and $\mathbf{e}_3$. It follows that, upon an arbitrary permutation of the particles, the function $\psi_{\nu KLMl_1l_2}(\mathbf{a},\mathbf{b})$ remains a function of two vector arguments, while the function $\Psi_{\nu KLMl_1l_2}(\mathbf{p},\mathbf{q})$ becomes a function of five vector variables.

In Fock–Bargmann space, basis states allowed by the Pauli exclusion principle can be obtained easily from an analysis of the overlap integral of two generating determinants Φ and $\tilde{\Phi}$,

$$\langle\tilde{\Phi}|\Phi\rangle = \det\{\langle\tilde{\varphi}_i|\varphi_j\rangle\},\ \langle\tilde{\phi}_i|\phi_j\rangle = \exp(\tilde{\mathbf{R}}_{(i)}\cdot\mathbf{R}_{(j)}), \quad (7)$$

that is, the integral of the product of the two determinants with respect to all single-particle variables. The second determinant $\tilde{\Phi}$ differs from the first one only in that its generator parameters are tilde-labeled; hence, they take the form $\tilde{\mathbf{a}}$ and $\tilde{\mathbf{b}}$ in the c.m. frame. The tilde-labeled generator parameters of the second determinant are introduced in order that the matrix elements computed preliminarily for various operators between Φ and $\tilde{\Phi}$ could be used, at a later stage, to determine the matrix elements of the same operators between basis functions characterized by specific values of the quantum numbers.

It is well known [3] that the overlap integral of the two determinants Φ and $\tilde{\Phi}$ represents a determinant having a simple quasidiagonal structure. By eliminating, from (7), the factor that describes the motion of the center of mass, we can reduce the overlap integral to the sum of four exponential terms:

$$\det\{\langle\tilde{\varphi}_i|\varphi_j\rangle\} = \exp(\tilde{\mathbf{R}}\cdot\mathbf{R})\langle\tilde{\mathbf{a}},\tilde{\mathbf{b}}|\mathbf{a},\mathbf{b}\rangle; \tag{8}$$

$$\begin{aligned}\langle\tilde{\mathbf{a}},\tilde{\mathbf{b}}|\mathbf{a},\mathbf{b}\rangle &= \exp(\tilde{\mathbf{a}}\cdot\mathbf{a}+\tilde{\mathbf{b}}\cdot\mathbf{b})\\ &-\exp(\tilde{\mathbf{a}}\cdot\mathbf{a}^{(1)}+\tilde{\mathbf{b}}\cdot\mathbf{b}^{(1)})\\ &-\exp(\tilde{\mathbf{a}}\cdot\mathbf{a}^{(2)}+\tilde{\mathbf{b}}\cdot\mathbf{b}^{(2)})+\exp(\tilde{\mathbf{a}}\cdot\mathbf{a}^{(3)}+\tilde{\mathbf{b}}\cdot\mathbf{b}^{(3)}),\end{aligned} \tag{9}$$

$$(\mathbf{a}^{(i)},\mathbf{b}^{(i)}) = T^{(i)}(\mathbf{a},\mathbf{b}),$$

$$T^{(1)} = \begin{pmatrix} \frac{1}{4} & \sqrt{\frac{3}{8}} \\ \sqrt{\frac{3}{8}} & \frac{1}{2}\end{pmatrix},\quad T^{(2)} = \begin{pmatrix} \frac{1}{4} & -\sqrt{\frac{3}{8}} \\ -\sqrt{\frac{3}{8}} & \frac{1}{2}\end{pmatrix},$$

$$T^{(3)} = \begin{pmatrix} -\frac{1}{2} & 0 \\ 0 & 0\end{pmatrix}.$$

Expression (9), which includes complete sets of states allowed by the Pauli exclusion principle vanishes if we set

$$\mathbf{b} = \pm\sqrt{\frac{3}{2}}\mathbf{a}.$$

This is because neither of the two neutron clusters can occur in those states that are occupied by the neutrons of the alpha cluster. From any state $f(\mathbf{a},\mathbf{b})$ expressed in terms of the vector Jacobi variables, we can go over to an allowed state by applying the antisymmetrization operator to the former, where this operator annihilates, in general, the contribution of the forbidden state. Specifically, we have

$$\begin{aligned}f_a(\mathbf{a},\mathbf{b}) &= \hat{A}f(\mathbf{a},\mathbf{b})\\ &= f(\mathbf{a},\mathbf{b})-f(\mathbf{a}^{(1)},\mathbf{b}^{(1)})-f(\mathbf{a}^{(2)},\mathbf{b}^{(2)})+f(\mathbf{a}^{(3)},\mathbf{b}^{(3)}).\end{aligned} \tag{10}$$

The choice of J^π determines the total angular momentum and the parity of the nuclear state. In our case, $J=0$, while the parity is positive. For $L=0$ states, the orbital angular momentum l_1 of the vector $\mathbf{a}$ must be equal to the orbital angular momentum l_2 of the vector $\mathbf{b}$. In addition, we find that, for the singlet state of the two neutron clusters and the main Jacobi tree, the quantity $l = l_1 = l_2$ can take only even positive integral values. In the case being considered, the grand orbital is also even. It is obvious that, for case where the grand orbital does not exceed a specific value K_a, the number of independent states of an arbitrary degree of homogeneity in the hyperradius is equal to the number of basis functions with the corresponding quantum numbers. If $L=0$ and if $l_1 = l_2 = l$ and K are even, we have

$$\begin{aligned}\psi_{\nu Kl}(\mathbf{a},\mathbf{b}) &= N_{\nu K}\rho^{2\nu+K}N_K^l\cos^l\gamma\sin^l\gamma\\ &\times P_{K/2-l}^{l+1/2}(\cos 2\gamma)\frac{\sqrt{2l+1}}{4\pi}P_l(t).\end{aligned} \tag{11}$$

If the principal quantum number $2\nu + K$ is fixed, only one state forbidden by the Pauli exclusion principle can be constructed from these states. It appears to be an eigenfunction of the antisymmetrization operator, the corresponding eigenvalue being equal to zero. Of all allowed states, it is reasonable to consider, above all, states that are characterized by the lowest values of the grand orbital because, in the equation of motion, a kinematical repulsive potential that increases with increasing grand-orbital value corresponds to basis functions. In the following, we will set $K_a = 4$. As a result, we obtain three branches of allowed states.

In the approximation of orthogonal conditions, the branches of allowed states can be constructed in the following way. By setting the grand orbital to its limiting value K_a in the present approach, we first find the lowest allowed states. We then multiply them by $\rho^{2\nu}$ and normalize.

For the principal quantum number $2n = 2\nu + K$, there exist many 0^+ allowed singlet states. Of these, we consider only those three for which the grand-orbital values are minimal. Each of these will be associated with one of the three branches (or, what is the same, with one of the three scattering channels) in such a way that the grand-orbital content of the branch remains unchanged with increasing number ν of hyperradial quanta.

The orthonormalized states Ψ_n^s of the three channels ($s = 1, 2, 3$) are expressed in terms of the basis functions (11) as

$$\Psi_n^1 = \sqrt{\frac{4n}{29n+75}}\psi_{n00}+\sqrt{\frac{25(n+3)}{29n+75}}\psi_{n-1\,20},$$

$$n = 1, \ldots,$$

$$\Psi_n^2 = \sqrt{\frac{M_n}{M_n+N_n}}$$

$$\times\left(\sqrt{\frac{25(n+3)}{29n+75}}\psi_{n00}-\sqrt{\frac{4n}{29n+75}}\psi_{n-1\,20}\right)$$

$$+\sqrt{\frac{N_n}{M_n+N_n}}\left(\frac{7}{\sqrt{561}}\psi_{n-2\,40}-\frac{16\sqrt{2}}{\sqrt{561}}\psi_{n-2\,42}\right),\quad n = 2, \ldots,$$

$$M_n = \frac{9n(n-1)}{29n+75},\quad N_n = \frac{25(n+4)}{561},$$

$$\Psi_n^3 = \frac{16\sqrt{2}}{\sqrt{561}}\psi_{n-2\,40}+\frac{7}{\sqrt{561}}\psi_{n-2\,42},\quad n = 2, \ldots.$$

Further, we will use the generic representation

$$\Psi_n^s = \sum_{(K)=0}^{K_a(s)} \sum_{l=0}^{K/2} \beta_{Kl}^{sn} \psi_{\nu(n,K)Kl} \sim \rho^{2n}, \qquad \nu(n,K) = n - K/2, \tag{12}$$

where summation is performed over even K and where the coefficients for the main Jacobi tree are equal to zero at odd l. For the upper limit of summation in (12), we have $K(1) = 2$ and up to $K_a(2, 3) = 4$.

It immediately follows from (12) that the first expression is the only branch for $K_a = 2$ whose lowest state appears to be a linear combination of the vectors **a** and **b** raised to the second power:

$$\Psi_1^1 \sim (3a^2 - 2b^2). \tag{13}$$

In Fock–Bargmann space, this homogeneous combination of second order in **a** and **b** is the translation-invariant shell-model wave function of the ^{6}He ground state.

The allowed states (12) can also be represented in terms of the vectors of the another Jacobi tree. These states involve, with nonzero coefficients, basis functions associated with odd l values. Under the orthogonal change of variables, one set of basis functions transforms into another set as the result of the orthogonal transformation $G_K^{ll'}$ that does not change the grand-orbital value [6].

This transformation can be represented as

$$\Psi_n^s = \sum_{(K)=0}^{K_a(s)} \sum_{l=0}^{K/2} \beta'^{sn}_{Kl} \psi_{\nu(n,K)Kl}(\mathbf{a}', \mathbf{b}'), \qquad \beta'^{sn}_{Kl} = \sum_{l'=0}^{K/2} G_K^{ll'} \beta_{Kl'}^{sn}. \tag{14}$$

A transition to other Jacobi trees is necessary in calculating the matrix elements of the potential-energy operator for nucleon–nucleon interaction.

3. MATRIX ELEMENTS OF THE HAMILTONIAN BETWEEN ALLOWED STATES

We will determine the structure of allowed states by using the overlap integral of the generating functions with the identity operator. In order to investigate the dynamics of the relative motion of the clusters, we must find the matrix elements of the Hamiltonian between the chosen allowed states. For this, we first calculate the overlap integrals of the generating functions and the kinetic- and potential-energy operators and then project them onto the allowed states associated with the branches being considered.

The kinetic-energy operator can be associated with its transform in Fock–Bargmann space. When this transform is applied to the overlap integral featuring unity, we obtain overlap integrals involving the kinetic-energy operator. By way of example, we indicate that, for the single-particle functions, we have

$$\langle \tilde{\phi}_i | \hat{t} | \phi_j \rangle = \frac{\hbar^2}{4m_n r_0^2} (3 - (\tilde{\mathbf{R}}_{(i)} - \mathbf{R}_{(j)})^2) \langle \tilde{\phi}_i | \phi_j \rangle, \tag{15}$$

where m_n is the nucleon mass. Upon going over to the Jacobi vectors for the system considered as a discrete unit, it is easy to write the kinetic-energy operator for the cluster degrees of freedom in the Fock–Bargmann representation. This yields

$$\hat{T} = \hat{T}^+ + \hat{T}^0 + \hat{T}^-, \tag{16}$$

$$\hat{T}^0 = \frac{\hbar^2}{4m_n r_0^2} (2(\mathbf{a}\nabla_{\mathbf{a}} + \mathbf{b}\nabla_{\mathbf{b}}) + 6),$$

$$\hat{T}^+ = -\frac{\hbar^2}{4m_n r_0^2}(a^2 + b^2), \quad \hat{T}^- = -\frac{\hbar^2}{4m_0 r_0^2}(\Delta_{\mathbf{a}} + \Delta_{\mathbf{b}}).$$

The matrix elements of the operator $\hat{T}$ between the basis functions have the form

$$\langle \nu + 1, KL; l_1 l_2 | \hat{T} | \nu, KL; l_1 l_2 \rangle = -\frac{\hbar^2}{2m_n r_0^2} \sqrt{(\nu + K + 3)(\nu + 1)},$$

$$\langle \nu, KL; l_1 l_2 | \hat{T} | \nu, KL; l_1 l_2 \rangle = \frac{\hbar^2}{2m_n r_0^2} (2\nu + K + 3),$$

$$\langle \nu - 1, KL; l_1 l_2 | \hat{T} | \nu, KL; l_1 l_2 \rangle = -\frac{\hbar^2}{2m_n r_0^2} \sqrt{(\nu + K + 2)\nu}.$$

Let us write the full matrix element of the kinetic-energy operator for $\tilde{n}$ and n states of the corresponding branches $\tilde{s}$ and s at $L = 0$. We have

$$\langle \tilde{s}, \tilde{n} | \hat{T} | s, n \rangle = \sum_{K=0}^{K_a(\min(\tilde{s}, s))} \sum_{l=0}^{K/2} \beta_{Kl}^{\tilde{s}\tilde{n}} \times \beta_{Kl}^{sn} \langle \tilde{\nu}(\tilde{n}, K), K | T | \nu(n, K), K \rangle. \tag{17}$$

The kinetic-energy matrix in the representation of states of the single channel has a tridiagonal form. Only the elements appearing on its principal diagonal and on the two neighboring diagonals are nonzero. Apart from this, there exist matrix elements relating the states of the first and the second channel:

$$\langle 2, n | \hat{T} | 1, n - 1 \rangle = -\frac{\hbar^2}{2m_n r_0^2} \times \sqrt{\frac{M_n}{M_n + N_n}} \frac{30}{\sqrt{(29n + 75)(29n + 104)}}.$$

Because the problem involves many channels, the Hamiltonian matrix consists of submatrices. In the calculations, the dimensions of these submatrices are chosen in such a way that the principal quantum number takes the same value in all channels.

The nucleon–nucleon interaction is simulated by the Minnesota potential [7], which has the form of the sum of three Gaussian functions with coefficients that depend on the spin and isospin of the interacting particles:

$$U(\mathbf{r}_i, \mathbf{r}_j) = \sum_{p=1}^{3} V_{2S+1,\,2T+1}(p) \exp\left(-\frac{(\mathbf{r}_i - \mathbf{r}_j)^2}{\mu(p)^2}\right).$$

The potential energy of the system formed by an alpha particle and two neutrons was reckoned from the energy that this system has when all three clusters constituting it are separated by infinitely large distances. Here, we are interested only in the interactions of neutron clusters with each other and with the alpha-particle cluster. The overlap integral of the direct interaction of two nucleons was calculated as the integral of the product of the nucleon potential and two generating functions that differ only by the notation for the generator parameters. We performed a permutation of the coordinates of the interacting nucleons in one of the generating functions in order to take into account exchange interaction. As the final result of this stage of the calculation, we obtained the generating matrix element of the potential-energy operator in the form

$$\langle \tilde{\Phi}|U|\Phi\rangle = \sum_{w=1}^{4} \langle \tilde{\Phi}|U_w|\Phi\rangle, \tag{18}$$

$$\langle \tilde{\Phi}|U_w|\Phi\rangle = \sum_{p=1}^{3} z^{3/2}(p) A(p, w)$$

$$\times \exp(\tilde{\mathbf{a}}_w \cdot \mathbf{a}_w + B(p, w)\tilde{\mathbf{b}}_w \cdot \mathbf{b}_w + D(p, w)(\tilde{b}_w^2 + b_w^2)),$$

$$(\mathbf{a}_w, \mathbf{b}_w) = (\mathbf{a}, \mathbf{b}), \quad w = 1, 2;$$

$$(\mathbf{a}_w, \mathbf{b}_w) = (\mathbf{a}', \mathbf{b}'), \quad w = 3, 4;$$

$$z(p) = \left(1 + \frac{2r_0^2}{\mu(p)^2}\right)^{-1}.$$

In this expression, each term corresponds to a specific interaction in the system. The first and the second term are associated with, respectively, the direct and the exchange interaction of the neutron clusters. The third and the fourth term correspond to, respectively, the direct and the exchange neutron–alpha interaction. These terms are calculated by using the vectors of an auxiliary Jacobi tree.

The parameters B and D in the generating matrix elements for various w and the factors A in front of them are given by

w	B	D	A
1	z	$(z-1)/2$	$(V_{33} + V_{13})/2$
2	$-z$	$(z-1)/2$	$-(V_{33} - V_{13})/2$
3	$(3+5z)/8$	$5(z-1)/16$	$(9V_{33} + 3V_{31} + 3V_{13} + V_{11})/2$
4	$(3-5z)/8$	$5(z-1)/16$	$-(9V_{33} - 3V_{31} - 3V_{13} + V_{11})/2.$

(19)

At the next stage, we project the generating matrix elements (18) onto basis states characterized by specific values of the angular quantum numbers. Specifically, we have

$$\langle \tilde{\nu}\tilde{K}l_1l_2\left|\exp(\tilde{\mathbf{a}} \cdot \mathbf{a} + B\tilde{\mathbf{b}} \cdot \mathbf{b} + D(\tilde{b}^2 + b^2))\right|\nu K l_1 l_2\rangle$$

$$= \sum_{n_1=0}^{\min(\tilde{\nu}+\tilde{m},\,\nu+m)} \sum_{n_2=0}^{\min(\tilde{\nu}+\tilde{m}-n_1,\,\nu+m-n_1)} \frac{(4\pi)^2 B^{2n_2+l_2} D^{\tilde{\nu}+\nu+\tilde{m}+m-2n_1-2n_2}}{(2n_1)!!(2n_1+2l_1+1)!!(2n_2)!!(2n_2+2l_2+1)!!}$$

$$\times \frac{C_K^{n_1,\,\tilde{\nu}+\tilde{m}-n_1}(l_1, l_2) C_K^{n_1,\,\nu+m-n_1}(l_1, l_2)}{(\tilde{\nu}+\tilde{m}-n_1-n_2)!(\nu+m-n_1-n_2)!} \frac{1}{N_{\tilde{\nu}\tilde{K}} N_{\nu K}},$$

where

$$C_K^{n_1, n_2}(l_1, l_2) = \frac{1}{2} N_K^{l_1 l_2} \sum_{m_1+m_2=m} \frac{(-1)^{m_2} n_1! n_2!}{m_1! m_2! (n_1-m_1)! (n_2-m_2)!} B\left(n_1 + m - m_1 + l_1 + \frac{3}{2}, n_2 + m - m_2 + l_2 + \frac{3}{2}\right),$$

$$\tilde{m} = (\tilde{K} - l_1 - l_2)/2, \quad m = (K - l_1 - l_2)/2.$$

We now represent the full matrix element of the cluster-interaction operator between the allowed states under consideration as

$$\langle \tilde{s}, \tilde{n}|\hat{U}|s, n\rangle = \sum_{p=1}^{3}\sum_{w=1}^{4} A(p, w) z^{3/2}(p)$$

$$\times \sum_{(K)=0}^{K_a(s)} \sum_{(\tilde{K})=0}^{K_a(\tilde{s})} \sum_{l=0}^{\min(K/2, \tilde{K}/2)} \beta_{\tilde{K}l}^{\tilde{s}\tilde{n}}(w)\beta_{Kl}^{sn}(w)$$

$$\times \langle \tilde{\nu}(\tilde{n}, \tilde{K}), \tilde{K}, l|u(B(p, w), D(p, w))|\nu(n, K), K, l\rangle.$$

The coefficients of the basis functions are determined by the Jacobi tree on which the calculation of the generating matrix element was performed.

By numerically evaluating the matrix elements of the Hamiltonian and by solving the set of algebraic equations that is obtained from the wave equation in the approximation chosen here, we arrive at the eigenfunctions

$$\Psi_s(r) = \sum_n C_n^{(s)} \Psi_n^s(r)$$

for various channels. They are expressed in terms of the allowed basis states and eigenvectors of the Hamiltonian matrix.

4. ASYMPTOTIC BEHAVIOR OF EXPANSION COEFFICIENTS

It is well known that, in the *K*-matrix representation, the asymptotic form of the expressions that the algebraic version of the resonating-group method (AVRGM) yields for the coefficients $C_n^{(s)}$ in the expansion of the continuous-state wave function in the harmonic-oscillator basis appears to be a linear superposition of a regular and a singular solution to the wave equation in those regions of coordinate space where the potential can be disregarded or where the potential reduces to the Coulomb potential. Here, it is necessary to determine the coefficients in the above linear superposition or the *K*-matrix elements associated with them.

In the minimal approximation of the method of hyperharmonics, where only the basis functions of the first channel are taken into account, the coefficients $C_n^{(1)}$ in the expansion of continuous-state wave functions in the basis of allowed states have simple asymptotic forms that are determined by the set of AVRGM equations in the limit of large *n*. The coefficients of the basis functions in allowed states then cease to depend on *n* and can be expressed in terms of the *K*-matrix elements. Therefore, we further write β_{Kl}^{s}. Via the matrix elements of the kinetic-energy operator $\hat{T}$, each of the asymptotic equations relates only three coefficients—$C_{n-1}^{(1)}$, $C_n^{(1)}$, and $C_{n+1}^{(1)}$. If $x = n + 3/2 = \nu + K/2 + 3/2 \gg 1$, the expansion

$$\langle \nu, K|\hat{T}|\nu \pm 1, K\rangle \simeq -\frac{\hbar^2}{2m_n r_0^2} x\left(1 \pm \frac{1}{2x} - \frac{(K+2)^2}{8x^2}\right) \quad (20)$$

in inverse powers of *x* holds for the nondiagonal matrix elements of the operator $\hat{T}$. In the limit $x \gg 1$, there is also a nonzero diagonal matrix element [8] of that part of the potential-energy operator which decreases slowly with increasing hyperradius. At very large values of *n*, we can also disregard that diagonal element. Assuming that the coefficients $C_n^{(1)}$ become, in this case, continuous functions of the hyperradius $r = 2\sqrt{x}$ of configuration space, we can then go over from the algebraic equations

$$x\left(2C_n^{(1)} - (C_{n-1}^{(1)} + C_{n+1}^{(1)}) - \frac{1}{2x}(C_{n+1}^{(1)} - C_{n-1}^{(1)}) + \frac{\mu_{(1)}^2}{8x^2}(C_{n-1}^{(1)} + C_{n+1}^{(1)})\right) = \varepsilon C_n^{(1)},$$

$$\varepsilon = \frac{2mr_0^2 E}{\hbar^2}, \quad \mu_{(1)}^2 = \frac{416}{29}$$

to the differential Bessel equation

$$\frac{d^2C^{(1)}}{dr^2} + \frac{1}{r}\frac{dC^{(1)}}{dr} + \left(\varepsilon - \frac{\mu_{(1)}^2}{r^2}\right)C^{(1)} = 0. \quad (21)$$

The index value of $\mu_{(1)}^2 = 416/29$ for the asymptotic equation of the minimal approximation reflects the fact that the allowed states of the first branch appear to be a superposition of hyperharmonics with the different grand-orbital values of $K = 0$ and 2.

Thus, we conclude that, in the minimal one-channel approximation, the asymptotic form of the coefficients $C_n^{(1)}$ appears to be a linear combination of cylindrical functions; that is,

$$C_n^{(1)} \simeq AJ_{\mu_{(1)}}(\sqrt{\varepsilon}\sqrt{4n+6}) + BN_{\mu_{(1)}}(\sqrt{\varepsilon}\sqrt{4n+6}). \quad (22)$$

Actual calculations reveal that, because of a small decrease of the diagonal matrix element of the potential-energy operator [in proportion to $1/(4n+6)^{3/2}$], a limiting transition to Bessel equations at the energy of

a continuum state about a few MeV is possible for $n > 10^3$. This value increases with decreasing energy. The resulting technical difficulties do not create serious problems and can be sidestepped easily. We note that the above algebraic equations can be treated as three-term recursion relations. By specifying, at large n, a regular (Bessel function) or a singular (Neumann function) basis solution in the absence of a potential and using the above recursion relations, we can straightforwardly go over to small n and construct each of the basis solutions with allowance for the effect of a slowly decreasing potential. As a result, the problem reduces to a set of a moderately small number of equations with asymptotic conditions in the form of a linear combination of the rearranged regular and the rearranged singular solution, and it is the coefficients in this combination that are quantities to be determined. Let us explain the character of the above rearrangement in some detail.

We begin by indicating that, in the approximation of three channels and in the limit of very large n, in which case we disregard the matrix elements of the potential-energy operator, three separate sets of equations cannot be obtained even by using hyperspherical quantum numbers for a basis of allowed states. The sets of equations remain coupled via the matrix elements of the kinetic-energy operator; this is because, despite the orthogonality of the basis functions of different channels, they do not contain, by virtue of the Pauli exclusion principle, components characterized by the same value of the grand orbital. In order to remove this coupling, it is necessary to apply an additional orthogonal transformation to the initially chosen basis states of various channels. The matrix elements of this orthogonal transformation are determined upon going to the asymptotic form of the relevant equations.

For our choice of three branches of allowed states, the matrix elements of the kinetic-energy operator relate the first and the second channel. For $n \gg 1$, in which case the coefficients $C_n^{(s)}$ are almost continuous functions of the variable $r = \sqrt{4n+6}$, the set of algebraic equations reduces to a set of three differential equations for the coefficients $C^{(s)}(r) = C_n^{(s)}$. The matrix form of this set of equations is

$$\left(\frac{d^2}{dr^2} + \frac{1}{r}\frac{d}{dr} + \varepsilon\right)\mathbf{C} - \frac{1}{r^2}\hat{\mu}^2\mathbf{C} = 0,$$

$$\mathbf{C} = \begin{pmatrix} C^{(1)}(r) \\ C^{(2)}(r) \\ C^{(3)}(r) \end{pmatrix}, \tag{23}$$

where

$$\hat{\mu}^2 = \begin{pmatrix} \mu_{(1)}^2 & \mu_{(12)}^2 & 0 \\ \mu_{(12)}^2 & \mu_{(2)}^2 & 0 \\ 0 & 0 & \mu_3^2 \end{pmatrix}, \tag{24}$$

$$\mu_{(s)}^2 = \sum_{(K)=0}^{K_a(s)} \sum_{l=0}^{K/2} (\beta_{Kl}^s)^2 (K+2)^2,$$
$$\mu_{(12)}^2 = \sum_{(K)=0}^{2} (\beta_{K0}^{(1)}\beta_{K0}^{(2)})(K+2)^2. \tag{25}$$

By using a simple transformation of the linear equations for the first two channels, we can go over to uncoupled Bessel equations with the indices

$$\mu_1^2 \simeq 14.34, \quad \mu_2^2 \simeq 9.47, \quad \mu_3^2 = \mu_{(3)}^2 = 36, \tag{26}$$

which are eigenvalues of the matrix $\hat{\mu}^2$ and which determine the asymptotic behavior of the rearranged solutions:

$$\bar{\mathbf{C}} = \begin{pmatrix} \bar{C}^{(1)}(r) \\ \bar{C}^{(2)}(r) \\ \bar{C}^{(3)}(r) \end{pmatrix}$$
$$= \begin{pmatrix} \cos\phi C^{(1)}(r) + \sin\phi C^{(2)}(r) \\ -\sin\phi C^{(1)}(r) + \cos\phi C^{(2)}(r) \\ C^{(3)}(r) \end{pmatrix}. \tag{27}$$

The angle $\phi = 0.504$ rad plays the role of the parameter in the orthogonal transformation from the original solutions to the rearranged ones.

In the case of small values of n, it is necessary to take into account both the diagonal matrix elements of the potential-energy operator and the nondiagonal matrix elements, which couple different channels. If, for example, the asymptotic basis solution in one of the channels can be represented by a Bessel function, the recursion relations that follow from the AVRGM equations therefore generate, in going over to small values of n, nonzero components of this basis solution in other channels that are coupled to the original channel via the matrix elements of the potential. In this way, a regular basis solution is spread over all coupled channels. The same happens to other regular and singular asymptotic basis solutions that are then used to determine the asymptotic behavior of the expansion coefficients at comparatively small values of n.

It should be emphasized that the problem in question is associated with the long-range character of the three-cluster potential and with the structure of allowed

states, which leads to the matrix elements of the kinetic and potential energies. This resembles the problem that arises in studying the polarizability of Coulomb systems.

In order to construct the wave functions of the continuous spectrum and to reproduce scattering data, we first determine the K-matrix elements by expressing the asymptotic forms of the rearranged eigenfunctions of the three channels in terms of these matrix elements:

$$\bar{C}_n^{(s)} = \delta_{s's} J_{\mu_s}(\sqrt{\varepsilon}\sqrt{4n+6}) - K_{s's} N_{\mu_s}(\sqrt{\varepsilon}\sqrt{4n+6}). \quad (28)$$

Here, the index s' indicates which regular solution of the three possible ones forms a continuum state. Recall that we consider a problem featuring three open channels. In order to find the K matrix, it is therefore necessary to have three independent solutions [9] to the set of algebraic equations of the resonating-group method or the method of orthogonal conditions. After that, we go over to the S matrix [9]

$$\hat{S} = (1 - i\hat{K})(1 + i\hat{K})^{-1} \quad (29)$$

and calculate its eigenphases δ_k according to the relation

$$S_{jk} = \delta_{jk}\exp(-2i\delta_k). \quad (30)$$

These phases provide a full characterization of data on $3 \longrightarrow 3$ scattering in each of the three channels.

5. APPROXIMATION OF AN ASYMPTOTIC POTENTIAL

The mean value of the hyperradius of the ground-state ^{6}He nucleus exceeds the range of nuclear forces; therefore, the approximation of an asymptotic potential is valid, in which case the exact values of the matrix elements of the potential-energy operator are replaced by their asymptotic values. In each channel, there then remain only the diagonal matrix elements and only those of nondiagonal ones that couple states that belong to different channels, but which are characterized by the same value of the principal quantum number (see [8]).

By way of example, we consider the asymptotic behavior of the matrix elements of the potential-energy operator. Let us first evaluate an auxiliary integral of the operator of the potential energy of nucleon–nucleon interaction and the normalized hyperspherical harmonics,

$$\langle Kl_1l_2|V_0\exp(-\alpha q^2)|\tilde{K}l_1l_2\rangle_{\rho\to\infty}$$

$$\approx V_0 M_{K\tilde{K}}^{l_2;\,l_1}\frac{1}{\Gamma(l_2+3/2)}\frac{\alpha^{l_2+3/2}}{r^{2l_2+3}},$$

$$M_{K\tilde{K}}^{l_2;\,l_1} = N_K^{l_1l_2}N_{\tilde{K}}^{l_1l_2}P_m^{l_2+1/2,\,l_1+1/2}(1)P_{\tilde{m}}^{l_2+1/2,\,l_1+1/2}(1),$$

and make use of the fact that, in coordinate space, the hyperradial oscillator basis functions $R_{\nu K}(r)$ possess the remarkable general property [10]

$$R_{\nu K}(r)r^3 \simeq \sqrt{2}\delta(r - \sqrt{4n+6}).$$

The value of $r_n = \sqrt{4n+6}$ with $n = \nu + K/2$ corresponds to the classical turning point in the oscillator potential $r^2/2$. For the asymptotic matrix elements of the potential-energy operator between the allowed states, we eventually obtain

$$\langle\tilde{s},\tilde{n}|U|s,n\rangle = \sum_{l=0}^{K_a(\min(s,s'))/2}\frac{A_l^{\tilde{s}s}}{(4n+6)^{2l+3}}\delta_{n\tilde{n}}, \quad (31)$$

$$A_l^{\tilde{s}s} = \sum_{p=1}^{3}\sum_{w=1}^{4}\sum_{(K)=2l}^{K_a(s)}\sum_{(\tilde{K})=2l}^{K_a(\tilde{s})}\frac{A(p,w)M_{K\tilde{K}}^l}{\Gamma(l+3/2)}$$

$$\times\frac{z^{3/2}B(p,w)^l}{(-2D(p,w))^{l+3/2}}\beta_{Kl}^s(w)\beta_{\tilde{K}l}^{\tilde{s}}(w).$$

The matrix elements in (31) couple states that belong to different channels, but which are characterized by the same value of the principal quantum number n—that is, states that have the same degree of homogeneity in the hyperradius ρ in Fock–Bargmann space.

Of course, expressions (31) approximate the matrix elements of the potential-energy operator only in the case of $n \gg 1$. Since the ^{6}He nucleus has a rather extended structure, we will use, however, the approximation in (31) for the entire set of allowed states. Our preliminary estimates reveal that this does not lead to significant errors; at the same time, the scheme for reproducing scattering data is significantly simplified within this framework. In addition, the parameters of the asymptotic potential at nonzero l that correspond to the interior of the nucleus were corrected by introducing a factor of 1.76 in order to reproduce the observed values of the energy and the root-mean-square radius of the ^{6}He ground state.

6. RESULTS OF THE CALCULATIONS AND THEIR DISCUSSION

6.1. One-Channel Approximation

It was indicated above that, in the one-channel approximation implemented within the model used here, the ^{6}He nucleus has a 0^+ bound state at 0.96 MeV, its root-mean-square radius being 2.48 fm. In the same approximation, Fig. 1*a* shows the phase shift for $3 \longrightarrow 3$ elastic scattering as a function of energy E. We will now indicate some special features in the behavior of this phase shift.

First, its derivative with respect to energy grows indefinitely at the threshold point, as it must [11], because, in the three-cluster system, the potential energy generated by attractive nucleon–nucleon forces

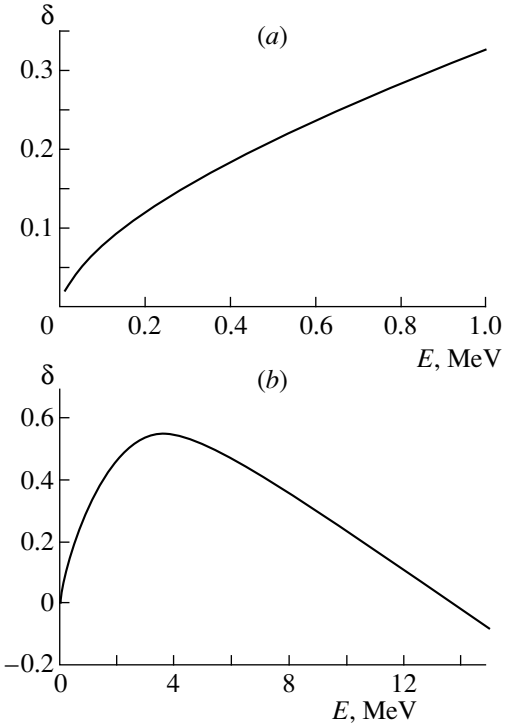

Fig. 1. Phase shift δ in the approximation of the minimal grand orbital (*a*) at low energies and (*b*) at higher energies.

decreases in inverse proportion to the hyperradius cubed. In the vicinity of the threshold, the phase shift is therefore proportional to the square root of energy (see [12]), the proportionality factor being 0.26. In numerical calculations, precautions must be taken, however, to reproduce faithfully the energy dependence of the phase shift in the region of low energies. The point is that the lower the energy, the larger the distances at which the slowly decreasing potential begins to affect the asymptotic behavior of the wave function.

Second, the phase shift grows from zero energy and attains a maximum value of 0.55 rad at $E = 3.6$ MeV (see Fig. 1*b*). In this region, the derivative of the phase shift with respect to energy decreases monotonically, which rules out the existence of a resonance.

Of practical interest is in fact the region of comparatively low energies from zero to 10 MeV; nonetheless, we performed our calculations at higher energies as well in order to verify the extent to which general requirements are satisfied. Taking into account Levinson's theorem [13] and considering that only one bound state (0^+) exists in our system, we can assume that, as the energy grows indefinitely, the limiting value of the phase shift must be $-\pi$. In fact, the phase shift continues to decrease slowly upon reaching the value of $-\pi$. This phenomenon is explained by the effect of the Pauli exclusion principle on the structure of the wave functions of the 0^+ allowed basis states. These wave functions vanish when the neutron clusters occur in the orbits of the 1*s* shell of the alpha-particle cluster. In the system in question, there arises an effective repulsion at small values of the hyperradius. For this reason, the matrix elements of the operator of the kinetic energy of a three-cluster system differ from the matrix elements of the same operator for the free motion of three clusters, where no account is taken of the effect of the Pauli exclusion principle and where the phase shift for $3 \longrightarrow 3$ scattering vanishes identically if the matrix elements of the potential-energy operator are disregarded. The elimination of states that are forbidden by the Pauli exclusion principle is equivalent to the emergence of an effective repulsion in the system at small values of the hyperradius. As follows from our calculations, the effect of this repulsion on the phase shifts is similar to that of a hard core of small radius. As a result, there arises a nonzero phase shift even if the AVRGM equations do not feature matrix elements of the potential-energy operator. This phase shift is negative and depends linearly on energy. But when the potential is taken into account, the phase shift falls below the expected limiting value of $-\pi$ at large energies owing to the impact of the effective repulsion. In the absence of the repulsion caused by the Pauli exclusion principle, the difference of the phase shift and the value of $-\pi$ at large values of the energy E would be equal to $C_\infty E^{-1/2}$, where $C_\infty = 6.4$ MeV$^{1/2}$.

6.2. Three-Channel Approximation

In the three-channel approximation, the continuous spectrum is triply degenerate—that is, at any specific energy of the continuous spectrum, there exist three solutions that differ by the number of the channel featuring both a converging and a diverging wave, only diverging waves being present in the remaining two channels. In order to obtain clear and compact information, we will make use of the S matrix in the representation of its eigenvectors, where only unimodular diagonal elements are nonzero; therefore, it is sufficient to know in that case only the energy dependences of the three phase shifts. These dependences are illustrated in Fig. 2. Indicated immediately below are their basic features.

In the vicinity of zero energy value, only two phase shifts vary in direct proportion to the square root of energy (Fig. 2*a*), the proportionality factors being 0.147 and 0.314 here. At the origin, the third phase has a zero derivative, and its values are negative. In this eigenchannel, the potential energy decreases in inverse proportion to the fifth power of the hyperradius, and it is this circumstance that explains the behavior of the third phase shift of the channel at zero energy.

At an energy value of $E = 6.4$ MeV, there is a quasi-intersection of two phase shifts (Fig. 2*b*). It reflects the general property of the eigenvalues of a unitary S matrix reduced to a diagonal form.

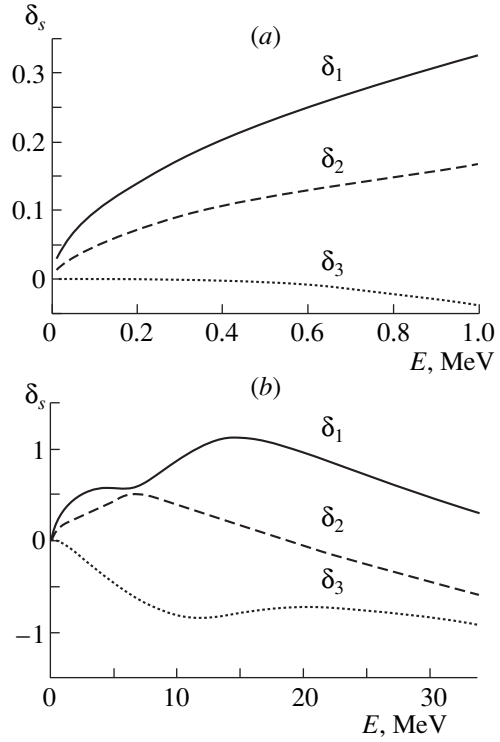

Fig. 2. Eigenphases δ_1, δ_2, and δ_3 of the S matrix in the three-channel approximation (*a*) at low energies and (*b*) at higher energies.

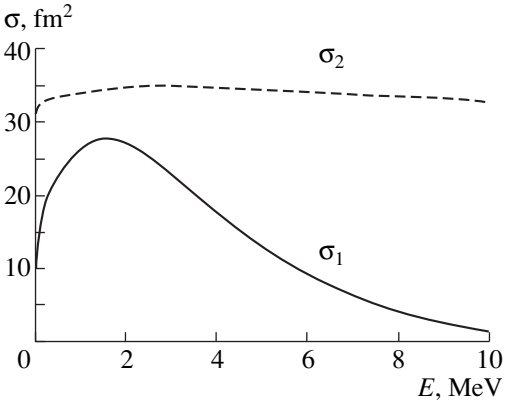

Fig. 3. Scattering cross sections: (σ_1) cross section in the approximation of a minimal grand orbital and (σ_2) total cross section in the three-channel approximation.

Although the system has only one bound state, all three phase shifts sink to the value of $-\pi$ with increasing energy. In the region of energies at which our calculations were performed, two phase shifts fall below this value, whereas the third one only approaches it. The continuum-state energy at which the channel phase shift is equal to $-\pi$ must be much greater than the potential energy in this channel. Therefore, the lesser the difference between the phase shift and the value of $-\pi$, the greater is the actual potential energy.

In just the same way as the cross section for binary processes, the cross section for $3 \longrightarrow 3$ scattering is expressed in terms of S-matrix elements. Here, it is necessary to consider that transitions from the input channel featuring a converging wave into other channels may occur and that these transitions are accompanied by changes in the grand-orbital value. As a result, the total cross section for $3 \longrightarrow 3$ scattering is now equal to the sum of three cross sections (see Fig. 3). In the energy region below 10 MeV, where the main contribution comes from two terms, this sum considerably exceeds the cross section in the one-channel approximation. This circumstance is important for obtaining an accurate estimate of the probability of nonradiative neutron capture by an alpha particle, a quantity that is of importance for astrophysics. A detailed calculation of the probability of this nonradiative neutron capture, as well as a calculation of the probability of electromagnetic transitions from the continuous spectrum to the ground state of ^{6}He, is also possible within the approach considered here, and we hope to present the results of such calculations in our forthcoming publication.

7. CONCLUSION

A basis of harmonic-oscillator states has been constructed from those linear combinations of hyperspherical functions that are allowed by the Pauli exclusion principle. This basis has been used to study the continuous spectrum of the ^{6}He nuclear system above the threshold for its three-body breakup. In the approximation of three 0^+ channels with minimal grand-orbital values, the behavior of the eigenphases of the S matrix for $3 \longrightarrow 3$ scattering highlights the important role of long-range potential components, which form the energy dependences of these phases in the region extending from the threshold to 5 MeV. If noncentral forces are disregarded, these phase shifts show no evidence for the existence of 0^+ resonances in the ^{6}He nuclear system. The effect of forbidden states on the energy dependences of the phases shifts becomes noticeable with increasing energy when the phase shifts fall below the value of $-\pi$.

A priori, we cannot rule out the importance of such three-body-breakup channels, for which the convergence of the method of hyperspherical functions is poor and which can substantially affect resonance widths. This problem is beyond the scope of the present article, but we hope to discuss it elsewhere.

REFERENCES

1. M. V. Zhukov, B. V. Danilin, D. V. Fedorov, *et al.*, Phys. Rep. **231**, 151 (1993).
2. G. F. Filippov, K. Kato, and S. V. Korennov, Prog. Theor. Fiz. **96**, 575 (1996).
3. G. F. Filippov, I. Yu. Rybkin, S. V. Korennov, *et al.*, J. Math. Phys. **36**, 4571 (1995).

4. D. M. Brink, *Enrico Fermi International School in Physics* (Academic, New York, 1995), Course 36, p. 247.
5. A. M. Perelomov, *Generalized Coherent States and Their Applications* (Nauka, Moscow, 1987; Springer-Verlag, New York, 1986).
6. J. Reinal and J. Revai, Nuovo Cimento A **68**, 612 (1970).
7. D. R. Thompson, M. LeMege, and Y. C. Tang, Nucl. Phys. A **286**, 53 (1977).
8. G. F. Filippov, A. D. Bazavov, K. Kato, *et al.*, Yad. Fiz. **60**, 635 (1997) [Phys. At. Nucl. **60**, 554 (1997)].
9. A. I. Baz', Ya. B. Zel'dovich, and A. M. Perelomov, *Scattering, Reactions and Decays in Nonrelativistic Quantum Mechanics*, transl. of 1st Russ. ed. (2nd ed., Nauka, Moscow, 1971; Israel Program of Scientific Translations, Jerusalem, 1966).
10. G. F. Filippov, Yad. Fiz. **33**, 928 (1981) [Sov. J. Nucl. Phys. **33**, 488 (1981)].
11. G. F. Filippov, I. Yu. Rybkin, and S. V. Korennov, Yad. Fiz. **59**, 616 (1996) [Phys. At. Nucl. **59**, 584 (1996)].
12. L. D. Landau and E. M. Lifshitz, *Quantum Mechanics: Non-Relativistic Theory*. Transl. of 3rd Russ. ed. (4th ed., Nauka, Moscow, 1989; Pergamon, Oxford, 1977).
13. N. Levinson, K. Dan, Vidensk. Selsk. Mat. Fys. Medd. **25** (9), 1 (1949).

Translated by A. Isaakyan

Physics of Atomic Nuclei, Vol. 63, No. 2, 2000, pp. 191–194. Translated from Yadernaya Fizika, Vol. 63, No. 2, 2000, pp. 244–247.

NUCLEI
Theory

Relation between Signature Splitting in Rotational Bands of Odd Nuclei and the Amplitude of the Ω = 1/2 Component

R. V. Jolos

Joint Institute for Nuclear Research, Dubna, Moscow oblast, 141980 Russia

Received November 17, 1998; in final form, April 5, 1999

Abstract—The relation between signature splitting in the spectra of rotational bands of odd nuclei and the structure of wave functions of these states is investigated. Rotational bands are considered both in axisymmetric nuclei and in nuclei that do not possess axial symmetry. A simple formula is obtained that makes it possible to extract the amplitude of the Ω = 1/2 wave-function component from experimental data on energy spectra. *© 2000 MAIK "Nauka/Interperiodica".*

1. INTRODUCTION

Both phenomenological and microscopic methods for studying the structure of deformed nuclei are based on the concept of mean field that is not spherically symmetric, but which can possess, for example, axial symmetry. Since the mean field is not spherically symmetric, many phenomena associated with the structure of deformed nuclei are analyzed in terms of a coordinate frame that is rigidly bound with the mean field [1, 2]. In the case of deformed nuclei, the mean field does not possess the symmetry of the total Hamiltonian; therefore, the symmetry of the intrinsic wave function is lower than the symmetry of the total wave function. This is because dynamical variables associated with the corresponding symmetry transformations are separated upon going over to the intrinsic coordinate frame. Upon this transition, some discrete symmetries survive, however, and we arrive at two-component intrinsic wave functions characterized by constructive or destructive interference, depending on the parity of the angular momentum. By way of example, we indicate that, in the case of axially deformed odd nuclei, states having positive and negative projections of the angular momentum of an odd particle onto the axial-symmetry axis (Ω) are degenerate in energy, so that both components are present in the wave function [1].

Of course, a fixed value of Ω corresponds to an idealized case. Interaction mixes components having different Ω values. Because of Coriolis forces, it looks as if the system moves along the Ω axis. Thus, we can see that, in the case being considered, we are dealing with a dynamical system that can be described by the one-dimensional Schrödinger equation in a potential having two symmetric minima. It is well known (see, for example, [3]) that, in the case of a potential featuring two symmetric minima, states having a positive and a negative parity with respect to the reversal of the coordinate sign are split in energy, the magnitude of this splitting being determined by the wave-function value at the barrier separating the two minima. Manifestations of such phenomena include a nonmonotonic angular-momentum dependence of the energy of states belonging to rotational bands of even nuclei [4]. As was shown in [5, 6], a change in the orientation of the angular momentum of an odd particle with respect to the angular momentum associated with a collective rotation can be considered as a motion that is governed by a potential featuring two symmetrically situated minima and which occurs along the coordinate appearing to be the projection of the angular momentum of an odd particle onto the symmetry axis. In this case, so-called favored and unfavored states are, respectively, symmetric and antisymmetric with respect to the reversal of the sign of Ω.

Since there are very accurate data on a nonmonotonic behavior of the energy of states belonging to the rotational bands of even nuclei, it would be useful to establish a relationship between the signature splitting of levels belonging to rotational bands, which appears to be quantitative measure of the above nonmonotonic behavior, and the amplitude of the Ω = 1/2 component. Having such a relation at our disposal, we can then deduce information about the wave functions of rotational states from the energy spectra. Specifically, a particle-plus-rotor model featuring an isolated *j* level is considered for the cases where the even–even core either possesses axial symmetry or is nonaxial.

2. AXISYMMETRIC CORE

In the case of an axisymmetric even–even core, the wave function of an odd-nucleus state characterized by an angular momentum I and its projection M can be represented as

$$\Psi_{IM} = \sum_{\Omega} C_{Ij}(\Omega) D^{I}_{M\Omega} \psi_{j\Omega}, \qquad (1)$$

where $D^{I}_{M\Omega}$ is a Wigner function, while $\psi_{j\Omega}$ is the wave

1063-7788/00/6302-0191$20.00 © 2000 MAIK "Nauka/Interperiodica"

function of an odd particle. The amplitudes $C_{Ij}(\Omega)$ possess the following symmetry property:

$$C_{Ij}(-\Omega) = (-1)^{I-j} C_{Ij}(\Omega). \quad (2)$$

Thus, the amplitudes $C_{Ij}(\Omega)$ are symmetric or antisymmetric functions of Ω, depending on the sign of $(-1)^{I-j}$ (signature). However, we can formally consider two solutions to the Schrödinger equation for each value of the angular momentum I: of these, one is symmetric under the reversal of the sign of Ω, while the other is antisymmetric. One solution is physical, and the other is unphysical. That the use of the two solutions for each value of I is convenient can be seen from the following considerations. Instead of studying the energy difference between the physical states that are characterized by the angular momenta $I + 1$ and I and which are distinguished in signature, we will consider the energy splitting of two states—a symmetric and an antisymmetric one—for each value of I. The magnitude of splitting is a smooth function of the angular momentum. The energies of unphysical states corresponding to forbidden combinations of the angular momentum I and parity with respect to the reversal of the sign of Ω can be obtained by means of an interpolation between the experimental values of the energies of the states having the angular momenta $I + 1$ and $I - 1$ and the same parity under the reflection $\Omega \longrightarrow -\Omega$ as that of the unphysical state having the angular momentum I. This is possible because the energies of states corresponding to a specific parity with respect to the reversal of the sign of Ω represent a smooth function of I.

In order to derive the sought relation, we consider the Schrödinger equation for the symmetric and antisymmetric wave functions [$C_{Ij}^{(+)}(\Omega)$ and $C_{Ij}^{(-)}(\Omega)$, respectively]. We have

$$\sum_{\Omega'} \langle I\Omega|H|I\Omega'\rangle C_{Ij}^{(+)}(\Omega') = E_I^{(+)} C_{Ij}^{(+)}(\Omega), \quad (3)$$

$$\sum_{\Omega'} \langle I\Omega|H|I\Omega'\rangle C_{Ij}^{(-)}(\Omega') = E_I^{(-)} C_{Ij}^{(-)}(\Omega). \quad (4)$$

Let us multiply equation (3) by $C_{Ij}^{(-)}(\Omega)$ and equation (4) by $C_{Ij}^{(+)}(\Omega)$ and subtract the second of the resulting expressions from the first one. This is the first step in a conventional procedure used in textbooks on quantum mechanics to prove that states corresponding to different eigenvalues are orthogonal. In contrast to what is done next in this procedure, we will sum here the resulting difference only over the positive values of Ω. This yields

$$E_I^{(-)} - E_I^{(+)} = -2\langle I, 1/2|H|I, -1/2\rangle \frac{C_{Ij}^{(+)}(1/2) C_{Ij}^{(-)}(1/2)}{\sum_{\Omega = 1/2}^{j} C_{Ij}^{(+)}(\Omega) C_{Ij}^{(-)}(\Omega)}. \quad (5)$$

As was mentioned above, the energy difference $(E_I^{(-)} - E_I^{(+)})$ can be determined on the basis of experimental data. In our case, the matrix element $\langle I, 1/2|H|I, -1/2\rangle$ is given by

$$-\frac{\hbar^2}{2\mathcal{I}}(I + 1/2)(j + 1/2). \quad (6)$$

Let us now consider the sum in the denominator on the right-hand side of equation (5):

$$\sum_{\Omega = 1/2}^{j} C_{Ij}^{(+)}(\Omega) C_{Ij}^{(-)}(\Omega). \quad (7)$$

In the case of weak Coriolis interaction, in which case only one value of Ω appears in the wave function with a large weight, the sum is equal to 1/2 by virtue of the normalization condition. When the Coriolis interaction is strong, which corresponds to a strong alignment of the angular momentum of an odd particle, the sum in (7) takes the minimum possible value. In order to assess it, we make use of the wave functions of a one-dimensional harmonic oscillator and calculate the overlap integral of the ground-state wave function [even function appearing to be an analog of $C_{Ij}^{(+)}(\Omega)$] and the wave function of the one-phonon state [odd function appearing to be an analog of $C_{Ij}^{(-)}(\Omega)$] over the region of positive values of the coordinate Ω (the corresponding sum over all positive and negative values of Ω vanishes because of orthogonality). This sum is equal to $0.5\sqrt{2/\pi} \approx 0.40$. Thus, the sum in (7) is bounded from above by the value of 0.50 and from below by the value of 0.40. We therefore set it to 0.45 ± 0.05 and use this value in extracting the amplitude of the $\Omega = 1/2$ component from experimental data.

That the amplitude of an unphysical state appears in [5] presents one more problem. If the signature splitting in energy is small—that is, the alignment of the single-particle angular momentum along the collective-rotation axis is weak, and the corresponding amplitudes $C_{Ij}^{(\pm)}$ $(\Omega = 1/2)$ are small—the physical and unphysical amplitudes are close to each other at positive Ω and have nearly equal absolute values and opposite signs at negative Ω. In the case of strong alignment, a smooth dependence of the amplitudes on the angular momentum I gives every reason to believe that the unphysical amplitude at an angular-momentum value of I is approximately equal to the arithmetic mean of the physical amplitudes at angular-momentum values of $I + 1$ and $I - 1$, these amplitudes having identical parities under the reversal of the sign of Ω. For the case of sufficiently strong Coriolis interaction—and this is precisely the case of our prime interest—we eventually find that, as parameters, equation (5) will involve only the amplitudes of physical states, experimental data,

and a quantity that is specified numerically to a fairly high precision.

3. NONAXISYMMETRIC CORE

In the case of a core not possessing axial symmetry, the wave function can be represented as

$$\Psi_{IM} = \sum_{\Omega} C_{Ij}(K, \Omega) D^{I}_{MK} \psi_{j\Omega}. \tag{8}$$

For physical states, we have

$$C_{Ij}(-K, -\Omega) = (-1)^{I-j} C_{Ij}(K, \Omega). \tag{9}$$

In just the same way as above, we consider two solutions to the Schrödinger equation for each value of the angular momentum I that are characterized by the amplitudes $C^{(\pm)}_{Ij}(K, \Omega)$ possessing the symmetry property

$$C^{(\pm)}_{Ij}(-K, -\Omega) = \pm C^{(\pm)}_{Ij}(K, \Omega). \tag{10}$$

Since the matrix elements of the Hamiltonian satisfy the relation

$$\begin{aligned} &\langle I, K, \Omega | H | I, K', \Omega' \rangle \\ &= \langle I, -K', -\Omega' | H | I, -K, -\Omega \rangle \end{aligned} \tag{11}$$

and since the Hamiltonian is a Hermitian operator, the two wave functions corresponding to the symmetric and antisymmetric solutions are eigenfunctions of the Hamiltonian.

As in the preceding section, we can obtain the relation

$$\begin{aligned} &C^{(-)}_{Ij}(K, \Omega) \sum_{K', \Omega'} \langle I, K, \Omega | H | I, K', \Omega' \rangle C^{(+)}_{Ij}(K', \Omega') \\ &- C^{(+)}_{Ij}(K, \Omega) \sum_{K', \Omega'} \langle I, K, \Omega | H | I, K', \Omega' \rangle C^{(-)}_{Ij}(K', \Omega') \\ &= (E^{(+)}_I - E^{(-)}_I) C^{(+)}_{Ij}(K, \Omega) C^{(-)}_{Ij}(K, \Omega). \end{aligned} \tag{12}$$

We must now perform summation in relation (12) over K and Ω by using, as above, half of all points in the (K, Ω) plane. However, this can be done in two different ways. Two independent modes of motion in the (K, Ω) plane can be approximately separated into that which is associated with a variation of the angle between the single-particle and collective angular momenta and that which is associated with a variation of the orientation of the axis of collective rotation. The first mode is softer in the case of strong Coriolis interaction, a principle subject of our concern. In the harmonic approximation, the ratio of the corresponding frequencies is $1 : 3$ at $\gamma = 30°$ [6]. With decreasing γ, this distinction between the frequencies becomes ever more pronounced. The hardest mode is associated with a variation of the difference $(K - \Omega)$, which is equal precisely to the projection of the angular momentum on the quantization axis. Thus, this mode corresponds to oscillations of the direction of collective rotation. This type of motion, the hardest one, can be described in the harmonic approximation. Thus, the motion in the (K, Ω) plane occurs within a narrow valley that is stretched in the direction nearly parallel to the $(K + \Omega)$ axis. Therefore, we can approximately factorize the dependence of the amplitudes on $(K - \Omega)$ and, say, $(K + \Omega)$. Accordingly, we have

$$\begin{aligned} C^{(\pm)}_{Ij}(K, \Omega) &\longrightarrow C^{(\pm)}_{Ij}(K + \Omega, K - \Omega) \\ &\approx C^{(\pm)}_{Ij}(K + \Omega, 0) w(K - \Omega), \end{aligned} \tag{13}$$

where $w(K - \Omega)$ is a normalized Gaussian function. The quantity $(K - \Omega)$ takes the values of 0, ±2, ±4, …. It is now clear that, in order to obtain the sought relation, we must perform summation in (12) over all values of $(K - \Omega)$ and over positive values of $(K + \Omega)$. For the sake of brevity, we introduce the notation $x = K + \Omega$ and $y = K - \Omega$. The possible values of x are ±1, ±3, …. Performing summation in (12) over all values of y and over positive values of x, we obtain

$$\begin{aligned} &(E^{(+)}_I - E^{(-)}_I) \sum_{x>0} C^{(+)}_{Ij}(x, 0) C^{(-)}_{Ij}(x, 0) \\ &= 2 \sum_{y} (\langle I, -1, y | H | I, 1, y \rangle w(y)^2 \\ &+ \langle I, 1, y | H | I, -1; y - 2 \rangle w(y) w(y - 2) \\ &+ \langle I, 1, y | H | I, -11, y + 2 \rangle w(y) w(y + 2)) \\ &\times C^{(+)}_{Ij}(x = 1, y = 0) C^{(-)}_{Ij}(x = 1, y = 0). \end{aligned} \tag{14}$$

In connection with the presence of unphysical amplitudes in (14), we can adduce the same arguments as in Section 2 to arrive at the relation that involves only physical quantities. The Hamiltonian matrix elements in (14) are known. They depend only on one parameter (γ) and appear to be smooth functions of y. Relation (14) can be used to extract information about the amplitudes $C^{(\pm)}_{Ij}(x = 1, y = 0)$.

4. CONCLUSION

We have considered signature splitting in the spectra of rotational bands of odd nuclei. It has been shown that this splitting is determined by the amplitude of the aligned wave-function component. Thus, experimental information about the spectra of rotational bands can be used to estimate these amplitudes.

ACKNOWLEDGMENTS

This work was supported in part by the Russian Foundation for Basic Research (project nos. 97-02-16030 and 96-15-96729).

REFERENCES

1. A. Bohr and B. R. Mottelson, *Nuclear Structure*, Vol. 2: *Nuclear Deformations* (Benjamin, New York, 1975; Mir, Moscow, 1977).
2. V. G. Soloviev, *Theory of Complex Nuclei* (Nauka, Moscow, 1971; Pergamon, Oxford, 1976).
3. L. D. Landau and E. M. Lifshitz, *Quantum Mechanics: Non-Relativistic Theory*. Transl. of 3rd Russ. ed. (4th ed., Nauka, Moscow, 1989; Pergamon, Oxford, 1977).
4. I. M. Pavlichenkov, Phys. Rep. **226**, 175 (1993).
5. R. V. Jolos and A. Gelberg, Phys. Lett. B **317**, 495 (1993).
6. R. Jolos, P. von Brentano, and A. Gelberg, in *Proceedings of International Conference "Frontiers of Nuclear Structure," Tokyo, 1994* (World. Sci., 1996), p. 243.

Translated by A. Isaakyan

Physics of Atomic Nuclei, Vol. 63, No. 2, 2000, pp. 195–203. Translated from Yadernaya Fizika, Vol. 63, No. 2, 2000, pp. 248–256.

NUCLEI
Theory

Supermultiplet Symmetry and Near-Threshold Levels in Systems Featuring Two or Three Extremely Light Clusters

V. M. Lebedev, V. G. Neudatchin, and A. A. Sakharuk[1)]

Institute of Nuclear Physics, Moscow State University, Vorob'evy gory, Moscow, 119899 Russia

Received January 6, 1999; in final form, March 23, 1999

Abstract—On the basis of the supermultiplet potential model for the interaction of extremely light clusters (formalism of Young diagrams), it is explained why the $d + t$ system does not feature a $(1/2)^+$ ($L = 0$) level allied to $(3/2)^+$ ($L = 0$) thermonuclear resonance. By using known data on the quasielastic knockout of nucleons from the inner 1*s* shell of light nuclei, a systematics of near-threshold states in the $t + d + d$, $t + t + d$, and $t + t + t$ systems is constructed in terms of excited Young diagrams like $\{f\} = \{322\}$. The emergence of similar states in going over from the $d + d$ and $t + t$ systems (which feature no such states) to the $\alpha + d + d$, $\alpha + t + d$, and $\alpha + t + t$ systems (where they appear owing to the binding effect of the alpha particle) is discussed. The three-cluster states being considered may be important not only for nuclear physics proper but also for nuclear astrophysics.

1. INTRODUCTION

It is well known that the $(3/2)^+$ ($L = 0$) narrow near-threshold level in the $d + t$ system underlies the physics of thermonuclear reactions [1]. This brings about the natural question of why there is no the allied $(1/2)^+$ ($L = 0$) level.

In the present study, we attempt to clarify this problem by using the general—and rather simple—formalism of the supermultiplet potential model [2], which is capable of providing a good simultaneous description (or predictions in cases where there is no relevant data) of the cross sections for $d + p$, $d + d$, $d + t$, and $t + p$ elastic scattering (that is, for the elastic scattering of extremely light clusters); for scattering processes where the deuteron spin and isospin are flipped (say, in the reaction $d + t \longrightarrow d_s + t$); and for photonuclear reactions like $^3\mathrm{He} + \gamma \longrightarrow d + p$, $d + t \longrightarrow {}^5\mathrm{He} + \gamma$, and $^4\mathrm{He} + \gamma \longrightarrow t + p$ [2].

In contrast to the simplest potential approaches, the model in question takes into account the interference of channels associated with different Young diagrams. To illustrate this, we indicate that, when the $d + d$ system is in the state where its total spin is $S = 0$—this corresponds to even values of the orbital angular momentum L of relative motion—the amplitudes associated with the spatial Young diagrams $\{f\} = \{22\}$ and $\{f\} = \{4\}$, which correspond to totally different potentials of deuteron interaction (a deep and a shallow one) interfere in scattering (continuum) states. In other words, a conventional potential description of *dd* scattering in the $S = 0$ channel is impossible. It is the interference of amplitudes characterized by different Young diagrams that makes it possible to understand the reason behind the absence of the $(1/2)^+$ thermonuclear level in the $d + t$ system.

Another merit of the model used is that the formalism of Young diagrams provides a consistent mathematical formulation of orthogonality (nonorthogonality) of various cluster channels to one another. By way of example, we indicate that, in the $t + t$ system, odd-L states are characterized by the Young diagram $\{f\} = \{33\}$ and are orthogonal to the αnn channel, where the energy release is high, whereas even-L states correspond to $\{f\} = \{42\}$, whence it follows that a transition into the αnn channel is allowed for such states (for selection rules in nuclear reactions according to Young diagrams, see [3, 4]). Similarly, the $t + d$ system characterized by the Young diagram $\{f\} = \{32\}$ is orthogonal to the $\alpha + n$ cluster channel—that is, the decay process $td \longrightarrow \alpha n$ is suppressed. It follows that the aforementioned $(3/2)^+$ resonance, which corresponds to $\{f\} = \{3/2\}$ symmetry [2, 5] is narrow, appearing to be a long-lived state. Such properties are of importance both for thermonuclear reactions and for nucleosynthesis [6].

Despite numerous theoretical investigations of systems featuring two or three extremely light clusters [7–11], the question of whether there exist similar states of the cluster type in systems of three clusters ($d + d + d$, $t + d + d$, $t + t + d$, and $t + t + t$) has not yet received a systematic study. But it is just the systematic study that provides a general pattern and makes it possible to determine nuclear excitation energies at which we can expect the emergence of near-threshold levels of a specific cluster origin. In constructing the systematics of such states, we rely on symmetry considerations expressed in terms of excited Young diagrams and on experimental information about the quasielastic knockout of nucleons from the inner 1*s* shell of light nuclei.

[1)] Brest State University, Brest, Belarus.

1063-7788/00/6302-0195$20.00

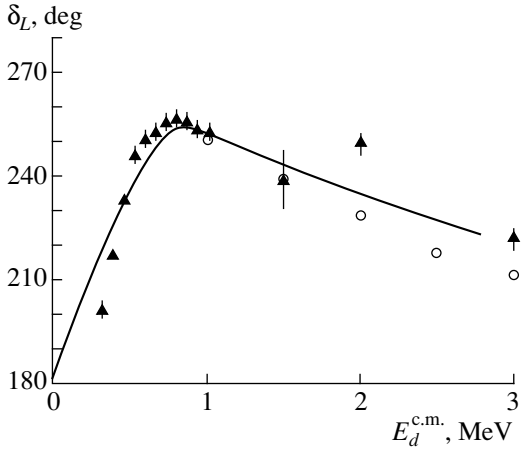

Fig. 1. Phase shifts for $d + h$ scattering in the $S = 3/2$, $L = 0$ channel: (solid curve) results of the calculation from [2] for the $\{f\} = 32\}$ channel, (open circles) RGM phase shifts from [10], and (closed triangles) results of the phase-shift analysis from [14].

This scheme differs crucially from that in the Wigner–Baz' theory of threshold states [12], first, by the microscopic many-body description of the system (in terms of symmetry properties) and, second, by the fact that, in the present case, the set of states belonging to a specific supermultiplet is generally distributed over a rather wide region of high nuclear excitations. Owing to this, the efficiency of the scheme becomes higher because a determination of the positions of some states belonging to the supermultiplet makes it possible to predict reliably the position of those states that occur in the energy region near the threshold for the three-body breakup of the corresponding compound nucleus. For example, highly excited levels of the ^{8}Li nucleus that have permutation symmetry specified by the Young diagram $\{f\} = \{332\}$, negative parity, a low orbital angular momentum of $L = 1$, and a spin of $S = 2$ characterize the $t + t + d$ system; that is, a dominant virtual decay through this channel is allowed by the Young diagram $\{f\}$. These levels are of interest just because their position near the threshold for one of the values of J ($\mathbf{J} = \mathbf{L} + \mathbf{S}$) is combined with the fact that the real decay $^8\text{Li}^* \longrightarrow {}^7\text{Li} + n$, which is accompanied by a significant energy release, is forbidden.

In this example, the deuteron binds the $t + t$ pair, $\{f\} = \{33\}$, for which there are no resonances, and creates a resonance in the three-cluster system undergoing thermonuclear decay. The triton in the $t + d + d$ system ($\{f\} = \{322\}$), the alpha particle in the $\alpha + d + d$ system ($\{f\} = \{422\}$), and the alpha particle in the $\alpha + t + t$ system ($\{f\} = \{433\}$) system play a similar role. A theoretical merit of the proposed approach is that we can make use of the well-known results obtained in calculating the set of levels within the multiparticle shell model [13] for s^4p^n configurations. Experimental prospects are associated with the belief that such states can be excited intensively in cluster-transfer reactions like (^{3}He, p), (^{6}Li, α), and (^{7}Li, α) at energies that admit the occurrence of a direct process with a high probability (approximately 20 MeV for ^{3}He beams and 50–60 MeV for Li nuclei). Strange though it may seem, the entire body of such data obtained thus far is scanty.

For all three-cluster levels discussed here, it is important to know the degree to which the quantum number $\{f\}$ is good, a quantity on the basis of which we can conclude whether a given resonance is sufficiently narrow and well-defined. According to the shell-model calculations from [13], this degree is not high (70–80%), but it is obviously reduced by a strong impact of the shell effect associated with spin–orbit interaction. In loose cluster systems, this effect is suppressed to a considerable extent. By way of example, we indicate that, according to experimental data, the width of the $(3/2)^+$ level in the $t + d$ system is close to the resonance width in the potential model and that the forbidden decay into the $\alpha + n$ channel has virtually no effect on this width. We will return to the question of accuracy of Young diagrams $\{f\}$ in the section devoted to cluster-transfer reactions.

2. COMPARISON OF THE ORIGINS OF THE $(3/2)^+$ AND $(1/2)^+$ STATES IN THE $t + d$ SYSTEM

For the $t + d$ and $h + d$ ($h \equiv {}^3$He) systems, the admissible types of symmetry (signature) are $\{f\} = \{41\}$ and $\{f\} = \{32\}$, irrespective of L parity because the particles involved are not identical. The Young diagram $\{f\} = \{41\}$ corresponds to the total spin of $S = 1/2$, whereas $\{f\} = \{32\}$ admits both $S = 1/2$ and $S = 3/2$ [2, 5]. Thus, the value of $S = 3/2$ is associated exclusively with the signature $\{f\} = \{32\}$. At the same time, amplitudes characterized by the Young diagrams $\{41\}$ and $\{32\}$ interfere in the $S = 1/2$ scattering channels. We see that, although the effect of the total spin S on the character of $t + d$ interaction is indirect—this effect is exerted through the signature $\{f\}$—it is quite significant.

According to our model [2], each signature $\{f\}$ generates an individual *td* potential, these potentials being strongly different for different $\{f\}$.

Thus, we conclude that, by origin, the $(3/2)^+$ ($L = 0$, $S = 3/2$) thermonuclear level represents a potential-scattering resonance that corresponds to the Young diagram $\{f\} = \{32\}$. Indeed, the potential $V_L^{\{32\}}(R)$ reproduces faithfully all $S = 3/2$ phase shifts for $h + d$ scattering over a broad energy interval [2] (for nonidentical particles, this potential has slightly different forms for even and odd values of L). The general pattern of the region where the $h + d$ system develops the resonance of our prime interest is shown in Fig. 1. We can see that the potential model describes fairly well both the general behavior of the phase shift and the resonance proper (its position and width). The wave function of the $h + d$ system at the resonance has, in just the same

way as the $S = 2$ state of the $d + d$ system at low energies does [2], a nodal character associated with the fact that the lowest admissible shell configuration corresponds to s^3p^2. In constructing the projections onto the $h + d$ channel, two oscillator quanta are concentrated, in this case, in the wave function of relative motion in the $h + d$ system [4] {in the potential $V^{\{32\}}_{\text{even}}(R)$, there is a forbidden nodeless S-wave bound state occurring at $E = -5$ MeV [2] and corresponding to the configuration s^5}. Thus, the effect of antisymmetrization arises even if we restrict our consideration to the classification of permutation-symmetry types according to Young diagrams without explicitly invoking the operator of full antisymmetrization in the system {this is characteristic of the resonating-group method (RGM) [15], rendering the procedure very cumbersome and hindering the construction of a simple general pattern}.

It goes without saying that, for the $3/2^+$ resonance, the thermonuclear forbidden channel $t + d \longrightarrow \alpha + n$ is of prime interest [7, 8], but it does not affect the general conclusions about the nature of this resonance, because the degree of suppression is 10^{-1} for this channel [8].

Going over to the $(1/2)^+$ resonance, we will make use of an efficient formalism for clarifying the reason why there is no such resonance in $t + d$ scattering despite the fact that the important $\{f\} = \{32\}$ component of the wave function in the $L = 0$, $S = 1/2$ channel resonates. Since the scattering amplitudes corresponding to the signatures $\{f_1\} = \{32\}$ and $\{f_2\} = \{41\}$ interfere in the $S = 1/2$ case for the $t + d$ system, the S matrix and the phase shifts can be taken in the conventional form from [2]; that is,

$$S^{\text{el}}_{L,S} = \eta_{L,S}\exp(2i\delta_{L,S}), \tag{1}$$

$$\delta_{L,1/2} = \frac{1}{2}\delta_L^{\{f_1\}} + \frac{1}{2}\delta_L^{\{f_2\}}. \tag{2}$$

If the channel of spin–isospin flip into a singlet state, $d + t \longrightarrow d_s + t$, were open, the resulting nonunitarity of elastic scattering in the case of $S = 1/2$ would be determined by the inelasticity factor [2]

$$\eta_{L,1/2} = \left|\cos(\delta_L^{\{f_1\}} - \delta_L^{\{f_2\}})\right|. \tag{3}$$

In our case, where this channel is closed, we have $\eta_{L,1/2} = 1$ (unitarization of the elastic channel). Thus, we arrive at

$$S^{\text{el}}_{L,1/2} = \exp[i(\delta_L^{\{f_1\}} + \delta_L^{\{f_2\}})]. \tag{4}$$

In the polarization experiment reported in [14], the phase shifts $\delta_{L,1/2}(E)$ and $\delta_{L,3/2}(E)$, which correspond to the values of $S = 1/2$ and $3/2$, respectively, can be separated (these data can be supplemented with the numerical results obtained in [10] on the basis of the RGM). Knowing the $S = 3/2$ phase shifts and relying on the supermultiplet formalism, we can determine the phase shift $\delta_L^{\{32\}}(E)$ as a function of energy. In this way, we can reconstruct the aforementioned potential $V_L^{\{32\}}(R)$. On the basis of the phase shift $\delta_{L,1/2}(E)$ determined experimentally, we then reconstruct the supermultiplet phase $\delta_L^{\{41\}}(E)$ by using equation (2) and the already known phase shift $\delta_L^{\{32\}}(E)$. This enables us to reconstruct the potential $V_L^{\{41\}}(R)$ [2], for which there exists a forbidden S-wave state with a large binding energy of 16 MeV (the lowest shell configuration compatible with the symmetry $\{f\} = \{41\}$ and $L = 0$ corresponds to the $s^3p^2 + s^42s$—not to the s^5—configuration of the forbidden state).

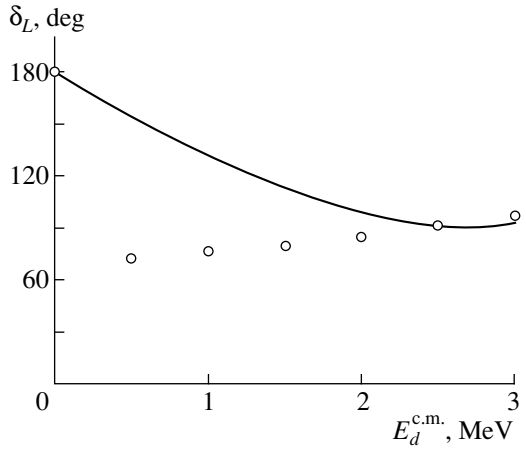

Fig. 2. Phase shifts for $d + h$ scattering in the $\{f\} = \{41\}$, $L = 0$ channel: (solid curve) results of the calculation from [2] on the basis of the potential $V^{\{41\}}_{L=0}$ and (open circles) pure phase shift $\delta^{\{41\}}_{L=0}$ as calculated on the basis of the RGM phase shift from [10] by using equation (2).

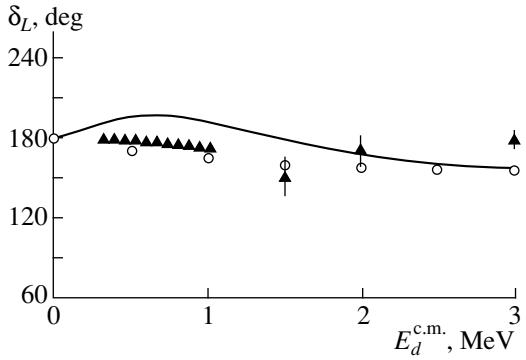

Fig. 3. Phase shifts for $d + h$ scattering in the $S = 1/2$, $L = 0$ channel: (solid curve) results of the calculation by equation (2), (open circles) RGM phase shifts from [10], and (closed triangles) experimental phase shifts from [14].

Figure 2 shows the reconstructed S-wave phase shift $\delta_0^{\{41\}}(E)$ in the region of low energies; we can see that this phase shift decreases rather fast from the value of 180° at zero energy [this behavior of the phase shift is

in accord with the position of the aforementioned forbidden level in the potential $V^{\{41\}}(R)$]. We can conclude that the pragmatic use of the RGM data for the phase shifts $\delta_{0,3/2}$ and $\delta_{0,1/2}$ on the basis of equation (2) leads to a noticeably different result, which cannot be tested directly in experiments.

Despite the fact that the term $\delta_0^{\{32\}}$ in the total phase shift $\delta_{0,1/2}(E) = \frac{1}{2}\delta_0^{\{32\}} + \frac{1}{2}\delta_0^{\{41\}}$ resonates (as is seen in Fig. 1), this total phase shift cannot correspond to a resonance behavior when the phase shift $\delta_0^{\{41\}}(E)$ decreases in the way described above. It should be noted that a wide interval of energies was considered in [2] and that some fine details—such as the behavior of the phase shift $\delta_{0,1/2}(E)$ at low energies—were successfully reproduced there.

The above example, where the resonance disappears when we go over, within the supermultiplet potential model, from the one-channel problem ($S = 3/2$, $\{f\} = \{32\}$) to the two-channel problem ($S = 1/2$, $\{f_1\} = \{32\}$ and $\{f_2\} = \{41\}$), may be of general interest in discussing the methodological problems of quantum mechanics (see the monograph quoted in [16]). Conceptually, this approach has never been invoked in applying the RGM scheme, but it can be implemented easily by using the RMG equations projected on a definite total Young diagram [17].

The effect of the decay $t + d \longrightarrow \alpha + n$ in the $S + 1/2$, $L = 0$, $\{f\} = \{41\}$ channel induces the emergence of the imaginary part of the S-wave phase shift for $d + t$ scattering in this channel and leads to the broadening of the relevant resonance, should it appear.

Let us now consider the $d + d$ and $t + t$ cluster pairs. For the $d + d$ system with symmetry $\{f\} = \{22\}$, the reconstructed dd potential [2] is overly shallow for the formation of a physical S-wave bound state or a resonance, although there is a forbidden S-wave state in this potential (in the $d + d$ system, the $\{f\} = 4$ symmetry corresponds to the ground state of the ^{4}He nucleus).

If there exists a resonance in the $t + d$ system ($\{f\} = \{32\}$), there then arises the question of why there is no such resonance in the $t + t$ system ($\{f\} = \{33\}$). Needless to say, it would occur for an S-wave state, but the $\{f\} = \{33\}$ symmetry is compatible only with the L-odd waves; proceeding further, we indicate that, even at $L = 1$, the strength of the potential is insufficient for the formation of a bound state or of a resonance (although there is a noticeable growth of the P-wave phase shift at $E_{\text{c.m.}} \sim 3$ MeV) [2, 18]. As to the $\{f\} = \{42\}$ symmetry for the $t + t$ system, it leads to a tightly bound physical S-wave state in the corresponding potential, the ground state of the ^{6}He nucleus (the relevant spectroscopic factor is $S^{tt}_{^6\text{He}} \simeq 0.5$ [18]). Similarly, the $\{f\} = \{41\}$ symmetry for the $t + d$ system considered above leads to a tightly bound physical doublet state in the potential $V^{\{41\}}(R)$, the $(3/2)^-$ ground state of the ^{5}He nucleus and the closest $(1/2)^-$ level. These well-known states are not considered here.

3. LOOSELY BOUND STATES AND RESONANCES IN SYSTEMS FEATURING THREE CLUSTERS OF THE *d* AND *t* TYPES

In this section, we discuss the possible existence of near-threshold three-cluster states that are characterized by excited Young diagrams of the type $\{f\} = \{332\}$ and which are orthogonal to channels involving α particles. In principle, they could exist as narrow resonances whose decay through the above alpha-particle channels, which is accompanied by a large energy release, is forbidden. In this case, data on photonuclear reactions and on reactions of quasielastic nucleon knockout would be very useful, but such data have not yet been invoked in solving problems of this type.

As the simplest example of three-cluster states in a continuum near the three-body threshold, we will consider the high-energy part (group B) of the giant dipole resonance (GDR) in the ^{6}Li and ^{7}Li nuclei, $|s^3p^3\{321\}L = 1;\ S = 1;\ T = 1\rangle$ and $|s^3p^4\{331\}L = 0, 2;\ S = 1/2;\ T = 1/2, 3/2\rangle$ (the conventions used here are described in detail elsewhere [19, 20]). Of these states, the lowest (in the group B, we consider here only that part which is the closest one to the threshold) lie above the thresholds for the three-cluster decays $^6\text{Li}^* \longrightarrow t(h) + d + p(n)$ and $^7\text{Li}^* \longrightarrow t(h) + t + p(n)$, which play an important role in processes occurring in stars, by, respectively, 2–4 and 6–8 MeV [19] (see also data on photomesonic reactions [20]). For such states, the above type of decay according to the rows of the Young diagram is superallowed, whence it follows that, even at energies above the threshold value of $E \simeq 3$ MeV, these states correspond to rather wide maxima of the cross section. We are interested, however, in states like $|s^3p^3\{321\}L = 1;\ S = 2;\ T = 0\rangle$ and $|s^3p^4\{331\}L = 0, 2;\ S = 3/2;\ T = 1/2\rangle$ that lie much lower and for which alpha decays are not forbidden in isospin. Taking into account the energy difference between the $|s^4p^3\{421\}L = 1;\ S = 1/2;\ T = 3/2\rangle$ and $|s^4p^3\{421\}L = 1;\ S = 3/2;\ T = 1/2\rangle$ levels, which is, on average, 3.5 MeV [13], and the analogous difference between the $|s^4p^4\{431\}L = 1;\ S = 0;\ T = 1\rangle$ and $|s^4p^4\{431\}L = 1;\ S = 1;\ T = 0\rangle$ levels, about 4 MeV, we arrive at the conclusion that the $|s^3p^3\{321\}L = 1;\ S = 2;\ J^\pi = 3^-;\ T = 0\rangle$ and $|s^3p^4\{331\}L = 0;\ S = 3/2;\ J^\pi = 3/2^+;\ T = 1/2\rangle$ states lie in the region of the $t + d + p$ three-body threshold and above the $t + t + p$ threshold, respectively. In the ^{6}Li nucleus, $\{f\} = \{321\}$, the analogous $L = 1$, $S = 2$, $T = 0$, $J^\pi = 2^-$ and 1^- levels also lie above the threshold.

There arises the natural question of how the energy of the system (we reckon here this energy from the threshold for the above three-body decay) changes upon going over from the $t + d + p$ ($\{f\} = \{321\}$) system to the $t + d + d$ ($\{f\} = \{322\}$) system or from the $t + t +$

p ($\{f\} = \{331\}$) system to the $t + t + d$ ($\{f\} = \{332\}$) system and further to the $t + t + t$ ($\{f\} = \{333\}$) system. Here—in just the same way as in the theory of photonuclear reactions—systematic data obtained (as far back as the 1970s) for the nucleon binding energies in the 1s and 1p shells from an investigation into quasielastic-knockout processes of the (p, 2p) and (e, $e'p$) types at high energies (a few hundred MeV) [21] play an important role. It is well known that, as the p shell is filled, the proton binding energy in the 1s state grows according to the law

$$E_{1s}^{\text{bind}}(1s^n 1p^n) \simeq E_{1s}^{\text{bind}}(^4\text{He}) + 2n \ \ (\text{MeV}). \qquad (5)$$

In particular, we have $E_{1s}^{\text{bind}}(^{10}\text{B}) \simeq 31$ MeV for the ^{10}B nucleus. Here, it is important to note that, with increasing n, the type of the symmetry of the configuration p^n changes substantially (for example, $\{f\} = \{3\}$ for the ^{7}Li nucleus, $\{f\} = \{41\}$ for the ^{9}Be nucleus, etc.), and so do the binding energies of valence nucleons; at the same time, equation (5) retains a linear character, and the binding energy of the 1s nucleon is independent of the above features of the wave function of the configuration p^n. Therefore, the statement that equation (5) is valid not only for the ground state but also for excited states (in particular, for those whose symmetry $\{f\}$ is rearranged) remains in force for a fixed nucleus as well, provided that the consideration is restricted to the configuration p^n with a fixed value of n. This is the reason why our derivation of the estimate for ^{10}B employs the same value of 31 MeV for the lowest state with symmetry $\{f\} = \{433\}$ $|s^4p^6\{433\}^{33}P_2\rangle$ ($E^* = 11.6$ MeV) as well [13]; that is, the proton binding energy $E_{1s}^{\text{bind}}(^{10}\text{B})$ between some 30 and 31 MeV is associated with the transition $|s^4p^6\{433\}^{33}P_2\rangle \longrightarrow |s^3p^6\{333\}^{44}P_{5/2}\rangle$. Since this state of the ^{10}B nucleus occurs 5 MeV above the threshold for proton emission, the ^{9}Be state in which we are interested, $|s^3p^6\{333\}^{44}P_{5/2}\rangle$, corresponds to the excitation energy $E^*(\{333\})$ between 35 and 36 MeV, which is only 1 to 2 MeV in excess of the threshold for the decay process $^9\text{Be} \longrightarrow h + t + t$. The last value is appropriate (since $T = 3/2$) for the analogous state of the ^{9}Li nucleus as well, a state of our direct interest, which decays via the process $^9\text{Li} \longrightarrow t + t + t$. Thus, the $t + t + t$ system can have near-threshold bound or resonance $J^\pi = 5/2^+, 3/2^+, 1/2^+$ states $|s^3p^6\{333\}^{44}P_J\rangle$. Needless to say, this system, featuring a very weak two-body resonance, calls for a more detailed quantitative investigation aimed at clarifying the question of whether there is here a clear-cut three-body resonance.

In principle, the three-cluster method of resonating groups in the conventional form (which is unfortunately cumbersome) is applicable here, because the maximal possible spin of $S = 3/2$ and the maximal possible isospin $T = 3/2$ in the system are compatible only with one orbital Young diagram $\{f\} = \{333\}$ (in a more general case, it would be necessary to project the RGM equations onto the given symmetry $\{f\}$ [17]). However, we can also use a simpler approach, that which relies on using the known tt potential for the $\{f\} = \{33\}$ symmetry (odd orbital angular momenta of relative motion) [2]—or even the first term of its separable expansion [23]—and on solving the Faddeev equations for the case of pair potentials involving forbidden states [24].

Going over to the $t + t + d$ system with orbital symmetry $\{f\} = \{332\}$, we consider here, as above, the lowest states of the ^{9}Be nucleus with signature $\{f\} = \{432\}$—namely, the $|s^4p^5\{432\}^{24}P_J\rangle$ multiplet whose levels have the quantum numbers $J^\pi = 1/2^-$, $3/2^-$, and $5/2^-$ and occur at, respectively, $E^* = 9.8$. 10.6, and 11.5 MeV [13]. A transition to the $J^\pi = 1^-$, 2^-, and 3^- $|s^3p^5\{332\}^{35}P_J\rangle$ hole states in the ^{8}Li and ^{8}Be nuclei corresponds to the 1s-nucleon binding energy $E_{1s}^{\text{bind}}(^9\text{Be}^*)$ between 28 and 29 MeV. A transition to the ground state of the ^{8}Be nucleus from the multiplet levels would be accompanied by the emission of neutrons with energies of 8, 9, and 10 MeV, respectively. Thus, our estimates predict that, in the ^{8}Be nucleus, the $|s^3p^5\{332\}^{35}P_J\rangle$ states lie in the interval $\Delta E^*(\{332\})$ of excitation energies between 36 and 39 MeV, the threshold for the three-cluster breakup $^8\text{Be} \longrightarrow h + t + d$ corresponding to the energy of $E_n = 38.1$ MeV. It can be seen that the E_n value occurs nearly at the midpoint of the interval $\Delta E^*(1s^{-1})$. This conclusion remains in force for the threshold in the $t + t + d$ system with respect to the interval $\Delta E^*(1s^{-1})$ of excitation energies of the ^{8}Li nucleus, because the Coulomb corrections to the quantities E_n and $E^*(1s^{-1})$ in the ^{8}Be nucleus prove to be identical to those in the ^{8}Li nucleus. Thus, the probability for the $t + t + d$ system with $\{f\} = \{332\}$ symmetry to occur in the region around the threshold for the three-cluster breakup of the ^{8}Li nucleus seems noticeably higher than that for the above-discussed $t + t + t$ system with $\{f\} = \{333\}$ symmetry. We would like to emphasize here that the former case requires a more detailed theoretical study. It should be recalled that the potential of dt interaction for the $\{f\} = \{32\}$ symmetry is well known (see above).

In order to analyze the $t + d + d$ system, $\{f\} = \{332\}$, we will consider the lowest level with $\{f\} = \{422\}$ symmetry in the ^{8}Be nucleus: this is the $|s^4p^4\{422\}^{15}P_4\rangle$ level at $E^* = 19.5$ MeV [13]. It occurs 2.2 MeV above the threshold for the decay $^8\text{Be} \longrightarrow {}^7\text{Li} + p$ [22]. It should also be borne in mind that, when the ^{7}Li $|s^3p^4\{322\}^{26}D_{9/2}\rangle$ hole state in which we are interested is formed as the result of 1s-nucleon knockout from the above excited state of the ^{8}Be nucleus, it turns out that $E_{1s}^{\text{bind}}(^8\text{Be}^*)$ is between some 27 and 28 MeV [21]. Thus, the excitation energy $E^*(\{322\})$ between 29 and 30 MeV, which is approximately 3 MeV above the threshold for the three-cluster decay $^7\text{Li} \longrightarrow t + d + d$

(E_n^* = 26.3 MeV [22]), corresponds to the ^{7}Li lowest state with $\{f\} = \{322\}$ symmetry in question. This situation is also of interest for a theoretical analysis, but is not so important as that for the $t + t + d$ system, a case of the greatest interest for a quantitative theoretical investigation.

Obviously, the $d + d + d$ system is not realized as a bound state; it lies high in a continuum.

4. NEAR-THRESHOLD STATES OF THREE-CLUSTER SYSTEMS FEATURING ONE ALPHA PARTICLE

It was indicated above that, if the $d + d$ ($\{f\} = \{22\}$) or the $t + t$ ($\{f\} = \{33\}$) system is not bound, the addition of a triton, a deuteron, or an alpha particle as the third cluster in processes of star burning will play the role of a stabilizer (binding center) that facilitates the formation of near-threshold $\alpha + d + d$ ($\{f\} = \{422\}$), $\alpha + t + d$ ($\{f\} = 432\}$), and $\alpha + t + t$ ($\{f\} = \{433\}$) states with physically important forbidden decays through the ^{7}Li + p, ^{8}Be + n, and ^{8}Be + 2n channels characterized by specific energy releases. In this case, however, the Coulomb barrier increases substantially, but it does not exceed the analogous barrier for the Bethe carbon cycle $\alpha + \alpha \longrightarrow {}^8\mathrm{Be}(0^+)$, $^8\mathrm{Be}(0^+) + \alpha \longrightarrow {}^{12}\mathrm{C}(0_2^+)$ [25].

For this case, basic theoretical information is contained in the calculations presented in [13]; a particularly important point here is that the near-threshold three-cluster nuclear states of our prime interest can be directly studied in experiments implementing cluster transfer in processes like ^{6}Li(^{3}He, p)^{8}Be* and ^{7}Li(^{7}Li, α)^{10}Be* at incident-particle energies lying in the range from about 30 to 50 MeV. In order to obtain, in this way, a reliable systematic pattern of three-cluster states characterized by three-row Young diagrams, the boundaries of the energy region studied in the spectra of emitted particles must be offset by at least ±5 MeV from the three-cluster threshold. However, such systematic measurements have not been performed so far—there are only separate fragments of required data [26–31]. By way of example, we indicate that, in the review article of Abramovich *et al.* [26], threshold states are discussed exclusively in connection with Wigner–Baz' theory [12] without considering the shell structure of excited nuclear states and cluster spectroscopic factors S_x, symmetries, and other features associated with this structure. Some primary experimental data are contained in [27–29], but orbital-angular-momentum transfers are not indicated there; nor do those studies establish, within the method of distorted waves, the S_x values of clusters captured by a nucleus.

We will illustrate the above by considering the example of the s^4p^4 levels of the ^{8}Be nucleus characterized by the Young diagram $\{f\} = \{422\}$ (the threshold for the decay $^8\mathrm{Be} \longrightarrow \alpha + d + d$ is E_n = 23.8 MeV). Of these, the simplest is the $|s^4p^4\{422\}^{11}S\rangle$ state, but it occurs at E^* = 32.3 MeV (that is, rather high) [13]. We are interested in the lower lying S-wave state ^{15}S having a spin value of $S = 2$ ($J^\pi = 2^+$, $T = 0$) and occurring at energy $E^* \simeq 20.6$ MeV [13]. Comparing the $\{422\}^{11}S$ and $\{422\}^{15}S$ states, which are separated by so wide an energy interval, we can once again evaluate the well-known predictive power of the multiparticle shell model, which has not been used so far in such problems. The ^{15}S state being considered must be excited, with a large spectroscopic factor of $S_d \simeq 1$, in deuteron transfer to a ^{6}Li nucleus in processes like (^{3}He, p) (the orbital-angular-momentum transfer is $L_d = 0$) and must be weakly excited in processes like ^{7}Li(d, n)^{8}Be* and ^{9}Be(d, t)^{8}Be*. This follows from selection rules according to Young diagrams [3] and from the calculations performed in [13] for the cluster spectroscopic factors on the basis of the shell theory of nucleon clustering [4, 32]. Experimental data corresponding to the above criteria are required not only for the ^{15}S state but also for $^{15}D_J$ levels having the quantum numbers of $J^\pi = 0^+$ ($E \simeq$ 26.8 MeV), $J^\pi = 1^+$ ($E^* \simeq 26.2$ MeV), and $J^\pi = 2^+$ ($E^* \simeq$ 24.4 MeV; this level lies 0.6 MeV above the threshold for the breakup process $^8\mathrm{Be} \longrightarrow \alpha + d + d$), $J^\pi = 3^+$ ($E^* \simeq 22.1$ MeV), and $J^\pi = 4^+$ ($E^* \simeq 19.5$ MeV), which also correspond to the $\{f\} = \{422\}$ symmetry. A value of $L_d = 2$ is peculiar to all levels of the $^{15}D_J$ multiplet.

Of all levels observed experimentally, the ^{8}Be state at E^* = 19.9 MeV is associated best with the $^{15}S_2$ level. This state is excited intensively in the deuteron-cluster-transfer reactions ^{6}Li(^{6}Li, α)^{8}Be* and ^{6}Li(^{3}He, p)^{8}Be* [27] (where, however, the value of $L_d = 0$ was not determined); it was also observed in the reaction ^{6}Li(α, d)^{8}Be* [28], where this state is excited much more weakly, possibly because of a large binding energy of the alpha particle. At the same time, there is no information, quite expectably, about a noticeable excitation of this state in the reaction ^{7}Li(d, n)^{8}Be* [22].

At still higher excitations, the level at an energy of 22.8 MeV is well manifested in the reaction ^{6}Li(^{6}Li, α)^{8}Be* [27]. This level can correspond to the aforementioned $^{15}D_3$ state, although neither the value of L_d = 2 nor the value of the spectroscopic factor S_d was established in [27]. It is surprising that the experiment did not revel other levels of the $\{422\}^{15}D_J$ multiplet.

A level at E^* = 25.2 MeV [29], which can be associated, in a natural way, with the aforementioned $^{15}D_2$ state, is clearly manifested in the resonance near-threshold reaction $^6\mathrm{Li} + d \longrightarrow \alpha + \alpha$. Unfortunately, an experimental verification of the values of L_d and S_d was not performed in [29] either.

Let us now consider states corresponding to the s^4p^5 configuration with $\{f\} = \{432\}$ symmetry, in which case the threshold energy E^* for the breakup process $^9\mathrm{Be} \longrightarrow \alpha + t + d$ is 19.2 MeV. Here, a leading role is played by the $^{22}P_J$ multiplet featuring the $J^\pi = (1/2)^-$ level at E^* = 17.8 MeV and the $J^\pi = (3/2)^-$ level at E^* =

18.2 MeV, the $^{22}D_J$ multiplet featuring the $J^\pi = (5/2)^-$ level at $E^* = 19.5$ MeV and the $J^\pi = (3/2)^-$ level at $E^* = 21.6$ MeV, the $^{22}F_J$ multiplet featuring the $J^\pi = (7/2)^-$ level at $E^* = 22.4$ MeV and the $J^\pi = (5/2)^-$ level at $E^* = 23.5$ MeV, the $^{24}F_J$ multiplet featuring the $J^\pi = (7/2)^-$ level at $E^* = 17.4$ MeV, and the $^{24}D_J$ multiplet featuring the $J^\pi = (1/2)^-$ level at $E^* = 15.5$ MeV (see [13]).

From the existing experimental observations of highly excited states of the ^{9}Be nucleus, the results presented in [27], where it was established that, in the reactions ^{6}Li(^{7}Li, α)^{9}Be and ^{7}Li(^{6}Li, α)^{9}Be, the ^{9}Be levels at $E^* = 17.8$ ($^{22}P_{1/2}$) and 21 MeV (the latter can correspond to the aforementioned $^{22}D_{3/2}$ state at $E^* = 21.6$ MeV) are the most readily excited states (the most intense groups in the spectra). These levels are observed in the reactions ^{7}Li(α, d)^{9}Be and ^{6}Li(α, p)^{9}Be [25], but the probability of their excitation is five to six times smaller, as might have been expected because of a large binding energy in the virtual-decay channels $\alpha \longrightarrow d + d$ and $\alpha \longrightarrow t + p$, than in reactions induced by lithium ions.

A noticeable excitation of levels at the lower energies of $E^* = 15.2$ and 11.8 MeV was observed in [27]. The former can be identified with the three-cluster $J^\pi = (1/2)^-$ $\{432\}^{22}P$ state at $E^* = 15.5$ MeV, which was predicted in [13], while the latter can be associated with at least three states: $J^\pi = (3/2)^-$ $\{432\}^{24}P$ state at $E^* = 10.6$ MeV, $J^\pi = (5/2)^-$ $\{432\}^{24}P$ state at $E^* = 11.5$ MeV, and $J^\pi = (7/2)^-$ $\{432\}^{24}D$ state at $E^* = 11.4$ MeV.

Eventually, levels corresponding to the s^4p^6 configuration are peculiar to the ^{10}B and ^{10}Be nuclei and the $\{f\} = \{433\}$ symmetry: these are the $J^\pi = 1^+$ ^{11}P state at $E^* = 18.0$ MeV for the ^{10}B nucleus, the $J^\pi = 0^+$ ^{33}P state at $E^* = 14.6$ MeV for the ^{10}Be nucleus, and the $J^\pi = 2^+$ ^{33}P state at $E^* = 10.1$ MeV and the $J^\pi = 1^+$ ^{33}P state at $E^* = 11.3$ MeV for the ^{10}Be nucleus. Of some interest are also the $J^\pi = 4^+$ ($E^* = 17.1$ MeV), $J^\pi = 3^+$ ($E^* = 17.8$ MeV), and $J^\pi = 2^+$ ($E^* = 20.9$ MeV) levels of the $^{33}F_J$ multiplet [13]. The reaction ^{7}Li(^{7}Li, α)^{10}Be is one of the most appropriate ones for the formation of the corresponding three-cluster systems. It turned out, however [27] that, in this reaction, the states of the ^{10}Be nucleus at excitation energies in the range 10–15 MeV either are not manifested or are excited along with lower states [27]. A strong excitation of the near-threshold levels at $E^* = 17.9$ MeV (this level is excited 30 times more intensely than the ground state of the ^{10}Be nucleus) and 18.8 MeV was observed in the above reaction. The level at 17.9 MeV seems to correspond to the aforementioned $\{433\}^{33}F_3$ state, while the level at 18.8 MeV can be identified with $J^\pi = 3^+$ state at $E^* = 19.5$ MeV, where the $\{433\}$ symmetry, albeit nondominant, plays a substantial role [13] (the threshold energy E_n^* for the decay $^{10}\text{Be}^* \longrightarrow \alpha + t + t$ is 19.7 MeV [21]). The estimate presented in [30] for the relative values of the spectroscopic factors for the stripping mechanism in the reaction ^{7}Li(^{7}Li, α)^{10}Be is in excellent agreement with experimental results. There are also relevant experimental data on the reaction ^{7}Li(α, p)^{10}Be [30, 31], but these are less clear (see above).

Thus, experiments confirm the theoretical prediction that, in light nuclei like ^{8}Be, ^{9}Be, and ^{10}Be, there exist near-threshold three-cluster states in which the alpha-particle cluster plays a stabilizing role. It is worth noting that the majority of experimentally established near-threshold states can be associated with three-cluster systems characterized by large contributions of the relevant components of the wave functions obtained within the multiparticle shell model. This confirms the value of the supermultiplet scheme used: the states being discussed are seen against the background of levels having a different origin. Of course, the above three-cluster states call for a quantitative theoretical investigation, which can be performed by using the combined shell–cluster approach [33], the RGM (where there is experience of studying the 3α system [34]), the Faddeev equations for three-cluster systems [24], and the stochastic variational method [35, 36] as applied to three-cluster systems [37]. Simplifications of the pair t matrix like those of unitary-pole-approximation type [38] can also be useful for loose systems.

Unfortunately, the number of experiments that studied three-cluster systems of the $\alpha + d + t$ type is scanty. Because of this, definite theoretical states predicted long ago cannot be reliably associated, at present, with each highly excited state found experimentally. In particular, a further investigation of the aforementioned reactions with ^{6}Li, ^{7}Li, etc., nuclei is of special interest. It is necessary to measure the angular distributions of the products of these reactions in order to determine the orbital-angular-momentum transfers and the corresponding spectroscopic factors. Such a systematic investigation will also make it possible to resolve the question of the accuracy of the quantum number $\{f\}$ for near-threshold three-cluster states. Recall that this accuracy is expected to be 80–90% (see above).

5. CONCLUSION

The problem of the near-threshold states of two- and three-cluster systems has been systematically surveyed. In considering these states, we have exhaustively used the classification of states according to Young orbital schemes (this automatically solves the problem of the orthogonality of wave functions describing different cluster partitions), data on quasielastic-nucleon-knockout reactions, and previous calculations of the diagrams of energy levels in light nuclei on the basis of the multiparticle shell model (so far, very informative results of these calculations have found virtually no use for the present purposes). We have arrived at the conclusion that the thermonuclear $S = 3/2$, $L = 0$ level in the $t + d$ system is the only near-threshold level in extremely

light two-cluster systems and have clarified the reasons behind the absence of the $S = 1/2$, $L = 0$ level, a natural counterpart of the latter. But for light three-cluster systems, which are of great topical interest for nuclear astrophysics, the total number of near-threshold states that can be involved in reactions accompanied by a significant energy release appears to be rather large. A system like $t + t + d$ is inaccessible to a direct laboratory investigation, but the cases in which an alpha particle plays the role of one of the clusters can be thoroughly studied in direct nuclear reactions of cluster transfer such as (h, p), $(^6\mathrm{Li}, \alpha)$, and $(^7\mathrm{Li}, \alpha)$. An attractive feature of such reactions is their universality, since they are efficient both below and above the threshold for three-cluster decay. There are only fragmentary data on this point, which is of great importance not only for nuclear physics proper but also for nuclear astrophysics. In this connection, it would be advisable to conduct coordinated experiments of the required type in Almaty, Kiev, and Moscow, where appropriate accelerators are available.

As to a theoretical development, a natural approach would be to invoke the Faddeev equations for three-cluster systems [24], in which case use is made of pair potentials involving forbidden states [2, 18]. Here, simple estimates can be obtained within the approximation of separable potentials [38, 39], which oscillate [40] owing to the presence of forbidden states. The stochastic variational method developed in [35–37] is more involved, but it is of a microscopic character; moreover, this method takes explicitly into account antisymmetrization in nucleons.

In recent years, much attention has been given to systems featuring a few alpha particles (more than three). Such systems have very high moments of inertia [11]. This gives grounds for speculations about various chain configurations and so on, but a consistent analysis of such possibilities has yet to be performed.

ACKNOWLEDGMENTS

It is a pleasure to acknowledge that the present study was stimulated by discussions with V.B. Belyaev. We are grateful to N.S. Zelenskaya, V.I. Kukulin, and Yu.M. Tchuvil'sky.

REFERENCES

1. M. Hagler and M. Kristiansen, *An Introduction to Controlled Thermonuclear Fusion* (Lexington Books, Lexington, 1977).
2. B. Iskra, A. I. Mazur, V. G. Neudatchin, *et al.*, Yad. Fiz. **48**, 1674 (1988) [Sov. J. Nucl. Phys. **48**, 1003 (1988)]; V. G. Neudatchin, V. I. Kukulin, V. N. Pomerantsev, *et al.*, Phys. Rev. C **45**, 1512 (1992); V. G. Neudatchin, A. A. Sakharuk, and Yu. F. Smirnov, Fiz. Élem. Chastits At. Yadra **23**, 479 (1992) [Sov. J. Part. Nucl. **23**, 210 (1992)]; V. G. Neudatchin, A. A. Sakharuk, and S. B. Dubovichenko, Few-Body Syst. **18**, 159 (1995).
3. V. G. Neudatchin, V. G. Shevchenko, and N. P. Yudin, Phys. Lett. **10**, 180 (1964); V. G. Neudatchin and Yu. F. Smirnov, Nucl. Phys. **66**, 25 (1965).
4. V. G. Neudatchin and Yu. F. Smirnov, *Nucleon Clusters in Light Nuclei* (Nauka, Moscow, 1969).
5. Yu. F. Smirnov, K. V. Shitikova, and S. Kh. El Samarai, Vestn. Mosk. Univ., Ser. 3: Fiz., Astron., No. 2, 33 (1968).
6. V. I. Kukulin, Izv. Akad Nauk SSSR, Ser. Fiz. **52**, 2088 (1988).
7. Y. Fujiwara and Y. C. Tang, Phys. Rev. C **27**, 2457 (1983); H. M. Hoffmann and D. Fick, Phys. Rev. Lett. **52**, 2038 (1984); W. Von Oertzen, Z. Phys. A **354**, 37 (1996).
8. B. De Facio, R. K. Umerjee, and J. L. Gammel, Phys. Rev. **151**, 819 (1966).
9. V. T. Voronchev, B. I. Kukulin, V. M. Krasnopolsky, *et al.*, Yad. Fiz. **37**, 271 (1983) [Sov. J. Nucl. Phys. **37**, 161 (1983)]; V. S. Vasilevsky, I. F. Gutich, and I. P. Okhrimenko, Yad. Fiz. **46**, 757 (1987) [Sov. J. Nucl. Phys. **46**, 427 (1987)]; A. M. Gorbatov, P. Yu. Nikishov, and V. L. Skopich, Izv. Akad. Nauk, Ser. Fiz. **59** (1), 52 (1995); V. S. Popov, B. M. Karnakov, and V. D. Mur, Zh. Éksp. Teor. Fiz. **110**, 1537 (1996) [JETP **83**, 849 (1996)].
10. F. S. Cwieroth, R. E. Brown, Y. C. Tang, *et al.*, Phys. Rev. C **8**, 938 (1973); H. Kamada, T. Kaneko, P. N. Shen, *et al.*, Nucl. Phys. A **457**, 93 (1986).
11. J. Yao, H. Sun, H. Lu, *et al.*, Nucl. Phys. A **519**, 602 (1990); A. C. Merchant and W. D. M. Rao, Nucl. Phys. A **549**, 431 (1992); S. G. Anagnostatos, Phys. Rev. C **51**, 152 (1995); M. Dufour and P. Descouvemont, Nucl. Phys. A **605**, 160 (1996).
12. A. I. Baz', Ya. B. Zel'dovich, and A. M. Perelomov, *Scattering, Reactions and Decays in Nonrelativistic Quantum Mechanics*. Transl. of 1st Russ. ed. (2nd ed., Nauka, Moscow, 1971; Israel Program of Scientific Translations, Jerusalem, 1966).
13. S. Cohen and D. Kurath, Nucl. Phys. **73**, 1 (1965); A. N. Boyarkina, *Structure of the p-Shell Nuclei* (Mosk. Gos. Univ., Moscow, 1973); D. Kurath and D. J. Miller, Nucl. Phys. A **238**, 269 (1975).
14. B. Jenny, W. Gruebler, P. A. Schmelzbach, *et al.*, Nucl. Phys. A **337**, 77 (1980).
15. Y. C. Tang, M. Le Mere, and D. R. Thompson, Phys. Rep. **47**, 167 (1978).
16. B. N. Zakhar'ev, *Lessons in Quantum Intuition* (JINR, Dubna, 1996).
17. V. Iskra, A. I. Mazur, V. G. Neudatchin, *et al.*, Yad. Fiz. **49**, 672 (1989) [Sov. J. Nucl. Phys. **49**, 416 (1989)].
18. O. F. Nemets, V. G. Neudatchin, A. T. Rudchik, *et al.*, *Nucleon Clustering in Nuclei and Nuclear Reactions of Multinucleon Transfer* (Naukova Dumka, Kiev, 1988).
19. B. S. Ishkhanov, I. M. Kapitonov, and V. G. Neudatchin, Fiz. Élem. Chastits. At. Yadra **12**, 905 (1981) [Sov. J. Part. Nucl. **12**, 362 (1981)]; R. A. Eramzhyan, B. S. Ishkhanov, I. M. Kapitonov, *et al.*, Phys. Rep. **136**, 229 (1986).
20. B. S. Ishkhanov, I. M. Kapitonov, V. G. Neudatchin, *et al.*, Usp. Fiz. Nauk **160** (3), 57 (1990).

21. J. Mougey, Nucl. Phys. A **335**, 35 (1980); S. Frullani and J. Mougey, Adv. Nucl. Phys. **15**, 1 (1983).
22. F. Ajzenberg-Selove, Nucl. Phys. A **490**, 1 (1988).
23. W. Glockle, *The Quantum Mechanical Few-Body Problem* (Springer-Verlag, 1983); R. H. Landau and M. Sagan, Phys. Rev. C **33**, 447 (1986); I. Bombaci and U. Lombardo, Phys. Rev. C **44**, 1892 (1991).
24. V. I. Kukulin, V. G. Neudatchin, and V. N. Pomerantsev, Yad. Fiz. **24**, 298 (1976) [Sov. J. Nucl. Phys. **24**, 155 (1976)]; J. Phys. G **4**, 1409 (1978); Sh. Oryu and H. Kamada, Nucl. Phys. A **493**, 91 (1989).
25. A. Bohr and B. R. Mottelson, *Nuclear Structure*, Vol. 1: *Single-Particle Motion* (Benjamin, New York, 1969).
26. S. N. Abramovich, B. Ya. Guzhovskiĭ, and L. M. Lazarev, Fiz. Élem. Chastitz At. Yadra **23**, 305 (1992) [Sov. J. Part. Nucl. **23**, 129 (1992)].
27. Yu. A. Glukhov, B. G. Novatskiĭ, A. A. Ogloblin, *et al.*, Yad. Fiz. **13**, 277 (1971) [Sov. J. Nucl. Phys. **13**, 154 (1971)].
28. N. T. Burtebaev, A. A. Vinogradov, A. D. Vongai, *et al.*, Izv. Akad Nauk Kaz. SSR, Ser. Fiz.-Mat. **2**, 59 (1975).
29. G. J. Clark, D. J. Sullivan, and P. B. Treacy, Nucl. Phys. A **98**, 473 (1967).
30. N. T. Burtebaev, A. D. Vongai, Yu. A. Glukhov, *et al.*, Izv. Akad. Nauk SSSR, Ser. Fiz. **39**, 2160 (1975).
31. S. Hamada, M. Yasue, S. Kubono, *et al.*, Phys. Rev. C **49**, 3192 (1994).
32. V. V. Balashov, V. G. Neudachin, Yu. F. Smirnov, *et al.*, Zh. Éksp. Teor. Fiz. **37**, 1385 (1959) [Sov. Phys. JETP **10**, 983 (1959)]; Yu. F. Smirnov and D. Chlebovska, Nucl. Phys. **26**, 306 (1961); Yu. F. Smirnov, Nucl. Phys. **39**, 346 (1962); I. Rotter, Nucl. Phys. A **122**, 567 (1968); **135**, 378 (1969).
33. Yu. F. Smirnov, I. T. Obukhovsky, Yu. M. Tchuvil'sky, *et al.*, Nucl. Phys. A **235**, 289 (1974).
34. Y. Fukushima and M. Kamimura, in *Proceedings of International Conference on Nuclear Structure, Tokyo, 1977*, Ed. by T. Marumori, J. Phys. Soc. Jpn. Suppl. **44**, 225 (1978).
35. V. I. Kukulin and V. M. Krasnopolsky, Yad. Fiz. **22**, 1110 (1975) [Sov. J. Nucl. Phys. **22**, 578 (1975)]; J. Phys. G **3**, 795 (1977).
36. K. Varga and Y. Suzuki, Phys. Rev. C **52**, 2885 (1995); Y. Suzuki, K. Varga, and J. Usukura, Nucl. Phys. A **631**, 91c (1998).
37. A. Csótó, H. Oberhummer, and R. Pichler, Phys. Rev. C **53**, 1589 (1996); R. Pichler, H. Oberhummer, A. Csoto, *et al.*, Nucl. Phys. A **618**, 55 (1997).
38. S. Nakaishi-Maeda, Phys. Rev. C **51**, 1633 (1995).
39. Sh. Oryu, H. Kamada, H. Sekine, *et al.*, Nucl. Phys. A **534**, 221 (1991).
40. V. I. Kukulin and V. G. Neudatchin, Nucl. Phys. A **157**, 609 (1970).

Translated by A. Isaakyan

Physics of Atomic Nuclei, Vol. 63, No. 2, 2000, pp. 204–209. Translated from Yadernaya Fizika, Vol. 63, No. 2, 2000, pp. 257–263.

NUCLEI
Theory

Relativistic Expressions for Current Electric Moments of Nuclei

A. J. Silenko

Institute of Nuclear Problems, Belarussian State University, ul. Bogdanovicha 153, Minsk, 240040 Belarus

Received August 25, 1998; in final form, January 27, 1999

Abstract—Relativistic expressions for the operators of current electric moments caused by electromagnetic spin–orbit interaction are obtained. Formulas for the matrix elements of the current electric moments of nuclei are derived. The contributions of the current electric moments to the quadrupole moment of the deuteron and to its root-mean-square radius are calculated with allowance for relativistic effects. © *2000 MAIK "Nauka/Interperiodica".*

1. INTRODUCTION

It well known that the electromagnetic spin–orbit interaction of intranuclear nucleons, which is proportional to the electric-field strength **E**, generates electromagnetic corrections to the electric moments of nuclei. These corrections are taken into account in the theory of the deuteron [1–5], as well as in the theory of other nuclei [4, 5]. Spin–orbit interaction results from the motion of the magnetic moments of particles, which causes a nonzero charge density. The effect of the spin–orbit interaction on the charge-density distribution in some nuclei was investigated in [6, 7]. Variations in the charge density lead to the emergence of electric moments, which were called current electric moments (CEM) in [4, 5, 8–10]. It was shown in [4, 5] that the contribution of the current electric quadrupole moments (CEQM) to the total quadrupole moments of some nuclei cannot be neglected. The expressions for the current electric dipole moment and for corrections to the root-mean-square charge radius that are associated with electrostatic contact interaction of a current origin were found in [10].

In [1–3], relativistic corrections to the quadrupole moment of the deuteron and to its root-mean-square radius were calculated within the conventional impulse approximation. The application of this approach involves rather cumbersome calculations; moreover, this does not lead to the relatively simple equations that were obtained in [4, 5, 10] and which are convenient for evaluating the CEQM of other nuclei. The calculations in [4, 5, 10] relied on the Foldy–Wouthuysen representation, where the relations between relevant operators are identical to the relations between the corresponding classical quantities and where the static moments are equal to the expectation values of the corresponding operators.

In all articles quoted above, the static moments of a current origin were calculated in the nonrelativistic approximation. Here, we derive relativistic expressions for the corresponding moments.

Throughout this article, we use the system of units where $\hbar = c = 1$.

2. OPERATORS OF CURRENT ELECTRIC MOMENTS

In classical theory, a moving particle whose magnetic moment in its rest frame is $\boldsymbol{\mu}$ develops an electric dipole moment **d** in the laboratory frame. This dipole moment is given by (see [11])

$$\mathbf{d} = [\mathbf{v} \times \boldsymbol{\mu}]. \tag{1}$$

The relativistic expression for the energy of intranuclear-nucleon interaction (or for the energy of electron interaction in an atom) with an external nonuniform electrostatic field is obtained from a power-series expansion of the field potential ϕ. We have

$$W = d_i \frac{\partial \phi(\mathbf{R})}{\partial X_i} + \frac{1}{6} Q_{ij} \frac{\partial^2 \phi(\mathbf{R})}{\partial X_i \partial X_j} + \frac{1}{6} \tau \frac{\partial^2 \phi(\mathbf{R})}{\partial X_i^2}, \tag{2}$$

$$Q_{ij} = 3d_i x_j + 3d_j x_i - 2\delta_{ij} \mathbf{d} \cdot \mathbf{r}, \quad \tau = 2\mathbf{d} \cdot \mathbf{r},$$

where **R** is the radius vector of the center of inertia of the nucleus (atom), and **r** is the nucleon radius vector with respect to the center of inertia. The quantity **d** is given by equation (1), and summation is performed over the dummy indices. The nuclear moments are determined as the sums of the quantities Q_{ij} and τ corresponding to different nucleons (the dipole moments of the nuclei are equal to zero). We denote by τ_t the sum of the quantities τ (of both charge and current origins) over all nucleons. The root-mean-square radius of the nucleus is then given by

$$\bar{r} = \sqrt{\tau_t / Ze},$$

where Ze is the charge of nucleus.

Let us consider CEM operators in quantum theory. In the Foldy–Wouthuysen representation, these operators can be constructed on the basis of the relativistic expression for the energy of spin–orbit interaction by

expanding the electric-field strength **E** in powers of r/R [10] in just the same way as in (2).

In constructing the CEM operators, we can make use of the relations for the operator of spin–orbit interaction that were obtained in [12–14]. For Dirac particles featuring no anomalous magnetic moment (AMM), the operator of spin–orbit interaction has the form [12]

$$W = \frac{e(\mathbf{E}\cdot[\mathbf{v}\times\boldsymbol{\sigma}])}{2(\epsilon+m)},$$
$$\epsilon = \frac{m}{\sqrt{1-\mathbf{v}^2}} = \sqrt{\boldsymbol{\pi}^2+m^2}, \quad \boldsymbol{\pi} = \mathbf{p}-e\mathbf{A}, \tag{3}$$

where **v**, ϵ, and $\boldsymbol{\pi}$ are the velocity, kinetic-energy, and kinetic-momentum operators, respectively; $\mathbf{p} = -i\nabla$ is the momentum operator; **A** is the vector potential of the external field; and m is the particle mass.

Since the operator W must be a Hermitian operator, the product of noncommuting operators in expressions of the type (3) must be replaced by the anticommutators $\{\ldots,\ldots\}_+$.

For relativistic particles with an AMM, the operator of spin–orbit interaction has the form [14]

$$W = \frac{1}{2}\left\{\left(\frac{\mu_0 m}{\epsilon+m}+\mu'\right)\frac{1}{\epsilon}, ([\boldsymbol{\sigma}\times\mathbf{p}]\cdot\mathbf{E})\right\}_+,$$

where $\mu_0 = e/2m$, $\mu' = \mu - \mu_0$, and μ are, respectively, the Dirac, the anomalous, and the total magnetic moments. Since the weak-field approximation was used in [14], terms that are quadratic in the field were not taken into account in the above expression.

Recall that the spin–orbit interaction and CEM appear only in the case of a moving particle; therefore, the interaction operator must be proportional to the velocity operator **v**, which is equal to the commutator of the Hamiltonian and the operator **r**:

$$\mathbf{v} = \dot{\mathbf{r}} = i[\mathscr{H}, \mathbf{r}]. \tag{4}$$

The refined expression for the energy of the spin–orbit interaction has the form

$$W = \frac{1}{4}\left\{\left(\frac{\mu_0 m}{\epsilon+m}+\mu'\right), ([\boldsymbol{\sigma}\times\mathbf{v}]\cdot\mathbf{E}-[\mathbf{v}\times\boldsymbol{\sigma}]\cdot\mathbf{E})\right\}_+. \tag{5}$$

In equation (5), we have considered that **v** and $\boldsymbol{\sigma}$ can be noncommuting operators. To the required precision, the velocity operator **v** can be found by using equation (4) and the expression obtained in [14] for the Hamiltonian. This yields

$$\mathbf{v} = \frac{1}{2}\left\{\frac{1}{\epsilon}, (\mathbf{p}-e\mathbf{A})\right\}_+ - \frac{1}{2}\left\{\left(\frac{\mu_0 m}{\epsilon+m}+\mu'\right)\frac{1}{\epsilon}, [\boldsymbol{\sigma}\times\mathbf{E}]\right\}_+.$$

Upon the substitution of this expression into equation (5), the first term, which is linear in **E**, is fully in accord with the relations obtained in [12, 13] for the energy of the spin–orbit interaction. It is worth noting that the analysis in [13] relied on the nonrelativistic approximation ($\epsilon \approx m$) with allowance for relativistic corrections. The second term, which is quadratic in **E** and which is much smaller then the first term, can be recast, after a simplification of the product of Pauli matrices, into the form

$$W' = \left\{\left(\frac{\mu_0 m}{\epsilon+m}+\mu'\right)^2\frac{1}{\epsilon}, E^2\right\}_+.$$

For Dirac particles ($\mu' = 0$), the terms in the Hamiltonian that are quadratic in **E** are determined by the relation

$$W'' = \frac{e^2E^2}{8\epsilon^3} - \frac{e^2(\mathbf{E}\cdot\mathbf{v})^2}{8\epsilon^3},$$

which was obtained in [12] and which is somewhat different in form from the preceding expression. Although the quantities W' and W'' are on the same order of magnitude, only in the nonrelativistic limit do they coincide for Dirac particles. In this limit, the expression for W' is simplified to become

$$W' = \frac{1}{2m}(\mu_0^2 + 4\mu_0\mu' + 4\mu'^2)E^2.$$

In the Hamiltonian obtained in [13] for particles featuring an AMM, the term proportional to E^2 is given by

$$W''' = \frac{1}{2m}(\mu_0^2 + \mu_0\mu' + \mu'^2)E^2. \tag{6}$$

The quantities W' and W''' differ by the factor in front of E^2, but they are also on the same order of magnitude. The difference between W', on one hand, and W'' and W''', on the other hand, is explained by the fact that equation (5) does not take into account all relativistic corrections to the electric moments of nuclei and atoms. In addition to those that can be found by means of equations (5) and (6), there are the corrections that are due to the presence of terms in the Hamiltonian that are proportional to higher powers of the potentials and field strengths. However, the corrections determined by CEM are leading ones since we have $|W'| \sim |W''| \sim |W'''| \ll |W|$.

Expanding, as in [10], the vector strength of the static electric field in power series in x_i and retaining only zero-order and linear terms,

$$E_i(\mathbf{r}) = -\frac{\partial\phi(\mathbf{R})}{\partial X_i} - x_j\frac{\partial^2\phi(\mathbf{R})}{\partial X_i\partial X_j},$$

we obtain, by means of a procedure similar to that relying on (2), the operator relation for W. With the aid of it, we find that the sought CEM operators can be represented as

$$\mathbf{d} = \frac{1}{4}\{\omega, ([\mathbf{v}\times\boldsymbol{\sigma}]-[\boldsymbol{\sigma}\times\mathbf{v}])\}_+,$$

$$\mathcal{Q}_{ij} = \frac{3}{8}\{\omega, \{(e_{ikl}x_i + e_{ikl}x_j), \{v_k, \sigma_l\}_+\}_+\}_+$$
$$-\frac{1}{4}\delta_{ij}\{\omega, \{\boldsymbol{\sigma}, ([\mathbf{r}\times\mathbf{v}] - [\mathbf{v}\times\mathbf{r}])\}_+\}_+, \quad (7)$$
$$\tau = \frac{1}{4}\{\omega, \{\boldsymbol{\sigma}, ([\mathbf{r}\times\mathbf{v}] - [\mathbf{v}\times\mathbf{r}])\}_+\}_+,$$
$$\omega = \frac{\mu_0 m}{\epsilon + m} + \mu',$$

where $\mathbf{d}$ and $\mathcal{Q}_{ij}$ are, respectively, the operator of the current electric dipole moment and the operator of CEQM, while the operator τ characterizes the electrostatic contact interaction of current origin. The relations in (7) provide a relativistic generalization of the equations obtained in [4, 5, 10].

3. TRANSFORMATION OF THE CEQM OPERATOR

Following [4, 5, 10], we can express the CEQM in terms of the operator $\boldsymbol{\lambda} = ([\mathbf{r}\times\mathbf{v}] - [\mathbf{v}\times\mathbf{r}])/2$. Here, we employ a transformation method that is more rigorous than that in the articles quoted immediately above and which does not invoke the current-density operator $\mathbf{j}$. By using the expression for the total time derivative,

$$\left\langle \frac{d}{dt}\{\omega, x_i x_k \sigma_l\}_+ \right\rangle = \frac{1}{2}\langle\{\omega, \{x_k\sigma_l, v_i\}_+\}_+\rangle$$
$$+\frac{1}{2}\langle\{\omega, \{x_i\sigma_l, v_k\}_+\}_+\rangle$$
$$+\frac{1}{2}\langle\{\omega, \{x_i x_k, \dot{\sigma}_l\}_+\}_+\rangle + \langle\{\dot{\omega}, x_i x_k \sigma_l\}_+\rangle,$$

and the fact that the expectation value of the time derivative of a Hermitian operator in a stationary state is zero, $\left\langle \frac{d}{dt}\{\omega, x_i x_k \sigma_l\}_+ \right\rangle = 0$, we obtain

$$e_{jkl}\langle\{\omega, \{x_i, \{v_k, \sigma_l\}_+\}_+\}_+\rangle$$
$$= e_{jkl}e_{ikm}\langle\{\omega, \{\sigma_l, \lambda_m\}_+\}_+\rangle$$
$$-e_{jkl}\langle\{\omega, \{x_i x_k, \dot{\sigma}_l\}_+\}_+\rangle - 2e_{jkl}\langle\{\dot{\omega}, x_i x_k \sigma_l\}_+\rangle.$$

It follows that the CEQM $Q_{ij} = \langle\mathcal{Q}_{ij}\rangle$ is also equal to the expectation value of the operator

$$\mathcal{Q}'_{ij} = D^{(1)}_{ij} + D^{(2)}_{ij} + D^{(3)}_{ij},$$
$$D^{(1)}_{ij} = -\frac{3}{8}\left\{\omega, [\{\sigma_i, \lambda_j\}_+ + \{\sigma_j, \lambda_i\}_+ - \frac{2}{3}\delta_{ij}(\boldsymbol{\sigma}\cdot\boldsymbol{\lambda} + \boldsymbol{\lambda}\cdot\boldsymbol{\sigma})]\right\}_+, \quad (8)$$
$$D^{(2)}_{ij} = -\frac{3}{8}\{\omega, \{(e_{jkl}x_i + e_{ikl}x_j)x_k, \dot{\sigma}_l\}_+\}_+,$$
$$D^{(3)}_{ij} = -\frac{3}{4}\{\dot{\omega}, (e_{jkl}x_i + e_{ikl}x_j)x_k\sigma_l\}_+,$$

that is, $Q_{ij} = \langle\mathcal{Q}'_{ij}\rangle$. In going over to the nonrelativistic approximation, we can neglect the operator $D^{(3)}_{ij}$. As a result, we arrive at the well-known expression for the operator $\mathcal{Q}'_{ij}$ (see [4, 5]). In this approximation, the operator $D^{(2)}_{ij}$ is not always small because the tensor interaction between nucleons, which determines the operator $\dot{\boldsymbol{\sigma}}$, may be sufficiently large. It was shown in [4, 5], however, that, upon summation of the contributions from various nucleons, this operator is commensurate with the operator $D^{(1)}_{ij}$ only for a small number of extremely light odd–odd nuclei.

For the majority of nuclei, we can set $\boldsymbol{\lambda} = \mathbf{l}/m$ ($\mathbf{l}$ is the angular-momentum operator), which renders equation (8) convenient for calculating CEQMs [4, 5]. When relativistic corrections are taken into account, however, the calculation of the terms featuring time derivatives by evaluating the commutators of the corresponding operators and the Hamiltonian by means of equation (8) becomes rather cumbersome. In this case, it is more convenient to use equation (7).

4. SPIN–ORBIT CORRECTIONS TO CEM OPERATOR

Dominant corrections to the velocity operator come from the spin–orbit interaction of nucleons.[1)] Taking the operator of spin–orbit interaction in the form [15]

$$W_{LS} = -\frac{1}{2}f(r)(\boldsymbol{\sigma}\cdot[\mathbf{r}\times\mathbf{p}])$$

and using equation (4), we find that the velocity operator can be represented as

$$\mathbf{v} = \frac{\mathbf{p}}{\epsilon} + \frac{1}{2}f(r)[\mathbf{r}\times\boldsymbol{\sigma}].$$

Electromagnetic corrections to the velocity operator can be neglected. In this case, relations (7) for the CEM operators become

$$\mathbf{d} = -\frac{1}{2}\left\{\omega, \left(\frac{[\boldsymbol{\sigma}\times\mathbf{p}]}{m} + f(r)\mathbf{r}\right)\right\}_+,$$
$$\mathcal{Q}_{ij} = \frac{3}{4m}\{\omega, \{(e_{jkl}x_i + e_{ikl}x_j), p_k\sigma_l\}_+\}_+$$
$$-\frac{1}{m}\delta_{ij}\{\omega, \boldsymbol{\sigma}\cdot\mathbf{l}\}_+ - \{\omega, (3x_i x_j - \delta_{ij}r^2)f(r)\}_+, \quad (9)$$

[1)] We means here strong interaction, which must be distinguished from electromagnetic spin–orbit interaction resulting in the emergence of CEMs.

$$\tau = \left\{\omega, \left[\frac{\boldsymbol{\sigma}\cdot\mathbf{l}}{m} - r^2 f(r)\right]\right\}_+.$$

It follows from equations (9) that, with respect to dominant terms, spin–orbit corrections to the CEM operator are of order

$$\frac{mr^2 f(r)}{l} \sim \frac{mvr\cdot f(r)rp}{lpv} \sim \frac{|W_{LS}|}{pv} \sim \frac{|W_{LS}|}{|W|},$$

where W is the total interaction operator. In accordance with this estimate, spin–orbit corrections are usually of order of v/c, appearing to be dominant relativistic corrections to CEMs. If terms that are retained in taking into account relativistic corrections have the order of smallness not higher than v/c, we obtain $\omega \approx \mu_0/2 + \mu'$. In this case, the calculation of the matrix elements of the CEM operators yields[2)]

$$\left\langle jm;\ j-\frac{1}{2}\middle|\mathcal{Q}_{zz}\middle|jm;\ j-\frac{1}{2}\right\rangle$$

$$= \kappa\frac{3m^2 - j(j+1)}{j}\left(-1 + \frac{M}{j+1}\langle r^2 f(r)\rangle\right),$$

$$\left\langle jm;\ j+\frac{1}{2}\middle|\mathcal{Q}_{zz}\middle|jm;\ j+\frac{1}{2}\right\rangle$$

$$= \kappa\frac{3m^2 - j(j+1)}{j+1}\left(1 + \frac{M}{j}\langle r^2 f(r)\rangle\right), \qquad (10)$$

$$\left\langle jm;\ j-\frac{1}{2}\middle|\tau\middle|jm;\ j-\frac{1}{2}\right\rangle = \kappa(2j - 1 - 2M\langle r^2 f(r)\rangle),$$

$$\left\langle jm;\ j+\frac{1}{2}\middle|\tau\middle|jm;\ j+\frac{1}{2}\right\rangle$$

$$= -\kappa(2j + 3 + 2M\langle r^2 f(r)\rangle), \quad \kappa = \omega/M.$$

The calculation of the matrix elements of the CEQM operator on the basis of equations (8) leads to the same results. If the CEQM of nuclei is determined by one nucleon, it is characterized by the quantity $\langle jj;\ j \pm 1/2|\mathcal{Q}_{zz}|jj;\ j \pm 1/2\rangle$. From (10), it follows that

$$\left\langle jj;\ j-\frac{1}{2}\middle|\mathcal{Q}_{zz}\middle|jj;\ j-\frac{1}{2}\right\rangle$$

$$= \kappa(2j-1)\left(-1 + \frac{M}{j+1}\langle r^2 f(r)\rangle\right),$$

$$\left\langle jj;\ j+\frac{1}{2}\middle|\mathcal{Q}_{zz}\middle|jj;\ j+\frac{1}{2}\right\rangle \qquad (11)$$

$$= \kappa\frac{j(2j-1)}{j+1}\left(1 + \frac{M}{j}\langle r^2 f(r)\rangle\right).$$

The spin–orbit corrections to the CEMs of multinucleon nuclei can be found by the method that is identical to that which was used to determine the additional magnetic moment of nucleons (see [15]). Since the function $f(r)$ decreases fast toward the center of the nucleus, the factor r^2 can be replaced, upon averaging, by R^2, where R is the radius of the nucleus; that is, $\langle r^2 f(r)\rangle = R^2\langle f(r)\rangle$. The quantity $\langle f(r)\rangle$ can be expressed in terms of the spin–orbit splitting ΔE of the $j = l \pm 1/2$ levels as [15]

$$\langle f(r)\rangle = \frac{\Delta E}{l + 1/2}.$$

5. EVALUATION OF THE DEUTERON CEM

Relativistic corrections to the quadrupole moment and the root-mean-square radius of the deuteron that are associated with the electromagnetic spin–orbit interaction were calculated in [2–5]. These corrections to the quadrupole moment determine the deuteron CEQM. We will calculate the CEQM and the corresponding corrections to the root-mean-square charge radius of the deuteron, taking into account the contribution to the velocity operator from strong spin–orbit interaction.

In [4, 5], the deuteron CEQM was calculated by means of an equation that is similar to (8) (without taking into account relativistic corrections). However, this method of calculation seems less efficient than that which is based on equation (7). Although relations (7) and (8) are equivalent, the procedure relying on equation (8) involves a determination of the operator $\dot{\boldsymbol{\sigma}}$ via evaluating the commutator of the Hamiltonian and the operator $\boldsymbol{\sigma}$ with the result that the calculation on the basis of (8) becomes more cumbersome and less precise. Here, we use relation (7) to determine the deuteron CEMs. In the calculations, it is necessary to take into account the motion of the proton and of the neutron and to consider that their masses are approximately equal. For the case of the deuteron, we can neglect v^2/c^2 corrections to the CEMs and set $\omega \approx (\mu_0 + 2\mu')/2M$ in equations (7). At the same time, we must take into account corrections to the velocity operator that are associated with the spin–orbit (so) interaction, the quadratic spin–orbit ($so2$) interaction, and the interaction quadratic in the angular momentum ($L2$). They are proportional to the corresponding corrections to the current operator and are determined by equation (4). In the above approximation, the proton- and neutron-velocity operators are given by

$$\mathbf{v}_1 = \frac{\mathbf{p}}{M} + \Delta\mathbf{v}_1, \quad \mathbf{v}_2 = -\frac{\mathbf{p}}{M} + \Delta\mathbf{v}_2.$$

[2)]All the relations presented above are valid for any spin-1/2 particle species, including electrons in atoms. In what follows, we consider only nuclei and employ a conventional notation for the nucleon mass (M), for the total angular momentum of the nucleon (j), and for the projection of the total angular momentum (m).

The operators $\Delta\mathbf{v}_1$ and $\Delta\mathbf{v}_2$ are determined by the commutators of the corresponding terms in the Hamiltonian and the operator $\mathbf{r}$.

We will first find the CEMs, neglecting the contributions of the operators $\Delta\mathbf{v}_1$ and $\Delta\mathbf{v}_2$. In this case, the CEM operators are given by

$$\mathcal{Q}_{ij} = -\frac{1}{4}(\kappa_p + \kappa_n)$$

$$\times (3\{[\mathbf{S}\times\mathbf{p}]_i, x_j\}_+ + 3\{[\mathbf{S}\times\mathbf{p}]_j, x_i\}_+ + 4\delta_{ij}\mathbf{L}\cdot\mathbf{S}),$$

$$\tau = (\kappa_p + \kappa_n)\mathbf{L}\cdot\mathbf{S},$$

where $\kappa_p = \omega_p/M$ and $\kappa_n = \omega_n/M$.

Introducing the standard notation $u = rR_s(r)$ and $w = rR_d(r)$ for the deuteron wave functions, we express the CEM as

$$Q_0 = \langle\mathcal{Q}_{zz}\rangle = \frac{3\sqrt{2}}{5}(\kappa_p + \kappa_n)$$

$$\times\int_0^\infty rw\left(\frac{u}{r}\right)' dr + \frac{3}{10}(\kappa_p + \kappa_n)P_D, \qquad (12)$$

$$\tau_0 = \langle\tau\rangle = -3(\kappa_p + \kappa_n)P_D,$$

where $P_D = \int_0^\infty w^2\,dr$. Performing integration by parts as

$$\int_0^\infty w^2 dr = -2\int_0^\infty rww'dr,$$

we can reduce the expression for Q_0 to the form

$$Q_0 = \frac{3\sqrt{2}}{5}(\kappa_p + \kappa_n)\int_0^\infty r^2 w\left[\left(\frac{u}{r}\right)' - \frac{1}{\sqrt{2}}\frac{w'}{r}\right]dr. \qquad (13)$$

Relation (13) and expression (12) for τ_0 are fully in accord with the results presented in [2], because the coefficients κ_p and κ_n are related to the form factors used in the present article by the equation $\kappa_p + \kappa_n = (2G_M^S - G_E^S)/4M^2$. Relativistic corrections to the CEM operators were disregarded in [1–5].

For the parameters Q_0 and τ_0, the calculations by equations (12) yield the following results in the case of the Paris [16] and Bonn [17] potentials, respectively:

$$Q_0 = -1.81\times10^{-3}\ \text{fm}^2, \quad \tau_0 = -1.46\times10^{-3}\ \text{fm}^2,$$

$$Q_0 = -1.74\times10^{-3}\ \text{fm}^2, \quad \tau_0 = -1.08\times10^{-3}\ \text{fm}^2.$$

In the former case, the above results agree with those obtained by Kohno [2], who also used the Paris potential. In [5], the quadrupole moment was calculated by a formula similar to (8), and the absolute value of the result obtained for it is greater by a factor of about 2. It seem that this is because small distances play a more important role for the CEQM than for charge quadrupole moment. For such distances, the one-pion-exchange potential used in [5] for nucleon interaction has insufficient accuracy. It is therefore preferable to employ equations (12), which does not involve interaction potentials.

6. RELATIVISTIC CORRECTIONS TO THE DEUTERON CEM

Relativistic corrections to the deuteron CEM stem from the corrections to the velocity operator that are calculated on the basis of equation (4). In the potential of nucleon–nucleon interaction, the operator of spin–orbit interaction, $W_{so} = V_{so}(r)\mathbf{L}\cdot\mathbf{S}$; the operator of quadratic spin–orbit interaction, $W_{so2} = V_{so2}(r)\frac{1}{2}[(\boldsymbol{\sigma}_1\cdot\mathbf{L})(\boldsymbol{\sigma}_2\cdot\mathbf{L}) + (\boldsymbol{\sigma}_2\cdot\mathbf{L})(\boldsymbol{\sigma}_1\cdot\mathbf{L})]$; and the operator of interaction quadratic in the angular momentum, $W_{L2} = V_{L2}(r)\mathbf{L}^2$, do not commute with the operator $\mathbf{r}$. Frequently, use is made of the operator $W_{LS2} = V_{LS2}(r)(\mathbf{L}\cdot\mathbf{S})^2$, which can be expressed in terms of the above operators with the aid of the well-known relation

$$(\mathbf{L}\cdot\mathbf{S})^2 = \frac{1}{2}\mathbf{L}^2 - \frac{1}{2}\mathbf{L}\cdot\mathbf{S}$$

$$+\frac{1}{4}[(\boldsymbol{\sigma}_1\cdot\mathbf{L})(\boldsymbol{\sigma}_2\cdot\mathbf{L}) + (\boldsymbol{\sigma}_2\cdot\mathbf{L})(\boldsymbol{\sigma}_1\cdot\mathbf{L})].$$

The aforementioned corrections to the velocity operator are relatively small, because the operators W_{so}, W_{so2}, and W_{L2} characterize interaction at small distances, which is rather weak for the deuteron (see [3]).

The calculation of the relativistic corrections to the deuteron CEM yields

$$Q_{\text{corr}} = (\omega_p + \omega_n)$$

$$\times\int_0^\infty\left[\left(\frac{2\sqrt{2}}{5}V_{so}(r) - \frac{9\sqrt{2}}{10}V_{so2}(r) - \frac{9\sqrt{2}}{10}V_{L2}(r)\right)u\right.$$

$$\left.+\left(-\frac{1}{5}V_{so}(r) + \frac{9}{10}V_{so2}(r) + \frac{3}{10}V_{L2}(r)\right)w\right]wr^2dr, \qquad (14)$$

$$\tau_{\text{corr}} = (\omega_p + \omega_n)$$

$$\times\int_0^\infty\left[V_{so}(r)u^2 + \left(V_{so}(r) - \frac{9}{2}V_{so2}(r) - 3V_{L2}(r)\right)w^2\right]r^2dr.$$

Their numerical values calculated with the wave functions for the Paris and Bonn potentials are, respectively,[3)]

$$Q_{\text{corr}} = -1\times10^{-5}\ \text{fm}^2, \quad \tau_{\text{corr}} = 2.2\times10^{-4}\ \text{fm}^2,$$

[3)]Since high accuracy of calculations is not required in this case, the quantities $V_{so}(r)$, $V_{so2}(r)$, and $V_{L2}(r)$ were determined with the aid of the Argonne potential [3].

$$Q_{\text{corr}} = -6 \times 10^{-6} \text{ fm}^2, \quad \tau_{\text{corr}} = 2.2 \times 10^{-4} \text{ fm}^2.$$

It follows that the deuteron CEMs found with allowance for the relativistic corrections ($Q = Q_0 + Q_{\text{corr}}$ and $\tau = \tau_0 + \tau_{\text{corr}}$) are

$$Q = -1.8 \times 10^{-3} \text{ fm}^2, \quad \tau = -1.2 \times 10^{-3} \text{ fm}^2,$$

$$Q = -1.7 \times 10^{-3} \text{ fm}^2, \quad \tau = -0.9 \times 10^{-3} \text{ fm}^2$$

for the Paris and Bonn potentials, respectively. Thus, the above relativistic corrections are sizable only for the quantity τ, which characterizes the contact interaction of a current origin. This quantity determines the corresponding correction to the root-mean-square radius $\bar{r}$ of the deuteron. The smallness of the corrections to the quadrupole moment stems from the cancellation of the contributions from the spin–orbit interaction, the quadratic spin–orbit interaction, and the interaction quadratic in the angular momentum.

7. CONCLUSION

Relativistic expressions have been obtained for the operators of the CEMs of nuclei. Current electric quadrupole moments and corrections to root-mean-square charge radii that are due to contact electrostatic interaction of a current origin have been considered for nuclei. The matrix elements of nuclear CEMs have also been obtained with allowance for corrections originating from the strong spin–orbit interaction of nucleons. These corrections can be deduced from the spin–orbit splitting of energy levels.

The calculation of the deuteron CEMs is of greatest physical interest. Expressions derived for this case without taking into account relativistic corrections comply with the results obtained in [1, 2] within the impulse approximation. The inclusion of relativistic corrections to the CEMs from the spin–orbit interaction, the quadratic spin–orbit interaction, and the interaction quadratic in the angular momentum affects noticeably only the quantity τ.

The resulting values of the deuteron CEMs are within one percent of the total (charge and current) values of these quantities. For other nuclei, the CEM contribution can be considerably greater [4, 5]. Constructing the relativistic theory of CEMs is of paramount importance for developing methods that make it possible to calculate the moments of nuclei within the Foldy–Wouthuysen representation (not the basis of the impulse approximation). In this representation, relativistic corrections can be taken into account quite straightforwardly, which is of great importance, for example, in calculating the magnetic moments of nuclei. It is planned to consider this problem in the future.

REFERENCES

1. J. L. Friar, Ann. Phys. (N.Y.) **81**, 322 (1973).
2. M. Kohno, J. Phys. G **9**, L85 (1983).
3. R. B. Wiringa, V. G. J. Stoks, and R. Schiavilla, Phys. Rev. C **51**, 38 (1995).
4. A. Ya. Silenko, Yad. Fiz. **60**, 432 (1997) [Phys. At. Nucl. **60**, 361 (1997)].
5. A. Ya. Silenko, Izv. Akad. Nauk, Ser. Fiz. **61**, 2132 (1997).
6. W. Bertozzi *et al.*, Phys. Lett. B **41**, 408 (1972).
7. J. Martorell and D. W. L. Sprung, Z. Phys. A **298**, 153 (1980).
8. A. Ya. Silenko, Izv. Vyssh. Uchebn. Zaved., Fiz., No. 7, 53 (1991).
9. A. J. Silenko, J. Phys. B **25**, 1661 (1992).
10. A. Ya. Silenko, Izv. Vyssh. Uchebn. Zaved., Fiz., No. 4, 66 (1995).
11. J. Frenkel, Z. Phys. **37**, 243 (1926); Ya. I. Frenkel', *Collected Papers* (AN SSSR, Moscow, 1958), Vol. 2, p. 460.
12. E. I. Blount, Phys. Rev. **128**, 2454 (1962).
13. A. I. L'vov, Preprint No. 344, FIAN (Lebedev Institute of Physics, USSR Academy of Sciences, 1987).
14. A. Ya. Silenko, Teor. Mat. Fiz. **105**, 46 (1995).
15. L. D. Landau and E. M. Lifshitz, *Quantum Mechanics: Non-Relativistic Theory.* Transl. of 3rd Russ. ed. (4th ed. Nauka, Moscow, 1989; Pergamon, Oxford, 1977).
16. M. Lacombe *et al.*, Phys. Rev. C **21**, 861 (1980).
17. R. Machleidt, K. Holinde, and Ch. Elster, Phys. Rep. **149**, 1 (1987).

Translated by S. Slabospitsky

Physics of Atomic Nuclei, Vol. 63, No. 2, 2000, pp. 210–215. Translated from Yadernaya Fizika, Vol. 63, No. 2, 2000, pp. 264–270.

NUCLEI
Theory

Interpretation of an Empirical Systematics of Coherence Widths

G. A. Prokopets

Taras Shevchenko Kiev State University, ul. Glushkova 6, Kiev, 252022 Ukraine

Received June 16, 1998; in final form, October 2, 1998

Abstract—On the basis of the continuity equation, the concept of a complex potential, and the exciton model of nuclear reactions, an expression was derived that establishes the relation between three time characteristics associated with different reaction stages. It is shown that an empirical systematics relating the coherence widths to the temperature of compound nuclei is a high-temperature limit of this expression, which determines empirical coefficients in terms of quantities similar to volume absorption integrals per nucleon that appear in optical-model calculations. The possibility of estimating the energy dependence of these quantities on the basis of experimental data on the total widths of neutron resonances, measured mean lifetimes of compound nuclei, and data on coherence widths is discussed. © *2000 MAIK "Nauka/Interperiodica".*

1. INTRODUCTION

It is well known [1, 2] that the values of the coherence width Γ_c that are extracted by means of an autocorrelation analysis of the experimental excitation functions for the effective cross sections for various nuclear reactions are closely approximated by the expression

$$\Gamma_c \approx 14\exp[-4.69(A/U)^{1/2}], \qquad (1)$$

where A is the mass number of a compound nucleus formed by the projectile particle with a mass number A_p and the target nucleus with a mass number A_t, while U is the excitation energy of the compound nucleus (both U and Γ_c are given in MeV). The approximation in (1) is in accord with experimental data not only in the excitation-energy range $U \approx 17$–21 MeV and for light projectile particles, where it was initially tested, but also for higher energies and for heavy ions [3, 4] in processes where a considerable contribution comes from the mechanism of compound-nucleus formation.

Whereas the role of the temperature factor $T \sim (U/A)^{1/2}$ was emphasized as far back as [1], the physical meaning of the numerical coefficients in formula (1) is less obvious. Under the assumption that the decays in question are exponential, we have $\Gamma_c = \hbar/\tau_c$, where τ_c is the mean lifetime of the compound nucleus. It therefore seems natural to perform an analysis of relation (1) along with a consideration of the time evolution of compound nuclear systems. An attempt at this is made here on the basis of a simple sketchy model.

2. DESCRIPTION OF THE MODEL

In the collision process, the wave function Ψ of a set of particles that is governed by a Hamiltonian $\hat{H}$ satisfies the time-dependent Schrödinger equation, which can be recast into the continuity equation

$$\partial\rho/\partial t = 2\mathrm{Im}(\Psi^*\hat{H}\Psi)/\hbar, \qquad (2)$$

where $\rho = \Psi^*\Psi$ is the probability density.

The concept of a complex optical potential makes it possible to reduce a many-body problem to a one-body problem. We consider a broad wave packet in the input channel (short pulse of particles bombarding the target nucleus) and denote by $\hat{H}_0$ the optical-model Hamiltonian. One-particle states of the continuous spectrum within a sphere of radius R_a will then satisfy the equation

$$dP_{R_a}(t)/dt \cong -\Phi_{R_a0}(t) + 2\overline{W}_a(t)P_{R_a}(t)/\hbar, \qquad (3)$$

where

$$P_{R_a}(t) = \int_0^{\pi}\int_0^{2\pi}\int_0^{R_a}\rho_a(\mathbf{r}, t)d\mathbf{r}$$

is the probability of the formation of a compound system through an a channel, while

$$\Phi_{R_a0}(t) = \int_{V_a}\mathrm{div}\,\mathbf{j}_a(\mathbf{r}, t)dV_a$$

is the flux of the probability current density $\mathbf{j}_a$ in the a channel through the surface of a spherical volume V_a of radius R_a for the Hamiltonian $\hat{H}_0$, which determines the divergence of the probability current density as

$$\mathrm{div}\,\mathbf{j}_a = -2\mathrm{Im}(\Psi_a^*\mathrm{Re}\,\hat{H}_0\Psi_a)/\hbar.$$

The imaginary part $W_a(\mathbf{r}) \equiv \mathrm{Im}\hat{H}_0$ of the complex potential takes effectively into account the coupling of the particle in the input channel to the internal degrees of freedom of the target nucleus. The quantity $\overline{W}_a(t)$

1063-7788/00/6302-0210$20.00

entering into equation (3) is related to this imaginary part by the equation

$$\overline{W}_a(t) = \int_0^{\pi}\int_0^{2\pi}\int_0^{R_a} W_a(\mathbf{r})\rho_a(\mathbf{r},t)d\mathbf{r} \Big/ \int_0^{\pi}\int_0^{2\pi}\int_0^{R_a} \rho_a(\mathbf{r},t)d\mathbf{r},$$

where the upper limit of integration, R_a, corresponds to the "radius of absorption" of the incident beam; it is defined is such a way that the potential $W_a(\mathbf{r})$ is negligibly small for $r > R_a$. In what follows, we assume, for the sake of simplicity, that $\overline{W}_a(t) = \langle W\rangle_{R_a}$, where $\langle W\rangle_{R_a}$ is a time-independent constant. This is justified only in the case where $W_a(\mathbf{r})$ = const for $r < R_a$ or in the case where $\rho_a(\mathbf{r}, t) = \rho_{1a}(\mathbf{r})\rho_{2a}(t)$. In a time-independent problem, which may arise, for example, when experimental conditions fix the energy of the system at some real value E, we have the relation

$$\Phi_{R_a 0} = 2\langle W\rangle_{R_a} P_{R_a}/\hbar = \text{const}(t), \qquad (4)$$

which determines the cross section for compound-nucleus formation within the optical model.

In contrast to the optical-model Hamiltonian $\hat{H}_0$, the total Hamiltonian $\hat{H}$ of the system must be Hermitian and must include a term caused by the residual interaction $\hat{H}'$ between particle a and the constituent nucleons of the target nucleus. On one hand, this residual interaction drives the evolution of the single-particle input state of the compound system to the compound nucleus c, where the excitation energy is distributed between a large number of degrees of freedom; on the other hand, it causes the decay of the compound nucleus through open channels.

After a fairly large amount of time has elapsed since the passage of a short pulse of projectiles, the wave function Ψ_c in the interior region represents a superposition of stationary states of the resonance type in the beam-energy interval ΔE [5]. We assume that this energy averaging over a large number of resonances will result in a time dependence similar to that in the case of an isolated resonance. A comprehensive analysis of the problem revealed [6] that this time dependence is expected at least for an energy region where the following conditions are satisfied:

$$\Delta E \gg \Gamma \gg D, \text{ but } \Gamma \ll nD/2\pi.$$

Here, Γ and D are the mean resonance widths and spacing, and n is the number of open channels. An analysis of effects caused by deviations from the exponential character of compound-nucleus decays is beyond the scope of this study; it can be a subject of a separate publication.

On the basis of the above assumption and equation (2), we can write the relation

$$dP_c/dt = -\Phi_c \exp(-\Gamma_c t/\hbar). \qquad (5)$$

Here, $P_c = \int_{V_c} \rho_c\, dV_c$, where integration is performed over the volume of the compound nucleus, $\Gamma_c = \hbar/\tau_c$ is the effective width determining the mean lifetime τ_c of the compound nucleus with respect to decays through open channels, and Φ_c is the time-independent part of the probability flux $\Phi_c(t)$ from the volume V_c (this quantity is generated by the real Hamiltonian $\hat{H}$). The probability flux is given by

$$\Phi_c(t) = \exp(-\Gamma_c t/\hbar)\sum_i \varphi_{ci}, \qquad (6)$$

where summation is performed over all open decay channels i.

At time instants preceding that at which particles from the short pulse of the incident beam achieve the spatial region occupied by the target nucleus, the flux in equation (3) must be directed toward the interior of this region. Since it is assumed that the same residual interaction causes the decay of the already existent compound nucleus through open channels, on one hand, and distributes each one-particle state in its interior over a large number of compound states, on the other hand, we will simulate this flux by the expression

$$\Phi_{ca} = -\varphi_{ca}\exp(-\Gamma_c t/\hbar). \qquad (7)$$

Provided that the restrictions hold, equation (3) can therefore be recast into the form

$$dP_{R_a}(t)/dt \cong \varphi_{ca}\exp(-\Gamma_c t/\hbar) - \Gamma_a P_{R_a}(t)/\hbar \qquad (8)$$

or into the form

$$d^2P_{R_a}(t)/dt^2 + \hbar^{-1}(\Gamma_a + \Gamma_c)dP_{R_a}(t)/dt + \hbar^{-2}\Gamma_a\Gamma_c P_{R_a}(t) \cong 0, \qquad (9)$$

where $\Gamma_a = \hbar/\tau_a = -2\langle W\rangle_{R_a}$.

For the initial conditions $P_{R_a}(0) = 0$ and $[dP_{R_a}(t)/dt]_{t=0} = P_0' > 0$, the solution to equation (9) is

$$P_{R_a}(t) = \hbar P_0'[\exp(-\Gamma_c t/\hbar) - \exp(-\Gamma_a t/\hbar)]/(\Gamma_a - \Gamma_c). \qquad (10)$$

This expression describes the time evolution of the compound nuclear system formed through the channel a.

The concept that a nuclear reaction proceeds through the formation of a relatively long-lived compound nucleus also implies that the intermediate compound system arising at the first stage of the reaction in question is characterized by a small relaxation time; that is,

$$\tau_a \ll \tau_c. \qquad (11)$$

It follows that expression (10) for P_{R_a} peaks at the time instant

$$t_{\max} = \hbar \ln(\Gamma_a/\Gamma_c)/(\Gamma_a - \Gamma_c). \quad (12)$$

From (10) and (11), it follows that, for times t much greater than $t_{\max}$, the probability $P_{R_a}(t)$ for the system to occur within a spatially limited region without undergoing transitions to open channels depends exponentially on time, the mean lifetime being τ_c. Owing to this, $t_{\max}$ can be identified with the time t_{eq} required for statistical equilibration in the compound nuclear system. In the time-independent formalism, the width of the "internal" mixing $\Gamma_\downarrow = \hbar/t_{eq}$ of one-particle configurations by the residual interaction $\hat{H}'$ corresponds to the latter time. As a result, we arrive at the relation

$$\Gamma_c = \Gamma_a \exp[-(\Gamma_a - \Gamma_c)/\Gamma_\downarrow]. \quad (13)$$

3. NUMERICAL CALCULATIONS

In order to estimate $\Gamma_\downarrow$, the mean widths with respect to intranuclear transitions at a known number $n = p + h$ of quasiparticles (particles and holes) near equilibrium, in which case $\bar{n} = (2gU)^{1/2}$, where g is the density of single-particle levels at the Fermi surface, can be borrowed from the exciton model [7]:

$$\Gamma_\downarrow \cong \Gamma_{n\to\bar{n}} = 2\pi\langle|M|^2\rangle\omega_f(\bar{n}). \quad (14)$$

For the density of available final states, we take the expression

$$\omega_f(\bar{n}) = g^2U[(2gU)^{1/2} - 1]/2, \quad (15)$$

which is used, for example, in the STAPRE code [8].

For the quantity obtained by averaging the square of the matrix element of the residual interaction over allowed transitions, we employed the phenomenological expression

$$\langle|M|^2\rangle = K/(A^3U) \quad (16)$$

(K is an empirical normalization factor), which is extensively used in the calculations of precompound processes.

From (14), we then obtain the estimate

$$\Gamma_\downarrow \cong [3^{-1/2}\pi^2Kg^3(1 - 1/\bar{n})/A^3]T = \eta T, \quad (17)$$

where $T = (U/a)^{1/2}$ is the thermodynamic temperature of the compound nucleus in the Fermi gas model, $a = \pi^2g/6$ being the level-density parameter. In the Fermi gas model, which, on average, describes well the nuclear-level density at excitation energies U in excess of the nucleon binding energy, we have $g = A/13$; for the constant K, an analysis of experimental emission spectra of various particles originating from nuclear reactions yields $K \cong 400 \pm 50$ MeV^3 [7, 8]. Considering that, at sufficiently high excitation energies, $\bar{n} \gg 1$ and using expression (17), we then obtain

$$\eta \cong \text{const} \cong 1.04 \pm 0.13 \text{ and}$$
$$\Gamma_\downarrow \cong T(U, A) \cong 3(U/A)^{1/2}. \quad (18)$$

Neglecting the ratio Γ_c/Γ_a, which is much less than unity, we find that expression (13) then becomes coincident with the empirical approximation (1) in functional form and, in the case of $\Gamma_a = 14$ MeV, in absolute value.

However, expressions (13) and (17), which relate different widths that determine the formation and decay of compound nuclei in collisions, are more general than empirical dependence (1); in particular, they permit analyzing data with allowance for the energy dependence of $\Gamma_a = -2\langle W\rangle_{R_a}$, which is implied by the above empirical dependence.

For example, $\langle W\rangle_{R_n}$ for the imaginary part of the optical potential can be estimated for various target nuclei in the excitation-energy region of compound nuclei formed by incident neutrons whose energies are close to the neutron binding energy ($U \approx B_n$), where there are detailed data on the neutron-resonance parameters [9]. After corresponding averaging, this yields

$$\Gamma_c(B_n) = \langle 1/\Gamma\rangle^{-1}, \quad (19)$$

where Γ are the total widths of individual resonances falling within the energy range of averaging, and $\hbar/\Gamma$ stands for their lifetimes. Therefore, no additional information is required for estimating $\langle W(B_n)\rangle_{R_n}$ for each individual nucleus on the basis of relations (13)–(19).

It should be noted that such estimations are usually performed on the basis of expression (4), which holds in the time-independent optical model; they are implemented by using the relation between the quantity obtained by averaging, over resonances, the effective cross section for the escape of particles from the beam and the neutron strength functions as determined from the ratios $\langle\Gamma_n\rangle/D$, where Γ_n is the mean partial widths with respect to resonance decay via neutron emission, while D is the mean spacing between resonances with a given spin–parity.

An alternative method for estimation consists in extrapolating, to zero kinetic energy, the results that can be obtained from an analysis of measured differential effective cross sections for low-energy elastic scattering within the spherical optical model. The results of the calculations reveal the highest sensitivity to the volume absorption integral per nucleon, an averaged characteristic of the imaginary part of the potential,

$$J_w = -4\pi(A_tA_p)^{-1}\int_0^\infty W(r)r^2dr. \quad (20)$$

Thus, it can easily be seen that relation (13) provides an alternative method for estimating the energy dependence of the averaged contribution of the imaginary potential to the particle–nucleus interaction. This may be of some interest because the results presented by different authors on the form of the energy dependence of J_w and on its absolute values differ widely. By way of example, we indicate that, for neutrons with energies in the range $0 < E_n \leq 40$ MeV, a determination of J_{wn} for the same nuclei from experimental data [10] may lead either to a linear increase in this quantity with energy, or to its linear decrease, or to a nonlinear increase toward a constant value, or to its almost complete invariability with energies; in the limit $E_n \cong 0$, the results show a scatter within an order of magnitude.

For several nuclear species, $J_{wn}(E_n \cong 0)$ values obtained from data presented in [11–16] for the parameters of phenomenological optical potentials are displayed in Table 1, along with the values of

$$J_{wn}[\tau_c(B_n)] = -4\pi r_0^3 \langle W(B_n)\rangle_{R_n}/3. \qquad (21)$$

The errors in the latter quantities—they are lso quoted in this table—were obtained from an analysis of experimental data from [9] on the averaged lifetimes τ_c of neutron resonances, which was performed on the basis of relations (13)–(19). The calculations employed the typical values of $K = 420$ MeV^3 and $r_0 = 1.25$ fm for, respectively, the constant that specifies, according to (16), the quantity obtained by averaging the square of the matrix element of the residual interaction over allowed transitions and the radial parameter specifying the radius $R_n = r_0 A_t^{1/3}$ of the region where the imaginary potential is operative.

The quoted errors include both the contribution associated with the resonance widths and the contribution from the uncertainty in the normalization of the square of the matrix element of the residual interaction.

The results presented in Table 1 demonstrate that, by and large, the integral characteristics of the imaginary potential that are determined by expression (21) are in accord with those that are determined by expression (20). It should be noted that our results agree with data of authors who quote values smaller than those of other authors. Considering that the estimates obtained by different authors for the absolute values of the integrals $J_{wn}(E_n \cong 0)$ and for their energy dependences differ considerably (for example, these results for the ^{208}Pb nucleus show a scatter between 14 and 70 MeV fm^3 [10]), we state that the method proposed here for determining the absorption integrals J_w can provide independent estimates of reasonable accuracy.

For 77 nuclei in the mass-number range $A_t = 27$–238, the quantities $J_{wn}(\Gamma_\downarrow)$ as obtained from experimental data on the neutron-resonances parameters [9] by using expressions (13)–(19) and (21) are shown in the figure as functions of the fragmentation width $\Gamma_\downarrow$ determined by according to (17). It can be seen from the figure that, with increasing $\Gamma_\downarrow$, the quantity $J_{wn}(\Gamma_\downarrow)$ exhibits a tendency toward saturation and can be represented, on average, in the form

$$J_{wn}(\Gamma_\downarrow) \approx J_{wn}(\infty)[1 - \exp(-\Gamma_\downarrow^2/\gamma^2)]. \qquad (22)$$

The corresponding approximated curve is also shown in the figure, the fitted parameter values being

$$J_{wn}(\infty) = 56.6 \pm 1.5 \text{ MeV fm}^3, \quad \gamma = 0.537 \pm 0.017 \text{ MeV}. \qquad (23)$$

According to (21), this yields

$$\Gamma(\infty) = -2\langle W(\infty)\rangle_R = 13.8 \pm 0.4 \text{ MeV}. \qquad (24)$$

Table 1. Absorption integrals per nucleon, $J_{wn}[\tau_c(B_n)]$, as calculated from data on the mean lifetimes of neutron resonances along with the corresponding $J_{wn}(E_n \cong 0)$ values taken from other studies, where they were obtained from a spherical-optical-model analysis of data on the energy dependence of the differential cross sections for neutron scattering

Target ^AX	$J_{wn}[\tau_c(B_n)]$, MeV fm^3	$J_{wn}(E_n \cong 0)$, MeV fm^3
^{32}S	71 ± 8	82 [11]
^{51}V	51 ± 6	53 [12]
^{52}Cr	50 ± 5	46 [13]
^{56}Fe	60 ± 8	46 [13]
^{93}Nb	55 ± 7	52 [14]
^{115}In	52 ± 7	53 [15]
^{208}Pb	14.6 ± 1.8	13.5 [13]
^{209}Bi	27 ± 3	31 [12]
^{238}U	30 ± 4	43.5 [16]

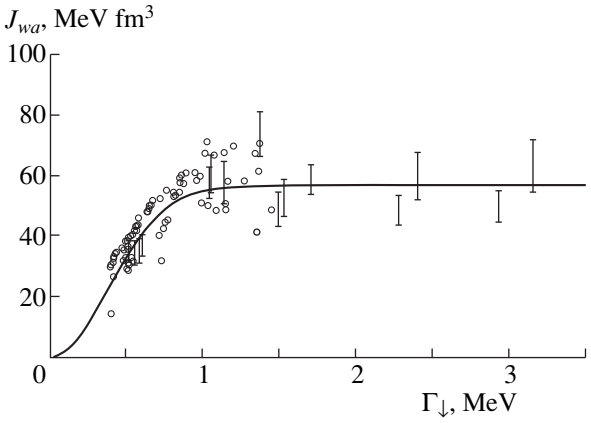

Absorption volume integrals per nucleon, J_{wa}, as calculated on the basis of equations (13) and (21) by using experimental data from [1, 6, 9, 17–23] on the mean lifetimes of compound nuclei and on coherence widths versus the averaged width $\Gamma_\downarrow$ (14) of intranuclear transitions. Points represent experimental data for (◦) neutron resonances and (□) nuclear reactions induced by charged particles. The curve shows the results of fitting these data to the form (22).

Table 2. Absorption integrals per nucleon, J_{wn}, as determined from an analysis of fluctuations of the effective cross sections (Γ_c) or from the results of direct measurements of the mean delay times (τ_c) in reactions that are induced by various charged particles and which proceed through the formation of compound nuclei ^AX at a mean excitation energy $\langle U \rangle$

^AX	$\langle U \rangle$, MeV	$\Gamma_\downarrow$, MeV	Input data	J_{wn}, MeV fm^3	^AX	$\langle U \rangle$, MeV	$\Gamma_\downarrow$, MeV	Input data	J_{wn}, MeV fm^3
^{16}O	20	2.94	Γ_c [1]	50 ± 5	^{113}Sb	15	1.05	τ_c [6]	58 ± 5
^{27}Al	19	2.28	Γ_c [17]	49 ± 5	^{117}Sb	25.9	1.37	τ_c [21]	74 ± 7
^{28}Si	21.5	2.41	Γ_c [18]	60 ± 8	^{200}Pb	65	1.71	τ_c [22]	59 ± 4
^{28}Si	35	3.16	Γ_c [19]	63 ± 9	^{234}U	7.7	0.52	τ_c [23]	35 ± 3
^{52}Cr	15	1.50	Γ_c [20]	49 ± 6	^{234}U	10	0.60	τ_c [23]	37 ± 3
^{57}Co	17	1.54	Γ_c [1]	53 ± 6	^{235}U	8.7	0.56	τ_c [23]	35 ± 4
^{107}In	14.6	1.06	τ_c [6]	61 ± 6	^{235}U	9.6	0.59	τ_c [23]	35 ± 4
^{108}Cd	17	1.14	Γ_c [1]	58 ± 7					

In all probability, the scatter of the $J_{wn}(\Gamma_\downarrow)$ for individual nuclei around the smooth curve corresponding to (22) is due to the averaging of resonances over an insufficiently wide interval ($\Gamma_\downarrow \approx 1$ MeV for lighter nuclei) and to structural features associated with magic and near-magic nuclei.

Since relation (18) holds for $\Gamma_\downarrow \geq 1$ MeV, we can conclude that the empirical systematics (1), which relates coherence widths to the temperature of compound nuclei, represents the high-temperature limit of equation (13), which was obtained above and which determines the corresponding empirical factors in terms of quantities like the volume absorption integrals per nucleon, which appear in optical-model calculations.

By way of illustration, some J_{wa} values for various particles a (p, ^{3}He, α, ^{16}O) that bombarded various target nuclei from aluminum to thorium with the result that compound nuclei with excitation energies from about 8 to about 65 MeV were formed are also displayed in the figure. These values of J_{wa}, which are also presented in Table 2, were obtained from formulas (13) and (21) by iteratively calculating Γ_a with the aid of data from [1, 6, 17–23] on coherence widths Γ_c or mean lifetimes τ_c measured for compound nuclei by the dark-field method or method of K vacancies. It can be seen that these results are in good agreement with data on neutron resonances in the region $\Gamma_\downarrow \approx 0.5$–1 MeV and, in accordance with the approximation in (22), show no systematic deviations from a constant at large $\Gamma_\downarrow$ values up to $\Gamma_\downarrow \approx 3.5$ MeV.

We note that relation (13) possesses one more feature of importance. At first glance, a value that it predicts for the mean lifetime of a compound nucleus that is characterized by an excitation energy U and a mass number A must depend noticeably on the set of the mass numbers A_p and A_t in the input channel. Nevertheless, both the empirical systematics (1) and all what was said above in connection with the discussion of data presented in the figure indicate that there is no such regular dependence or that it is relatively weak. This suggests that the temperature of the nascent compound nucleus affects crucially the values of the absorption integrals J_{wa} (21); at the same time, distinctions associated with angular-momentum distributions do not play any significant role. That there is no pronounced angular-momentum dependence of the J_{wa} values extracted from the measured mean lifetimes τ_c or from the measured coherence widths Γ_c is probably due to the fact that these data are sensitive primarily to the most long-lived components of the spin distribution, so that the resulting Γ_c value appears to be much closer to the minimal width Γ_{min} than to the mean width $\langle \Gamma \rangle$ of the excited compound-nucleus states, which appears in the calculations of effective cross sections.

4. CONCLUSION

On the basis of a simple sketchy model, the numerical coefficients in the empirical systematics of experimental data from [1, 2] on the coherence widths Γ_c and mean lifetimes τ_c of compound nuclei have been related to the quantity obtained by averaging the imaginary part of the optical potential over the nuclear volume, $\langle W \rangle_R$ and to the mean width $\Gamma_\downarrow$ with respect to intranuclear transitions near the state of statistical equilibrium.

It has been shown that, for compound systems with excitation energies above the neutron binding energy B_n, the results obtained from an analysis of the spectra of preequilibrium particle emission in nuclear reactions [7, 8] are agreement, within errors (about 15%), with the equality $\Gamma_\downarrow \cong T$, where T is the thermodynamic temperature of the compound nucleus.

For 77 nuclei with mass numbers $28 \leq A \leq 239$, the lifetimes $\tau_c(B_n)$ averaged over allowed resonances have been evaluated on the basis of experimental data on the parameters of neutron resonances [9]. Within the proposed model, this made it possible to calculate $\langle W(B_n) \rangle_{R_n}$ values and $J_{wn}(B_n)$ values, which are proportional to them [see equation (21)]. A comparison has revealed that the latter are associated with the absorp-

tion integrals per nucleon, which are extensively cited in the literature and which are obtained from an optical-model analysis of the differential cross sections for elastic scattering. Because the accuracy of such an analysis is rather poor, in particular, at low energies of incident particles, the proposed model description of data obtained in time measurements and in a correlation analysis of fluctuations in the energy dependence of the effective cross sections for various channels of nuclear reactions can be used as an independent method for estimating the integral characteristics of the imaginary part of the optical potential.

The extracted $J_{wn}(B_n)$ values represented as functions of the width $\Gamma_\downarrow$ increase, on average, in the range $0.4 \le \Gamma_\downarrow \le 1.5$ MeV with increasing $\Gamma_\downarrow$, reaching saturation near $\Gamma_\downarrow \approx 1$ MeV.

An approximation of these data by the two-parameter dependence (22) yields the following saturation value for $\Gamma_\downarrow \ge 1$ MeV:

$$-2\langle W(\infty)\rangle_R = 13.8 \pm 0.4 \text{ MeV}.$$

Since this result agrees with the corresponding numerical coefficient in the empirical systematics of the coherence widths (1), we can consider this systematics as the high-temperature limit of the more general relation (13) derived in this study. The systematics in (1) is based on an analysis of fluctuations in the energy dependence of the effective cross sections for nuclear reactions induced by charged particles—in particular, by heavy ions—and covers the range $1 \le \Gamma_\downarrow \le 3$ MeV.

In our consideration, we have also included rather scanty data from direct measurements of the mean lifetimes of compound nuclei by the dark-field method and method of *K* vacancies.

These results, obtained for reactions induced by protons and ^{3}He, ^{4}He, and ^{16}O ions, cover the range $0.5 \le \Gamma_\downarrow \le 1.7$ MeV, where their behavior proved similar to the behavior of data for resonance neutrons and, within the errors, are in satisfactory agreement with them, as well as with data obtained from a correlation analysis and with the approximation in (22).

In summary, the proposed model of the time evolution of compound nuclear systems provides a systematization of a rather wide variety of experimental data and establishes the relation between the following three time characteristics of nuclear reactions proceeding through the formation of a compound nucleus: the time that determines the rate of absorption of the incident beam of particles *a* at the first stage of the reaction, $\tau_a = -\hbar/(2\langle W\rangle_{R_a})$; the time over which the internal mixing of nucleon configurations in the compound nucleus occurs, $\tau_\downarrow = \hbar/\Gamma_\downarrow$; and the lifetime $\tau_c = \hbar/\Gamma_c$ with respect to emission from the compound nucleus.

Satisfactory agreement of the present model calculations with various experimental data is evidence for correctness of physical principles underlying the model.

REFERENCES

1. T. Ericson and T. Mayer-Kuckuk, Annu. Rev. Nucl. Sci. **16**, 183 (1966).
2. D. Shapira, R. G. Stokstad, and D. A. Bromley, Phys. Rev. C **10**, 1063 (1974).
3. J. Gómez Del Campo, M. E. Órtiz, A. Dacal, *et al.*, Nucl. Phys. A **262**, 125 (1976).
4. M. Hugi, J. Lang, R. Müller, *et al.*, Phys. Rev. C **25**, 2403 (1982).
5. A. M. Lane and R. G. Thomas, Rev. Mod. Phys. **30**, 257 (1958).
6. V. L. Lyuboshits, in *Proceedings of XIX LINP Winter School* (Leningrad, 1984), p. 33.
7. F. A. Zhivopistsev, E. I. Kebin, and V. G. Sukharevskiĭ, *Preequilibrium Nuclear Reaction* (Mosk. Gos. Univ., Moscow, 1984), Part 1.
8. M. Uhl and B. Strohmaier, Preprint No. 76/01, IRK (Institut für Radiumstrahlung und Kernforschung, Vienna, 1976).
9. S. F. Mughabghab *et al.*, *Neutron Cross Sections* (Academic, New York, 1981), Vol. 1, Parts A, B.
10. O. V. Konshin, in *Proceedings of Advisory Group Meeting* (Beijing, 1987), p. 85.
11. B. Holmqvist and T. Wiedling, J. Nucl. Energy **27**, 543 (1973).
12. A. B. Smith, P. T. Guenter, and R. D. Lawson, in *Texts of Invited Papers Presented during the Second Research Coordination Meeting* (Vienna, 1988), p. 25.
13. J. Rapaport, V. Kulkarni, and R. W. Finlay, Nucl. Phys. A **330**, 15 (1979).
14. P. E. Hodgson, in *Texts of Invited Papers Presented during the Second Research Coordination Meeting* (Vienna, 1988), p. 49.
15. I. E. Kashuba and T. A. Kostyuk, in *Proceedings of 5th All-Union Conference on Neutron Physics* (Kiev, 1980), Part 1, p. 289.
16. E. H. Auerbach and S. O. Moore, Phys. Rev. B **135**, 895 (1964).
17. B. W. Allardyce, P. J. Dallimore, I. Hall, *et al.*, Nucl. Phys. **85**, 193 (1966).
18. R. V. Elliott and R. H. Spear, Nucl. Phys. **84**, 209 (1966).
19. R. Bonetti, L. Colli Milazzo, M. Melanotte, *et al.*, Nucl. Phys. A **25**, 717 (1982).
20. C. M. Lamba, N. Sazma, N. S. Thampi, *et al.*, Nucl. Phys. A **110**, 111 (1968).
21. M. V. Aprelev, Yu. V. Kangropol', and Yu. G. Kudryavtsev, Izv. Akad. Nauk SSSR, Ser. Fiz. **54**, 98 (1990).
22. S. A. Karamian, Fiz. Élem. Chastits At. Yadra **17**, 753 (1986) [Sov. J. Part. Nucl. **17**, 333 (1986)].
23. D. O. Eremenko, V. O. Kordyukevich, S. Yu. Platonov, *et al.*, Yad. Fiz. **60**, 206 (1997) [Phys. At. Nucl. **60**, 149 (1997)].

Translated by R. Tyapaev

Physics of Atomic Nuclei, Vol. 63, No. 2, 2000, pp. 216–222. Translated from Yadernaya Fizika, Vol. 63, No. 2, 2000, pp. 271–277.

NUCLEI
Theory

Microscopic Calculation of Low-Energy Deuteron–Deuteron Scattering on the Basis of the Cluster-Reduction Method

I. N. Filikhin and S. L. Yakovlev

St. Petersburg State University, Universitetskaya nab. 7/9, St. Petersburg, 199164 Russia

Received December 30, 1998; in final form, April 8, 1999

Abstract—The cluster-reduction method is used to solve numerically the differential equations for the *s*-wave Yakubovsky components characterizing the *nnpp* system in the $S = 2$ spin state. Elastic deuteron–deuteron scattering is analyzed for the case where nucleon–nucleon interaction is simulated by the MT I–III potentials. Effective equations describing the relative motion of clusters is derived. The scattering length and phase shifts for low-energy deuteron–deuteron scattering are calculated. © *2000 MAIK "Nauka/Interperiodica".*

1. INTRODUCTION

This article reports a continuation of the investigation of the four-nucleon *nnpp* system by the method of cluster reduction of the equations for Yakubovsky components [1]. The Yakubovsky equations have some advantages over standard approaches to studying the continuous spectrum of the *nnpp* system [2–9]. In particular, the Yakubovsky equations describe correctly the asymptotic behavior of the wave function in two- and three-particle scattering channels. The differential form of these equations [10] makes it possible to include Coulomb interaction in consideration quite straightforwardly. Unfortunately, the differential formalism yields cumbersome sets of three-dimensional integro-differential equations even in the simplest case of the *s*-wave approximation. Only with the aid of supercomputers is it possible to construct directly numerical solutions to such sets of equations. The cluster-reduction method [11] is used here to solve the differential equations for the Yakubovsky components describing the *nnpp* system. Within this method, the solution to the original set of equations is sought in the form of an expansion in the basis formed by the eigenfunctions of the Hamiltonians of three-nucleon subsystems. By constructing projections onto the conjugate basis, we can derive a set of equations for functions describing the relative motion of the clusters. The resulting set of equations can be solved numerically by means of a simpler procedure that is implementable with a conventional computer.

In the present study, we consider deuteron–deuteron scattering in the $S = 2$ spin state of the *nnpp* system. We perform our calculations within the *s*-wave approximation, simulating nucleon–nucleon interaction on the basis of the MT I–III potential model [12] modified as in [13]. In a similar formulation of the problem, scattering in the $S = 0$ state of the *nnpp* system was considered in [1].

2. BASIC RELATIONS

We consider the four-nucleon system consisting of two neutrons and two protons. The pair interaction potentials represent the sums of the short-range and Coulomb components. In order to describe the system in configuration space, we employ the relative coordinates $\mathbf{X} = \{\mathbf{x}_i, \mathbf{y}_i, \mathbf{z}_i\}$, where the subscript $i = 1$ and 2 corresponds to the 3 + 1 and 2 + 2 partitions of the system, respectively. The relative coordinates are expressed in terms of the particle radius vectors $\mathbf{r}_k$ ($k = 1, 2, 3, 4$) as

$$\mathbf{x}_1 = \mathbf{r}_2 - \mathbf{r}_1, \quad \mathbf{y}_1 = (\mathbf{r}_1 + \mathbf{r}_2)/2 - \mathbf{r}_3,$$

$$\mathbf{z}_1 = (\mathbf{r}_1 + \mathbf{r}_2 + \mathbf{r}_3)/3 - \mathbf{r}_4,$$

$$\mathbf{x}_2 = \mathbf{r}_2 - \mathbf{r}_1, \quad \mathbf{y}_2 = \mathbf{r}_4 - \mathbf{r}_3,$$

$$\mathbf{z}_2 = (\mathbf{r}_1 + \mathbf{r}_2)/2 - (\mathbf{r}_3 + \mathbf{r}_4)/2.$$

The wave function Ψ of the system is a spinor in the space $\mathcal{H} = \mathcal{H}_T \otimes \mathcal{H}_S$, where $\mathcal{H}_S$ ($\mathcal{H}_T$) is a linear space where we specify possible spin (isospin) states of the system. In the isospin formalism, all particles of the system are treated as identical objects. For the system under consideration, the modified differential equations for the Yakubovsky components U_1 and U_2 are given by

$$\begin{aligned}
&(H_0 + V - E + V^{\mathrm{Coul}})U_1 + V(P_4^+ + P_4^-)U_1 \\
&\quad = -V[(P_1^+ - P^+)U_1 + (P_1^+ + P_4^+)U_2], \\
&(H_0 + V - E + V^{\mathrm{Coul}})U_2 + V(P^+P^+)U_2 \\
&\quad = -V[(P^+ - P_1^+)P^+U_1],
\end{aligned} \tag{1}$$

where H_0 is the kinetic-energy operator; V is the potential of pair nuclear interaction; the Coulomb potential V^{Coul} is included in the unperturbed Hamiltonian; P^+ are the operators of cyclic permutations in the four-particle

system; and $P_k^{\pm}$ are the operators of cyclic permutations in the possible three-particle systems, the subscript k labeling the particle not involved in a specific permutation. The Yakubovsky components U_1 and U_2 are spinors from $\mathcal{H}$ and correspond to the 3 + 1 and 2 + 2 partitions of the system, respectively. The coordinate parts of the components U_i depend on the relative coordinates $\{\mathbf{x}_i, \mathbf{y}_i, \mathbf{z}_i\}$, $i = 1, 2$.

2.1. Spin–Isospin Analysis

Since the MT I–III potential does not involve spin–isospin and tensor components, the total spin and the total orbital angular momentum of the system are conserved. Bases in the subspaces $\mathcal{H}_S$ ($\mathcal{H}_T$) are associated with two possible partitions that determine a scheme for the addition of the angular momenta of the subsystems into the total angular momentum. The basis elements in the subspace $\mathcal{H}_S$ are given by

$$|\chi^{(1)}\rangle = |(((1/2, 1/2)s_{12}, 1/2)s_{123})S, S_z\rangle,$$

$$|\chi^{(2)}\rangle = |((1/2, 1/2)s_{12}(1/2, 1/2)s_{34})S, S_z\rangle$$

for two schemes of addition of the angular momenta. The basis functions in the subspace $\mathcal{H}_T$ are constructed in a similar way and are denoted by $|\eta^{(k)}\rangle$. The basis elements of the space $\mathcal{H}$ then have the form

$$|e^{(k)}\rangle = |\chi^{(k)}\rangle|\eta^{(k)}\rangle. \quad (2)$$

The corresponding sets of the quantum numbers $e^{(k)}$ are given by

$$e^{(1)} = (s_{12}, s_{123}, S, S_z)(t_{12}, t_{123}, T, T_z),$$

$$e^{(2)} = (s_{12}, s_{34}, S, S_z)(t_{12}, t_{34}, T, T_z).$$

The components of the spinor U_k can be expanded in bases (2) as

$$U_k(\mathbf{X}) = \sum_e \mathcal{U}_e^k(\mathbf{x}_k, \mathbf{y}_k, \mathbf{z}_k)|e^{(k)}\rangle. \quad (3)$$

A conventional procedure for constructing projections onto the basis elements leads to the set of equations for coordinate functions. Since there is no interaction in the singlet–isosinglet and triplet–isotriplet states of the nucleon pair, the elements of the spin–isospin basis that correspond to these states are excluded from expansion (3). Thereafter, the spin–isospin bases include only two elements $e_k^{(i)}$, where k takes the values of 1 or 2 and where the superscript i, also taking the values of 1 or 2, labels basis elements that correspond to the different schemes of addition of the particle spins and isospins. The elements of the spin–isospin basis and the corresponding states of the *nnpp* system are listed in Tables 1 and 2. Further, we obtain representations for the particle-permutation operators from equations (1) in terms of basis (2). Here, we display only the final results of the calculations. The nuclear interaction depends only on the total spin of a nucleon pair; therefore, the operator V has the diagonal form

Table 1. Components of the spin–isospin basis that are associated with the 3 + 1 partition and corresponding spin–isospin states of the system

Basis components	S_{12}	T_{12}	S_{123}	T_{123}	S	T
$e_1^{(1)}$	1	0	3/2	1/2	2	0
$e_2^{(1)}$	1	0	3/2	1/2	2	1

Table 2. Components of the spin–isospin basis that are associated with the 2 + 2 partition and corresponding spin–isospin states of the system

Basis components	S_{12}	T_{12}	S_{34}	T_{34}	S	T
$e_1^{(2)}$	1	0	1	0	2	0
$e_2^{(2)}$	1	0	1	1	2	1

$$V = \mathrm{diag}\{V^{\mathrm{t}}, V^{\mathrm{t}}\},$$

where V^{t} is the triplet potential component. In the basis in the question, the matrices of the particle-permutation operators can be represented as

$$\langle 1|P_4^{\pm}|1\rangle = \begin{pmatrix} -1/2 & 0 \\ 0 & -1/2 \end{pmatrix},$$

$$\langle 2|P^+P^+|2\rangle = \begin{pmatrix} 1 & 0 \\ 0 & 0 \end{pmatrix},$$

$$\langle 1|P_1^+|1\rangle = \begin{pmatrix} -1/12 & 0 \\ 0 & 1/2 \end{pmatrix},$$

$$\langle 1|P^+|1\rangle = -\langle 1|P_1^+|1\rangle,$$

$$\langle 1|P_4^+|2\rangle = \langle 1|P_4^+|1\rangle,$$

$$\langle 1|P_1^+|2\rangle = \langle 1|P_1^+|1\rangle.$$

The Coulomb potential is given by

$$V^{\mathrm{Coul}} = \sum_{i>j} V_{ij}(|\mathbf{x}_{ij}|)\frac{(1 + 2\tau_i^z)(1 + 2\tau_j^z)}{4}.$$

Here, τ_i^z is the operator of the projection of the isospin of the ith particle, while $V_{ji}(|\mathbf{x}_{ij}|) = n/|\mathbf{x}_{ji}|$, where $i, j = 1, 2, 3, 4$ and $i > j$; $\mathbf{x}_{ji} = \mathbf{r}_j - \mathbf{r}_i$; and $n = e^2m/\hbar^2$, m being the nucleon mass. The matrices of the Coulomb interaction

between the spin–isospin basis elements (2) are given by

$$\langle k|V^{\mathrm{Coul}}|k\rangle = W_1\left(\frac{n}{|\mathbf{x}_{23}|}+\frac{n}{|\mathbf{x}_{13}|}\right)+W_2\left(\frac{n}{|\mathbf{x}_{14}|}+\frac{n}{|\mathbf{x}_{24}|}\right),$$

where $k = 1$ or 2 and

$$W_1 = \begin{pmatrix} 1/4 & 1/4 \\ 1/4 & 1/4 \end{pmatrix},$$

$$W_2 = \begin{pmatrix} 1/4 & -1/4 \\ -1/4 & 1/4 \end{pmatrix}.$$

2.2. s-Wave Approximation

A further analysis will be performed in the *s*-wave approximation; that is, we set all orbital angular momenta of the system and of each subsystem to zero. For the $S = 2$ spin state, the set of equations (1) reduces to a set of three equations for the components $\mathcal{U}_i^1$, $i = 1, 2$, and $\mathcal{U}_1^2$. In diagonalizing the matrix of the Coulomb interaction in equations (1) for the components corresponding to 3 + 1 partition, it is convenient to go over to a new spin–isospin basis of the 3 + 1 type via the orthogonal transformation

$$e_i^{(1)'} = \sum_{j=1}^{2} A_{ij} e_j^{(1)}, \quad i = 1, 2,$$

where the matrix of the orthogonal transformation A has the form

$$A = \frac{1}{\sqrt{2}}\begin{pmatrix} 1 & 1 \\ -1 & 1 \end{pmatrix}.$$

The matrix of the Coulomb interaction transforms as

$$\langle 1|V^{\mathrm{Coul}}|1\rangle = \begin{pmatrix} w_{11} & 0 \\ 0 & \bar{w}_{11} \end{pmatrix},$$

where

$$w_{11} = \frac{1}{2}\left(\frac{n}{|\mathbf{x}_{12}|}+\frac{n}{|\mathbf{x}_{23}|}\right), \quad \bar{w}_{11} = \frac{1}{2}\left(\frac{n}{|\mathbf{x}_{14}|}+\frac{n}{|\mathbf{x}_{24}|}\right).$$

Eventually, the set of equations for the coordinate parts of *s*-wave Yakubovsky components can be written as

$$(h_0^1 + V_1(x) - \varepsilon)\mathcal{U}^1(x,y,z) + V_1(x)$$
$$\times \int_{-1}^{1} dv \frac{xy}{x_1 y_1} B_1 \mathcal{U}^1(x_1,y_1,z_1) + \mathcal{W}^1\mathcal{U}^1(x,y,z)$$
$$= -\frac{1}{2}V_1(x)\int_{-1}^{1}du\int_{-1}^{1}dv\left\{\frac{xyz}{x_2y_2z_2}D\mathcal{U}^1(x_2,y_2,z_2)\right.$$
$$\left. + \frac{xyz}{x_3y_3z_3}C_1\mathcal{U}^2(x_3,y_3,z_3)\right\}, \qquad (4)$$

$$(h_0^2 + V_2(x) - \varepsilon)\mathcal{U}^2(x,y,z)$$
$$+ V_2B_2\mathcal{U}^2(x,y,z) + \mathcal{W}^2\mathcal{U}^2(x,y,z)$$
$$= -\frac{1}{2}V_2(x)\int_{-1}^{1}dv\frac{xyz}{x_4y_4z_4}C_2\mathcal{U}^1(x_4,y_4,z_4).$$

Here, x, y, and z are the absolute values of the Jacobi coordinates; $V_k(x) = \mathrm{diag}\{v^t(x), v^t(x)\}$, where $v^t(x) = (m/\hbar^2)V^t(x)$, $\varepsilon = (m/\hbar^2)E$, $\mathcal{W}^k = \frac{1}{2}\int_{-1}^{1}\langle k|V^{\mathrm{Coul}}|k\rangle du$, $k = 1$ or 2; and $B_1 = \langle 1|P_4^+ + P_1^-|1\rangle$, $D = \langle 1|P_1^+ - P^+|1\rangle$, $B_2 = \langle 2|P^+P^+|2\rangle$, $C_1 = \langle 1|P_1^+ + P_4^+|2\rangle$, and $C_2 = \langle 2|(P^+ - P_1^+)P^+|1\rangle$ are numerical matrices representing the permutation operators from equations (1) in the spin–isospin bases (2). Explicitly, these matrices are given by

$$B_1 = \begin{pmatrix} -1/2 & 0 \\ 0 & -1/2 \end{pmatrix},$$

$$D = \begin{pmatrix} 0 & 1/2 \\ 1/2 & 0 \end{pmatrix},$$

$$C_1 = \begin{pmatrix} -1/2 \\ 1/2 \end{pmatrix},$$

$$B_2 = 1, \quad C_2 = (1/2, -1/2).$$

For the operators h_0^k appearing in equations (4), we have

$$h_0^1 = -\left(\partial_x^2 + \frac{3}{4}\partial_y^2 + \frac{2}{3}\partial_z^2\right),$$

$$h_0^2 = -\left(\partial_x^2 + \partial_y^2 + \frac{1}{2}\partial_z^2\right).$$

For x_i, y_i, and z_i, $i = 1, 2, 3, 4$, in the integral terms of equations (4), the transformation of the relative coordinates by the particle-permutation operators appearing in (1) yields

$$x_1 = \left[\frac{x^2}{4} + y^2 - xyv\right]^{1/2},$$

$$y_1 = \left[\left(\frac{3x}{4}\right)^2 + \frac{y^2}{4} + \frac{3}{4}xyv\right]^{1/2},$$

$$x_2 = x_1, \quad x_3 = x_1, \quad x_4 = y,$$

$$y_2 = \left[\left(\frac{y_1}{3}\right)^2 + z^2 + \frac{2}{3}y_1zu\right]^{1/2},$$

$$z_2 = \left[\left(\frac{8y_1}{9}\right)^2 + \frac{z^2}{9} - \frac{16}{27}y_1zu\right]^{1/2},$$

$$y_3 = \left[\left(\frac{2y_1}{3}\right)^2 + z^2 + \frac{4}{3}y_1zu\right]^{1/2},$$

$$z_3 = \left[\left(\frac{2y_1}{3}\right)^2 + \frac{z^2}{4} - \frac{2}{3}y_1zu\right]^{1/2},$$

$$y_4 = \left[\left(\frac{x}{2}\right)^2 + z^2 - xzv\right]^{1/2}, \quad z_4 = \frac{2}{3}[x^2 + z^2 + 2xzv]^{1/2}.$$

The equations obtained above must be supplemented with the boundary conditions corresponding to deuteron–deuteron scattering at the energies below the threshold for three-cluster disintegration of the system. The corresponding boundary-value problem is solved by the cluster-reduction method [11]. In doing this, we expand the sought solution to the original equations in the bases formed by the eigenfunctions of the Faddeev operator for the three-body subsystems with zero boundary conditions at the origin and at the boundary of the rectangular region specified by the parameters R_x and R_y, which determine the dimensions of the asymptotic region in the coordinates x and y, respectively. A detailed description of the cluster-reduction method is given elsewhere [11].

3. EFFECTIVE EQUATIONS

By constructing projections onto the bases that are generated by the Hamiltonians of the subsystems, we find that the Yakubovsky components satisfy the reduced equations

$$\left(\frac{\partial^2}{\partial z^2} + E_i^{(1)}\right)F_i^{(1)}(z) = -3\sum_j \int_0^{R_x}\int_0^{R_y} dx\,dy\,\tilde{\phi}_i^{(1)}(x,y)\,v^{\mathrm{t}}(x)$$
$$\times \int_{-1}^{1} du \int_{-1}^{1} dv \left\{\frac{xyz}{x_2y_2z_2}\phi_j^{(2)}(x_2,y_2)F_j^{(2)}(z_2) + \frac{xyz}{x_3y_3z_3}\phi_j^{(3)}(x_3,y_3)F_j^{(3)}(z_3)\right\},$$

$$\left(\frac{\partial^2}{\partial z^2} + E_i^{(2)}\right)F_i^{(2)}(z) - 12\sum_j \int_0^{R_x}\int_0^{R_y} dx\,dy\,\tilde{\phi}_i^{(2)}(x,y)$$
$$\times v_1^{\mathrm{Coul}}(x,y,z)\phi_j^{(2)}(x,y)F_j^{(2)}(z)$$
$$= -3\sum_j \int_0^{R_x}\int_0^{R_y} dx\,dy\,\tilde{\phi}_i^{(2)}(x,y)\,v^{\mathrm{t}}(x)$$
$$\times \int_{-1}^{1} du \int_{-1}^{1} dv \left\{\frac{xyz}{x_2y_2z_2}\phi_j^{(1)}(x_2,y_2)F_j^{(1)}(z_2) + \frac{xyz}{x_3y_3z_3}\phi_j^{(3)}(x_3,y_3)F_j^{(3)}(z_3)\right\},$$

$$\left(\frac{\partial^2}{\partial z^2} + E_i^{(3)}\right)F_i^{(3)}(z) - 16\sum_j \int_0^{R_x}\int_0^{R_y} dx\,dy\,\tilde{\phi}_i^{(3)}(x,y)$$
$$\times v_2^{\mathrm{Coul}}(x,y,z)\phi_j^{(3)}(x,y)F_j^{(3)}(z)$$
$$= 8\sum_j \int_{-1}^{1}\int_{-1}^{1} du\,dv\,\tilde{\phi}_i^{(3)}(x,y)\,v^{\mathrm{t}}(x)$$
$$\times \int_{-1}^{1} du \frac{xyz}{x_4y_4z_4}\{\phi_j^{(1)}(x_4,y_4)F_j^{(1)}(z_4) + \phi_j^{(2)}(x_4,y_4)F_j^{(2)}(z_4)\}.$$

Here,

$$E_i^{(k)} = \frac{3}{2}[p^2 + (2\epsilon_d - \epsilon_i^{(k)})], \quad k = 1, 2,$$

$$E_i^{(3)} = p^2 + (2\epsilon_d - \epsilon_i^{(3)}),$$

where ϵ_d is the deuteron binding energy;

$$v_1^{\mathrm{Coul}} = n\begin{cases} \dfrac{1}{z} \ \text{for} \ z > \dfrac{x}{2} + \dfrac{y}{3} \\ \dfrac{1}{xy}\left(\dfrac{2}{3}\dfrac{1}{z}\left(z^2 - \left(\dfrac{3}{4}x - \dfrac{1}{2}y\right)^2\right) + 2\left(\dfrac{3}{4}x + \dfrac{1}{2}y - z\right)\right) \\ \text{for} \ \left|\dfrac{1}{2}x - \dfrac{1}{3}y\right| < z < \dfrac{1}{2}x + \dfrac{1}{3}y \\ \dfrac{2}{x} \ \text{for} \ x > \dfrac{2}{3}y, \quad z < \left|\dfrac{1}{2}x - \dfrac{1}{3}y\right| \\ \dfrac{3}{y} \ \text{for} \ x < \dfrac{2}{3}y, \quad z < \left|\dfrac{1}{2}x - \dfrac{1}{3}y\right|, \end{cases}$$

$$v_2^{\mathrm{Coul}} = n\begin{cases} \dfrac{1}{z} \ \text{for} \ z > \dfrac{x+y}{2} \\ \dfrac{1}{xy}\left(-\dfrac{1}{z}\left(\left(\dfrac{x-y}{2}\right)^2 + x + y - z\right)\right) \\ \text{for} \ \left|\dfrac{x-y}{2}\right| < z < \dfrac{x+y}{2} \\ \dfrac{2}{x} \ \text{for} \ x > y, \quad z < \left|\dfrac{x-y}{2}\right| \\ \dfrac{2}{y} \ \text{for} \ x < y, \quad z < \left|\dfrac{x-y}{2}\right|. \end{cases}$$

The asymptotic behavior of the functions $F_i^{(k)}(z)$, $k = 1, 2, 3$ and $i = 1, 2, \ldots$, for $z \longrightarrow \infty$ is given by

$$F_i^{(k)}(z) \sim 0, \quad k = 1, 2, \quad i = 1, 2, \ldots,$$
$$F_1^{(3)}(z) \sim F_0(\eta, pz) + a(p)G_0(\eta, pz), \tag{5}$$
$$F_i^{(3)}(z) \sim 0, \quad i = 2, 3, \ldots,$$

where $F_0(\eta, pz)$ and $G_0(\eta, pz)$ are the regular and irregular Coulomb functions, respectively, and $\eta = n/p$. The amplitude $a(p)$ is related to the phase shift ${}^{2S+1}\delta$ ($S = 2$) for dd scattering by the equation

$$a(p) = \tan({}^5\delta).$$

The scattering length ${}^5A_{dd}$ is defined as the limit of the function $-\dfrac{\tan({}^5\delta)}{pC_0^2(\eta)}$ when the energy tends to zero:

$$\begin{aligned} {}^5A_{dd} &= -\lim_{p\to 0}\frac{\tan({}^5\delta)}{pC_0^2(\eta)}, \\ C_0^2(\eta) &= \frac{2\pi\eta}{\exp(2\pi\eta)-1}. \end{aligned} \tag{6}$$

At $p = 0$, the asymptotic form of the function $F_1^{(3)}(z)$ for $z \longrightarrow \infty$ is

$$F_1^{(3)}(z) \sim zF(\tilde{z}) + {}^5A_{dd}K(\tilde{z}), \tag{7}$$

where $F(\tilde{z}) = I_1(2\sqrt{\tilde{z}})/\sqrt{\tilde{z}}$, $K(\tilde{z}) = 2\sqrt{\tilde{z}}\,K_1(2\sqrt{\tilde{z}})$, and $\tilde{z} = 2nz$, I_1 and K_1 being modified Bessel functions of the first order. The basis functions $\phi_i^{(k)}(x, y)$ are the solutions to the boundary-value problems

$$(h_{0xy}^{(1)} + V^{\mathrm{t}}(x) - \epsilon_i^{(1)})\phi_i^{(1)}(x, y) + V_0^{\mathrm{Coul}}(x, y)\phi_i^{(1)}(x, y)$$
$$= \frac{1}{2}V^{\mathrm{t}}(x)\int_{-1}^{1} du\frac{xy}{x_1y_1}\phi_i^{(1)}(x, y),$$
$$\phi_i^{(1)}(x, 0) = \phi_i^{(1)}(0, y)$$
$$= \phi_i^{(1)}(R_x, y) = \phi_i^{(1)}(x, R_y) = 0,$$
$$(h_{0xy}^{(1)} + V^{\mathrm{t}}(x) - \epsilon_i^{(2)})\phi_i^{(2)}(x, y)$$
$$= \frac{1}{2}V^{\mathrm{t}}(x)\int_{-1}^{1} du\frac{xy}{x_1y_1}\phi_i^{(2)}(x, y), \tag{8}$$
$$\phi_i^{(2)}(x, 0) = \phi_i^{(2)}(0, y)$$
$$= \phi_i^{(2)}(R_x, y) = \phi_i^{(2)}(x, R_y) = 0,$$
$$(h_{0xy}^{(2)} + V^{\mathrm{t}}(x) - \epsilon_i^{(3)})\phi_i^{(3)}(x, y) = -V^{\mathrm{t}}(x)\phi_i^{(3)}(y, x),$$
$$\phi_i^{(3)}(x, 0) = \phi_i^{(3)}(0, y)$$
$$= \phi_i^{(3)}(R_x, y) = \phi_i^{(3)}(x, R_y) = 0,$$

where,

$$h_{0xy}^{(1)} = \frac{3}{4}\frac{\partial^2}{\partial y^2} + \frac{\partial^2}{\partial x^2}, \quad h_{0xy}^{(2)} = \frac{\partial^2}{\partial y^2} + \frac{\partial^2}{\partial x^2},$$
$$V_0^{\mathrm{Coul}} = n\begin{cases} 2/x & \text{for } x > 2y \\ 1/y & \text{for } x < 2y. \end{cases}$$

The functions $\tilde{\phi}_i^{(k)}(x, y)$ are the solutions to the corresponding conjugate equations with boundary conditions similar to (8) [14, 15]. The functions $\tilde{\phi}_i^{(k)}(x, y)$ and $\phi_i^{(k)}(x, y)$ are normalized by the condition

$$\langle\tilde{\phi}_i^k|\phi_j^k\rangle = 8\int_0^{R_x} dx\int_0^{R_y} dy\tilde{\phi}_i^{(k)}(x, y)\phi_j^{(k)}(x, y) = \delta_{ij},$$
$$k = 1, 2.$$

The expansion of solutions to equations (4) in the bases determined above has the form

$$\begin{aligned} \Psi_k^1(x, y, z) &= \sum_{j=1}^{N}\phi_j^{(k)}(x, y)F_j^{(k)}(z), \quad k = 1, 2, \\ \Psi_1^2(x, y, z) &= \sum_{j=1}^{N}\phi_j^{(3)}(x, y)F_j^{(3)}(z). \end{aligned} \tag{9}$$

4. RESULTS OF THE CALCULATIONS

The effective equations derived in the preceding section for the functions $F_i^{(k)}(z)$ describing relative motion were solved numerically by using a finite-difference approximation on an equidistant grid in the relative coordinate z. The basis functions required for this were obtained by numerically solving equations (8). The functions were determined within the rectangular region of dimensions $R_x = 20$ fm and $R_y = 17$ fm. We denote by R_z the radius in z at which the asymptotic boundary conditions (5) and (7) are imposed and by N_z the number of nodes in this coordinate. In our calculations, we set $R_z = 20$ fm and $N_z = 25$. The self-consistency of the calculation was tested by varying the parameters involved in this calculation. The error in numerically solving equations (4) was determined predominantly by the error in calculating the basis functions. The requirement that the functions $\tilde{\phi}_i^{(k)}$ and $\phi_j^{(k)}$ be biorthogonal was used as a criterion of accuracy of

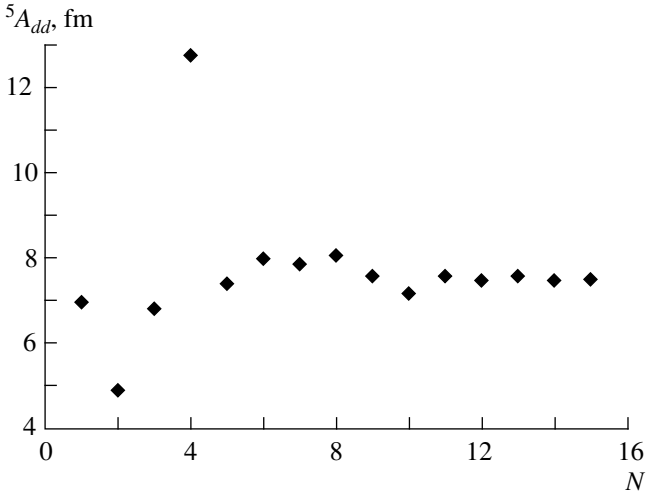

Fig. 1. Deuteron–deuteron scattering length $^5A_{dd}$ versus the number N of terms retained in the expansion in (9).

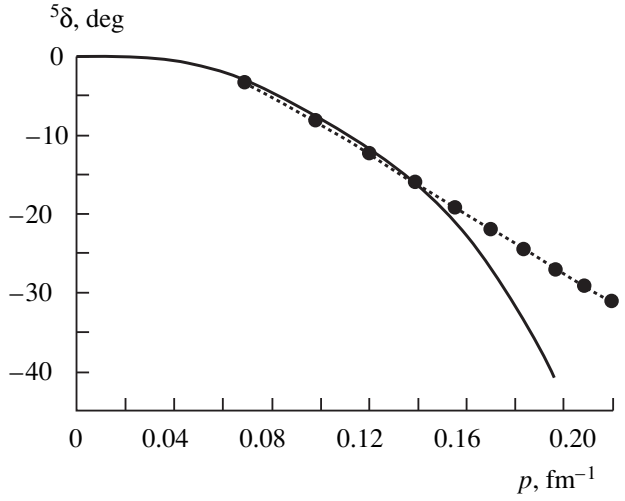

Fig. 2. Phase shift for *s*-wave deuteron–deuteron scattering versus the momentum p of the relative motion of the deuterons involved: (solid curve) our results and (points) results obtained in [8, 16] from an *R*-matrix analyses of experimental data.

our calculations. The basis functions satisfy the estimate

$$\max_{i \le j} \left| \langle \tilde{\phi}_i^k | \phi_j^k \rangle - \delta_{ij} \right| \le 5 \times 10^{-4}, \quad k = 1, 2.$$

We calculated the deuteron–deuteron scattering length and the corresponding low-energy *s*-wave phase shifts. According to (5), the scattering length $^5A_{dd}$ can either be calculated as the limit in (6) or be determined directly by using the asymptotic representation (7) at zero energy. Within the errors of the calculations, the two methods yield the same value of $^5A_{dd} = 7.5$ fm. For comparison, we note that our value of the scattering length $^5A_{dd}$ is somewhat less than the value obtained in [1] for the real part of the singlet deuteron–deuteron scattering length [$\mathrm{Re}(^1A_{dd}) = 10.2$ fm]. The number N of the basis functions that must be taken into account in the expansion in (9) to ensure the convergence of the results is an important parameter. Figure 1 illustrates the convergence of the calculated deuteron–deuteron scattering length $^5A_{dd}$ for various N values. As can be seen from Fig. 1, N does not exceed the value of $N_{\max} = 15$. The closed channel that involves rearrangement and which is described by the 3 + 1 components affects considerably the solution to set of equations (4). The scattering length calculated without allowing for the 3 + 1 components in equations (4) is small in magnitude and negative (–0.1 fm). The solid curve in Fig. 2 represents the calculated *s*-wave phase shift $^5\delta$ as a function of the momentum p of the relative motion of the scattered deuterons. The points in Fig. 2 correspond to the results obtained in [8, 16], on the basis of an *R*-matrix analysis of experimental data. We note that calculations within the resonating-group method were also performed in [8] and the result proved to be in agreement with those of the *R*-matrix analysis. The fact that, at energies in excess of 0.5 MeV, the value that we obtained for the *s*-wave phase shift differs from the results presented in [8, 16] can be explained by the presence of the low-lying *d*-wave 2^+ resonance state in the system [8]. The effect of this resonance is disregarded in the *s*-wave model used here. At low energies, where the contribution of higher partial waves is small, our results are in good agreement with those obtained from the *R*-matrix analysis [16] and from the calculation within the resonating-group method [8].

ACKNOWLEDGMENTS

This work was supported by the Russian Foundation for Basic Research (project no. 98-02-18190).

REFERENCES

1. S. L. Yakovlev and I. N. Filikhin, Yad. Fiz. **63**, 63 (2000) [Phys. At. Nucl. **63**, 55 (2000)]; nucl-th/9701020.
2. D. R. Thompson, Nucl. Phys. A **143**, 304 (1970).
3. H. M. Hofman, W. Zahn, and H. Stowe, Nucl. Phys. A **357**, 139 (1981).
4. H. Kamada, T. Kaneko, and Y. C. Tang, Phys. Rev. C **34**, 22 (1986).
5. V. S. Vasilevsky, T. N. Kovalenko, and G. F. Filippov, Yad. Fiz. **48**, 346 (1988) [Sov. J. Nucl. Phys. **48**, 217 (1988)].
6. V. S. Vasilevsky, I. Yu. Rybkin, and G. F. Filippov, Yad. Fiz. **51**, 112 (1990) [Sov. J. Nucl. Phys. **51**, 71 (1990)].
7. S. B. Dubovichenko, Yad. Fiz. **58**, 1973 (1995) [Phys. At. Nucl. **58**, 1866 (1995)].
8. H. M. Hofman and G. M. Hale, Nucl. Phys. A **613**, 69 (1997); nucl-th/9608046.

9. A. Csótó and G. M. Hale, nucl-th/9701006.

10. S. P. Merkuriev and S. L. Yakovlev, Dokl. Akad. Nauk SSSR **262**, 591 (1982) [Sov. Phys. Doklady **27**, 39 (1982)]; Teor. Mat. Fiz. **56**, 60 (1983); S. P. Merkuriev and L. D. Faddeev, *Quantum Scattering Theory for Few-Body Systems* (Nauka, Moscow, 1985).

11. S. L. Yakovlev and I. N. Filikhin, Yad. Fiz. **56** (12), 98 (1993) [Phys. At. Nucl. **56**, 1676 (1993)]; Yad. Fiz. **58**, 817 (1995) [Phys. At. Nucl. **58**, 754 (1995)]; Yad. Fiz. **60**, 1962 (1997) [Phys. At. Nucl. **60**, 1794 (1997)].

12. R. A. Malfliet and J. A. Tjon, Ann. Phys. (N.Y.) **61**, 425 (1970).

13. N. W. Schellingerhout, J. J. Schut, and L. P. Kok, Phys. Rev. C **46**, 1192 (1992).

14. S. L. Yakovlev, Teor. Mat. Fiz. **102**, 323 (1995); **107**, 513 (1996).

15. V. A. Rudnev and S. L. Yakovlev, Yad. Fiz. **58**, 1762 (1995) [Phys. At. Nucl. **58**, 1662 (1995)].

16. G. M. Hale, private communication.

Translated by R. Tyapaev

Physics of Atomic Nuclei, Vol. 63, No. 2, 2000, pp. 223–228. Translated from Yadernaya Fizika, Vol. 63, No. 2, 2000, pp. 278–284.

NUCLEI
Theory

Calculation of the Binding Energy and of the Parameters of Low-Energy Scattering in the Λ*np* System

I. N. Filikhin and S. L. Yakovlev

St. Petersburg State University, Universitetskaya nab. 7/9, St. Petersburg, 199164 Russia

Received December 22, 1998; in final form, March 4, 1999

Abstract—The cluster-reduction method is used to solve the differential Faddeev equations for $S = 1/2$, $T = 0$ and $S = 3/2$, $T = 0$ spin–isospin states of the Λ*np* system in the *s*-wave approximation. The *NN* interaction is simulated on the basis of the MT I–III potential model, and the Λ*N* potential is set to $V_{\Lambda N} = V_{NN}/2$. This simple option makes it possible to reproduce faithfully the binding energy of the hypertriton ${}^{3}_{\Lambda}\mathrm{H}$. The doublet and quadruplet Λ*d* scattering lengths and the low-energy phase shifts are calculated. It is shown that the effective-range approximation is applicable to the cases of doublet and quadruplet scattering. © *2000 MAIK "Nauka/Interperiodica".*

1. INTRODUCTION

For a long time, Faddeev equations [1, 2] have been used successfully to explore systems consisting of three identical particles—in particular, three-nucleon systems (^{3}H, ^{3}He) [3–5]. Of great interest to nuclear physics are, however, three-body systems involving two identical particles and a particle different from them. The Λ*NN* system, which has a bound state (the hypertriton ${}^{3}_{\Lambda}\mathrm{H}$), belongs to this class. In the case where the system under consideration involves nonidentical particles, the set of relevant equations includes a greater number of coupled Faddeev equations, so that the problem of constructing numerical solutions for such systems is more complicated. Only in recent years have attempts therefore been made to analyze the Λ*NN* system on the basis of the Faddeev equations with realistic *NN* and *YN* potentials [6–8]. Unfortunately, only the bound state was considered in [6, 7], and doublet Λ-hyperon scattering on a deuteron was explored in [8] only in the zero-energy limit. The doublet scattering length for the Λ*np* system was calculated in [9], where the *NN* and Λ*N* interactions were simulated by model separable potentials and the procedure used was based on integral equations for the relevant amplitudes.

In the present study, the Λ*np* system is treated on the basis of the Faddeev equations in configuration space. A numerical solution to these equations is constructed by the cluster-reduction method. In [10–13], the cluster-reduction method was used to study three- and four-nucleon systems. The *s*-wave *NN* interaction was simulated by the MT I–III potential [14] modified as in [15]. The choice of potential model for the Λ*N* interaction requires some comments. The effect of variations in the parameters of the Λ*N* potential on the calculated binding energy of the Λ*np* system was analyzed in [8], where it was found that the binding energy of the system is tightly related to the value of the singlet Λ*N* scattering length. Provided that this scattering length is fixed, variations in the potential parameters affect only slightly the calculated binding energy of ${}^{3}_{\Lambda}\mathrm{H}$. Taking this into consideration, we employ here the model Λ*N* potential $V_{\Lambda N} = V_{NN}/2$ because, for the singlet Λ*N* scattering length, it leads to a value that is close to that required for correctly reproducing the binding energy of the Λ*np* system.

This article is organized as follows. In Section 2, we formulate the problem and present the differential Faddeev equation for two *s*-wave spin–isospin states, $S = 1/2$, $T = 0$ and $S = 3/2$, $T = 0$. The cluster-reduction method for solving equations from Section 2 is briefly described in Section 3. In Section 4, we summarize the results of the calculations for the hypertriton binding energy and for the parameters of low-energy Λ*d* scattering. The wave function constructed in our calculations for the ${}^{3}_{\Lambda}\mathrm{H}$ nucleus is used to evaluate the root-mean-square radius and to determine the region where the hyperon is localized in the nucleus with the highest probability. The resulting hyperon-distribution density and squared modulus of the wave function of the system are plotted in the figures. For the doublet ($S = 1/2$) and quadruplet ($S = 3/2$) spin states, the scattering lengths and phase shifts are calculated at energies below the deuteron-breakup threshold. We present curves for the phase shifts $\delta(p)$ and for the function $p\cot(\delta(p))$. The graphs for the calculated parameters of low-energy Λ*N* scattering (singlet and triplet scattering lengths and effective ranges) are presented to illustrate the applicability of the Λ*N* potential used here.

1063-7788/00/6302-0223$20.00

2. DIFFERENTIAL FADDEEV EQUATIONS IN THE *s*-WAVE APPROXIMATION

The differential Faddeev equations for the three-body system involving two identical particles (for the sake of definiteness, they are assigned the numbers of 1 and 2) have the form

$$\begin{aligned}(H_0^u + V_{12} - E)U &= -V_{12}(W - P_{12}W),\\ (H_0^w + V_{13} - E)W &= -V_{13}(U - P_{12}W),\end{aligned} \tag{1}$$

where the components U and W of the total wave function Ψ describe the pairs of particles {12} and {13}, respectively, the corresponding kinetic-energy operators being H_0^u and H_0^w; P_{ik} stands for the operator of permutation in a pair of particles $\{ik\}$; and V_{ik} is the interaction potential within the pair of particles $\{ik\}$. Each of the above component is a function of the corresponding relative coordinates, which are expressed in terms of the particle radius vectors $\mathbf{r}_k$, $k = 1, 2, 3$. The component U depends on the relative coordinates

$$\mathbf{x} = \mathbf{r}_2 - \mathbf{r}_1, \quad \mathbf{y} = \frac{\mathbf{r}_1 + \mathbf{r}_2}{2} - \mathbf{r}_3, \tag{2}$$

while the component W depends on

$$\mathbf{x} = \mathbf{r}_3 - \mathbf{r}_1, \quad \mathbf{y} = \frac{m\mathbf{r}_1 + m_3\mathbf{r}_3}{m + m_3} - \mathbf{r}_2, \tag{3}$$

where m is the mass of each of the particles 1 and 2, while m_3 is the mass of particle 3. The total wave function of the system can be represented as

$$\Psi = U + (I - P_{12})W.$$

It should be noted here that, in studying the Λnp system on the basis of equations (1), we do not consider Λ–Σ conversion. The *s*-wave *NN* interaction is represented here by the MT I–III potential [14] modified as in [15], and the ΛN potential is taken in the form $V_{\Lambda N} = V_{NN}/2$. Since the *NN* potential does not involve spin–orbit and tensor interactions, the total spin and the total orbital angular momentum of the system are conserved. Here, we consider $S = 1/2$, $T = 0$ and $S = 3/2$, $T = 0$ spin–isospin states of the system. The bound state of the Λnp system corresponds to the quantum number values of $S = 1/2$, $T = 0$. In this case, the Faddeev equations for the *s*-wave states form a set of three equations for the coordinate components of the spinors U and W:

$$\begin{aligned}(h_0^u + v_{12}^t(x) - E)U(x,y) &= v_{12}^t(x)\\ \times\left[\frac{\sqrt{6}}{4}\int_{-1}^{1} dv\,\frac{xy}{x'y'}W_1(x',y') - \frac{\sqrt{2}}{4}\int_{-1}^{1} dv\,\frac{xy}{x'y'}W_2(x',y')\right],&\end{aligned}$$

$$\begin{aligned}(h_0^u + v_{13}^s(x) - E)W_1(x,y)&\\ = -v_{13}^s(x)\left[\frac{\sqrt{6}}{4}\int_{-1}^{1} dv\,\frac{xy}{x_1y_1}U(x_1,y_1)\right.&\\ \left. + \frac{1}{4}\int_{-1}^{1} dv\,\frac{xy}{x_2y_2}W_1(x_2,y_2) - \frac{\sqrt{3}}{4}\int_{-1}^{1} dv\,\frac{xy}{x_2y_2}W_2(x_2,y_2)\right],&\end{aligned} \tag{4}$$

$$\begin{aligned}(h_0^w + v_{13}^t(x) - E)W_2(x,y)&\\ = v_{13}^t(x)\left[\frac{\sqrt{2}}{4}\int_{-1}^{1} dv\,\frac{xy}{x_1y_1}U(x_1,y_1)\right.&\\ \left. + \frac{\sqrt{3}}{4}\int_{-1}^{1} dv\,\frac{xy}{x_2y_2}W_1(x_2,y_2) + \frac{1}{4}\int_{-1}^{1} dv\,\frac{xy}{x_2y_2}W_2(x_2,y_2)\right].&\end{aligned}$$

In the case of $S = 3/2$, $T = 0$, we have a set of two equations:

$$\begin{aligned}(h_0^u + v_{12}^t(x) - E)U(x,y)&\\ = -v_{12}^t(x)\int_{-1}^{1} dv\,\frac{xy}{x'y'}W(x',y'),&\\ (h_0^u + v_{13}^t(x) - E)W(x,y) &= -\frac{1}{2}v_{13}^t(x)\\ \times\left[\int_{-1}^{1} dv\,\frac{xy}{x_1y_1}U(x_1,y_1) + \int_{-1}^{1} dv\,\frac{xy}{x_2y_2}W(x_2,y_2)\right].&\end{aligned} \tag{5}$$

Here,

$$h_0^u = -\frac{1}{4}\frac{2m + m_3}{m_3}\partial_y^2 - \partial_x^2,$$

and

$$h_0^w = -\frac{1}{2}\frac{2m + m_3}{m + m_3}\partial_y^2 - \frac{m + m_3}{2m_3}\partial_x^2$$

are the *s*-wave projections of the kinetic-energy operators h_0^u and h_0^w, respectively; $x = |\mathbf{x}|$ and $y = |\mathbf{y}|$; m and m_3 are, respectively, the nucleon and Λ-hyperon masses; and v_{12}^s (v_{12}^t) and v_{13}^s (v_{13}^t) are the singlet (triplet) components of the *NN* and ΛN potentials, respectively. The coordinates x, y, x_1, y_1, x_2, and y_2 are related by the transformations

$$x' = \left(\frac{1}{4}x^2 + y^2 + xyv\right)^{1/2},$$

$$y' = \left((ax)^2 + (by)^2 - 2abxyv\right)^{1/2},$$

$$x_1 = ((bx)^2 + y^2 - 2bxyv)^{1/2},$$
$$y_1 = \left((ax)^2 + \frac{1}{4}y^2 + axyv\right)^{1/2},$$
$$x_2 = ((cx)^2 + y^2 + 2cxyv)^{1/2},$$
$$y_2 = (4(abx)^2 + (cy)^2 - 4abcxyv)^{1/2},$$

where $a = \frac{1}{2}\frac{2m + m_3}{m + m_3} \approx 0.728$, $b = \frac{m_3}{m + m_3} \approx 0.543$, and $c = \frac{m}{m + m_3} \approx 0.456$. The sets of equations (4) and (5) must be supplemented with the asymptotic boundary conditions corresponding to the bound state and to the Λd scattering at energies below the deuteron-breakup threshold, respectively. For the bound state, these are zero boundary conditions for $x, y \longrightarrow 0$ and for $x, y \longrightarrow \infty$. The asymptotic boundary conditions for scattering are given by

$$U \sim \phi_d(x)[\chi_p(y) - a(p)\cos(py)],$$
$$W \sim (0, 0)^T, \quad y \longrightarrow \infty, \tag{6}$$

where $\phi(x)$ is the deuteron wave function; the function $\chi_p(y) = \sin(py)/p$ describes the asymptotically free motion of the deuteron and the hyperon; and $\frac{1}{4}\frac{2m + m_3}{m_3}p^2 = E - \varepsilon_d$, ε_d being the deuteron binding energy. The scattering length is calculated as the limit of the function $a(p)$ at zero energy. The phase shift ${}^{2S+1}\delta_0$ is related to the function $a(p)$ by the equation

$$\frac{\tan({}^{2S+1}\delta_0)}{p} = -a(p).$$

3. SOLVING EQUATIONS (4) AND (5)

The set of Faddeev equations (4) and (5) will be solved by the cluster-reduction method. This method, which was proposed in [10–13] and which was used previously to calculate the bound states and low-energy scattering in three- and four-nucleon systems, relies on expansions of solutions to the original equations in the bases formed by the eigenfunctions of the Hamiltonians of the possible two-body subsystems. That such expansions can be constructed follows from the asymptotic boundary conditions corresponding to two-cluster scattering at energies below the threshold for the decay of a bound cluster [2]. The procedure for constructing projections leads to a set of equations for the functions that describe the relative motion of clusters. Concurrently, the dimensionality of the equations to be solved is reduced. For the problem being considered, this means that the original two-dimensional equations go over to a set of one-dimensional equations. We seek solutions to equations (4) and (5) in the form of the expansions

$$U(x, y, a) = \sum_{l=0}^{N_l} \phi_l^a(x) f_l^a(y),$$
$$W(x, y, a) = \sum_{l=0}^{N_l} \psi_l^a(x) g_l^a(y), \tag{7}$$

where the superscript a specifies the spin–isospin variables of the system. The functions $\phi_l^a(x)$ and $\psi_l^a(x)$, $l = 1, \ldots, N_l$, are sought, in the class functions satisfying zero boundary conditions $\phi_l^a(0) = \phi_l^a(R_x) = 0$ and $\psi_l^a(0) = \psi_l^a(R_x) = 0$, as the solutions to the eigenvalue problems for the Hamiltonians of the subsystems,

$$(-\partial_x^2 + v^a(x))\phi_l^a(x) = \varepsilon_l^{a,u}\phi_l^a(x),$$
$$\left(-\frac{m + m_3}{2m_3}\partial_x^2 + v^a(x)\right)\psi_l^a(x) = \varepsilon^{a,w}\psi_l^a(x), \tag{8}$$

and form orthonormalized sets of functions. The procedure for constructing projections reduces the sets of two-dimensional integro-differential equations (4) and (5) to sets of one-dimensional equations for the functions $f_l^a(y)$ and $g_l^a(y)$ describing the relative motion of the clusters. By taking the projection of (6), we find that, for $y \longrightarrow \infty$, the functions $f_l^a(y)$ and $g_l^a(y)$ satisfy the asymptotic boundary conditions

$$f_l^a(y) \sim \delta_{l0}[\chi_p(y) - a(p)\cos(py)],$$
$$g_l^a(y) \sim 0.$$

4. RESULTS OF THE CALCULATIONS

The set of differential equations for the functions $f_l^a(y)$ and $g_l^a(y)$ describing the relative motion of the clusters was solved numerically by using a finite-difference approximation on an equidistant grid. The cutoff radius R_y specifying the asymptotic region in the variable y and the number of nodes on the grid, N_y, were the grid parameters. The basis functions (8) were calculated at $R_x = R_y$. At a relative error set to 0.5%, the convergence of the results of the calculations was achieved at the parameter values of $R_x = R_y = 40$ fm and $N_y = 70$. The number N_l of terms that must be retained in the expansions in (7) is a factor that has the strongest impact on the efficiency of the method used here. It has been found that, at a relative-error level of 0.5%, the results of the calculations for the scattering lengths, phase shifts, and binding energies are stabilized at $N_l = 16$ both for doublet ($S = 1/2$) and for quadruplet ($S = 3/2$) spin states of the system. For the sake of comparison, we note that, for the three-nucleon system, the val-

Table 1. Hypertriton binding energy $E({}^{3}_{\Lambda}\mathrm{H})$ and doublet and quadruplet scattering lengths ${}^{2}A_{\Lambda d}$ and ${}^{4}A_{\Lambda d}$, respectively

References	*NN* potential	Λ*N* potential	$E({}^{3}_{\Lambda}\mathrm{H})$, MeV	${}^{2}A_{\Lambda d}$, fm	${}^{4}A_{\Lambda d}$, fm
This study	MT I–III		–2.37	15.3	4.9
[7]	Bonn	Nijmegen	–2.37	–	–
[8]	G3	E1r	–2.37	15.7	–
	GS1	Y5rb	–2.374	15.3	–
[9]			–2.439	13.29	–

ues of N_l from [11] were 15 and 5 for the corresponding spin states.

The calculated values of the hypertriton binding energy are displayed in Table 1, along with the calculated values of the Λ*d* scattering lengths ${}^{2}A_{\Lambda d}$ and ${}^{4}A_{\Lambda d}$ in the doublet and quadruplet spin states, respectively. The experimental value of the ${}^{3}_{\Lambda}\mathrm{H}$ binding energy is -2.35 ± 0.05 MeV [16]. Thus, our result is seen to be in good agreement both with the results obtained in [7, 8] and with the above experimental value.

Figure 1 shows the hyperon-density distribution $\rho_\Lambda(r)$ in the nucleus, the normalization condition being $\int_0^\infty r^2\rho_\Lambda(r)dr = 1$. For the sake of comparison, the nucleon density in the triton nucleus ${}^{3}\mathrm{H}$ as calculated in a similar way with the MT I–III *NN* potential is also shown in Fig. 1. For the root-mean-square radius of the hypertriton, we obtained the value of $\langle r^2\rangle^{1/2} = 5.69$ fm.

The most probable configuration of the particles of the system being considered is determined by the position of a local maximum of the squared modulus of the wave function of the system, $|\Psi(x, y, v)|^2$. The quantity $|\Psi(x, y, v)|^2$ peaks at the point specified by the values of $x = 0.86$ fm, $y = 0.61$ fm, and $v = 0$. Figures 2 and 3 illustrate the most probable position of the Λ hyperon in the nucleus. Figure 2 shows the squared modulus $|\Psi(x, y, v)|^2$ of the wave function of the Λ*np* system at the fixed value of $x = 0.86$ fm. Along the axes, we plotted the projections yv and $y\sqrt{1-v^2}$ of the vector **y** directed from the center of mass of the nucleon pair to the hyperon rather than the variables y and v. Figure 3 displays the function $|\Psi(x, y, v = 0)|^2$. From Figs. 2 and 3, we can see that, according to the direct determination of the point at which the function $|\Psi(x, y, v)|^2$ peaks, the most probable position of the hyperon is on the straight line that passes through the center of mass of the *np* pair and which is orthogonal to the relative vector **x**.

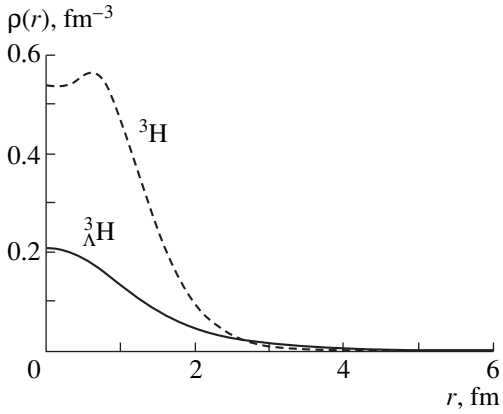

Fig. 1. Λ-particle-distribution density $\rho_\Lambda(r)$ (solid curve) in the hypertriton nucleus ${}^{3}_{\Lambda}\mathrm{H}$ and nucleon-distribution density $\rho_N(r)$ (dashed curve) in the triton nucleus ${}^{3}\mathrm{H}$.

The total wave function $\Psi(x, y, v)$ of the ${}^{3}_{\Lambda}\mathrm{H}$ hypernucleus as obtained in our calculation was used to estimate the degree of deuteron clustering in the bound system Λ*np* by considering the parameter

$$P_d = \frac{\langle \Psi_d, \Psi\rangle}{\langle \Psi, \Psi\rangle},$$

where Ψ_d is the wave function of the system as calculated with the component $U(x, y)$ represented as $U(x, y) = \phi_d(x)f_1(y)$; this corresponds to taking into account only the first term in the expansion in (7). The parameter P_d measures the degree of deuteron clustering in the ${}^{3}_{\Lambda}\mathrm{H}$ nucleus. We obtained the value of $P_d = 0.988$, which indicates that the clustering of the bound state of the Λ*np* system is considerable. An evaluation of this parameter in [7] yielded $P_d = 0.987$.

In addition to the Λ*d* scattering lengths, we have also calculated the phase shifts at energies of relative motion that are below the deuteron-breakup threshold. Figure 4 shows the doublet and quadruplet phase shifts (${}^{2}\delta_0$ and ${}^{4}\delta_0$, respectively) as functions of energy. The results of our study indicate that to a high precision, the function $p\cot({}^{2S+1}\delta)$ can be represented in the form of the effective-range expansion

$$p\cot({}^{2S+1}\delta_0) = -\frac{1}{{}^{2S+1}A_{\Lambda d}} + \frac{{}^{2S+1}r}{2}p^2,$$

where the parameter values of ${}^{2}r = 3.78$ fm and ${}^{4}r = 2.45$ fm. Figure 5 shows the functions $p\cot({}^{2S+1}\delta_0)$ for

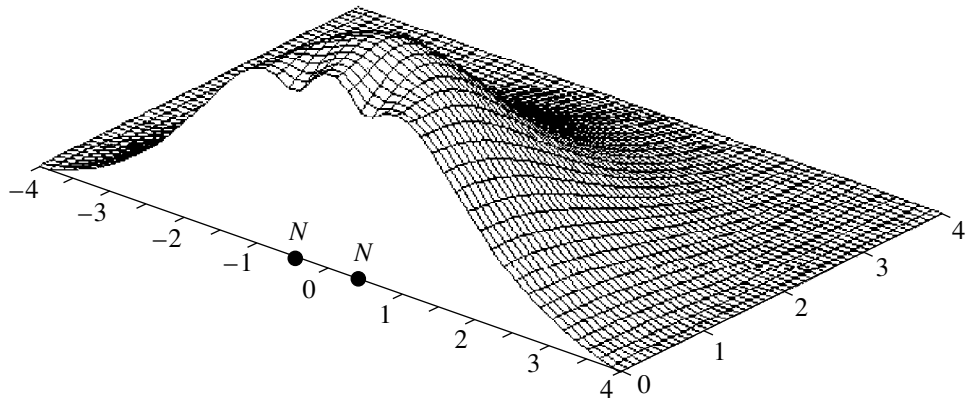

Fig. 2. Squared modulus $|\Psi(x, y, v)|^2$ of the wave function of the Λnp system. The distance between nucleons is fixed at the value of $x = 0.26$ fm; the projections yv and $y\sqrt{1-v^2}$ are plotted along the axes.

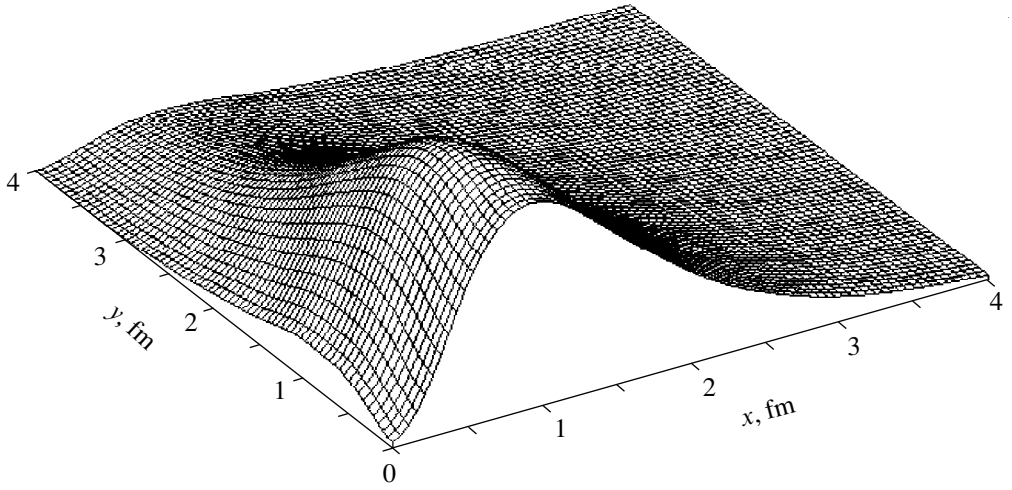

Fig. 3. Squared modulus $|\Psi(x, y, v = 0)|^2$ of the wave function of the Λnp system.

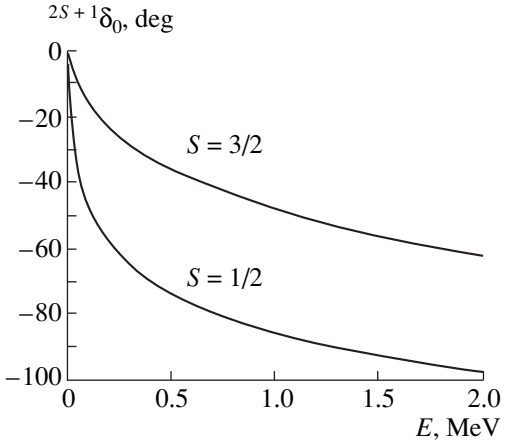

Fig. 4. Doublet ($S = 1/2$) and quadruplet ($S = 3/2$) phase shifts $^{2S+1}\delta_0$ for Λd scattering as functions of energy.

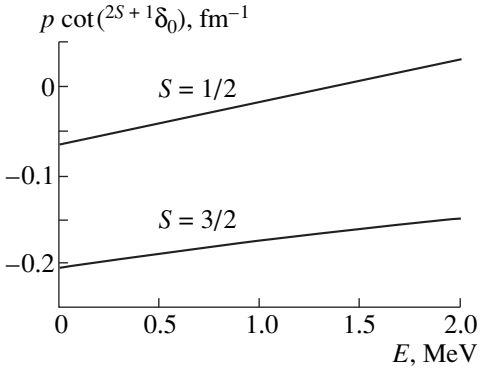

Fig. 5. Function $p\cot(^{2S+1}\delta_0)$ for the doublet ($S = 1/2$) and quadruplet ($S = 3/2$) phase shifts for Λd scattering.

Table 2. Parameters of low-energy Λ*N* scattering that are calculated by using various Λ*N* potentials

References	a^s, fm	r^s, fm	a^t, fm	r^t, fm
This study	–1.90	4.8	–6.85	2.9
Nijmegen [7]	–2.45	–	–1.51	–
[9]	–1.80	2.8	–1.60	3.3
E1r [8]	–1.86	3.68	–1.55	3.85
Y5rb [8]	–2.27	3.13	–1.05	3.87

$S = 1/2$ and $S = 3/2$. In order to compare the Λ*N* potential used in this study with well-known potentials, we have calculated the singlet and triplet Λ*N* scattering lengths and the effective ranges. The results of the calculations are presented in Table 2.

5. CONCLUSION

By using model *NN* and Λ*N* potentials, we solved numerically the differential Faddeev equations for the Λ*np* system in the *s*-wave approximation. The resulting value of the binding energy of the ${}^{3}_{\Lambda}\mathrm{H}$ hypernucleus is in good agreement with the values obtained in [7, 8], where the Faddeev equations were solved with realistic potentials (moreover, Λ–Σ conversion was taken into account in [7]). A detailed comparison of the Λ-hyperon-distribution densities in the hypertriton nucleus indicates that our results for the wave function are consistent with those from [7].

The ${}^{3}_{\Lambda}\mathrm{H}$ binding energy was calculated in [8] by using various hyperon–nucleon potentials. From an analysis of the results obtained there, it was deduced in [8] that an accurate determination of the singlet Λ*N* scattering length is necessary for correctly reproducing the binding energy of the hypertriton for a given Λ*N* potential. Our calculations support this conclusion.

The low-energy parameters of Λ-hyperon scattering on a deuteron in the doublet and quadruplet spin states have been calculated here. The results for doublet Λ*d* scattering differ considerably from the results for corresponding *Nd* scattering. In particular, a conventional effective-range expansion proves to be valid for doublet Λ*d* scattering at low energies.

We are going to apply the cluster-reduction method to the differential equations for Yakubovsky components describing the four-body Λ*NNN* system. For such equations, we expect an even more considerable reduction of computational difficulties within the cluster-reduction method.

ACKNOWLEDGMENTS

This work was supported by the Russian Foundation for Basic Research (project no. 98-02-18190).

REFERENCES

1. L. D. Faddeev, Zh. Éksp. Teor. Fiz. **39**, 1459 (1960) [Sov. Phys. JETP **12**, 1014 (1960)].
2. S. P. Merkuriev and L. D. Faddeev, *Quantum Scattering Theory for Few-Body Systems* (Nauka, Moscow, 1985).
3. H. Kamada and W. Glöckle, Nucl. Phys. A **548**, 205 (1992).
4. A. A. Kvitsinskiĭ, Yu. A. Kuperin, *et al.*, Fiz. Élem. Chastits At. Yadra **17**, 267 (1986) [Sov. J. Part. Nucl. **17**, 113 (1986)].
5. C. R. Chen, G. L. Payne, J. L. Friar, *et al.*, Phys. Rev. C **39**, 1261 (1989).
6. K. Miyagawa and W. Glöckle, Phys. Rev. C **48**, 2576 (1993).
7. K. Miyagawa, H. Kamada, W. Glöckle, *et al.*, Phys. Rev. C **51**, 2905 (1995).
8. A. Gobis, A. S. Jensen, and D. V. Fedorov, nucl-th/9608026.
9. V. B. Belyaev and V. V. Pupyshev, Yad. Fiz. **35**, 905 (1982) [Sov. J. Nucl. Phys. **35**, 526 (1982)].
10. S. L. Yakovlev and I. N. Filikhin, Yad. Fiz. **56** (12), 98 (1993) [Phys. At. Nucl. **56**, 1676 (1993)].
11. S. L. Yakovlev and I. N. Filikhin, Vestn. S.-Peterb. Univ., Ser. 4: Fiz. Khim., No. 3, 24 (1992).
12. S. L. Yakovlev and I. N. Filikhin, Yad. Fiz. **58**, 817 (1995) [Phys. At. Nucl. **58**, 754 (1995)].
13. S. L. Yakovlev and I. N. Filikhin, Yad. Fiz. **60**, 1962 (1997) [Phys. At. Nucl. **60**, 1794 (1997)].
14. R. A. Malfliet and J. A. Tjon, Ann. Phys. (N.Y.) **61**, 425 (1970).
15. N. W. Schellingerhout, J. J. Schut, and L. P. Kok, Phys. Rev. C **46**, 1192 (1992).
16. M. Juric *et al.*, Nucl. Phys. B **52**, 1 (1973).

Translated by R. Tyapaev

Physics of Atomic Nuclei, Vol. 63, No. 2, 2000, pp. 229–232. From Yadernaya Fizika, Vol. 63, No. 2, 2000, pp. 285–289.

NUCLEI
Theory

Breakup of Exotic Nuclei and Correlations of Halo Neutrons*

G. D. Alkhazov

Petersburg Nuclear Physics Institute, Russian Academy of Sciences, Gatchina, 188350 Russia

Received March 22, 1999

Abstract—We show that cross sections for nuclear fragmentation and Coulomb dissociation depend essentially on the correlation between halo neutrons, and thus the experimental data for the given processes may serve as a source of information on this correlation. The recently obtained data on the Coulomb dissociation of ^{6}He, when combined with the data on the proton elastic scattering, have allowed us to conclude that the motion of the halo neutrons in ^{6}He is significantly correlated, the size of the dineutron cluster, in particular, being 2.0 ± 0.5 fm. © *2000 MAIK "Nauka/Interperiodica".*

1. INTRODUCTION

The correlation of halo neutrons presents one of the intriguing questions in the physics of exotic nuclei. There were several attempts [1–8] to obtain information on this correlation, in particular, from the investigation of nuclear fragmentation and Coulomb dissociation of the nuclei under study. The idea of the often used approach consisted in the following. It was supposed that the mentioned processes might be described within the frames of the "sudden approximation." According to this approximation, the reaction mechanism does not distort significantly the momenta of the emitted neutrons and fragments, so that these measured momenta can be considered the same as those that the neutrons and fragments had in the exotic nucleus before the nuclear breakup took place. Thus, comparing the widths of the measured momentum distributions, or studying directly the correlation between the measured momenta, we intended to obtain information on the correlation between the halo neutrons. However, as became evident later, the reaction mechanism may dramatically influence the observed momenta of the neutrons and the fragments. For this reason, this approach turns out to be not meaningful (see [9, 10]) and cannot be applied for studying nucleon correlations. The results of investigations [1–8], where the correlation of halo neutrons was studied, are contradictory. At present, from the mentioned works, it is difficult to make definite conclusions concerning this correlation.

Recently, we discussed that the correlation between the halo neutrons may be, in principle, studied using intermediate energy proton elastic scattering [11]. Here, we discuss another approach for studying this correlation. We show that the differential cross sections for the nuclear fragmentation and the Coulomb dissociation as functions of the square of the sum of the momenta for the core fragment and the emitted halo neutrons are rather sensitive to the correlation between the halo neutrons. Therefore, a study of the processes of nuclear fragmentation and Coulomb dissociation may be used to get information on the correlation between the halo neutrons. Note that this approach does not employ the doubtful "sudden approximation," which cannot be applied in fact for quantitative description of nuclear fragmentation and Coulomb dissociation.

As is known, when a fast beam of nuclei interacts with a target, the breakup of nuclei occurs due to nuclear fragmentation, induced by strong interaction, and due to Coulomb dissociation, induced by electromagnetic interaction. In the present paper, we consider nuclear fragmentation of exotic nuclei on a proton target and Coulomb dissociation of exotic nuclei on a nuclear target with high charge number Z_t. We neglect a contribution of the Coulomb dissociation in the first case and a contribution of the nuclear fragmentation in the second case. We consider the above processes at intermediate energy and small momentum transfers for two-neutron halo nuclei, such as ^{6}He and ^{11}Li. We suppose that these nuclei consist of a compact inert core and two halo neutrons and that due to interaction with the target they disintegrate to the core and the halo neutrons.

2. NUCLEAR FRAGMENTATION

In agreement with the Glauber theory [12], the scattering amplitude of the discussed processes may be written as

$$F_{fi}(\mathbf{q}) = \langle f|\hat{F}(\mathbf{q})|i\rangle, \tag{1}$$

$$\hat{F}(\mathbf{q}) = ik/2\pi\int \exp(i\mathbf{q}\cdot\mathbf{b})\hat{\Gamma}(\mathbf{b})d^2b, \tag{2}$$

$$\begin{aligned}\hat{\Gamma}(\mathbf{b}) &= \Gamma_{tn1}(\mathbf{b}-\mathbf{s}_1) + \Gamma_{tn2}(\mathbf{b}-\mathbf{s}_2)\\ &+ \Gamma_{tc}(\mathbf{b}-\mathbf{s}_c) - \Delta\Gamma(\mathbf{b}, \mathbf{s}_1, \mathbf{s}_2, \mathbf{s}_c).\end{aligned} \tag{3}$$

Here, $\mathbf{q}$ is the momentum transfer from the target to the halo nucleus; k is the magnitude of the wave vector $\mathbf{k}$ of the projectile; $\mathbf{b}$ is the impact parameter ($\mathbf{b} \perp \mathbf{k}$); $\mathbf{s}_1$, $\mathbf{s}_2$,

* This article was submitted by the author in English.

and $\mathbf{s}_c$ are the transverse coordinates of the halo neutrons and of the core; $\Gamma_{tn1}(\mathbf{b}-\mathbf{s}_1)$, $\Gamma_{tn2}(\mathbf{b}-\mathbf{s}_2)$, and $\Gamma_{tc}(\mathbf{b}-\mathbf{s}_c)$ are the profile functions for interaction of the halo neutrons and the core with the target; and the term $\Delta\Gamma(\mathbf{b}, \mathbf{s}_1, \mathbf{s}_2, \mathbf{s}_c)$ describes rescattering of the halo neutrons and the core on the target. The contribution of the last term in case of scattering of exotic nuclei is relatively small, and it will not be considered here. Substituting (3) into (2), and neglecting the term $\Delta\Gamma(\mathbf{b}, \mathbf{s}_1, \mathbf{s}_2, \mathbf{s}_c)$, we obtain

$$\hat{F}(\mathbf{q}) = f_{tn}(\mathbf{q})[\exp(i\mathbf{q}\cdot\mathbf{r}_1)+\exp(i\mathbf{q}\cdot\mathbf{r}_2)] + f_{tc}(\mathbf{q})\exp(i\mathbf{q}\cdot\mathbf{r}_c). \quad (4)$$

Here, $f_{tn}(\mathbf{q})$ and $f_{tc}(\mathbf{q})$ are the amplitudes of scattering of the free neutrons and free core on the target, and $\mathbf{r}_1$, $\mathbf{r}_2$, and $\mathbf{r}_c$ are the position vectors of the two neutrons and the core relative to the center of mass (c.m.) of the whole nucleus. Supposing that the halo nucleus has no bound excited states, to obtain the differential cross section $d\sigma/d^2q$ for the disintegration of the nucleus to the core and the halo nucleons, we have to sum up $k^{-2}|F_{fi}(\mathbf{q})|^2$ over all final states except $f = i$. Making use of closure, we obtain

$$d\sigma/d^2q = k^{-2}\sum_{f\neq i}|F_{fi}|^2 = k^{-2}\{\langle i|\hat{F}(\mathbf{q})\hat{F}^*(\mathbf{q})|i\rangle - |\langle i|\hat{F}(\mathbf{q})|i\rangle|^2\}. \quad (5)$$

To calculate $d\sigma/d^2q$, we have to take into account in (4) the contributions of scattering from the halo nucleons and from the core. However, as was discussed in [13], in the case of nuclear fragmentation at small momentum transfers, the contribution from scattering on halo nucleons dominates. Let us consider this contribution. Substituting (4) into (5) and assuming that the target is a proton, we obtain

$$d\sigma/d^2q = k^{-2}|f_{pn}(\mathbf{q})|^2 \times\{2+2\langle i|\exp[i\mathbf{q}\cdot(\mathbf{r}_1-\mathbf{r}_2)]|i\rangle - 4|\langle i|\exp(i\mathbf{q}\cdot\mathbf{r}_1)|i\rangle|^2\}. \quad (6)$$

Introducing the halo form factor $S_h(\mathbf{q})$ as

$$S_h(\mathbf{q}) = \langle i|\exp(i\mathbf{q}\cdot\mathbf{r}_1)|i\rangle \quad (7)$$

and the correlation function $C(\mathbf{q})$, defined in [14] as

$$C(\mathbf{q}) = \langle i|\exp[i\mathbf{q}\cdot(\mathbf{r}_1-\mathbf{r}_2)]|i\rangle - \langle i|\exp(i\mathbf{q}\cdot\mathbf{r}_1)|i\rangle\langle i|\exp(-i\mathbf{q}\cdot\mathbf{r}_2)|i\rangle, \quad (8)$$

we finally obtain

$$d\sigma/d^2q = 2k^{-2}|f_{pn}(\mathbf{q})|^2\{1-S_h^2(\mathbf{q})+C(\mathbf{q})\}. \quad (9)$$

We see that the resulting differential cross section depends directly on the correlation function $C(\mathbf{q})$, which describes the correlation between the halo nucleons.

In the absence of correlations between the halo nucleons, the correlation function $C(\mathbf{q})$ is equal to zero, and the expression for $d\sigma/d^2q$ becomes

$$d\sigma/d^2q = 2k^{-2}|f_{pn}(\mathbf{q})|^2\{1-S_h^2(\mathbf{q})\}. \quad (10)$$

If we consider the extreme case of strong correlation when $\mathbf{r}_1 = \mathbf{r}_2$, we obtain

$$C(\mathbf{q}) = 1-S_h^2(\mathbf{q}), \quad (11)$$

$$d\sigma/d^2q = 4k^{-2}|f_{pn}(\mathbf{q})|^2\{1-S_h^2(\mathbf{q})\}. \quad (12)$$

On the other hand, for the extreme case of anticorrelation when $\mathbf{r}_1 = -\mathbf{r}_2$, we obtain

$$C(\mathbf{q}) = S_h(2\mathbf{q})-[S_h(\mathbf{q})]^2, \quad (13)$$

$$d\sigma/d^2q = 2k^{-2}|f_{pn}(\mathbf{q})|^2\{1-2S_h^2(\mathbf{q})+S_h(2\mathbf{q})\}. \quad (14)$$

Of course, the extreme cases of the correlations considered above are not realistic. However, they show how much the effects from correlations may be in principle in the cross section $d\sigma/d^2q$.

Let us consider a more realistic case of correlations when the halo neutrons are bound into a dineutron cluster of size $R_{dn} \equiv \langle(\mathbf{r}_1-\mathbf{r}_2)^2/4\rangle^{1/2}$. Introducing a form factor of the dineutron cluster

$$S_{dn}(\mathbf{q}) = \langle i|\exp[i\mathbf{q}\cdot(\mathbf{r}_1-\mathbf{r}_2)/2]|i\rangle, \quad (15)$$

we can write the correlation function $C(\mathbf{q})$ as

$$C(\mathbf{q}) = S_{dn}(2\mathbf{q})-S_h^2(\mathbf{q}). \quad (16)$$

In the figure, we compare the cross sections $d\sigma/d^2q$, calculated using (10) and (9) and (16) for the case of p^{11}Li scattering at 1 GeV assuming $R_h \equiv \langle\mathbf{r}_1^2\rangle^{1/2} = 8$ fm and $R_{dn} = 3$ fm, the cluster and halo form factors being parametrized by Gaussian functions. It is seen that the correlation between the halo neutrons may significantly influence the absolute value and the shape of the cross section for the nuclear fragmentation. Of course, in the calculation of the cross section $d\sigma/d^2q$ with the purpose to get information on the correlation between the halo nucleons from the data on the nuclear fragmentation, one has to consider all scattering terms in (5). In this connection, we have to note that the contribution to the cross section $d\sigma/d^2q$ from scattering on the core, though being relatively small, may not be neglected, and taking this term into account makes the whole picture more complicated.

3. COULOMB DISSOCIATION

Now, let us consider the Coulomb dissociation. Retaining in (3) only the term $\Gamma_{tc}(\mathbf{b}-\mathbf{s}_c)$, and performing a similar consideration, for the cross section of the Coulomb dissociation, we obtain

$$d\sigma/d^2q = k^{-2}|f_{tc}^{\mathrm{Coul}}(\mathbf{q})|^2\{1-S_c^2(\mathbf{q})\}. \quad (17)$$

Here $f_{tc}^{\mathrm{Coul}}(\mathbf{q})$ is the Coulomb amplitude of elastic scattering of the free core on the target

$$|f_{tc}^{\mathrm{Coul}}(\mathbf{q})|^2 = 4n^2q^{-4}S_t^2(\mathbf{q})[S_c'(\mathbf{q})]^2, \quad (18)$$

n is the Sommerfeld parameter $n = Z_t Z_c \alpha/\beta$, Z_c is the charge number of the core, α is the fine structure constant, $\beta = v/c$, v is the relative velocity of the exotic nucleus and the target, $S_t(\mathbf{q})$ is the charge form factor of the target, $S_c'(\mathbf{q})$ is the charge form factor of the free core, and $S_c(\mathbf{q})$ is the form factor corresponding to the distribution of the core c.m. radius $\mathbf{r}_c$.

At small momentum transfers q, the form factor $S_c(\mathbf{q})$ may be approximated by

$$S_c(\mathbf{q}) \approx 1 - \mathbf{q}^2 \tilde{R}_c^2/6, \tag{19}$$

where $\tilde{R}_c^2 \equiv \langle \mathbf{r}_c^2 \rangle$. Inserting (19) into equation (17), for the cross section $d\sigma/d^2q$ at small momentum transfers we have

$$d\sigma/d^2q \approx k^{-2} \left| f_{tc}^{\mathrm{Coul}}(\mathbf{q}) \right|^2 \mathbf{q}^2 \tilde{R}_c^2/3. \tag{20}$$

At small momentum transfers, the form factors $S_t(\mathbf{q})$ and $S_c'(\mathbf{q})$ are close to one, so that some uncertainty in these form factors is of little importance. Thus, we see that the only unknown parameter that determines the magnitude of the cross section for the Coulomb dissociation of an exotic nucleus at small momentum transfers is the value of $\tilde{R}_c$. On the other hand,

$$\mathbf{r}_c = -(\mathbf{r}_1 + \mathbf{r}_2)/A_c, \tag{21}$$

$$\tilde{R}_c^2 = 2R_h^2\{1 + \eta\}/A_c^2, \tag{22}$$

where A_c in the number of nucleons in the core, and η is the correlation factor

$$\eta = \langle \mathbf{r}_1 \cdot \mathbf{r}_2 \rangle / R_h^2, \quad -1 < \eta < 1. \tag{23}$$

Therefore, studying the process of Coulomb dissociation of exotic nuclei at small momentum transfers, one can derive information on the correlation factor η which characterizes the degree of correlation between the halo neutrons. Of course, the total cross section for the Coulomb dissociation is also sensitive to the correlation between the halo neutrons. However, it is at small momentum transfers that the process of Coulomb dissociation dominates over that of nuclear fragmentation, and thus it can be easily separated out.

We have to note that since the energy conservation and nuclear binding are neglected in the Glauber approach, cross section (17) for the Coulomb dissociation diverges in the forward direction. We also remind the reader that, strictly speaking, only the transverse momentum transfer is considered in the Glauber theory. It is well known that the accuracy of the Glauber formulas obtained is significantly improved by replacing the transverse momentum transfer $\mathbf{q}_\perp$ by the total one including the longitudinal component $\mathbf{q}_\parallel$. The value of $\mathbf{q}_\parallel$ may be estimated at small transverse momentum transfers as $q_\parallel = \omega/\gamma v$ [15, 16], where ω is the transferred energy, and γ is the Lorents factor $\gamma = (1 - \beta^2)^{-1/2}$.

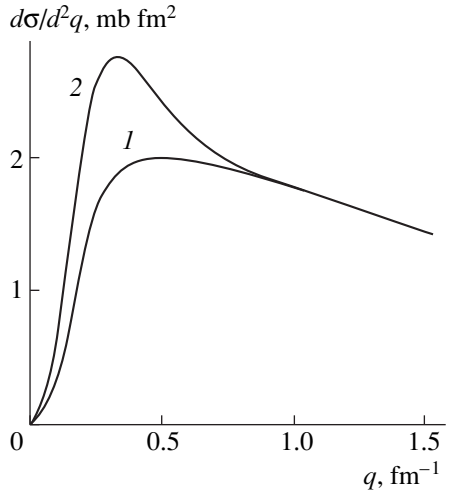

The fragmentation cross sections $d\sigma/d^2q$ as a function of the transverse momentum q for the case of p^{11}Li scattering at 1 GeV. Curve *1* corresponds to the assumed halo radius of 8 fm for uncorrelated motion of the halo neutrons ($C(q) = 0$). Curve *2* corresponds to the halo radius of 8 fm, the two neutrons being bound in a dineutron cluster of 3-fm radius. The calculations are performed using (9) and (16).

The procedure of taking the longitudinal momentum into account solves the divergency problem. However, even in this case, equation (17) overestimates the cross section for the Coulomb dissociation at very small transverse momentum transfers $q_\perp \le q_\perp^* = n\omega/\gamma v$ (see, for example, [15, 16]). To avoid this problem, when comparing the calculated cross section (17) to the experimental one, with the aim of deducing the value of $\tilde{R}_c$, the region of $q \le q_\perp^*$ may be excluded from the analysis. Note that for sufficiently high energy of the experiment and low excitation energies, this region is rather narrow. We see that the discussed method of obtaining information on the radius $\tilde{R}_c$ is based on the analysis of the absolute values of the measured cross sections. An alternative way of deducing $\tilde{R}_c$ from the data for the Coulomb dissociation may be, in principle, based on the analysis of the shape of the spectrum of the excitation energies, since the value of $\tilde{R}_c^2$ is proportional to the inverse value of the "mean excitation energy" (see [17]).

4. SPATIAL STRUCTURE OF ^{6}He

Recently, Aumann *et al*. [18] have investigated Coulomb dissociation of ^{6}He nuclei at the projectile energy of 240 MeV/u. The value of $\tilde{R}_c$ was extracted from the experimentally obtained total dipole strength making use of the energy-weighted and non-energy-weighted cluster sum rules. The cross section for the Coulomb dissociation was calculated in the quasiclassical

approximation under the assumption that the contribution of excitations with multipolarities higher than $L = 1$ may be neglected. The deduced value is $\tilde{R}_c = 1.12 \pm 0.13$ fm. This value, in combination with the results of the study of p^6He elastic scattering at intermediate energy [19], allows us to get valuable information on the spatial structure of the ^{6}He nucleus and, in particular, on the correlation of the halo neutrons.

We first note that using the overall core size $R_c = 1.88 \pm 0.12$ fm [19] and the value of $\tilde{R}_c$ mentioned above, we can determine the core internal size $R_c^* = (R_c^2 - \tilde{R}_c^2)^{1/2} = 1.51 \pm 0.18$ fm. We see that the core internal size of ^{6}He is consistent with that of a free α-particle, the latter being $R_\alpha = 1.49(1)$ fm, which corresponds to the charge radius of 1.67 fm, after taking the form factors of a proton and a neutron into account.

Then, using the value of the halo size $R_h = 2.97 \pm 0.26$ fm [19] and the value of $\tilde{R}_c$ as above, we determine the correlation factor $\eta = (A_c\tilde{R}_c/R_h)^2/2 - 1 = 0.14 \pm 0.33$. This result is compatible with uncorrelated motion of the halo neutrons around the c.m. of the ^{6}He nucleus. It should be kept in mind, however, that, even if one imagines the situation when the halo neutrons move around the core independently, nevertheless, due to the c.m. constraint, the correlation factor η will be nonzero. Thus, assuming that $\langle \mathbf{r}_{n1,c} \cdot \mathbf{r}_{n2,c} \rangle = 0$, where $\mathbf{r}_{n1,c} = \mathbf{r}_1 - \mathbf{r}_c$ and $\mathbf{r}_{n2,c} = \mathbf{r}_2 - \mathbf{r}_c$, we find $\eta = -0.38$. Therefore, the deduced value of $\eta = 0.14 \pm 0.33$ should be interpreted, in fact, as evidence for a quite significant positive (attractive) correlation between the halo neutrons. To make judgments about the dynamical correlations between the halo neutrons, it is also helpful to introduce a correlation factor $\tilde{\eta}$ defined as

$$\tilde{\eta} = \langle \mathbf{r}_{n1,c} \cdot \mathbf{r}_{n2,c} \rangle / \langle \mathbf{r}_{n1,c}^2 \rangle. \quad (24)$$

For ^{6}He, we find $\tilde{\eta} = 0.50 \pm 0.26$.

Another insight into the correlated structure of ^{6}He may be provided if we deduce the size R_{dn} of the dineutron cluster or, otherwise, the halo size in its own c.m. system. We find $R_{dn} = [R_h^2 - A_c^2\tilde{R}_c^2/4]^{(1/2)} = 1.95 \pm 0.50$ fm. The deduced value of R_{dn} may be compared with theoretical predictions. For example, according to [20], $R_{dn} = 2.3$–2.5 fm.

5. CONCLUSION

We have shown that the differential cross section $d\sigma/d^2q$ for the nuclear fragmentation on a hydrogen target at small momentum transfers q is sensitive to the correlation function $C(q)$ describing the halo neutron–neutron correlation. A very efficient means of getting information on the correlation between the halo neutrons happens to be the Coulomb dissociation on a high-Z target at small momentum transfers. Combining the results of investigations of the Coulomb dissociation of ^{6}He [18] and of the p^6He elastic scattering at intermediate energy [19], we have obtained unambiguous quantitative information on the correlated structure of the ^{6}He nucleus in its ground state. It is important that the information obtained here is free from distortion effects of final-state interaction, in contrast to some previous approaches that we discussed before.

The quantities deduced are as follows. The ^{6}He core internal size is $R_c^* = 1.51 \pm 0.18$ fm; the dynamical n–n correlation factor is $\tilde{\eta} = 0.50 \pm 0.26$; the size of the dineutron cluster is $R_{dn} = 1.95 \pm 0.50$ fm. To reduce the uncertainties in these quantities, it would be helpful to measure cross sections for p^6He elastic scattering at higher momentum transfers and also to perform a more careful analysis of the data for the Coulomb dissociation of ^{6}He.

REFERENCES

1. I. Tanihata, T. Kobayashi, T. Suzuki, *et al.*, Phys. Lett. B **287**, 307 (1992).
2. H. Esbensen, D. Kurath, and T. S. H. Lee, Phys. Lett. B **287**, 289 (1992).
3. T. Kobayashi, Nucl. Phys. A **553**, 465c (1993).
4. D. Sackett, K. Ieki, A. Galonsky, *et al.*, Phys. Rev. C **48**, 118 (1993).
5. S. Shimoura, T. Nakamura, M. Ishihara, *et al.*, Phys. Lett. B **348**, 29 (1995).
6. K. Ieki, A. Galonsky, D. Sackett, *et al.*, Phys. Rev. C **54**, 1589 (1996).
7. T. Kobayashi, K. Yoshida, A. Ozava, *et al.*, Nucl. Phys. A **616**, 223c (1997).
8. G. M. Ter-Akopian, A. M. Rodin, A. S. Fomichev, *et al.*, Phys. Lett. B **426**, 251 (1998).
9. I. Tanihata, Prog. Part. Nucl. Phys. **35**, 505 (1995).
10. I. Tanihata, J. Phys. G **22**, 157 (1996).
11. G. D. Alkhazov, Yad. Fiz. **62**, 765 (1999) [Phys. At. Nucl. **62**, 715 (1999)].
12. R. J. Glauber, in *Lectures in Theoretical Physics*, Ed. by W. E. Brittin (Interscience, New York, 1959), Vol. 1, p. 315.
13. G. D. Alkhazov, Pis'ma Zh. Éksp. Teor. Fiz. **67**, 296 (1998).
14. O. Kofoed-Hansen and C. Wilkin, Ann. Phys. (N.Y.) **63**, 309 (1971).
15. K. Soutome, S. Yamaji, and M. Sano, Prog. Theor. Phys. **87**, 599 (1992).
16. K. Soutome, S. Yamaji, and M. Sano, Prog. Theor. Phys. **88**, 703 (1992).
17. S. Funada, Prog. Theor. Phys. **93**, 373 (1995).
18. T. Aumann, D. Aleksandrov, L. Axelsson, *et al.*, Preprint No. GST-99-01, GSI (Darmstadt, 1999).
19. G. D. Alkhazov, M. N. Andronenko, A. V. Dobrovolsky, *et al.*, Phys. Rev. Lett. **78**, 2313 (1997).
20. M. V. Zhykov, B. V. Danilin, D. V. Fedorov, *et al.*, Phys. Rep. **231**, 151 (1993).

Physics of Atomic Nuclei, Vol. 63, No. 2, 2000, pp. 233–239. From Yadernaya Fizika, Vol. 63, No. 2, 2000, pp. 290–296.

ELEMENTARY PARTICLES AND FIELDS
Theory

Anti-helium Flux As a Signature for Antimatter Globular Clusters in Our Galaxy*

K. M. Belotsky[1)], Yu. A. Golubkov[2)], M. Yu. Khlopov[3)], R. V. Konoplich[4)], and A. S. Sakharov[4)]

Moscow State Engineering Physics Institute (Technical University), Kashirskoe sh. 31, Moscow, 115409 Russia

Received August 7; in final form April 6, 1999

Abstract—The Alpha Magnetic Spectrometer experiment is shown to be sensitive to test the hypothesis on the existence of antimatter globular cluster in our Galaxy. The hypothesis follows from the analysis of possible tests for the mechanisms of baryosynthesis and uses antimatter domains in the matter-dominated Universe as the probe for the physics underlying the origin of matter. The interval of masses for the antimatter in our Galaxy is fixed from below by the condition of antimatter domain survival in the matter-dominated Universe and from above by the observed gamma-ray flux. For this interval, the expected fluxes of anti-helium-3 and anti-helium-4 are calculated with account for their interaction with the matter in the Galaxy. © *2000 MAIK "Nauka/Interperiodica".*

1. ANTIMATTER IN BARYON-ASYMMETRIC UNIVERSE

The modern Big Bang theory is based on inflationary models with baryosynthesis and nonbaryonic dark matter. The physical basis for all three phenomena lies outside the experimentally proven theory of elementary particles. This basis follows from the extensions of the Standard Model. Particle theory considers such extensions as aesthetically appealing such as Grand Unification, as necessary to remove internal inconsistencies in the Standard Model with the use of supersymmetry and axion or simply as theoretically possible ideas of neutrino mass or lepton and baryon number violation. Most of these theoretical ideas cannot be tested directly, and particle theory considers cosmological relevance as the important component of their indirect test. In the absence of direct methods of study, one should analyze the set of indirect effects, which specify the models of particles and cosmology. The expected progress in the measurement of cosmic-ray fluxes and gamma-ray background and in the search for cosmic antinuclei makes cosmic-ray experiments the important source of information on the possible cosmological effects of particle theory. The first step in this direction may be done on the basis of the Alpha Magnetic Spectrometer (AMS) Shuttle experiment.

The specifics of the AMS Shuttle experimental program puts a stringent restriction on the possible choice of cosmic signatures for the new physics. At this stage, it cannot be related to positrons, gamma rays, or multi-GeV antiprotons. It makes us reduce the analysis to the antinuclear signal as the profound signature of new physics and cosmology, related to the existence of antimatter in the Universe.

The generally accepted motivation for a baryon-asymmetric Universe is the observed absence of the macroscopic amounts of antimatter up to the scales of clusters of galaxies. According to the Big Bang theory, a baryon-symmetric homogeneous mixture of matter and antimatter cannot survive after local annihilation, taking place at the first millisecond of cosmological evolution. Spatial separation of matter and antimatter can provide their survival in the baryon-symmetric Universe, but should satisfy severe constraints on the effects of annihilation at the border of domains. The most recent analysis finds that the size of domains should be only a few times smaller than the modern cosmological horizon to escape the contradictions to the observed gamma-ray background [1]. In a baryon-asymmetric universe, the Big Bang theory predicts the exponentially small fraction of primordial antimatter and virtually excludes the existence of primordial antinuclei. The secondary antiprotons may appear as a result of cosmic-ray interaction, with the matter. In such interaction, it is impossible to produce any sizeable amount of secondary antinuclei. Thus, nonexponential small amounts of antiprotons in the Universe, in the period from 10^{-3} to 10^{16} s, and antinuclei in the modern Universe are the profound signature for new phenomena, related to the cosmological consequences of particle theory.

The inhomogeneity of baryon-excess generation and antibaryon-excess generation as the reflection of this inhomogeneity represents one of the most important examples of such consequences. It has turned out [2–4] that virtually all the existing mechanisms of

* This article was submitted by the authors in English.

1) Institute of Applied Mathematics and Center for CosmoParticle Physics "Cosmion," Russia.
2) Moscow State University, Institute of Nuclear Physics and "Cosmion," Russia.
3) Moscow State Engineering Physics Institute and Institute of Applied Mathematics and "Cosmion," Russia.
4) Moscow State Engineering Physics Institute and "Cosmion."

baryogenesis can lead to the generation of antibaryon excess in some places, when the baryon excess, averaged over the whole space, is positive. So domains of antimatter in a baryon-asymmetric universe provide a probe for the physical mechanism of the matter generation.

Sakharov's original scenario of baryosynthesis [5] has found physical grounds in GUT models. It assumes *CP*-violating effects in out-of-equilibrium *B*-nonconserving processes, which generate baryon excess proportional to the *CP*-violating phase. If the sign and magnitude of this phase varies in space, the same out-of-equilibrium *B*-nonconserving processes, leading to baryon asymmetry, result in $B < 0$ in the regions where the phase is negative. The same argument is appropriate for the models of baryosynthesis based on electroweak-baryon-charge nonconservation at high temperatures, as well as on its combination with lepton-number-violation processes, related to the physics of the Majorana mass of a neutrino. In all these approaches to baryogenesis, independent of the physical nature of *B* nonconservation, the inhomogeneity of baryon excess and generation of antibaryon excess is determined by the spatial dependence of the *CP*-violating phase.

Spatial dependence of this phase is predicted in models of spontaneous *CP* violation, modified to escape the supermassive domain wall problem (see [2, 3] and references therein).

In this type of models, the *CP*-violating phase acquires discrete values $\phi_+ = \phi_0 + \phi_{sp}$ and $\phi_- = \phi_0 - \phi_{sp}$ where ϕ_0 and ϕ_{sp} are, respectively, a constant and spontaneously broken *CP* phase, and antibaryon domains appear in the regions with $\phi_- < 0$, provided that $\phi_{sp} > \phi_0$.

In models where the *CP*-violating phase is associated with the amplitude of an invisible axion field, the spatially variable phase ϕ_{vr} changes continuously from $-\pi$ to $+\pi$. The amplitude of the axion field plays the role of ϕ_{vr} in the period starting from Peccei–Quinn symmetry breaking phase transition until the axion mass is switched on at $T \approx 1$ GeV. The net phase changes continuously, and, if baryosynthesis takes place in the considered period, axion-induced baryosynthesis implies continuous spatial variation of the baryon excess given by [6]:

$$b(x) = A + b\sin\theta(x). \quad (1)$$

Here, *A* is the baryon excess induced by the constant *CP*-violating phase, which provides the global baryon asymmetry of the Universe, and *b* is the measure of axion-induced asymmetry. If $b > A$, antibaryon excess is generated along the direction $\theta = 3\pi/2$, the stronger will be the inequality $b > A$, and the larger interval of θ around the layer $\theta = 3\pi/2$ provides generation of antibaryon excess [6]. In the case $b - A = \delta \ll A$, the antibaryon excess is proportional to δ^2 and the relative volume occupied by it is proportional to δ.

The axion-induced antibaryon excess forms the Brownian structure looking like an infinite ribbon along the infinite axion string (see [7]). The minimal width of the ribbon is of the order of horizon in the period of baryosynthesis and is equal to m_{Pl}/T_{BS}^2. At $T < T_{BS}$, this size experiences red shift and is equal to

$$l_h(T) \approx \frac{m_{Pl}}{T_{BS}T}. \quad (2)$$

This structure is smoothed by the annihilation at the border of matter and antimatter domains. When the antibaryon diffusion scale exceeds $l_h(T)$, the infinite structure decays into separated domains. The distribution with respect to domain sizes turns out to be strongly model dependent and will be presented in our successive paper.

The size and amount of antimatter in domains, generated as a result of local baryon-nonconserving out-of-equilibrium processes, is related to the parameters of models of *CP* violation and/or invisible axion (see [2, 4]). SUSY GUT motivated mechanisms of baryon asymmetry imply flatness of superpotential relative to the existence of squark condensate. Such a condensate, being formed with $B > 0$, induces baryon asymmetry, after squarks decay into quarks and gluinos. The mechanism does not fix the value and sign of *B* in the condensate, opening the possibilities for inhomogeneous baryon charge distribution and antibaryon domains [4]. The size and amount of antimatter in such domains are determined by the initial distribution of squark condensate.

Thus, antimatter domains in a baryon-asymmetric universe are related to virtually all the mechanisms of baryosynthesis and serve as the probe for the mechanisms of *CP* violation and primordial baryon-charge inhomogeneity. The size of domains depends on the parameters of these mechanisms.

With the account of all possible mechanisms for inhomogeneous baryosynthesis, predicted on the basis of various, and generally independent, extensions of the Standard Model, the general analysis of possible domain distributions is rather complicated. Fortunately, the test for the possibility of the existence of antistars in our Galaxy, offered in [6], turns out to be virtually model independent and, as we show here, may be accessible to cosmic-ray experiments, to AMS experiment, in particular.

2. ANTIMATTER GLOBULAR CLUSTER IN OUR GALAXY

Assume a distribution of antimatter domains which satisfies the constraints on antimatter annihilation in the early Universe. Domains surviving after such annihilation should have a mass exceeding

$$M_{min} \approx (b/A)\rho_b l_a^3, \quad (3)$$

where ρ_b is the mean cosmological baryon density. The mass fraction of such domains relative to total baryon

mass is strongly model dependent. Note that, since the diffusion to the border of antimatter domain is determined on the RD stage by the radiation friction, the surviving scale fixes the size of the surviving domain. On the other hand, the constraints on the effects of annihilation put the upper limit on the mass of annihilated antimatter.

The modern antimatter-domain distribution should be cut at the masses given due to annihilation of smaller domains, and it is the general feature of any model of antibaryosynthesis in a baryon-asymmetric universe. The specific form of the domain distribution is model dependent. At scales smaller than (3), the spectrum should satisfy the constraints on the relative amount of annihilating antimatter. Provided that these constraints are satisfied, one may consider the conditions for antimatter object formation. One should take into account that the estimation of the annihilation scale after recombination gives, for this scale, the value close to the Jeans mass in the neutral baryon gas after recombination. So, the development of gravitational instability may take place in antimatter domains resulting in the formation of astronomical objects of antimatter.

Formation of an antimatter object has the time scale of the order of $t_f \approx (\pi G\rho)^{-1/2}$. The object is formed provided that this time scale is smaller than the time scale of its collision with the matter clouds. The latter is the smallest in the beginning of the object formation, when the clouds forming objects have a large size.

Note that the isolated domain cannot form an astronomical object smaller than a globular cluster [6]. The isolated antistar cannot be formed in surrounding matter since its formation implies the development of thermal instability, during which cold clouds are pressed by hot gas. Pressure of the hot matter gas on the antimatter cloud is accompanied by the annihilation of antimatter. Thus, antistars can be formed in the antimatter surroundings only, which may take place when such surroundings have at least the scale of a globular cluster.

One should expect to find antimatter objects among the oldest population of the Galaxy [6]. It should be in the halo, since, owing to strong annihilation of antimatter and matter gas, the formation of secondary antimatter objects in the disc component of our Galaxy is impossible. So, in the estimation of antimatter effects, we can use the data on the spherical component of our Galaxy as well as the analogy with the properties of the old population stars in globular clusters and elliptical galaxies.

In the spherical component of our Galaxy, the antimatter globular cluster should move at high velocity (which follows from the velocity dispersion in halo ($v \approx 150$ km/s) through the matter gas with very low number density ($n \approx 3 \times 10^{-4}$ cm^{-3}). Owing to small number density of the antimatter gas, effects of annihilation with the matter gas within the antimatter globular cluster are small. These effects, however, deserve special analysis for a future search for antimatter cluster as the gamma source.

The integral effects of an antimatter cluster may be estimated by the analysis of antimatter pollution of the Galaxy by the globular cluster of antistars.

There are two main sources of such pollution: the antistellar wind (the mass flow from antistars) and the antimatter supernova explosions. The first source provides the stationary inflow of antimatter particles with the velocity 10^7–10^8 to the Galaxy. From the analogy with the elliptical galaxies, for which one has the mass loss $10^{-12}M_\odot$ per solar mass per year, one can estimate the stationary admixture of antimatter gas in the Galaxy and the contribution of its annihilation into the gamma-ray background. The estimation strongly depends on the distribution of magnetic fields in the Galaxy, trapping charged antiparticles. Crude estimation of the gamma flux from the annihilation of this antimatter flux is compatible with the observed gamma background for the total mass of antimatter cluster less than $10^5M_\odot$. This estimation puts an upper limit on the total mass fraction of antimatter clusters in our Galaxy. Their integral effect should not contradict the observed gamma-ray background.

The uncertainty in the distribution of magnetic fields causes even more problems in the reliable estimation of the expected flux of antinuclei in cosmic rays. It also is accomplished by the uncertainty in the mechanism of cosmic-ray acceleration. The relative contribution of disc and halo particles into the cosmic-ray spectrum is also unknown.

To have some feeling of the expected effect, we may assume that the mechanisms of acceleration of matter and antimatter cosmic rays are similar and that the contribution of antinuclei into the cosmic-ray fluxes is proportional to the mass ratio of globular cluster and Galaxy. Putting together the lower limit on the mass of the antimatter globular cluster from the condition of survival of antimatter domain and the upper limit on this mass following from the observed gamma-ray background, one obtains [6] the expected flux of antihelium nuclei in the cosmic rays with the energy exceeding 0.5 GeV/nucleon to be 10^{-8}–10^{-6} of helium nuclei observed in the cosmic rays.

Such estimation assumes that annihilation does not influence the antinucleus composition of cosmic rays, which may take place if the cosmic-ray antinuclei are initially relativistic. If the process of acceleration takes place outside the antimatter globular cluster, one should take into account the Coulomb effects in the annihilation cross section of nonrelativistic antinuclei, which may lead to suppression of their expected flux.

On the other hand, antinuclear annihilation invokes a new factor in the problem of their acceleration, which is evidently absent in the case of cosmic ray nuclei. This factor may play a very important role in the account of antimatter supernovae as the possible source of cosmic-ray antinuclei. From the analogy with elliptical galaxies, one may expect [6] that, in the antimatter globular cluster, supernovae of the I type (SNI) should

explode with a frequency of about $2 \times 10^{-13}/M_\odot$ per year. On the basis of theoretical models and observational data on SNI (see [8]), one expects in such explosions the expansion of a shell with a mass of about $1.4M_\odot$ and velocity distribution up to 2×10^9 cm/s. The internal layers with the velocity $v < 8 \times 10^8$ cm/s contain anti-iron ^{56}Fe and the outer layers with higher velocity contain lighter elements such as anti-calcium or anti-silicon. Another important property of supernovae of the I type is the absence of hydrogen lines in their spectra. Theoretically, this is explained as the absence of a hydrogen mantle in the presupernova. In the case of antimatter supernova, it may lead to strong enhancement of antinuclei relative to antiprotons in the cosmic-ray effect. Note that a similar effect is suppressed in the nuclear component of cosmic rays, since supernovae of the II type are also related to the matter cosmic ray origin in our Galaxy, in which massive hydrogen mantles (with the mass up to a few solar masses) are accelerated.

In contrast with the ordinary supernova, the expanding antimatter shell is not decelerated owing to the acquirition of the interstellar matter gas and is not stopped by its pressure, but is annihilated with it [6]. As a result of annihilation with hydrogen, of which the matter gas is dominantly composed, semirelativistic antinucleus fragments are produced. The reliable analysis of such a cascade of antinucleus annihilation may be based on the theoretical models and experimental data on antiproton nucleus interaction. This program is now under way. The important qualitative result is the possible nontrivial contribution into the fluxes of cosmic-ray antinuclei with $Z \le 14$ and the enhancement of antihelium flux. With the account of this argument, the estimation of anti-helium flux from its direct proportionality to the mass of antimatter globular cluster seems to give the lower limit for the expected flux.

Here, we study another important qualitative effect in the expected antinuclear composition of cosmic rays. Cosmic-ray annihilation in the galactic disc results in the significant fraction of anti-helium-3, so that anti-helium-3 to anti-helium-4 ratio turns out to be the signature of the antimatter globular cluster.

3. EQUATIONS FOR DIFFERENTIAL FLUXES

Considering the $\overline{^4\mathrm{He}}$ nuclei travelling through the Galactic disk, we have to take into account two processes:

(i) the destruction of a nucleus in the inelastic interactions with the protons of the galactic media;

(ii) the energy losses whilst traveling through the Galaxy.

For the $\overline{^3\mathrm{He}}$ nuclei, we need to take into account also the possibility of the $\overline{^3\mathrm{He}}$-nucleus production due to the reaction

(iii) $\overline{^4\mathrm{He}} + p \longrightarrow \overline{^3\mathrm{He}} + all.$

The energy losses occur due to four kinds of processes:

(a) the energy losses on ionization and excitation of the hydrogen atoms in the disk matter;

(b) the bremsstrahlung radiation on the galactic hydrogen atoms;

(c) the inverse Compton scattering on the relic photons; and

(d) the synchrotron radiation in the galactic magnetic fields.

The processes (b)–(d) are proportional to $(m_e/M_{\mathrm{He}})^2$ and can be neglected at not very high energies of the He nuclei. The energy losses due to ionization and excitation of the hydrogen atoms per one collision are being described by the expression [9]:

$$\kappa(\beta, z) = \frac{4\pi Z(z\alpha)^2}{m_e\beta^2}\left[\ln\frac{2m_e\beta^2}{I(1-\beta^2)} - \beta^2\right], \qquad (4)$$

where I is the ionization potential of the hydrogen atom, $I \approx 15$ eV; $Z = 1$ and $z = 2$ are the electric charges of the hydrogen and helium nuclei, respectively; $\beta = v/c$ is the dimensionless velocity; and $\alpha = 1/137$ is the fine structure constant.

The rates of the energy losses and of the $\overline{^4\mathrm{He}}$ nucleus destruction are

$$\frac{dE_{3,4}}{dt} = -n_{\mathrm{H}} v_{3,4}\kappa_{3,4},$$
$$\frac{dn_{3,4}}{dt} = -n_{\mathrm{H}} v_{3,4}\sigma_{\mathrm{ann}}^{(3,4)} n_{3,4}, \qquad (5)$$

where n_{H} is the particle density of H atoms in the Galactic disc.

The source of $\overline{^3\mathrm{He}}$ nuclei can be written in the form

$$\frac{dn_3^{(+)}(t, E_3)}{dt} = -\int_{E_3}^{\infty} dn_4(t, E_4)\frac{\partial W(E_4; E_3)}{\partial E_3}; \qquad (6)$$

$\partial W(E_4; E_3)/\partial E_3$ describes the probability of producing $\overline{^3\mathrm{He}}$ in the inelastic collision $\overline{^4\mathrm{He}} + p \longrightarrow \overline{^3\mathrm{He}} + all$, with the normalization condition

$$\int_0^{\infty} dE_3 \frac{\partial W(E_4; E_3)}{\partial E_3} = W_3(E_4).$$

If we introduce the differential flux

$$J(t, E) = v\frac{\partial n(t, E)}{\partial E}$$

and the energy per nucleon ($E \longrightarrow E/A$), with $A = 4$ being the atomic weight of the anti-helium nucleus, we

finally obtain a system of the integro-differential equations describing the behavior of $^4\overline{\text{He}}$ and $^3\overline{\text{He}}$ nuclei in the Galaxy:

$$\begin{aligned}
\frac{dJ(t,E_4)}{dt} &= -n_{\text{H}}c\beta_4\left[\sigma_{\text{inel}}(p_4) - A\frac{m_p^2}{p_4E_4^2}\frac{d\kappa(\beta_4)}{d\beta_4}\right]J(t,E_4),\\
\frac{dE_4}{dt} &= -n_{\text{H}}cA^{-1}\beta_4\kappa(\beta_4),\\
\frac{dJ(t,E_3)}{dt} &= -n_{\text{H}}c\beta_3\\
&\times\left[\sigma_{\text{inel}}(p_3) - (A-1)\frac{m^2}{p_3E_3^2}\frac{d\kappa(\beta_3)}{d\beta_3}\right]J(t,E_3)\\
&+ n_{\text{H}}c\beta_3\int_{E_3}^{\infty}dE_4\sigma_4(p_4)\frac{\partial W(E_4;E_3)}{\partial E_3}J_4(t,E_4),\\
\frac{dE_3}{dt} &= -n_{\text{H}}c(A-1)^{-1}\beta_3\kappa(\beta_3).
\end{aligned} \tag{7}$$

4. THE ANNIHILATION CROSS SECTIONS

Because the cross section for the coherent interaction of the nucleon with the nuclei is not larger than 10–15% of the inelastic cross section (see, e.g., [10]), we can neglect such processes and set

$$\sigma_{\text{ann}}(N\ \text{He}) \approx \sigma_{\text{inel}}(N\ \text{He}), \tag{8}$$

where $\sigma_{\text{ann}}(N\ \text{He})$ is the cross section for the annihilation of $^4\overline{\text{He}}$ at its collision with the nucleon and $\sigma_{\text{inel}}(N\ \text{He})$ is the inelastic cross section.

Total and elastic cross sections for the pp, pn, $\bar{p}p$, $\bar{p}n$, and $\bar{p}d$ (d is the deuteron) can be found in [11]. For total cross sections at laboratory momentum $P_{\text{lab}} > 50$ GeV/c, we used the parametrization following from the Regge phenomenology [11]:

$$\sigma(pN)_{\text{tot}} = Xs^{\epsilon} + Ys^{-\eta}, \tag{9}$$

where

$$\begin{aligned}
X_{ab} &= X_{\bar{a}b},\\
X_{pp} &= 22.0 \pm 0.6,\\
X_{pn} &= 22.6 \pm 0.6,\\
Y_{pp} &= 56.1 \pm 4.4,\\
Y_{\bar{p}p} &= 98.2 \pm 9.5,\\
Y_{pn} &= 55.0 \pm 4.1,\\
Y_{\bar{p}n} &= 92.7 \pm 8.6,\\
\eta &= 0.46 \pm 0.3,\\
\epsilon &= 0.079 \pm 0.003.
\end{aligned} \tag{10}$$

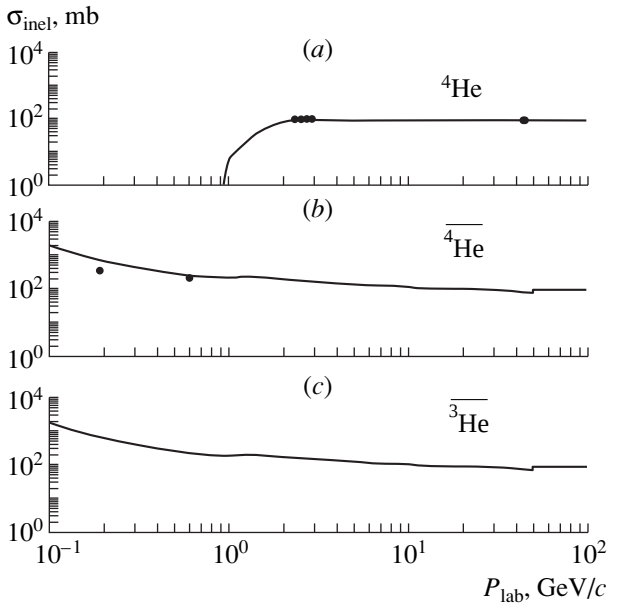

Fig. 1. Inelastic cross sections for: (*a*) (^{4}Hep), (*b*) ($^4\overline{\text{He}}p$), and (*c*) ($^3\overline{\text{He}}p$) interactions. The closed circles are the experimental points for $\sigma_{\text{inel}}(p^4\text{He})$ [12, 13] and $\sigma_{\text{inel}}(\bar{p}\,^4\text{He})$ [10, 16].

At $0.1 < P_{\text{lab}} < 50$ GeV/c, we used plots from [11] for the total and elastic cross sections.

Very scarce experimental data on total and elastic cross sections for p^4He can be found in [12, 13] and for $\bar{p}\,^4$He in [10, 14, 15]. Using these data, we found the A dependence of the cross sections in the form

$$\begin{aligned}
\sigma(^4\text{He}p) &= A^{0.84}\times\frac{1}{2}[\sigma(pp)+\sigma(np)],\\
\sigma(^4\overline{\text{He}}p) &= A^{0.84}\times\frac{1}{2}[\sigma(\bar{p}p)+\sigma(\bar{n}p)].
\end{aligned} \tag{11}$$

We also used the above A dependence for the inelastic cross section of $^3\overline{\text{He}}p$ collisions. The inelastic cross sections for the interaction of ^{4}He, $^4\overline{\text{He}}$, and $^3\overline{\text{He}}$ with protons, are shown in Fig. 1. In this picture, we also plotted the experimental points for $\sigma_{\text{inel}} = \sigma_{\text{tot}} - \sigma_{\text{el}}$ of the reaction p^4He and $\bar{p}\,^4$He.

5. RESULTS OF THE CALCULATIONS

For the probability of the production of the $^3\overline{\text{He}}$ nucleus in a $^4\overline{\text{He}}p$ collision, the experimental data from [10, 15] yield

$$\frac{\sigma(\bar{p}\,^4\text{He} \longrightarrow {}^3\text{He} + \text{all})}{\sigma_{\text{ann}}(\bar{p}\,^4\text{He})} \approx 0.25, \quad P_{\text{lab}} = 193\ \text{MeV}/c. \tag{12}$$

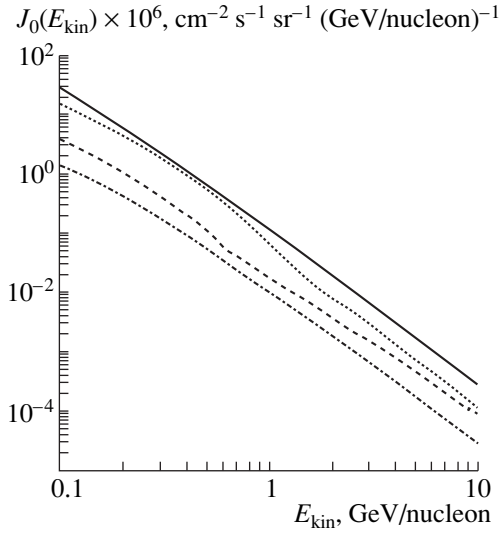

Fig. 2. Calculated fluxes of $\overline{^4\text{He}}$ (dashed curve), ^{4}He (dotted curve), and $\overline{^3\text{He}}$ (dash-dotted curve). The solid curve presents initial flux for ^{4}He nuclei. The confinement time has been chosen equal to 10^7 yr.

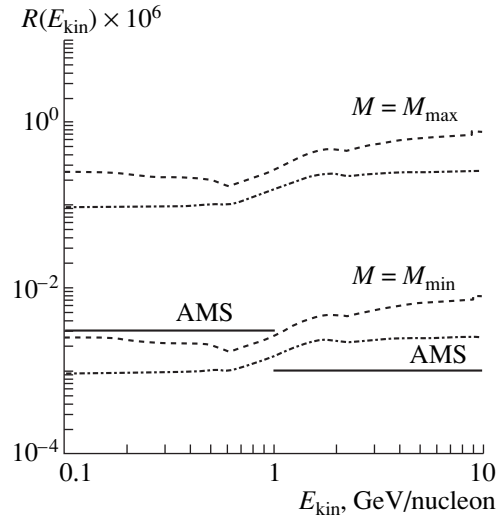

Fig. 3. Ratios of fluxes $\overline{^4\text{He}}/^4$He (dashed curve) and $\overline{^3\text{He}}/^4$He (dash-dotted curve). The two upper curves correspond to the case of maximal possible mass of antimatter globular cluster $M_{max} = 10^5 M_\odot$ and the two lower curves to the case of the minimal possible mass of such clusters $M_{min} = 10^3 M_\odot$. The results of calculations are compared with the expected sensitivity of AMS experiment [17] (solid curve).

We suggested that a relative contribution to $\overline{^3\text{He}}$ does not depend on energy and used the above value.

For simplicity, we suggested that the probability $dW(E_4; E_3)/dE_3$ in (6) could be approximated by the δ function:

$$\frac{\partial W(E_4; E_3)}{\partial E_3} = W_3 \delta(E_4 - E_3),$$

with W_3 from (12).

The initial fluxes for ^{4}He and $\overline{^4\text{He}}$ we choose in the form

$$J_4(0, E) = 0.07 \times \frac{1.93\beta}{E^{2.7}} \times 10^{-6}, \text{ cm}^{-2}\text{ s}^{-1}\text{ sr}^{-1}\text{ (GeV/nucleon)}^{-1}, \quad (13)$$

$$J_3(0, E) = 0.$$

As the confinement time for He nuclei in the galactic disc, where the hydrogen number density is $n_H \approx 1$ atom/cm^3, we choose the typical time scale $T_{conf} = 10^7$ yr. We also accounted for the very low density of the matter in the Galactic halo.

Results of our calculations are shown in Fig. 2. The solid curve shows initial He flux, and the dashed and dash-dotted curves represent final fluxes of $\overline{^4\text{He}}$ and $\overline{^3\text{He}}$, respectively.

The first two equations in (7) can be applied to the ^{4}He nuclei, if by σ_{ann} one can understand the inelastic interaction cross section of the ^{4}He nucleus with the proton.

For comparison, we also plotted the final flux of the ^{4}He by the dotted line, suggesting that the initial flux is the same as for $\overline{^4\text{He}}$.

In Fig. 3, we plotted the ratios of fluxes $\overline{^4\text{He}}/^4$He and $\overline{^3\text{He}}/^4$He for two masses of the anticluster of the upper curve for $M_{max} = 10^5 M_\odot$ and two lower curves for $M_{min} = 10^3 M_\odot$. These results are compared with the expected sensitivity of the AMS experiment to anti-helium flux. One finds the AMS experiment accessible to a complete test of the hypothesis on the existence of an antimatter globular cluster in our Galaxy.

6. DISCUSSION

The important result of the present work is that we found the substantial contribution of anti-helium-3 into the expected antinuclear flux. Even in the case of negligible anti-helium-3 flux originated in the halo, its contribution into the antinucleus flux in the galactic disc should be comparable with the one of anti-helium-4.

The estimations of [6], on which our calculations are based, assumed stationary inflow of antimatter in the cosmic rays. In case supernovae play the dominant role in the cosmic-ray origin, the inflow is defined by their frequency. One may find from [6] that the interval of possible masses of antimatter cluster 3×10^3–$10^5 M_\odot$ gives the time scale of antimatter inflow 1.6×10^9–5×10^7 yr,

which exceeds the generally estimated lifetime of cosmic rays in the Galaxy. The succession of antinucleus annihilations may result, in this case, in the dominant contribution of anti-helium and, in particular, anti-helium-3 into the expected antinuclear flux. It makes the anti-helium signature sufficiently reliable even in this case.

Thus, with all the reservations mentioned above on the basis of the hypothesis on antimatter globular cluster in our Galaxy, one may predict at the level of the expected 600 antiprotons up to ten anti-helium events in the AMS Shuttle experiment. Their detection would be an exciting indication favoring this hypothesis. Even the upper limit on anti-helium flux will lead to an important constraint on the fundamental parameters of particle theory and cosmology to be discussed in our successive publications.

Note that the important source of background for antinuclear events in AMS Shuttle experiment may be cosmic antiproton interaction with the matter of the shuttle. Such interaction should give a significant back-directed flux of helium-4, imitating anti-helium events in the AMS detector. To have a feeling of this effect, we may use the results of the numerical simulations by Lozhkin and Kramarovsky, who estimated the secondary nuclei multiplicities in the antiproton–iron interactions.

According to these estimations, which can be qualitatively correct at least for not very heavy nuclei, the helium-3 to helium-4 ratio in such interactions does not exceed 1 : 8. Moreover, contrary to the case of antinuclei, back-directed nuclear flux contains a significant admixture of metastable isotopes, tritium, in particular. According to Lozhkin–Kramarovsky calculations, the tritium-to-helium-4 ratio reaches, in this case, 1 : 3.5, which may be important for the removal of background events from the experimental data. Another interesting feature of the multiplicity distributions of secondary nuclei is that, being peaked at $z = 2$, it exceeds the level of 5% for $z \leq 6$ and then falls down to (1–2)% for higher z, giving negligible output for $z > 18$.

ACKNOWLEDGMENTS

We express our gratitude to H. Hofer, Ya.M. Kramarovsky, O.M. Lozhkin, S.G. Rubin, A.L. Sudarikov, and J.Ulbricht for fruitful discussions and to ETHZ for the permanent support of studies undertaken on the base of Cosmion–ETHZ collaboration. This work was performed in the framework of international projects Astrodamus, Eurocos–AMS, and Cosmion–ETHZ.

REFERENCES

1. A. Cohen, A. DeRujula, and S. Glashow, Astrophys. J. **495**, 539 (1998).
2. V. M. Chechetkin, M. Yu. Khlopov, and M. G. Sapozhnikov, Riv. Nuovo Cimento **5**, 1 (1982).
3. V. M. Chechetkin, M. Yu. Khlopov, M. G. Sapozhnikov, *et al*., Phys. Lett. B **118**, 329 (1982).
4. M. Yu. Khlopov, in *Cosmion'94: Proceedings of the 1st International Conference on Cosmoparticle Physics*, Ed. by M. Yu. Khlopov *et al.* (Frontieres, 1996), p. 67.
5. A. D. Sakharov, JETP Lett. **5**, 17 (1967).
6. M.Yu. Khlopov, Grav. Cosm. **4**, 1 (1998).
7. A. S. Sakharov, and M. Yu. Khlopov, Phys. At. Nucl. **57**, 485 (1994).
8. N. N. Chugaĭ, S. I. Blinnikov, and T. A. Lozinskaya, Preprint No. 43, ITEP (Moscow, 1986).
9. V. B. Berestetskiĭ, E. M. Lifshitz, and L. P. Pitaevskiĭ, *Quantum Electrodynamics*, 2nd ed. (Nauka, Moscow, 1980; Pergamon, Oxford, 1982).
10. F. Balestra, Yu. A. Batusov, G. Bendiscioli, *et al*., Phys. Lett. B **305**, 18 (1993).
11. Particle Data Group, Phys. Rev. D **54**, 191 (1996).
12. G. N. Velichko, A. A. Vorobjev, A. V. Dobrovolskiĭ, *et al.*, Yad. Fiz. **42**, 1325 (1985) [Sov. J. Nucl. Phys. **42**, 837 (1985)].
13. A. Bujak, P. Devenski, E. Jenkins, *et al.*, Preprint No. E1-81-289, JINR (Dubna, 1981).
14. F. Balestra, S. Bossolasco, M. P. Bussa, *et al.*, Phys. Lett. B **230**, 36 (1989).
15. F. Balestra, M. P. Bussa, *et al.*, Phys. Lett. B **165**, 265 (1985).
16. Yu. A. Batusov, S. A. Bunyatov, I. V. Falomkin, *et al.*, Yad. Fiz. **52**, 1222 (1990) [Sov. J. Nucl. Phys. **52**, 776 (1990)]; Preprint No. E1-90-328, JINR (Dubna, 1990).
17. H. L. Hoofer and F. Pauss, in *Cosmion'96: Proceedings of the International Conference on Cosmoparticle Physics*, Ed. by M. Yu. Khlopov *et al.* (1998), p. 596.

Physics of Atomic Nuclei, Vol. 63, No. 2, 2000, pp. 240–243. Translated from Yadernaya Fizika, Vol. 63, No. 2, 2000, pp. 297–300.

ELEMENTARY PARTICLES AND FIELDS
Theory

Production of Ultrarelativistic Positronium Beams in γe Interactions

A. P. Martynenko and V. A. Saleev[1), *]

Samara State University, ul. Akademika Pavlova 1, Samara, 443011 Russia

Received October 28, 1998

Abstract—The possibility of producing ultrarelativistic positronium beams with a Lorentz factor of $\gamma \sim 10^6$ by means of laser-photon conversion on high-energy electron beams ($E_e > 0.5$ GeV) is considered. © *2000 MAIK "Nauka/Interperiodica".*

1. INTRODUCTION

The production of relativistic positronium beams is of considerable interest for testing basic principles of QED [1] and of the relativistic theory of bound states [2]. In particular, the production of intense beams of parapositronium atoms (that is, the e^+e^- state with quantum numbers $^1S_0$) and of P-wave positronium atoms ($l = 1$) with large Lorentz factors γ can contribute to improving considerably the precision to which their lifetimes are measured. Efforts along these lines are motivated by the improved accuracy of theoretical predictions [3]. In the region of ultrarelativistic values of $\gamma \sim 10^6$, the length of formation (that is, the distance that an e^+e^- pair travels from the instant of its generation to the instant of the formation of a stationary bound state) of a positronium atom in the $n = 1$ state, n being the principal quantum number, reaches macroscopic values on the order of a few centimeters [4]. This makes it possible to test directly the law according to which the probability for the formation of an e^+e^- stationary state decreases exponentially with increasing distance from the generation point (either in a vacuum or in a medium).

Various methods of producing relativistic positronium beams have been proposed in recent years. First of all, this is the method that relies on the mechanism of positronium generation in π^0-meson decay at proton synchrotrons and which has already been tested experimentally [5].

Relativistic positronia can be produced in the interactions of high-energy photons and electrons with matter (see [6] and [7], respectively). Calculations of positronium yields from relativistic-ion collisions were performed in [8].

In the present study, we consider the generation of ultrarelativistic positronium beams ($\gamma \simeq 10^6$) via laser-photon conversion on a fast electron beam ($E_e > 0.5$ TeV). In practice, this possibility can be implemented upon commissioning new-generation linear accelerators (linac) capable of producing $E_e \approx 1$ TeV electrons.

The idea of the method is analogous to that proposed in [9] to implement γe and $\gamma\gamma$ collisions at linear e^+e^- colliders. A high-intensity beam of laser photons (about 10^{20} photons per pulse)—we assume, for the sake of definiteness, that their energy is $\omega = 1$ eV—undergoes backward scattering on a beam of high-energy electrons from a linear accelerator, transforming into a hard-photon beam, the conversion coefficient being close to unity. At a laser power in a pulse of about 10 J and a laser-pulse-repetition frequency multiple to the frequency of linac operation ($f = 10$–100 Hz), there are so many photons in a pulse per electron that it would transfer its energy to one of the incident photons with a probability close to unity.

It is clear that, under these conditions, the ratio of the cross section for positronium production in the process $\gamma + e \longrightarrow \mathrm{Ps} + e$ (Ps stands for a positronium atom in the $^3S_1$ or the $^1S_0$ state) to the cross section for the Compton scattering process $\gamma + e \longrightarrow \gamma + e$,

$$\mathcal{K} = \frac{\sigma(\gamma + e \longrightarrow \mathrm{Ps} + e)}{\sigma(\gamma + e \longrightarrow \gamma + e)}, \qquad (1)$$

determines the number of product positronia per electron of the primary beam. Like converted photons, the positronia will travel within a narrow cone along the electron-beam direction and have a hard energy spectrum.

2. PROCESS $\gamma + e \longrightarrow \mathrm{Ps} + e$

Within the nonrelativistic approximation, where the positronium atom is treated as the system formed by an electron and a positron having zero relative momentum and zero binding energy, the projection operator describing the production of an e^+e^- system in various spin states with principal quantum number $n = 1$ has the form [10]

$$\hat{P}(^3S_1) = \frac{\Psi(0)}{\sqrt{2m}}\hat{\varepsilon}(\hat{p}/2 + m), \qquad (2)$$

[1)] Nayanova Samara Municipal University, Samara, Russia.

* e-mail: saleev@ssu.samara.ru

$$\hat{P}(^1S_0) = \frac{\Psi(0)}{\sqrt{2m}}\gamma_5(\hat{p}/2 + m), \quad (3)$$

where $\hat{\varepsilon} = \varepsilon^\mu(p)\gamma_\mu$, $\varepsilon^\mu(p)$ being the orthopositronium polarization 4-vector (p is the positronium 4-momentum); m is the electron mass; and $\Psi(0) = \sqrt{m^3\alpha^3/8\pi}$ is the wave function of the positronium ground state at the origin.

In the leading order in the coupling constant $\alpha = e^2/4\pi$, positronium production in the process $\gamma + e \longrightarrow \mathrm{Ps} + e$ is described by the Feynman diagrams in Fig. 1 (*1–6* for parapositronium and *1–4*, *7*, and *8* for orthopositronium).

The amplitudes corresponding to diagrams (1)–(8) in Fig. 1 are given by

$$M_1 = e^3\bar{U}(q_2)\gamma^\mu\hat{P}\gamma_\mu(\hat{q}_1 + \hat{k} + m)\hat{\varepsilon}(k) \times U(q_1)/((q_1 + k)^2 - m^2)(p/2 - q_2)^2, \quad (4)$$

$$M_2 = e^3\bar{U}(q_2)\gamma^\mu\hat{P}\hat{\varepsilon}(k)(\hat{p}/2 - \hat{k} + m)\gamma_\mu \times U(q_1)/((p/2 - k)^2 - m^2)(q_2 + p/2)^2, \quad (5)$$

$$M_3 = e^3\bar{U}(q_2)\hat{\varepsilon}(k)(\hat{q}_2 - \hat{k} + m)\gamma^\mu\hat{P}\gamma_\mu \times U(q_1)/((q_2 - k)^2 - m^2)(q_1 - p/2)^2, \quad (6)$$

$$M_4 = e^3\bar{U}(q_2)\gamma^\mu(-\hat{p}/2 + \hat{k} + m)\hat{\varepsilon}(k)\hat{P}\gamma_\mu \times U(q_1)/((p/2 - k)^2 - m^2)(q_1 - p/2)^2, \quad (7)$$

$$M_5 = e^3\bar{U}(q_2)\gamma^\mu U(q_1)\mathrm{tr}[\hat{P}\hat{\varepsilon}(k)(-\hat{k} + \hat{p}/2 + m) \times \gamma_\mu]/(q_1 - q_2)^2((p/2 - k)^2 - m^2), \quad (8)$$

$$M_6 = e^3\bar{U}(q_2)\gamma^\mu U(q_1)\mathrm{tr}[\hat{P}\gamma_\mu(-\hat{p}/2 + \hat{k} + m) \times \hat{\varepsilon}(k)]/(q_1 - q_2)^2((p/2 - k)^2 - m^2), \quad (9)$$

$$M_7 = e^3\bar{U}(q_2)\gamma^\mu(\hat{q}_1 + \hat{k} + m)\hat{\varepsilon}(k)U(q_1) \times \mathrm{tr}[\gamma_\mu\hat{P}]/p^2((q_1 + k)^2 - m^2), \quad (10)$$

$$M_8 = e^3\bar{U}(q_2)\hat{\varepsilon}(k)\gamma^\mu(-\hat{p} + \hat{q}_1 + m)U(q_1) \times \mathrm{tr}[\gamma_\mu\hat{P}]/p^2((p - q_1)^2 - m^2). \quad (11)$$

Under the conditions $E_e \gg m \gg \omega \sim 1$ eV, the Mandelstam variables for the process $\gamma + e \longrightarrow \mathrm{Ps} + e$ can be written as

$$s = (q_1 + k)^2 \simeq m^2 + 4\omega E_e, \quad (12)$$

$$t = (k - p)^2 \simeq 4m^2 - 2E_e\omega(1 + \cos\theta), \quad (13)$$

$$u = (q_1 - p)^2 \simeq 5m^2 - 2E_eE(1 - \cos\theta), \quad (14)$$

where $k = (\omega, 0, 0, -\omega)$ is the laser-photon 4-momentum; $q_1 = (E_e, 0, 0, E_e)$ is the primary-electron 4-momentum, E_e being the primary-electron energy; q_2 is the scattered-electron 4-momentum; and $p = (E, 0, E\sin\theta, E\cos\theta)$ is the positronium 4-momentum, E and θ being, respectively, the positronium energy and the angle between the primary-electron and the positronium momentum. For this angle, we have

$$\cos\theta \simeq 1 - \frac{4\omega E_e + 4m^2}{2EE_e}. \quad (15)$$

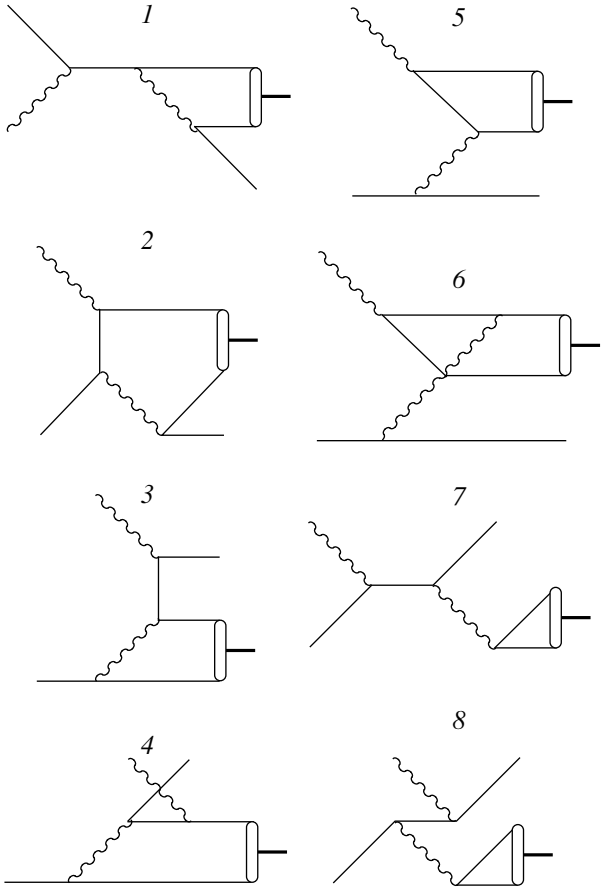

Fig. 1. Feynman diagrams for the process $\gamma + e \longrightarrow \mathrm{Ps} + e$.

The differential cross section for the process in question with respect to the variable $y = E/E_e \simeq (4m^2 - t)/(s - m^2)$ is expressed in terms of the squared modulus of the amplitude as

$$\frac{d\sigma}{dy}(\gamma + e \longrightarrow \mathrm{Ps} + e) = \frac{\overline{|M|^2}}{16\pi(s - m^2)}. \quad (16)$$

The total cross section $\sigma(\gamma + e \longrightarrow \mathrm{Ps} + e)$ is obtained from (16) by means of integration with respect to y between the limits

$$y_{\substack{\max\\\min}} = \frac{1}{s - m^2}\left[2m^2 + \frac{(s + m^2)(s - 3m^2)}{2s} \pm \frac{(s - m^2)}{2s}\sqrt{(s - 9m^2)(s - m^2)}\right]. \quad (17)$$

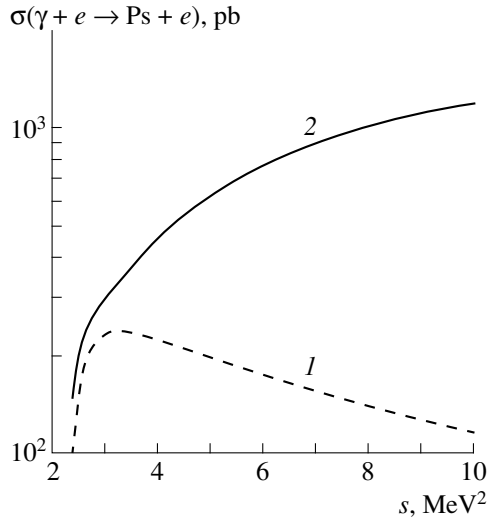

Fig. 2. Cross section $\sigma(\gamma + e \longrightarrow \mathrm{Ps} + e)$ as a function of s at a laser-photon energy of $\omega = 1$ eV. Here and in the caption under Fig. 3, Ps stands for either (curve *1*) orthopositronium or (curve *2*) parapositronium.

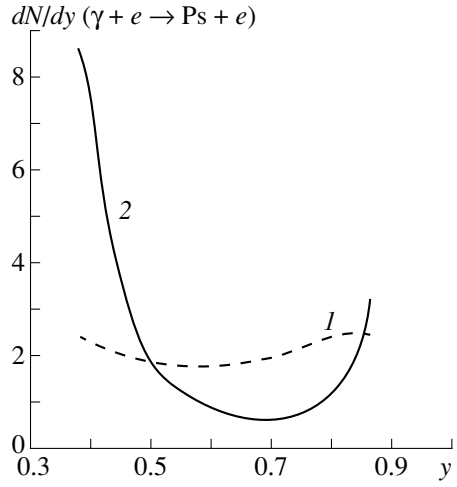

Fig. 3. Positronium spectrum dN/dy ($y = E/E_e$) for the process $\gamma + e \longrightarrow \mathrm{Ps} + e$. The notation for the curves is identical to that in Fig. 2.

3. RESULTS OF THE CALCULATIONS

We note that, on one hand, the minimum value of the invariant s is $s_{\min} = 9m^2$, whence it follows that the threshold energy for the electrons in the scattering process $\gamma + e \longrightarrow \mathrm{Ps} + e$ is

$$E_{e,\min} = \frac{s_{\min} - m^2}{4\omega} = \frac{2m^2}{\omega}. \qquad (18)$$

At the laser-photon energy of $\omega \simeq 1$ eV, this yields $E_{e,\min} = 522$ GeV. On the other hand, the value of $s = 4.2$ MeV^2 corresponds to the energy of $E_e = 1$ TeV at $\omega = 1$ eV. Figure 2 shows the calculated cross sections for orthopositronium and parapositronium production (curves *1* and *2*, respectively) as functions of the invariant s. The cross section for orthopositronium production peaks at $s = 3.2$ MeV^2 (which corresponds to $E_e = 735$ GeV); we then have $\sigma(\gamma + e \longrightarrow {}^3S_1 + e) \approx 237$ pb and $\sigma(\gamma + e \longrightarrow {}^1S_0 + e) \approx 325$ pb.

With increasing s, the cross section for orthopositronium production decreases, while the cross section for parapositronium production grows logarithmically. The latter is due to the contributions of diagrams *4* and *5* in Fig. 1. At $E_e = 1$ TeV ($s \approx 4.2$ MeV^2), we have $\sigma(\gamma + e \longrightarrow {}^3S_1 + e) \approx 218$ pb and $\sigma(\gamma + e \longrightarrow {}^1S_0 + e) \approx 494$ pb.

The above values and the curves in Fig. 2 correspond to the cross sections for the production of $n = 1$ S-wave states. The total positronium-production cross section summed over all levels is obtained by multiplying (7) by $\zeta(3) = \sum_{n=1}^{\infty} \frac{1}{n^3} \simeq 1.202$.

The values of the ratio $\mathcal{K}$ (1) are listed in the table for various values of s. By way of example, we indicate that, at $E_e = 1$ TeV and $n = 2 \times 10^{11}$ electrons per accelerator burst (this corresponds to the project of the VLEPP e^+e^- linear collider), we obtain some 1200 parapositronia and some 500 orthopositronia per pulse. At the accelerator frequency of $f = 100$ Hz, this yields 1.2×10^5 and 0.5×10^5 positronia per second, respectively. This is one order of magnitude greater than the flux of positronia in the recombination process $e^+ + e^- \longrightarrow \mathrm{Ps} + \gamma$ at e^+e^- storage rings [11]. A rough estimate of the P-wave-positronium yield (which is about 10^{-4} less than that for the S-wave-positronium yield) is 100 at/sec. It seems that so great a yield of ultrarelativistic ($\gamma \sim 10^6$) P-wave positronia is sufficient for a precise (and unique) measurement of their decay widths.

Figure 3 shows positronium spectra at $s = 3.2$ MeV^2 that are normalized to unity. The positronia are produced within the kinematical region $0.375 \le y \le 0.869$—that is, with ultrarelativistic Lorentz factors in the range $0.27 \times 10^6 \le \gamma \le 0.64 \times 10^6$. The parapositronium spectrum shows two distinct peaks near the kinematical boundaries. The mean value of $y = E/E_e$ at $s = 3.2$ MeV^2 is $\langle y \rangle \approx 0.54$ for parapositronium and $\langle y \rangle \approx 0.63$ for orthopositronium.

A positronium beam produced by means of laser-photon conversion on fast electrons is expected to be

Values of the ratio $\mathcal{K} = \sigma(\gamma + e \longrightarrow \mathrm{Ps} + e)/\sigma(\gamma + e \longrightarrow \gamma + e)$

s, MeV^2	${}^3S_1$	${}^1S_0$
3.2	2.35×10^{-9}	3.23×10^{-9}
4.2	2.61×10^{-9}	5.88×10^{-9}

free from hadron admixtures since the energy threshold for the production of even one pion pair has a formidable value of $E_{min} \approx 2 \times 10^4$ TeV in relation to the laser-photon energy of $\omega \approx 1$ eV.

ACKNOWLEDGMENTS

We are grateful to E.K. Kuraev, L.L. Nemenov, I.N. Meshkov, V.G. Serbo, R.N. Faustov, and I.B. Khriplovich for stimulating discussions on the physics of relativistic positronia.

This work was supported in part by the Russian Foundation for Basic Research (project nos. 98-02-16185 and 98-15-96040) and by the program "Universities of Russia—Fundamental Research" (project no. 2759).

REFERENCES

1. *Quantum Electrodynamics*, Ed. by T. Kinoshita (World Sci., Singapore, 1990).
2. V. V. Dvoeglazov, Yu. N. Tyukhtyaev, and R. N. Faustov, Fiz. Élem. Chastits At. Yadra **25**, 144 (1994) [Phys. Part. Nucl. **25**, 58 (1994)]; A. P. Martynenko and R. N. Faustov, Yad. Fiz. **60**, 1407 (1997) [Phys. At. Nucl. **60**, 1272 (1997)].
3. G. S. Adkins, A. A. Salahuddin, and K. E. Schalm, Phys. Rev. A **45**, 7774 (1992); P. Labelle, G. P. Lepage, and U. Magnea, Phys. Rev. Lett. **72**, 2006 (1994); E. A. Kuraev, G. V. Kukhto, and Z. K. Silagadze, Yad. Fiz. **51**, 1638 (1990) [Sov. J. Nucl. Phys. **51**, 1036 (1990)]; A. I. Mil'shteĭn and I. B. Khriplovich, Zh. Éksp. Teor. Fiz. **106**, 689 (1994) [JETP **79**, 379 (1994)]; A. P. Martynenko, V. A. Saleev, and R. N. Faustov, Phys. Rev. A **51**, 4520 (1995); Yad. Fiz. **58**, 1454 (1995) [Phys. At. Nucl. **58**, 1370 (1995)].
4. L. L. Nemenov, Preprint No. R1-89-14, JINR (1989).
5. L. L. Nemenov, Yad. Fiz. **15**, 1047 (1972) [Sov. J. Nucl. Phys. **15**, 582 (1970)]
6. S.M. Bilen'kiĭ *et al.*, Yad. Fiz. **10**, 125 (1969); G. V. Meledin, V. G. Serbo, and A. K. Slivkov, Pis'ma Zh. Éksp. Teor. Fiz. **13**, 98 (1971) [JETP Lett. **13**, 68 (1971)]; H. A. Olsen, Phys. Rev. D **33**, 2033 (1986); V. L. Lyuboshitz, Yad. Fiz. **45**, 1099 (1987) [Sov. J. Nucl. Phys. **45**, 682 (1987)].
7. A. A. Akhundov, D. Yu. Bardin, and L. L. Nemenov, Yad. Fiz. **27**, 1542 (1978) [Sov. J. Nucl. Phys. **27**, 812 (1978)]; E. Holvik and H. A. Olsen, Phys. Rev. D **35**, 2124 (1987).
8. A. P. Martynenko and V. A. Saleev, Vestn. Samarskogo Gos. Univ. **2**, 103 (1996); S. R. Gevorkyan *et al.*, Preprint No. 11/98, VL-NTZ (1998); hep-ph/9804264.
9. I. F. Ginzburg, G. L. Kotkin, V. G. Serbo, *et al.*, Pis'ma Zh. Éksp. Teor. Fiz., **34**, 514 (1981) [JETP Lett. **34**, 491 (1981)].
10. R. N. Cahn *et al.*, Phys. Lett. B **82**, 113 (1973).
11. I. N. Meshkov, Fiz. Élem. Chastits At. Yadra **28**, 495 (1997) [Phys. Part. Nucl. **28**, 198 (1997)]; G. I. Budker and A. N. Skrinskiĭ, Usp. Fiz. Nauk **124**, 561 (1978) [Sov. Phys. Usp. **21**, 277 (1978)].

Translated by O. Chernavskaya

Physics of Atomic Nuclei, Vol. 63, No. 2, 2000, pp. 244–253. Translated from Yadernaya Fizika, Vol. 63, No. 2, 2000, pp. 301–311.

ELEMENTARY PARTICLES AND FIELDS
Theory

Semileptonic Decays of Pseudoscalar Mesons in the Instant Form of Relativistic Hamiltonian Dynamics

E. V. Balandina[1)], A. F. Krutov, V. E. Troitsky[1)], and O. I. Shro

Samara State University, ul. Akademika Pavlova, Samara, 443011 Russia

Received March 16, 1998; in final form, February 16, 1999

Abstract—A formalism for describing semileptonic decays of pseudoscalar mesons is developed on the basis of the instant form of relativistic Hamiltonian dynamics. By way of example, this formalism is applied to the decay process $K^- \longrightarrow \pi^0 + \mu^- + \bar{\nu}_\mu$. Relevant calculations are performed with wave functions that correspond to various models of constituent-quark interactions in mesons. Free parameters that appear in these models are determined from a fit to the root-mean-square radii of the kaons and pions. The results of the calculations agree well with experimental data. © *2000 MAIK "Nauka/Interperiodica".*

1. INTRODUCTION

Describing the properties of mesons on the basis of constituent-quark models is an important line of investigations in elementary-particle physics. Interest in such issues is provoked, first, by a vast body of available experimental information about mesons [1], which permits fixing model parameters involved and making quantitative predictions; second, by the experiments that are being now conducted at JLab [2], where much attention is being given to studying the properties of mesons; and, third, by the inability of the present-day theory to reproduce, on the basis of QCD first principles, the majority of the meson properties, which are determined primarily by large- and intermediate-distance physics not described by perturbation theory. The existing approaches that treat mesons on the basis of constituent-quark models differ both by underlying principles and, to a considerable extent, by results [3–24]. Therefore, searches for new formulations of the constituent-quark model are of great topical interest.

In studying the properties of mesons, an important role is played by weak decays, which furnish rich information about quark interaction in mesons. In particular, many important parameters of the Standard Model, such as the elements of the Cabibbo–Kobayashi–Maskawa matrix, can be extracted from data on semileptonic decays [21]. A constituent-quark-model calculation of the decays of mesons featuring heavy quarks makes it possible to determine the coefficients in the expansion of transition form factors in inverse powers of the heavy-quark mass. It is well known that these coefficients appear in heavy-quark effective theory as well and that, at present, they cannot be computed on the basis of QCD first principles [14].

Special features of quark systems stem from the relativistic nature of quarks. This concerns primarily systems formed by light quarks; however, relativistic effects can be pronounced even in systems featuring heavy quarks. Among relativistic formulations of the constituent-quark model, the following are the most popular ones: (i) quasipotential approach [11, 14], (ii) dispersion method [15], (iii) methods of relativistic Hamiltonian dynamics (see, for example, [3, 5, 13, 17–24] and references therein), and (iv) methods that are closely related to the preceding group and which formulate a constituent-quark model in the infinite-momentum frame [4, 6].

In the present study, a formalism for describing semileptonic decays of pseudoscalar mesons is developed on the basis of the instant form of relativistic Hamiltonian dynamics [17, 18, 22]. This formalism is then applied to describing semileptonic kaon decays.

This article is organized as follows. In Section 2, we give a brief account of the formalism of relativistic Hamiltonian dynamics. In Section 3, a general procedure for parametrizing the matrix elements of local operators is used to obtain an expression for the matrix element of the weak current for the semileptonic-decay process and to derive an integral representation for the corresponding form factors. In the impulse approximation, the form factors for the semileptonic-decay process are expressed in terms of the relativistic wave functions of quarks in mesons and so-called free two-particle form factors. In Section 4, the latter are calculated by the methods of relativistic kinematics. In Section 5, the advantages of the developed formalism are demonstrated by applying it to the decay $K^- \longrightarrow \pi^0 + \mu^- + \bar{\nu}_\mu$. The calculations are performed with wave functions based on essentially different models of constituent-quark interaction in mesons. The results that we obtained without recourse to any fitting procedure—all

[1)] Institute of Nuclear Physics, Moscow State University, Vorob'evy gory, Moscow, 119899 Russia.

free parameters of the problem are independently fixed in evaluating the root-mean-square parameters of the pion and of the kaon within the same models [18]—comply well with experimental data.

2. FUNDAMENTALS OF RELATIVISTIC HAMILTONIAN DYNAMICS

In treating constituent-quark systems within a relativistic theory, there exist two essentially different approaches.

The first of these relies on field-theoretical methods. Based on the principles of QCD, it is justifiably deemed to be the most consistent approach to solving the problem in question. The limitation of conventional perturbative QCD is that it provides reliable computational recipes only in dealing with hard processes, but the calculation of the features of hadrons requires considering soft processes, where perturbative QCD fails.

Within field theory proper, there exist various methods for sidestepping this problem. These include the popular method of QCD sum rules [25], approaches relying on the Bethe–Salpeter equation [8, 9, 26], quasipotential approaches [27, 28] (their application to quark systems is discussed in [11, 14]), and the dispersion-relation approach.

The second method in the theory of composite systems—it is the method that we will use here—is based on a direct realization of the algebra of the Poincaré group on the set of dynamical variables of the composite system being considered. This approach is referred to as the theory of direct interaction or relativistic Hamiltonian dynamics.

Fundamentally, relativistic Hamiltonian dynamics differs from quantum fields theories in that the former describes a composite system in terms of a finite number of degrees of freedom. In order to render a description within relativistic Hamiltonian dynamics covariant, a single-valued unitary representation of the non-homogeneous $SL(2, C)$ group, which appears to be a universal cover of the Poincaré group, is constructed in the Hilbert space of states of the composite system featuring a finite number of degrees of freedom. It is worth noting from the outset that establishing connections between relativistic Hamiltonian dynamics and field theory is a challenging problem that has yet to be solved conclusively [23, 30].

Presently, light-front dynamics [3, 5, 10, 13, 19, 21, 23, 24] is the most popular form of relativistic Hamiltonian dynamics. In its traditional formulation, this form of dynamics possesses, along with a number of merits, a serious flaw—it is not invariant under rotations. One of the consequences of this is that the form factors of composite systems cannot be determined unambiguously [16]. In this connection, there appeared studies that rely on alternative forms of dynamics—for example, a pointlike one [20, 31].

In the present study, we make use of the instant form of relativistic Hamiltonian dynamics in the formulation developed in [12, 17, 18, 22].

The fundamentals of relativistic Hamiltonian dynamics are considered in detail elsewhere [32–35].

We will briefly describe the way in which the wave function is introduced in relativistic Hamiltonian dynamics. By analogy with nonrelativistic quantum mechanics, the wave function of a composite system in relativistic Hamiltonian dynamics is defined as an eigenfunction of a complete set of commuting operators of dynamical variables [33]. However, a novel feature of the relativistic approach in relation to the nonrelativistic one is that, in the former, dynamical variables satisfy algebraic relations of the Poincaré group [33]. In the instant form of dynamics, the above complete set is chosen to be

$$\hat{M}_I^2, \quad \hat{J}^2, \quad \hat{J}_3, \quad \hat{\mathbf{P}}. \tag{1}$$

Here, $\hat{M}_I^2 = \hat{M}_0^2 + \hat{U}$ is the operator of the square of the mass of the system of particles being considered, where $\hat{M}_0^2$ is the analogous operator for the same system of particles with interaction switched off, and $\hat{U}$ is the interaction operator; $\hat{J}^2$ is the operator of the square of the total angular momentum; $\hat{J}_3$ is the operator of its third component; and $\hat{\mathbf{P}}$ is the operator of the total 3-momentum. The last three operators coincide with the corresponding operators for the system of noninteracting particles.

In order to calculate the wave function, it is necessary to choose a basis in the Hilbert space of the states of the system. Of all possible bases, we will consider below only two. Since relativistic Hamiltonian dynamics is specified in terms of a finite number of degrees of freedom, the Hilbert space of the states of the system of interacting particles represents a direct product of single-particle Hilbert spaces. For example, the Hilbert space of the states of a meson appears to be the direct product of two spaces corresponding to a quark q and an antiquark $\bar{q}$: $\mathcal{H}_{q\bar{q}} \equiv \mathcal{H}_q \otimes \mathcal{H}_{\bar{q}}$. Thus, we can see that, in relativistic Hamiltonian dynamics, a meson-state vector appears to be a superposition of only two-particle states; hence, a basis in $\mathcal{H}_{q\bar{q}}$ can be chosen, for example, as follows:

$$\begin{aligned} |\mathbf{p}_1, m_1; \mathbf{p}_2, m_2\rangle &= |\mathbf{p}_1, m_1\rangle \otimes |\mathbf{p}_2, m_2\rangle, \\ \langle \mathbf{p}, m|\mathbf{p}', m'\rangle &= 2p_0\delta(\mathbf{p}-\mathbf{p}')\delta_{mm'}. \end{aligned} \tag{2}$$

Here, $\mathbf{p}_1$ and $\mathbf{p}_2$ are the quark and antiquark 3-momenta, while m_1 and m_2 are the corresponding spin projections onto the z axis.

In the following, we will use an alternative representation where the basis is chosen in such a way that center-of-mass motion is singled out explicitly:

$$|\mathbf{P}, \sqrt{s}, J, l, S, m_J\rangle. \tag{3}$$

Here, $P_\mu = (p_1 + p_2)_\mu$ with $P_\mu^2 = s$, $\sqrt{s}$ being the invariant mass of the two-particle system in question; l is the orbital angular momentum in the c.m. frame; S is the total spin in the c.m. frame [$\mathbf{S}^2 = (\mathbf{S}_1 + \mathbf{S}_2)^2 = S(S+1)$]; J is the total angular momentum; and m_J is the third projection of the total angular momentum.

The basis in (3) is related to the basis in (2) via the Clebsch–Gordan expansion of the Poincaré group. A more detailed description of the relevant procedure can be found in [36]. Here, we only present the eventual result, which has the form

$$|\mathbf{P}, \sqrt{s}, J, l, S, m_J\rangle = \sum_{m_1 m_2} \int \frac{d\mathbf{p}_1}{2p_{10}} \frac{d\mathbf{p}_2}{2p_{20}} |\mathbf{p}_1, m_1; \mathbf{p}_2, m_2\rangle \times \langle \mathbf{p}_1, m_1; \mathbf{p}_2, m_2 | \mathbf{P}, \sqrt{s}, J, l, S, m_J\rangle. \quad (4)$$

The Clebsch–Gordan coefficient appearing in (4) is given by

$$\langle \mathbf{p}_1, m_1; \mathbf{p}_2, m_2 | \mathbf{P}, \sqrt{s}, J, l, S, m_J\rangle = \sqrt{2s}[s^2 - 2s(M_q^2 + M_{\bar{q}}^2) + (M_q^2 - M_{\bar{q}}^2)^2]^{-1/2} \times 2P_0 \delta(P - p_1 - p_2) \sum_{\tilde{m}_1 \tilde{m}_2} \left\langle m_1 \middle| D^{1/2}(p_1 P) \middle| \tilde{m}_1 \right\rangle \quad (5)$$
$$\times \left\langle m_2 \middle| D^{1/2}(p_2 P) \middle| \tilde{m}_2 \right\rangle \sum_{m_l m_S} \langle 1/2\ 1/2 \tilde{m}_1 \tilde{m}_2 | S m_S \rangle \times Y_{l m_l}(\vartheta, \varphi) \langle S l m_S m_l | J m_J \rangle,$$

where M_q and $M_{\bar{q}}$ are, respectively, the quark and the antiquark mass; $Y_{lm_l}(\vartheta, \varphi)$ are spherical harmonies; and D^j are rotation matrices, which are necessary for the composition of particle spins in a Lorentz invariant way. For a spin of one-half, the required rotation matrix has the form

$$D^{1/2}(p_1, p_2) = \cos(\omega/2) - 2i(\mathbf{k} \cdot \mathbf{j}) \sin(\omega/2),$$
$$[j_i, j_k] = i\varepsilon_{ikl} j_l, \quad \mathbf{k} = \frac{[\mathbf{p}_1 \times \mathbf{p}_2]}{|[\mathbf{p}_1 \times \mathbf{p}_2]|}, \quad (6)$$
$$\omega = 2 \arctan \frac{|[\mathbf{p}_1 \times \mathbf{p}_2]|}{(p_{10} + M_1)(p_{20} + M_2) - (\mathbf{p}_1 \cdot \mathbf{p}_2)}.$$

From the group-theory point of view, the vectors in (3) form a basis of that irreducible representation of the $SL(2, C)$ group which describes the system of two noninteracting particles that is characterized by a fixed invariant mass and a fixed total angular momentum. In this representation, a vector is determined by eigenvalues of the complete set of commuting operators constructed from the generators of the Poincaré group for the system of noninteracting particles:

$$\hat{M}_0^2 = \hat{P}^2, \hat{J}^2, \hat{J}_3, \hat{\mathbf{P}}. \quad (7)$$

The orbital-angular-momentum and the total-spin operator taken separately are not generators of the $SL(2, C)$ group; therefore, they do not enter into the complete commuting set in (7). At a fixed value of the total angular momentum J, the total spin S and the orbital angular momentum l are not fixed in general; that is, the quantities S and l singled out in the c.m. frame play the role of degeneracy parameters. These quantities can be defined in an invariant way [36]. In describing scalar and pseudoscalar mesons, there is no degeneracy in these variables ($l = 0$ and $S = 0$), so that they are immaterial here.

The representation that corresponds to the set of operators in (7) and which describes the system of two noninteracting particles differs from the representation that is determined by the set of operators in (1) and which describes the set of interacting particles; however, the operators $\hat{J}^2$, $\hat{J}_3$, and $\hat{\mathbf{P}}$ enter both into (1) and into (7).

The calculation of the wave function of two noninteracting particles amounts to diagonalizing the set of operators in (1). If the basis in (3) is used for this, then three operators that enter both in (1) and in (7) will appear to be diagonal. Thus, the problem of calculating the wave function in basis (3) can be reduced to diagonalizing the operator $\hat{M}_I^2$.

In all versions of relativistic Hamiltonian dynamics, the eigenvalue problem for the operator $\hat{M}_I^2$ is formulated in terms of the nonrelativistic Schrödinger equation [33]. It follows that, apart from the normalization factor, the nonrelativistic meson wave function calculated within some model featuring a phenomenological potential can be chosen for a wave function within relativistic Hamiltonian dynamics.

The wave function for pseudoscalar mesons in the instant form of dynamics has the form

$$\langle \mathbf{P}', \sqrt{s}', J', l', S', m_J' | p_c \rangle = N_C \delta(\mathbf{P}' - \mathbf{p}_c) \delta_{JJ'} \delta_{m_J m_J'} \delta_{ll'} \delta_{SS'} \varphi_c(k),$$
$$k = \frac{[s^2 - 2s(M_q^2 + M_{\bar{q}}^2) + (M_q^2 - M_{\bar{q}}^2)^2]^{1/2}}{2\sqrt{s}}, \quad (8)$$
$$N_C = \sqrt{2p_{c0}} \sqrt{\frac{N_{CG}}{4k}}, \quad N_{CG} = \frac{(2P_0)^2}{8k\sqrt{s}}.$$

In the following, we will consider only pseudoscalar mesons; that is, we set $J = l = S = m_J = 0$.

The wave function of internal motion is given by

$$\varphi_c(k(s)) = \sqrt{\sqrt{s}[1 - (M_q^2 - M_{\bar{q}}^2)^2/s^2]}\, u(k) k \quad (9)$$

and is normalized by the condition

$$\int u^2(k) k^2 dk = 1. \quad (10)$$

As was discussed above, any model wave function can be taken for $u(k)$.

The relativistic wave function in the form (9) coincides with the wave function constructed in [37] by means of a minimal relativization. The wave function obtained within the scheme of a minimal relativization differs from the corresponding nonrelativistic wave function by a normalization factor whose explicit form is obtained from the normalization condition featuring the relativistic density of states. This can clearly be demonstrated by setting $M_q = M_{\bar{q}} = M$ in (9), in which case the transition to the relativistic density of states reduces to the substitution $k^2dk \longrightarrow k^2dk/2\sqrt{(k^2 + M^2)}$.

Thus, we can see that, within relativistic Hamiltonian dynamics, the conditions of relativistic invariance that are expressed in the form of algebraic relations of the Poincaré group can be made consistent with potential approaches to describing composite systems.

In calculating the electroweak properties of mesons, we use the following model wave functions:

(i) the harmonic-oscillator wave function (see, for example, [5])

$$u(k) = N_{\mathrm{HO}}\exp(-k^2/2b^2); \tag{11}$$

(ii) the wave function that was presented in [13] and which involves negative power-law exponents,

$$u(k) = N_{\mathrm{PL}}(k^2/b^2 + 1)^{-n}, \quad n = 2, 3; \tag{12}$$

(iii) the wave function featuring linear confinement and a Coulomb behavior at small distances [38],

$$\begin{aligned} u(r) &= N_{\mathrm{T}}\exp(-\alpha r^{3/2} - \beta r), \\ \alpha &= \frac{2}{3}\sqrt{2M_{\mathrm{r}}a}, \quad \beta = M_{\mathrm{r}}b, \end{aligned} \tag{13}$$

where a and b are the parameters of, respectively, the linear and Coulomb components of the potential, while M_{r} is the reduced mass of the two-particle system.

3. FORM FACTORS FOR SEMILEPTONIC DECAYS OF PSEUDOSCALAR MESONS

In the following, we consider weak decays of the types

$$K \longrightarrow \pi^0 + l + \nu_l,$$
$$B \longrightarrow D + l + \nu_l, \quad D \longrightarrow K + l + \nu_l.$$

The invariant amplitudes for these processes can be represented as (see, for example, [39])

$$W = \frac{G_{\mathrm{F}}}{\sqrt{2}}\left\langle \mathbf{p}_c\middle|J^\mu\middle|\mathbf{p}'_{c'}\right\rangle\left\langle l^-\nu_l\middle|j_l^\mu\middle|0\right\rangle, \tag{14}$$

where $\langle l^-\nu_l|j_l^\mu|0\rangle$ and $\langle \mathbf{p}_c|J^\mu|\mathbf{p}'_{c'}\rangle$ are, respectively, leptonic and hadronic components of the amplitudes; $\mathbf{p}'_{c'}$ and $\mathbf{p}_c$ are the momenta of the initial and final mesons; and G_{F} is the Fermi constant of weak interaction.

For the matrix element of the transition current in terms of the form factors, the conditions of relativistic covariance yield the conventional expression

$$\left\langle \mathbf{p}_c\middle|J^\mu\middle|\mathbf{p}'_{c'}\right\rangle = P_-^\mu F_-(t) + P_+^\mu F_+(t), \tag{15}$$

where $P_-^\mu = (p_c - p'_{c'})^\mu$, $P_+^\mu = (p_c + p'_{c'})^\mu$, and $t = (p_c - p'_{c'})^2$.

Let us expand the matrix element (15) in the basis given by (3). Since the relations $J = l = S = 0$ hold for pseudoscalar mesons, we will henceforth suppress the corresponding symbols in the basis vectors. Taking into account (8), we obtain

$$\begin{aligned} &\int N_{\mathrm{C}}N'_{\mathrm{C}}\frac{d\sqrt{s}}{N_{\mathrm{CG}}}\frac{d\sqrt{s'}}{N'_{\mathrm{CG}}}\varphi_c(k(s)) \\ &\times\left\langle \mathbf{p}_c, \sqrt{s}\middle|J^\mu\middle|\mathbf{p}'_{c'}, \sqrt{s'}\right\rangle\varphi_{c'}(k(s')) \\ &= P_-^\mu F_-(t) + P_+^\mu F_+(t), \end{aligned} \tag{16}$$

where $\varphi_{c'}$ and φ_c are the wave functions of, respectively, the initial and the final meson.

In the integrand on the left-hand side of (16), we will now consider the matrix element of the weak-current operator. The current operator describes a weak transition of the system consisting of two interacting quarks and depends on interaction. Under the Poincaré group, it transforms according to the representation determined by the set of operators in (1). Recall that, in the instant form of dynamics, the generators of Lorentz transformations depend on interaction [33]. In view of this, the conditions of Lorentz covariance impose severe constraints on the current operator. In particular, the condition of Lorentz covariance is violated by the representation of the current operator as the sum of single-particle (quark) currents; that is, the popular impulse approximation [31] employing the current in the form

$$J^\mu \simeq j_1^\mu \otimes I_2 + j_2^\mu \otimes I_1 = J^{(0)\mu}, \tag{17}$$

where $j_{1,2}^\mu$ are single-particle operators and $I_{1,2}$ are identical operators acting in the corresponding single-particle spaces, is incompatible with Lorentz covariance. As a matter of fact, the current-operator representation in the form (17) amounts to replacing the current operator of the system of two interacting particles by that for two free particles, the latter being denoted in (17) by $J^{(0)\mu}$.

The noncovariance of the approximation specified by (17) is clarified by the following argument. The operators J^μ and $J^{(0)\mu}$ transform according to different representations of the Poincaré group [those that are determined by the operators in (1) and (7), respec-

tively]. Since the Lorentz transformation operator in the instant form of relativistic Hamiltonian dynamics depends on the interaction operator, which mixes the variables of the first and second particles, we can state that, upon the application of the Lorenz transformation in representation (1) to (17), two-particle currents must appear in the new reference frame, in addition to single-particle currents.

The problem of rendering the conditions of covariance of the current matrix elements consistent with approximations of the type (17), an important problem in relativistic Hamiltonian dynamics indeed, is discussed in many studies (for an overview, see [34]; for a more recent discussion, see, for example, the study of Lev [31]). It should be noted that other relativistic formulations of the constituent-quark model run into a similar problem [40].

In the present study, we follow the procedure adopted in [12, 17, 18, 22]; that is, we begin by determining, on that basis of the Lorentz covariance conditions, the most general form of the current-operator matrix element in (16) and then formulate the impulse approximation in terms of form factors that parametrize the current matrix element.

In order to establish the most general form of the above matrix element, we generalize the method for parametrizing the matrix elements of local operators that was developed in [41].

For the current-operator matrix element on the left-hand side of (16), we will use a representation similar to that for the current matrix element in (15). The difference of the current matrix elements in (15) and in (16) consists in that the basis of representation (1) and the basis of representation (7) are used in (15) and (16), respectively. It is worth noting that, in (15), both the basis vectors and the operator itself transform according to the same representation of the Poincaré group. It is this feature that makes it possible to construct the covariant part of representation (15)—that is, the 4-vectors on the right-hand side of (15)—from variables entering into the vectors. On the contrary, the operator and vectors in (16) transform according to different representations of the Poincaré group [those that are specified by (1) and (7), respectively]; therefore, the covariant part of the matrix element cannot be constructed here from variables entering into the vectors.

The current-operator matrix element on the left-hand side of (16) will be sought in a form that is dictated by the covariant properties of the current operator as a 4-vector. Specifically, we set

$$\frac{N_C}{N_{CG}}\frac{N'_C}{N'_{CG}}\left\langle \mathbf{p}_c, \sqrt{s}\left|J^\mu\right|\mathbf{p}'_{c'}, \sqrt{s'}\right\rangle \tag{18}$$

$$= a^\mu(s, t, s')G_1(s, t, s') + b^\mu(s, t, s')G_2(s, t, s'),$$

where $a^\mu(s, t, s')$ and $b^\mu(s, t, s')$ are some 4-vectors whose explicit form will be indicated later, while $G_1(s, t, s')$ and $G_2(s, t, s')$ are invariant functions (form factors). A feature that distinguishes the parametrization in (18) from the parametrization in (15) is that, in the former, both the form factors and the 4-vectors depend on additional variables, the invariant masses of the initial and of the final state.

With the aid of (18), we further recast equation (16) into the form

$$\int d\sqrt{s}d\sqrt{s'}\varphi_c(k(s))[a^\mu(s, t, s')G_1(s, t, s') + b^\mu(s, t, s')G_2(s, t, s')]\varphi_{c'}(k(s')) \tag{19}$$

$$= P_-^\mu F_-(t) + P_+^\mu F_+(t).$$

The explicit expressions for the vectors a_μ and b_μ in (19) can be found in the following way. Relation (19) represents an equality of two 4-vectors that is bound to hold for any wave function of internal motion. It should be emphasized that, in varying the wave function of internal motion—that is, in going over from one model of quark interaction in a meson to another—the vectors P_-^μ and P_+^μ remain unchanged, because they are expressed in terms of the meson 4-momentum [see equation (15)], which is independent of the internal motion of the constituent quarks. Only the form factors $F_-(t)$ and $F_+(t)$ change under the above variations. Thus, we conclude that, for any wave function describing the internal motion of the quarks, the 4-vector on the right-hand side of equation (19) appears to be a linear combination of the 4-vectors P_-^μ and P_+^μ; that is, it lies in the hyperplane spanned by these two vectors.

At the same time, the dependence of the 4-vectors a_μ and b_μ on the variables of integration implies that, in the case of an arbitrary choice of the wave function, the 4-vector on the left-hand side of (19) is generally arbitrary as well; that is, it is not bound to lie in the hyperplane spanned by the 4-vectors P_-^μ and P_+^μ.

Thus, we conclude that, for the equality in (19) to hold for any wave function of internal motion, it is sufficient that the 4-vectors a_μ and b_μ be constant (independent of the integration variables s and s') and be linear combinations of the 4-vectors P_-^μ and P_+^μ. Taking into account this and the fact that the 4-vectors P_-^μ and P_+^μ are linearly independent, we obtain two scalar equalities that can be represented as

$$F_\pm(t) = \int d\sqrt{s}d\sqrt{s'}\varphi_c(k(s))G_\pm(s, t, s')\varphi_{c'}(k(s')). \tag{20}$$

The form factors $G_+(s, t, s')$ and $G_-(s, t, s')$ are linear combinations of the form factors $G_1(s, t, s')$ and $G_2(s, t, s')$ from (18).

The equality in (20) was obtained from the requirement of gauge covariance; it expresses the form factors for semileptonic decays of pseudoscalar mesons in

terms of the wave functions (8) in relativistic Hamiltonian dynamics and the form factors $G_{\pm}(s, t, s')$ parametrizing the weak-current-operator matrix elements in the basis given by (3).

Let us now formulate the impulse approximation according to (17), but now in terms of the form factors $G_{\pm}(s, t, s')$. As was indicated above, the representation (17) of the weak-current operator implies physically that the current operator that describes a weak transition of the system featuring two interacting quarks is replaced by the so-called free-current operator that describes a transition in the system of two noninteracting quarks. In our formulation, this approximation means that, in expression (20), the form factors $G_{\pm}(s, t, s')$, which parametrize the current-operator matrix element in the case where the interaction, is present are replaced by form factors that parametrize the matrix element of the free-current operator $J^{(0)\mu}$ in basis (3). In the following, the latter will be referred to as free two-particle form factors. The next section will be devoted to calculating these quantities by the methods of relativistic kinematics.

Let us now discuss the problem of unambiguity in calculating the form factors for composite systems within our approach to relativistic Hamiltonian dynamics. Since sectors featuring a fixed numbers of particles are considered in relativistic Hamiltonian dynamics, different options for current matrix elements or different options for reference frames can lead to different solutions for the sought form factors [42, 43, 23]. In this connection, it was proposed in [43] to introduce explicitly the dependence of current matrix elements on some spacelike 4-vector λ_μ determining the surface on which initial conditions are specified for the vectors of states of the composite system in question. The form factor for this vector describes nonphysical contributions to the matrix element that arise because of the use of only those sectors that feature a fixed number of particles. This form factor is referred to as a nonphysical one [23].

It should be noted that expression (15), which was used previously for the weak current, is derived from the conditions of relativistic covariance exclusively and is independent of λ_μ—that is, it has nothing to do with any model concepts of the internal structure of mesons.

The criterion proposed in (43) for choosing a solution for form factors in relativistic Hamiltonian dynamics prescribes that matrix elements that are independent of the nonphysical form factor be taken for calculating form factors. For semileptonic meson decays, this procedure was implemented in [23].

The λ_μ dependence of the matrix element (15) of the meson current according to [43] can be considered within our formalism as well. In this case, the right-hand side of (19) will involve, as an additional term, the vector λ_μ multiplied by the nonphysical form factor. At the same time, all form factors will generally depend on some additional scalar composed of the 4-vectors λ_μ, P_-^μ, and P_+^μ. Thus, we can see that, upon a variation of the wave function in a way similar to that used to derive equation (20), we obtain the right-hand side in the form of a vector that appears to be a linear combination of the independent 4-vectors λ_μ, P_-^μ, and P_+^μ. If we additionally require fulfillment of the equality in (19) for any wave functions describing the internal motion of the quarks in a meson, the vectors on the left-hand side will prove to be constant (independent of the variables of integration) and have the form of linear combinations of the same three 4-vectors. In view of the independence of these 4-vectors, integral representations similar to (20) are obtained for all form factors. It follows that the result will not then depend on the choice of the 4-vector λ_μ.

We further emphasize that, for physical form factors, it is convenient to use the relativistic impulse approximation that is formulated in terms of the form factors $G_{\pm}(s, t, s')$ and which was discussed above. In this approximation, the dependence of physical form factors on the additional scalar drops out, since the free two-particle form factors do not feature this scalar.

4. FREE FORM FACTORS FOR SEMILEPTONIC DECAYS OF PSEUDOSCALAR MESONS

In the conventional impulse approximation, the current operator for the system of two interacting particles is replaced, according to (17), by the current operator for the corresponding system of free particles. Bearing this in mind, we will consider the system of two free quarks. For this system, the matrix element of the weak transition current can be written in the basis (2) of the individual quark momenta and spins. In the impulse approximation, this matrix element has the form

$$\begin{aligned}&\left\langle \mathbf{p}_1', m_1'; \mathbf{p}_2', m_2' \middle| J^{(0)\mu} \middle| \mathbf{p}_1, m_1; \mathbf{p}_2, m_2 \right\rangle \\ &= \left\langle \mathbf{p}_1', m_1' | \mathbf{p}_1, m_1 \right\rangle \left\langle \mathbf{p}_2', m_2' \middle| j_2^\mu \middle| \mathbf{p}_2, m_2 \right\rangle,\end{aligned} \tag{21}$$

where it has been considered that only one quark of the system undergoes a weak transition (see Fig. 1). In (21), the right-hand side, which involves a single-particle current, can be expressed in terms of single-particle

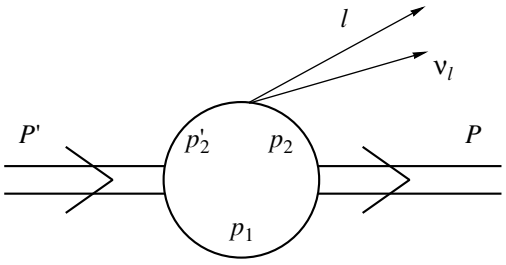

Fig. 1. Diagram for the semileptonic decay of a pseudoscalar meson.

form factors for the quarks. In the standard Dirac parametrization, the relevant expression has the form

$$\langle \mathbf{p}, m|j^{\mu}|\mathbf{p}', m'\rangle = \bar{u}_m(p)[F_1P^{\mu} + F_2q^{\mu} + F_3\gamma^{\mu} + F_4\gamma^5\gamma^{\mu} + F_5\gamma^5q^{\mu} + F_6\gamma^5P^{\mu}]u_{m'}(p'), \quad (22)$$

where $u_{m'}(p')$ and $u_m(p)$ are Dirac bispinors, while $F_i = F_i(t)$ with $t = q^2 = (p - p')^2$ are Dirac form factors. It the following, it is, however, more convenient to use the matrix element of the single-particle current from (21) in a different parametrization, that from [41],

$$\langle \mathbf{p}, m|j^{\mu}|\mathbf{p}', m'\rangle = \sum_{m''}\langle m|D^{1/2}(p', p)|m''\rangle \times\langle m''|f_1P^{\mu} + f_3q^{\mu} + (f_2P^{\mu} + f_4q^{\mu})[p\Gamma(p')] + f_5\Gamma^{\mu}(p') + f_6R^{\mu}|m'\rangle. \quad (23)$$

Here, $\Gamma^{\mu}(p')$ is the quark-spin 4-vector, $R^{\mu} = \epsilon^{\mu\nu\lambda\rho}\times p_{\nu}p'_{\lambda}\Gamma_{\rho}(p')$, and $D^{1/2}_{m'm''}$ is the spin-rotation matrix [41].

The form factors appearing in (22) and (23) can be related easily to one another. Here, we present only those relations that we will need in the following. We have

$$f_1(t) = \frac{[(M_3 + M_2)^2 - t]F_1(t) + (M_3 + M_2)F_3(t)}{\sqrt{(M_3 + M_2)^2 - t}},$$

$$f_3(t) = \frac{[(M_3 + M_2)^2 - t]F_2(t) - (M_2 - M_3)F_3(t)}{\sqrt{(M_3 + M_2)^2 - t}}, \quad (24)$$

$$f_6(t) = -\frac{4M_2F_3(t)}{M_3^2\sqrt{(M_3 + M_2)^2 - t}}.$$

Let us now express the matrix element of the current of the system of two free particles in terms of free two-particle form factors. It is the objective of this section to calculate these form factors. The corresponding transition current can be written in the basis given by (3). For the matrix element of the current in this basis, we can make use of the general parametrization procedure from [41]. As a result, we obtain

$$\langle \mathbf{P}, \sqrt{s}|J^{(0)\mu}|\mathbf{P}', \sqrt{s'}\rangle = Q^{\mu}G^{(0)}_{-}(s, t, s') + \tilde{P}^{\mu}G^{(0)}_{+}(s, t, s'), \quad (25)$$

where $Q^{\mu} = (P - P')^{\mu}$, $\tilde{P}^{\mu} = (P + P')^{\mu}$, and $G^{(0)}_{\pm}(s, t, s')$ are free two-particle form factors for semileptonic decays. For these form factors, we will obtain explicit expressions, which will be further substituted for $G_{\pm}(s, t, s')$ into the representation (20) of the form factors for semileptonic decays.

The representation in (25) is similar to that in (15), differing from it only in that the invariant functions in (25) depend on additional invariant variables s and s'.

The matrix elements in the bases given by (2) and (3) are related via the Clebsch–Gordan expansion as [17, 36]

$$\langle \mathbf{P}, \sqrt{s}|J^{(0)\mu}|\mathbf{P}', \sqrt{s'}\rangle = \int\frac{d\mathbf{p}_1}{2p_{10}}\frac{d\mathbf{p}_2}{2p_{20}}\frac{d\mathbf{p}'_1}{2p'_{10}}\frac{d\mathbf{p}'_2}{2p'_{20}}\langle \mathbf{P}, \sqrt{s}|\mathbf{p}_1, m_1; \mathbf{p}_2, m_2\rangle \times\langle \mathbf{p}_1, m_1; \mathbf{p}_2, m_2|J^{(0)\mu}|\mathbf{p}'_1, m'_1; \mathbf{p}'_2, m'_2\rangle \times\langle \mathbf{p}'_1, m'_1; \mathbf{p}'_2, m'_2|\mathbf{P}', \sqrt{s'}\rangle, \quad (26)$$

where $\langle \mathbf{p}_1, m_1; \mathbf{p}_2, m_2|\mathbf{P}, \sqrt{s}\rangle$ stands for the Clebsch–Gordan coefficients of the Poincaré group, which are given by (5).

Substituting (5), (21), (23), and (25) into (26) and performing integration in the resulting expression in the reference frame where $P' = (P'_0, 0, 0, 0)$ and $P = (P_0, 0, 0, P)$, we find that the free two-particle form factors $G^{(0)}_{\pm}(s, t, s')$ can be represented as

$$\begin{aligned}
G^{(0)}_{+}(s, t, s') &= g(s, t, s')\{[-f_3(t)\lambda(s, t, s')(s - s' - t) \\
&\quad - 2f_1(t)s'[t(s + s' - t) - \eta_1(s - s' - t) \\
&\quad + \eta_2(s - s' + t)]]\cos\alpha + f_6(t)M_2\xi(s, t, s')s't\sin\alpha\}, \\
G^{(0)}_{-}(s, t, s') &= g(s, t, s')\{[f_1(t)[(s + s' - t)^2(s - s') \\
&\quad + 2s'\eta_1(s + 3s' - t) - 2s'\eta_2(3s + s' - t)] \\
&\quad - f_3(t)\lambda(s, t, s')(s + s' - t)]\cos\alpha \\
&\quad - f_6(t)M_2\xi(s, t, s')s'(s - s')\sin\alpha\},
\end{aligned} \quad (27)$$

$$g(s, t, s') = \frac{\sqrt{s}(s + s' - t)\Theta(s, t, s')}{4\sqrt{s'}[\lambda(s, t, s')]^{3/2}\sqrt{\lambda(s', M_1^2, M_2^2)\lambda(s, M_1^2, M_3^2)}},$$

$$\eta_1 = M_3^2 - M_1^2, \quad \eta_2 = M_2^2 - M_1^2, \quad \eta_3 = M_2^2 - M_3^2,$$

$$\Theta(s, t, s') = \theta(s - s_1) - \theta(s - s_2),$$

$$\lambda(a, b, c) = a^2 + b^2 + c^2 - 2(ab + bc + ac),$$

$$\xi(s, t, s') = \{-M_1^2\lambda(s, t, s') - ss't - s\eta_2(s - s' - t) - s\eta_2^2 - s'\eta_1^2 + s'\eta_1(s - s' + t) + \eta_1\eta_2(s + s' - t)\}^{1/2},$$

where θ is a Heaviside step function; M_i, $i = 1, 2, 3$, are the quark masses in the process displayed in Fig. 1 ($p_1^2 = M_1^2$ and $p_2^2 = M_3^2$); s_1 and s_2 are variables that determine the kinematically admissible range of s and s' and which are given by

$$s_{1,2} = s' + t - \frac{1}{2M_2^2}(s' + \eta_2)(t + \eta_3) \mp \frac{1}{2M_2^2}\sqrt{\lambda(s', M_1^2, M_2^2)\lambda(t, M_3^2, M_2^2)};$$

and $\alpha = \omega_1 + \omega_2 + \omega_3$, ω_i being the spin-rotation parameters from the Clebsch–Gordan expansion relating the bases in (2) and (3) according to (4) and (5) [see also the parametrization in (23)]. Explicitly, these parameters are given by

$$\tan\omega_1 = \frac{\xi(s, t, s')}{M_3(s + s' - t + 2\sqrt{ss'}) + \sqrt{ss'}(\sqrt{s} + \sqrt{s'}) - \eta_2\sqrt{s} - \eta_1\sqrt{s'}},$$

$$\tan\omega_2 = \frac{\xi(s, t, s')}{M_3(s + s' - t + 2\sqrt{ss'}) + \sqrt{s}(s - t + \sqrt{ss'}) + \eta_2\sqrt{s} + \eta_1\sqrt{s'}},$$

$$\tan\omega_3 = \frac{\xi(s, t, s')}{M_3 s' + M_2(s - t) + \sqrt{s'}[(M_3 + M_2)^2 - t] + \eta_2(M_2 + M_3)}.$$

In the impulse approximation formulated in terms of the form factors, we replace the form factors $G_\pm(s, t, s')$ by free two-particle form factors (27). Within this framework, the form factors for semileptonic decays can eventually be written as

$$F_\pm(t) = \int d\sqrt{s}\, d\sqrt{s'}\, \varphi_c(k(s)) G_\pm^{(0)}(s, t, s') \varphi_{c'}(k(s')). \quad (28)$$

As to meson electromagnetic form factors and meson decay constants for leptonic transitions, the expressions for these quantities in the impulse approximation are obtained in quite a similar way (see [18] and [22], respectively). It is interesting to note that, in the latter case, the method used here to construct matrix elements leads to the same expressions for the constants of leptonic meson decays as those that are obtained within light-front dynamics.

5. RESULTS OF THE CALCULATIONS

Expressions (20) and (28), which we obtained for the form factors in question, can be used to calculate semileptonic decays of any pseudoscalar mesons. By way of illustration, we will consider the semileptonic decay $K^- \longrightarrow \pi^0 + \mu^- + \bar{\nu}_\mu$. For this decay, the form factors $F_\pm(t)$ (15) were computed by formula (28). For the free two-particle form factors $G_\pm^{(0)}$, we used expressions (27) with $M_1 = M_3$ and M_2 set to the u-quark mass m_u and s-quark mass m_s, respectively. In our calculations, we relied on the approximation of pointlike quarks. In this approximation, the quark form factors in (22) and (24) take the values of

$$F_1(t) = F_2(t) = 0, \quad F_3(t) = 1. \quad (29)$$

The calculations were performed with the wave functions (11), (12), and (13). The quark masses $m_u = m_d$ and m_s, along with the wave-function parameters b [in (11) and (12)] and a [in (13)], are quantities to be fixed. The constituent-quark masses were set to the values of $m_u = m_d = 0.25$ GeV and $m_s = 0.35$, which are used most often in relativistic calculations. The wave-function parameters were determined by fitting the root-mean-square radii of the pion and the kaon, whose electromagnetic properties were computed in [18]. The values obtained in this way for the parameters of the wave functions (11)–(13) are quoted in the table. In the calculations on the basis of the model specified by equation (13), the parameter b was fixed at 0.7867, which corresponds to the value of $\alpha_s = 0.59$ at a scale of light meson masses. Thus, our calculation of the semileptonic decay of the kaon involves no free parameters. In order to perform a comparison with the results produced by other approaches and with experimental data, we have computed the quantities $F_+(0)$, λ_+, and λ_0, which appear in the expansions of the form factors for semileptonic decays at low momentum transfers:

$$F_+(t) = F_+(0)\left\{1 + \frac{\lambda_+}{m_\pi^2}t + \ldots\right\},$$

$$F_0(t) = F_0(0)\left\{1 + \frac{\lambda_0}{m_\pi^2}t + \ldots\right\}, \quad (30)$$

$$F_0(t) = F_+(t) - \frac{t}{M_K^2 - m_\pi^2}F_-(t).$$

In accordance with [1], the pion and kaon masses were chosen to be $m_\pi = 139.5679 \pm 0.0007$ MeV and $M_K = 493.646 \pm 0.009$ MeV.

As can be seen from the table, the calculation with each of the wave functions reproduces rather closely the experimental values of λ_+ ($\lambda_+ = 0.033 \pm 0.008$ [1], $\lambda_+ = 0.029 \pm 0.024$ [45]). The value of $\lambda_0 = 0.004 \pm 0.007$, which is presented in [1], was deduced by averaging the results of several experiments. In this connec-

Values of $F_+(0)$, λ_+, and λ_0, which determine the slopes of the form factors (30) at low momentum transfers

Model	*b*, *a*		$F_+(0)$	λ_+	λ_0
	Pion	Kaon			
(11)	0.207	0.225	0.93	0.028	0.082
(12) at $n = 2$	0.274	0.339	0.94	0.026	0.073
(12) at $n = 3$	0.388	0.480	0.93	0.026	0.074
(13)	0.0183	0.0318	0.93	0.031	0.075
Experiment				0.033 ± 0.008 [1]	0.004 ± 0.007 [1]
				0.029 ± 0.024 [45]	0.062 ± 0.024 [45]

Note: The wave-function parameters were obtained by fitting the root-mean-square radii of the pion and the kaon from the electromagnetic calculations presented in [18]. The quark masses were set to $m_u = m_d = 0.25$ GeV and $m_s = 0.35$ GeV. In the model specified by equation (13), we used the value of $b = 0.7867$. The parameter b in the wave functions (11) and (12) and the parameter a in the wave function (13) are measured in GeV and GeV^2 units, respectively.

tion, it was indicated in [45] that it is not quite clear whether this averaging of λ_0 is correct, because different experiments yield markedly different results. In particular, a new value of λ_0 ($\lambda_0 = 0.062 \pm 0.024$) was obtained experimentally in [45]. We emphasize that our calculations of λ_0 result in good agreement with the experimental value from [45], irrespectively of which function of the three listed above was used in these calculations. Thus, we have reproduced available experimental data on weak kaon decay. Many studies (see, for example, [10]) devoted to calculating semileptonic decays quote the $F_+(0)$ value appearing in (30). The $F_+(0)$ values calculated in the present study (see table) are very close to those obtained within light-front dynamics [10].

The results that we obtained here comply well with the electromagnetic features of the pion and of the kaon [18]. The parameter values quoted in the table provide a good description of the electromagnetic form factors for the pion and the kaon at all values of momentum transfers.

That our results depend only slightly on the choice of model at low momentum transfers is worthy of special note.

In order to assess the model dependence of our calculations, we computed the form factors $F_\pm(t)$ at high momentum transfers. The results are displayed in Figs. 2 and 3. It can be seen that the model dependence in question becomes pronounced at high momentum transfers. This circumstance is also in accord with the results pre-

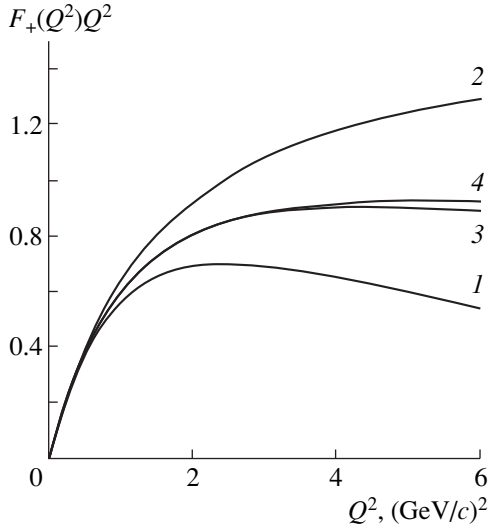

Fig. 2. Values calculated for $F_+(Q^2)Q^2$, $Q^2 = -t$, versus Q^2 by using the (*1*) wave function (11), (*2*) wave function (12) with $n = 2$, (*3*) wave function (12) with $n = 3$, and (*4*) wave function (13) with $b = 0.7867$. The quark masses were set to the values of $m_u = m_d = 0.25$ GeV and $m_s = 0.35$ GeV. The wave-function parameters are quoted in the table.

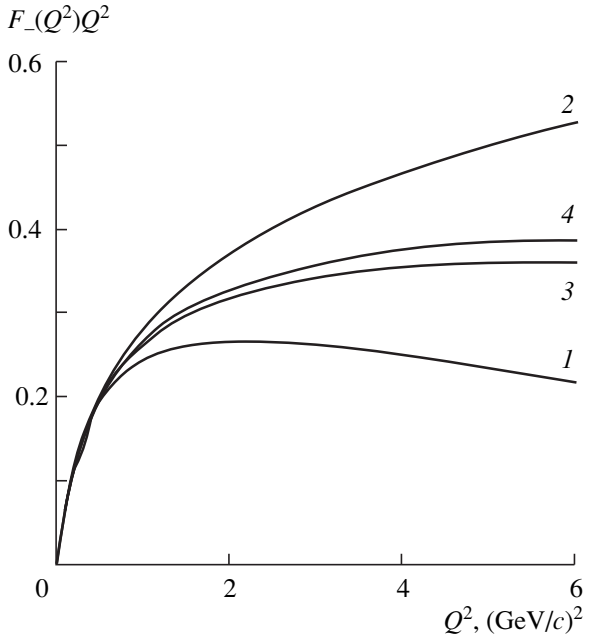

Fig. 3. As in Fig. 2, but for $F_-(Q^2)Q^2$.

sented in [18], where the electromagnetic properties of the pion and the kaon were calculated and where a significant model dependence of electromagnetic form factors was obtained at large t.

In summary, an approach to describing semileptonic decays of pseudoscalar mesons has been developed within the instant form of relativistic Hamiltonian dynamics. The advantages of the formalism have been demonstrated by considering semileptonic kaon decay, where we arrived at good agreement with experimental data. The results of our calculations for semileptonic kaon decay are consistent with the results of the calculations performed in [18] for the electromagnetic properties of the pion and the kaon. In particular, the parameter values obtained by fitting the root-mean-square radii of the pion and the kaon ensure accurate results for the semileptonic decay under study as well.

ACKNOWLEDGMENTS

We are grateful to N.P. Yudin for numerous stimulating discussions.

This work was supported by the Russian Foundation for Basic Research (project no. 96-02-17288).

REFERENCES

1. Particle Data Group, Phys. Rev. **45**, No. 11, Part II (1992).
2. CEBAF Program Advisory Committee, Report (June 14–18, 1993).
3. M. V. Terentjev, Yad. Fiz. **24**, 207 (1976) [Sov. J. Nucl. Phys. **24**, 106 (1976)]; V. B. Berestetskiĭ and M. V. Terentjev, Yad. Fiz. **24**, 1044 (1976) [Sov. J. Nucl. Phys. **24**, 547 (1976)]; **25**, 653 (1977) [**25**, 347 (1977)].
4. I. G. Aznauryan and K. A. Oganessyan, Yad. Fiz. **47**, 1731 (1988) [Sov. J. Nucl. Phys. **47**, 1097 (1988)].
5. P. L. Chung, F. Coester, and W. N. Polyzou, Phys. Lett. B **205**, 545 (1988).
6. I. G. Aznauryan, S. V. Esajbegyan, K. A. Oganessyan, *et al.*, Preprint No. YERPHI-1185(62)-89 (Yerevan Physics Institute, 1989).
7. N. Isgur and M. Wise, Phys. Lett. B **232**, 113 (1989); **237**, 527 (1990).
8. O. C. Jakob and L. S. Kisslinger, Phys. Lett. B **243**, 323 (1990).
9. H. Ito, W. W. Buck, and F. Gross, Phys. Lett. B **248**, 323 (1990).
10. W. Jaus, Phys. Rev. D **44**, 2851 (1991).
11. V. O. Galkin, A. Yu. Mishurov, and R. N. Faustov, Yad. Fiz. **55**, 2175 (1992) [Sov. J. Nucl. Phys. **55**, 1207 (1992)].
12. A. F. Krutov and V. E. Troitsky, J. Phys. G **19**, L127 (1993).
13. F. Cardarelli, I. L. Grach, I. M. Narodetskii, *et al.*, Phys. Lett. B **332**, 1 (1994).
14. R. N. Faustov and V. O. Galkin, Z. Phys. C **66**, 119 (1995).
15. D. Melikhov, Phys. Rev. D **53**, 2460 (1996).
16. B. D. Keister, Phys. Rev. D **49**, 1500 (1994).
17. E. V. Balandina, A. F. Krutov, and V. E. Troitsky, Teor. Mat. Fiz. **103**, 41 (1995).
18. E. V. Balandina, A. F. Krutov, and V. E. Troitsky, J. Phys. G **22**, 1585 (1996).
19. S. Simula, Phys. Lett. B **373**, 193 (1996).
20. B. D. Keister, hep-ph/9703310.
21. N. B. Demchuk, P. Yu. Kulikov, I. M. Narodetskiĭ, *et al.*, Yad. Fiz. **60**, 1429 (1997) [Phys. At. Nucl. **60**, 1292 (1997)].
22. A. F. Krutov, Yad. Fiz. **60**, 1442 (1997) [Phys. At. Nucl. **60**, 1305 (1997)].
23. L. A. Kondratyuk and D. V. Tchekin, Yad. Fiz. **61**, 337 (1998) [Phys. At. Nucl. **61**, 285 (1998)].
24. Hai-Yang Cheng, Chi-Yee Cheung, and Chien-Wen Hwang, Phys. Rev. D **55**, 1559 (1997).
25. B. L. Ioffe and A. V. Smilga, Nucl. Phys. B **216**, 373 (1983).
26. F. Gross, *Relativistic Quantum Mechanics and Field Theory* (Wiley, New York, 1993).
27. A. A. Logunov and A. N. Tavkhelidze, Nuovo Cimento **29**, 380 (1963).
28. R. Blankenbecler and R. Sugar, Phys. Rev. **142**, 1051 (1966).
29. Yu. V. Novozhilov, *Introduction to Elementary Particle Theory* (Nauka, Moscow, 1972; Pergamon, Oxford, 1975).
30. S. J. Brodsky and F. Schlumpf, Preprint No. SLAC-PUB-6431 (Stanford, 1994).
31. F. M. Lev, Ann. Phys. (N.Y.) **237**, 355 (1995).
32. L. A. Kondratyuk, F. M. Lev, and V. G. Soloviev, Few-Body Syst. **7**, 55 (1989).
33. W. N. Polyzou, Ann. Phys. (N.Y.) **193**, 367 (1989).
34. B. D. Keister and W. N. Polyzou, Adv. Nucl. Phys. **20**, 225 (1991).
35. F.M. Lev, Riv. Nuovo Cimento **16**, 1 (1993).
36. V. P. Kozhevnikov, V. E. Troitsky, S. B. Trubnikov, *et al.*, Teor. Mat. Fiz. **10**, 47 (1972).
37. L. L. Frankfurt, I. L. Grach, L. A. Kondratyuk, *et al.*, Phys. Rev. Lett. **62**, 387 (1989).
38. H. Tezuka, J. Phys. A **24**, 5267 (1991).
39. L. B. Okun, *Leptons and Quarks*, 2nd ed. (Nauka, Moscow, 1982; North-Holland, Amsterdam, 1984).
40. F. Coester and D. O. Riska, Ann. Phys. (N.Y.) **234**, 141 (1994); J. W. van Orden, N. Devine, and F. Gross, Phys. Rev. Lett. **75**, 4369 (1995).
41. A. A. Cheshkov and Yu. M. Shirokov, Zh. Éksp. Teor. Fiz. **44**, 1982 (1963) [Sov. Phys. JETP **17**, 1333 (1963)].
42. I. L. Grach and L. A. Kondratyuk, Yad. Fiz. **39**, 316 (1984) [Sov. J. Nucl. Phys. **39**, 198 (1984)].
43. V. A. Karmanov, Fiz. Élem. Chastits At. Yadra, **19**, 525 (1988) [Sov. J. Part. Nucl. **19**, 228 (1988)]; B. Desplanques, V. A. Karmanov, and J.-F. Mathiot, Nucl. Phys. A **589**, 697 (1995); Phys. Rep. **300**, 215 (1998); V. A. Karmanov and J.-F. Mathiot, Nucl. Phys. A **602**, 388 (1996).
44. E. V. Balandina, Candidate's Dissertation in Mathematical Physics (Moscow, 1996).
45. V. M. Artemov *et al.*, Preprint No. R1-95-330, JINR (1995).

Translated by A. Isaakyan

Physics of Atomic Nuclei, Vol. 63, No. 2, 2000, pp. 254–259. Translated from Yadernaya Fizika, Vol. 63, No. 2, 2000, pp. 312–318.

ELEMENTARY PARTICLES AND FIELDS
Theory

Implications of Collider Experiments for Detecting Cold Dark Matter

V. A. Bednyakov*

Joint Institute for Nuclear Research, Dubna, Moscow oblast, 141980 Russia

Received January 26, 1999; in final form, May 5, 1999

Abstract—By investigating the space of parameters of the minimal supersymmetric extension of the Standard Model, it is shown that an observation of at least one supersymmetric particle in high-energy experiments would increase considerably the importance of highly sensitive low-energy experiments aimed at detecting cold-dark-matter particles assumed to be neutralinos, the lightest supersymmetric particles, which are stable. On the other hand, nonobservation of direct signals from dark matter in such experiments can have a pronounced effect on the strategy of high-energy searches for the light charged Higgs boson. *© 2000 MAIK "Nauka/Interperiodica".*

It was indicated in [1, 2] that, owing to the concept unifying all interactions on the basis of supersymmetry (SUSY), low-energy experiments aimed at detecting cold-dark-matter particles appear to be an important supplement to collider experiments devoted to searches for SUSY particles at ultrahigh energies. It is well known [3] that *R*-parity conservation in supersymmetric models implies the existence of the lightest supersymmetric particle (LSP), which is stable. The neutralino, should it appear to be the LSP, provides a natural (and currently the most popular) solution to the problem of dark matter in the Universe.

Precision low-energy experiments are of importance in their own right and, sometimes—for example, in the case of proton decay—prove to be a unique source of fundamental experimental data. Searches for dark matter may also furnish information that can hardly be extracted from collider experiments.

In this study, we provide a specific example of how additional information from the high-energy domain (for instance, a determination of the mass of at least one SUSY particle) can increase the importance of highly sensitive low-energy experiments aimed at detecting cold-dark-matter particles. At the same time, "zero" signal from dark-matter detectors could, in certain situations, rule out the possibility of discovering light Higgs bosons at modern colliders.

If the masses of some superpartners are determined from high-energy experiments, it will imply that there exists a lower bound on the rate of counting of relic LSPs in direct-detection studies. The level of this bound will presumably be reached by dark-matter detectors in the near future [4–7]. This additional information would at least constrain the range of possible LSP mass values because all sfermions and gauginos must be heavier than the LSP. For this reason, the region of possible values that the parameters of the minimal supersymmetric extension of the Standard Model (MSSM) can take would be restricted. In some cases, this is accompanied by the emergence of a lower bound on the event counting rate in cold-dark-matter detectors. The most spectacular effect is expected for the case where the squark mass and the mass of the charged Higgs boson are known.

The basic issue is that of assessing the extent to which investigation of supersymmetric particles at high energies can affect the strategies and prospects of searches for direct signals from dark matter. These searches are usually conducted by recording recoil nuclei resulting from the elastic scattering of relic nonrelativistic particles of dark matter in a highly sensitive detector.

For this purpose, the MSSM parameter space was explored at an electroweak scale of about 100 GeV. In doing this, no account was taken of theoretical constraints that follow from unification of gauge and Yukawa coupling constants, scalar-particle masses, and so on. On the other hand, the following conditions were imposed in studying the constraints on the MSSM parameter space in the way indicated above. The calculated spectrum of supersymmetric particles must be consistent with nonobservation of such particles in the collider experiments. The relic density of neutralinos must agree with the known age of the Universe, and the probabilities of some rare processes must be compatible with available data. Such a phenomenological approach makes it possible to reveal only the most general regularities, but it is the search of such regularities that forms the subject of the present consideration. Specific realizations of the MSSM (such as supergravity) possess a higher predictive power, involve a smaller number of parameters, and exhibit special forms of interplay of model features at the electroweak scale, but

* e-mail: bedny@nu.jinr.ru

each of these realization is expected to show general regularities as well.

At the electroweak scale, the MSSM parameter space involves the neutralino, chargino, sfermion (squark and slepton), and Higgs boson mass matrices. The explicit expressions for these matrices are given below.

In the notation corresponding to the third generation, the squark and slepton mass matrices are given by [8]

$$M_{\tilde{t}}^2 = \begin{pmatrix} M_{\tilde{Q}}^2 + m_t^2 + m_Z^2\left(\frac{1}{2} - e_u s_W^2\right)\cos 2\beta & m_t(A_t - \mu\cot\beta) \\ m_t(A_t - \mu\cot\beta) & M_{\tilde{U}}^2 + m_t^2 + m_Z^2 e_u s_W^2\cos 2\beta \end{pmatrix},$$

$$M_{\tilde{b}}^2 = \begin{pmatrix} M_{\tilde{Q}}^2 + m_b^2 - m_Z^2\left(\frac{1}{2} + e_d s_W^2\right)\cos 2\beta & m_b(A_b - \mu\tan\beta) \\ m_b(A_b - \mu\tan\beta) & M_{\tilde{D}}^2 + m_b^2 + m_Z^2 e_d s_W^2\cos 2\beta \end{pmatrix},$$

$$M_{\tilde{\nu}}^2 = M_{\tilde{L}}^2 + \frac{1}{2}m_Z^2\cos 2\beta,$$

$$M_{\tilde{\tau}}^2 = \begin{pmatrix} M_{\tilde{L}}^2 + m_\tau^2 - m_Z^2\left(\frac{1}{2} - s_W^2\right)\cos 2\beta & m_\tau(A_\tau - \mu\tan\beta) \\ m_\tau(A_\tau - \mu\tan\beta) & M_{\tilde{E}}^2 + m_\tau^2 - m_Z^2 s_W^2\cos 2\beta \end{pmatrix},$$

where m_Z is the Z-boson mass; $m_{t(b)}$ is the mass of the conventional top (bottom) quark; m_τ is the τ-lepton mass; $e_u = 2/3$; $e_d = -1/3$; $s_W^2 \equiv \sin^2\theta_W$; and $\tan\beta \equiv \langle H_2^0\rangle/\langle H_1^0\rangle$, $\langle H_i^0\rangle$ being nonzero vacuum expectation values of the neutral Higgs fields. The eigenstates of these matrices correspond to sfermions with masses fixed at $m_{\tilde{t}_{1,2}}$, $m_{\tilde{b}_{1,2}}$, and $m_{\tilde{\tau}_{1,2}}$.

The chargino mass matrix, which appears in the interaction Lagrangian, has the form (m_W is the W-boson mass)

$$X = \begin{pmatrix} M_2 & \sqrt{2}m_W\sin\beta \\ \sqrt{2}m_W\cos\beta & \mu \end{pmatrix}.$$

The eigenvalues of this matrix denoted by $\tilde{\chi}_{1,2}^+$ describe the physical states of the charginos with definite masses.

In the interaction basis $\tilde{B}-\tilde{W}^3-\tilde{H}_1^0-\tilde{H}_2^0$, the mass matrix for the neutral Majorana fermions (neutralinos) has the form

$$Y = \begin{pmatrix} M_1 & 0 & -m_Z c_\beta s_W & m_Z s_\beta s_W \\ 0 & M_2 & m_Z c_\beta c_W & -m_Z s_\beta c_W \\ -m_Z c_\beta s_W & m_Z c_\beta c_W & 0 & -\mu \\ m_Z s_\beta s_W & -m_Z s_\beta c_W & -\mu & 0 \end{pmatrix},$$

where $s_\beta = \sin\beta$, $c_\beta = \cos\beta$, etc. The four eigenstates of this matrix describe the four physical states of the neutralino. As was mentioned above, the lightest of these, LSP, is stable.

With allowance for radiative corrections, the mass matrix for the CP-even Higgs bosons is given by [9]

$$H \equiv \begin{pmatrix} H_{11} & H_{12} \\ H_{21} & H_{22} \end{pmatrix} = \frac{1}{2}\begin{pmatrix} \tan\beta & -1 \\ -1 & \cot\beta \end{pmatrix}M_A^2\sin 2\beta$$

$$+ \frac{1}{2}\begin{pmatrix} \cot\beta & -1 \\ -1 & \tan\beta \end{pmatrix}m_Z^2\sin 2\beta + \omega\begin{pmatrix} \Delta_{11} & \Delta_{12} \\ \Delta_{21} & \Delta_{22} \end{pmatrix},$$

where $\omega = \dfrac{3g_2^2}{16\pi^2 m_W^2}$ and

$$\Delta_{11} = \frac{m_b^4}{c_\beta^2}\left(\ln\frac{m_{\tilde{b}_1}^2 m_{\tilde{b}_2}^2}{m_b^4} + \frac{2A_b(A_b - \mu\tan\beta)}{m_{\tilde{b}_1}^2 - m_{\tilde{b}_2}^2}\ln\frac{m_{\tilde{b}_1}^2}{m_{\tilde{b}_2}^2}\right)$$

$$+ \frac{m_b^4}{c_\beta^2}\left(\frac{A_b(A_b - \mu\tan\beta)}{m_{\tilde{b}_1}^2 - m_{\tilde{b}_2}^2}\right)^2 g(m_{\tilde{b}_1}^2, m_{\tilde{b}_2}^2)$$

$$+ \frac{m_t^4}{s_\beta^2}\left(\frac{\mu\left(A_t - \dfrac{\mu}{\tan\beta}\right)}{m_{\tilde{t}_1}^2 - m_{\tilde{t}_2}^2}\right)^2 g(m_{\tilde{t}_1}^2, m_{\tilde{t}_2}^2);$$

$$\Delta_{22} = \frac{m_t^4}{s_\beta^2}\left(\ln\frac{m_{\tilde{t}_1}^2 m_{\tilde{t}_2}^2}{m_t^4} + \frac{2A_t\left(A_t - \frac{\mu}{\tan\beta}\right)}{m_{\tilde{t}_1}^2 - m_{\tilde{t}_2}^2}\ln\frac{m_{\tilde{t}_1}^2}{m_{\tilde{t}_2}^2}\right)$$

$$+ \frac{m_t^4}{s_\beta^2}\left(\frac{A_t\left(A_t - \frac{\mu}{\tan\beta}\right)}{m_{\tilde{t}_1}^2 - m_{\tilde{t}_2}^2}\right)^2 g(m_{\tilde{t}_1}^2, m_{\tilde{t}_2}^2)$$

$$+ \frac{m_b^4}{c_\beta^2}\left(\frac{\mu(A_b - \mu\tan\beta)}{m_{\tilde{b}_1}^2 - m_{\tilde{b}_2}^2}\right)^2 g(m_{\tilde{b}_1}^2, m_{\tilde{b}_2}^2);$$

$$\Delta_{12} = \Delta_{21} = \frac{m_t^4}{s_\beta^2}\frac{\mu\left(A_t - \frac{\mu}{\tan\beta}\right)}{m_{\tilde{t}_1}^2 - m_{\tilde{t}_2}^2}$$

$$\times\left(\ln\frac{m_{\tilde{t}_1}^2}{m_{\tilde{t}_2}^2} + \frac{A_t\left(A_t - \frac{\mu}{\tan\beta}\right)}{m_{\tilde{t}_1}^2 - m_{\tilde{t}_2}^2}g(m_{\tilde{t}_1}^2, m_{\tilde{t}_2}^2)\right)$$

$$+ \frac{m_b^4}{c_\beta^2}\frac{\mu(A_b - \mu\tan\beta)}{m_{\tilde{b}_1}^2 - m_{\tilde{b}_2}^2}$$

$$\times\left(\ln\frac{m_{\tilde{b}_1}^2}{m_{\tilde{b}_2}^2} + \frac{A_b(A_b - \mu\tan\beta)}{m_{\tilde{b}_1}^2 - m_{\tilde{b}_2}^2}g(m_{\tilde{b}_1}^2, m_{\tilde{b}_2}^2)\right).$$

Here, $c_\beta^2 = \cos^2\beta$, $s_\beta^2 = \sin^2\beta$, and $g(m_1^2, m_2^2) = 2 - \frac{m_1^2 + m_2^2}{m_1^2 - m_2^2}\ln\frac{m_1^2}{m_2^2}$. The eigenvalues of the matrix H represent the masses of the *CP*-even Higgs bosons:

$$m_{H,h}^2 = \frac{1}{2}\left\{H_{11} + H_{22}\right.$$

$$\left. \pm\sqrt{(H_{11} + H_{22})^2 - 4(H_{11}H_{22} - H_{12}^2)}\right\}.$$

The mass of the charged Higgs boson is

$$m_{H^\pm}^2 = m_W^2 + m_A^2 + \omega\Delta_{ch},$$

where Δ_{ch} is the contribution of radiative corrections [9].

Thus, the parameters of the gaugino mass matrix, M_1, M_2, $\tan\beta$, and μ; the mass of the *CP*-odd (or axial) Higgs boson, M_A; the parameters of the mass matrices for the first- and second-generation squarks and sleptons, $m_{\tilde{Q}}^2$, $m_{\tilde{U}}^2$, $m_{\tilde{D}}^2$, $m_{\tilde{L}}^2$, and $m_{\tilde{E}}^2$; the parameters of the mass matrix for the third-generation sfermions $m_{\tilde{Q}_3}^2$, $m_{\tilde{T}}^2$, $m_{\tilde{B}}^2$, $m_{\tilde{L}_3}^2$, and $m_{\tilde{\tau}}^2$; and the trilinear coupling constants for the third generation, A_t, A_b, and A_τ, appear to be free parameters of the model. This parameter set makes it possible to calculate the masses of all SUSY particles at the electroweak scale. Here, the parameter values were varied in the ranges

$$-1000 < M_1 < 1000\ \text{GeV},$$
$$-2000 < M_2 < 2000\ \text{GeV},$$
$$1 < \tan\beta < 50,$$
$$-2000 < \mu < 2000\ \text{GeV},$$
$$60 < M_A < 1000\ \text{GeV},$$
$$10 < m_{\tilde{Q}_{1,2}}^2 < 1000000\ \text{GeV}^2,$$
$$10 < m_{\tilde{L}}^2 < 1000000\ \text{GeV}^2,$$
$$10 < m_{\tilde{Q}_3}^2 < 1000000\ \text{GeV}^2,$$
$$10 < m_{\tilde{L}_3}^2 < 1000000\ \text{GeV}^2,$$
$$-2000 < A_t < 2000\ \text{GeV}.$$

Without considerable loss of generality, the remaining sfermion mass parameters $m_{\tilde{U}_{1,2}}^2$, $m_{\tilde{D}_{1,2}}^2$, $m_{\tilde{E}_{1,2}}^2$, $m_{\tilde{T}}^2$, $m_{\tilde{B}}^2$, and $m_{\tilde{E}_3}^2$ were set to $m_{\tilde{Q}_{1,2}}^2$, $m_{\tilde{L}}^2$, $m_{\tilde{Q}_3}^2$, and $m_{\tilde{L}_3}^2$, respectively; the trilinear parameters A_b and A_τ were set to zero. The main argument behind the above choice of region for the parameters involved was that their values seemed natural (in the case being considered, this implied that the mass values in SUSY models must not be considerably greater than 1 TeV). In addition, the regions forbidden by available constraints on the masses of the sparticles and of the Higgs bosons should be avoided from the outset.

Procedures for directly detecting of the relic cold-dark-matter particles rely on recording, by a highly sensitive detector, recoil nuclei originating from the scattering of dark-matter particles on detector nuclei. The number of such events per unit time depends on the velocity distribution of relic neutralinos and on their density in the vicinity of the Earth. It also depends on the cross section for the elastic scattering of these particles on the nuclei of a detector material; this cross section in turn depends on a specific realization of a supersymmetric model and on its parameters [1, 3]. In our calculations, we employed standard formulas that can be found, for example, in [10]. Since the present analysis is aimed at an investigation of the most general properties of relevant domains in the parameter space and at searches for those domains where the event counting rate reaches extreme values, it is sufficient to use, for this purpose, the total event counting rate R (an

integral characteristic of the procedure), the quantity defined as an average over the spectrum of recoil nuclei and over some other parameters. For a typical dark-matter detector, we consider here a detector based on ^{73}Ge nuclei.

For our analysis to be realistic, we must consider that, if dark matter in the Universe is dominated by neutralinos, the density of relic neutralinos must satisfy known cosmological constraints associated with the age of the Universe and with the character of its evolution. It is generally believed [11] that the contribution of any particle species χ must obey the condition $\Omega_\chi h_0^2 < 1$, where the relic-density parameter $\Omega_\chi = \rho_\chi/\rho_{cr}$ is the ratio of the relic mass density of neutralinos, ρ_χ, to the critical density $\rho_{cr} = 1.88 \times 10^{-29} h_0^2$ g cm^{-3}, and h_0 is the Hubble constant normalized in a special way. On the other hand, the contribution to the relic density from neutralinos must not be overly small; otherwise, they could not play the role of dark-matter particles. It is reasonable to consider the range $0.025 < \Omega_\chi h_0^2 < 1$ [12]. The quantity $\Omega_\chi h_0^2$ was calculated by the standard approximate formula from [13, 14] with allowance for all possible channels of neutralino annihilation. In the MSSM, the neutralinos appear to be various linear combinations of the gauginos and higgsinos; therefore, there are various annihilation channels—for example, those that feature Z^0-boson or Higgs boson exchange in the s channel, as well as those that feature the t-channel exchange of a scalar particle like a selectron in [15]. By taking all the above into account, the region admissible for model-parameter values can be considerably reduced [13, 16, 17].

The precision measurement of the branching ratio for the decay mode $b \longrightarrow s\gamma$ by the CLEO collaboration [10, 18], $1.0 \times 10^{-4} < \mathrm{Br}(b \longrightarrow s\gamma) < 4.2 \times 10^{-4}$, imposes an additional constraint on the region of admissible model-parameter values. Within the MSSM, this process is governed by quark-flavor-changing neutral currents which receive contributions from the $H^\pm$–t, $\tilde{\chi}^+$–$\tilde{t}$, and $\tilde{g}$–$\tilde{q}$ loop diagrams, as well as from the Standard Model W–t loop diagram.

Lower limits on the masses of supersymmetric particles can be derived from nonobservation of these particles at the CERN and Fermilab high-energy colliders. In our analysis, we assumed that the masses of both charginos, the masses of the neutralinos other than the LSP, the masses of the sneutrino, the masses of the selectrons, the masses of the first- and second-generation squarks, the mass of the lightest top squark, the masses of all neutral Higgs bosons, and the mass of the charged Higgs boson are constrained from below as $m_{\tilde{\chi}^+_{1,2}} \geq 91$ GeV; $m_{\tilde{\chi}^0_{1,2,3}} \geq 52$, 84, 127 GeV; $m_{\tilde{\nu}} \geq 66$ GeV; $m_{\tilde{e}_R} \geq 60$ GeV; $m_{\tilde{q}} \geq 200$ GeV; $m_{\tilde{t}_1} \geq 85$ GeV; $m_{H^0} \geq 62.5$ GeV; and $m_{H^\pm} \geq 62.5$ GeV. These constraints reduce further the region of admissible model-parameter values.

With allowance for all the above accelerator and cosmological constraints, we scanned the parameter space of the model under study. In doing this, we took, at random, a point in the above regions of the parameter space and calculated, at this point, the mass spectrum of the supersymmetric particles (including the LSP mass M), the relic density, and other observables. If all the necessary conditions were satisfied—that is, the point fell within the allowed region—the expected event counting rate R in a germanium detector for a direct detection of LSPs was computed; otherwise, the point in question was discarded. Since this testing procedure was repeated about 10^8 times, it was possible to determine the allowed regions for the expected event counting rate R and the relic-neutralino mass M. It turned out that, in the parameter space, a single point that obeys all the above conditions and constraints corresponds to each allowed point within the closed curves. Within an error controllable in principle (which we do not discuss here), we can state that all these points form a region of R and M values allowed by the entire body of experimental data. These regions, which result from the concerted action of all the above constraints, are shown in Figs. 1 and 2.

In either figure, the shaded region bounded by the thick solid curve was obtained as the result of scanning the parameter space without introducing additional assumptions about the mass values of the supersymmetric particles. It should be emphasized that the event counting rate is bounded from below. With increasing LSP mass, the corresponding bound decreases from about 10^{-4} events per day in 1 kg of germanium at $M \sim 7$ GeV to 10^{-7} events/kg/day at the maximum LSP mass of about 800 GeV.

In Fig. 1, we can see four contours within the shaded domain that bound allowed regions corresponding to different additional restrictions. The dotted curve encloses the allowed region in the R–M plane for the case where the lightest chargino mass lies in the range $100 < m_{\chi^+_1} < 140$ GeV. It can be seen that the constraint $R > 5 \times 10^{-6}$ event/kg/day is a straightforward consequence of the existence of an upper bound on the LSP mass ($M < 140$ GeV). A very similar constraint ($R > 10^{-5}$ events/kg/day) is obtained if the mass of the selectron (sneutrino) is in the range $150 < m_{(\tilde{\nu}),\tilde{e}} < 200$ GeV. This is shown by the solid (dashed) curve. The region bounded by the remaining (solid) curve in Fig. 1 extends from 10^{-3} event/kg/day upward along the axis; this region corresponds to the assumption that the mass of the lightest squark in the first and second generations lies in the range $190 < m_{\tilde{q}} < 230$ GeV. The above increase in the lower bound on R comes as no surprise because the existence of at least one light squark in the

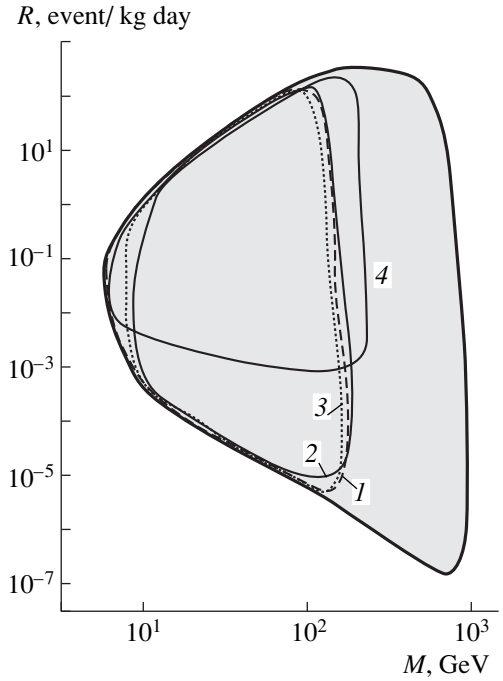

Fig. 1. Regions (within contours) of admissible values of the total event counting rate R (in number of events per day in 1 kg of a ^{73}Ge detector) and the LSP mass M (in GeV). The curves within the shaded region correspond to hypothetical fixed values of the sfermion masses (see main body of the text): (curve *1*) sneutrino mass of $m_{(\tilde{\nu})} = 175$ GeV, (curve *2*) selectron mass of $m_{\tilde{e}} = 175$ GeV, (curve *3*) chargino mass of $m_{\chi_1^+} = 140$ GeV, and (curve *4*) squark mass of $m_{\tilde{q}} = 210$ GeV.

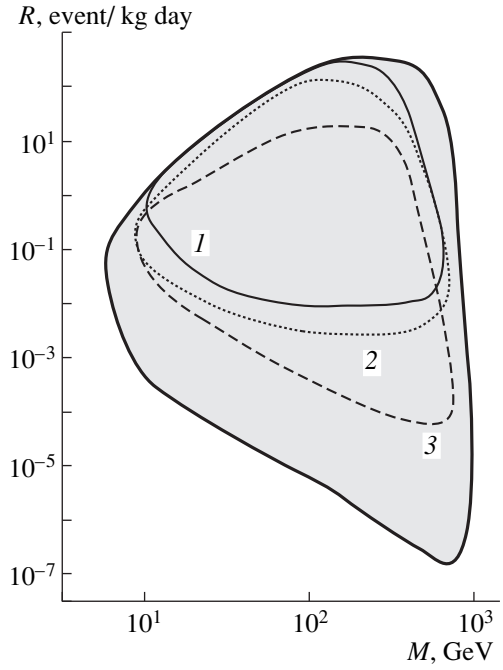

Fig. 2. As in Fig. 1, but for fixed values of the mass $m_{H^\pm}$ of the charged Higgs boson. Curves *1*, *2*, and *3* correspond to $m_{H^\pm} = 150$, 200, and 300 GeV, respectively.

particle spectrum renders scalar interaction mediated by this squark quite sizable. For the top-squark mass in the range $150 < m_{\tilde{t}_1} < 200$ GeV, the lower bound on R decreases slightly.

The curves in Fig. 2 that are associated with the light Higgs bosons are of the greatest physical interest. The three curves in this figure correspond to the masses of the charged Higgs boson in the ranges $290\ \text{GeV} < m_{H^\pm} < 310\ \text{GeV}$ (dashed curve), $190\ \text{GeV} < m_{H^\pm} < 210\ \text{GeV}$ (dotted curve), and $140 < m_{H^\pm} < 160$ GeV (solid curve). In the last case, where it was also assumed that all fermions are sufficiently heavy ($500\ \text{GeV} < m_{\tilde{f}}$), the lower limit on the event counting rate was at a level 10^{-2} event/kg/day for almost all admissible values of the LSP mass. This value of R is thought to become attainable in the near future for dark-matter detectors like HDMS [4] and GENIUS [7]. As the mass of the charged Higgs boson increases from 150 to 200 GeV and further, the lower bound on R decreases to the value of about 10^{-3} event/kg/day and further to about 10^{-4} event/kg/day at $m_{H^\pm} = 300$ GeV. So high a value of the lower bound on R for the case of light charged Higgs bosons is also naturally explained: a small value of $m_{H^\pm}$ implies that the masses of all other neutral Higgs bosons are relatively small. Hence, the strength of the scalar interaction that is mediated by *CP*-even neutral Higgs bosons and which is dominant in the case of ^{73}Ge cannot be less than some definite value.

From Fig. 2, it can seen that, if the mass of the charged Higgs boson is sufficiently small (about 200 GeV), precision dark-matter detectors must record signals from a direct interaction of dark-matter particles in a detector.

This observation seems to provide an additional incentive to searches for the charged Higgs bosons at high-energy accelerators because, should they be discovered (and they must be sufficiently light), the importance of searches for dark-matter particles by means of their direct detection will increase considerably. Thereby, high-energy experiments aimed at searches for light Higgs bosons, together with low-energy experiments devoted to searches for dark matter, become especially important for testing supersymmetric models.

On the other hand, nonobservation of dark matter with highly precise detectors like GENIUS would imply that, if we are going to remain within the MSSM, all Higgs bosons are rather heavy. In this case, charged Higgs bosons can hardly be observed at present-day

accelerators because their energies are not sufficient for this.

In conclusion, it should be emphasized that it will be necessary to revise some current concepts, including those on the abundance of relic neutralinos, on the character of their interaction with matter, and on the principles of detection, if the results of searches for light Higgs bosons at accelerators and the results of direct searches for signals from dark matter in low-energy experiments prove positive and negative, respectively.

The present study highlights the importance of combining the above two types of current experiments in the searches for new physical phenomena.

ACKNOWLEDGMENTS

I am grateful to S. G. Kovalenko and H. F. Klapdor-Kleingrothaus for stimulating discussions.

This work was supported in part by the GNTB grant no. 215 Nucleon from the Ministry of Science and Technology of Russian Federation and by the joint grant no. 96-02-00082 from the Russian Foundation for Basic Research and the German Association for Scientific Research.

REFERENCES

1. M. Drees and M. M. Nojiri, Phys. Rev. D **48**, 3483 (1993).
2. H. F. Klapdor-Kleingrothaus and A. Schtaudt, *Nonaccelerator Elementary-Paricle Physics* (Nauka, Moscow, 1997).
3. G. Jungman, M. Kamionkowski, and K. Griest, Phys. Rep. **267**, 195 (1996).
4. H. F. Klapdor-Kleingrothaus, in *Proceedings of International Workshop "Double Beta Decay and Related Topics"* (World Sci., Singapore, 1996), p. 3; L. Baudis *et al.*, Nucl. Instrum. Methods Phys. Res., Sect. A **385**, 265 (1997).
5. M. Bühler *et al.*, Nucl. Instrum. Methods Phys. Res., Sect. A **370**, 1 (1996); W. Seidel *et al.*, J. Low Temp. Phys. **93**, 797 (1993).
6. N. Coron *et al.*, Nucl. Phys. B (Proc. Suppl.) **35**, 169 (1994).
7. H. F. Klapdor-Kleingrothaus, Yad. Fiz. **61**, 967 (1998) [Phys. At. Nucl. **61**, 875 (1998)]; hep-ex/9802007.
8. H. E. Haber and G. L. Kane, Phys. Rep. **117**, 75 (1985); G. F. Gunion and H. E. Haber, Nucl. Phys. B **272**, 1 (1986).
9. J. Ellis, G. Ridolfi, and F. Zwirner, Phys. Lett. B **257**, 83 (1991); J. L. López and D. Nanopoulos, Phys. Lett. B **266**, 397 (1991).
10. V. A. Bednyakov, H. F. Klapdor-Kleingrothaus, and S. G. Kovalenko, Phys. Rev. D **55**, 503 (1997); V. A. Bednyakov, H. F. Klapdor-Kleingrothaus, S. G. Kovalenko, *et al.*, Z. Phys. A **357**, 339 (1997); V. A. Bednyakov, H. F. Klapdor-Kleingrothaus, and S. G. Kovalenko, Yad. Fiz. **59**, 1777 (1996) [Phys. At. Nucl. **59**, 1718 (1996)].
11. E. W. Kolb and M. S. Turner, *The Early Universe* (Addison-Wesley, Redwood City, 1990).
12. K. Griest and D. Seckel, Phys. Rev. D **43**, 3191 (1991); P. Nath and R. Arnowitt, Phys. Rev. Lett. **70**, 3696 (1993); G. Gelmini and P. Gondolo, Nucl. Phys. B **360**, 145 (1991).
13. M. Drees and M. M. Nojiri, Phys. Rev. D **47**, 376 (1991).
14. J. Ellis *et al.*, Nucl. Phys. B **238**, 453 (1984).
15. J. Steigman, K. A. Olive, D. N. Schramm, *et al.*, Phys. Lett. B **176**, 33 (1986); J. Ellis, K. Enquist, D. Nanopoulos, *et al.*, Phys. Lett. B **176**, 457 (1986).
16. L. Roszhkowski, Phys. Rev. D **50**, 4842 (1994); P. Nath and R. Arnowitt, Phys. Rev. Lett. **70**, 3696 (1993); G. B. Gelmini, P. Gondolo, and E. Roulet, Nucl. Phys. B **351**, 623 (1991).
17. G. L. Kane, G. Kolda, L. Roszkowski, *et al.*, Phys. Rev. D **49**, 6173 (1994); A. Bottino *et al.*, Astropart. Phys. **2**, 77 (1994); P. Gondolo and J. Edsjö, Yad. Fiz. **61**, 1181 (1998) [Phys. At. Nucl. **61**, 1081 (1998)].
18. S. Bertolini, F. Borzumati, A. Masiero, *et al.*, Nucl. Phys. B **353**, 591 (1991); N. Oshimo, Nucl. Phys. B **404**, 20 (1993); R. Barbieri and G. Giudice, Phys. Lett. B **309**, 86 (1993).

Translated by R. Rogalyov

Physics of Atomic Nuclei, Vol. 63, No. 2, 2000, pp. 260–263. From Yadernaya Fizika, Vol. 63, No. 2, 2000, pp. 319–323.

ELEMENTARY PARTICLES AND FIELDS
Theory

Transverse Muon Polarization in the $K^0_{\mu 3}$ Decay Induced by Electromagnetic Final-State Interaction*

V. P. Efrosinin and Yu. G. Kudenko

Institute for Nuclear Research, Russian Academy of Science, ul. Shestidesyatiletiya Oktyabrya 7a, Moscow, 117312 Russia

Received November 5, 1998

Abstract—A calculation of transverse muon polarization in the $K^0_{\mu 3}$ decay due to the electromagnetic interaction in a final state in one-loop approach is presented. Average transverse muon polarization is found to be $(2.4 \pm 0.1) \times 10^{-3}$ in the Dalitz plot region. © *2000 MAIK "Nauka/Interperiodica".*

One of the few observables that offer good prospects for detecting *CP* violation beyond the Standard Model (SM) is the transverse muon polarization (P_T) in the kaon decays $K^0 \longrightarrow \pi^-\mu^+\nu$, $K^+ \longrightarrow \pi^0\mu^+\nu$, and $K^+ \longrightarrow \mu^+\nu\gamma$. In the Standard Model, *CP* violation originates from the complex Kobayashi–Maskawa matrix in the quark sector [1, 2], whereas, in the lepton sector, there is no mixing and therefore no *CP* violation. The transverse muon polarization in these kaon decays vanishes in the SM because only one diagram at the tree level induces these decays and there are no interference effects, i.e., no *CP* violation. A nonzero P_T must arise from new *CP*-violation sources beyond the SM. Nonstandard effects for P_T in the $K_{\mu 3}$ decays were examined in [3, 4]. It was demonstrated that effective scalar and pseudoscalar interactions can induce a nonzero value of P_T at the level of 10^{-3}. While the final-state electromagnetic interactions (FSI) induce small P_T^{em} of the order of 10^{-6} in the decay $K^+ \longrightarrow \pi^0\mu^+\nu$, one needs to distinguish the real *CP*-violation effect from the FSI in the decays $K^0 \longrightarrow \pi^-\mu^+\nu$ and $K^+ \longrightarrow \mu^+\nu\gamma$, where P_T^{em} is predicted to be as large as 10^{-3}. Note that in the decay $K^+ \longrightarrow \pi^0\mu^+\nu$, P_T^{em} is zero in the one-loop approximation.

One way to obtain the *T*-violation polarization in the $K^0_{\mu 3}$ decays is a measurement of the difference between the muon polarization in

$$K^0 \longrightarrow \pi^-\mu^+\nu \qquad (1)$$

and

$$\bar{K}^0 \longrightarrow \pi^+\mu^-\bar{\nu}. \qquad (2)$$

For these two modes, the FSI induce the same P_T^{em} (both signs and absolute values), whereas *CP* violation gives rise to the transverse muon polarization with the same absolute value but opposite signs. However, measurement of the polarization of the μ^- in the decay $\bar{K}^0 \longrightarrow \pi^+\mu^-\bar{\nu}$ is very difficult because of a nuclear capture of stopped μ^- and its depolarization in any material. Therefore, a precise calculation of the P_T^{em} induced by the FSI is needed for extraction of the *T*-odd polarization in $K^0 \longrightarrow \pi^-\mu^+\nu$.

The calculations of P_T^{em} in the $K^0_{\mu 3}$ decay performed in [5, 6] did not include the pion electromagnetic form factor and form factors of the weak vertex. The value of P_T^{em} obtained in [6] depends on the ultraviolet cutoff parameter. These form factors were taken into account [7], and an additional form factor was introduced whose value cannot be extracted from the experiment. The value of P_T^{em} obtained in [7] is different from the polarization of [5] by a factor of minus two. A calculation of P_T^{em} using the covariant procedure which ignored the form factors of the $K^0_{\mu 3}$ decay was performed in [8]. The result of [8] agrees with [7], but differs from P_T^{em} of [5] by the same factor of minus two.

The polarization P_T^{em} in the decays $K_L \longrightarrow \pi^{\mp} l^{\pm} \nu_l$ was obtained in [9] through the usual nonrelativistic procedure of calculation of Coulomb corrections to decay amplitudes using the Fermi–Watson theorem.

Thus, it would be important to perform new calculations of the P_T^{em} using updated form factors of the $K^0_{\mu 3}$ decay. In our calculations, we followed the approach of [7].

* This article was submitted by the authors in English.

The transverse muon polarization $P_T^{\rm em}$ in the $K^0_{\mu 3}$ decay arises from the interference of the Born diagram of Fig. 1*a* and the one-loop diagram of Fig. 1*b*. The polarization $P_T^{\rm em}$ is proportional to the imaginary part of the diagram shown in Fig. 1*b*. The amplitude of the decay $K^0 \longrightarrow \pi^-\mu^+\nu$ can be expressed as

$$M_+ = \frac{G_{\rm F}}{\sqrt{2}} V_{us}^* l_+^\mu \times [(p_K + p_\pi)_\mu f_+^{K^0\pi^-}(t) + (p_K - p_\pi)_\mu f_-^{K^0\pi^-}(t)], \quad (3)$$

where

$$f_+^{K^0\pi^-}(t) = 1 + \lambda_+ \frac{t}{m_\pi^2},$$

$$t = (p_K - p_\pi)^2,$$

$$l_+^\mu = \bar{u}(p_\nu)\gamma^\mu(1-\gamma_5)v(p_\mu),$$

$$\xi(t) = f_-^{K^0\pi^-}(t)/f_+^{K^0\pi^-}(t).$$

In our calculations, we use the current PDG values of λ_+, $\xi(0)$, V_{us}, and $G_{\rm F}$ [10]:

$$\lambda_+ = 0.034 \pm 0.005,$$
$$\xi(0) = -0.11 \pm 0.09,$$
$$|V_{us}| = 0.2196, \quad (4)$$
$$G_{\rm F} = 1.16639 \times 10^{-5},$$

where $G_{\rm F}$ is the Fermi coupling constant, and V_{us} is the individual matrix element of the Kobayashi–Maskawa mixing matrix. For the amplitude of the decay $\bar{K}^0 \longrightarrow \pi^+\mu^-\bar{\nu}$, we have the expression

$$M_- = \frac{G_{\rm F}}{\sqrt{2}} V_{us} l_-^\mu \times [(p_K + p_\pi)_\mu f_+^{\bar{K}^0\pi^+}(t) + (p_K - p_\pi)_\mu f_-^{\bar{K}^0\pi^+}(t)], \quad (5)$$

where

$$l_-^\mu = \bar{u}(p_\mu)\gamma^\mu(1-\gamma_5)v(p_\nu).$$

In the calculation of transverse muon polarization induced by the FSI, we assume that *CP* holds.

In the K^0 rest frame, the partial width of the decay is written as

$$d\Gamma = \frac{1}{2m_K}|M|^2(2\pi)^4\delta(p_K - p_\mu - p_\nu - p_\pi) \times \frac{d\mathbf{p}_\pi}{(2\pi)^3 2E_\pi}\frac{d\mathbf{p}_\mu}{(2\pi)^3 2E_\mu}\frac{d\mathbf{p}_\nu}{(2\pi)^3 2E_\nu}. \quad (6)$$

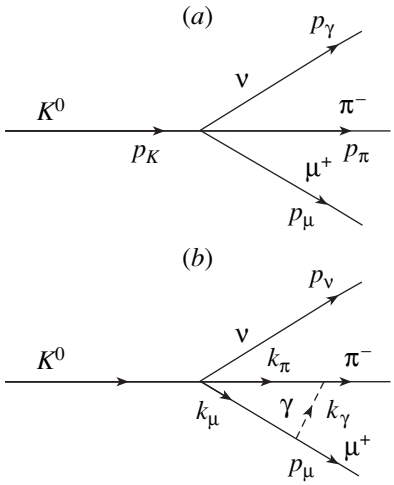

Fig. 1. Diagrams of the $K^0_{\mu 3}$ decay: (*a*) Born approximation and (*b*) one-loop correction.

The square of the matrix element of the $K^0_{\mu 3}$ decay can be written as

$$|M|^2 = \rho_0(y,z)[1 + (P_L\mathbf{e}_L + P_N\mathbf{e}_N + P_T\mathbf{e}_T)\cdot\mathbf{u}]. \quad (7)$$

Here, $\mathbf{u}$ is a unit vector along the direction of the muon spin in its rest frame,

$$y = \frac{2E_\mu}{m_K}, \quad z = \frac{2E_\pi}{m_K}; \quad (8)$$

$\mathbf{e}_i$ ($i = L, N, T$) are unit vectors along the longitudinal, normal, and transverse components of the muon polarization,

$$\mathbf{e}_L = \frac{\mathbf{p}_\mu}{|\mathbf{p}_\mu|},$$
$$\mathbf{e}_N = \frac{\mathbf{p}_\mu \times [\mathbf{p}_\pi \times \mathbf{p}_\mu]}{|\mathbf{p}_\mu \times [\mathbf{p}_\pi \times \mathbf{p}_\mu]|}, \quad (9)$$
$$\mathbf{e}_T = \frac{\mathbf{p}_\pi \times \mathbf{p}_\mu}{|\mathbf{p}_\pi \times \mathbf{p}_\mu|};$$

and, also,

$$P_i(y,z) = \frac{\rho_i(y,z)}{\rho_0(y,z)} \quad (i = L, N, T). \quad (10)$$

The Dalitz plot density of $K^0_{\mu 3}$ can be written as

$$\rho_0(y,z) = 8G_{\rm F}^2|V_{us}|^2\left|f_+^{K^0\pi^-}(t)\right|^2\Phi, \quad (11)$$

where

$$\Phi = 2(p_\mu p_K)(p_\nu p_K) - m_K^2(p_\mu p_\nu) + 2{\rm Re}\chi_+ m_\mu^2(p_\nu p_K)$$

$$+ m_\mu^2|\chi_+|^2(p_\mu p_\nu) = \frac{m_K^4}{2}[(y + 2\mathrm{Re}\chi_+ r_l)(2 - y - z) - (1 - |\chi_+|^2 r_l)(1 - z + r - r_l)], \quad (12)$$

$$\chi_+ = \frac{1}{2}(\xi(0) - 1), \quad r_l = m_\mu^2/m_K^2, \quad r = m_\pi^2/m_K^2. \quad (13)$$

The transverse muon polarization is proportional to the imaginary part of the parameter ξ,

$$P_T = m_\mu m_K \mathrm{Im}(\xi)|\mathbf{p}_\pi \times \mathbf{p}_\mu|/\Phi, \quad (14)$$

where

$$|\mathbf{p}_\pi \times \mathbf{p}_\mu| = \sqrt{|\mathbf{p}_\pi|^2|\mathbf{p}_\mu|^2 - (E_\mu E_\pi - (p_\pi p_\mu))^2}. \quad (15)$$

Thus, if Im(ξ) is induced by the FSI (assuming *CP* invariance holds), we have

$$\mathrm{Im}\chi_+ = \mathrm{Im}\chi_-. \quad (16)$$

If a weak *CP* violation occurs and if the FSI in $K^0_{\mu 3}$ decay is negligible, we have

$$\mathrm{Im}\chi_+ = -\mathrm{Im}\chi_-. \quad (17)$$

The requirement of unitarity of the *S*-matrix is used for determination of the imaginary part of the diagram shown in Fig. 1*b*. In addition, the amplitudes of the $K^0_{\mu 3}$ decays are supposed to be *CP* invariant, and the form factors in expressions (3) and (5) are real.

The imaginary part of the diagram of Fig. 1*b* is as follows:

for $K^0 \longrightarrow \pi^-\mu^+\nu$ decay,

$$\mathrm{Im}M_{\mathrm{el}}^+ = -\frac{\alpha}{\pi}\frac{G_\mathrm{F}}{\sqrt{2}}V_{us}^*\bar{u}(p_\nu)\int\frac{d\mathbf{k}_\pi}{2\omega_\pi}\frac{d\mathbf{k}_\mu}{2\omega_\mu}\delta^4(k_\pi + k_\mu - p) \times f_+^{K^0\pi^-}(t')\frac{F_\pi(k_\gamma^2)}{k_\gamma^2}[\hat{p}_K + \chi_+\hat{k}_\mu] \times (1 - \gamma_5)(\hat{k}_\mu - m_\mu)(\hat{p}_\pi + \hat{k}_\pi)v(p_\mu); \quad (18)$$

for $\bar{K}^0 \longrightarrow \pi^+\mu^-\bar{\nu}$ decay,

$$\mathrm{Im}M_{\mathrm{el}}^- = -\frac{\alpha}{\pi}\frac{G_\mathrm{F}}{\sqrt{2}}V_{us}\bar{u}(p_\mu)\int\frac{d\mathbf{k}_\pi}{2\omega_\pi}\frac{d\mathbf{k}_\mu}{2\omega_\mu}\delta^4(k_\pi + k_\mu - p) \times f_+^{\bar{K}^0\pi^+}(t')\frac{F_\pi(k_\gamma^2)}{k_\gamma^2}(\hat{p}_\pi + \hat{k}_\pi) \times (\hat{k}_\mu + m_\mu)[\hat{p}_K + \chi_-\hat{k}_\mu](1 - \gamma_5)v(p_\nu), \quad (19)$$

where

$$t' = (p_\nu + k_\mu)^2 = m_\mu^2 + 2(p_\nu k_\mu), \quad (20)$$

$$p = p_\mu + p_\pi. \quad (21)$$

The momenta k_π, k_μ, and k_γ are defined in Fig. 1*b*, and $F_\pi(k_\gamma^2)$ is the pion electromagnetic form factor:

$$F_\pi(k_\gamma^2) = 1 + (1/6)k_\gamma^2\langle r_\pi^2\rangle. \quad (22)$$

The experimental value is [11]

$$\langle r_\pi^2\rangle = 0.432 \pm 0.016\ \mathrm{fm}^2. \quad (23)$$

One can rewrite the expression (22) in the form

$$F_\pi(k_\gamma^2) = 1 + k_\gamma^2/\Lambda_\pi^2, \quad (24)$$

where

$$\Lambda_\pi^2 = \frac{6(0.197)^2}{0.432}\ \mathrm{GeV}^2 = 0.541\ \mathrm{GeV}^2. \quad (25)$$

The procedure of integration of (18) and (19) is similar to that used in [7], so that the terms containing infrared divergences do not contribute to the transverse muon polarization. We obtain the following expression for Im(ξ^{em}):

$$\mathrm{Im}(\xi^{\mathrm{em}}) = \frac{\alpha}{\sqrt{(p_\pi p_\mu)^2 - m_\pi^2 m_\mu^2}} \times\left(1 + \lambda_+\frac{t}{m_\pi^2}\right)^{-1}\left[b\left(1 + \frac{2l^2}{\Lambda_\pi^2}\right) + \frac{b_1}{\Lambda_1^2}\right]. \quad (26)$$

Here

$$b = (p_\pi p)\left(1 - |\chi|^2\frac{m_\mu^2}{p^2}\right), \quad (27)$$

Average values of transverse muon polarization $\bar{P}_T^{\mathrm{em}}$ and Im(ξ^{em}) in $K^0_{\mu 3}$ decay [column A: expressions (3) and (21) were used for $f_+^{K^0\pi^-}(t)$ and $F_\pi(k_\gamma^2)$, respectively; column B: $f_+^{K^0\pi^-}(t) = 1$ and $F_\pi(k_\gamma^2) = 1$]

Quantity	Method of calculation	
	A	B
Im(ξ^{em})	0.011	0.012
$\bar{P}_T^{\mathrm{em}}$	2.44×10^{-3}	2.45×10^{-3}
Br($K^0_{\mu 3}$)	28.12%	23.51%

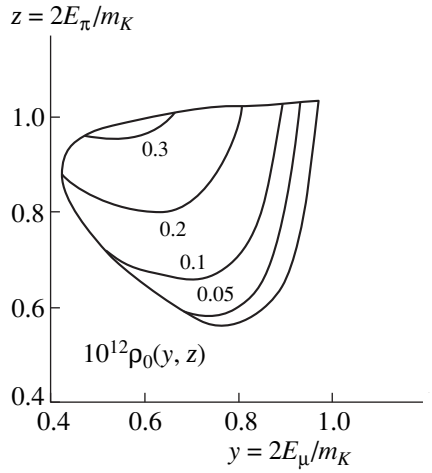

Fig. 2. Dalitz plot of $\rho_0(y, z)$ for $K^0_{\mu 3}$.

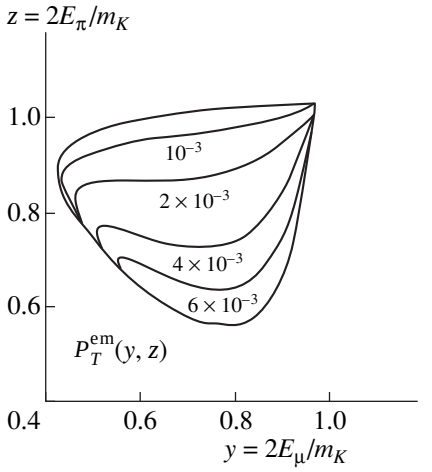

Fig. 3. Contour plot of P_T^{em}.

$$\Lambda_1^2 = m_\pi^2/\lambda_+, \tag{28}$$

$$b_1 = b[(p_\nu l) + 2(p_\nu p)(p_\mu p)/p^2 + m_\mu^2] - \left[1 + 2\chi + \chi^2\frac{m_\mu^2}{p^2}\right](p_\nu)l^2, \tag{29}$$

$$l = p_\mu\frac{(p_\pi p)}{p^2} - p_\pi\frac{(p_\mu p)}{p^2}, \tag{30}$$

$$l^2 = [(p_\mu p_\pi)^2 - m_\pi^2 m_\mu^2]/p^2. \tag{31}$$

Figure 2 shows the Dalitz plot of the density $\rho_0(y, z)$ obtained using (11) with the parameters (4). The contour plot of P_T^{em} is given in Fig. 3. It ranges from 1×10^{-3} to 6×10^{-3} and has a high value at low pion energy.

The values of $\bar{P}_T^{em}$ and $\mathrm{Im}(\xi^{em})$, averaged over the Dalitz plot, and the branching ratio (Br) of the $K^0_{\mu 3}$ decay are shown in the table (column A). The calculated branching ratio is in good agreement with the experimental value of $(27.0 \pm 0.4)\%$ [10]. As seen from the table, correctly taking into account the form factors hardly affects the average values of $\bar{P}_T^{em}$ and $\mathrm{Im}(\xi^{em})$ because the form factors only slightly depend on t'. As a result, our values of $\bar{P}_T^{em}$ and $\mathrm{Im}(\xi^{em})$, presented in the table, are very close to those obtained in the assumption of $f_+^{K^0\pi^-}(t) = 1$ and $F_\pi(k_\gamma^2) = 1$ (column B).

A variation of λ_+, $\xi(0)$, and $\langle r_\pi^2\rangle$ in the intervals limited by two experimental errors did not show any significant deviation of $\bar{P}_T^{em}$ from the value in the table. In these limits, $\bar{P}_T^{em} = (2.4 \pm 0.1) \times 10^{-3}$. This, therefore, allows us to clearly separate the *T*-violating muon polarization, if it exists at the level of 10^{-3}, from the background $\bar{P}_T^{em}$ in the case of the decay $K^0 \longrightarrow \pi^-\mu^+\nu$, when the experimental accuracy in the measurement of P_T reaches a level of 1×10^{-3}. Note that the calculated value of $\bar{P}_T^{em}$ is well below the experimental limit of 5.6×10^{-3} (σ) reached in [12].

ACKNOWLEDGMENTS

This work was supported in part by the Russian Foundation for Basic Research (project no. 96-02-16081).

REFERENCES

1. M. Kobayashi, and T. Maskawa, Prog. Theor. Phys. **49**, 652 (1973).
2. C. Jarlskog, Z. Phys. C **29**, 491 (1985).
3. M. Leurer, Phys. Rev. Lett. **62**, 1967 (1989); G. Belanger, and C. Q. Geng, Phys. Rev. D **44**, 2789 (1991).
4. P. Castoldi, J. M. Frere, and G. L. Kane, Phys. Rev. D **39**, 2633 (1989); R. Garisto, and G. Kane, Phys. Rev. D **44**, 2038 (1991).
5. N. Byers, S. W. MacDowell, and C. N. Yang, in *Proceedings of the International Seminar on High Energy Physics and Elementary Particles* (Vienna, 1965), p. 953.
6. E. S. Ginsberg, and J. Smith, Phys. Rev. D **8**, 3887 (1973).
7. L. B. Okun, and I. B. Khriplovich, Yad. Fiz. **6**, 821 (1966) [Sov. J. Nucl. Phys. **6**, 598 (1967)].
8. G. S. Adkins, Phys. Rev. D **28**, 2885 (1983).
9. J. C. Brodine, Nucl. Phys. B **30**, 545 (1971).
10. Particle Data Group (R. Barnett *et al.*), Phys. Rev. D **54**, 1 (1996).
11. S. R. Anendolia *et al.*, Phys. Lett. B **146**, 116 (1984); **178**, 435 (1986).
12. W. M. Morse, L. B. Leipuner, and R. C. Larsen, Phys. Rev. D **21**, 1750 (1980).

Physics of Atomic Nuclei, Vol. 63, No. 2, 2000, pp. 264–273. Translated from Yadernaya Fizika, Vol. 63, No. 2, 2000, pp. 324–333.

ELEMENTARY PARTICLES AND FIELDS
Theory

Pionic Decay of a Possible Dibaryon d' and Quark Models of πB and $\pi d'$ Couplings

I. T. Obukhovsky and A. I. Obukhovsky[1)]

Institute of Nuclear Physics, Moscow State University, Vorob'evy gory, Moscow, 119899 Russia

Received December 25, 1998; in final form, February 3, 1999

Abstract—The pionic decay of a possible dibaryon, $d' \longrightarrow \pi NN$, is studied in the model assuming the production of $^3P_0$ quark–antiquark pairs and in other models of effective quark–pion coupling. The vertex constants and the form factors for pion–baryon and pion–dibaryon couplings are calculated. The effect of the internal pion structure on decay widths is investigated. It is shown that the quark structure of the nucleon–nucleon wave function in the overlap region plays an important role in dibaryon decays, and known models of nucleon–nucleon interaction are analyzed with allowance for this circumstance. The decay width of a dibaryon is estimated as a function of its effective mass in nuclear matter. © *2000 MAIK "Nauka/Interperiodica".*

1. INTRODUCTION

Double-charge-exchange reactions of the $(Z, A) + \pi^+ \longrightarrow (Z + 2, A) + \pi^-$ type have been considered for some years in the literature as a promising tool for studying short-range nucleon–nucleon correlations in nuclei (see, for example, the review article of Kaminskiĭ [1] and references therein). Of particular interest is a resonance-like behavior that the relevant cross sections displayed at energies of $T_\pi \approx 50$ MeV for all $A \geq 12$ nuclei studied thus far [2]. In [2–4], these results were interpreted as a possible manifestation of a narrow dibaryon resonance commonly known as d' (alternative interpretations are also possible [1]). An investigation of angular distributions revealed that, in all probability, this resonance decays via the emission of an S-wave pion and a pair of S-wave protons. This decay mode is compatible with the quantum numbers $J^P = 0^-$, $T = 0$ of the dibaryon, which was previously considered within the quark-bag model. The πNN channel is the only allowed mode of d' decays. This explains partly the small resonance width of $\Gamma_{d'} \approx 0.5$ MeV. However, the dibaryon mass of $M_{d'} \approx 2065$ MeV proved overly small to be matched with the results of six-quark calculations based on qq interaction fitted to the baryon spectrum. In various versions of the nonrelativistic quark model, the d' mass lies in the range 2.3–2.5 GeV [6, 7].

We deem that the observed deficit of the d' mass may be due to a conventional modification of hadron properties in nuclear matter. For example, the shift (reduction) of the Δ-isobar mass by 30–40 MeV is well known [8]. Quantitative estimates of this shift can be obtained by considering the virtual decay $\Delta \longrightarrow \pi + N$ and the propagation of the interacting pion–nucleon system in nuclear matter [9]. A similar mechanism can be realized for d' as well, in which case the corresponding virtual decay is $d' \longrightarrow \pi NN$. Since the d' mass $M_{d'}$ is close to the πNN threshold (2.02 GeV), even small variations in this mass can cause substantial changes in the decay width (near-threshold effect of the three-body phase space). It follows that, if a dibaryon is formed beyond nuclear matter, even a small distinction between its vacuum mass and the mass $M_{d'}$ that is observed in experiments with nuclei may result in so great a broadening of the resonance that it would be difficult to isolate it against a background. This is supported by recent data of the CHAOS collaboration [10], who studied the (π^+, π^-) reaction on ^{4}He, and by the results of an investigation of the production of $\pi^+\pi^-$ pairs in proton–proton collisions at the CELSIUS accelerator [11] (see also data presented in [12] for d' photoproduction on a deuteron). Although the cross sections for double-charge-exchange reactions showed a distinct resonance behavior for all $A \geq 12$ target nuclei studied thus far, the existence of a resonance peak has not yet been confirmed, with sufficient statistical significance, in processes occurring on light systems like $p + p$, d, or ^{4}He. It is quite possible that the distinctions between these data from those for heavier nuclei are due to resonance broadening beyond nuclear matter. In this connection, theoretical estimates of the branching fraction for the decay $d' \longrightarrow \pi + N + N$ and a determination of the decay width $\Gamma_{d'}$ of the dibaryon as a function of its mass $M_{d'}$ may prove useful in resolving the question of whether the dibaryon d' exists in nuclei and beyond them.

The first estimates showed that the width $\Gamma_{d'}$ depends substantially on the off-mass-shell behavior of the amplitude of nucleon–nucleon scattering (that is, on the nucleon–nucleon interaction at small distances) and on the form of the effective Hamiltonian of quark–pion

[1)] Institute for Nuclear Research, Russian Academy of Sciences, pr. Shestidesyatiletiya Oktyabrya 7a, Moscow, 117312 Russia.

coupling. The latter requires some clarifications. Since the d' mass is close to the πNN threshold, the behavior of the transition matrix element is of importance in the limit where the emitted-pion momentum $\mathbf{k}$ tends to zero. In the nonrelativistic quark model, a consideration of the pseudoscalar and the pseudovector version of quark–pion coupling in the lowest order of an expansion in v/c leads to qualitatively different results when $\mathbf{k} \longrightarrow 0$ (that is, to zero and a nonzero limit for the former and the latter version, respectively). At the same time, a relativistic calculation proper [16] (and even the inclusion of only first-order corrections in v/c [13]) reveals that the above matrix element for the case of pseudoscalar coupling does not vanish in the limit $\mathbf{k} \longrightarrow 0$, its limiting value being determined, in just the same way as for pseudovector coupling, by off-mass-shell effects. In our opinion, it is useful to take into account other off-mass-shell effects as well—for example, those that are associated with the internal $(q\bar{q})$ structure of the pion. In the nonrelativistic quark model, the pion is usually treated as a Goldstone particle having no internal structure. It is well known, however, that, in many cases—for example, in considering the electromagnetic form factor for the pion and pionic-decay widths of mesons [17] and baryons [18]—it is impossible to dispense with taking into account the internal structure of the pion.

In the present study, we consider the problem of $\pi d'$ coupling and calculate the decay width of a hypothetical d' dibaryon as a function of its mass $M_{d'}$ within the model relying on the mechanism of the production of quark–antiquark pairs (PQAP) in the $^3P_0$ spin–orbit state. This model was successfully invoked in describing the pionic decays of light hadrons [17, 20] on the basis of the relativistic Isgur–Paton quark model [21], where vacuum quark–antiquark pairs are produced via the rupture of color-flux tubes. It is important to note that, in the limit of zero pion radius, the PQAP model is equivalent to the assumption of effective pseudovector quark–pion coupling. It follows that, by varying the pion radius b_π, we obtain, within this approach, the results for the pseudovector-coupling case as well. Owing to this, the phenomenological coupling constant of the PQAP model can be normalized to the value of the pion–nucleon pseudovector-coupling constant $f_{\pi NN}$.

2. EFFECTIVE QUARK–PION COUPLING

As a starting point, we will make use of the ansatz of the PQAP model (see, for example, [20] and references therein)—that is, the amplitude for the production of a quark–antiquark pair via the rupture of the color-flux tube in the form

$$t_{q\bar{q}} = -\gamma \sum_{\alpha,\beta} \int d\mathbf{p}_q d\mathbf{p}_{\bar{q}} \delta(\mathbf{p}_q + \mathbf{p}_{\bar{q}}) C_{\alpha\bar{\beta}} F_{\alpha\bar{\beta}} Z(\mathbf{p}_q, \mathbf{p}_{\bar{q}}) \times \sum_m (1m1-m|00) \chi^m_{\alpha\bar{\beta}} \mathcal{Y}_1^{-m}(\mathbf{p}_q - \mathbf{p}_{\bar{q}}) b^+_\alpha(\mathbf{p}_q) d^+_{\bar{\beta}}(\mathbf{p}_{\bar{q}}), \quad (1)$$

where $\alpha = \{s_\alpha, f_\alpha, c_\alpha\}$ ($\bar{\beta} = \{s_{\bar{\beta}}, f_{\bar{\beta}}, c_{\bar{\beta}}\}$) is a complete set of the projections of the quark (antiquark) spin, flavor, and color; $C_{\alpha\bar{\beta}} = \frac{1}{\sqrt{3}}\delta_{c_\alpha c_{\bar{\beta}}}$ and $F_{\alpha\bar{\beta}} = \frac{1}{\sqrt{3}}\delta_{f_\alpha f_{\bar{\beta}}}$ are, respectively, the color and the flavor component of the wave function of the product $q\bar{q}$ pair; $\chi^m_{\alpha\bar{\beta}} = \frac{1}{\sqrt{2}}\{\sigma_m\}_{s_\alpha s_{\bar{\beta}}}$ is the spin component of this wave function; and $\mathcal{Y}_1^{-m}(\mathbf{p}_q - \mathbf{p}_{\bar{q}})$ is a vector spherical harmonic. Expression (1) corresponds to the production of a $q\bar{q}$ pair in the $^3P_0$ spin–orbit state with vacuum quantum numbers $J^P = 0^+$ and $I^C = 0^+$, the production amplitude being proportional to the relative momentum in the pair, $\mathbf{p}_q - \mathbf{p}_{\bar{q}}$, and to the phenomenological constant γ. This hypothesis is justified in the pointlike-pion limit, where the amplitude in the form (1) leads to conventional pseudovector coupling, provided that the requirement of Galilean invariance is taken additionally into account [18]. The function $Z(\mathbf{p}_q, \mathbf{p}_{\bar{q}})$ is nonzero only in the region bounded by the surface of the color tube (usually, this is a cigarlike or a spherical region) and determines the (relative) intensity of the production of $q\bar{q}$ pairs in this region. The calculations from [17, 20] revealed, however, that the shape of the region is immaterial for a successful description of pionic decays, because the hadron wave functions effectively bound the region where the $q\bar{q}$ pairs are produced. Therefore, this function can be replaced by a constant, $Z(\mathbf{p}_q, \mathbf{p}_{\bar{q}}) = 1$, in which case our treatment is equivalent to the use of the conventional nonrelativistic version of the PQAP model [18, 19].

The amplitudes of the transition resulting in pion emission (pion–baryon and pion–dibaryon vertices) are defined as the matrix elements

$$M_3 = \langle \pi^\lambda N | t_{q\bar{q}} | B \rangle, \quad M_6 = \langle \pi^\lambda NN | t_{q\bar{q}} | d' \rangle, \quad (2)$$

which involve hadron wave functions in the form of the simplest quark configurations $|N\rangle = |s^3(b_3)[3]_X(ST = 1/2\ 1/2)\rangle$ and $|\pi^\lambda\rangle = |s^2(b_\pi)[2]_X(ST = 01, T_z = \lambda)\rangle$ and the dibaryon wave function

$$|d'\rangle = |s^5 p(b_6)[51]_X[321]_{CS} LST = 110\ J^P = 0^-\rangle \quad (3)$$

of the translation-invariant shell model. The space components of these configurations,

$$\psi_N(\boldsymbol{\rho}_1, \boldsymbol{\rho}_2) \equiv |s^3(b_3)[3]_X\rangle \sim \exp\left[-2^{-1} b_3^{-2}\left(\frac{1}{2}\rho_1^2 + \frac{2}{3}\rho_2^2\right)\right],$$

$$\psi_\pi(\boldsymbol{\rho}_\pi) \equiv |s^2(b_\pi)[2]_X\rangle \sim \exp\left[-2^{-1} b_\pi^{-2}\left(\frac{1}{2}\rho_\pi^2\right)\right],$$

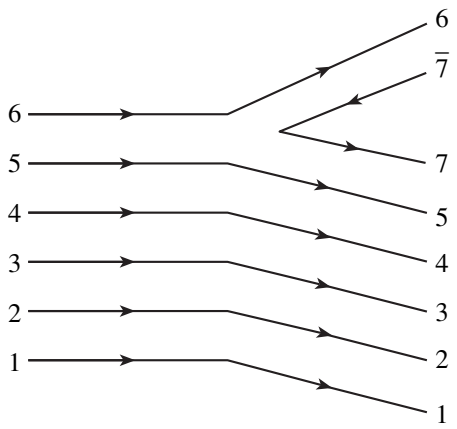

Fig. 1. Diagram describing pion production from a vacuum $q\bar{q}$ pair.

etc., depend only on the relative coordinates of the quarks involved, $\boldsymbol{\rho}_n = \frac{1}{n}(\mathbf{r}_1 + \mathbf{r}_2 + \ldots + \mathbf{r}_n) - \mathbf{r}_{n+1}$ (n = 1, 2, …, 5) and $\boldsymbol{\rho}_\pi = \mathbf{r}_6 - \mathbf{r}_{\bar{7}}$ (the numbering of quarks in pion–hadron vertices is illustrated in Fig. 1).

Expressions (2) for pion–hadron vertices can be represented in the form of matrix elements of the operator of effective quark–pion coupling by defining this operator via the relation

$$H_\lambda = \langle \pi^\lambda | t_{q\bar{q}} I_{q'q''} | 0 \rangle, \tag{4}$$

which employs, as is usually done, the identity operator

$$I_{q'q''} = \sum_\gamma \int d\mathbf{p}_{q'} d\mathbf{p}_{q''} \delta(\mathbf{p}_{q'} - \mathbf{p}_{q''}) b_\gamma(\mathbf{p}_{q'}) b^+_\gamma(\mathbf{p}_{q''}),$$

whereby one of the quarks (q') of the initial hadron (it simultaneously appears to be one of the quarks, q'', of the final pion–hadron state—see Fig. 1) is formally included in our consideration along with the $q\bar{q}$ pair. By using the identity of quarks and by performing permutations of quark indices, along with redefining them (for details, see [18]), we arrive at the required operator of quark–pion coupling. In the coordinate representation for the relative coordinate of the sixth quark, $\boldsymbol{\rho}_5$ (in the following, we suppress everywhere the index 5), it has the form

$$H^{(6)}_\lambda(\boldsymbol{\rho}, \boldsymbol{\rho}') = v\tau^{(6)}_{-\lambda} e^{i\frac{5}{6}\mathbf{k}\cdot\boldsymbol{\rho}'} \hat{O}^{(6)}(\boldsymbol{\rho}, \boldsymbol{\rho}')\boldsymbol{\sigma}^{(6)} \times \left[\frac{\omega_\pi}{2m_q}\left(\frac{2}{i}\nabla_\rho + \frac{5}{6}\mathbf{k}\right) + \left(1 + \frac{\omega_\pi}{12m_q}\right)\mathbf{k}\right]. \tag{5}$$

In order to ensure Galilean invariance, the factor ω_π/m_q was introduced here in front of the gradient term, as is usually done. The nonlocal factor $\hat{O}^{(6)}$ in (5) is proportional to the pion wave function:

$$\hat{O}^{(6)}(\boldsymbol{\rho}, \boldsymbol{\rho}') = e^{-i\frac{1}{2}\mathbf{k}\cdot(\boldsymbol{\rho}-\boldsymbol{\rho}')} \psi_\pi(2^{-1/2}(\boldsymbol{\rho} - \boldsymbol{\rho}')). \tag{6}$$

In (6), we have changed the conventional normalization of ψ_π via the substitution $\psi_\pi \longrightarrow (4\pi b_\pi^2)^{-3/4}\psi_\pi = (4\pi b_\pi^2)^{-3/2}\exp[-(4b_\pi^2)^{-1}(\boldsymbol{\rho} - \boldsymbol{\rho}')^2]$ and, simultaneously, renormalized the phenomenological constant of $q\bar{q}$-pair production in (1) as $\gamma \longrightarrow v = (4\pi b_\pi^2)^{3/4}\gamma$. It can be seen easily that, in the pointlike-pion limit, $b_\pi \longrightarrow 0$, the nonlocal factor in (6) goes over to the contact term proportional to a delta function, $\psi_\pi \longrightarrow \delta(\boldsymbol{\rho} - \boldsymbol{\rho}')$; along with this, expression (5) reduces to the operator of local quark–pion coupling. Comparing the result that we obtained with the standard form of a v/c expansion of the pseudovector-coupling operator (see, for example, [22]), we can see that, in the lowest order in v/c, the two expressions coincide. Assuming that the factor v is independent of b_π, we find that, in this approximation, it can be expressed in terms of the constant $f_{\pi qq}$ of effective quark–pion pseudovector coupling as

$$v = -i\frac{f_{\pi qq}}{m_\pi}\frac{1}{(2\pi)^{3/2}(2\omega_\pi)^{1/2}}. \tag{7}$$

The latter in turn is related to the pion–nucleon coupling constant $f_{\pi NN}$ by the standard equation of the quark model: $f_{\pi qq} = \frac{3}{5} f_{\pi NN}$. Thus, the phenomenological parameter γ in (1) can be treated as a running coupling constant, which is proportional to $b_\pi^{-3/2}$ for $b_\pi \longrightarrow 0$.

3. BARYON VERTICES

The efficiency of this approach was tested by considering the baryon sector for $B \longrightarrow \pi N$ transitions. With respect to standard hadron phenomenology, the present approach is advantageous in that it features a smaller number of free parameters ($f_{\pi qq}$, b_π, and b_3) and in that the vertex form factors are now related to the internal structure of hadrons. By using the simplest configurations $s^3[3]_X$, $s^2p[21]_X$, and $sp^2[3]_X$ and the radius value of b_3 = 0.6 fm, which is common to all baryons and which is peculiar to the nonrelativistic quark model, we have calculated the vertex constants and form factors for the $B = N$, Δ, $N^*(1535)$, and $N^{**}(1440)$ baryons. For the pion radius, there are presently rather accurate data from the relativistic quark model [17, 20] ($b_\pi \approx 0.26$ fm); in our simplified approach (based on the nonrelativistic quark model), however, we varied the parameter b_π in the wider interval $0 \le b_\pi \le b_3$ in order to investigate, within this model, the general dependence of the pionic-decay widths of baryons, $\Gamma_{\pi NB}$, on b_π.

Let us now represent the vertex amplitude in the factorized form

$$\langle N(b_3)m_f t_f|3H_\lambda^{(3)}|B(b_3)m_i t_i\rangle = f_{\pi NB}F_{\pi NB}(k^2)K^{(3)}_{\pi NB}(k;\lambda, m_f t_f, m_i t_i), \quad (8)$$

where m_i (m_f) and t_i (t_f) are the third projections of, respectively, the spin and the isospin of the initial baryon (final nucleon); $f_{\pi NB}$ is the vertex constant; and $F_{\pi NB}(k^2)$ is the vertex form factor satisfying the normalization condition $F_{\pi NB}(0) = 1$. The operator of quark–pion coupling for the three-quark system, $H_\lambda^{(3)}$, differs only slightly from $H_\lambda^{(6)}$. Its explicit form can be established by making the substitution $\boldsymbol{\rho}_5 \longrightarrow \boldsymbol{\rho}_2$ and by replacing the factors 5/6 and 1/12 by 2/2 and 1/6, respectively, in expression (5). The last factor on the right-hand side of (8) is a kinematical factor, whose values are given in Table 1. As a matter of fact, the product $f_{\pi NB}K^{(3)}_{\pi NB}$ determines the vertex amplitudes for point-like structureless hadrons, and we obtain it by going over, in (5), to the limit where $b_\pi \longrightarrow 0$ and $b_3 \longrightarrow 0$ under the condition $b_\pi/b_3 = \text{const}$. In addition to the standard normalization factors from (7), the expression for $K^{(3)}_{\pi NB}$ involves only the spin–isospin matrix elements of operators like $\sigma^{(N)}\tau^{(N)}$ and $S^{(N\Delta)}T^{(N\Delta)}$ for $B \longrightarrow N$ transitions and the dimensionless parameters k/m_π, ω_π/m_π, and $(m_q b_3)^{-1}$. Because of the last of these, a transition to the limit $b_3 \longrightarrow 0$ in the matrix element (8) is nontrivial because, in the case of N^* and N^{**}, the factor $(m_q b_3)^{-1}$ is not compensated, so that the entire expressions diverges. This means that a transition to a point-like baryon must be accompanied by an indefinite increase in the quark mass at a fixed value of the product $(m_q b_3)$ ($m_q b_3 = \text{const} \approx 1$). The last condition is equivalent to the use of running mass $m_q \sim b_3^{-1}$ in the limit $b_3 \longrightarrow 0$ [this is analogous to employing the running constant γ in (1) in the limit $b_\pi \longrightarrow 0$].

Table 2 lists the values of the vertex constants and of the pionic-decay widths of baryons, $\Gamma_{\pi NB}$. The latter were calculated on the basis of the transition matrix elements by the standard formula

$$\Gamma_{\pi NB} = 2\pi\int d\mathbf{k}\,\delta(M_B - E_N(k) - \omega_\pi(k)) \times \frac{1}{2J_i+1}\sum_{m_i t_i}\sum_{m_f t_f}\left|\left\langle Nm_f t_f\left|3H_\lambda^{(3)}\right|Bm_i t_i\right\rangle\right|^2, \quad (9)$$

where $E_N(k) = \sqrt{M_N^2 + k^2}$ and $\omega_\pi(k) = \sqrt{m_\pi^2 + k^2}$. The expressions for the form factors $F_{\pi NB}$ are given in the Appendix. In presenting our results, we make use of the following notation:

$$x_3^2 = \frac{b_\pi^2}{b_3^2}\left(1 + \frac{2}{3}\frac{b_\pi^2}{b_3^2}\right)^{-1}, \quad N_3 = \left(1 + \frac{2}{3}\frac{b_\pi^2}{b_3^2}\right)^{3/2},$$
$$x_6^2 = \frac{b_\pi^2}{b_6^2}\left(1 + \frac{5}{6}\frac{b_\pi^2}{b_6^2}\right)^{-1}, \quad N_6 = \left(1 + \frac{5}{6}\frac{b_\pi^2}{b_6^2}\right)^{3/2}. \quad (10)$$

Table 1. $B \longrightarrow \pi + N$ vertices for structureless baryons

B	$(2\pi)^{3/2}(2\omega_\pi)^{1/2}K^{(3)}_{\pi NB}(k;\lambda, m_f t_f, m_i t_i)$
N	$-i\left\langle Nm_f t_f\left\|\frac{k}{m_\pi}(\boldsymbol{\sigma}^{(N)}\cdot\hat{\mathbf{k}})\tau^{(N)}_{-\lambda}\right\|Nm_i t_i\right\rangle$
Δ	$-i\left\langle Nm_f t_f\left\|\frac{k}{m_\pi}(\mathbf{S}^{(N\Delta)}\cdot\hat{\mathbf{k}})T^{(N\Delta)}_{-\lambda}\right\|\Delta m_i t_i\right\rangle$
$N^*(1535)$	$\frac{1}{m_q b_3}\left\langle Nm_f t_f\left\|\frac{\omega_\pi}{m_\pi}\delta_{m_f m_i}\tau^{(N)}_{-\lambda}\right\|N^* m_i t_i\right\rangle$
$N^{**}(1440)$	$-\frac{i}{m_q b_3}\left\langle Nm_f t_f\left\|\frac{k}{m_\pi}(\boldsymbol{\sigma}^{(N)}\cdot\hat{\mathbf{k}})\tau^{(N)}_{-\lambda}\right\|Nm_i t_i\right\rangle$

As can be seen from Table 2, the decay widths $\Gamma_{\pi NB}$ calculated for $N^*(1535)$ and $N^{**}(1440)$ depend strongly on the ratio of the pion and baryon radii, b_π/b_3, the value of $b_\pi/b_3 \approx 0.5$ being, in all probability, optimal for the purpose of describing the widths of the two resonances. We note that, if the pion dimension of $b_\pi = (0.5\text{–}1)b_3$ is disregarded, even a correct order of magnitude cannot be reproduced for the width of the Roper resonance $N^{**}(1440)$.

At the same time, it should be emphasized that the simplified approach used here (Born approximation for transition amplitudes in the lowest order in v/c) can provide only rough (order-of-magnitude) estimates of decay widths. More accurate estimates could be obtained either by using well-known methods for the unitarization of the Born amplitude or by calculating self-energy contributions and corrections to vertex functions within procedures for approximately solving the Schwinger–Dyson equation (see, for example, the recent study of Kondratyuk and Scholten [23] and references therein). More rigorous estimates of those types will be given elsewhere. Nonetheless, we note that even estimates in the Born approximation may prove very informative, as is demonstrated by the above example of the Roper resonance.

4. DIBARYON VERTICES

In deriving estimates for the pionic width of the dibaryon d', we follow the same scheme as that used in the case of baryons. A significant feature that distinguishes the case of d' is that, here, the decay process

Table 2. Coupling constants $f_{\pi NB}$ and baryon widths $\Gamma_{\pi NB}$ with respect to decays through the πN channel

B	$f_{\pi NB}/f_{\pi qq}$		$\Gamma_{\pi NB}$, MeV			
	$b_\pi/b_3 = 0$	$b_\pi/b_3 \neq 0$	$b_\pi/b_3 = 0$	$b_\pi/b_3 = 0.5$	$b_\pi/b_3 = 1$	Experiment
N	$\frac{5}{3}\left(1+\frac{m_\pi}{6m_q}\right)$	$\frac{5}{3N_3}\left(1+\frac{m_\pi}{6m_q}\right)$	–	–	–	–
Δ	$2\sqrt{2}\left(1+\frac{m_\pi}{6m_q}\right)$	$\frac{2\sqrt{2}}{N_3}\left(1+\frac{m_\pi}{6m_q}\right)$	69	68.7	68	115
N^*	$\frac{2\sqrt{2}}{3\sqrt{3}}$	$\frac{2\sqrt{2}}{3\sqrt{3}N_3}\left(1-\frac{1}{6}x_3^2\right)$	58.5	26.2	8.1	$(0.35–0.55)\Gamma^{\text{tot}}_{N^*}$ [a]
N^{**}	$\frac{5}{9\sqrt{3}}m_\pi b_3$	$\frac{5}{9\sqrt{3}N_3}m_\pi b_3 P(x_3^2)$ [b]	4.3	25.3	118	$(0.6–0.7)\Gamma^{\text{tot}}_{N^{**}}$ [a]

[a] $\Gamma^{\text{tot}}_{N^*}$ = 100–250 MeV, $\Gamma^{\text{tot}}_{N^{**}}$ = 250–450 MeV.

[b] $P(x_3^2) = 1+\frac{1}{6}\left(1+18\frac{m_q}{m_\pi}\right)x_3^2+\frac{5}{9}x_3^4$.

produces a two-nucleon system in a scattering state (in the $^1S_0$ wave). Near the threshold, the S-wave phase shifts for nucleon–nucleon scattering are large, which implies that they must be taken into account in calculating the decay width. Here, we make use of the circumstance that the initial state (3) has a characteristic hadronic dimension of $b_6 \approx b_3 \leq 1$ fm, whence it follows that, in the final state, only the region of small nucleon–nucleon distances will contribute substantially to the transition amplitude. In order to single out the contribution of small distances, we project the wave function of nucleon–nucleon scattering onto six-quark configurations, the most important ones in the region $r_{NN} \leq 1$ fm. For this purpose, expression (2) for the transition amplitude will be written in terms of the complete set of intermediate states $|n, f\rangle$, $I = \sum_{n,f}|n,f\rangle\langle n,f|$, $|n,f\rangle$ being precisely the six-quark configurations in question (n is the number of oscillator excitation quanta, while f is a symbolic notation for Young diagrams $[f_X]$, $[f_{CT}]$ used to classify states). Specifically, we have

$$M_6 = \sum_{n,f}\langle NN|n,f\rangle\left\langle n,f\left|6H_\lambda^{(6)}\right|d'\right\rangle. \qquad (11)$$

It is clear that, upon the emission of S-wave pions, the single-particle operator of quark–pion coupling, $H_\lambda^{(6)}$, initiates transitions only into configurations that differ from (3) either by the $s \longrightarrow p$ excitation or by the $p \longrightarrow s$ excitation of one of the quarks (see Fig. 2), the contribution of possible radial excitations [higher values of n in (11)] decreasing fast with increasing principal quantum number n because of orthogonality of states in the overlap integral $\langle NN|n,f\rangle$. In view of this, we take into account only the contribution of $2s$ excitations—an analysis reveals that they play an important role in the nucleon–nucleon system at small distances—and consider the following six-quark configurations in the final state:

$$|d_0\rangle = |s^6(b_6)[6]_X[2^3]_{CT}LST = 001\ J^P = 0^+\rangle,$$

$$|d_2\rangle = |(s^4p^2 - s^52s)(b_6)[6]_X[2^3]_{CT}LST = 001\ J^P = 0^+\rangle, \qquad (12)$$

$$|d_f\rangle = |s^4p^2(b_6)[42]_X[f_{CT}]LST = 001\ J^P = 0^+\rangle.$$

In the configuration $s^4p^2[42]_X$, we take into account all Young diagrams that are contained in the inner product $[2^3]_C \circ [42]_T$ ($[f_{CT}] = [42]$, $[321]$, $[2^3]$, $[31^3]$, and $[21^4]$) because each of these satisfies the Pauli exclusion prin-

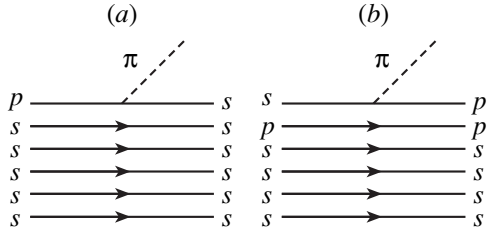

Fig. 2. Modes of the (*a*) deexcitation and (*b*) excitation of the s^5p quark configuration that are associated with the emission of an S-wave pion.

Table 3. Pion–dibaryon coupling constants $f_{\pi d_j d'}$ and coefficients $U^{NN}_{\{f\}}$ for projections onto states belonging to the nucleon–nucleon channel

d_j	$\{f\}$	$f_{\pi d_j d'}/f_{\pi qq}$		$U^{NN}_{\{f\}}$
		$b_\pi/b_6 = 0$	$b_\pi/b_6 \neq 0$	
d_0	$\{[6]_X, [2^3]_{CT}\}$	$\frac{5\sqrt{2}}{3\sqrt{3}}$	$\frac{5\sqrt{2}}{3\sqrt{3}N_6}\left(1-\frac{5}{6}x_6^2\right)$	$\frac{1}{3}$
d_2	$\{[6]_X, [2^3]_{CT}\}$	$\frac{2\sqrt{5}}{9}$	$\frac{2\sqrt{5}}{9N_6}\left[1-\frac{5}{12}x_6^2\left(7-\frac{25}{6}x_6^2\right)\right]$	$\frac{1}{3}$
d_f	$\{[42]_X, [42]_{CT}\}$	0	0	$-\frac{3}{2\sqrt{5}}$
d_f	$\{[42]_X, [321]_{CT}\}$	$-\frac{5}{9}$	$-\frac{5}{9N_6}\left(1-\frac{5}{6}x_6^2\right)$	$\frac{4}{3\sqrt{5}}$
d_f	$\{[42]_X, [2^3]_{CT}\}$	$\frac{4\sqrt{5}}{9}$	$\frac{4\sqrt{5}}{9N_6}\left(1-\frac{5}{6}x_6^2\right)$	$\frac{1}{6}$
d_f	$\{[42]_X, [31^3]_{CT}\}$	$\frac{\sqrt{10}}{9}$	$\frac{\sqrt{10}}{9N_6}\left(1-\frac{5}{6}x_6^2\right)$	$-\frac{1}{3\sqrt{2}}$
d_f	$\{[42]_X, [21^4]_{CT}\}$	$-\frac{2\sqrt{5}}{9}$	$-\frac{2\sqrt{5}}{9N_6}\left(1-\frac{5}{6}x_6^2\right)$	0

ciple, in contrast to the configurations $|d_0\rangle$ and $|d_2\rangle$, which possess the trivial coordinate symmetry $[6]_X$ and which are compatible with only one Young diagram, $[2^3]_{CT}$.

The computational scheme developed in the preceding section is applicable within the limited basis of final states that is given by (12). We begin by determining the coupling constants $f_{\pi d_0 d'}$, $f_{\pi d_2 d'}$, and $f_{\pi d_f d'}$ and the form factors $F_{\pi d_0 d'}(k^2)$, $F_{\pi d_2 d'}(k^2)$, and $F_{\pi d_f d'}(k^2)$ for the transitions from the initial state (3) to the six-quark configurations (12):

$$\begin{aligned}&\langle d_j(b_6)t_f\big|6H^{(6)}_\lambda\big|d'(b_6)\rangle\\ &= f_{\pi d_j d'}F_{\pi d_j d'}(k^2)K^{(6)}_{\pi d_j d'}(k;\lambda,t_f).\end{aligned} \tag{13}$$

The kinematical factors $K^{(6)}_{\pi d_j d'}$ defined, as in the baryon case, via a transition to the limit where $b_6 \longrightarrow 0$ and $b_\pi \longrightarrow 0$ at constant b_π/b_6 take the same value for all dibaryon states $d_j = d_0, d_2, d_f$. Specifically, we have

$$K^{(6)}_{\pi d_j d'}(k;\lambda,t_f) = \frac{1}{m_q b_6}\frac{\omega_\pi}{m_\pi}\frac{\delta_{t_f,-\lambda}}{(2\pi)^{3/2}(2\omega_\pi)^{1/2}}. \tag{14}$$

The resulting values of the coupling constants $f_{\pi d_j d'}$ are quoted in Table 3, along with the algebraic factors $U^{NN}_{\{f\}}$ determining, in *CST* space, the projections of the configurations $|n, f\rangle$ onto the *NN* channel (for details, see [14]). Analytic expressions for the vertex form factors $F_{\pi d_j d'}(k^2)$ are presented in the Appendix.

The developed technique makes it possible to obtain an analytic approximation for the total transition amplitude (11) in the plane-wave approximation for the final nucleon–nucleon state. Substituting the plane-wave final state $|NN(b_3)\mathbf{q}, t_f\rangle_{\rm pw}$ into (11) and performing a summation over configurations (12) in the intermediate state, we obtain

$$\begin{aligned}&M^{\rm pw}_6\\ &= \sum_{d_j}{}_{\rm pw}\langle NN(b_3)\mathbf{q}, t_f|d_j(b_6), t_f\rangle\big\langle d_j, t_f\big|6H^{(6)}_\lambda\big|d'\big\rangle\\ &= \Phi_{NN}(q^2)K^{(6)}_{\pi d_j d'}(k;\lambda,t_f)\Big\{F_{\pi d_0 d'}(k^2)f_{\pi d_0 d'}U^{NN}_{\{f_0\}}\\ &\quad -\sqrt{\frac{3}{10}}\left(1-\frac{4}{9}q^2b_6^2\right)\Big[F_{\pi d_2 d'}(k^2)f_{\pi d_2 d'}U^{NN}_{\{f_2\}}\\ &\quad +\frac{2}{3}F_{\pi d_f d'}(k^2)\sum_{\{f\}}f_{\pi d_f d'}U^{NN}_{\{f\}}\Big]\Big\},\end{aligned} \tag{15}$$

where all functions dependent on q, including the function

$$\Phi_{NN}(q^2) = \sqrt{10}\frac{2^{3/4}b_6^{3/2}}{3^{1/4}\pi^{3/4}}\left(\frac{2b_6/b_3}{1+b_6^2/b_3^2}\right)^6 e^{-q^2b_6^2/3}, \quad (16)$$

are projections of the coordinate components of configurations (12) onto plane waves in the NN channel. All calculations of overlap integrals and transition matrix elements in the basis of quark configurations can be performed easily [14] by using the technique of fractional-parentage coefficients (see, for example, [25]). The first term in the braced expression from (15) corresponds to the transition $d' \longrightarrow d_0$ resulting in the deexcitation of configuration (3) (deexcitation mode), while the remaining part of this expression represents contributions from the transitions $d' \longrightarrow d_2, d_f$ involving the orbital or radial excitations of this configuration (excitation mode).

Substituting the values of the coefficients $U^{NN}_{\{f\}}$ from Table 3 into (15), we can see that, because of the destructive interference of the contributions of the d_2 and d_f configurations, the contributions of the excitation mode to the transition amplitude is a few times as small as the contribution of the deexcitation mode. In the following, this circumstance will be used in studying the dependence of the decay width of the dibaryon d' on the strength of nucleon–nucleon interaction at small distances.

5. INCLUSION OF NUCLEON–NUCLEON INTERACTION

The total width with respect to the decay $d' \longrightarrow \pi NN$ is obtained by integrating the square of the Born amplitude (11) over the entire phase space and by summing the result over the projections of the isospin t_f:

$$\Gamma^{\text{tot}}_{d'} = 2\pi\int d\mathbf{q}\int d\mathbf{k}_\pi\delta(M_{d'}-E_{NN}-\omega_\pi) \times\sum_{t_f}\left|\sum_{d_j}\langle NN(b_3)\mathbf{q}, t_f|d_j(b_6), t_f\rangle\left\langle d_j, t_f\left|6H^{(6)}_\lambda\right|d'\right\rangle\right|^2. \quad (17)$$

In contrast to equation (15), which features plane waves, the wave function $|NN(b_3)\mathbf{q}, t_f\rangle$ in (17) takes fully into account nucleon–nucleon interaction [the eigenstate $\Psi^{(-)}$ corresponds to the asymptotic boundary condition in the form of the plane wave $|NN(b_3)\mathbf{q}, t_f\rangle_{\text{pw}}$ for $t \longrightarrow \infty$]. As a result, expression (17) can be used to test various models of nucleon–nucleon interaction at small distances. We have performed our calculations for two alternative models of nucleon–nucleon interaction: the one-boson-exchange (OBE) potential, which implies short-range repulsion, and the Moscow potential, which implies attraction at small distances and forbidden states in the discrete spectrum. Here, some brief comments on these qualitatively different approaches to nucleon–nucleon interaction at small distances are in order.

In the first approach (see, for example, [26]), only hadronic degrees of freedom are taken into account in deriving the effective nucleon–nucleon potential; as a result, it proves rather close, at small distances, to well-known phenomenological potentials featuring a repulsive core. The second approach relies on the microscopic (quark) picture of nucleon overlap, as analyzed previously in [24, 25, 27, 28]. An analysis revealed that the characteristic behavior of the phase shifts for nucleon–nucleon scattering at intermediate energies in the lowest partial waves (constant negative slope of the energy dependence of the S- and P-wave phase shifts) admits two different interpretations. By way of example, we will consider this point in detail for S waves.

(i) Suppose that the s^6 and s^4p^2 quark configurations interfere destructively in the region of nucleon overlap. In this case, the wave function dies out at distances $r_{NN} \le b_3$ (in just the same way as in the OBE model featuring a repulsive core). For the wave function to die out completely, it is necessary that the two configurations have close weights in the region of overlap [24].

(ii) Suppose that the weight of the s^4p^2 configuration is greater than the weight of the s^6 configuration. Owing to this, the wave function in the nucleon–nucleon channel develops a node at a distance of $r_{NN} \approx b_3$. The above dominance of the $s^4p^2[42]_X$ configuration is possible in principle (an opposite standpoint is advocated in [29], however), provided that the influence of exchange forces in the six-quark system is equivalent to effective attraction in states characterized by the nontrivial Young diagram $[42]_X$ and to repulsion in the symmetric $[6]_X$ state (see [27]). That the node of the radial wave function stably occurs at $r_{NN} \approx 0.6$ fm over a wide energy interval plays the same role for nucleon–nucleon scattering as a repulsive core of radius $r_c \approx 0.6$ fm [30].

In comparing the contributions of the $s^5p[51]_X$ and $s^3p^3[3^2]_X$ configurations to the nucleon–nucleon wave function at small distances, a similar pattern was revealed in the P waves as well.

In accordance with this analysis, a phenomenological model of the Moscow potential, where the node character of the wave function in the S and P waves was proposed and where the condition of orthogonality of the wave function in the nucleon–nucleon channel to the symmetric configurations (of the six-quark-bag type) $s^6[6]_XL = 0$ and $s^5p[51]_XL = 1$ was used, was proposed in [30–32]. The last version of the Moscow potential from [32] describes nucleon–nucleon scattering to the same degree of accuracy as the high-precision potential versions featuring a core (Argonne and Nijmegen potentials). Thus, the two models of nucleon–nucleon interaction (OBE potential and Moscow potential) lead to similar phase shifts, but they produce scattering amplitudes differing by their off-mass-shell properties.

The above off-mass-shell distinctions, which stem from the use of the different dynamical models of nucleon–nucleon interaction at small distances, manifest themselves most vividly in the decay of a hypothetical baryon d'. The total decay width $\Gamma_{d'}^{\text{tot}}$ as a function of the dibaryon mass $M_{d'}$ is displayed in Fig. 3 for two alternative models of nucleon–nucleon interaction: the OBE potential in the separable approximation [33] and the Moscow potential from [32] with two different values of the quark radius of the pion, $b_\pi = 0$ and $0.5b_3$ (for the sake of simplicity, we use here identical quark radii of the baryons and dibaryons, $b_3 = b_6 = 0.6$ fm). At $b_\pi = 0$, we arrive at results corresponding to effective pseudovector quark–pion coupling; for the sake of comparison, we also present results obtained for the case of pseudoscalar coupling. In Fig. 3, the mass $M_{d'}$ is varied in the interval from the πNN threshold (2.02 GeV) to the value of 2.3 GeV, which was obtained in the calculations presented in [6, 7] and which is peculiar to the nonrelativistic quark model. Over this interval, the decay width calculated on the basis of the OBE interaction is several times as great as that corresponding to the Moscow potential. This means that, in either case, final-state nucleon–nucleon interaction does not violate the destructive interference of the amplitudes for transitions into the excited configurations $s^4p^2[42]_X$ and $(s^4p^2 - s^52s)[6]_X$ that was indicated at the end of the preceding section, where it was established on the basis of plane-wave calculations. As a result, the conclusion that the probability of a transition into the symmetric $s^6[6]_X$ state (six-quark bag) exceeds considerably the probability of a transition into a full superposition of excited states, which corresponds to a nodal wave function in the nucleon–nucleon channel, remains in force even upon taking the interaction into account. By definition, the wave function in the Moscow potential is orthogonal to the $s^6[6]_X$ configuration; hence, the total width of d' must be anomalously narrow in this model in relation to the results generated by the OBE potential. If the dimensions of the pion are assumed to be finite ($b_\pi = 0.5b_3$), the orthogonality condition is somewhat relaxed, but this only leads to a decrease in the decay width in both models (Fig. 3, curves *2*).

The experimental values of $\Gamma_{d'}$ and $M_{d'}$ (Fig. 3, point) are compatible with the dashed curves calculated within the Moscow potential model; at the same time, the OBE results (solid curves) yield a d' width greater than that by a factor of about 4 in this mass region. With increasing d' mass, this difference becomes greater, achieving an order of magnitude at $M_{d'} \approx 2.3$ GeV. For $M_{d'} \geq 2.3$ GeV, the value of $\Gamma_{d'}^{\text{tot}}$ in the OBE model may exceed 100 MeV.

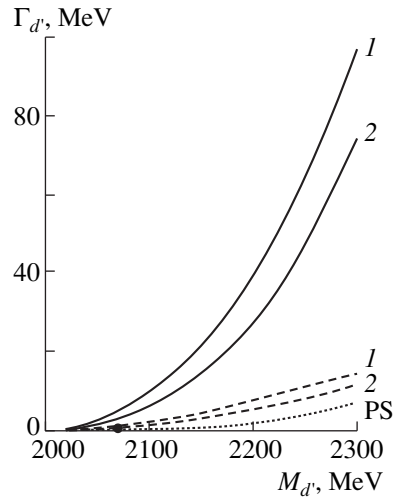

Fig. 3. Total decay width of the dibaryon d' as a function of its mass for the nucleon–nucleon interaction simulated by (solid curves) the OBE potential [33] or (dashed curves) the Moscow potential [32]: (curves *1*) results of the calculation at $b_\pi = 0$ and (curves *2*) results of the calculation at $b_\pi = 0.3$ fm. The results obtained in [14] for the case of pseudovector (PS) coupling are represented by the dotted curve.

6. CONCLUSION

On the basis of our results, we may conclude that the experimental dibaryon-width value of $\Gamma_{d'} \approx 0.5$ MeV is quite compatible with the assumption of the quark origin of the resonance, provided that the mass $M_{d'}$ observed in experiments with nuclear targets is substantially smaller than values in the range 2.3–2.5 GeV, which are peculiar to the quark model. It is quite possible that the observed value of $M_{d'} \approx 2.065$ GeV, which differs significantly from theoretical estimates based on the quark model, stems from a modification of the properties of a dibaryon in nuclear matter. At the same time, we note that, if the quark dibaryon d' being considered had a vacuum mass (that is, the mass outside nuclei) in the interval 2.3–2.5 GeV, its width with respect to decay through the πNN channel could be greater than 100 MeV (as follows from the data in Fig. 3, this estimate depends greatly on the choice of model for nucleon–nucleon interaction at small distances). This would complicate the isolation of a resonance peak against the background from other pion-production processes leading, for example, to the excitation of baryon resonances in the same mass region.

In this connection, we deem it desirable to estimate theoretically the shift of the d' mass in nuclear matter. The model of quark–pion, pion–baryon, and pion–dibaryon couplings that was developed here may prove very useful in deriving such estimates. It is also necessary to conduct experiments aimed at studying d' formation outside nuclei (for example, in electro- and photoproduction on deuterons and in proton–proton collisions), because a comparatively narrow resonance peak ($\Gamma_{d'} \approx 10$ MeV) peculiar, in particular, to models like

those where nucleon–nucleon interactions are simulated by the Moscow potential can manifest itself even outside a nuclear medium.

ACKNOWLEDGMENTS

We are grateful to V.I. Kukulin, V.G. Neudatchin, N.P. Yudin, A. Faessler, M.V. Kazarnovsky,† M.G. Shchepkin, and A. Buchmann for stimulating discussions and critical comments.

This work was supported in part by the Russian Foundation for Basic Research (project nos. 96-02-18071 and 96-02-18072).

APPENDIX

The vertex form factors for $B \longrightarrow \pi + N$ transitions are given by

$$F_{\pi NN}(k^2) = F_{\pi N\Delta}(k^2) = \exp\left[-\frac{k^2 b_3^2}{6}\left(1+\frac{x_3^2}{6}\right)\right];$$

$$F_{\pi NN^*}(k^2) = \left[1-\frac{k^2 b_3^2}{18}\frac{\left(1-\frac{4}{3}x_3^2\right)\left(1+\frac{1}{3}x_3^2\right)}{\left(1-\frac{2}{3}x_3^2\right)} - \frac{m_q}{\omega_\pi}\frac{k^2 b_3^2}{3}\frac{\left(1+\frac{1}{3}x_3^2\right)}{\left(1-\frac{2}{3}x_3^2\right)}\right]F_{\pi NN}(k^2);$$

$$F_{\pi NN^{**}}(k^2) = \left[\frac{m_\pi}{m_q}\left(1+\frac{1}{6}x_3^2+\frac{5}{9}x_3^4\right)+3x_3^2\right]^{-1}\left\{\frac{\omega_\pi}{m_q}\times\left[1+\frac{1}{6}x_3^2+\frac{5}{9}x_3^4-\frac{k^2 b_3^2}{12}\left(1-\frac{4}{3}x_3^2\right)\left(1+\frac{2}{3}x_3^2+\frac{1}{9}x_3^4\right)\right] + 3x_3^2-\frac{k^2 b_3^2}{2}\left(1+\frac{2}{3}x_3^2+\frac{1}{9}x_3^4\right)\right\}F_{\pi NN}(k^2).$$

The vertex form factors for the transitions $d' \longrightarrow \pi + d_j$ are

$$F_{\pi d_0 d'}(k^2) = \left[1+\frac{5}{216}k^2 b_6^2 x_6^2\frac{1+\frac{1}{6}x_6^2}{1-\frac{5}{6}x_6^2} - \frac{m_q}{\omega_\pi}\left(1+\frac{\omega_\pi}{12 m_q}\right)\frac{k^2 b_6^2}{3}\left(\frac{1+\frac{1}{6}x_6^2}{1-\frac{5}{6}x_6^2}\right)\right]\times\exp\left[-\frac{5}{24}k^2 b_6^2\left(1+\frac{x_6^2}{30}\right)\right],\quad F_{\pi d_f d'}(k^2) = F_{\pi d_0 d'}(k^2);$$

$$F_{\pi d_2 d'}(k^2) = \left\{1+\left[1-\frac{5}{12}x_6^2\left(7-\frac{25}{6}x_6^2\right)\right]^{-1}\times\left[\frac{5}{72}k^2 b_6^2+\frac{5}{432}k^2 b_6^2 x_6^2\left(17-\frac{35}{6}x_6^2+\frac{25}{18x_6^4}\right) + \frac{25}{5184}k^4 b_6^4 x_6^2\left(1-\frac{x_6^2}{6}-\frac{x_6^4}{36}+\frac{x_6^6}{216}\right)\right] + \frac{m_q}{\omega_\pi}\left(1+\frac{\omega_\pi}{12 m_q}\right)\left[1-\frac{5}{12}x_6^2\left(7-\frac{25}{6}x_6^2\right)\right]^{-1}\times\left[\frac{k^2 b_6^2}{3}\left(1-\frac{5}{24}k^2 b_6^2\right)-\frac{k^2 b_6^2}{36}x_6^2\left(1-\frac{25}{6}x_6^2\right) + \frac{5}{216}k^4 b_6^4 x_6^2\left(1+\frac{x_6^2}{6}-\frac{x_6^4}{36}\right)\right]\right\}\exp\left[-\frac{5}{24}k^2 b_6^2\left(1+\frac{x_6^2}{30}\right)\right].$$

† Deceased.

REFERENCES

1. V. A. Kaminskiĭ, Fiz. Élem. Chastitz At. Yadra **26**, 362 (1995) [Phys. Part. Nucl. **26**, 148 (1995)].
2. R. Bilger, B. M. Barnet, H. Clement, *et al.*, Phys. Lett. B **269**, 247 (1991); R. Bilger, H. Clement, K. Föhl, *et al.*, Z. Phys. A **343**, 941 (1992); H. Clement, M. Schepkin, G. J. Wagner, *et al.*, Phys. Lett. B **337**, 43 (1994).
3. B. V. Martem'yanov and M. G. Shchepkin, Pis'ma Zh. Éksp. Teor. Fiz. **53**, 776 (1991).
4. R. Bilger, H. A. Clement, and M. G. Schepkin, Phys. Rev. Lett. **71**, 42 (1993); R. Bilger, πN Newsletter **10**, 47 (1995).
5. P. J. Mulders, A. T. Aerts, and J. J. de Swart, Phys. Rev. Lett. **40**, 1543 (1978); Phys. Rev. D **21**, 2653 (1980).
6. G. Wagner, L. Ya. Glozman, A. J. Buchmann, *et al.*, Nucl. Phys. A **594**, 263 (1995).
7. A. J. Buchmann, G. Wagner, and A. Faessler, Phys. Rev. C **57**, 3340 (1998).
8. V. G. Ableev *et al.*, Pis'ma Zh. Éksp. Teor. Fiz. **40**, 35 (1984) [JETP Lett. **40**, 763 (1984)].
9. M. Betz and T.-S. H. Lee, Phys. Rev. C **23**, 375 (1981).
10. CHAOS Collab. (J. Gräter *et al.*), Phys. Lett. B **240**, 37 (1998).
11. H. Clement, private communication.
12. R. Bilger, H. Clement, *et al.*, Nucl. Phys. A **596**, 586 (1996).
13. K. Itonaga, A. J. Buchmann, G. Wagner, *et al.*, Nucl. Phys. A **609**, 422 (1996).
14. I. T. Obukhovsky, K. Itonaga, G. Wagner, *et al.*, Phys. Rev. C **56**, 3295 (1997).
15. I. Obukhovsky and A. Obukhovsky, in *16th European Conference on Few-Body Problems in Physics, Autrans, 1998*, Abstract Booklet, Ed. by K. Protasov (Grenoble, 1998), p. 91.
16. A. Samsonov and M. Shchepkin, nucl-th/9712079.
17. S. Godfrey and N. Isgur, Phys. Rev. D **32**, 189 (1985).

18. F. Cano, P. González, S. Noguera, *et al.*, Nucl. Phys. A **603**, 257 (1996).
19. L. Mecu, Nucl. Phys. B **10**, 521 (1969); A. Le Yaouanc, L. Oliver, O. Rene, *et al.*, Phys. Rev. D **8**, 2223 (1973).
20. S. Capstick and W. Roberts, Phys. Rev. D **47**, 1994 (1993).
21. N. Isgur and J. Paton, Phys. Rev. D **31**, 2910 (1985).
22. T. E. O. Ericson and W. Weise, *Pions and Nuclei* (Clarendon, Oxford, 1988).
23. S. Kondratyuk and O. Scholten, nucl-th/9807077.
24. A. M. Kusainov, V. G. Neudatchin, and I. T. Obukhovsky, Phys. Rev. C **44**, 2343 (1991).
25. I. T. Obukhovsky, Yu. F. Smirnov, and Yu. M. Tchuvil'sky, J. Phys. A **15**, 7 (1982); I. T. Obukhovsky, Prog. Part. Nucl. Phys. **36**, 359 (1996).
26. R. Machleid, Adv. Nucl. Phys. **19**, 189 (1989).
27. I. T. Obukhovsky, V. G. Neudatchin, Yu. F. Smirnov, *et al.*, Phys. Lett. B **88**, 231 (1979).
28. M. Harvey, Nucl. Phys. A **352**, 301 (1981).
29. Fl. Stancu, S. Pepin, and L. Ya. Glozman, Phys. Rev. C **56**, 2779 (1997).
30. Yu. L. Dorodnykh, V. G. Neudatchin, N. P. Yudin, *et al.*, Phys. Rev. C **43**, 2499 (1991).
31. V. I. Kukulin, V. M. Krasnopol'sky, V. N. Pomerantsev, *et al.*, Phys. Lett. B **153**, 7 (1985).
32. V. I. Kukulin, V. N. Pomerantsev, A. Faessler, *et al.*, Phys. Rev. C **57**, 535 (1998).
33. T. Ueda, K. Tada, and T. Kameyama, Prog. Theor. Phys. **95**, 115 (1996).

Translated by A. Isaakyan

Physics of Atomic Nuclei, Vol. 63, No. 2, 2000, pp. 274–286. Translated from Yadernaya Fizika, Vol. 63, No. 2, 2000, pp. 334–347.

ELEMENTARY PARTICLES AND FIELDS
Theory

Spectroscopy of Doubly Heavy Baryons

S. S. Gershteĭn, V. V. Kiselev*, A. K. Likhoded, and A. I. Onishchenko**

Institute for High Energy Physics, Protvino, Moscow oblast, 142284 Russia

Received November 5, 1998; in final form, April 29, 1999

Abstract—Within a nonrelativistic quark model featuring a QCD-motivated Buchmüller–Tye potential, the mass spectra for the families of doubly heavy baryons are calculated by assuming the quark–diquark structure of the baryon wave functions and by taking into account spin-dependent splitting. Physically motivated evidence that, in the case where heavy quarks have identical flavors, quasistationary excited states may be formed in the heavy-diquark subsystem is analyzed. © *2000 MAIK "Nauka/Interperiodica".*

1. INTRODUCTION

The first observation of the B_c^+ meson by CDF collaboration at FNAL [1] opened a new era in the physics of hadrons that contain heavy quarks. On one hand, the B_c^+ meson is the last of the heavy quarkonia ($Q\bar{Q}'$) and heavy mesons featuring open charm that have become accessible to observation. On the other hand, this is the first long-lived hadron containing two heavy quarks. In this sense, the B_c^+ meson appears to be at the beginning of some families that also include the doubly heavy baryons Ξ_{cc}, Ξ_{bc}, and Ξ_{bb} (for the classification of hadrons on the basis of the quark model, see the Review of Particle Properties in [2]). The experimental observation of the B_c^+ meson was preceded by thorough inquiries into its spectroscopy and into the mechanisms of its decay and production (for an overview, see [3]). In just the same way, an observation of doubly heavy baryons requires detailed and reliable knowledge of their properties. The first theoretical steps toward obtaining relevant predictions were made (i) in (4), where the lifetimes of the Ξ_{cc}^+ and Ξ_{cc}^{++} baryons were estimated within the operator-product expansion in the inverse heavy-quark mass; (ii) in the series of articles listed in [5], which were devoted to studying the differential and total cross sections for $\Xi_{QQ'}$ production in various interactions within the fragmentation model, within the intrinsic-charm model [6] (for Ξ_{cc} hadroproduction), and within a perturbative QCD calculation to $O(\alpha_s^4)$ terms inclusive that takes into account not only fragmentation, which is dominant at high transverse momenta ($p_T \gg M$), but also the prefragmentation regime; and (iii) in the series of studies quoted in [7], which were aimed at estimating the masses of some low-lying states of doubly heavy baryons and the masses of Ξ_{cc} excitations [8].

In the present study, we analyze basic spectroscopic features of the families of doubly heavy baryons $\Xi_{QQ'} = (QQ'q)$, where $q = u$, d, and $\Omega_{QQ'} = (QQ's)$.

Qualitatively, the formation of bound states in the $(QQ'q)$ system is governed by the existence of two distance scales that are specified by the dimension of the doubly heavy diquark QQ', $r_{QQ'}$, in the color-antitriplet state and by the confinement scale for the light quark q, Λ_{QCD}. For these two scales, we have the inequalities

$$r_{QQ'}\Lambda_{\mathrm{QCD}} \ll 1, \quad \Lambda_{\mathrm{QCD}} \ll m_Q.$$

Under these conditions, the compact diquark QQ' appears to be merely a static source of a color QCD field for the light quark, provided that we use the approximation of a diquark local field. In view of this, we can use some reliable results obtained within models of heavy mesons featuring one heavy quark [in which case there is merely a static local source in the antitriplet representation of the $SU(3)_c$ group]: this may be, for example, potential models [9] or heavy-quark effective theory [10], where the expansion is performed in terms of the inverse heavy-quark mass. Here, we invoke the nonrelativistic quark model based on the Buchmüller–Tye potential [11]. Theoretically, we can speak of the rough approximation for a light quark ($m_q^{\mathrm{QCD}} \ll \Lambda_{\mathrm{QCD}}$)—which is therefore relativistic—in the system featuring a finite number of degrees of freedom and an instantaneous interaction $V(\mathbf{r})$. This is because the confinement phenomenon implies the dressing of a light quark with a sea (an infinite number of gluons and quark pairs) and nonperturbative effects beyond the potential approach, the correlation times of these effects, τ_{QCD}, being about $1/\Lambda_{\mathrm{QCD}}$. Phenomenologically, however, the use of the constituent mass m_q^{NP} of about Λ_{QCD} as a basic parameter that governs the interaction with QCD condensates makes it possible to tune the nonrelativistic potential model to a high preci-

* e-mail: kiselev@mx.ihep.su
** e-mail: likhoded@mx.ihep.su

sion ($\delta M \approx 30$–40 MeV) on the basis of available experimental data. Owing to this, the approach being discussed becomes a reliable tool for predicting the masses of hadrons containing heavy and light quarks.

As to the diquark QQ', it is, by and large, similar to the heavy quarkonium $Q\bar{Q}'$, but there are some significant distinctions. The most important ones are the following:

(i) The $(QQ')_{\bar{3}_c}$ system features an open color.

(ii) For quarks of the same flavor, $Q = Q'$, it is necessary to take into account the Pauli exclusion principle for identical fermions.

It can be seen easily that, because of the second feature, the total-quark-spin values of $S = 0$ and 1 are forbidden for, respectively, symmetric P-even and antisymmetric P-odd diquark space wave functions $\Psi_d(\mathbf{r})$ (the corresponding values of the orbital angular momentum for these two cases are, respectively, $L_d = 2n$ and $L_d = 2n + 1$, $n = 0, 1, 2, \ldots$). At the same time, a nonzero color charge of the system (first feature) generates two problems.

First, the hypothesis of confinement in the form of a confining potential (an indefinite growth of energy with increasing size of the system) is generally inapplicable to interactions within such an object. Physically, it is rather difficult, however, to imagine a situation where a color object of large dimensions ($r > 1/\Lambda_{\mathrm{QCD}}$) possessing a bounded self-interaction energy interacts with another color source within a color-singlet [with respect to $SU(3)_c$] state in such a way that it is confined within a hadron of dimension $r \sim 1/\Lambda_{\mathrm{QCD}}$. Moreover, the hadronic-string framework, which proved highly reliable, leads to the following picture: for baryons, the string tension in a diquark with an external leg is only one-half as great as that in the quark–antiquark pair of the $q\bar{q}'$ meson; since the energy of a diquark also grows in direct proportion to its dimension, there occurs an effect similar to quark confinement. In addition, quark coupling can be viewed as that which is realized via an effective single exchange of a color object in the octet representation of $SU(3)_c$ (it is common practice to take the sum of scalar and vector exchanges), so that the potentials in the singlet ($q\bar{q}'$) and antitriplet (qq') states again differ only by the color factor of 1/2; this means the presence of a confining potential (a linearly growing term) in QCD-motivated models for the heavy diquark $(QQ')_{\bar{3}_c}$. In the present study, the nonrelativistic model based on the Buchmüller–Tye potential is used for the diquark as well.

Second, the total spin S of the quarks and their total orbital angular momentum L are conserved individually in the color-singlet state of the $Q\bar{Q}'$ system, because the contributions of the QCD operators governing transitions between levels that are specified by these quantum numbers are suppressed. Indeed, it can be shown [12] that, within a multipole QCD expansion, the amplitudes of chromomagnetic and chromoelectric dipole transitions are suppressed, the suppression factor being in inverse proportion of the heavy-quark mass; this is, however, not the whole story, since of crucial importance are the following two circumstances: the above transitions can proceed only via the emission of a color-singlet object—that is, at least two gluons are emitted (an extra order in $1/m_Q$)—and it is necessary to take into account the actual phase space in the physical spectrum of massive hadrons, in which case the situation is naturally different from that for massless gluons. As to the probability of a hybrid-state admixture—for example, an admixture featuring an octet ($Q\bar{Q}'$) subsystem and an extra gluon (that is, the Fock state $|Q\bar{Q}'_{8_c} g\rangle$)—it is suppressed owing to the small dimensions of the system and to the nonrelativistic motion of the quarks (for details, see [13]). In the color-antitriplet state, the emission of a soft nonperturbative gluon via a transition between diquark levels determined by the spin S_d and orbital angular momentum L_d is not forbidden, provided that there are no other prohibitions or small parameters of suppression. If the quarks forming a diquark are of the same flavor, the Pauli exclusion principle results in that transitions may occur only between levels that either differ both by the spin ($\Delta S_d = 1$) and by the orbital angular momentum ($\Delta L_d = 2n + 1$), or belong to the same series of radial excitations, or are characterized by the orbital angular momentum difference of $\Delta L_d = 2n$. In the second case, the transition amplitudes are suppressed in proportion to the ratio of the diquark recoil momentum to the diquark mass; in the first case, the transition operator changing both the spin of the diquark and its orbital angular momentum has an additional order of smallness either because of an extra factor $1/m_Q$ or because of the small dimension of the diquark. In view of this, we can state that there must exist quasistationary states determined by the quantum numbers S_d and L_d. In a diquark formed by quarks of different flavors (bc), the operators of QCD dipole transitions resulting in a single emission of a soft gluon are not forbidden, so that the lifetimes of the levels can be commensurate with the times of bound-state formation or with inverse level spacings. In that case, we cannot therefore be positive about the existence of a set of diquark excitations characterized by specific values of the spin and the orbital angular momentum.[1)]

Thus, the presence of two physical scales is used here to factorize the wave function in the problem that involves a heavy diquark and a light constituent quark and which is treated within the nonrelativistic quark model. In this way, the problem of calculating the mass

[1)]In other words, the presence of the gluon sea in the baryon Ξ_{bc} results in unsuppressed $\Delta S_d = 1$ or $\Delta L_d = 1$ transitions of the $|bc\rangle \longrightarrow |bcg\rangle$ type between different excited states of the diquark.

spectrum and the characteristics of bound states in the doubly heavy baryon reduces to two standard problems of searches for stationary energy levels in a two-body system. After that, we take into account relativistic quark-spin-dependent corrections in each of the two subsystems under study. The threshold energy for decay into a heavy baryon and a heavy meson is a natural boundary of the region where the stable states of doubly heavy baryons exist. It was shown in [14] that the presence of such a threshold in various systems can be associated with the existence of a universal feature of confinement in QCD, a limiting interquark distance that cannot be increased without violating the stability of the quark–gluon field (that is, the generation of quark–antiquark pairs from the sea begins as soon as the interquark distance exceeds this value). In other words, a hadronic string of length greater than the critical one decays, with a probability close to unity, into strings of smaller dimensions. Within the potential approach, this effect can be taken into account by restricting a consideration of diquark excited states to the region where the diquark dimensions are less than the critical distance, $r_{QQ'} < r_{\text{conf}} \approx 1.4$–$1.5$ fm. Moreover, the pair-interaction model segregating the diquark structure is reliable only for diquark dimensions smaller than the distance to the light quark, $r_{QQ'} < r_l$.

A feature peculiar to the quark–diquark interpretation of a doubly heavy baryon is that the higher excitations of the diquark that are characterized by different quantum-number values can be mixed owing to the interaction with a light quark, so that we can hardly associate such excitations with specific values of the quantum numbers. Below, the mechanism and character of this effect will be described in detail.

The ensuing exposition is organized as follows. In Section 2, we give an account of a general procedure that makes it possible to calculate the mass spectrum of doubly heavy baryons and which admits the inclusion of quark-spin-dependent corrections to the QCD-motivated potential. We present the results of relevant numerical calculations in Section 3 and briefly discuss our conclusions in Section 4.

2. NONRELATIVISTIC POTENTIAL MODEL

As was indicated in the Introduction, the problem of calculating the mass spectrum of baryons featuring two heavy quarks is reduced here to a consecutive calculation of diquark energy levels and the energy levels of the system formed by a pointlike diquark with the predetermined parameters and a light constituent quark interacting with this diquark. In each stage of the calculation, we apply a two-step procedure: in accordance with the effective theory where the QCD interaction is expanded in terms of the inverse quark mass, the nonrelativistic Schrödinger equation with a QCD-motivated model potential is solved for a first approximation, whereas quark-spin-dependent corrections are introduced as a perturbation at the second step.

2.1. Potential

For a model potential, we make use of that which is due to Buchmüller and Tye. This potential takes into account Coulomb-like corrections in the region of small distances, so that the effective constant of octet-color-state exchange between the quarks is approximated by the QCD running coupling constant in the two-loop approximation; at large distances, a linear growth of the interaction energy is ensured, which leads to confinement. These two regimes appear to be extreme cases of the effective model Gell-Mann–Low beta function, which is presented explicitly. In the antitriplet state, we take into account the factor of 1/2 arising from the color structure of the quark–quark bound state. In the interaction of the diquark with a light constituent quark, this factor is equal to unity.

As was shown in [15], the nonperturbative constituent correction to the nonrelativistic-quark mass coincides with the additive constant subtracted from the Coulomb-like potential. Having determined the heavy-quark masses from a fit of the model to the actual spectrum of charmonium and bottomonium,

$$m_c = 1.486 \text{ GeV}, \quad m_b = 4.88 \text{ GeV} \tag{1}$$

(so that the mass of the heavy-quarkonium level was calculated, for example, as $M(c\bar{c}) = 2m_c + E$, where E is the energy of the corresponding time-independent solution to the Schrödinger equation with a model potential V), we set the mass of the meson featuring one heavy quark to $M(Q\bar{q}) = m_Q + m_q + E$, where the last term is now given by $E = \langle T \rangle + \langle V - \delta V \rangle$. Here, the additive correction to the potential was introduced because the constituent mass is determined as a part of the interaction energy, so that $\delta V = m_q$, where a value of 0.385 GeV is used for m_q according to our fit to the heavy-meson masses.

For various systems, Table 1 quotes the energies of levels as obtained on the basis of the Schrödinger equation with the Buchmüller–Tye potential. Some features of the corresponding wave functions are given in Table 2.

It turned out that, to a high accuracy, the binding energy and the wave function of the light quark are virtually independent on heavy-quark flavors, since the large diquark mass makes but a small contribution to the reduced mass of the system and leads, in this case, to insignificant corrections in the Schrödinger equation. For states under the threshold for the decay of a doubly heavy baryon into a heavy baryon and a heavy meson, the calculated energies of levels of the light constituent quark are

$$E(1s) = 0.38 \text{ GeV},$$
$$E(2s) = 1.09 \text{ GeV}, \quad E(2p) = 0.83 \text{ GeV}.$$

Here, the energy of a level was determined as the sum of the constituent mass and the energy eigenvalue associated with the relevant solution to the time-independent Schrödinger equation. Heavy-quark effective the-

Table 1. Spectrum of the QQ'-diquark levels without allowing for spin splittings: masses and root-mean-square radii

Diquark level	M, GeV	$\langle r^2\rangle^{1/2}$, fm	Diquark level	M, GeV	$\langle r^2\rangle^{1/2}$, fm
		bb			
1*S*	9.74	0.33	2*P*	9.95	0.54
2*S*	10.02	0.69	3*P*	10.15	0.86
3*S*	10.22	1.06	4*P*	10.31	1.14
4*S*	10.37	1.26	5*P*	10.45	1.39
5*S*	10.50	1.50	6*P*	10.58	1.61
3*D*	10.08	0.72	4*D*	10.25	1.01
5*D*	10.39	1.28	6*D*	10.53	1.51
4*F*	10.19	0.87	5*F*	10.34	1.15
6*F*	10.47	1.40	5*G*	10.28	1.01
6*G*	10.42	1.28	6*M*	10.37	1.15
		bc			
1*S*	6.48	0.48	3*P*	6.93	1.16
2*S*	6.79	0.95	4*P*	7.13	1.51
3*S*	7.01	1.33	3*D*	6.85	0.96
2*P*	6.69	0.74	4*D*	7.05	1.35
4*F*	6.97	1.16	5*F*	7.16	1.52
5*G*	7.09	1.34	6*H*	7.19	1.50
		cc			
1*S*	3.16	0.58	3*P*	3.66	1.36
2*S*	3.50	1.12	4*P*	3.90	1.86
3*S*	3.76	1.58	3*D*	3.56	1.13
2*P*	3.39	0.88	4*D*	3.80	1.59

ory employs the scale $\bar{\Lambda} = E(1s)$, whence we conclude that our estimate complies well with the results produced by different approaches. This confirms once again the reliability of phenomenological predictions. For the corresponding radial wave functions and their derivatives at the origin, we have

$$R_{1S}(0) = 0.527\ \text{GeV}^{3/2},$$

$$R_{2S}(0) = 0.278\ \text{GeV}^{3/2}, \quad R'_{2P}(0) = 0.127\ \text{GeV}^{5/2}.$$

The analogous features of the bound state formed by a c quark and a bb diquark are

$$E(1s) = 1.42\ \text{GeV},$$
$$E(2s) = 1.99\ \text{GeV}, \quad E(2p) = 1.84\ \text{GeV}$$

for the energies and

$$R_{1S}(0) = 1.41\ \text{GeV}^{3/2},$$

$$R_{2S}(0) = 1.07\ \text{GeV}^{3/2}, \quad R'_{2P}(0) = 0.511\ \text{GeV}^{5/2}$$

for the wave functions.

For the coupling of the constituent strange quark, we add a current mass of $m_s \approx 100$–150 MeV.

2.2. Spin-Dependent Corrections

Following [16], we introduce spin-dependent corrections that are responsible for the splitting of nL levels both in the diquark and in the system formed by a light constituent quark and a diquark (here, $n = n_r + L + 1$ is the principal quantum number, n_r and L being, respectively, the number of a radial excitation and the orbital angular momentum). For a heavy diquark formed by identical quarks, we have

$$V_{SD}^{(d)}(\mathbf{r}) = \frac{1}{2}\left(\frac{\mathbf{L}_d\cdot\mathbf{S}_d}{2m_Q^2}\right)\left(-\frac{dV(r)}{rdr}+\frac{8}{3}\alpha_s\frac{1}{r^3}\right)$$

$$+\frac{2}{3}\alpha_s\frac{1}{m_Q^2}\frac{\mathbf{L}_d\cdot\mathbf{S}_d}{r^3}+\frac{4}{3}\alpha_s\frac{1}{3m_Q^2}\mathbf{S}_{Q1}\cdot\mathbf{S}_{Q2}[4\pi\delta(\mathbf{r})] \qquad (2)$$

$$-\frac{1}{3}\alpha_s\frac{1}{m_Q^2}\frac{1}{4\mathbf{L}_d^2-3}[6(\mathbf{L}_d\cdot\mathbf{S}_d)^2+3(\mathbf{L}_d\cdot\mathbf{S}_d)-2\mathbf{L}_d^2\mathbf{S}_d^2]\frac{1}{r^3},$$

Table 2. Features of the radial wave function of the QQ' diquark: $R_{d(ns)}(0)$ ($\mathrm{GeV}^{3/2}$) and $R'_{d(np)}(0)$ ($\mathrm{GeV}^{5/2}$)

nL	$R_{d(ns)}(0)$	nL	$R'_{d(np)}(0)$
		bb	
1*S*	1.346	2*P*	0.479
2*S*	1.027	3*P*	0.539
3*S*	0.782	4*P*	0.585
4*S*	0.681	5*P*	0.343
		bc	
1*S*	0.726	2*P*	0.202
2*S*	0.601	3*P*	0.240
3*S*	0.561	4*P*	
		cc	
1*S*	0.530	2*P*	0.128
2*S*	0.452	3*P*	0.158

where $\mathbf{L}_d$ is the orbital angular momentum in the diquark system and $\mathbf{S}_d$ is the total spin of the quarks constituting the diquark. Upon taking into account the interaction with the light constituent quark, we obtain ($\mathbf{S} = \mathbf{S}_d + \mathbf{S}_l$)

$$V_{SD}^{(l)}(\mathbf{r}) = \frac{1}{4}\left(\frac{\mathbf{L}\cdot\mathbf{S}_d}{2m_Q^2} + \frac{2\mathbf{L}\cdot\mathbf{S}_l}{2m_l^2}\right)\left(-\frac{dV(r)}{rdr} + \frac{8}{3}\alpha_s\frac{1}{r^3}\right)$$
$$+ \frac{1}{3}\alpha_s\frac{1}{m_Q m_l}\frac{(\mathbf{L}\cdot\mathbf{S}_d + 2\mathbf{L}\cdot\mathbf{S}_l)}{r^3}$$
$$+ \frac{4}{3}\alpha_s\frac{1}{3m_Q m_l}(\mathbf{S}_d + \mathbf{L}_d)\cdot\mathbf{S}_l[4\pi\delta(\mathbf{r})] \qquad (3)$$
$$-\frac{1}{3}\alpha_s\frac{1}{m_Q m_l}\frac{1}{4\mathbf{L}^2 - 3}[6(\mathbf{L}\cdot\mathbf{S})^2 + 3(\mathbf{L}\cdot\mathbf{S}) - 2\mathbf{L}^2\mathbf{S}^2$$
$$- 6(\mathbf{L}\cdot\mathbf{S}_d)^2 - 3(\mathbf{L}\cdot\mathbf{S}_d) + 2\mathbf{L}^2\mathbf{S}_d^2]\frac{1}{r^3},$$

where the first term is associated with the relativistic correction to effective scalar exchange, whereas the remaining terms are generated by corrections to effective one-gluon exchange characterized by the constant α_s.

The effective parameter α_s can be evaluated in the following way. In the *s*-wave heavy quarkonium ($Q_1\bar{Q}_2$), the splitting is given by

$$\Delta M(ns) = \frac{8}{9}\alpha_s\frac{1}{m_1 m_2}|R_{nS}(0)|^2, \qquad (4)$$

where $R_{nS}(0)$ is the radial wave function of the quarkonium at the origin. From the experimental value of

$$\Delta M(1S, c\bar{c}) = 117 \pm 2 \text{ MeV} \qquad (5)$$

and from the value of $R_{1S}(0)$ as determined on the basis of our model, we can find the parameter $\alpha_s(\Psi)$.

By using the one-loop expression for the QCD running coupling constant,

$$\alpha_s(p^2) = \frac{4\pi}{b\ln(p^2/\Lambda_{\mathrm{QCD}}^2)}, \qquad (6)$$

where $b = 11 - 2n_f/3$ with $n_f = 3$ for $p^2 < m_c^2$, we will further take into account the dependence of this parameter on the reduced mass of the system (μ). From the phenomenology of potential models, it is well known that the mean kinetic energy of quark motion in a bound state is virtually independent of quark flavors and is given by

$$\langle T_d\rangle \approx 0.2 \text{ GeV}, \qquad (7)$$

and

$$\langle T_l\rangle \approx 0.4 \text{ GeV} \qquad (8)$$

for the antitriplet and singlet couplings, respectively. Substituting the definition of nonrelativistic kinetic energy,

$$\langle T\rangle = \langle p^2\rangle/2\mu, \qquad (9)$$

into (6), we arrive at

$$\alpha_s(p^2) = \frac{4\pi}{b\ln(2\langle T\rangle\mu/\Lambda_{\mathrm{QCD}}^2)}. \qquad (10)$$

From (4) and (5), we can obtain the numerical value of $\Lambda_{\mathrm{QCD}} \approx 113$ MeV.

For identical quarks in a diquark, the scheme for calculating *LS*-coupling corrections that is well known from the physics of heavy quarkonium is applicable; for the interaction with a light quark, we make use of the *jj*-coupling scheme (here, $\mathbf{L}\cdot\mathbf{S}_l$ is diagonal for given $\mathbf{J}_l$, $\mathbf{J}_l = \mathbf{L} + \mathbf{S}_l$ and $\mathbf{J} = \mathbf{J}_l + \bar{\mathbf{J}}$, where $\mathbf{J}$ is the total spin of the baryon and $\bar{\mathbf{J}} = \mathbf{S}_d + \mathbf{L}_d$ is the total angular momentum of the diquark).

In order to estimate various contributions and the mixing of states, we can make use of the basis transformations (in the following, we set $\mathbf{S} = \mathbf{S}_l + \bar{\mathbf{J}}$)

$$|J;\ J_l\rangle = \sum_S (-1)^{(\bar{J}+S_l+L+J)}$$
$$\times\sqrt{(2S+1)(2J_l+1)}\begin{Bmatrix} \bar{J} & S_l & S \\ L & J & J_l \end{Bmatrix}|J;\ S\rangle, \qquad (11)$$

$$|J;\ J_l\rangle = \sum_{J_d}(-1)^{(\bar{J}+S_l+L+J)} \times \sqrt{(2J_d+1)(2J_l+1)}\begin{Bmatrix} \bar{J} & L & J_d \\ S_l & J & J_l \end{Bmatrix}|J;\ J_d\rangle. \quad (12)$$

Thus, we have given a detailed account of the procedure for calculating the mass spectrum of doubly heavy baryons. The results that we obtained on the basis of this procedure are presented in the next section.

3. NUMERICAL RESULTS

In this section, we display the mass spectra calculated with allowance for the quark-spin-dependent splitting of levels. As was explained in the Introduction, doubly heavy baryons formed by identical heavy quarks admit quite a reliable interpretation in terms of the total angular momentum and the orbital angular momentum of diquark excitations. For the *bc* diquark, we present only the results for the spin splitting of the 1*S* ground state since, for higher excitations of this diquark, the allowed emission of a soft gluon disturbs the above classification of levels.

It is obvious that, within the quark–diquark model of bound states of doubly heavy baryons, the most reliable results are obtained for the system featuring the quarks of the largest mass—that is, for Ξ_{bb}.

3.1. Ξ_{bb} *Baryons*

The quantum numbers of the levels will be denoted here by $n_dL_dn_lL_l$; that is, each level is specified in terms of four quantum numbers: the principal quantum number in the diquark, n_d; the orbital angular momentum in the diquark, L_d; the principal quantum number of light-quark excitation, n_l; and the orbital angular momentum of the light quark, L_l. According to our calculations, the splitting $\Delta^{(J)}$ of the 1*S*2*p* level is given by

$$\Delta^{(5/2)} = 10.3\ \text{MeV}.$$

States that are characterized by the total spin of $J = 3/2$ (or 1/2) may have different J_l values, whence it follows that, in the calculations by perturbation theory constructed on the basis of pure states in the total angular momentum of the light constituent quark, such states acquire nonzero mixing. For $J = 3/2$, the mixing matrix has the form

$$\begin{pmatrix} -3.0 & -0.5 \\ -0.5 & 11.4 \end{pmatrix}\text{MeV}.$$

It can be seen that, in practice, the mixing can be disregarded here and that the shifts of the levels are given by

$$\lambda_1' = -3.0\ \text{MeV}, \quad \lambda_1 = 11.4\ \text{MeV}.$$

For $J = 1/2$, the mixing matrix appears to be

$$\begin{pmatrix} -5.7 & -17.8 \\ -17.8 & -14.9 \end{pmatrix}\text{MeV}.$$

Its eigenvectors are

$$\left|1S2p\left(\frac{1'}{2}\right)\right\rangle = 0.790\left|J_l = \frac{3}{2}\right\rangle - 0.613\left|J_l = \frac{1}{2}\right\rangle,$$

$$\left|1S2p\left(\frac{1}{2}\right)\right\rangle = 0.613\left|J_l = \frac{3}{2}\right\rangle + 0.790\left|J_l = \frac{1}{2}\right\rangle,$$

while the corresponding eigenvalues are given by

$$\lambda_2' = 8.1\ \text{MeV}, \quad \lambda_2 = -28.7\ \text{MeV}.$$

For the 2*S*2*p* level, the splitting is

$$\Delta^{(5/2)} = 10.3\ \text{MeV}.$$

For $J = 3/2$, the mixing matrix has the form

$$\begin{pmatrix} -3.6 & -0.5 \\ -0.5 & 12.4 \end{pmatrix}\text{MeV},$$

so that we have

$$\lambda_1' = -3.6\ \text{MeV}, \quad \lambda_1 = 12.4\ \text{MeV}.$$

For $J = 1/2$, the mixing matrix appears to be

$$\begin{pmatrix} -6.1 & -17.6 \\ -17.6 & -13.5 \end{pmatrix}\text{MeV}.$$

Its eigenvectors are given by

$$\left|1S2p\left(\frac{1'}{2}\right)\right\rangle = 0.776\left|J_l = \frac{3}{2}\right\rangle - 0.631\left|J_l = \frac{1}{2}\right\rangle,$$

$$\left|1S2p\left(\frac{1}{2}\right)\right\rangle = 0.631\left|J_l = \frac{3}{2}\right\rangle + 0.776\left|J_l = \frac{1}{2}\right\rangle.$$

The corresponding eigenvalues are

$$\lambda_2' = 8.2\ \text{MeV}, \quad \lambda_2 = -27.8\ \text{MeV}.$$

From the above, it can be seen immediately that the distinction between the wave functions that is due to variations in the mass of the diquark subsystem is indeed immaterial.

The splitting of diquark levels, $\Delta^{(J_d)}$, takes the following values:

for 3*D*1*s*,

$$\Delta^{(3)} = -0.06\ \text{MeV},$$

$$\Delta^{(2)} = 0.2\ \text{MeV},$$

$$\Delta^{(1)} = -0.2 \text{ MeV};$$

for $4D1s$,

$$\Delta^{(3)} = -2.6 \text{ MeV},$$

$$\Delta^{(2)} = -0.8 \text{ MeV},$$

$$\Delta^{(1)} = -4.6 \text{ MeV};$$

for $5D1s$,

$$\Delta^{(3)} = 2.6 \text{ MeV},$$

$$\Delta^{(2)} = -0.9 \text{ MeV},$$

$$\Delta^{(1)} = -4.7 \text{ MeV};$$

for $5G1s$,

$$\Delta^{(5)} = -0.3 \text{ MeV},$$

$$\Delta^{(4)} = 0.3 \text{ MeV},$$

$$\Delta^{(3)} = 1.1 \text{ MeV},$$

$$\Delta^{(2)} = 1.7 \text{ MeV},$$

$$\Delta^{(1)} = 2.0 \text{ MeV};$$

for $6G1s$,

$$\Delta^{(5)} = 3.2 \text{ MeV},$$

$$\Delta^{(4)} = -0.5 \text{ MeV},$$

$$\Delta^{(3)} = -4.4 \text{ MeV},$$

$$\Delta^{(2)} = -7.9 \text{ MeV},$$

$$\Delta^{(1)} = -10.5 \text{ MeV}.$$

It can be seen that, for the excitations of a diquark whose dimensions are smaller than the distance to the light quark—that is, for a diquark state characterized by a moderately small value of the principal quantum number—the above corrections are insignificant in relation to the uncertainties of the method ($\delta M \approx 30$–40 MeV).

For the hyperfine spin–spin splitting in the quark–diquark system, we have

$$\Delta^{(l)}_{\text{h.f}} = \frac{2}{9}\left[J(J+1) - \bar{J}(\bar{J}+1) - \frac{3}{4}\right] \times \alpha_s(2\mu T)\frac{1}{m_c m_l}|R_l(0)|^2,$$

where $R_l(0)$ is the radial wave function of the light constituent quark at the origin. For the analogous shift of the diquark level, the result is

$$\Delta^{(d)}_{\text{h.f}} = \frac{1}{9}\alpha_s(2\mu T)\frac{1}{m_c^2}|R_d(0)|^2.$$

The mass spectrum of the Ξ^-_{bb} and Ξ^0_{bb} baryons is presented in Fig. 1 and in Table 3, where we quoted our results only for *S*, *P*, and *D* levels.

As can be seen from Fig. 1, the most reliable predictions were obtained for the masses of the $1S1s$ ($J^P = 3/2^+, 1/2^+$), $2P1s$ ($J^P = 3/2^-, 1/2^-$), and $3D1s$ ($J^P = 7/2^+, \ldots, 1/2^+$) baryons. We note that the $2P1s$ level is metastable because, for a transition to the ground state to occur, both the orbital angular momentum and the total spin of the heavy quarks in the diquark must undergo changes. As an analog of such a transition, we can indicate the transition between the ortho- and parahydrogen states in an H_2 molecule in the nonuniform external field that is generated by the magnetic moments of other molecules. For the $2P1s \longrightarrow 1S1s$ transition, the role of such an external field is played by the nonuniform chromomagnetic field of the light quark. The corresponding perturbation has the form

$$\delta V \sim \frac{1}{m_Q}[\mathbf{S}_1 \cdot \mathbf{H}_1 + \mathbf{S}_2 \cdot \mathbf{H}_2 - (\mathbf{S}_1 + \mathbf{S}_2) \cdot \langle \mathbf{H} \rangle]$$

$$= \frac{1}{2m_Q}(\nabla \cdot \mathbf{r}_d)(\mathbf{S}_1 - \mathbf{S}_2) \cdot \mathbf{H}$$

$$\sim \frac{1}{m_Q}\frac{\mathbf{r}_l \cdot \mathbf{r}_d}{m_q r_l^5}(\mathbf{S}_1 - \mathbf{S}_2) \cdot \mathbf{J}_l f(r_l),$$

where $f(r_l)$ is a dimensionless nonperturbative function that depends on the coordinate of the light quark with respect to the diquark. It is obvious that the perturbation δV also changes the orbital angular momentum of the light quark. It mixes states having identical values of J^P. If the splitting is not small (for example, that for $2P1s$–$1S2p$, where $\Delta E \sim \Lambda_{\text{QCD}}$), the mixing is suppressed:

$$\delta V/\Delta E \sim \frac{1}{m_Q m_q}\frac{r_d}{r_l^4}\frac{1}{\Delta E} \ll 1.$$

Since the $1S2p$ admixture in the $2P1s$ state is small, the $2P1s$ levels are quasistationary; that is, the hadronic transitions that occur from them to the ground state and which are accompanied by pion emission are suppressed (there is also additional suppression associated with the smallness of the phase space). In view of this, the spectra of $\Xi_{bb}\pi$ pairs are expected to display anomalously narrow resonances associated with the decays of such $J^P = 3/2^-, 1/2^-$ quasistationary states. A direct experimental observation of the above-type levels would suggest the existence of diquark excitations and would furnish information about the character of the dependence $f(r_l)$—that is, about the origin of the nonhomogeneous chromomagnetic field in the nonperturbative region.

It is obvious that the $J^P = 7/2^+, 5/2^+$ $3D1s$ states—within a QCD multipole expansion, these states deexcite into the ground-state level via a quadrupole gluon emission ($E2$ hadronization process $gq \longrightarrow q'\pi$)—are also quasistationary ones.

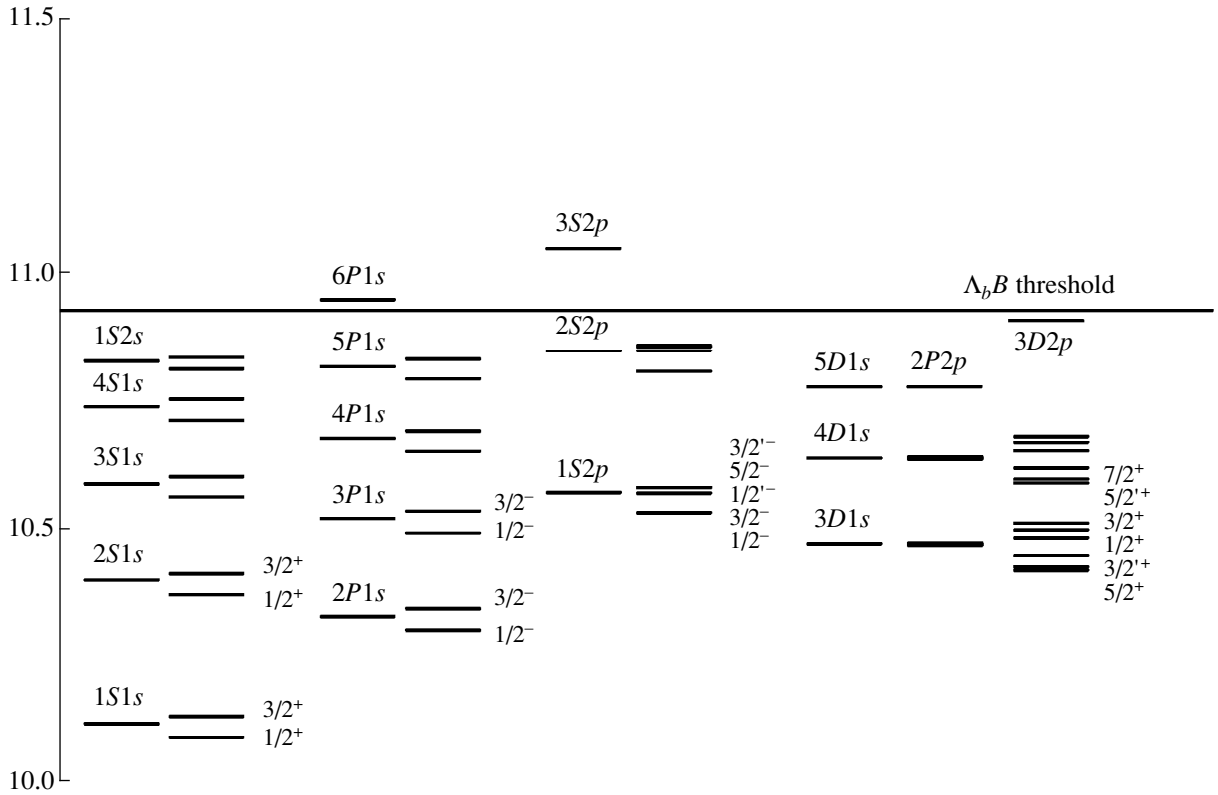

Fig. 1. Spectrum of the Ξ_{bb}^- and Ξ_{bb}^0 baryons featuring two b quarks with allowance for the quark-spin-dependent splitting of low-lying excitations (masses are presented in GeV).

As to higher excitations, we can indicate by way of example that the energies of the $3P1s$ states are close to the energies of the $J^P = 3/2^-$, $1/2^-$ $1S2p$ levels; therefore, the contributions of the operators changing the diquark orbital angular momentum and spin can lead to a substantial mixing (with the amplitude $\Delta V_{nn'}/\Delta E_{nn'} \sim 1$), despite the fact that these contributions are suppressed in direct proportion to the inverse heavy-quark mass and the small dimension of the diquark. We believe, however, that this mixing shifts the masses of the states only slightly. A more important circumstance is that a significant $1S2p$ admixture in the $3P1s$ state renders it unstable to transitions to the $1S1s$ ground state via $E1$ gluon emission; in the physical spectrum of hadrons, this leads to decays accompanied, for example, by pion emission.[2)]

The $J^P = 5/2^-$ $1S2p$ level has definite values of the light-quark and diquark quantum numbers, because there are no close levels with the same values of J^P. However, its width with respect to the transition to the ground-state level via pion emission is suppressed by no factor, so that it is expected to be great ($\Gamma \sim 100$ MeV).

We also note that

$$3/2^- \longrightarrow 3/2^+\pi \text{ in the } S \text{ wave},$$

$$3/2^- \longrightarrow 1/2^+\pi \text{ in the } D \text{ wave},$$

$$1/2^- \longrightarrow 3/2^+\pi \text{ in the } D \text{ wave},$$

$$1/2^- \longrightarrow 1/2^+\pi \text{ in the } S \text{ wave}.$$

Here, the D-wave transitions are suppressed in proportion to the small ratio of the recoil momenta of the baryon involved to its mass.

The width of the low-lying $J^P = 3/2^+$ state is completely determined by the radiative electromagnetic $M1$ transition to the $J^P = 1/2^+$ ground state.

3.2. Ξ_{cc} Baryons

For the doubly charmed baryon, the above computational procedure leads to the results listed below.

For the $1S2p$ state, the splitting is given by

$$\Delta^{(5/2)} = 17.4 \text{ MeV}.$$

For $J = 3/2$, mixing is determined by the matrix

$$\begin{pmatrix} 4.3 & -1.7 \\ -1.7 & 7.8 \end{pmatrix} \text{MeV}.$$

[2)]We recall that the $\Xi_{QQ'}$ baryons are isodoublets.

Table 3. Mass spectrum of the Ξ_{bb}^{-} and Ξ_{bb}^{0} baryons

$(n_dL_dn_lL_l)$, J^P	Mass, GeV	$(n_dL_dn_lL_l)$, J^P	Mass, GeV
$(1S1s)1/2^+$	10.093	$(3P1s)1/2^-$	10.493
$(1S1s)3/2^+$	10.133	$(3D1s)5/2'^+$	10.497
$(2P1s)1/2^-$	10.310	$(3D1s)7/2^+$	10.510
$(2P1s)3/2^-$	10.343	$(3P1s)3/2^-$	10.533
$(2S1s)1/2^+$	10.373	$(1S2p)1/2^-$	10.541
$(2S1s)3/2^+$	10.413	$(1S2p)3/2^-$	10.567
$(3D1s)5/2^+$	10.416	$(1S2p)1/2'^-$	10.578
$(3D1s)3/2'^+$	10.430	$(1S2p)5/2^-$	10.580
$(3D1s)1/2^+$	10.463	$(1S2p)3/2'^-$	10.581
$(3D1s)3/2^+$	10.483	$(3S1s)1/2^+$	10.563

Its eigenvectors appear to be

$$\left|1S2p\left(\frac{3'}{2}\right)\right\rangle = 0.986\left|J_l = \frac{3}{2}\right\rangle + 0.164\left|J_l = \frac{1}{2}\right\rangle,$$

$$\left|1S2p\left(\frac{3}{2}\right)\right\rangle = -0.164\left|J_l = \frac{3}{2}\right\rangle + 0.986\left|J_l = \frac{1}{2}\right\rangle.$$

The corresponding eigenvalues are

$$\lambda_1' = 3.6 \text{ MeV}, \quad \lambda_1 = 8.5 \text{ MeV}.$$

For $J = 1/2$, the mixing matrix has the form

$$\begin{pmatrix} -3.6 & -55.0 \\ -55.0 & -73.0 \end{pmatrix} \text{MeV}.$$

Its eigenvectors can be written as

$$\left|1S2p\left(\frac{1'}{2}\right)\right\rangle = 0.957\left|J_l = \frac{3}{2}\right\rangle - 0.291\left|J_l = \frac{1}{2}\right\rangle,$$

$$\left|1S2p\left(\frac{1}{2}\right)\right\rangle = 0.291\left|J_l = \frac{3}{2}\right\rangle + 0.957\left|J_l = \frac{1}{2}\right\rangle,$$

while the corresponding eigenvalues are

$$\lambda_2' = 26.8 \text{ MeV}, \quad \lambda_2 = -103.3 \text{ MeV}.$$

For the splitting of the $3D$ diquark level, we have

$$\Delta^{(3)} = -3.02 \text{ MeV},$$

$$\Delta^{(2)} = 2.19 \text{ MeV},$$

$$\Delta^{(1)} = 3.39 \text{ MeV}.$$

We must further take into account hyperfine spin–spin corrections in the quark–diquark system.

For the $1S$- and $2S$-wave levels of the diquark, the shifts of the vector states are

$$\Delta(1S) = 6.3 \text{ MeV},$$

$$\Delta(2S) = 4.6 \text{ MeV}.$$

The mass spectra of Ξ_{cc}^{++} and Ξ_{cc}^{+} baryons are presented in Fig. 1 and in Table 4.

3.3. Ξ_{bc} Baryons

It was indicated in the Introduction that, in all probability, a heavy diquark formed by quarks of different flavors is unstable with respect to the emission of soft gluons; therefore, the Fock state of such a baryon must have a considerable nonperturbative admixture of configurations that include gluons and a diquark with different values of the spin S_d and the angular orbital momentum L_d,

$$|B_{bcq}\rangle = O_B|bc\bar{3}_c^{S_d, L_d}, q\rangle + H_1|bc\bar{3}_c^{S_d \pm 1, L_d}, g, q\rangle + H_2|bc\bar{3}_c^{S_d, L_d \pm 1}, g, q\rangle + \ldots,$$

the amplitudes H_1 and H_2 being commensurate with O_B. In the heavy quarkonium, the contributions of analogous operators of color-octet states are suppressed by the probability of emission from nonrelativistic quarks in a small volume determined by the dimension of the singlet quark–antiquark system. In the present case, however, a soft gluon is constrained only by the conventional confinement scale, so that there is no suppression.

In this situation, we deem that it would not be quite correct to calculate the masses of excited Ξ_{bc} baryons according to the above scheme. For this reason, we quote here only the result for the $J^P = 1/2^+$ ground state:

$$M_{\Xi_{bc}'} = 6.85 \text{ GeV}, \quad M_{\Xi_{bc}} = 6.82 \text{ GeV}.$$

For the vector diquark, we assumed that, in the interaction with the light constituent quark, the spin-dependent splitting is determined by the conventional contact interaction of the magnetic moments of two pointlike subsystems. The diagram of baryon levels that takes no

Table 4. Mass spectrum of the Ξ_{cc}^{++} and Ξ_{cc}^{+} baryons

$(n_dL_dn_lL_l)$, J^P	Mass, GeV	$(n_dL_dn_lL_l)$, J^P	Mass, GeV
$(1S1s)1/2^+$	3.478	$(3P1s)1/2^-$	3.972
$(1S1s)3/2^+$	3.61	$(3D1s)3/2'^+$	4.007
$(2P1s)1/2^-$	3.702	$(1S2p)3/2'^-$	4.034
$(3D1s)5/2^+$	3.781	$(1S2p)3/2^-$	4.039
$(2S1s)1/2^+$	3.812	$(1S2p)5/2^-$	4.047
$(3D1s)3/2^+$	3.83	$(3D1s)5/2'^+$	4.05
$(2P1s)3/2^-$	3.834	$(1S2p)1/2'^-$	4.052
$(3D1s)1/2^+$	3.875	$(3S1s)1/2^+$	4.072
$(1S2p)1/2^-$	3.927	$(3D1s)7/2^+$	4.089
$(2S1s)3/2^+$	3.944	$(3P1s)3/2^-$	4.104

account of the spin-dependent perturbation, which is suppressed in inverse proportion to the heavy-quark mass, is shown in Fig. 3.

3.4. Doubly Heavy Baryons Featuring a Strange Quark: $\Omega_{QQ'}$

In the leading approximation, we assume that the wave functions and the excitation energies of the strange quark are close to the analogous features for baryons featuring u and d quarks. Apart from the additive upward shift of the masses by the current mass of the strange quark, $m_s \approx M(D_s) - M(D) \approx M(B_s) - M(B) \approx 0.1$ GeV, the set of levels of the $\Omega_{QQ'}$ baryons that disregards the quark-spin-dependent splitting is therefore expected to reproduce the set of levels of the $\Xi_{QQ'}$ baryons.

Further, we assume that the spin–spin splitting of low-lying states of the $\Omega_{QQ'}$ baryons for $2P1s$ and $3D1s$ n_dSn_ls levels is 20–30% smaller than the corresponding

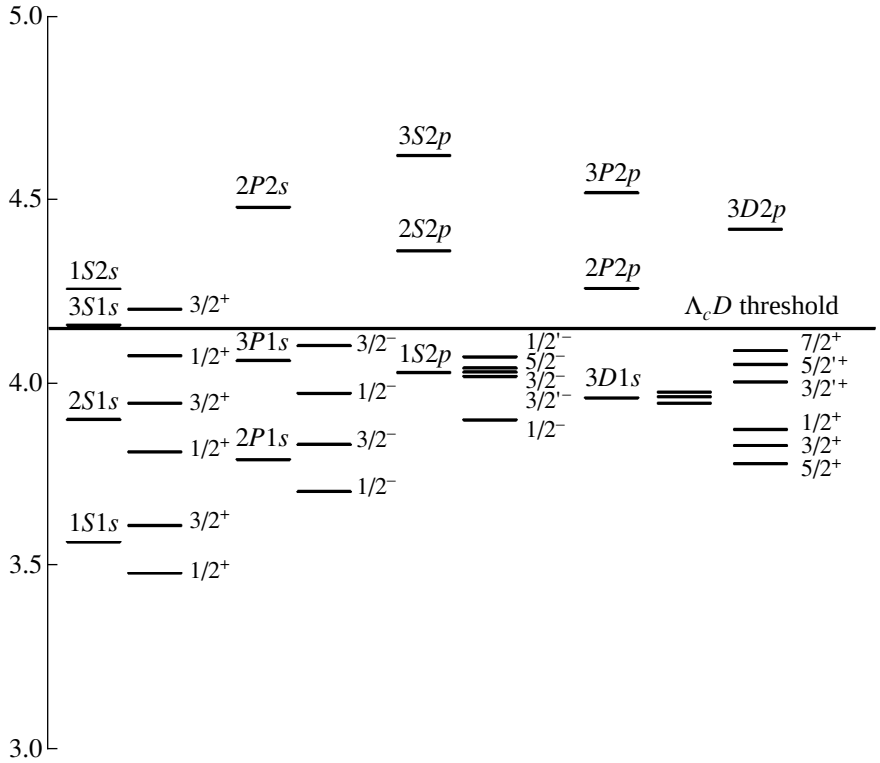

Fig. 2. Spectrum of the Ξ_{cc}^{++} and Ξ_{cc}^{+} baryons (masses are presented in GeV).

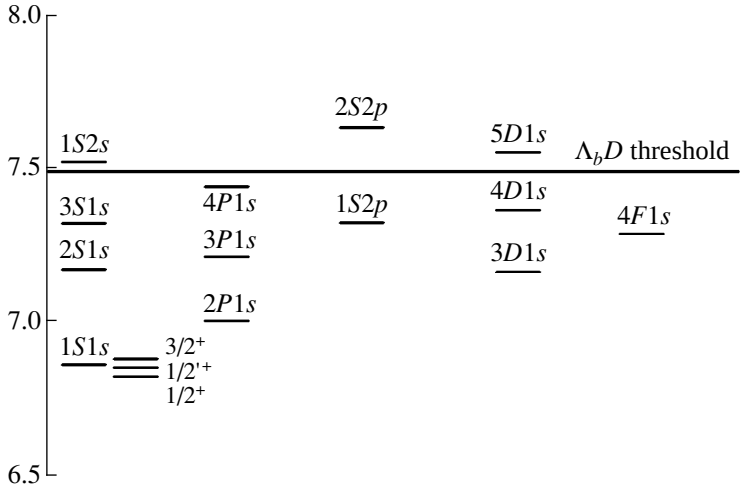

Fig. 3. Spectrum of the Ξ_{bc}^{+} and Ξ_{bc}^{0} baryons without allowing for the splitting of higher excitations (masses are presented in GeV).

splitting in the $\Xi_{QQ'}$ baryons (factor of $m_{u,d}/m_s$). For the $1S2p$ level, we can use the computational procedure described above. By way of example, we indicate that, in the Ω_{bb} baryons, the matrix that describes the mixing of states characterized by different values of the total angular momentum of the light constituent quark can be closely approximated by a diagonal matrix. This means that a dominant perturbative term has the form

$$\frac{1}{4}\left(\frac{2\mathbf{L}\cdot\mathbf{S}_l}{2m_l^2}\right)\left(-\frac{dV(r)}{rdr}+\frac{8}{3}\alpha_s\frac{1}{r^3}\right).$$

Therefore, we can assume that the splitting of the $1S2p$ level is determined by the factor $m_{u,d}^2/m_s^2$; that is, it is very small (40% less than in Ξ_{bb}).

In the Ω_{cc} baryon, the factor m_s/m_c is not small, whence it follows that, for $1S2p$, the matrix describing the mixing of states characterized by different values of the total angular momentum is nondiagonal; as a result, the order of the $1S2p$ spin states in Ω_{cc} can be somewhat different from that in Ξ_{cc}.

The $\Omega_{QQ'}$ baryons have a much more interesting feature. Even with allowance for the mixing of levels characterized by different spins and orbital angular momenta of the subsystems, the lowest S and P excitations of the diquark are quasistationary with respect to strong-interaction-induced decays since the emission of a gluon is accompanied by its hadronization into kaons (transitions $\Omega_{QQ'} \longrightarrow \Xi_{QQ'} + K$) and since single pion emission is forbidden by the isospin- and strangeness-conservation laws; in addition, relevant hadronic transitions featuring kaons do not occur because of an insufficient mass splitting between the levels of $\Omega_{QQ'}$ and $\Xi_{QQ'}$, whereas decays resulting in the emission of isosinglet pion pairs are suppressed because of the small phase space or are merely forbidden. Thus, radiative electromagnetic transitions to the ground-state level appear to be dominant modes of the decays of low-lying excitations of $\Omega_{QQ'}$.

3.5. Ω_{bbc} Baryons

Within the quark–diquark picture, it is possible to construct the model of baryons featuring three heavy quarks (*bbc*). However, our calculations revealed that the dimensions of the diquark are commensurate with the root-mean square distance to the charmed quark; therefore, the model assumption about a compact heavy diquark may prove, in this case, to be insufficiently accurate for calculating the masses of the levels. As to spin-dependent splitting, it is negligibly small for interactions within the diquark (see above). The spin–spin splitting in the system formed by the vector diquark and a charmed quark is given by

$$\Delta(1s) = 33\ \text{MeV}, \quad \Delta(2s) = 18\ \text{MeV}.$$

For the splitting of the $1S2p$ state, the shifts of the levels are small, so that the correction of –33 MeV must be taken into account only for one of the $J^P = 1/2$ levels. In the $3D1s$ state, the splitting is determined by spin–spin interaction. The features of charmed-quark excitations in the model based on the Buchmüller–Tye potential were indicated above. Eventually, we arrive at the diagram of levels of the Ω_{bbc} baryons that is represented in Fig. 4 and in Table 5.

We further note that, because of the small splitting of levels, the excitations over the ground state of the Ω_{bbc}^{0} can be mixed in some cases rather strongly (with large amplitudes, but with small mass shifts)—for example, this is so in the case of $3P1s$–$1S2p$ mixing for $J^P = 1/2^-, 3/2^-$ and in the case of $2S1s$–$3D1s$ mixing for $J^P = 1/2^+, 3/2^+$. We believe that the predictions that we

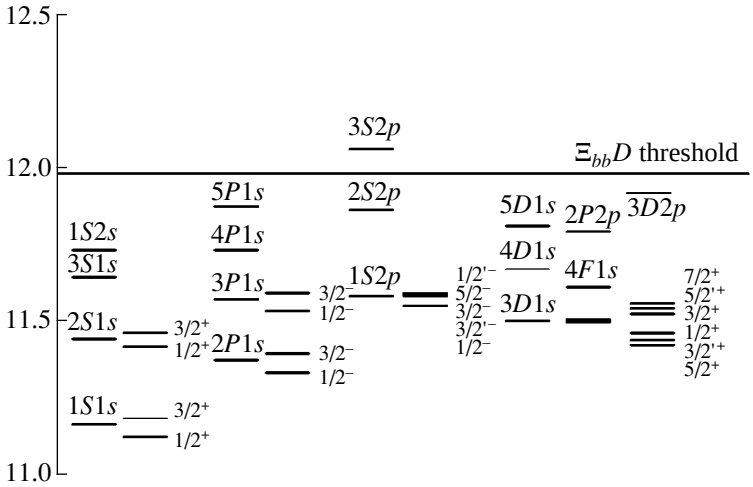

Fig. 4. Spectrum of the Ω^0_{bbc} baryons with allowance for the quark-spin-dependent splitting of low-lying excitations (masses are presented in GeV).

obtained are quite reliable for $J^P = 1/2^+$, $3/2^+$ $1S1s$; $J^P = 5/2^-$ $1S2p$; and $J^P = 5/2^+$, $7/2^+$ $3D1s$ states. It is for these excitations that the multipole expansion makes it possible to predict reliably the widths with respect to radiative electromagnetic transitions to the ground state. As to the widths with respect to transitions involving mixed states, they are greatly affected by the model-dependent amplitudes of admixtures. In this connection, an experimental investigation of electromagnetic transitions in the family of the Ω^0_{bbc} baryons could furnish valuable information about the mechanism of mixing of various levels in baryon systems. It should be noted that the sum of the contribution of electromagnetic transitions and the contribution from pion-pair emission—if the latter is not forbidden by the phase-space conditions—saturates the total widths of the excited levels of Ω^0_{bbc}. There are reasons to expect that the total width in question lies in the range $\Gamma \sim 10$–100 keV.

Thus, the Ω^0_{bbc} system can be characterized by a large number of narrow quasistationary states.

4. CONCLUSION

A detailed analysis of the spectroscopic features of baryons involving two heavy quarks has been performed in the approximation of a quark–diquark factorization of the baryon wave functions. This analysis relies on the nonrelativistic constituent-quark model employing the Buchmüller–Tye potential. The applicability range of the above approximations has been outlined.

Quark-spin-dependent relativistic corrections to the potential have been taken into account in the diquark

Table 5. Mass spectrum of the Ω^0_{bbc} baryons

$(n_dL_dn_lL_l)$, J^P	Mass, GeV	$(n_dL_dn_lL_l)$, J^P	Mass, GeV
$(1S1s)1/2^+$	11.12	$(3D1s)3/2'^+$	11.52
$(1S1s)3/2^+$	11.18	$(3D1s)5/2'^+$	11.54
$(2P1s)1/2^-$	11.33	$(1S2p)1/2^-$	11.55
$(2P1s)3/2^-$	11.39	$(3D1s)7/2^+$	11.56
$(2S1s)1/2^+$	11.40	$(1S2p)3/2'^-$	11.58
$(3D1s)5/2^+$	11.42	$(1S2p)3/2^-$	11.58
$(3D1s)3/2^+$	11.44	$(1S2p)1/2'^-$	11.59
$(3D1s)1/2^+$	11.46	$(1S2p)5/2^-$	11.59
$(2S1s)3/2^+$	11.46	$(3P1s)3/2^-$	11.59
$(3P1s)1/2^-$	11.52	$(3S1s)1/2^+$	11.62

subsystem and in the system formed by a light quark and a diquark. As a result, a set of bound excited states that are quasistable with respect to hadronic transitions to the ground-state level has been found below the threshold for the hadronic decay of our system into a heavy baryon and a heavy meson, each containing one heavy quark. Physical reasons for this quasistability of the above levels have been considered in detail. In particular, the property of quasistability must be peculiar to baryons featuring two identical quarks, where the Pauli exclusion principle effect combined with the fact that the contributions of the operators responsible for hadronic decays and for the mixing of levels are suppressed in proportion to the inverse heavy-quark mass and to the small dimension of the diquark. This suppression stems from the need for changing simultaneously the spin and the orbital angular momentum of the compact diquark. In baryonic systems formed by two heavy quarks and a strange quark, the quasistability of low-lying excitations of the diquark is additionally ensured by the fact that transitions accompanied by single kaon emission are forbidden by the isospin- and strangeness-conservation laws.

The characteristics of the wave functions can be used in calculating the cross sections for the production of doubly heavy baryons in the quark–diquark approximation.

ACKNOWLEDGMENTS

This work was supported in part by the Russian Foundation for Basic Research (project nos. 96-02-18216 and 96-15-96575).

REFERENCES

1. F. Abe *et al*., Preprint No. FERMILAB-PUB-98-157-E, FERMILAB (1998); hep-ex/9805034; Preprint No. FERMILAB-PUB-98-121-E, FERMILAB (1998); hep-ex/9804014.
2. Particle Data Group (C. Caso *et al.*), Eur. Phys. J. C **3**, 1 (1998).
3. S. S. Gershtein *et al.*, Preprint No. IHEP 98-22, IHEP (1998); hep-ph/9803433; Usp. Fiz. Nauk **165**, 3 (1995) [Sov. Phys Usp. **38**, 1 (1995)].
4. V. V. Kiselev, A. K. Likhoded, and A. I. Onishchenko, Preprint No. 98-079, DESY (1998); hep-ph/9807354.
5. V. V. Kiselev, A. K. Likhoded, and M. V. Shevlyagin, Phys. Lett. B **332**, 411 (1994); A. Falk *et al.*, Phys. Rev. D **49**, 555 (1994); A. V. Berezhnoy, V. V. Kiselev, and A. K. Likhoded, Yad. Fiz. **59**, 909 (1996) [Phys. At. Nucl. **59**, 870 (1996)]; S. P. Baranov, Phys. Rev. D **56**, 3046 (1997); A. V. Berezhnoy, V. V. Kiselev, A. K. Likhoded, *et al.*, Phys. Rev. D **57**, 4385 (1998).
6. S. J. Brodsky, P. Hoyer, C. Peterson, *et al.*, Phys. Lett. B **93**, 451 (1980); S. J. Brodsky, C. Peterson, and N. Sakai, Phys. Rev. D **23**, 2745 (1981); R. Vogt and S. J. Brodsky, Nucl. Phys. B **438**, 261 (1995); **478**, 311 (1996).
7. E. Bagan, M. Chabab, and S. Narison, Phys. Lett. B **306**, 350 (1993); E. Bagan, H. G. Dosch, P. Gosdzinsky, *et al.*, Z. Phys. C **64**, 57 (1994); J. G. Körner, M. Krämer, and D. Pirjol, Prog. Part. Nucl. Phys. **33**, 787 (1994); R. Roncaglia, D. B. Lichtenberg, and E. Predazzi, Phys. Rev. D **52**, 1722 (1995); D. Ebert, R. N. Faustov, V. O. Galkin, *et al.*, Z. Phys. C **76**, 111 (1997).
8. S. S. Gershtein *et al.*, Preprint No. 98-080, DESY (1998); hep-ph/9807375.
9. C. Quigg and J. L. Rosner, Phys. Rep. **56**, 167 (1979).
10. M. Neubert, Phys. Rep. **245**, 259 (1994).
11. W. Buchmüller and S.-H. H. Tye, Phys. Rev. D **24**, 132 (1981).
12. K. Gottfried, Phys. Rev. Lett. **40**, 598 (1978); M. Voloshin, Nucl. Phys. B **154**, 365 (1979); M. Peskin, Nucl. Phys. B **156**, 365 (1979).
13. G. T. Bodwin, E. Braaten, and G. P. Lepage, Phys. Rev. D **51**, 1125 (1995); **55**, 5853 (Erratum) (1997).
14. J. L. Rosner, Phys. Lett. B **385**, 293 (1996).
15. A. H. Hoang, M. C. Smith, T. Stelzer, *et al.*, Preprint No. UCSD-PTH-98-13 (1998); hep-ph/9804227.
16. E. Eichten and F. Feinberg, Phys. Rev. D **23**, 2724 (1981); D. Gromes, Z. Phys. C **26**, 401 (1984).

Translated by A. Isaakyan

Physics of Atomic Nuclei, Vol. 63, No. 2, 2000, pp. 287–302. From Yadernaya Fizika, Vol. 63, No. 2, 2000, pp. 348–364.

ELEMENTARY PARTICLES AND FIELDS
Theory

Subthreshold and Near-Threshold K^+-Meson Production on Light Nuclei by Protons*

É. Ya. Paryev

Institute for Nuclear Research, Russian Academy of Sciences, pr. Shestidesyatiletiya Oktyabrya 7a, Moscow, 117312 Russia

Received October 19, 1998; in final form, January 5, 1999

Abstract—Inclusive K^+-meson production in proton–nucleus collisions in the near-threshold and subthreshold energy regimes is analyzed with respect to the one-step ($pN \longrightarrow K^+YN$, $Y = \Lambda, \Sigma$) and two-step ($pN \longrightarrow NN\pi$, $NN2\pi$; $\pi N \longrightarrow K^+Y$) incoherent production processes. An appropriate folding model is used that properly takes into account the struck-target-nucleon-removal energy and the momentum distribution (nucleon spectral function), novel elementary cross sections for proton–nucleon reaction channel close to threshold, as well as nuclear-mean-field-potential effects on the one-step and two-step kaon-creation processes. A detailed comparison of the model calculations of the K^+ total and differential cross sections for the $p + {}^9$Be and $p + {}^{12}$C interactions with the existing experimental data is given, which displays both the relative role of the primary and secondary production channels at considered incident energies and those features of the cross sections that are sensitive to the high-momentum and high-removal-energy parts of the nucleon spectral function. It is found that, contrary to previous studies known in the literature, the pion–nucleon production channels do not necessarily dominate in *pA* collisions at subthreshold energies and that the relative strength of the proton- and pion-induced reaction channels for light target nuclei in the subthreshold energy regime is governed by the kinematics of the experiment under consideration. © *2000 MAIK "Nauka/Interperiodica"*.

INTRODUCTION

Kaon production in proton–nucleus reactions at incident energies less than threshold energies in a collision of free nucleons has been extensively studied both experimentally and theoretically in recent years [1–12]. Since kaons have a long mean free path inside the nucleus, it is expected to extract from these studies valuable information about the nuclear structure at short nucleon–nucleon separations as well as about the dynamics of the reaction and properties of the produced particles in the nuclear environment. The first theoretical investigations of subthreshold kaon production on nuclei have been mainly performed in the framework of the respective folding models based both on the direct mechanism [1, 2, 6, 11, 12] of K^+ production ($pN \longrightarrow K^+\Lambda N$) and on the two-step mechanism [1, 3–5] associated with the production of kaons by intermediate pions ($pN_1 \longrightarrow \pi NN$, $\pi N_2 \longrightarrow K^+\Lambda$) using different parametrizations for the elementary kaon-production cross sections as well as for the internal-nucleon-momentum distribution. Subthreshold K^+ production by protons on multiquark clusters in nuclei formed from 2, 3 and 4 intranuclear nucleons has been explored in [7]. This approach is able to reproduce both the energy and A dependences of the measured [1] total kaon-production cross sections. However, it suffers from the drawback that it uses a free parameter, the admixture of the multiquark clusters in nuclei, to give the absolute normalization. In the above folding models, only the nucleon momentum distribution has been used, and the off-shell propagation of the struck target nucleon has been neglected or has been taken into account most crudely, but it could be significant in the threshold heavy-meson-production processes, since they are limited by the phase space. Later [8–10], the full nucleon momentum and binding (removal) energy distribution (nucleon spectral function) was properly taken into account in calculating the subthreshold kaon production in *p*C and *p*Pb collisions. It was shown that, within the spectral-function approach, the measured total [1] and differential [8] K^+-production cross sections are underestimated significantly at subthreshold incident energies by calculations assuming only that first-chance collisions are unaffected [8, 10] by the nuclear medium or are affected [9] by the repulsive impinging-proton optical potential. When the two-step kaon-production processes with intermediate pions have been taken into consideration, the results of calculations [8, 9] are in much better agreement with the experimental data, while the ones from [10] have shown that, without the in-medium modifications of the invariant energies available for pion and kaon production due to the corresponding optical potentials, it is not possible to reproduce the considered experimental data on total [1] and differential [8] K^+ cross sections from *p*C interactions at subthreshold energies via the secondary pion-induced channels. However, in order to gain a deeper insight into the relative role of the primary and second-

* This article was submitted by the author in English.

ary reaction channels, it is obviously necessary, as was pointed out in [10], to carry out a detailed study of subthreshold kaon production in *p*A collisions on the basis of the spectral function approach that includes consistently the mean-field potential effects both on the one-step and on two-step kaon-production processes. This is the main purpose of the present article. In doing this, it is extremely important to incorporate, in the calculations, new experimental data points for the total cross section of the $pp \longrightarrow K^+\Lambda p$ reaction in the threshold region covering the excess energy range up to 7 MeV from the COSY-11 collaboration at COSY-Jülich [13], which lie above the current parametrizations [10, 14, 15] employed in the recent studies of the subthreshold kaon production in proton–nucleus [10] and heavy-ion [14, 15] reactions, as well as to analyze other experimental data on subthreshold and near-threshold K^+ production in *p*A interactions obtained at the ITEP proton synchrotron [11, 12] together with those presented in [1, 8].

In the present work, we have performed an analysis of K^+ production from *p*Be and *p*C interactions in the near-threshold and subthreshold energy regimes using the spectral function approach [10] that has been modified to take into account the new data points for the reaction $pp \longrightarrow K^+\Lambda p$ close to threshold [13] and to treat the mean-field potential effects on the primary and secondary creation processes on equal footing. This approach is explained in detail in [10]; here, we only describe the respective modifications.

1. THE MODEL AND INPUTS

1.1. Direct K^+-Production Processes

Apart from participation in elastic scattering, an incident proton can produce a K^+ meson directly in the first inelastic *pN* collision due to nucleon Fermi motion. Since we are interested in a few-GeV region (up to 3 GeV), we have taken into account [16] the following elementary processes characterized by the lowest free production thresholds:

$$p + N \longrightarrow K^+ + \Lambda + N, \quad (1)$$

$$p + N \longrightarrow K^+ + \Sigma + N. \quad (2)$$

Following the predictions of the effective chiral Lagrangian approach by Kaplan and Nelson [17], we assume that the mass of the produced kaon is not changed in the nuclear medium (see also [14, 15, 18]) due to an approximate cancellation of attractive scalar and repulsive vector mean fields;[1)] i.e., the total energy E_{K^+} of the K^+ meson with momentum $\mathbf{p}_{K^+}$ is given by

$$E_{K^+} = \sqrt{\mathbf{p}_{K^+}^2 + m_K^2}, \quad (3)$$

where m_K is the rest mass of a kaon in free space. The effective masses m_h^* of other final hadrons (nucleon and hyperon) participating in the K^+-production processes (1) and (2), which have to be incorporated in our model [10] (see below) instead of their free-space masses m_h to allow for the influence of the nuclear environment on the K^+ production, are defined by the dispersion relation [27–33]

$$E_h^2 = \mathbf{p}_h^2 + m_h^{*2} = \left(\sqrt{\mathbf{p}_h^2 + (m_h + U_s^h)^2} + U_v^h\right)^2, \quad (4)$$

where U_s^h and U_v^h are the scalar and vector (timelike component) self-energies of hadron *h* and $\mathbf{p}_h$ denotes its canonical three-momentum.[2)]

The use of the relativistic dispersion relation for the quasiparticle given by the left-hand side of (4) enables us to keep on dealing with relativistic kinematics as in the on-mass-shell case. The effective masses m_h^* include the effective scalar mean-field potentials U_{eff}^h, needed for our calculations:

$$m_h^* = m_h + U_{\text{eff}}^h. \quad (5)$$

Equations (4) and (5) allow us to extract these potentials, provided that the scalar and vector fields U_s^h and U_v^h are known. In the general case, these fields are density- and momentum-dependent [27, 31–33]. However, for the purposes of the present study, as well as for reasons of simplicity, it is sufficient to neglect the explicit momentum dependence of U_s^h and U_v^h and to evaluate the effective fields U_{eff}^h using the quantities U_s^h and U_v^h within only limited density and momentum range relevant for the observed [1, 8, 11, 12] subthreshold kaon production in *pA* interactions. K^+ creation due to first-chance *pN* collisions [(1) and (2)] occurs mainly inside the target nucleus [34] and populates, as our calculations showed, the outgoing nucleon and hyperon in a limited kinematical range with the mean kinetic energies $\lesssim 0.1$ GeV for the most part of kinematical conditions of the experiments on subthreshold kaon production that are analyzed below. Therefore, the potentials U_s^h and U_v^h should be estimated at the normal nuclear-matter density for the above characteristic energy. Employing the recent parametrization for the nucleon scalar and vector potentials from [33], obtained within the self-consistent Dirac–Brueckner approach, we can

[1)]It should be noted that the actual magnitude of these fields is still a matter of current debate [19–25], although recent studies [15, 26] indicate that a weakly repulsive kaon potential (~30 MeV at the normal nuclear matter density) cannot be excluded by the present data on kaon transverse flow in heavy-ion collisions, measured by the FOPI collaboration at SIS/GSI.

[2)]The spacelike components of the vector self-energies are neglected here [33].

readily find that the nucleon effective potential $U_{\rm eff}^N$ at a kinetic energy of 100 MeV for normal matter density becomes $U_{\rm eff}^N = -34$ MeV. It may be pointed out that this value of the effective potential $U_{\rm eff}^N$ is in good agreement [10] with the characteristic depth of a potential well gained in the noninteracting Fermi gas model.

At present, there are a few models for the hyperon mean-field potentials in nuclear medium [35–37], which give essentially different predictions for the actual magnitude of the potentials. By way of example, we indicate that, in the naive constituent quark model, the hyperon self-energies are about 2/3 of the nucleon self-energies. This assumption is widely used in the relativistic transport models for high-energy nucleus–nucleus collisions [15, 32, 37–39]. In view of the substantial uncertainties of the model hyperon self-energies, as well as since, at subthreshold energies, hyperons from primary pN interactions (1) and (2) are produced, as was noted above, in a limited kinematical range, it is natural to use, for the effective potentials $U_{\rm eff}^\Lambda$ and $U_{\rm eff}^\Sigma$ seen by the final low-energy Λ and Σ hyperons, the values of the corresponding optical potentials at normal nuclear-matter density, extracted from the properties of hypernuclei, namely, $U_{\rm eff}^\Lambda = -30$ MeV [37, 40, 41] and $U_{\rm eff}^\Sigma = -26$ MeV [41]. The set of parameters

$$U_{\rm eff}^N = -34 \text{ MeV}, \quad U_{\rm eff}^\Lambda = -30 \text{ MeV}, \quad U_{\rm eff}^\Sigma = -26 \text{ MeV} \tag{6}$$

will be used throughout our calculations. To examine the sensitivity of kaon-production cross section for the one-step processes (1) and (2) to the effective nucleon and hyperon potentials, we will also ignore these potentials in our calculations, as this has been done in the previous investigations [8–10] of subthreshold K^+ production in pA collisions within the spectral function approach.

Another medium effect that must be taken into account is the modification of the four-momentum $\hat{p}_0 = (E_0, \mathbf{p}_0)$ ($\hat{p}_0^2 = m_N^2$) of an incoming proton inside the target nucleus due to the nuclear optical potential V_0. Let $\hat{p}_0' = (E_0', \mathbf{p}_0')$ be the four-momentum of an incident proton under the influence of this potential, and let $\hat{p}_A = (M_A, 0)$ and $\hat{p}_A' = (M_A + \Delta\mathbf{p}^2/2M_A, \Delta\mathbf{p})$ be, respectively, the four-momenta of the initial target nucleus with mass M_A and the target nucleus recoiling (due to the refraction of a beam proton at the nuclear surface) with momentum $\Delta\mathbf{p}$. Energy and momentum conservation reads

$$\hat{p}_0 + \hat{p}_A = \hat{p}_0' + \hat{p}_A'. \tag{7}$$

This leads to the following expressions for the total energy E_0' and momentum $\mathbf{p}_0'$ of the incident proton inside the target nucleus:

$$E_0' = E_0 - \Delta\mathbf{p}^2/2M_A, \tag{8}$$

$$\mathbf{p}_0' = \mathbf{p}_0 - \Delta\mathbf{p}. \tag{9}$$

Considering that, on the other hand,

$$E_0' = \sqrt{(\mathbf{p}_0 - \Delta\mathbf{p})^2 + m_N^2} + V_0 \tag{10}$$

and assuming, for the sake of numerical simplicity, that the recoil momentum $\Delta\mathbf{p}$ of the target nucleus entering into equations (8) and (9) is parallel to the beam direction,

$$\Delta\mathbf{p} = \Delta p \frac{\mathbf{p}_0}{|\mathbf{p}_0|}, \tag{11}$$

we can readily get the following expression for the quantity Δp:

$$\Delta p = \frac{p_0 E_0^2 M_A \left(1 - \sqrt{1 - \dfrac{2V_0E_0^2}{p_0^2M_A} - \dfrac{2V_0m_N^2}{p_0^2E_0}}\right)}{(E_0^3 + m_N^2M_A)} \approx \frac{E_0}{p_0}V_0, \tag{12}$$

where $p_0 = |\mathbf{p}_0|$. According to [3, 5, 32, 33, 42], a proton incoming to a nucleus at a kinetic energy ϵ_0 of about $\epsilon_0 \approx 1$ GeV in the interior of the nucleus feels the repulsive optical potential of about $V_0 \approx 40$ MeV. We will use this value of potential V_0 also at higher beam energies considered in the present work. Then, in the energy range under consideration, i.e., when the energy ϵ_0 varies within the range of about 1–3 GeV, the "recoil momentum" Δp, as follows from equation (12), amounts approximately to 43 MeV/c.

Further, let E_t and $\mathbf{p}_t$ be the total energy and momentum of the struck nucleon N of the target just before the collisions (1) and (2). Taking into account the respective recoil and excitation energies of the residual (A – 1) system, one has [10, 43]

$$E_t = M_A - \sqrt{(-\mathbf{p}_t)^2 + (M_A - m_N + E)^2}, \tag{13}$$

where E is the removal energy of the struck target nucleon. It is easily seen that, in this case, the struck target nucleon is an off-shell one. After specifying the energies and momenta of all particles involved in the K^+-production processes (1) and (2), we can write out the corresponding laws of energy and momentum conservation:

$$E_0' + E_t = E_{K^+} + E_Y + E_N, \tag{14}$$

$$\mathbf{p}_0' + \mathbf{p}_t = \mathbf{p}_{K^+} + \mathbf{p}_Y + \mathbf{p}_N. \tag{15}$$

From (14) and (15), we obtain the squared invariant energy available in the first-chance pN collision:

$$s = (E_0' + E_t)^2 - (\mathbf{p}_0' + \mathbf{p}_t)^2. \quad (16)$$

On the other hand, according to the equations (14) and (15), one gets

$$s = (E_{K^+} + E_Y + E_N)^2 - (\mathbf{p}_{K^+} + \mathbf{p}_Y + \mathbf{p}_N)^2. \quad (17)$$

With allowance for (3)–(5), this leads to the following expression for the in-medium reaction thresholds:

$$\sqrt{s^*_{\rm thr}} = m_K + m_Y^* + m_N^* = \sqrt{s_{\rm thr}} + U_{\rm eff}^Y + U_{\rm eff}^N, \quad (18)$$

where $\sqrt{s_{\rm thr}} = m_K + m_Y + m_N$ are the threshold energies in free space and the effective potentials $U_{\rm eff}^{Y,N}$ are given by (6). Hence, the reduction of the K^+ threshold in the medium will be 64 MeV in the case of the reaction $pN \longrightarrow K^+\Lambda N$ and 60 MeV for the process $pN \longrightarrow K^+\Sigma N$. This will strongly enhance the K^+ production via first-chance pN collisions (see below).

Finally, neglecting the kaon final-state interactions [10], we can represent the invariant inclusive cross section of K^+ production on nuclei from the primary proton-induced reaction channels (1) and (2) as follows [10]:

$$E_{K^+}\frac{d\sigma^{(\rm prim)}_{pA\to K^+X}(\mathbf{p}_0)}{d\mathbf{p}_{K^+}} = I_V[A] \times\left\{\left\langle E_{K^+}\frac{d\sigma_{pN\to K^+\Lambda N}(\mathbf{p}_0,\mathbf{p}_{K^+})}{d\mathbf{p}_{K^+}}\right\rangle + \left\langle E_{K^+}\frac{d\sigma_{pN\to K^+\Sigma N}(\mathbf{p}_0,\mathbf{p}_{K^+})}{d\mathbf{p}_{K^+}}\right\rangle\right\}, \quad (19)$$

where

$$I_V[A] = A\int\rho(\mathbf{r})d\mathbf{r}\exp\left[-\mu(p_0)\int_{-\infty}^{0}\rho(\mathbf{r}+x\mathbf{\Omega}_0)dx\right], \quad (20)$$

$$\mu(p_0) = \sigma^{\rm in}_{pp}(p_0)Z + \sigma^{\rm in}_{pn}(p_0)N; \quad (21)$$

$$\left\langle E_{K^+}\frac{d\sigma_{pN\to K^+YN}(\mathbf{p}_0,\mathbf{p}_{K^+})}{d\mathbf{p}_{K^+}}\right\rangle = \iint P(\mathbf{p}_t,E)d\mathbf{p}_t dE \times\left[E_{K^+}\frac{d\sigma_{pN\to K^+YN}(\sqrt{s},\mathbf{p}_{K^+})}{d\mathbf{p}_{K^+}}\right]. \quad (22)$$

Here, $E_{K^+}d\sigma_{pN\to K^+YN}(\sqrt{s},\ \mathbf{p}_{K^+})/d\mathbf{p}_{K^+}$ are the in-medium invariant inclusive cross sections for K^+ production in reactions (1) and (2); $\rho(\mathbf{r})$ and $P(\mathbf{p}_t, E)$ are the density and nucleon spectral function normalized to unity; $\mathbf{p}_t$ and E are the internal momentum and removal energy of the struck target nucleon just before the collision; $\sigma^{\rm in}_{pN}(p_0)$ is the inelastic cross section for free pN interaction; Z and N are the numbers of protons and neutrons in the target nucleus $A = N + Z$; $\mathbf{\Omega}_0 = \mathbf{p}_0/p_0$ ($\mathbf{p}_0$ is the beam momentum); s is the pN center-of-mass energy squared. The expression for s is given above by formula (16). To derive equation (19), we assumed that the K^+-meson-production cross sections in pp and pn interactions are the same [8, 10], and any difference is disregarded between the proton and the neutron spectral functions [44]. In our approach, the invariant inclusive cross sections for K^+ production in the elementary processes (1) and (2) have been described by the three-body phase space calculations normalized to the corresponding total cross sections [10]:

$$E_{K^+}\frac{d\sigma_{pN\to K^+YN}(\sqrt{s},\mathbf{p}_{K^+})}{d\mathbf{p}_{K^+}} = \frac{\pi}{4} \times\frac{\sigma_{pN\to K^+YN}(\sqrt{s},\sqrt{s^*_{\rm thr}})}{I_3(s,m_K,m_Y^*,m_N^*)}\frac{\lambda(s_{YN},m_Y^{*2},m_N^{*2})}{s_{YN}}, \quad (23)$$

$$I_3(s,m_K,m_Y^*,m_N^*) = \left(\frac{\pi}{2}\right)^2 \times\int_{(m_Y^*+m_N^*)^2}^{(\sqrt{s}-m_K)^2}\frac{\lambda(s_{YN},m_Y^{*2},m_N^{*2})}{s_{YN}}\frac{\lambda(s,s_{YN},m_K^2)}{s}ds_{YN}, \quad (24)$$

$$\lambda(x,y,z) = \sqrt{[x-(\sqrt{y}+\sqrt{z})^2][x-(\sqrt{y}-\sqrt{z})^2]}, \quad (25)$$

$$s_{YN} = s + m_K^2 - 2(E_0'+E_t)E_{K^+} + 2(\mathbf{p}_0'+\mathbf{p}_t)\cdot\mathbf{p}_{K^+}. \quad (26)$$

Here, $\sigma_{pN\to K^+YN}(\sqrt{s},\sqrt{s^*_{\rm thr}})$ are the in-medium total cross sections for K^+ production in reactions (1) and (2); m_Y^* is the effective mass of the Y hyperon (Λ or Σ). The in-medium cross sections $\sigma_{pN\to K^+YN}(\sqrt{s},\sqrt{s^*_{\rm thr}})$ are equivalent [14, 15] to the vacuum cross sections $\sigma_{pN\to K^+YN}(\sqrt{s},\sqrt{s_{\rm thr}})$, where the free thresholds $\sqrt{s_{\rm thr}}$ are replaced by the effective thresholds $\sqrt{s^*_{\rm thr}}$ as given by equation (18). For the free total cross sections $\sigma_{pN\to K^+YN}(\sqrt{s},\sqrt{s_{\rm thr}})$, we have used the parametrization suggested in [10] that has been corrected for the new data points for the reaction $pp \longrightarrow K^+\Lambda p$ from the COSY-11 collaboration at COSY-Jülich [13] in the

Parameters in the approximation of the partial cross sections for the production of K^+ mesons in pp collisions

Reaction	A_Y, μb GeV^{-2}	B_Y, GeV^{-2}	C_Y, μb GeV^{-2}	$s_{\rm th}$, GeV^2
$p + p \longrightarrow K^+ + \Lambda + p$	122.943	2.015	2515.56	6.490
$p + p \longrightarrow K^+ + \Sigma + N$	104.026	1.006	0	6.880

threshold region covering the excess energy range up to 7 MeV, viz.,

$$\sigma_{pp\to K^+YN}(\sqrt{s}, \sqrt{s_{\rm thr}}) = \frac{A_Y(s-s_{\rm thr})^2}{4m_p^2 + B_Y(s-s_{\rm thr})^2} + C_Y(s-s_{\rm thr})^2[0.5-(s-s_{\rm thr})/{\rm GeV}^2]^{2.328} \times \Theta[0.5-(s-s_{\rm thr})/{\rm GeV}^2]/(4m_p^2), \quad (27)$$

where $\Theta(x) = (x + |x|)/2|x|$, while the constants A_Y, B_Y, C_Y, and $s_{\rm thr}$ are given in the table. The comparison of the results of our calculations given by (27) (solid curve) with the experimental data close to the threshold for the reaction $pp \longrightarrow K^+\Lambda p$ from the installation COSY-11 [13] (full squares), from the facility TOF at COSY [13] (full circles), as well as from the old bubble-chamber measurements BNL 62 [45] (open crosses), is shown in Fig. 1. It is seen that our parametrization (27) complies quite well with the world set of data for the $pp \longrightarrow K^+\Lambda p$ reaction in the threshold region.

Consider now the integral in (20), which represents the effective number of nucleons for the reaction $pN \longrightarrow K^+YN$ on nuclei. A simpler expression can be given [10] for $I_V[A]$ in the case of the Gaussian nuclear density [$\rho(\mathbf{r}) = (b/\pi)^{3/2}\exp(-br^2)$, with $b = 0.240$ fm^{-2} for ^{9}Be and $b = 0.248$ fm^{-2} for ^{12}C]:

$$I_V[A] = \frac{A}{x_G}\int_0^1 \frac{dt}{t}(1-e^{-x_G t}), \quad x_G = \mu(p_0)b/\pi. \quad (28)$$

Another very important ingredient for the calculation of the cross sections in proton–nucleus interactions in the subthreshold energy regime is the nucleon spectral function $P(\mathbf{p}_t, E)$, which represents the probability to find, in the nucleus, a nucleon with momentum $\mathbf{p}_t$ and removal energy E and contains the overall information on the structure of a target nucleus. When we consider the ground-state NN correlations, which are generated by the short-range and tensor parts of realistic NN interaction, the spectral function $P(\mathbf{p}_t, E)$ can be represented in the form [46–50]

$$P(\mathbf{p}_t, E) = P_0(\mathbf{p}_t, E) + P_1(\mathbf{p}_t, E), \quad (29)$$

where P_0 includes the ground and one-hole states of the residual $(A-1)$ nucleon system and P_1 stands for the contribution of more complex configurations (mainly $1p$–$2h$ states) that arise from the $2p$–$2h$ excited states generated in the ground state of the target nucleus by NN correlations. For K^+-production calculations in the case of ^{9}Be and ^{12}C target nuclei reported here, we have employed, for the single-particle (uncorrelated) part $P_0(\mathbf{p}_t, E)$ of the nucleon spectral function, the expression [10]

$$P_0(\mathbf{p}_t, E) = S_0 P_0^{\rm (MF)}(\mathbf{p}_t, E) \quad (30)$$

with $P_0^{\rm (MF)}(\mathbf{p}_t, E)$ being the harmonic-oscillator spectral function (see, e.g., [51]),

$$P_0^{\rm (MF)}(\mathbf{p}_t, E) = \frac{4}{A}n_{1s}(\mathbf{p}_t)\delta(E-|\epsilon_{1s}|) + \left(\frac{A-4}{A}\right)n_{1p}(\mathbf{p}_t)\delta(E-|\epsilon_{1p}|), \quad (31)$$

where the s- and p-shell nucleon momentum distributions $n_{1s}(\mathbf{p}_t)$ and $n_{1p}(\mathbf{p}_t)$ were taken from [52],

$$n_{1s}(\mathbf{p}_t) = (b_0/\pi)^{3/2}\exp(-b_0 p_t^2),$$
$$n_{1p}(\mathbf{p}_t) = \frac{2}{3}(b_0/\pi)^{3/2} b_0 p_t^2 \exp(-b_0 p_t^2) \quad (32)$$

[$b_0 = 77.5$ (GeV/c)$^{-2}$ for ^{9}Be and $b_0 = 68.5$ (GeV/c)$^{-2}$ for ^{12}C], and binding energies of $|\epsilon_{1s}| = 26$ MeV and $|\epsilon_{1p}| = 16$ MeV [53, 54] for the s and p shells, respectively, in the case of ^{9}Be nucleus; $|\epsilon_{1s}| = 34$ MeV and $|\epsilon_{1p}| = 16$ MeV [51] were used for ^{12}C target nucleus. The parameter S_0 in (30) takes into account the depletion of states below the Fermi sea due to the NN correlations. According to [46, 47, 50], $S_0 = 0.8$.

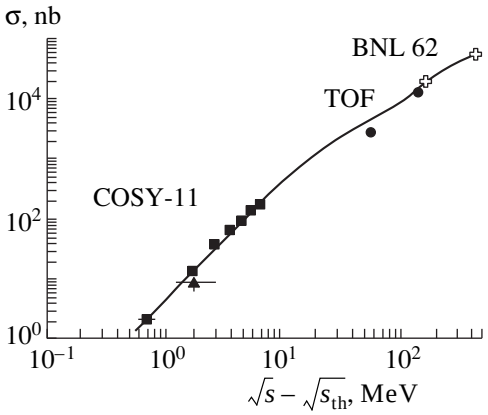

Fig. 1. The total cross section for the reaction $pp \longrightarrow K^+\Lambda p$ as a function of an excess energy ($\sqrt{s} - \sqrt{s_{\rm thr}}$). For notation see text.

Let us now focus on the high-momentum and high-removal-energy part (correlated part) $P_1(\mathbf{p}_t, E)$ of the nucleon spectral function $P(\mathbf{p}_t, E)$. As was shown in [48, 50], the function $P_1(\mathbf{p}_t, E)$ can be expressed as a convolution integral of the momentum distributions describing the relative and center-of-mass motions of a correlated *NN* pair embedded into the nuclear medium. An inspection of the convolution formula (53) from [50] for the spectral function $P_1(\mathbf{p}_t, E)$ leads to the following simple analytic expression for the $P_1(\mathbf{p}_t, E)$ proposed in [47] [formula (7)] (see, also, [10]):

$$P_1(\mathbf{p}_t, E) = a_1 n_1(\mathbf{p}_t) \times \exp\{-3[(A-2)/(A-1)]m_N \times [\sqrt{E-E_{\rm thr}} - \sqrt{E_1(p_t)-E_{\rm thr}}]^2/\langle p_{\rm cm}^2\rangle\}, \quad (33)$$

where

$$a_1 = \frac{3[(A-2)/(A-1)]m_N}{\left\{e^{-\alpha_0^2} + \alpha_0\sqrt{\pi}[1+\mathrm{erf}(\alpha_0)]\right\}\langle p_{\rm cm}^2\rangle}, \quad (34)$$

$$\alpha_0 = \frac{p_t}{\langle p_{\rm cm}^2\rangle^{1/2}}\sqrt{\frac{3}{2}\left(\frac{A-2}{A-1}\right)^2\left[1-\left(\frac{A-1}{A-2}\right)\gamma\right]}, \quad (35)$$

$$\mathrm{erf}(x) = \frac{2}{\sqrt{\pi}}\int_0^x e^{-t^2}dt,$$

$$E_1(p_t) = E_{\rm thr} + \left(\frac{A-2}{A-1}\right)\frac{p_t^2}{2m_N}\left[1-\left(\frac{A-1}{A-2}\right)\gamma\right], \quad \gamma = \frac{\langle p_{\rm cm}^2\rangle}{\langle p_{\rm rel}^2\rangle}. \quad (36)$$

Here, $n_1(\mathbf{p}_t)$ is the correlated part of the internal-nucleon-momentum distribution; a_1 is a proper normalization constant [such that $\int_{E_{\rm thr}}^{\infty} P_1(\mathbf{p}_t, E)dE = n_1(\mathbf{p}_t)$]; $E_{\rm thr} = M_{A-2} + 2m_N - M_A$ is the two-particle breakup threshold ($E_{\rm thr}$ is equal to 19 and 25 MeV for ^{9}Be and ^{12}C target nuclei, respectively); and $\langle p_{\rm cm}^2\rangle$ and $\langle p_{\rm rel}^2\rangle$ are the mean-square momenta associated with the low- and high-momentum parts of the momentum distribution describing the center-of-mass motion of a correlated *NN* pair and the momentum distribution describing the relative motion of this pair, respectively. In our calculations of the cross sections for K^+ production on ^{9}Be and ^{12}C target nuclei, we have used the values of $\langle p_{\rm cm}^2\rangle = 1.5$ fm^{-2} and $\langle p_{\rm rel}^2\rangle = 7.5$ fm^{-2} [48, 50]. The many-body momentum distribution $n_1(\mathbf{p}_t)$ for ^{12}C has been presented in [46, 47]. Taking into account the corresponding normalization of $n_1(\mathbf{p}_t)$ ($\int n_1(\mathbf{p}_t)d\mathbf{p}_t = S_1 = 1 - S_0 = 0.2$), we can parametrize it as [10]

$$n_1(\mathbf{p}_t) = \frac{S_1}{(2\pi)^{3/2}(1+\alpha_1)} \times\left[\frac{1}{\sigma_1^3}\exp(-p_t^2/2\sigma_1^2) + \frac{\alpha_1}{\sigma_2^3}\exp(-p_t^2/2\sigma_2^2)\right], \quad (37)$$

where $\sigma_1^2 = 0.162$ fm^{-2}, $\sigma_2^2 = 2.50$ fm^{-2}, and $\alpha_1 = 2.78$. This momentum distribution has been also employed in the case of ^{9}Be target nucleus [50]. The expressions (30) and (33) for the respective spectral functions were used in our calculations of K^+ production in *p*Be an *p*C collisions.

Let us now consider the two-step K^+-production mechanism.

1.2. Two-Step K^+-Production Processes

Kinematical considerations show that, in the bombarding-energy range of our interest (≤3.0 GeV), the following two-step production processes may not only contribute to the K^+ production in *pA* interactions but even dominate there [1, 3–5, 8–10] at subthreshold energies. An incident proton can produce, in the first inelastic collision with an intranuclear nucleon, also a pion through the elementary reactions

$$p + N_1 \longrightarrow N + N + \pi, \quad (38)$$

$$p + N_1 \longrightarrow N + N + 2\pi. \quad (39)$$

We recall that the free threshold energies for these reactions are, respectively, 0.29 and 0.60 GeV. Then, the intermediate pion, which is assumed to be on-shell, produces the kaon on a nucleon of the target nucleus via the elementary subprocesses with the lowest free production thresholds (respectively, 0.76 and 0.89 GeV):

$$\pi + N_2 \longrightarrow K^+ + \Lambda, \quad (40)$$

$$\pi + N_2 \longrightarrow K^+ + \Sigma, \quad (41)$$

provided that these subprocesses are allowed energetically. Since the main contribution to the K^+ production at subthreshold incident energies comes from extremely fast pions moving in the beam direction, the relevant kinetic energy ϵ_N of each nucleon produced in the reactions (38) and (39), together with a high-energy pion, can be approximately estimated as $\epsilon_N \approx 0.1$ GeV [10] at beam energies of our interest. As has been mentioned above [see (6)], such low-energy outgoing nucleons feel the attractive effective potential $U_{\rm eff}^N = -34$ MeV inside the nucleus that reduces their free masses in line with formula (5). Thus, it is necessary to incorporate properly the effective nucleon mass m_N^* in calculations of the K^+-production cross section from the two-step processes (38)–(41). Moreover, in these

calculations, the same in-medium modification of the masses of hyperons from secondary πN collisions (40) and (41) as that for hyperons from primary pN collisions due to the corresponding effective potentials U_{eff}^{Λ} and U_{eff}^{Σ} should also be taken into account [see (5) and (6)]. Keeping in mind this fact and using the results given in [10], we can get the following expression for the K^+-production cross section for pA interactions from the secondary pion-induced reaction channels (40) and (41), which includes the medium effects under consideration on the same covariant footing[3)] as those employed in calculation of the K^+-production cross section (19) from primary proton-induced reaction channels (1) and (2):

$$E_{K^+}\frac{d\sigma^{(\text{sec})}_{pA\to K^+X}(\mathbf{p}_0)}{d\mathbf{p}_{K^+}} = \sum_{i,\,j\,=\,0,\,1} E_{K^+}\frac{d\sigma^{(\text{sec})}_{ij}(\mathbf{p}_0)}{d\mathbf{p}_{K^+}}, \qquad (42)$$

where

$$E_{K^+}\frac{d\sigma^{(\text{sec})}_{ij}(\mathbf{p}_0)}{d\mathbf{p}_{K^+}} = \sum_{\pi\,=\,\pi^+,\,\pi^0,\,\pi^-}\iint P_i(\mathbf{p}_t, E)\,d\mathbf{p}_t dE$$

$$\times \int\limits_{p_\pi^{\text{abs}}}^{p_\pi^{\max}(\mathbf{p}_t,\,E)} p_\pi^2 dp_\pi \int\limits_{4\pi} d\mathbf{\Omega}_\pi I_V[A, \sigma^{\text{in}}_{pN}(p_0), \sigma^{\text{tot}}_{\pi N}(p_\pi), \vartheta_\pi] \qquad (43)$$

$$\times \frac{d\sigma_{pN\to\pi X}(\sqrt{s}, \mathbf{p}_\pi)}{d\mathbf{p}_\pi}$$

$$\times \iint P_j(\mathbf{p}'_t, E')\,d\mathbf{p}'_t dE' \left[E_{K^+}\frac{d\sigma_{\pi N\to K^+X}(\sqrt{s_1}, \mathbf{p}_{K^+})}{d\mathbf{p}_{K^+}}\right]$$

and

$$I_V[A, \sigma^{\text{in}}_{pN}(p_0), \sigma^{\text{tot}}_{\pi N}(p_\pi), \vartheta_\pi]$$

$$= A^2\iint d\mathbf{r}\,d\mathbf{r}_1\,\Theta(x_\parallel)\delta^{(2)}(\mathbf{x}_\perp)\rho(\mathbf{r})\rho(\mathbf{r}_1)$$

$$\times \exp\left[-\mu(p_0)\int\limits_{-\infty}^{0}\rho(\mathbf{r}_1 + x'\mathbf{\Omega}_0)dx'\right. \qquad (44)$$

$$\left. -\mu(p_\pi)\int\limits_{0}^{x_\parallel}\rho(\mathbf{r}_1 + x'\mathbf{\Omega}_\pi)dx'\right],$$

$$\mathbf{r} - \mathbf{r}_1 = x_\parallel\mathbf{\Omega}_\pi + \mathbf{x}_\perp, \quad \mathbf{\Omega}_\pi = \mathbf{p}_\pi/p_\pi,$$
$$\cos\vartheta_\pi = \mathbf{\Omega}_0\cdot\mathbf{\Omega}_\pi,$$
$$\mu(p_\pi) = (A/2)[\sigma^{\text{tot}}_{\pi p}(p_\pi) + \sigma^{\text{tot}}_{\pi n}(p_\pi)], \qquad (45)$$
$$\Theta(x_\parallel) = (x_\parallel + |x_\parallel|)/2|x_\parallel|;$$

$$\frac{d\sigma_{pN\to\pi X}(\sqrt{s}, \mathbf{p}_\pi)}{d\mathbf{p}_\pi} = \frac{Z}{A}\frac{d\sigma_{pp\to\pi X}(\sqrt{s}, \mathbf{p}_\pi)}{d\mathbf{p}_\pi} + \frac{N}{A}\frac{d\sigma_{pn\to\pi X}(\sqrt{s}, \mathbf{p}_\pi)}{d\mathbf{p}_\pi}, \qquad (46)$$

$$E_{K^+}\frac{d\sigma_{\pi N\to K^+X}(\sqrt{s_1}, \mathbf{p}_{K^+})}{d\mathbf{p}_{K^+}} = \frac{Z}{A}E_{K^+}\frac{d\sigma_{\pi p\to K^+X}(\sqrt{s_1}, \mathbf{p}_{K^+})}{d\mathbf{p}_{K^+}} + \frac{N}{A}E_{K^+}\frac{d\sigma_{\pi n\to K^+X}(\sqrt{s_1}, \mathbf{p}_{K^+})}{d\mathbf{p}_{K^+}}, \qquad (47)$$

$$s_1 = (E_\pi + E'_t)^2 - (\mathbf{p}_\pi + \mathbf{p}'_t)^2, \qquad (48)$$

$$E'_t = \begin{cases} M_A - E_t - \sqrt{(-\mathbf{p}_t - \mathbf{p}'_t)^2 + (M_A - 2m_N + E + E')^2} \\ \text{for } i = 0, \quad j = 0, 1 \\ M_{A-2} - \sqrt{(-\mathbf{p}'_t)^2 + (M_{A-2} - m_N + E')^2} \\ \text{for } i = 1, \quad j = 0, 1; \end{cases} \qquad (49)$$

$$p_\pi^{\max}(\mathbf{p}_t, E) = \left[\beta|\mathbf{p}'_0 + \mathbf{p}_t| + (E'_0 + E_t)\sqrt{\beta^2 - 4m_\pi^2 s}\right]/(2s), \qquad (50)$$

$$\beta = s + m_\pi^2 - 4m_N^{*2}.$$

Here, $d\sigma_{pp\,\to\,\pi X}/d\mathbf{p}_\pi$ ($d\sigma_{pn\,\to\,\pi X}/d\mathbf{p}_\pi$) is the in-medium inclusive differential cross section for pion production in pp (pn) collisions through the elementary reactions (38) and (39); $E_{K^+}\,d\sigma_{\pi p\to K^+X}/d\mathbf{p}_{K^+}$ ($E_{K^+}\,d\sigma_{\pi n\to K^+X}/d\mathbf{p}_{K^+}$) is the in-medium inclusive invariant differential cross section for K^+ production in πp (πn) collisions via the subprocesses (40) and (41); $\sigma^{\text{tot}}_{\pi N}(p_\pi)$ is the total cross section for free πN interaction; $\mathbf{p}_\pi$ and E_π are the momentum and total energy of a pion; and p_π^{abs} is the absolute threshold momentum for kaon production of the residual nucleus by an intermediate pion. The total energy E'_0 and momentum $\mathbf{p}'_0$ of the initial proton inside the target nucleus are defined above by formulas (8) and (9), respectively. The quantities s and $\mu(p_0)$ are defined above by equations (16) and (21), respectively.

[3)] It should be noted that, in [10], nuclear-mean-field effects on the kaon-production cross section from pion-induced reaction channels have been treated in a noncovariant manner. However, both treatments—present one and that given in [10], as is shown by our calculations—the lead to close results.

In our method, the differential cross sections $d\sigma_{pp\to\pi X}/d\mathbf{p}_\pi$ and $d\sigma_{pn\to\pi X}/d\mathbf{p}_\pi$ for pion production in pp and pn collisions have been described by the three- and four-body phase-space calculations normalized to the respective total cross sections. According to [10], one has

$$E_{\pi^+}\frac{d\sigma_{pp\to\pi^+X}(\sqrt{s},\mathbf{p}_{\pi^+})}{d\mathbf{p}_{\pi^+}} = \sigma_{pp\to pn\pi^+}(\sqrt{s})f_3(s,\mathbf{p}_{\pi^+}) + [\sigma_{pp\to pp\pi^+\pi^-}(\sqrt{s}) + \sigma_{pp\to pn\pi^+\pi^0}(\sqrt{s}) + 2\sigma_{pp\to nn\pi^+\pi^+}(\sqrt{s})]f_4(s,\mathbf{p}_{\pi^+}), \quad (51)$$

$$E_{\pi^0}\frac{d\sigma_{pp\to\pi^0X}(\sqrt{s},\mathbf{p}_{\pi^0})}{d\mathbf{p}_{\pi^0}} = \sigma_{pp\to pp\pi^0}(\sqrt{s})f_3(s,\mathbf{p}_{\pi^0}) + [\sigma_{pp\to pn\pi^+\pi^0}(\sqrt{s}) + 2\sigma_{pp\to pp\pi^0\pi^0}(\sqrt{s})]f_4(s,\mathbf{p}_{\pi^0}), \quad (52)$$

$$E_{\pi^-}\frac{d\sigma_{pp\to\pi^-X}(\sqrt{s},\mathbf{p}_{\pi^-})}{d\mathbf{p}_{\pi^-}} = \sigma_{pp\to pp\pi^+\pi^-}(\sqrt{s})f_4(s,\mathbf{p}_{\pi^-}); \quad (53)$$

$$E_{\pi^+}\frac{d\sigma_{pn\to\pi^+X}(\sqrt{s},\mathbf{p}_{\pi^+})}{d\mathbf{p}_{\pi^+}} = \sigma_{pn\to nn\pi^+}(\sqrt{s})f_3(s,\mathbf{p}_{\pi^+}) + [\sigma_{pn\to pn\pi^+\pi^-}(\sqrt{s}) + \sigma_{pn\to nn\pi^+\pi^0}(\sqrt{s})]f_4(s,\mathbf{p}_{\pi^+}), \quad (54)$$

$$E_{\pi^0}\frac{d\sigma_{pn\to\pi^0X}(\sqrt{s},\mathbf{p}_{\pi^0})}{d\mathbf{p}_{\pi^0}} = \sigma_{pn\to pn\pi^0}(\sqrt{s})f_3(s,\mathbf{p}_{\pi^0}) + [\sigma_{pn\to nn\pi^+\pi^0}(\sqrt{s}) + \sigma_{pn\to pp\pi^-\pi^0}(\sqrt{s}) + 2\sigma_{pn\to pn\pi^0\pi^0}(\sqrt{s})]f_4(s,\mathbf{p}_{\pi^0}), \quad (55)$$

$$E_{\pi^-}\frac{d\sigma_{pn\to\pi^-X}(\sqrt{s},\mathbf{p}_{\pi^-})}{d\mathbf{p}_{\pi^-}} = E_{\pi^+}\frac{d\sigma_{pn\to\pi^+X}(\sqrt{s},\mathbf{p}_{\pi^+})}{d\mathbf{p}_{\pi^+}}, \quad (56)$$

where

$$f_3(s,\mathbf{p}_\pi) = \frac{\pi}{4I_3(s,m_\pi,m_N^*,m_N^*)}\frac{\lambda(s_{NN},m_N^{*2},m_N^{*2})}{s_{NN}}, \quad (57)$$

$$s_{NN} = s + m_\pi^2 - 2(E_0' + E_t)E_\pi + 2(\mathbf{p}_0' + \mathbf{p}_t)\cdot\mathbf{p}_\pi, \quad (58)$$

$$f_4(s,\mathbf{p}_\pi) = I_3(s_{NN\pi},m_\pi,m_N^*,m_N^*)/[2I_4(s,m_\pi,m_\pi,m_N^*,m_N^*)], \quad (59)$$

$$I_4(s,m_\pi,m_\pi,m_N^*,m_N^*) = \frac{\pi}{2}\int_{4m_N^{*2}}^{(\sqrt{s}-2m_\pi)^2}\frac{\lambda(s_{NN},m_N^{*2},m_N^{*2})}{s_{NN}} \times I_3(s,m_\pi,\sqrt{s_{NN}},m_\pi)ds_{NN}, \quad (60)$$

$$s_{NN\pi} = s + m_\pi^2 - 2(E_0' + E_t)E_\pi + 2(\mathbf{p}_0' + \mathbf{p}_t)\cdot\mathbf{p}_\pi. \quad (61)$$

For the total cross sections $\sigma_{pN\to NN\pi}$ and $\sigma_{pN\to NN2\pi}$ entering into equations (51)–(55), we used the parametrization suggested in [55] (see, also, [10]) in which the threshold energy $\epsilon_{\rm thr}^{(k)}$ for the considered reaction k [(38) or (39)] has been properly corrected for the effective mass m_N^* of the secondary nucleons.

Taking into account the two-body kinematics of the elementary processes (40) and (41), we can readily get the following expression for the Lorentz invariant inclusive cross sections for these processes:

$$E_{K^+}\frac{d\sigma_{\pi N\to K^+Y}(\sqrt{s_1},\mathbf{p}_{K^+})}{d\mathbf{p}_{K^+}} = \frac{\pi}{I_2(s_1,m_Y^*,m_K)} \times\frac{d\sigma_{\pi N\to K^+Y}(s_1)}{d\mathbf{\Omega}^*}\frac{1}{(\omega + E_t')} \times\delta\left[\omega + E_t' - \sqrt{m_Y^{*2} + (\mathbf{Q} + \mathbf{p}_t')^2}\right], \quad (62)$$

$$I_2(s_1,m_Y^*,m_K) = \frac{\pi}{2}\frac{\lambda(s_1,m_Y^{*2},m_K^2)}{s_1}, \quad (63)$$

$$\omega = E_\pi - E_{K^+}, \quad \mathbf{Q} = \mathbf{p}_\pi - \mathbf{p}_{K^+}, \quad E_\pi = \sqrt{p_\pi^2 + m_\pi^2}. \quad (64)$$

Here, $d\sigma_{\pi N\to K^+Y}(s_1)/d\mathbf{\Omega}^*$ are the K^+ differential cross sections in the πN center-of-mass system. According to Cugnon *et al.* [56], we choose the K^+ angular distributions in the forms

$$\frac{d\sigma_{\pi^+n\to K^+\Lambda}(s_1)}{d\mathbf{\Omega}^*} = [1 + A_1(\sqrt{s_1})\cos\vartheta_{K^+}^*]\frac{\sigma_{\pi^+n\to K^+\Lambda}(\sqrt{s_1})}{4\pi}, \quad (65)$$

$$\frac{d\sigma_{\pi^0p\to K^+\Lambda}(s_1)}{d\mathbf{\Omega}^*} = \frac{1}{2}\frac{d\sigma_{\pi^+n\to K^+\Lambda}(s_1)}{d\mathbf{\Omega}^*}, \quad (66)$$

$$\frac{d\sigma_{\pi N\to K^+\Sigma}(s_1)}{d\mathbf{\Omega}^*} = [1 + |\cos\vartheta_{K^+}^*|]\frac{\sigma_{\pi N\to K^+\Sigma}(\sqrt{s_1})}{6\pi}. \quad (67)$$

The parameter A_1 and the total cross section $\sigma_{\pi^+n\to K^+\Lambda}$ of the reaction $\pi^+n \longrightarrow K^+\Lambda$ can be parametrized as [56]

$$A_1(\sqrt{s_1}) = \begin{cases} 5.26\left(\dfrac{\sqrt{s_1}-\sqrt{s_0}}{\text{GeV}}\right) \text{ for } \sqrt{s_0} < \sqrt{s_1} \le 1.8 \text{ GeV} \\ 1 \text{ for } \sqrt{s_1} > 1.8\text{GeV}, \end{cases} \quad (68)$$

$$\sigma_{\pi^+n\to K^+\Lambda}(\sqrt{s_1}) = \begin{cases} 10.0\left(\dfrac{\sqrt{s_1}-\sqrt{s_0}}{\text{GeV}}\right) \text{[mb] for } \sqrt{s_0} < \sqrt{s_1} \le 1.7 \text{ GeV} \\ 0.09\left(\dfrac{\text{GeV}}{\sqrt{s_1}-1.6\text{ GeV}}\right) \text{[mb] for } \sqrt{s_1} > 1.7 \text{ GeV}, \end{cases} \quad (69)$$

where $\sqrt{s_0} = m_K + m_\Lambda^*$ is the in-medium threshold energy. It is interesting to note that both the above parametrization (69) for the total cross section $\sigma_{\pi^+n\to K^+\Lambda}$ of reaction $\pi^+n \longrightarrow K^+\Lambda$ and those from [18, 57] lead to similar results for the respective kaon-production cross sections in *pA* collisions at subthreshold incident energies. For the total cross sections $\sigma_{\pi N\to K^+\Sigma}(\sqrt{s_1})$, we have used the following parametrization suggested in [58] on the basis of the resonance-model calculations:

$$\sigma_{\pi N\to K^+\Sigma}(\sqrt{s_1}) = \sum_{n=1}^{2} \frac{d_n(\sqrt{s_1}-\sqrt{\tilde{s}_0})^{f_n}}{(\sqrt{s_1}-c_n)^2 + b_n}, \quad (70)$$

where $\sqrt{\tilde{s}_0} = m_K + m_\Sigma^*$ is the in-medium threshold energy and the constants d_n, b_n, c_n, and f_n are given in [58]. Within the representation (62), the inclusive invariant differential cross sections $E_{K^+}d\sigma_{\pi p\to K^+X}/d\mathbf{p}_{K^+}$ and $E_{K^+}d\sigma_{\pi n\to K^+X}/d\mathbf{p}_{K^+}$ for kaon production in πp and πn interactions appearing in equation (47) can be written in the forms:

$$E_{K^+}\frac{d\sigma_{\pi^+p\to K^+X}(\sqrt{s_1},\mathbf{p}_{K^+})}{d\mathbf{p}_{K^+}} = E_{K^+}\frac{d\sigma_{\pi^+p\to K^+\Sigma^+}(\sqrt{s_1},\mathbf{p}_{K^+})}{d\mathbf{p}_{K^+}},$$

$$E_{K^+}\frac{d\sigma_{\pi^+n\to K^+X}(\sqrt{s_1},\mathbf{p}_{K^+})}{d\mathbf{p}_{K^+}} \quad (71)$$

$$= E_{K^+}\frac{d\sigma_{\pi^+n\to K^+\Lambda}(\sqrt{s_1},\mathbf{p}_{K^+})}{d\mathbf{p}_{K^+}} + E_{K^+}\frac{d\sigma_{\pi^+n\to K^+\Sigma^0}(\sqrt{s_1},\mathbf{p}_{K^+})}{d\mathbf{p}_{K^+}};$$

$$E_{K^+}\frac{d\sigma_{\pi^0p\to K^+X}(\sqrt{s_1},\mathbf{p}_{K^+})}{d\mathbf{p}_{K^+}} = E_{K^+}\frac{d\sigma_{\pi^0p\to K^+\Lambda}(\sqrt{s_1},\mathbf{p}_{K^+})}{d\mathbf{p}_{K^+}}$$

$$+ E_{K^+}\frac{d\sigma_{\pi^0p\to K^+\Sigma^0}(\sqrt{s_1},\mathbf{p}_{K^+})}{d\mathbf{p}_{K^+}}, \quad (72)$$

$$E_{K^+}\frac{d\sigma_{\pi^0n\to K^+X}(\sqrt{s_1},\mathbf{p}_{K^+})}{d\mathbf{p}_{K^+}} = E_{K^+}\frac{d\sigma_{\pi^0n\to K^+\Sigma^-}(\sqrt{s_1},\mathbf{p}_{K^+})}{d\mathbf{p}_{K^+}};$$

$$E_{K^+}\frac{d\sigma_{\pi^-p\to K^+X}(\sqrt{s_1},\mathbf{p}_{K^+})}{d\mathbf{p}_{K^+}} = E_{K^+}\frac{d\sigma_{\pi^-p\to K^+\Sigma^-}(\sqrt{s_1},\mathbf{p}_{K^+})}{d\mathbf{p}_{K^+}}, \quad (73)$$

$$E_{K^+}\frac{d\sigma_{\pi^-n\to K^+X}(\sqrt{s_1},\mathbf{p}_{K^+})}{d\mathbf{p}_{K^+}} = 0.$$

According to [10], a simpler expression like formula (90) from [10] can be given for the invariant differential cross section $E_{K^+}\dfrac{d\sigma_{ij}^{(\text{sec})}(\mathbf{p}_0)}{d\mathbf{p}_{K^+}}$ (43). As compared to equation (90) from [10], it includes the effective hyperon mass m_Y^* instead of its free mass m_Y. For the purpose of brevity of presentation, we did not give it here. Results of investigations [10] indicate that the main contribution to the K^+ production in the two-step reaction channels (38)–(41) both at subthreshold and above the free *NN* threshold incident energies comes from the uncorrelated part $P_0(\mathbf{p}_t, E)$ of the nucleon spectral function alone. Therefore, we will hereafter adopt only the $E_{K^+}\dfrac{d\sigma_{00}^{(\text{sec})}(\mathbf{p}_0)}{d\mathbf{p}_{K^+}}$ term in the sum (42) to calculate the K^+ yield in *pA* interactions from the secondary channels (40) and (41).

To show the validity of the present approach in the description of the kaon yield in *pA* collisions from these channels, it is obviously necessary to be able to reproduce, within this approach, the high-momentum parts of the charged-pion spectra measured at forward laboratory angles for the beam energies between 1 and 2 GeV. Taking into consideration the pion final-state absorption, as well as according to equations (19)–(22), we easily come to the following expression for the invariant inclusive cross section of pion production on nuclei from the primary proton-induced reaction channels (38) and (39) (see, also, [16]):

$$E_\pi\frac{d\sigma_{pA\to\pi X}^{(\text{prim})}(\mathbf{p}_0)}{d\mathbf{p}_\pi} = I_V'[A]\left\langle E_\pi\frac{d\sigma_{pN\to\pi X}(\mathbf{p}_0,\mathbf{p}_\pi)}{d\mathbf{p}_\pi}\right\rangle, \quad (74)$$

where

$$I_V'[A] = A\int\rho(\mathbf{r})d\mathbf{r}\exp\left[-\mu(p_0)\int_{-\infty}^{0}\rho(\mathbf{r}+x\mathbf{\Omega}_0)dx - \mu(p_\pi)\int_0^{\infty}\rho(\mathbf{r}+x\mathbf{\Omega}_\pi)dx\right], \quad (75)$$

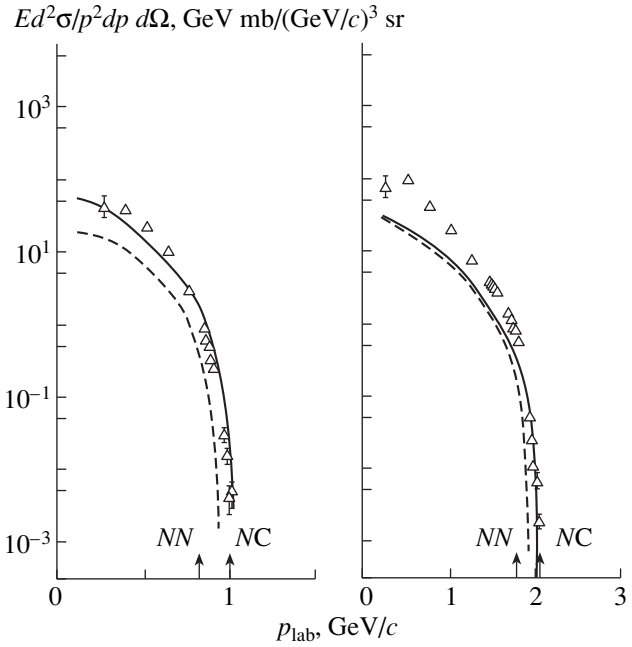

Fig. 2. Lorentz-invariant negative-pion inclusive cross sections versus the (lab) momentum at 0° for 1.05- (left) and 2.1-GeV (right) protons interacting with a carbon target. The experimental data (open triangles) are from [59]. The curves are our calculation. The solid and dashed curves are our calculation by (74)–(77) for primary production processes (38) and (39) with the total nucleon spectral function at V_0 = 40 MeV, $U^N_{\rm eff}$ = –34 MeV and V_0 = 0, $U^N_{\rm eff}$ = 0, respectively, The arrows indicate the kinematical limits for pion production from free nucleons as well as from nucleon–nucleus interactions.

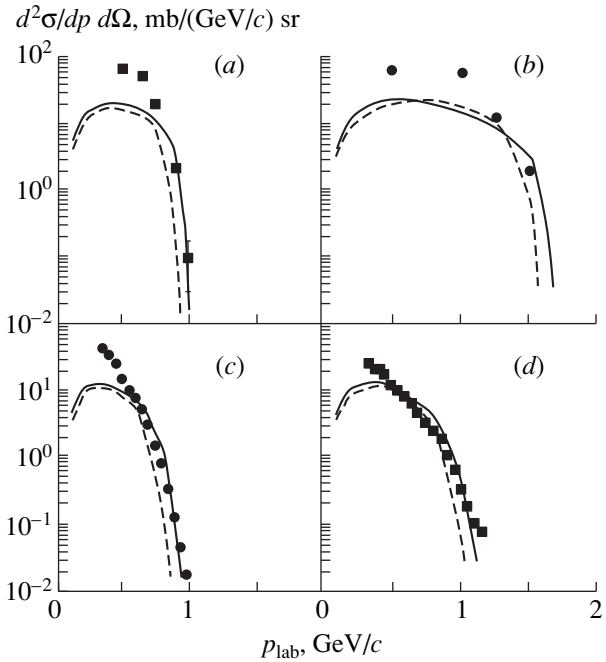

Fig. 3. Measured and calculated positive-pion-production cross sections in pC collisions at different bombarding energies and outgoing laboratory angles: (*a*) 1.05 GeV, 0° [60]; (*b*) 1.73 GeV, 0° [60]; (*c*) 1.2 GeV, 40° [8]; and (*d*) 1.5 GeV, 40° [8]. The curves are results of our model at V_0 = 40 MeV, $U^N_{\rm eff}$ = –34 MeV (solid curve) and at V_0 = 0, $U^N_{\rm eff}$ = 0 (dashed curve).

$$\left\langle E_\pi \frac{d\sigma_{pN\to\pi X}(\mathbf{p}_0, \mathbf{p}_\pi)}{d\mathbf{p}_\pi} \right\rangle = \int\int P(\mathbf{p}_t, E) d\mathbf{p}_t dE \left[E_\pi \frac{d\sigma_{pN\to\pi X}(\sqrt{s}, \mathbf{p}_\pi)}{d\mathbf{p}_\pi} \right]. \quad (76)$$

The quantity $\mu(p_\pi)$ entering into equation (75) and the differential cross sections for pion production in pN collisions are defined above by the formulas (45) and (46), (51)–(61), respectively. Since we are interested in the spectra of emitted pions at forward laboratory angles, i.e., when $\mathbf{\Omega}_\pi \approx \mathbf{\Omega}_0$, we can easily obtain, for a nucleus with the uniform density of nucleons of a radius $R = 1.3A^{1/3}$ fm, the following simple form for the integral (75) [16]:

$$I'_V[A] = \frac{3A}{(a_1 - a_2)a_2^2} \times \left\{ 1 - (1 + a_2)e^{-a_2} - \left(\frac{a_2}{a_1}\right)^2 [1 - (1 + a_1)e^{-a_1}] \right\}, \quad (77)$$

where $a_1 = 3\mu(p_\pi)/2\pi R^2$ and $a_2 = 3\mu(p_0)/2\pi R^2$. The comparison of the results of our calculations by (74)–(77) for the Lorentz invariant inclusive cross sections for the π^--meson production at 0° in the interactions of 1.05- and 2.1-GeV protons with ^{12}C nuclei with the experimental data [59] is given in Fig. 2. The elementary cross sections $\sigma^{\rm in}_{pN}$ and $\sigma^{\rm tot}_{\pi N}$ in the calculations were assumed to be, respectively, 30 and 35 mb [10]. One can see that our calculations reproduce quite well the high-momentum tails of the pion spectra only if we include the effect of the mean fields (mainly the nucleon effective potential $U^N_{\rm eff}$) on the one-step production processes (38) and (39). Let us now discuss the results for π^+-meson production. In Fig. 3, we present the results of our calculations by (74)–(77) for the double-differential cross sections for π^+ production in pC collisions at different incident energies and outgoing angles as well as the experimental data [8, 60]. It is seen that the agreement between the model calculations and the measurements in the high-momentum parts of the π^+ spectra is quite remarkable, as in the above comparison for the π^- spectra, only if we take into account the in-medium effects on secondary nucleons. Therefore, we are confident that our approach is realistic enough

to describe K^+ production through the reactions $\pi N \longrightarrow K^+Y$.

Let us now discuss the results of our calculations for kaon production in pBe and pC interactions in the framework of model outlined above.

2. RESULTS AND DISCUSSION

Figure 4 shows the invariant cross sections calculated by (19) and (42) for the production of K^+ mesons with a momentum of 1.28 GeV/c at the laboratory angle of 10.5° through the primary $pN \longrightarrow K^+YN$ and secondary $\pi N \longrightarrow K^+Y$ channels and the experimental data [11] for $p + {}^9\mathrm{Be} \longrightarrow K^+ + X$ reactions at the various bombarding energies. One can see that

(1) our model for primary and secondary kaon-production processes, based on the nucleon spectral function, completely fails to reproduce the experimental data at subthreshold beam energies (at energies $\lesssim$2.1 GeV for the kinematical conditions of the experiment [11]) without allowance for the influence of the corresponding effective potentials on the one-step [(1) and (2)] and two-step [(38)–(41)] production processes;

(2) our calculations of the one-step reaction channels (1) and (2) with the set of parameters V_0 = 40 MeV, U_{eff}^N = –34 MeV, U_{eff}^Λ = –30 MeV, and U_{eff}^Σ = –26 MeV [see (6)] reproduce quite well the experimental data [11] in the energy region far below the lowest threshold, but overestimate the data by a factor of 2 at higher bombarding energies, which indicates that there is no need for employing the medium effects considered by us at these energies;

(3) the results of our calculations of the kaon yield from the two-step reaction channels (38)–(41) with the same set of parameters for the effective potentials V_0, U_{eff}^N, U_{eff}^Λ, and U_{eff}^Σ as that used above in calculating the K^+ yield from the primary reaction channels (1) and (2) substantially underestimate the data [11] both at subthreshold and above-threshold incident energies, which means the dominance of the one-step K^+-production mechanism for the considered "hard"-kaon production at all beam energies of interest;

(4) the contributions to the K^+ production from the primary reaction channels (1) and (2) with Λ and Σ particles in the final states are comparable at bombarding energies $\epsilon_0 \gtrsim 2.2$ GeV, whereas, at lower incident energies, the primary production process (1) is more important than (2);

(5) the primary proton–nucleon production process (1) misses the experimental data in the far subthreshold region when the effective potential U_{eff}^Λ that is seen inside the nucleus by a slow Λ particle grows from the value of U_{eff}^Λ = –30 MeV, estimated from the study of the binding and decay of hypernuclei, to U_{eff}^Λ = –20 MeV,

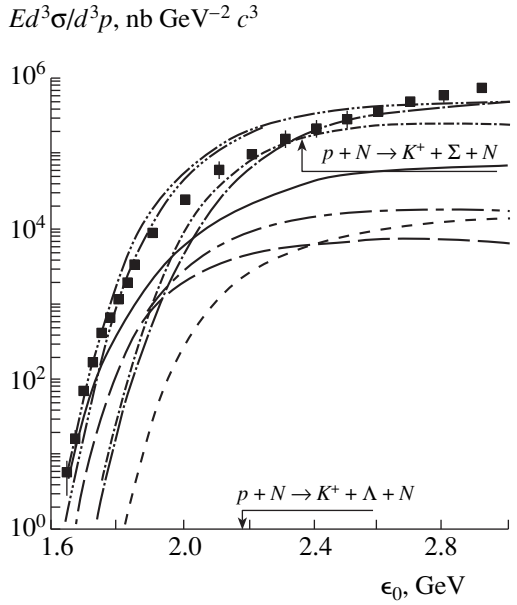

Fig. 4. Lorentz invariant cross sections for the production of K^+ mesons with a momentum of 1.28 GeV/c at the laboratory angle of 10.5° in $p + {}^9\mathrm{Be}$ reactions as functions of the laboratory energy of the proton. The experimental data (full squares) are from [11]. The curves are our calculation. The dashed curves with one, two, and three dots are calculations by (19) for primary production processes (1) and (2) with the total nucleon spectral function at $V_0 = 0$, $U_{\mathrm{eff}}^N = 0$, U_{eff}^Λ = 0, and U_{eff}^Σ = 0; V_0 = 40 MeV, U_{eff}^N = –34 MeV, U_{eff}^Λ = –30 MeV, and U_{eff}^Σ = –26 MeV; and V_0 = 40 MeV, U_{eff}^N = –34 MeV, U_{eff}^Λ = –20 MeV, and U_{eff}^Σ = –26 MeV, respectively. The two-dot-dashed curve represents our calculations by (19) for primary production process (2) with the total nucleon spectral function at V_0 = 40 MeV, U_{eff}^N = –34 MeV, U_{eff}^Σ = –26 MeV. The solid curve denotes the same as the dashed curve with two dots, but it is supposed that the total nucleon spectral function given by equations (29), (30), and (33) is replaced by its correlated part (33). The short- and long-dashed curves are calculations by (42) for the secondary production process (40) with the use of the uncorrelated part of the nucleon spectral function in the calculation of momentum–energy-averaged differential cross sections for pion and kaon production at $V_0 = 0$, $U_{\mathrm{eff}}^N = 0$, and $U_{\mathrm{eff}}^\Lambda = 0$ and V_0 = 40 MeV, U_{eff}^N = –34 MeV, and U_{eff}^Λ = –30 MeV, respectively. The curve with alternating short and long dashes represents calculations by (42) for the secondary production processes (40) and (41) with the use of the uncorrelated part of the nucleon spectral function in the calculation of momentum–energy-averaged differential cross sections for pion and kaon production at V_0 = 40 MeV, U_{eff}^N = –34 MeV, U_{eff}^Λ = –30 MeV, and U_{eff}^Σ = –26 MeV. The arrows indicate the thresholds for the reactions $pN \longrightarrow K^+\Lambda N$ and $pN \longrightarrow K^+\Sigma N$ occurring on a free nucleon.

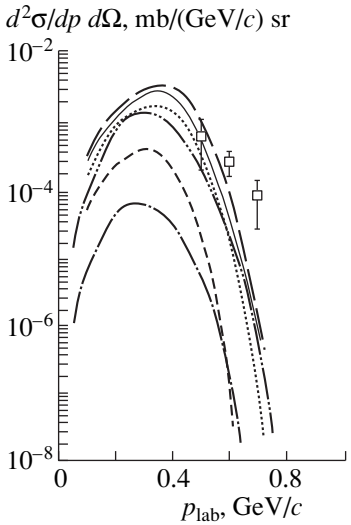

Fig. 5. Double-differential cross sections for the production of K^+ mesons at an angle of 40° in the interaction of 1.2-GeV protons with ^{12}C nuclei as functions of kaon momentum. The experimental data (open squares) are from [8]. The curves are our calculation. The dashed curves with one and two dots are calculations by (19) for the primary production process (1) with the total nucleon spectral function at $V_0 = 0$, $U_{\text{eff}}^N = 0$, $U_{\text{eff}}^\Lambda = 0$ and $V_0 = 40$ MeV, $U_{\text{eff}}^N = -34$ MeV, $U_{\text{eff}}^\Lambda = -30$ MeV, respectively. The short-, long-dashed, and dotted curves are calculations by (42) for the secondary production process (40) with the use of the uncorrelated part of the nucleon spectral function in the calculation of momentum–energy-averaged differential cross sections for pion and kaon production at $V_0 = 0$, $U_{\text{eff}}^N = 0$, and $U_{\text{eff}}^\Lambda = 0$; $V_0 = 40$ MeV, $U_{\text{eff}}^N = -34$ MeV, and $U_{\text{eff}}^\Lambda = -30$ MeV; and $V_0 = 40$ MeV, $U_{\text{eff}}^N = -34$ MeV, and $U_{\text{eff}}^\Lambda = 0$, respectively. The thin solid curve is the sum of the dashed curve with two dots and the dotted curve.

which implies the strong sensitivity of "hard"-kaon yield at "low" beam energies to the lambda potential in the nuclear matter;

(6) the kaon yield from the one-step K^+-production mechanism is entirely governed by the correlated part $P_1(\mathbf{p}_t, E)$ of the nucleon spectral function only in the vicinity of the absolute reaction threshold (at bombarding energies of $\epsilon_0 \approx 1.65$–1.70 GeV), which suggests the difficulty of extracting information on the high-momentum and high-removal-energy components within the target nucleus even from the "hard"-kaon-production experiment [11].

The results of our calculations by (19) and (42) for the double-differential cross sections for the production of "soft" K^+ mesons from primary $pN \longrightarrow K^+YN$ and secondary $\pi N \longrightarrow K^+Y$ channels at an angle of 40° in the interaction of protons with energies of 1.2, 1.5, and 2.5 GeV with ^{12}C nuclei and the experimental data [8] are displayed in Figs. 5–7. It is seen that

(1) our model calculations for proton- and pion-induced reaction channels underpredict significantly the data at 1.2- and 1.5-GeV incident energies without taking into account the medium effects on the hadrons produced in these channels, which is consistent with our previous findings of Fig. 4;

(2) the inclusion of the in-medium effects under consideration leads to the substantial enhancement of the K^+ cross sections both from primary and secondary kaon-production processes at 1.2- and 1.5-GeV beam energies as well as to a similar magnitude[4)] for these K^+-creation processes at the indicated bombarding energies;

(3) the "soft"-kaon yield from the secondary reaction channel (40) with Λ particle in the final state at 1.2- and 1.5-GeV beam energies is not too sensitive to the effective potential U_{eff}^Λ that is seen inside the nucleus by a lambda when this potential grows from $U_{\text{eff}}^\Lambda = -30$ MeV to $U_{\text{eff}}^\Lambda = 0$, and, moreover, the discrepancy between the calculations with allowance for the influence of this potential on the production process (40) and without it is more prominent with the lowering of the incident energy;

(4) the one-step K^+-production mechanism clearly dominates at 2.5-GeV proton beam energy both with and without the influence of the mean fields on the one-step production processes (1) and (2);

(5) the high-momentum tail[5)] ($p_{\text{lab}} \geq 0.9$ GeV/c) of the kaon spectrum measured in [8] at a 2.5-GeV incident energy is much better reproduced by our first-chance collision model when including the same influence of the mean fields on the one-step production processes (1) and (2) as that employed above (see Fig. 4) in the analysis of the energy dependence of the "hard"-kaon production taken in [11], whereas its low-momentum tail ($p_{\text{lab}} \leq 0.6$ GeV/c) is reasonably well described by the model both with and without this influence;

(6) our overall calculations {the sum of the results obtained both for the one-step [(1) and (2)] and two-step [(38)–(41)] reaction channels, thin solid curves in Figs. 5–7} reasonably reproduce the experimental data only if we include the effect of the respective effective potentials on the one-step kaon-production processes (1) and (2) and on pion production reactions (38) and (39).

It should be pointed out that the two-pion-production reactions (39) have been taken into account in the above calculations only at a 2.5-GeV incident labora-

[4)] It should be mentioned that the first-chance collision models [8, 10], based on nucleon spectral function as well as on discarding any self-energies for the produced hadrons, predict a minor role for the direct K^+-production processes (1) and (2) compared to that for the secondary K^+-reaction channels (40) and (41) in subthreshold kaon production in pC interactions at these bombarding energies.

[5)] It should be noticed that, for kinematical conditions of the experiment [8], the kaons emitted with the laboratory momenta $p_{\text{lab}} \geq 0.9$ GeV/c are subthreshold kaons.

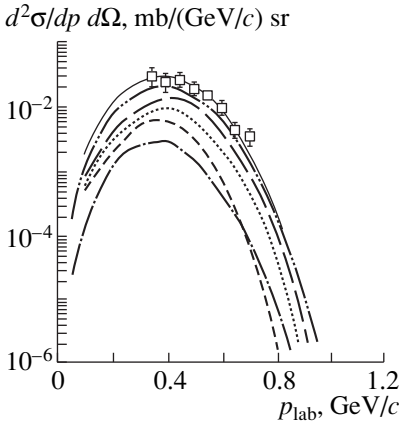

Fig. 6. Double-differential cross sections for the production of K^+ mesons at an angle of 40° in the interaction of 1.5-GeV protons with the ^{12}C nuclei as functions of kaon momentum. The dashed curves with one and two dots are calculations by (19) for primary production processes (1) and (2) with the total nucleon spectral function at $V_0 = 0$, $U^N_{\text{eff}} = 0$, $U^\Lambda_{\text{eff}} = 0$, and $U^\Sigma_{\text{eff}} = 0$ and $V_0 = 40$ MeV, $U^N_{\text{eff}} = -34$ MeV, $U^\Lambda_{\text{eff}} = -30$ MeV, and $U^\Sigma_{\text{eff}} = -26$ MeV, respectively. The rest of the notation is identical to that in Fig. 5.

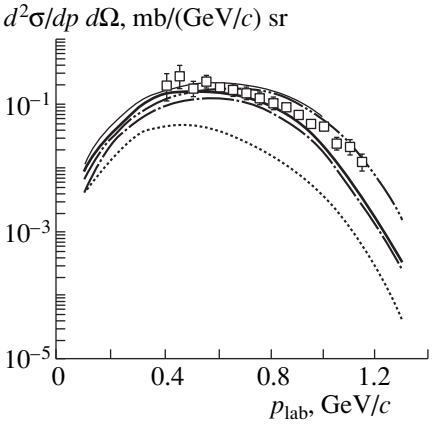

Fig. 7. Double-differential cross sections for the production of K^+ mesons at an angle of 40° in the interaction of 2.5-GeV protons with ^{12}C nuclei as functions of kaon momentum. The dotted curve is calculation by (42) for the secondary production processes (40) and (41) with the use of the uncorrelated part of the nucleon spectral function in the calculation of momentum–energy-averaged differential cross sections for pion and kaon production at $V_0 = 40$ MeV, $U^N_{\text{eff}} = -34$ MeV, $U^\Lambda_{\text{eff}} = 0$, and $U^\Sigma_{\text{eff}} = 0$. The dashed curves with one and two dots and the thin solid curve denote the same as in Fig. 5. The thick solid curve is the sum of the dash-dotted and dotted curves.

tory kinetic energy, where their contribution to the inelastic cross sections of free pN interaction is about 40%. It is also worth mentioning that the present model can simultaneously reproduce the π^+ spectra measured in the same experiment [8] (see Fig. 3).

Figure 8 presents a comparison of the results of our calculations by (19) and (42) for the Lorentz invariant inclusive cross sections for the production of K^+ mesons at the laboratory angle of 10.5° from the proton- and pion-induced reaction channels with the experimental data [12] for $p + {}^9\text{Be} \longrightarrow K^+ + X$ reactions at a 1.7-GeV beam energy. It can be seen that

(1) the model calculations for the primary and secondary kaon-production processes substantially underestimate the subthreshold data points,[6)] as in the above cases (cf. Figs. 4–7), without including the in-medium effects considered by us;

(2) the high-momentum part of the measured kaon spectrum is fairly well reproduced by the calculations for the one-step production processes (1) and (2) with allowance for the same influence of the nuclear mean fields on these processes as those adopted above in the analysis of the other experimental data [8, 11] on subthreshold kaon production in pBe and pC collisions (see Figs. 4–7), whereas its low-momentum part is overestimated in the calculations by a factor of about 2 to 3;

(3) our calculations of the kaon yield from the two-step production processes (38)–(41) with the same set of parameters for the effective potentials V_0, U^N_{eff}, U^Λ_{eff}, and U^Σ_{eff} as that employed above (see Figs. 5–7) in the analysis of the corresponding K^+ yield from pC interactions significantly underestimate the subthreshold data points, which indicates the dominance of the one-step K^+-production mechanism at the laboratory kaon momenta $p_{\text{lab}} > 0.8$ GeV/c;

(4) the high-momentum tail of the kaon spectrum from direct K^+-production mechanism is almost completely determined by the correlated part $P_1(\mathbf{p}_t, E)$ of the nucleon spectral function only in a very limited range of kaon momenta ($p_{\text{lab}} \approx 1.25$–$1.35$ GeV/c), which makes it difficult to extract this part from the experimental data [12].

In Fig. 9, we compare the results of our calculations by (19) and (42) for the total cross sections for K^+ production in p^{12}C collisions from primary $pN \longrightarrow K^+YN$ and secondary $\pi N \longrightarrow K^+\Lambda$ channels with the experimental data [1]. It is clearly seen that

(1) the calculations for primary and secondary kaon-production channels essentially miss the data in line with our findings inferred above from the analysis of the data on differential kaon-production cross sections when no self-energy effects have been employed and, moreover, the primary pN and secondary πN channels are of the same order of magnitude in this case;

[6)] It should be noted that, for kinematical conditions of the experiment [12], the data points which correspond to the laboratory kaon momenta $p_{\text{lab}} \geq 0.8$ GeV/c are the subthreshold data points.

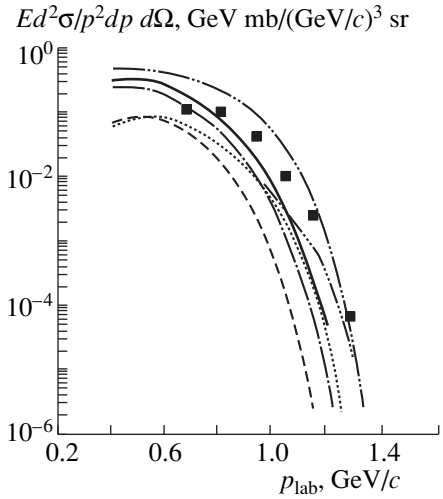

Fig. 8. Lorentz invariant inclusive cross sections for the production of K^+ mesons at an angle of 10.5° in the interaction of 1.7-GeV protons with ^{9}Be nuclei as functions of kaon momentum. The experimental data (full squares) are from [12]. The curves are our calculation. The dashed curves with one and two dots are calculations by (19) for primary production processes (1) and (2) with the total nucleon spectral function at $V_0 = 0$, $U^N_{\text{eff}} = 0$, $U^\Lambda_{\text{eff}} = 0$, and $U^\Sigma_{\text{eff}} = 0$ and $V_0 =$ 40 MeV, $U^N_{\text{eff}} = -34$ MeV, $U^\Lambda_{\text{eff}} = -30$ MeV, and $U^\Sigma_{\text{eff}} =$ –26 MeV, respectively. The dashed curve with three dots denotes the same as the dashed curve with two dots, but it is supposed that the total nucleon spectral function given by equations (29), (30), and (33) is replaced by its correlated part (33). The short-dashed and dotted curves are calculations by (42) for the secondary production processes (40) and (41), with the use of the uncorrelated part of the nucleon spectral function in the calculation of momentum-energy-averaged differential cross sections for pion and kaon production at $V_0 =$ 0, $U^N_{\text{eff}} = 0$, $U^\Lambda_{\text{eff}} = 0$, and $U^\Sigma_{\text{eff}} = 0$ and $V_0 = 40$ MeV, $U^N_{\text{eff}} =$ –34 MeV, $U^\Lambda_{\text{eff}} = 0$, and $U^\Sigma_{\text{eff}} = 0$, respectively. The thick solid curve is the sum of the dash-dotted and dotted curves.

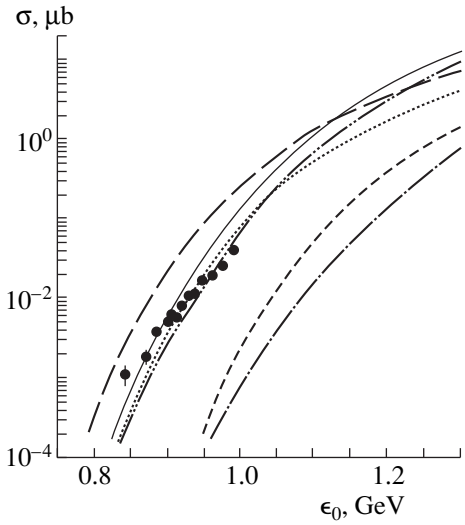

Fig. 9. The total cross sections for K^+ production in $p + {}^{12}$C interactions as functions of the laboratory energy of the proton. The experimental data (full circles) are from [1]. The curves are calculation. The dashed curves with one and two dots are calculations by (19) for primary production processes (1) and (2) with the total nucleon spectral function at $V_0 = 0$, $U^N_{\text{eff}} = 0$, $U^\Lambda_{\text{eff}} = 0$, and $U^\Sigma_{\text{eff}} = 0$ and $V_0 = 40$ MeV, $U^N_{\text{eff}} = -34$ MeV, $U^\Lambda_{\text{eff}} = -30$ MeV, and $U^\Sigma_{\text{eff}} = -26$ MeV, respectively. The short-, long-dashed, and dotted curves are calculations by (42) for the secondary production process (40) with Λ particle in the final state with the use of the uncorrelated part of the nucleon spectral function at $V_0 = 0$, $U^N_{\text{eff}} = 0$, and $U^\Lambda_{\text{eff}} = 0$; $V_0 = 40$ MeV, $U^N_{\text{eff}} = -34$ MeV, and $U^\Lambda_{\text{eff}} = -30$ MeV; and $V_0 = 40$ MeV, $U^N_{\text{eff}} = -34$ MeV, and $U^\Lambda_{\text{eff}} = 0$, respectively. The thin solid curve is the sum of the dashed curve with two dots and a dotted curve.

(2) approximately an equal magnitude[7)] for these channels is gained at beam energies below about 1.1 GeV, when the same influence of the nuclear mean fields on them as that which allowed us to describe the existing experimental data [8, 11, 12] on the differential kaon-production cross sections (cf. Figs. 4–8) has been included;

(3) our full calculations {the sum of results obtained both for the one-step [(1) and (2)] and for two-step [(38)–(40)] reaction channels, thin solid curve in Fig. 9}, which adopted the influence of the respective effective potentials on these channels, reasonably well reproduce the measured [1] total K^+-production cross sections[8)] at proton energies below about 900 MeV, but they slightly overestimate the data at higher bombarding energies.

Finally, Fig. 10 shows the same comparison as that presented in Fig. 9, but also includes data points at pro-

[7)]It should be emphasized that this finding is in disagreement with the conclusions of the authors of earlier studies [3–5] of the measured [1] total cross sections for K^+ production from pA collisions in the framework of the simple folding models, who claim the dominance of the secondary N channel for K^+ production in proton–nucleus reactions at subthreshold energies. This result also disagrees with the recent studies [9, 10] of the data [1] on total K^+-production cross section from pC interactions within the spectral-function approach without including any self-energy effect for hadrons created in direct processes (1) and (2), since it has been claimed in [9, 10] that the two-step kaon-production mechanism with an intermediate pion dominates in the subthreshold regime as in the folding models [3–5].

[8)]It is interesting to note that we are able to reproduce reasonably well these cross sections also within the simple folding model (cf. [3–5]) for the two-step K^+-production mechanism ($pN_1 \longrightarrow \pi NN$, $\pi N_2 \longrightarrow K^+\Lambda$) which is obtained from the present model by replacing the total nucleon spectral function by the shell-model momentum distribution (32), assuming the struck target nucleon to be on mass shell, and employing only the repulsive optical potential of about $V_0 \approx 50$ MeV in the entrance channel in line with [3, 5, 9].

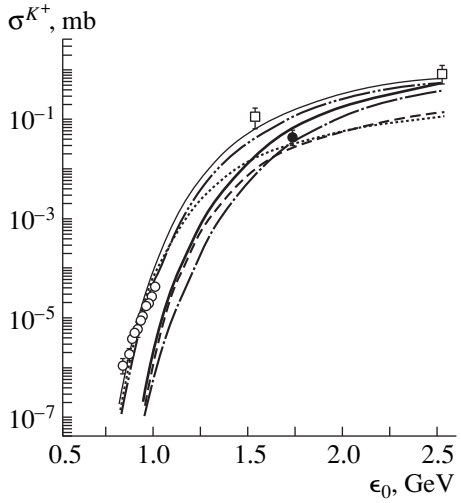

Fig. 10. The total cross sections for K^+ production in $p + {}^{12}C$ interactions as functions of the laboratory energy of the proton. The experimental data are from [1, 8, 61]. The curves are our calculation. The short-dashed and dotted curves are calculations by (42) for the two-step production processes (38)–(41) with the use of the uncorrelated part of the nucleon spectral function at $V_0 = 0$, $U^N_{\text{eff}} = 0$, $U^\Lambda_{\text{eff}} = 0$, and $U^\Sigma_{\text{eff}} = 0$ and $V_0 = 40$ MeV, $U^N_{\text{eff}} = -34$ MeV, $U^\Lambda_{\text{eff}} = 0$, and $U^\Sigma_{\text{eff}} = 0$, respectively. The thick solid curve is the sum of the dash-dotted and short-dashed curves. The rest of the notation is identical to that in Fig. 9.

ton energies of 1.5, 1.7, and 2.5 GeV. The data points at 1.5 and 2.5 GeV were taken from [8], where they have been deduced from the measured double differential cross section for K^+ production at these incident energies (see Figs. 6, 7). The data point at 1.7 GeV was taken from [61], where it has been extracted from the inclusive invariant cross sections for kaon production in p^9Be interactions, given in Fig. 8, assuming an $A^{2/3}$ scaling to make an extrapolation from ^{9}Be to ^{12}C target nuclei. It is nicely seen that our overall model calculations (the sum of results obtained both for primary and secondary kaon-production processes, thin solid curve in Fig. 10) including the same mean-field effects as those that allowed us to describe above the data both on differential [8, 11, 12] and total [1] kaon-production cross sections also reproduce fairly well the measured [8] total K^+-production cross sections at proton energies of 1.5 and 2.5 GeV and overestimate the data point [61] at 1.7 GeV by a factor of about 3.[9)]

The similar calculations with no mean-field effects (thick solid curve in Fig. 10) reasonably describe both this data point and that at 2.5 GeV, but completely fail to reproduce the data at lower incident energies, which counts in favor of the former model calculations. It is also seen that, at beam energies below about 1.5 GeV, the contributions from the two-step and one-step kaon-production processes are comparable in both calculations.

Taking into account the considered above, one may conclude that the relative strength of the proton- and pion-induced reaction channels in light target nuclei in the subthreshold energy regime is mainly governed by the kinematics of the experiment on inclusive kaon production in pA interactions. Our results also demonstrate that further measurements of the total (and differential) cross sections for K^+ production on light nuclei in the proton-energy range 1.0–1.7 GeV are extremely needed nowadays to test reliably the spectral-function approach presented in this study, as well as to deeply elucidate the underlying mechanism of subthreshold kaon production and the role played by nucleon–nucleon correlations in this phenomenon.

SUMMARY

In this study, we have calculated the total and differential cross sections for K^+ production in p^9Be and p^{12}C interactions in the near-threshold and subthreshold energy regimes by considering incoherent primary proton–nucleon and secondary pion–nucleon production processes in the framework of an appropriate folding model, which properly takes into account the struck-target-nucleon momentum and removal-energy distribution, novel elementary cross sections for proton–nucleon reaction channel close to threshold, as well as nuclear mean-field potential effects on the one-step and two-step kaon-production processes. The detailed comparison of the results of our calculations with the existing experimental data [1, 8, 11, 12] was made. It was shown that these effects are of importance to explain consistently both the considered experimental data on kaon production and the measured [8, 59, 60] charged-pion spectra at forward angles from p^{12}C interactions at beam energies between 1.05 and 2.1 GeV. It was also found that, contrary to previous studies carried out in the literature, the pion–nucleon-production channels do not necessarily dominate in pA collisions at subthreshold energies and the relative weight of the proton- and pion-induced reaction channels in light target nuclei in the subthreshold energy regime is governed by the kinematics of experiment under consideration; namely, the one-step K^+-production mechanism clearly dominates in the subthreshold "hard"-kaon production in p^9Be [11, 12] and p^{12}C [8] collisions, whereas, in the subthreshold "soft"-kaon production in p^{12}C reactions [1, 8], the contributions from the direct and two-step kaon-production processes are comparable. Our present results indicate that the kaon yield from the one-step K^+-production mechanism is almost completely determined by the correlated part of the nucleon spectral function only in a very limited range of kaon momenta (for kaon spectra) or bombarding energies (for energy dependence), which makes it difficult to

[9)]Compare to the analogous difference in the low-momentum region between the measured and calculated kaon-production cross sections presented in Fig. 8.

extract it from the data under consideration. Therefore, further measurements of the differential cross sections for subthreshold production of "hard" K^+ mesons on light nuclei are needed both to test reliably the spectral-function approach presented in this work and to elucidate deeply the underlying mechanism of subthreshold kaon production and the role played by nucleon–nucleon correlations in this phenomenon.

ACKNOWLEDGMENTS

I am very grateful to Yu.T. Kiselev and V.A. Sheĭnkman for their information on experimental results from the ITEP synchrotron on near-threshold and subthreshold kaon production in proton–nucleus collisions as well as for valuable discussions throughout this study. I am also thankful to L.A. Kondratyuk for interest in the work.

REFERENCES

1. V. P. Koptev *et al.*, Zh. Éksp. Teor. Fiz. **94** (11), 1 (1988) [Sov. Phys. JETP **67**, 2177 (1988)].
2. A. Shor *et al.*, Nucl. Phys. A **514**, 717 (1990).
3. W. Cassing *et al.*, Phys. Lett. B **238**, 25 (1990).
4. A. A. Sibirtsev and M. Böscher, Z. Phys. A **347**, 191 (1994).
5. W. Cassing *et al.*, Z. Phys. A **349**, 77 (1994).
6. A. Sibirtsev, Phys. Lett. B **359**, 29 (1995).
7. B. Z. Kopeliovich and F. Niedermeier, Yad. Fiz. **44**, 517 (1986) [Sov. J. Nucl. Phys. **44**, 333 (1986)].
8. M. Debowski *et al.*, Z. Phys. A **356**, 313 (1996).
9. A. Sibirtsev *et al.*, Z. Phys. A **358**, 357 (1997).
10. S. V. Efremov and É. Ya. Paryev, Eur. Phys. J. A **1**, 99 (1998).
11. A. V. Akindinov *et al.*, APH (N.S.), Heavy Ion Physics **4**, 325 (1996).
12. Yu. T. Kiselev *et al.*, Preprint No. 56-96 ITEP (Moscow, 1996).
13. W. Oelert, nucl-ex/9803004; J. T. Balewski *et al.*, nucl-ex/9803003; W. Eyrich, in *Proceedings of Seventh International Symposium on Meson–Nucleon Physics and the Structure of the Nucleon, Vancouver, 1997*, p. 373.
14. W. Cassing *et al.*, Nucl. Phys. A **614**, 415 (1997).
15. E. L. Bratkovskaya *et al.*, Nucl. Phys. A **622**, 593 (1997).
16. S. V. Efremov *et al.*, Yad. Fiz. **55**, 521 (1992) [Sov. J. Nucl. Phys. **55**, 290 (1992)].
17. D. B. Kaplan and A. E. Nelson, Phys. Lett. B **175**, 57 (1986); A. E. Nelson and D. B. Kaplan, Phys. Lett. B **192**, 193 (1987).
18. C. Fuchs *et al.*, Phys. Rev. C **56**, R606 (1997).
19. G. Q. Li *et al.*, Phys. Rev. Lett. **74**, 235 (1995).
20. G. Q. Li and C. M. Ko, Nucl. Phys. A **594**, 460 (1995).
21. Bao-An Li and C. M. Ko, Phys. Rev. C **54**, 3283 (1996).
22. T. Waas *et al.*, Phys. Lett. B **379**, 34 (1996).
23. J. Schaffner and I. N. Mishustin, Phys. Rev. C **53**, 1416 (1996).
24. G. E. Brown and M. Rho, Nucl. Phys. A **596**, 503 (1996).
25. T. Waas *et al.*, Nucl. Phys. A **617**, 449 (1997).
26. G. E. Brown *et al.*, nucl-th/9608039.
27. W. Cassing *et al.*, Nucl. Phys. A **545**, 123c (1992).
28. M. Cahay *et al.*, Nucl. Phys. A **411**, 524 (1983).
29. S. Teis *et al.*, Z. Phys. A **356**, 421 (1997).
30. M. Goncalves *et al.*, Phys. Lett. B **406**, 1 (1997).
31. S. Teis *et al.*, Phys. Rev. C **50**, 388 (1994).
32. W. Ehehalt and W. Cassing, Nucl. Phys. A **602**, 449 (1996).
33. C. H. Lee *et al.*, Phys. Lett. B **412**, 235 (1997).
34. Z. Rudy *et al.*, Z. Phys. A **351**, 217 (1995).
35. Y. Yamamoto and H. Bando, Phys. Lett. B **214**, 173 (1988).
36. M. Hjorth-Jensen *et al.*, Nucl. Phys. A **605**, 458 (1996).
37. G. Q. Li and C. M. Ko, Phys. Rev. C **54**, 1897 (1996).
38. X. S. Fang *et al.*, Nucl. Phys. A **575**, 766 (1994).
39. X. S. Fang *et al.*, Phys. Rev. C **49**, R608 (1994).
40. R. H. Dalitz and A. Gal, Phys. Lett. B **64**, 154 (1976).
41. C. B. Dove and G. E. Walker, Phys. Rep. **89**, 1 (1982).
42. G. Q. Li and C. M. Ko, Phys. Lett. B **349**, 405 (1995).
43. C. Ciofi degli Atti and S. Simula, Phys. Lett. B **325**, 276 (1994).
44. C. Ciofi degli Atti *et al.*, Phys. Rev. C **43**, 1155 (1991).
45. W. J. Fickinger, Phys. Rev. **125**, 2082 (1962).
46. C. Ciofi degli Atti and S. Liuti, Phys. Lett. B **225**, 215 (1989).
47. C. Ciofi degli Atti *et al.*, Phys. Rev. C **41**, 2474 (1990).
48. C. Ciofi degli Atti *et al.*, Phys. Rev. C **44**, R7 (1991).
49. O. Benhar *et al.*, Nucl. Phys. A **579**, 493 (1994).
50. C. Ciofi degli Atti and S. Simula, Phys. Rev. C **53**, 1689 (1996).
51. L. B. Weinstein and G. A. Warren, Phys. Rev. C **50**, 350 (1994).
52. S. V. Efremov and É. Ya. Paryev, Yad. Fiz. **59**, 2143 (1996) [Phys. At. Nucl. **59**, 2063 (1996)].
53. G. Jacob and Th. Maris, Rev. Mod. Phys. **38**, 121 (1966); **45**, 6 (1973).
54. H. Tyren, Nucl. Phys. **79**, 321 (1966).
55. J. Bystricky *et al.*, J. Phys. (Paris) **48**, 1901 (1987).
56. J. Cugnon and R. M. Lombard, Nucl. Phys. A **422**, 635 (1984).
57. J. J. Jones *et al.*, Phys. Rev. Lett. **26**, 860 (1971).
58. K. Tsushima *et al.*, Phys. Lett. B **337**, 245 (1994).
59. E. Moeller *et al.*, Phys. Rev. C **28**, 1246 (1983).
60. J. Papp *et al.*, Phys. Rev. Lett. **34**, 601, 991 (1975).
61. Yu. T. Kiselev and V. A. Sheĭnkman, private communication.

Physics of Atomic Nuclei, Vol. 63, No. 2, 2000, pp. 303–309. Translated from Yadernaya Fizika, Vol. 63, No. 2, 2000, pp. 365–372.

ELEMENTARY PARTICLES AND FIELDS
Theory

Production of Λ Hypernuclei in π^+A Interactions

Ye. S. Golubeva and A. S. Iljinov

Institute for Nuclear Research, Russian Academy of Sciences, pr. Shestidesyatiletiya Oktyabrya 7a, Moscow, 117312 Russia

Received March 16, 1999; in final form, June 2, 1999

Abstract—The production of Λ hyperons in π^+A interactions is studied on the basis of the intranuclear-cascade model, and the excitation-energy, momentum, angular-momentum, charge, and mass distributions of the ensemble of product hypernuclei are determined. The decay of excited hypernuclei via particle emission and fission is considered. It is shown that, for the production of heavy Λ hypernuclei, the optimal momentum of the incident π^+ meson is about 1 GeV/c. The cross section of the channel in which heavy-nucleus decay induced by a π^+ meson is accompanied by the emission of a K^+ meson is estimated, and it is proposed to use the reaction (π^+, K^+f) in measurements of the fission barrier in hypernuclei and of their level density. © *2000 MAIK "Nauka/Interperiodica".*

1. INTRODUCTION

Throughout the past years, much attention has been given to investigations of strangeness in hadrons and nuclei. The range of these investigations is very broad, extending from the spectroscopy of hypernuclei to the formation of strange matter in ultrarelativistic nucleus–nucleus collisions or in neutron stars [1–6]. Here, the effect of nuclear matter on the properties of strange particles is the subject of great topical interest. Since the lifetime of Λ hypernuclei is large on the scale of characteristic nuclear times, Λ hypernuclei are especially suitable for the investigation of strangeness in nuclear matter.

Various incident particles, including photons, pions, kaons, antiprotons, and heavy ions, can produce Λ hypernuclei in interactions with nuclear targets. Whether the product Λ hyperon is captured by a nucleus with the formation of a Λ hypernucleus depends crucially on the momentum transfer in an elementary process. In all elementary processes, with the exception of $K^-n \longrightarrow \Lambda\pi^-$, the momentum transfer is high, so that the product Λ hyperon has a sufficiently high energy. It can be captured by a nucleus only as the result of rescattering in a nuclear medium. In the rescattering process, the Λ hypernucleus receives a rather high excitation energy, momentum, and angular momentum and loses some nucleons.

The first detailed investigation of the characteristics of the product ensemble of Λ hypernuclei were performed in [7] for proton–nucleus reactions. A kinetic approach based on the Boltzmann–Uehling–Uhlenbeck equation was used there to describe pA interactions and the rescattering of Λ hyperons produced in them. The main contribution to the production of hypernuclei comes from Λ hyperons formed in the collisions of secondary pions with intranuclear nucleons.

In this study, we will analyze a simpler and physically clearer case of Λ-hypernucleus production by primary pions. Our analysis of πA interactions will also be performed within the kinetic approach relying on the intranuclear cascade (INC) model.

The ensuing exposition is organized as follows. The INC modification that was successfully used to study pion–nucleus [8] and multipion–nucleus ($\bar{p}A$ annihilation [9], photonuclear reactions [10]) interactions is described in Section 2. In Section 3, the excitation-energy, momentum, angular-momentum, charge, and mass distributions of hot hypernuclei are calculated on the basis of this model version. In Section 4, particle emission from excited hypernuclei and the process of their fission are described within the evaporation–fission model; as a result, we obtain the eventual momentum, mass, and charge distributions of Λ hypernuclei. In Section 5, we discuss the results of our analysis and the prospects of experimental investigations of Λ hypernuclei with pion beams.

2. DESCRIPTION OF THE COMPUTATIONAL METHOD

In this study, the interaction of an incident pion with a nucleus and the propagation of product particles in nuclear matter will be described on the basis of the INC model. The INC model reduces an inelastic πA interaction to a series of successive quasifree collisions of fast secondaries with intranuclear nucleons. The INC model is a numerical method for solving the kinetic equation for a multiparticle distribution function that describes the transport of cascade particles (pions, kaons, nucleons, Λ hyperons, etc.) in a nuclear medium (see [11] and references therein).

The INC model version used here provided a good description of similar nuclear processes, including pion–nucleus interactions [8] and multipion–nucleus interactions ($\bar{p}A$ annihilation [9] and γA interactions at energies of 1–5 GeV [10]). A detailed description of the

1063-7788/00/6302-0303$20.00

model is given elsewhere [8–10]. For this reason, only a brief account of its fundamentals will be given here, but the modification associated with the inclusion of channels featuring strangeness will be considered in greater detail.

A Λ hyperon is produced in the collision of an incident pion and an intranuclear nucleon:

$$\pi^+ + n \longrightarrow K^+ + \Lambda. \quad (1)$$

In the INC model, the target nucleus is a mixture of degenerate proton and neutron Fermi gases contained in a potential well. The radial dependence of the potential well for nucleons is identical to that of the density distribution in nuclear matter, $V_N(r) \sim \rho_N(r)$. The potential well for Λ hyperons is taken in the form $V_\Lambda(r) = 0.6V_N(r)$ [7], and its depth at the center of the nucleus is $V_\Lambda(0) = -30$ MeV.

In this study, we consider the interval of the initial energies near the threshold for meson production. As was shown in [12], the Fermi momentum distribution of intranuclear nucleons, which is used in the INC model, makes it possible to reproduce faithfully, in this energy interval, the cross section for η-meson production by protons and photons incident on nuclear targets. This confirms that the approximation used here is valid for kaon production near the threshold as well.

Near the threshold, the kaon-production cross section is a small fraction of the total inelastic cross section for π^+A interaction. In this interval of the initial energies, a kaon is produced in the first collision between a pion and an intranuclear nucleon with the probability

$$W_s = \sigma_{K\Lambda}/\sigma_{\pi n}^{\text{inel}}, \quad (2)$$

where $\sigma_{K\Lambda}$ is the cross section for the elementary process (1), while $\sigma_{\pi n}^{\text{inel}}$ is the total cross section for inelastic π^+n interaction. The first π^+n collision resulting in the strangeness-production reaction (1) is always simulated in the Monte Carlo calculation performed here for the intranuclear cascade, and the weight (2) of this collision is remembered. The use of the method of weights permits performing an effective Monte Carlo simulation of channels characterized by small cross sections. In calculating the cross section for the elementary process (1), we used the parametrization [7]

$$\sigma_{K\Lambda}[\text{mb}] = \frac{7.665 \times 10^{-3}(\sqrt{s} - \sqrt{s_0})^{0.1341}}{(\sqrt{s} - 1.72)^2 + 7.826 \times 10^{-3}}, \quad (3)$$

where $\sqrt{s_0} = m_\Lambda + m_K = 1.613$ GeV, and $\sqrt{s}$ is the total invariant energy in GeV. The angular distribution of Λ and K particles in the c.m. frame was assumed to be isotropic.

The product Λ hyperon can be rescattered within the nucleus. In calculating the cross section for elastic ΛN scattering, we used the parametrization [7]

$$\sigma_{\Lambda N}[\text{mb}] = \begin{cases} 114/[-1 + 0.2(\sqrt{s} - \sqrt{s_0})] + 6, & \sqrt{s} \geq \sqrt{s_0} + 10 \\ 120, & \sqrt{s} < \sqrt{s_0} + 10, \end{cases} \quad (4)$$

where $\sqrt{s}$ and $\sqrt{s_0}$ (both in MeV) are, respectively, the total invariant energy and the sum of the Λ and nucleon masses. The angular distribution in ΛN interaction is assumed to be identical to that in NN interaction.

In describing the propagation of kaons in nuclear matter, we took into account the elastic-rescattering processes

$$K^+N \longrightarrow K^+N, \quad K^0N \longrightarrow K^0N. \quad (5)$$

The values of the elastic-scattering cross sections in the kaon-momentum region $P_K < 1$ GeV/c (and this is precisely the region of our prime interest), $\sigma^{\text{el}}(K^+p) \sim 12$ mb and $\sigma^{\text{el}}(K^+n) \sim 12$ mb, were taken from the compilation of experimental data that was presented in [13]. For K^0 mesons, we used the relations $\sigma^{\text{el}}(K^0p) = \sigma^{\text{el}}(K^+n)$ and $\sigma^{\text{el}}(K^0n) = \sigma^{\text{el}}(K^+p)$. We also took into account the kaon-charge-exchange channels

$$K^+n \longrightarrow K^0p, \quad K^0p \longrightarrow K^+n. \quad (6)$$

The charge-exchange cross section $\sigma^{\text{ex}}(KN)$ was taken to be 6 mb [13]. The angular distributions for these reactions were assumed to be identical to those for the corresponding channels in πN interactions at the same c.m. energies.

The cascade stage of the inelastic pion–nucleus interaction is completed upon the escape of fast cascade particles from the nucleus and the capture of slow nucleons and of the Λ hyperon by the nuclear potential. The excitation energy of the residual nucleus is determined as the sum of the energies of the excitons that originate from the INC and which are formed by captured nucleons occupying nuclear levels above the Fermi energy and holes left in the Fermi sea by nucleons knocked out of the nucleus. In such an excited residual nucleus, thermodynamic equilibrium is established in a comparatively short time interval. The resulting compound nucleus is deexcited via the evaporation of nucleons and extremely light nuclei, as well as via fission. This stage of the inelastic πA interaction is treated on the basis of the evaporation–fission model. This unified cascade–evaporation–fission model describes successfully a wide variety of data on fission and isotope yields in the interaction of multipion systems with nuclei [14]. A detailed description of the evaporation–fission model can be found in [15]. Here, we only indicate that, in calculating the evaporation and fission of hypernuclei, the mass of the hypernucleus ${}^{N}_{Z}A_\Lambda$ and the fission barrier in it are assumed to be equal

to, respectively, the mass of the conventional nucleus ${}^{N+1}_{Z}A$ and the fission barrier in it.

3. FEATURES OF SECONDARIES AND EXCITED Λ HYPERNUCLEI PRODUCED IN THE INTRANUCLEAR CASCADE

Let us consider the results of the calculations performed on the basis of the model described above. The cross section for the production of kaons and Λ hyperons on nucleus increases sharply with the incident-pion momentum P_{π^+} near the threshold for kaon production, reaches saturation at $P_{\pi^+} \sim 1$ GeV/c, and changes only slightly as P_{π^+} increases further (see Fig. 1). Only a small number of the product Λ hyperons are captured by the nuclear potential, forming hypernuclei (Fig. 1). The cross section for the production of hypernuclei peaks at $P_{\pi^+} \sim 1$ GeV/c.

The rescattering of Λ hyperons on intranuclear nucleons plays a crucial role in the production of hypernuclei. This is because Λ hyperons produced in the primary π^+n collision are too fast to be captured by the nucleus. Only as the result of rescattering are some Λ hyperons moderated, forming hypernuclei (see Fig. 2). Figure 2 also illustrates the effect of rescattering on the spectrum of K^+ mesons. The same effects determine the production of K^0 mesons in the charge-exchange process (see Fig. 1).

The effects of rescattering depend on the nuclear size and on the primary energy. It is clear from Fig. 3 that Λ hyperons are strongly moderated in the nuclear matter of the heavy nuclei with $A \sim 150$. A further increase in the nuclear mass affects only slightly the probability W^{Λ}_{cap} of Λ-hyperon capture (the capture probability W^{Λ}_{cap} is defined as the ratio of the number of the captured Λ hyperons to total number of product Λ hyperons). At a fixed mass of the target nucleus, the probability W^{Λ}_{cap} decreases with increasing primary energy (see Fig. 3) because, in this case, more energetic Λ hyperons are produced, which require a greater number of rescatterings to be captured by the nucleus.

Mean features of the compound hypernuclei produced in the interactions of π^+ mesons with the ^{238}U nucleus are shown in Fig. 4 versus energy. The yield of the hypernuclei, Y_{HN}, per inelastic π^+U interaction grows fast with the primary momentum in the subthreshold energy interval, reaches a maximal value of $Y_{\text{HN}} \sim 10^{-3}$ at $P_{\pi^+} = 1$ GeV/c, and decreases as P_{π^+} increases further. The mean excitation energy of hypernuclei, $\langle E^*/A \rangle$, also grows fast with the primary momentum P_{π^+} below the threshold, reaching a value

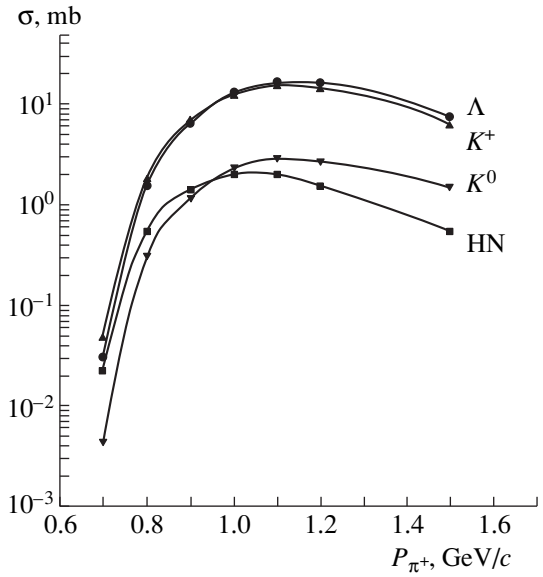

Fig. 1. Calculated cross sections for the production of K^+ and K^0 mesons, Λ hyperons, and hypernuclei (HN) by π^+ mesons incident on ^{238}U nuclei as functions of energy: (points) results of the calculation and (curves) interpolation between the calculated points.

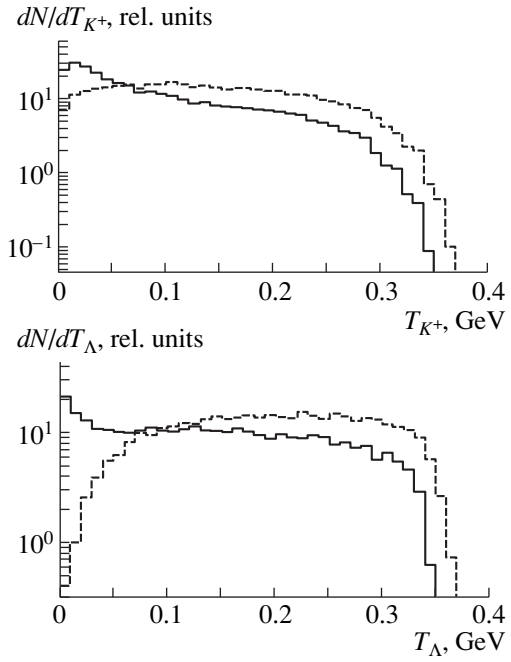

Fig. 2. Calculated energy spectra of K^+ mesons and Λ hyperons produced in the interactions of 1-GeV/c π^+ mesons with ^{238}U nuclei. The solid and dashed histograms represent the results obtained with and without allowance for rescattering, respectively.

of $\langle E^*/A \rangle = 0.49$ MeV at $P_{\pi^+} = 1$ GeV/c; at higher P_{π^+}, the growth of $\langle E^*/A \rangle$ becomes slower (see Fig. 4). The mean longitudinal momentum of hypernuclei, $\langle P_Z/A \rangle$, depends only slightly on the primary energy; at P_{π^+} =

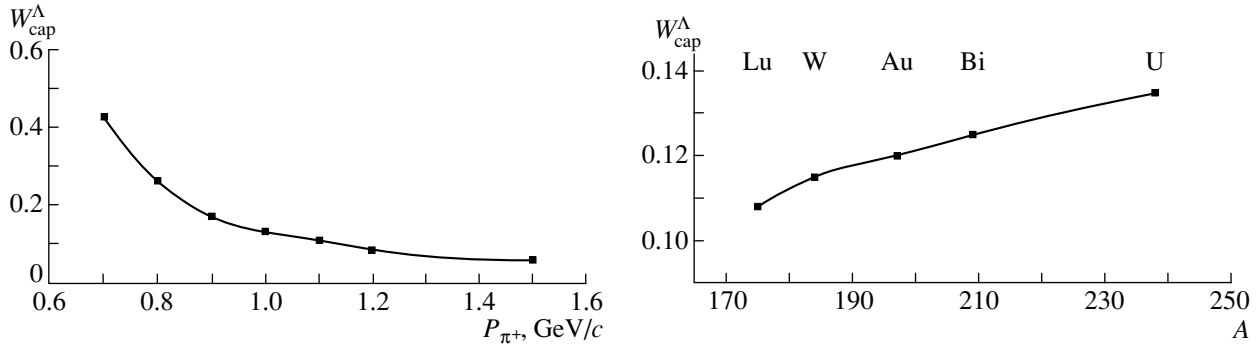

Fig. 3. Probability W^{Λ}_{cap} of Λ-hyperon capture of by a nucleus (left panel) as a function of the primary momentum of the π^+ meson interacting with a ^{238}U nucleus and (right panel) as a function of the mass number A of the target nucleus interacting with a 1-GeV/c π^+ meson. The notation is identical to that in Fig. 1.

1 GeV/c, it takes the value of $\langle P_Z/A\rangle$ = 2.24 MeV/c. The mean angular momentum of hypernuclei, $\langle I\rangle$, shows a similar energy dependence, its value at P_{π^+} = 1 GeV/c being $\langle I\rangle = 12.1\hbar$. The mean mass of the hypernucleus decreases with increasing P_{π^+}. At P_{π^+} = 1 GeV/c, two nucleons are knocked out of the target nucleus during the development of the INC: $\langle A\rangle$ = 235.8 (ΔA = 2.2).

Figure 5 displays the E^*/A, P_Z/A, I, and A distributions of the ensemble of compound hypernuclei. At the optimal momentum value of P_{π^+} = 1 GeV/c, the variances of these distributions are rather small: $a_{E^*/A}$ = 0.276 MeV, $a_{P_Z/A}$ = 1.013 MeV/c, $a_I = 5.56\hbar$, and

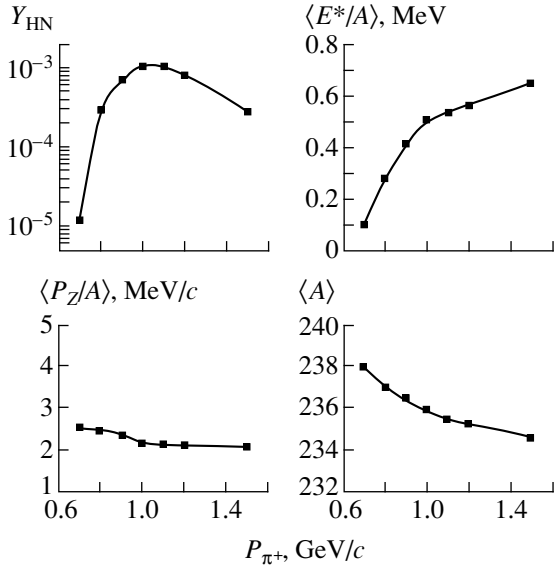

Fig. 4. Yield Y_{HN} (per event of inelastic interaction), mean excitation energy $\langle E^*/A\rangle$, mean longitudinal momentum $\langle P_Z/A\rangle$, and mean mass number $\langle A\rangle$ of Λ hypernuclei as functions of the primary momentum of π^+ mesons incident on ^{238}U nuclei. The notation is identical to that in Fig. 1.

a_A = 1.21. The product hypernuclei have comparatively low excitation energies (below 1 MeV per nucleon) and angular momenta (below 20$\hbar$). They are rather far from the critical values at which the properties and decay features of the excited nuclei change drastically.

Figure 6 presents the dependence of the mean characteristics of the composite hypernuclei on the mass number A of the target nucleus. It is clear from Fig. 6 that the mean yield of hypernuclei Y_{HN}, their excitation energy $\langle E^*/A\rangle$, and their longitudinal $\langle P_Z/A\rangle$ and angular $\langle I\rangle$ momenta weakly depend on A in the region of sufficiently heavy nuclei $A > 150$.

Although the different models were used here and in [7], it is worthwhile to draw at least a qualitative comparison of the basic features of the ensembles of the compound hypernuclei produced in pion–nucleus and proton–nucleus collisions at the optimal primary-energy values of T_{π^+} = 0.87 GeV and T_p = 1.5 GeV.

The inclusive cross section for the production of hypernuclei in π^+U interaction, $\sigma^{\pi^+}_{HN} \sim 1$ mb, is an order of magnitude larger than that in pU interactions, $\sigma^{p}_{HN} \sim$ 0.1 mb. The probability of Λ-hyperon capture with the formation of a hypernucleus in πU interaction is $W^{\pi\Lambda}_{cap}$ = 14%, which is close to the experimental value for the pion–nucleus interactions [5] and to the value of $W^{p\Lambda}_{cap}$ = 25% calculated for pU interactions [7].

The main difference between πU and pU interactions is that the proton introduces a significantly higher momentum P_Z/A, a significantly higher angular momentum I, and a significantly higher excitation energy E^*/A in the compound hypernucleus; it also knocks out a larger number A of nucleons of the target nucleus. In pU interactions at the primary energy of T_p = 1.5 GeV, the product hypernuclei have a mean excitation energy of $\langle E^*/A\rangle$ = 0.74 MeV, a mean longitudinal momentum of $\langle P_Z/A\rangle$ = 3.4 MeV/c, and a mean angular momentum of $\langle I\rangle = 28\hbar$, the number of knock-

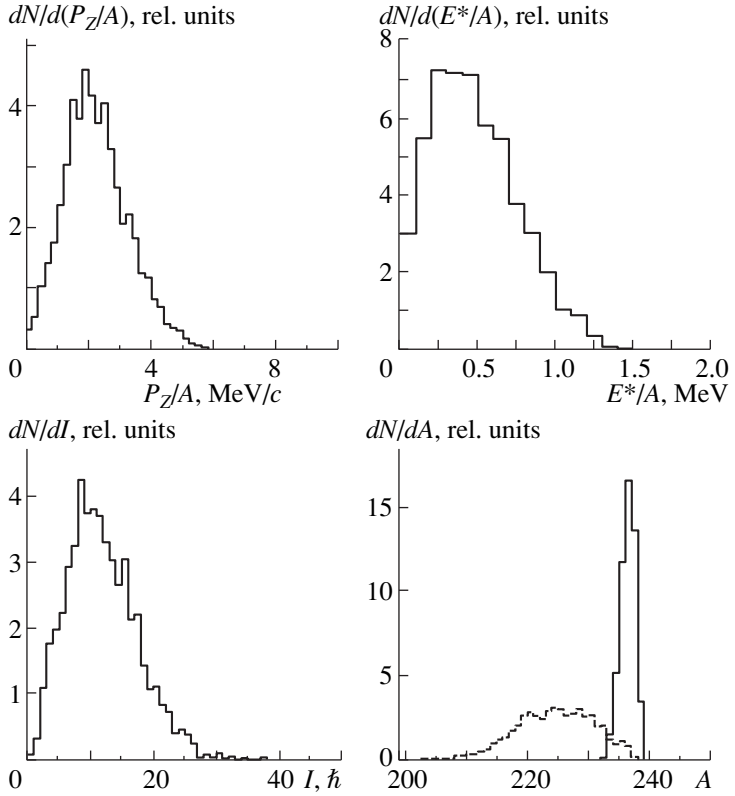

Fig. 5. Longitudinal-momentum (P_Z/A), excitation-energy (E^*/A), angular-momentum (I), and mass-number (A) distributions of Λ hypernuclei produced in the interaction of 1 GeV/c π^+ mesons with ^{238}U nuclei. The solid and dashed histograms represent the distributions of Λ hypernuclei formed upon the completion of the intranuclear and evaporation cascades, respectively.

on nucleons being $\langle \Delta A \rangle = 5$ [7]. These values exceed the corresponding values for π^+U interactions by a factor of 1.5–3.

To a still greater extent, these distinctions are manifested in the excitation-energy, longitudinal-momentum, angular-momentum, and mass distributions of compound hypernuclei. In pU interactions, the excitation-energy, longitudinal-momentum, angular-momentum, and mass-number distributions extend to the values of $E^*/A \simeq 2$ MeV, $P_Z/A \simeq 8$ MeV/c, $I = 60\hbar$, and $A = 230$, respectively, the corresponding variances being $a_{E^*/A} = 0.35$ MeV, $a_{P_Z/A} = 1.4$ MeV/c, $a_I = 12\hbar$, and $a_A = 1.75$) [7]. The compound nuclei produced in heavy-ions collisions have similarly high values of the excitation energy and of the angular momentum. It is well known that the decays of such nuclei (especially their fission) are strongly affected by thermal effects and the effects of high angular momenta. As to the decays of hot, quickly rotating hypernuclei, these effects in them have yet to be studied.

4. EVAPORATION AND FISSION OF EXCITED Λ HYPERNUCLEI

A hypernucleus that was produced upon the completion of the INC and which has a definite value of the excitation energy E^*, definite numbers of nucleons and protons (A and Z, respectively), and definite values of the momentum P and of the angular momentum I will emit particles (p, n, d, t, α, ^{3}He, and extremely light nuclei) and undergo fission. Since the excitation energy of the hypernucleus can reach a value of $E^* \sim 200$ MeV, this hypernucleus can emit successively a rather large

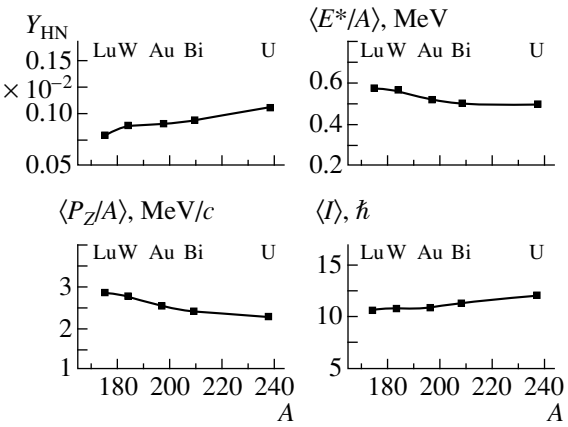

Fig. 6. Yield Y_{HN} (per event of inelastic interaction), mean excitation energy $\langle E^*/A \rangle$, mean longitudinal momentum $\langle P_Z/A \rangle$, and mean angular momentum $\langle I \rangle$ of Λ hypernuclei as functions of the mass number A of the target nucleus interacting with 1-GeV/c π^+ mesons. The notation is identical to that in Fig. 1.

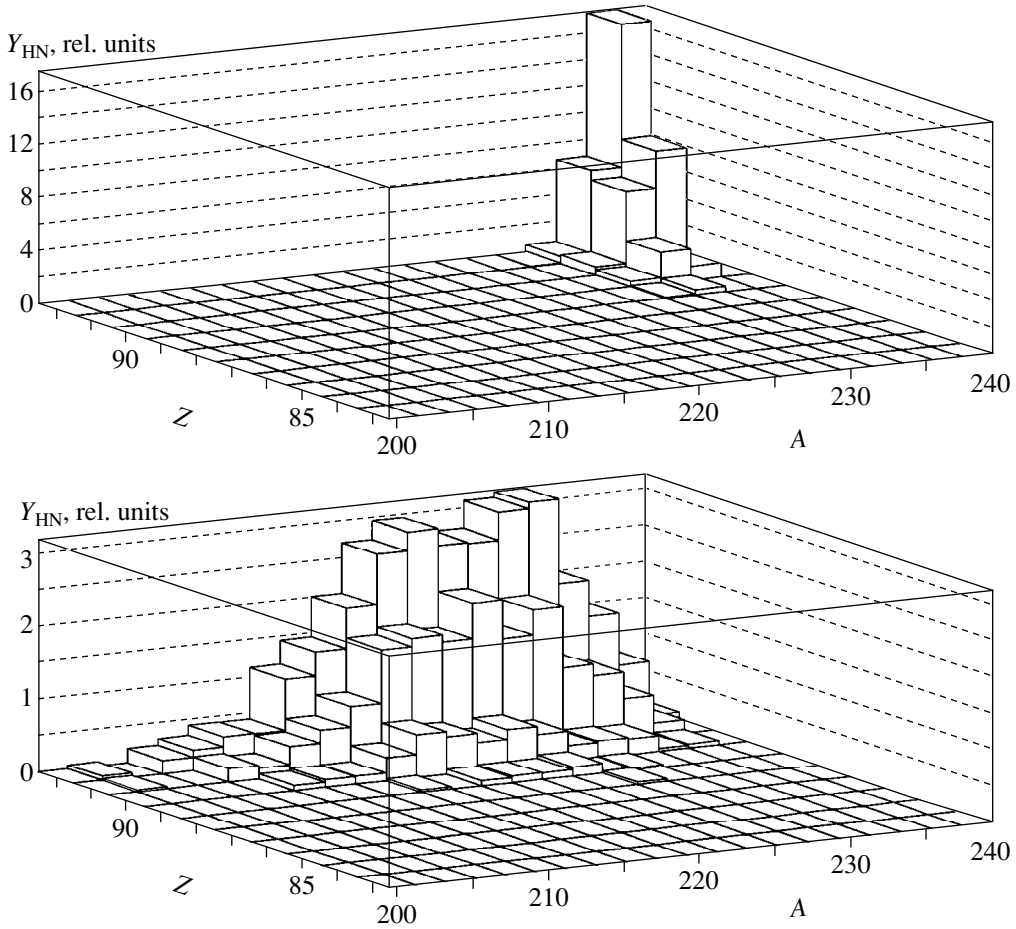

Fig. 7. Yield of hypernuclei with specific numbers of nucleons (A) and protons (Z) upon the completion of the (upper panel) intranuclear and (lower panel) evaporation cascades in the interaction of 1-GeV/c π^+ mesons with ^{238}U nuclei.

(up to 20) number of nucleons; in each unit of this chain, the nucleus can undergo fission with some probability. In the present study, such an evaporation cascade is described on the basis of the evaporation–fission model [15], which takes into account angular-momentum effects and the thermal damping of shell effects in nuclei. The parameters of this model were determined by fitting a vast body of experimental data on the statistical properties of excited nuclei formed in reactions featuring low-energy particles and heavy ions.

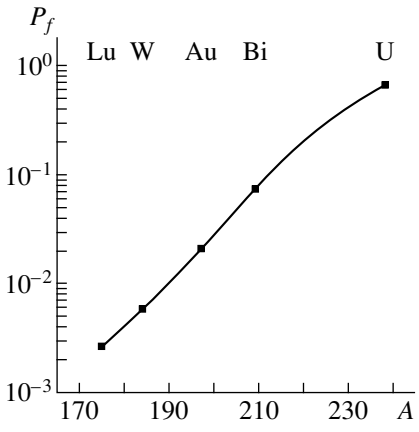

Fig. 8. Probability P_f for the fission of Λ hypernuclei produced in the interaction of 1-GeV/c π^+ mesons with various nuclei as functions of the target mass number A. The notation is identical to that in Fig. 1.

The deexcitation of a compound hypernucleus affects primarily the yield of a final hypernucleus with specific values of A and Z. The initially narrow distribution of compound nuclei with respect to A and Z becomes rather broad upon the completion of the evaporation cascade (see Fig. 7); this especially concerns the A distribution, because a heavy nucleus evaporates predominantly neutrons. In heavy nuclei, fission strongly competes with particle evaporation; as a result, the yield of final hypernuclei that escaped fission is reduced. (To the greatest extent, the fission process reduces the yield of neutron-deficit isotopes.) For the interaction of π^+ mesons with ^{238}U nuclei, the total fission probability is P_f = 0.67. This quantity (P_f) decreases fast with decreasing mass number of the tar-

get nucleus (Fig. 8); as a result, the effect of fission on the yield of final hypernuclei is negligible for $A < 200$.

On one hand, fission complicates the spectroscopic investigation of heavy hypernuclei because it reduces their yield. On the other hand, the high probability for the fission of a heavy hypernucleus provides the possibility of studying (π^+, K^+f) or (p, K^+f) reactions, opening a truly new line of investigations in the physics of hypernuclei. By measuring, at a specific angle, the energy spectrum of all kaons and that of kaons in coincidence with fission fragments, we can deduce, from the ratio of this spectra, the excitation-energy dependence of the fission probability P_f for the hypernucleus being investigated. The analysis of the dependence $P_f(E^*)$ will furnish information about the fission barrier and the level density in heavy hypernuclei in just the same way as this was done for usual nuclei in studying reactions like (d, pf) and (t, pf) [16]. Of course, this method can be used near the kaon-production threshold, where a small number of nucleons are emitted in the INC and where there therefore exists a tight relation between the kaon energy and the excitation energy of the product hypernucleus.[1)]

5. CONCLUSION

The primary pion momentum of $P_{\pi^+} = 1$ GeV/c is optimal for producing Λ hypernuclei. The integrated cross section for the production of hypernuclei at the corresponding energy is $\sigma_{HN} \sim 1$ mb. The product hypernuclei have moderately high excitation energies of $\langle E^*/A\rangle = 0.5$ MeV and moderately high angular momenta of $\langle I\rangle = 10\hbar$. In π^+ interactions with ^{238}U nuclei, the probability P_f for the fission of heavy hypernuclei reaches the value of $P_f \approx 0.7$. A measurement of the characteristics of (π^+, K^+f) reactions near the threshold furnishes information about the fission barrier and the level density in Λ hypernuclei. High-intensity pion beams of momentum 1 GeV/c from existing (for example, GSI in Germany) and future (for example, JNF in Japan) accelerators open new prospects for an experimental investigation of the production and properties of Λ hypernuclei. The proposed model and the predictions made on its basis for the production of Λ hypernuclei in π^+A interactions can be used in planning experiments at these accelerators.

[1)]It is worth noting that Krappe and Pashkevich [17] considered another interesting line of investigation of the fission of hypernuclei, that which is based on a measurement of the probability of Λ-hyperon capture by one of the fission products and which may provide unique information about the dynamics of the fission process.

ACKNOWLEDGMENTS

We are grateful to H. Krappe, L. A. Kondratyuk, and W. Cassing for discussions on the problems considered here.

This work was supported by INTAS, grant no. INTAS-93-1560.

REFERENCES

1. *Proceedings of the International Symposium on Hypernuclei and Strange Particle Physics*, in Nucl. Phys. A **547** (1992).
2. *Proceedings of the Workshop "Strangeness in Nuclei"* (World Sci., Cracow, 1992).
3. *Proceedings of the Workshop on Strange Quark Matter in Physics and Astrophysics*, in Nucl. Phys. B (Proc. Suppl.) **24** (1991).
4. *Proceedings of the 12th International Conference on Particles and Nuclei (PANIC)*, in Nucl. Phys. A **527** (1991).
5. H. Ejiri, Nucl. Phys. A **574**, 311 (1994).
6. B. F. Gibson and E. V. Hungerford, Phys. Rep. **257**, 349 (1995).
7. Z. Rudy *et al.*, Z. Phys. A **351**, 217 (1995); A **354**, 445 (1996).
8. A. S. Iljinov, V. I. Nazaruk, and S. E. Chigrinov, Yad. Fiz. **36**, 646 (1982) [Sov. J. Nucl. Phys. **36**, 376 (1982)].
9. Ye. S. Golubeva *et al.*, Nucl. Phys. A **483**, 539 (1988).
10. A. S. Iljinov *et al.*, Nucl. Phys. A **616**, 575 (1997).
11. A. S. Iljinov, M. V. Kazarnovsky, and É. Ya. Paryev, *Intermediate-Energy Nuclear Physics* (CRC, Boca Raton, 1994).
12. Ye. S. Golubeva *et al.*, Z. Phys. A **345**, 223 (1993); Nucl. Phys. A **562**, 389 (1993).
13. V. Flaminio *et al.*, Preprint No. CERN-HERA 83-02, CERN (1983).
14. D. I. Ivanov *et al.*, Z. Phys. A **352**, 191 (1995); P. Hofmann *et al.*, Phys. Rev. C **49**, 2555 (1994); Y. S. Kim *et al.*, Phys. Rev. C **54**, 2469 (1996).
15. A. S. Iljinov *et al.*, Nucl. Phys. A **543**, 517 (1992).
16. S. Bjornholm and J. F. Lynn, Rev. Mod. Phys. **52**, 725 (1980).
17. H. J. Krappe and V. V. Pashkevich, in *Proceedings of the 2nd International Conference on Dynamical Aspects of Nuclear Fission* (JINR Commun. No. E7-94-19, Dubna, 1994), p. 213.

Translated by M. Kobrinsky

Physics of Atomic Nuclei, Vol. 63, No. 2, 2000, pp. 310–317. Translated from Yadernaya Fizika, Vol. 63, No. 2, 2000, pp. 373–380.

ELEMENTARY PARTICLES AND FIELDS
Theory

Two-Photon Decay of the B_s Meson in Supersymmetric Models

G. G. Devidze* and G. R. Jibuti**

Institute for High Energy Physics, Tbilisi State University, Universitetskaya ul. 9, Tbilisi, 380086 Georgia

Received October 31, 1997; in final form, July 3, 1998

Abstract—The two-photon decay mode $B_s \longrightarrow \gamma\gamma$ is studied within the supersymmetric extension of the Standard Model. The contributions of one-particle-reducible and one-particle-irreducible diagrams to the decay amplitude are analyzed in detail. Exact expressions for the *CP*-even and *CP*-odd amplitudes are obtained. The contributions of supersymmetric particles to the partial width with respect the decay mode $B_s \longrightarrow \gamma\gamma$ are estimated. © *2000 MAIK "Nauka/Interperiodica".*

1. INTRODUCTION

Investigation of rare decays of the B_s mesons is of great interest for testing the Standard Model (SM) and for seeking the effect of new physics (in particular, manifestations of SUSY) beyond the SM. These decays are accessible to investigation in current experiments; another advantage of such studies is that, in contrast to what occurs in kaon decays, long-distance effects are insignificant in the decays of the B_s mesons. Rare *B*-meson decays within the SM, which are due to the transitions $b \longrightarrow s, d$, make it possible to estimate the elements of the Cabibbo–Kobayashi–Maskawa (CKM) matrix and to deduce some information about the properties of the third quark generation in the SM. The CLEO collaboration was able to observe a rare *B*-meson decay [1] and to measure its branching fraction for both charged and neutral *B* mesons:

$$\begin{aligned} \mathrm{Br}(B^+ \longrightarrow K^{*+}\gamma) &= (5.7 \pm 3.0) \times 10^{-5}, \\ \mathrm{Br}(B^0 \longrightarrow K^{*}\gamma) &= (4.0 \pm 1.9) \times 10^{-5}. \end{aligned} \quad (1)$$

These values of the branching fractions agree with the SM predictions taking into account QCD corrections. More precise experiments would show whether it is necessary to include effects beyond the SM in the theoretical framework.

The decay process $B_s \longrightarrow \gamma\gamma$ is similar to the transition $K^0 \longrightarrow \gamma\gamma$, which was investigated in [2, 3]. In contrast to the latter decay process, however, where large-distance effects are significant, the former is dominated by the contribution of small-distance effects. It should be noted that, here, two final-state photons may be either in the *CP*-even state described by the expression $F^{\mu\nu}F_{\mu\nu}$ or in the *CP*-odd state described by the expression $F^{\mu\nu}\tilde{F}_{\mu\nu}$. This circumstance may open a new possibility for studying *CP*-violation effects—in particular, in *B*-meson physics.

The two-photon decays of the *B* mesons are being vigorously studied at CERN. The L3 collaboration set an upper bound on the branching ratio for the decay mode $B_s \longrightarrow \gamma\gamma$ [4]:

$$\mathrm{Br}(B_s \longrightarrow \gamma\gamma) < 1.48 \times 10^{-4}. \quad (2)$$

Investigation of *B*-meson physics—and in particular, of rare decays of the *B* mesons—will be one of the main subjects for leading experimental collaborations at LHC–ATLAS, DESY, KEK, SLAC, and other research centers. Theoretical studies like those reported in [5–8] have also given impetus to experimental investigations of the issue. The low-energy Low theorem was used in [5] to calculate the amplitude of the process $B_s \longrightarrow \gamma\gamma$. Without invoking this technique, another group of authors (see [6, 7]) simplified their calculations by means of the on-mass-shell normalization of the self-energy operator for the transition $b \longrightarrow s$. The importance of the problem served as a motivation for the most precise computation of the $B_s \longrightarrow \gamma\gamma$ amplitude in [8], where the corresponding branching fraction and the weight of the *CP*-odd component of the final photon state were found within the SM. To order $1/M_W^2$, the authors of all the aforementioned studies obtained the identical analytic expressions for the amplitude and the same numerical value for the branching fraction,

$$\mathrm{Br}(B_s \longrightarrow \gamma\gamma) = (3.0 \pm 1.0) \times 10^{-7}. \quad (3)$$

It may turn out that rare processes are sensitive to new physics beyond the SM—for example, the physics of the minimal supersymmetric extension of the SM (MSSM) [9]. Rare decays may give indirect evidence for supersymmetry prior to a direct observation of supersymmetric effects at future colliders. Supersymmetry provides an elegant solution to the theoretical problems of the SM; in addition, the MSSM predicts that the masses of the supersymmetric particles (with the exception of the lightest supersymmetric particle) range from 100 GeV to a few TeV.

* e-mail: devidze@hepi.edu.ge
** e-mail: jibuti@hepi.edu.ge

Here, we study the rare decay $B_s \longrightarrow \gamma\gamma$ within the supersymmetric extension of the SM.

2. AMPLITUDE OF THE DECAY PROCESS $B_s \longrightarrow \gamma\gamma$

Having fixed the gauge of the final photons, we can represent the amplitude of the decay process $B_s \longrightarrow \gamma\gamma$ in the form

$$T(B_s \longrightarrow \gamma\gamma) = \epsilon_1^{\mu}(k_1)\epsilon_2^{\nu}(k_2)[Ag_{\mu\nu} + iB\epsilon_{\mu\nu\alpha\beta}k_1^{\alpha}k_2^{\beta}], \quad (4)$$

where $\epsilon_1^{\mu}(k_1)$ and $\epsilon_2^{\nu}(k_2)$ are the final-photon polarization vectors, while k_1 and k_2 are the 4-momenta of the final photons. The quantities A and B in (4) receive contributions from each diagram in Fig. 1. In order to determine the amplitude in (4), we must first evaluate the contributions of all these diagrams and then sum the parts contributing to A and B separately. Here, we aim at computing the amplitude in (4) as precisely as is possible. Within the MSSM, there are the following classes of diagrams contributing to the $B_s \longrightarrow \gamma\gamma$ amplitude (the diagrams are classified according to the particle species propagating in the loop): (i) charged gauge fermions and up-type squarks, (ii) charged Higgs particles and up-type quarks, (iii) neutral gauge fermions and down-type squarks, and (iv) gluinos and down-type squarks. The Lagrangians describing the interactions of the down-type quarks with the above supersymmetric particles are given by [9, 10]

$$L_{d\tilde{\chi}^*\tilde{u}} = -\frac{ig}{2}\left[V_{j1}(1+\gamma_5) - \frac{m_d U_{j2}^*}{\sqrt{2}M_W\cos\beta}(1-\gamma_5)\right]$$

$$\times C\Gamma_{ab}^L\bar{d}_a\tilde{\chi}^*\tilde{u}_{Lb} + \frac{igm_u V_{j2}}{2\sqrt{2}M_W\sin\beta}(1-\gamma_5)C\Gamma_{ab}^R\bar{d}_a\tilde{\chi}^*\tilde{u}_{Rb},$$

$$L_{dHu} = \frac{ig}{2\sqrt{2}M_W}$$

$$\times [m_d\tan\beta(1-\gamma_5) + m_u\cot\beta(1+\gamma_5)]O_{ab}\bar{d}_a H u_b,$$

$$L_{d\tilde{\chi}^0\tilde{u}} = -\frac{i}{\sqrt{2}}\left\{\frac{gm_d}{2M_W\cos\beta}N_{j3}^*(1-\gamma_5)\right.$$

$$\left. + \left[eQ_d N_{j1} - \frac{g}{\cos\theta_W}\left(\frac{1}{2} + Q_d\sin^2\theta_W\right)N_{j2}\right](1+\gamma_5)\right\} \quad (5)$$

$$\times F_{ab}^L\bar{d}_a\tilde{\chi}^0\tilde{u}_{Lb} - \frac{i}{\sqrt{2}}\left\{\frac{gm_d}{2M_W\cos\beta}N_{j3}(1+\gamma_5)\right.$$

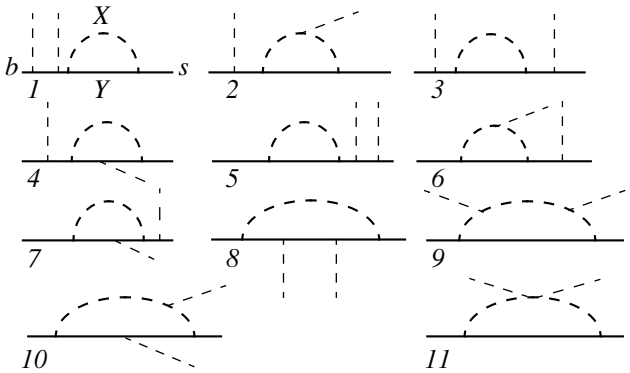

Fig. 1. One-particle-reducible (*1–7*) and one-particle-irreducible (*8–11*) diagrams contributing to the amplitude of the decay process $B_s \longrightarrow \gamma\gamma$ ($X = \tilde{u}_L, \tilde{u}_R, H, \tilde{d}_L, \tilde{d}_R, \tilde{d}_L, \tilde{d}_R$; $Y = \tilde{\chi}^*, \tilde{\chi}^*, u, \tilde{\chi}^0, \tilde{\chi}^0, \tilde{g}, \tilde{g}$).

$$\left. - \left[eQ_d N_{j1}^* - N_{j2}^*\frac{gQ_d\sin^2\theta_W}{\cos\theta_W}\right](1-\gamma_5)\right\}F_{ab}^R\bar{d}_a\tilde{\chi}^0\tilde{u}_{Rb},$$

$$L_{d\tilde{g}\tilde{d}} = -\sqrt{2}g_s\frac{\lambda_{ij}^a}{2}F_{ij}^L\frac{1+\gamma_5}{2}\bar{d}_i\tilde{g}_a\tilde{d}_{Lj}$$

$$+ \sqrt{2}g_s\frac{\lambda_{ij}^a}{2}F_{ij}^R\frac{1-\gamma_5}{2}\bar{d}_i\tilde{g}_a\tilde{d}_{Rj},$$

where $g = e\sin\theta_W$; θ_W is the Weinberg angle; V and U are the charged-gauge-fermion mixing matrices; C is the charge-conjugation operator; Γ^L and Γ^R are the up-type-squark mixing matrices; $\tan\beta = v_2/v_1$, v_1 and v_2 being the vacuum expectation values of the Higgs fields [9, 10]; O is the CKM matrix; N is the neutral-gauge-fermion mixing matrix [9, 10]; $Q_d = -1/3$; F^L and F^R are the down-type-squark mixing matrices; g_s is the coupling constant of strong interaction; and λ^a are the Gell-Mann matrices.

The gauge of final photons is fixed by the conditions

$$(\epsilon_1 k_1) = 0, \ (\epsilon_2 k_2) = 0, \quad (\epsilon_1 k_2) = 0, \quad (\epsilon_2 k_1) = 0. \quad (6)$$

Taking into account the momentum-conservation law and using relations (6), we arrive at the constraints

$$(\epsilon_i P) = (\epsilon_i p_1) = (\epsilon_i p_2) = 0, \quad (7)$$

where

$$P = k_1 + k_2, \quad p_1 = p_2 + k_1 + k_2. \quad (8)$$

From equations (6)–(8), we derive useful kinematical relations,

$$(k_1 k_2) = (Pk_1) = (Pk_2) = \frac{M_B^2}{2},$$

$$(p_1p_2) = -m_bm_s, \quad (Pp_1) = m_bM_B,$$
$$(p_1k_1) = (p_1k_2) = \frac{m_bM_B}{2}, \tag{9}$$
$$(p_2k_1) = (p_2k_2) = -\frac{m_sM_B}{2}, \quad (Pp_2) = -m_sM_B.$$

With the aid of (5)–(9), we can explicitly calculate the contribution of each diagram to the *CP*-even (A) and the *CP*-odd (B) component of the amplitude in (4). Our calculations were performed in the 't Hooft–Feynman gauge, and divergent integrals were evaluated by means of the dimensional-regularization technique. It should be noted that only one-particle-reducible diagrams lead to $\sim 1/\epsilon$ divergences, where $\epsilon = (4-n)/2$, with n being the dimensionality of spacetime.

The contributions to the *CP*-even amplitude A that come from the one-particle-reducible diagrams featuring charged gauge fermions and up-type left-handed squarks in the loops are given by

$$A_1 = -\frac{1}{4}CQ_d^2\frac{1}{m_b}\sum\lambda_l\left\{-\frac{M(\tilde{\chi}_j^*)}{\sqrt{2}M_W\cos\beta}\right.$$
$$\times(m_bV_{j1}U_{j2} - m_sV_{j1}^*U_{j2}^*)I_0(m(\tilde{u}_{Ll}), M(\tilde{\chi}_j^*), p_2)$$
$$\left. - m_s\left(|V_{j1}|^2 - \frac{m_sm_b|U_{j2}|^2}{2M_W^2\cos^2\beta}\right)I_1(m(\tilde{u}_{Ll}), M(\tilde{\chi}_j^*), p_2)\right\},$$

$$A_2 = \frac{1}{2}CQ_d\frac{M_B}{m_b}\sum\lambda_l\left(|V_{j1}|^2 - \frac{m_sm_b|U_{j2}|^2}{2M_W^2\cos^2\beta}\right)$$
$$\times R_{00}(m(\tilde{u}_{Ll}), m(\tilde{u}_{Ll}), M(\tilde{\chi}_j^*), p_1-k_1, p_2),$$

$$A_3 = \frac{1}{4}CQ_d\frac{M_B}{m_b}\sum\lambda_l\left\{\left(|V_{j1}|^2 - \frac{m_sm_b|U_{j2}|^2}{2M_W^2\cos^2\beta}\right)\right.$$
$$\times[(m_bM_B - m_l^2 + M^2(\tilde{\chi}_j^*))R_0 - 2m_lm_bR_{10}$$
$$+ m_l(m_l-m_b)R_{01} + 2R_{00} - R_{\alpha\alpha}]$$
$$+ (m_bV_{j1}U_{j2} - m_sV_{j1}^*U_{j2}^*)\frac{M_BM(\tilde{\chi}_j^*)}{\sqrt{2}M_W\cos\beta}$$
$$\left.\times R_0(M(\tilde{\chi}_j^*), M(\tilde{\chi}_j^*), m(\tilde{u}_{Ll}), p_1-k_1, p_2)\right\},$$

$$A_4 = \frac{1}{4}CQ_d^2\frac{1}{m_s}\sum\lambda_l\left\{\frac{M(\tilde{\chi}_j^*)}{\sqrt{2}M_W\cos\beta}\right. \tag{10}$$
$$\left.\times(m_bV_{j1}U_{j2} - m_sV_{j1}^*U_{j2}^*)I_0(m(\tilde{u}_{Ll}), M(\tilde{\chi}_j^*), p_1)\right\},$$

$$A_5 = \frac{1}{4}CQ_d^2\frac{1}{m_s}\sum\lambda_l\left\{-\frac{M(\tilde{\chi}_j^*)}{\sqrt{2}M_W\cos\beta}\right.$$
$$\times(m_bV_{j1}U_{j2} - m_sV_{j1}^*U_{j2}^*)I_0(m(\tilde{u}_{Ll}), M(\tilde{\chi}_j^*), p_1)$$
$$\left. + m_b\left(|V_{j1}|^2 - \frac{m_sm_b|U_{j2}|^2}{2M_W^2\cos^2\beta}\right)I_1(m(\tilde{u}_{Ll}), M(\tilde{\chi}_j^*), p_1)\right\},$$

$$A_6 = -\frac{1}{2}CQ_d\frac{M_B}{m_s}\sum\lambda_l\left(|V_{j1}|^2 - \frac{m_sm_b|U_{j2}|^2}{2M_W^2\cos^2\beta}\right)$$
$$\times R_{00}(m(\tilde{u}_{Ll}), m(\tilde{u}_{Ll}), M(\tilde{\chi}_j^*), p_1-k_1, p_1),$$

$$A_7 = \frac{1}{4}CQ_d\frac{M_B}{m_s}\sum\lambda_l\left\{\left(|V_{j1}|^2 - \frac{m_sm_b|U_{j2}|^2}{2M_W^2\cos^2\beta}\right)\right.$$
$$\times[(m_bM_B - m_l^2 + M^2(\tilde{\chi}_j^*))R_0 - 2m_lm_bR_{10}$$
$$+ m_l(m_l-m_b)R_{01} + 2R_{00} - R_{\alpha\alpha}]$$
$$- (m_bV_{j1}U_{j2} - m_sV_{j1}^*U_{j2}^*)\frac{M_BM(\tilde{\chi}_j^*)}{\sqrt{2}M_W\cos\beta}$$
$$\left.\times R_0(M(\tilde{\chi}_j^*), M(\tilde{\chi}_j^*), m(\tilde{u}_{Ll}), p_1-k_1, p_1)\right\},$$

where $C = e^2g^2f_B$, f_B being the B-meson decay constant; $\lambda_l = \Gamma_{ls}^L\Gamma_{lb}^L$; $Q_{d,u}$ are the charges of the up-type and down-type quarks; and $M_B \approx m_b + m_s$. The integrals R ($R \equiv \tilde{R}_0, R_{10}, R_{01}, R_{\alpha\alpha}$) depend on the set of the masses and momenta (m_1, m_2, m_3, q_1, q_2) (see Appendix).

For the hadronic matrix elements, we use the relations

$$\langle 0|\bar{s}\gamma_\mu\gamma_5 b|B_s(P)\rangle = -if_BP_\mu,$$
$$\langle 0|\bar{s}\gamma_5 b|B_s(P)\rangle = if_BM_B, \tag{11}$$
$$\langle 0|\bar{s}\gamma_\mu\gamma_\nu\gamma_5 b|B_s(P)\rangle = if_BM_Bg_{\mu\nu}.$$

Similar contributions to the *CP*-odd part of the amplitude are given by

$$B_{1,5} = -\frac{2}{M_B(m_b-m_s)}A_{1,5}, \quad B_{2,4,6} = \frac{2}{M_B^2}A_{2,4,6},$$
$$B_{3,7} = -\frac{2}{M_B^2}A_{3,7} \tag{12}$$
$$\times(U_{j2} \longrightarrow U_{j2}, U_{j2}^* \longrightarrow -U_{j2}^*, M(\tilde{\chi}_j^*) \longrightarrow -M(\tilde{\chi}_j^*)).$$

We note that, upon summation of formulas (10) and (12), the divergent parts of the integrals (those proportional to $1/\epsilon$) cancel each other.

Indicated below are the substitutions that must be made in (10) and (12) in order to derive the contributions of the other classes of the diagrams. The substitution rules for the charged gauge fermions and right-handed up-type squarks propagating in the loop are as follows:

$$V_{j1} \longrightarrow 0, \quad \frac{|U_{j2}|^2}{\cos^2\beta} \longrightarrow \frac{m^2(\tilde{u}_{Rl})}{m_b m_s}\frac{|V_{j2}|^2}{\sin^2\beta}, \qquad (13)$$
$$m(\tilde{u}_{Ll}) \longrightarrow m(\tilde{u}_{Rl}), \quad \Gamma^L_{li} \longrightarrow \Gamma^R_{li}.$$

The substitution rules for the charged Higgs particles and up-type quarks propagating in the loop are

$$V_{j1} \longrightarrow \cot\beta\frac{m(u_l)}{\sqrt{2}M_W}, \quad \frac{U_{j2}}{\cos\beta} \longrightarrow \tan\beta, \qquad (14)$$
$$M(\tilde{\chi}^*_j) \longrightarrow M(H), \quad \Gamma^L_{li} \longrightarrow O_{li},$$

where O_{li} are the elements of the CKM matrix and the replacements

$$M(\tilde{u}_{Ll}) \longrightarrow M(H), \quad M(\tilde{\chi}^*_j) \longrightarrow m(u_l) \qquad (15)$$

must be made in the integrands.

The substitution rules for the neutral gauge fermions and left-handed down-type squarks are

$$V_{j1} \longrightarrow 2\Big[\sin\theta_W N_{j1}$$
$$-\frac{1}{\cos\theta_W}\Big(\frac{1}{2} + Q_d\sin^2\theta_W\Big)N_{j2}\Big] \equiv t_{Lj}, \qquad (16)$$
$$U_{j2} \longrightarrow -N_{j3}, \quad Q_u \longrightarrow 0, \quad M(\tilde{\chi}^*_j) \longrightarrow M(\tilde{\chi}^0_j),$$
$$m(\tilde{u}_{Ll}) \longrightarrow m(\tilde{d}_{Ll}), \quad \Gamma^L_{li} \longrightarrow F^L_{li},$$

where F^L_{li} are the mixing-matrix elements for the left-handed down-type squarks, while N_{j1}, N_{j2}, and N_{j3} are the mixing-matrix elements for the neutral gauge fermions.

In order to obtain the contributions of the diagrams involving neutral gauge fermions and right-handed down-type squarks, we must make the following substitutions in the expressions for the diagrams involving neutral gauge fermions and left-handed down-type squarks:

$$t_{Lj} \longrightarrow \frac{m_s}{\sqrt{2}M_W\cos\beta}N_{j3}, \quad t^*_{Lj} \longrightarrow \frac{m_b}{\sqrt{2}M_W\cos\beta}N^*_{j3},$$
$$\frac{m_s}{\sqrt{2}M_W\cos\beta}N^*_{j3} \longrightarrow -\sqrt{2}\Big(\sin\theta_W Q_d N^*_{j1}$$
$$-Q_d\frac{\sin^2\theta_W}{\cos\theta_W}N^*_{j2} \equiv t^*_{Rj}, \qquad (17)$$
$$\frac{m_b}{\sqrt{2}M_W\cos\beta}N_{j3} \longrightarrow t_{Rj},$$
$$m(\tilde{d}_{Ll}) \longrightarrow m(\tilde{d}_{Rl}), \quad \Gamma^L_{li} \longrightarrow F^R_{li}.$$

The contributions of the diagrams featuring gluinos can be obtained by performing the following substitutions in the diagrams featuring neutral gauge fermions:

$$N_{j3} \longrightarrow 0, \quad g \longrightarrow \frac{4}{3}g_s, \quad t_{Lj} \longrightarrow \sqrt{2}, \quad \tilde{\chi}^0_j \longrightarrow \tilde{g}, \qquad (18)$$
$$N_{j3} \longrightarrow 0, \quad g \longrightarrow \frac{4}{3}g_s, \quad t_{Rj} \longrightarrow -\sqrt{2}, \quad \tilde{\chi}^0_j \longrightarrow \tilde{g}.$$

The *CP*-even part (A) and the *CP*-odd part (B) of the $B_s \longrightarrow \gamma\gamma$ amplitude (4) receive contributions not only from one-particle-reducible diagrams but also from one-particle-irreducible diagrams. Each of the contributions from the one-particle-irreducible diagrams is finite. Let us consider these contributions in more detail. Within the SM, contributions of order $1/M^2_W$ come from only one one-particle-irreducible diagram, that which features a W boson in the loop, so that both photons are emitted by virtual up-type quarks. It was shown in [2] that the diagram in question that features light virtual quarks makes a contribution of order $1/M^2_W$, whereas the analogous diagram featuring heavy virtual quarks makes a contribution of order $1/M^4_W$. The analogous diagrams in the MSSM—they involve charged gauge fermions in the loop, in which case both photons are emitted by scalar quarks—make contribution of order $1/M^4_W$, provided that the masses of all supersymmetric particles satisfy the constraint $m >$ 100 GeV. Similar arguments show that the contribution of the other one-particle-irreducible diagrams in the MSSM is of order $1/M^4_W$. Thus, the leading corrections from one-particle-irreducible diagrams are vanishingly small, provided that $m^2_i/M^2_W > 1$.

3. BRANCHING FRACTION FOR THE DECAY MODE $B_s \longrightarrow \gamma\gamma$

By using equation (4), we find that the partial width with respect to the decay mode $\Gamma(B_s \longrightarrow \gamma\gamma)$ is given by

$$\Gamma(B_s \longrightarrow \gamma\gamma) = \frac{1}{32\pi M_B}\Big[4|A|^2 + \frac{1}{2}M^4_B|B|^2\Big]. \qquad (19)$$

From Fig. 1, it can be seen that the effect of the permutation of final photons must be properly taken into account in a correct calculation. Under the kinematical conditions (6)–(8), which are valid in the case being

considered, this can be done by doubling the contributions of all diagrams, with the exception of diagram 11, which describes the emission of both photons from the same spacetime point; that is,

$$A = A_{11} + 2\sum_{i=1}^{10} A_i, \quad B = B_{11} + 2\sum_{i=1}^{10} B_i. \qquad (20)$$

Presented below is the total contribution of the diagrams to the amplitude derived under the assumption that the masses of all supersymmetric particles are greater than the *W*-boson mass. The contributions to the *CP*-even and *CP*-odd parts of the amplitude from the diagrams featuring charged gauge fermions and up-type squarks are given by

$$A = i\frac{\sqrt{2}m_b}{16\pi^2 m_s} G_F f_B (eQ_d)^2 M_B^2$$
$$\times \sum \lambda_l \left\{ \frac{\sqrt{2}M_W}{M(\tilde{\chi}_j^*)\cos\beta}\left(V_{j1}U_{j2} - \frac{m_s}{m_b}V_{j1}^* U_{j2}^*\right) f_1(x_l) \right.$$
$$\left. + \left(|V_{j1}|^2 - \frac{m_s m_b |U_{j2}|^2}{2M_W^2 \cos^2\beta}\right)\frac{M_W^2}{M^2(\tilde{\chi}_j^*)} f_2(x_l) \right\},$$
$$B = i\frac{\sqrt{2}m_b}{8\pi^2 m_s} G_F f_B (eQ_d)^2 \qquad (21)$$
$$\times \sum \lambda_l \left\{ \frac{\sqrt{2}M_W}{M(\tilde{\chi}_j^*)\cos\beta}\left(V_{j1}U_{j2} + \frac{m_s}{m_b}V_{j1}^* U_{j2}^*\right) f_1(x_l) \right.$$
$$\left. + \left(|V_{j1}|^2 + \frac{m_s m_b |U_{j2}|^2}{2M_W^2 \cos^2\beta}\right)\frac{M_W^2}{M^2(\tilde{\chi}_j^*)} f_2(x_l) \right\},$$

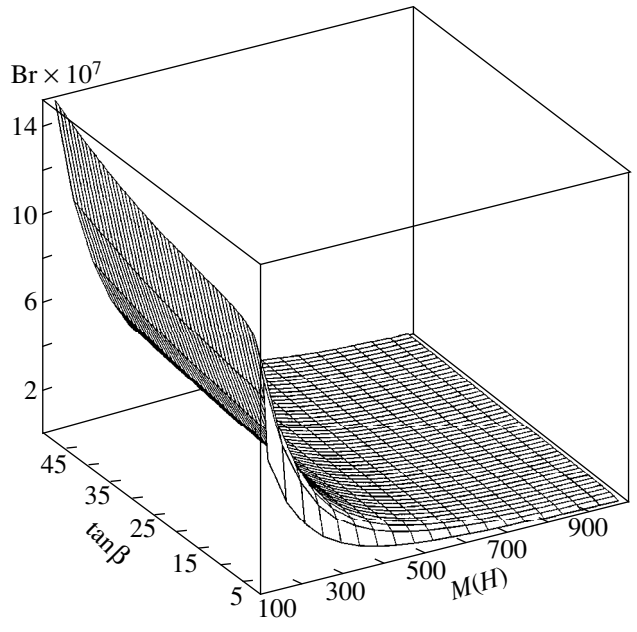

Fig. 2. Partial width with respect to the decay mode $B_s \longrightarrow \gamma\gamma$ as a function of tanβ and the Higgs boson mass $M(H)$ (in GeV).

where

$$x_l = \frac{m^2(\tilde{u}_{Ll})}{M^2(\tilde{\chi}_j^*)},$$

$$f_1(x) = \frac{5 - 12x + 7x^2 + (4x - 6x^2)\ln x}{2(1-x)^3}, \qquad (22)$$
$$f_2(x)$$
$$= \frac{29 - 96x + 111x^2 - 44x^3 + 6x(4 - 9x + 6x^2)\ln x}{6(1-x)^4}.$$

The contributions of the diagrams involving charged Higgs particles and up-type quarks can be represented as

$$A = i\frac{\sqrt{2}m_b}{16\pi^2 m_s} G_F f_B (eQ_d)^2 M_B^2$$
$$\times \sum \lambda_l \left\{ g_1(y_l) + \cot^2\beta g_2(y_l) - \tan^2\beta \frac{m_s m_b}{M^2(H)}\frac{1}{y_l} g_2(y_l) \right\}, \qquad (23)$$
$$B = i\frac{\sqrt{2}m_b}{8\pi^2 m_s} G_F f_B (eQ_d)^2$$
$$\times \sum \lambda_l \left\{ g_1(y_l) + \cot^2\beta g_2(y_l) + \tan^2\beta \frac{m_s m_b}{M^2(H)}\frac{1}{y_l} g_2(y_l) \right\},$$

where

$$y_l = \frac{m^2(u_l)}{M^2(H)},$$

$$g_1(y) = \frac{-3y + 8y^2 - 5y^3 + (6y^2 - 4y)\ln y}{2(1-y)^3}, \qquad (24)$$
$$g_2(y)$$
$$= \frac{31y - 84y^2 + 69y^3 - 16y^4 + 6y(y^2 - 6y + 4)\ln y}{12(1-y)^4}.$$

The contributions of the other diagrams can be obtained from (21)–(24) by using relations (13)–(18).

The contributions of supersymmetric particles to the partial width with respect to the two-photon mode $B_s \longrightarrow \gamma\gamma$ of B_s decay can be evaluated on the basis of equations (10) and (12)–(24). Numerical estimates show that the contributions of the diagrams featuring gauge fermions and gluinos are much smaller than the SM contributions ($\mathrm{Br}_{SM}(B_s \longrightarrow \gamma\gamma) \sim 10^{-7}$). The contri-

butions of these particles do not exceed 10^{-8}. This estimate corresponds to maximal mixing in the squark and gauge-fermion sectors. The gauge-fermions mass matrices and the angles of mixing of the charged gauge fermions can be represented in an analytic form [9, 10]. Since the contribution of these particles to the partial width does not exceed 10^{-8}, the formulas in question are not presented here. In estimating the maximum possible contribution of the gauge fermions and gluinos, we assumed that the masses of the supersymmetric particles are about 100 GeV and used the following values of the input parameters: $\Gamma_{tot}(B_s) = 5 \times 10^{-4}$ eV, f_B = 200 MeV, m_s = 0.5 GeV, m_b = 4.8 GeV, and M_B = 5.3 GeV. Figure 2 shows the partial width with respect to the decay $B_s \longrightarrow \gamma\gamma$ as a functions of tanβ and the mass of the Higgs particle.

4. CONCLUSION

We have investigated the rare B_s-meson decay $B_s \longrightarrow \gamma\gamma$ within the supersymmetric extension of the SM. The contributions of the neutral gauge fermions and gluinos have been found to be much smaller than the SM contributions. For large values of tanβ (tanβ > 10) and small values of $M(H)$ [$M(H) \approx 100$ GeV], supersymmetric contributions exceed the SM estimate. From Fig. 2, it can be seen that, in broad ranges of the parameters ($1 < \tan\beta < 50$, 100 GeV $< M(H) <$ 350 GeV), the supersymmetric contributions to the partial width are greater than or comparable with the SM estimate. In the near future, the most advanced experimental facilities will provide the possibility of observing rare decays characterized by partial-widths values of about 10^{-7} (and the more so by those of 10^{-6}).

ACKNOWLEDGMENTS

We are grateful to N.S. Amaglobeli, T.I. Kopaleishvili, and Z.Sh. Garuchava for stimulating discussions and support.

APPENDIX

In evaluating the diagrams in Fig. 1, we have to deal with integrals of the type

$$\{I_0; I_\alpha\}(p^2, m_1^2, m_2^2) = \int \frac{d^4q}{(2\pi)^4} \frac{(1, q_\alpha)}{[(q-p)^2 - m_1^2 + i\epsilon](q^2 - m_2^2 + i\epsilon)}, \quad \text{(A.1)}$$

$$\{R_0, R_\alpha, R_{\alpha\beta}\}(p_1^2, p_2^2, (p_1-p_2)^2, m_1^2, m_2^2, m_3^2) = \int \frac{d^4q}{(2\pi)^4}(1, q_\alpha, q_\alpha q_\beta)\{[(p_1-q)^2 - m_1^2 + i\epsilon] \times [(p_2-q)^2 - (m_2^2 + i\epsilon)](q^2 - m_3^2 + i\epsilon)\}^{-1}.$$

The Lorentz structures of the integrals I_α, R_α, and $R_{\alpha\beta}$ are the following:

$$I_\alpha(p^2, m_1^2, m_2^2) = p_\alpha I_1(p^2, m_1^2, m_2^2),$$

$$R_\alpha(p_1^2, p_2^2, (p_1-p_2)^2, m_1^2, m_2^2, m_3^2) = p_{1\alpha} R_{10}(p_1^2, p_2^2, (p_1-p_2)^2, m_1^2, m_2^2, m_3^2) + p_{2\alpha} R_{01}(p_1^2, p_2^2, (p_1-p_2)^2, m_1^2, m_2^2, m_3^2),$$

$$R_{\alpha\beta}(p_1^2, p_2^2, (p_1-p_2)^2, m_1^2, m_2^2, m_3^2) = g_{\alpha\beta} R_{00}(p_1^2, p_2^2, (p_1-p_2)^2, m_1^2, m_2^2, m_3^2) + p_{1\alpha}p_{1\beta} R_{20}(p_1^2, p_2^2, (p_1-p_2)^2, m_1^2, m_2^2, m_3^2) + p_{2\alpha}p_{2\beta} R_{02}(p_1^2, p_2^2, (p_1-p_2)^2, m_1^2, m_2^2, m_3^2) + (p_{1\alpha}p_{2\beta} + p_{2\alpha}p_{1\beta}) R_{11}(p_1^2, p_2^2, (p_1-p_2)^2, m_1^2, m_2^2, m_3^2). \quad \text{(A.2)}$$

Some of these integrals are divergent. Within the dimensional-regularization technique, the relevant divergences can be isolated in the form

$$I_0(p^2, m_1^2, m_2^2) = \frac{1}{\epsilon'} + \tilde{I}_0(p^2, m_1^2, m_2^2),$$

$$I_\alpha(p^2, m_1^2, m_2^2) = p_\alpha I_1(p^2, m_1^2, m_2^2) = p_\alpha \left\{ \frac{1}{2\epsilon'} + \tilde{I}_1(p^2, m_1^2, m_2^2) \right\}, \quad \text{(A.3)}$$

$$R_{00}(p_1^2, p_2^2, (p_1-p_2)^2, m_1^2, m_2^2, m_3^2) = \frac{1}{4\epsilon'} + \tilde{R}_{00}(p_1^2, p_2^2, (p_1-p_2)^2, m_1^2, m_2^2, m_3^2).$$

Here, $1/\epsilon' = \frac{i}{(4\pi)^2}[1/\epsilon - \gamma + \ln 4\pi]$, where γ is the Euler–Mascheroni constant ($\gamma = 0.5772157\ldots$) and $2\epsilon = 4 - n$, n being the dimension of spacetime. The integrals $\tilde{I}_0$ and $\tilde{I}_1$ can be approximated as

$$\tilde{I}_0(p^2, m_1^2, m_2^2) = -\frac{i}{(4\pi)^2}\left\{ \ln\frac{m_1^2}{\mu^2} + k_1(x) + \frac{p^2}{m_1^2}k_2(x) + \frac{p^4}{m_1^4}k_3(x) \right\},$$

$$\tilde{I}_1(p^2, m_1^2, m_2^2) = -\frac{i}{(4\pi)^2}\left\{ \frac{1}{2}\ln\frac{m_1^2}{\mu^2} + l_1(x) + \frac{p^2}{m_1^2}l_2(x) + \frac{p^4}{m_1^4}l_3(x) \right\}, \quad \text{(A.4)}$$

where μ is an arbitrary parameter having dimensions of mass and

$$k_1(x) = \frac{x-1-x\ln x}{1-x}, \quad k_2(x) = \frac{x^2-1-2x\ln x}{2(1-x)^3},$$

$$k_3(x) = \frac{x^3+9x^2-9x-1-6x(1+x)\ln x}{6(1-x)^5}, \qquad (A.5)$$

$$l_1(x) = \frac{-3x^2+4x-1+2x^2\ln x}{4(1-x)^2},$$

$$l_2(x) = \frac{-2x^3-3x^2+6x-1+6x^2\ln x}{6(1-x)^4},$$

$$l_3(x) = \frac{-3x^4-44x^3+36x^2+12x-1+12(3x^2+2x^3)\ln x}{24(1-x)^6},$$

$$x = \frac{m_2^2}{m_1^2}.$$

If one of the masses exceeds considerably the remaining masses, it convenient to approximate the integrals R_0 and $R_{\alpha\beta}$ as

$$R_0(p_1^2, p_2^2, (p_1-p_2)^2, m_1^2, m_1^2, m_2^2)$$
$$= -\frac{i}{(4\pi)^2}\frac{1}{m_1^2}\left\{e_1(x) + \frac{p_1^2+p_2^2}{m_1^2}e_2(x) + \frac{(p_1-p_2)^2}{m_1^2}e_3(x)\right\},$$

$$R_{10}(p_1^2, p_2^2, (p_1-p_2)^2, m_1^2, m_1^2, m_2^2)$$
$$= -\frac{i}{(4\pi)^2}\frac{1}{m_1^2}\left\{f_1(x) + \frac{p_1^2+2p_2^2}{m_1^2}f_2(x) + \frac{(p_1-p_2)^2}{m_1^2}f_3(x)\right\},$$

$$R_{01}(p_1^2, p_2^2, (p_1-p_2)^2, m_1^2, m_1^2, m_2^2)$$
$$= R_{10}(p_2^2, p_1^2, (p_1-p_2)^2, m_1^2, m_1^2, m_2^2),$$

$$\tilde{R}_{00}(p_1^2, p_2^2, (p_1-p_2)^2, m_1^2, m_1^2, m_2^2)$$
$$= -\frac{i}{(4\pi)^2}\left\{\frac{1}{4}\ln\frac{m_1^2}{\mu^2} + g_1(x) + \frac{p_1^2+p_2^2}{m_1^2}g_2(x) + \frac{(p_1-p_2)^2}{m_1^2}g_3(x)\right\}, \qquad (A.6)$$

$$R_{20}(p_1^2, p_2^2, (p_1-p_2)^2, m_1^2, m_1^2, m_2^2)$$
$$= -\frac{i}{(4\pi)^2}\frac{1}{m_1^2}\left\{h_1(x) + \frac{p_1^2+3p_2^2}{m_1^2}h_2(x) + \frac{(p_1-p_2)^2}{m_1^2}h_3(x)\right\},$$

$$R_{11}(p_1^2, p_2^2, (p_1-p_2)^2, m_1^2, m_1^2, m_2^2)$$
$$= -\frac{i}{(4\pi)^2}\frac{1}{m_1^2}\left\{\frac{1}{2}h_1(x) + \frac{p_1^2+p_2^2}{m_1^2}h_2(x) + \frac{2}{3}\frac{(p_1-p_2)^2}{m_1^2}h_3(x)\right\},$$

$$R_{02}(p_1^2, p_2^2, (p_1-p_2)^2, m_1^2, m_1^2, m_2^2)$$
$$= R_{20}(p_2^2, p_1^2, (p_1-p_2)^2, m_1^2, m_1^2, m_2^2),$$

where

$$e_1(x) = \frac{1-x+x\ln x}{(1-x)^2},$$

$$e_2(x) = \frac{1+4x-5x^2+2x(2+x)\ln x}{4(1-x)^4},$$

$$e_3(x) = \frac{1-6x+3x^2+2x^3-6x^2\ln x}{12(1-x)^4},$$

$$f_1(x) = \frac{1-4x+3x^2-2x^2\ln x}{4(1-x)^3},$$

$$f_2(x) = \frac{1-9x-9x^2+17x^3-6x^2(3+x)\ln x}{36(1-x)^5},$$

$$f_3(x) = \frac{1-6x+18x^2-10x^3-3x^4+12x^3\ln x}{36(1-x)^5},$$

$$g_1(x) = \frac{-1+4x-3x^2+2x^2\ln x}{8(1-x)^2}, \qquad (A.7)$$

$$g_2(x) = -\frac{1}{2}e_3(x),$$

$$g_3(x) = \frac{-2+9x-18x^2+11x^3-6x^3\ln x}{72(1-x)^4},$$

$$h_1(x) = -4g_3(x),$$

$$h_2(x) = \frac{1-8x+36x^2+8x^3-37x^4+12x^3(4+x)\ln x}{144(1-x)^6},$$

$$h_3(x) = \frac{3-20x+60x^2-120x^3+65x^4+12x^5-60x^4\ln x}{240(1-x)^6},$$

$$x = \frac{m_2^2}{m_1^2}.$$

At $x = 1$, expressions (A.5) and (A.7) can be evaluated as their limiting values for $x \longrightarrow 1$.

REFERENCES

1. Particle Data Group, Phys. Rev. D **54**, 1 (1996).
2. M. R. Gaillard and B. W. Lee, Phys. Rev. D **10**, 897 (1974).
3. F. Ma and A. Pramudita, Phys. Rev. D **24**, 2476 (1981).
4. L3 Collab., Preprint No. CERN-PPE-95-136, CERN (1995).
5. G.-L. Lin, J. Liu, and Y.-P. Yao, Phys. Rev. D **42**, 2314 (1990).
6. H. Simma and D. Wyler, Nucl. Phys. B **344**, 283 (1990).
7. S. Herrlich and J. Kalinowski, Nucl. Phys. B **371**, 1176 (1993).
8. G. G. Devidze, G. R. Jibuti, and A. G. Liparteliani, Nucl. Phys. B **468**, 241 (1996).
9. H. E. Haber and G. L. Kane, Phys. Rep. **117**, 75 (1985).
10. G. G. Volkov *et al.*, Fiz. Élem. Chastits. At. Yadra **19**, 1026 (1988) [Sov. J. Part. Nucl. **19**, 442 (1988)].

Translated by R. Rogalyov

Physics of Atomic Nuclei, Vol. 63, No. 2, 2000, pp. 318–321. Translated from Yadernaya Fizika, Vol. 63, No. 2, 2000, pp. 381–384.

ELEMENTARY PARTICLES AND FIELDS
Theory

Two-Center Problem for the Dirac Equation

V. I. Matveev*, D. U. Matrasulov, and H. Yu. Rakhimov**

Department of Thermal Physics, Academy of Sciences of Uzbekistan, ul. Karatal 28, Tashkent, 700135 Republic of Uzbekistan

Received July 10, 1998; in final form, March 26, 1999

Abstract—The ground-state wave function and the energy term of a relativistic electron moving in the field of two fixed Coulomb centers are calculated analytically by the LCAO method. The resulting analytic formula is used to calculate the critical internuclear distance at which the energy term crosses the boundary of the lower continuum. © *2000 MAIK "Nauka/Interperiodica".*

The two-center problem (that is, the problem of describing an electron moving in the field of two fixed centers that have charges Z_1 and Z_2 and which are separated by a distance R), a classical problem in nonrelativistic quantum mechanics, has applications in the theory of chemical bonding, in the physics of muon processes, and in many other realms of science. It was widely discussed in the literature (see, for example, [1–3]). The corresponding problem for the Dirac equation possesses some special features that complicate its solution:

(i) In the Dirac equation with potential $V = -\alpha(Z_1/r_1 + Z_2/r_2)$ ($\alpha = 1/137$), the variables can be separated in none of the systems of orthogonal coordinates.

(ii) For large Z values, collapse into the center occurs.

(iii) The wave function has many components, all of them being on the same order of magnitude at $Z\alpha \approx 1$.

Interest in the two-center problem was generated by the study of Gershteĭn and Zeldovich [4], who indicated that there is the possibility of testing QED in experiments studying heavy-ion collisions. It is well known [5–7] that, for charges of $Z \approx Z_{cr} = 170$, the lowest energy level of the one-center Dirac equation crosses the boundary of the lower continuum and that a spontaneous production of positrons begins as soon as this occurs. Since $Z \approx 170$ nuclei do not exist, it was proposed in [4] to generate such a field in heavy-ion collisions. To calculate the cross section for positron production, it is necessary to know the energy of the (Z_1, Z_2, e^-) quasimolecular state as a function of distance—that is, an energy term. In this connection, the energy term and the critical distance (the distance at which the energy term crosses the boundary of the lower continuum) were calculated both numerically [8] and analytically [5, 9]. Müller, Rafelski, and Greiner [7] and Müller and Greiner [8], who presented the results of their extensive numerical calculations, solved the Dirac equation for the two-center Coulomb potential by diagonalizing the Dirac Hamiltonian in a two-center basis. Approximate analytic calculations of the energy term and of the critical distance are presented in a series of articles by Popov [5, 9]. However, the expressions that he obtained permit calculating the energy term and the critical distance either only numerically or under the conditions that an excess over the critical charge is small ($(Z_1 + Z_2 - Z_{cr})/Z_{cr} \ll 1$) and that the centers are separated by small distances.

In the present study, we solve the Dirac equation for the two-center problem by a method similar to the LCAO method, which is widely used to solve the nonrelativistic two-center problem [2] and which makes it possible to calculate analytically the energy term for the hydrogen molecular ion and for the hydrogen molecule. Similar calculations for the Dirac electron have not been performed so far. The analytic formula obtained by applying the LCAO method to the relativistic two-center problem enabled us to calculate the energy term over a wide range of the total nuclear charge and a wide range of center-to-center distances.

Below, we use the system of units in which $\hbar = c = m_e = 1$ and denote by R the distance between the nuclei and by r_1 and r_2 the distances between the electron and the nuclei; we also assume that $Z_1 = Z_2 = Z$.

The motion of a relativistic electron in the field of two Coulomb centers is described by the time-independent Dirac equation

$$H\Psi = E\Psi, \tag{1}$$

where $H = \boldsymbol{\alpha} \cdot \mathbf{p} + \beta + V$ is the Dirac Hamiltonian, while $\boldsymbol{\alpha}$ and β are Dirac matrices.

We will solve equation (1) by the LCAO method, choosing the wave function in the form

$$\Psi = d_1\Psi_1 + d_2\Psi_2,$$

where Ψ_1 (Ψ_2) is the wave function of the electron moving in the field of the first (second) center. The details of the application of the variational principle to the Dirac equation are discussed in [9–12]. From the symmetry of the problem ($Z_1 = Z_2$), the normalization conditions $\langle\Psi|\Psi\rangle = 1$ and $\langle\Psi_j|\Psi_j\rangle = 1$ ($j = 1, 2$), and the

* e-mail: matveev@vict.sim.org
** e-mail: davron@silk.org

fact that the ground state does not have nodes, it follows that [2]

$$d_1 = d_2 = 1/\sqrt{2(1+S)},$$

where $S = \langle\Psi_1|\Psi_2\rangle$ is the overlap integral.

The energy of an electron can be calculated as the matrix element

$$E = \langle\Psi|H|\Psi\rangle, \tag{2}$$

where $\langle\Psi| = [\varphi\ \chi]$ ($|\Psi\rangle = \begin{bmatrix}\varphi\\ \chi\end{bmatrix}$) is a bispinor in the standard representation.

It was indicated above that, for the functions Ψ_1 and Ψ_2, we will take the relativistic wave functions of the hydrogen-like atom [13] with the effective charge $Q\alpha$; that is,

$$\varphi_j = Ag_j\begin{bmatrix}1\\0\end{bmatrix}, \quad \chi_j = iABg_j\begin{bmatrix}\cos\theta\\ e^{i\varphi}\sin\theta\end{bmatrix},$$

where $g_j = r_j^{\gamma-1}e^{-Q\alpha r_j}$ ($j = 1, 2$), and

$$A = \frac{(2Q\alpha)^{3/2}}{\sqrt{4\pi}}\sqrt{\frac{1+\gamma}{2\Gamma(1+2\gamma)}}(2Q\alpha)^{\gamma-1},$$

$$B = (1-\gamma)/Q\alpha, \quad \gamma = \sqrt{1-Q^2\alpha^2}.$$

Substituting these wave functions into (2), we reduce the expression for the energy term to a form involving five integrals that can be expressed analytically in terms of complete and incomplete Euler gamma functions [$\Gamma(x)$ and $\Gamma(x, y)$, respectively] [14]. Specifically, we have

$$E = \frac{2\pi A^2 bR^{2\gamma}}{1+S}\left[Q\alpha(I_1+I_2) + \frac{a\gamma}{2Q\alpha}(I_3+I_4) - 2Z\alpha(I_2+I_5)\right], \tag{3}$$

where the overlap integral S and the integrals I_1, I_2, I_3, I_4, and I_5 are given by

$$S = 2\pi A^2 R^{2\gamma+1}bI_4,$$

$$I_1 = \frac{1}{a^{2\gamma}}2\Gamma(2\gamma),$$

$$I_2 = \frac{1}{a^{2\gamma}}\left[\left(2-\frac{a^2}{3(2\gamma-1)}\right)\Gamma(2\gamma, a) + \left(\frac{1}{3}+\frac{a}{3(2\gamma-1)}\right)a^{2\gamma}e^{-a}\right],$$

$$I_3 = \frac{1}{a^{2\gamma+1}}4\gamma\Gamma(2\gamma),$$

$$I_4 = \frac{1}{a^{2\gamma+1}}\left[\left(4\gamma-\frac{2a^2\gamma}{3(2\gamma-1)}\right)\Gamma(2\gamma, a) + \left(2+\frac{2a\gamma}{3(2\gamma-1)}\right)a^{2\gamma}e^{-a}\right],$$

$$I_5 = \frac{1}{a^{2\gamma+1}}\left[(a-\gamma)\Gamma(2\gamma, 2a) + (a+\gamma)\Gamma(2\gamma) - \frac{1}{2}(2a)^{2\gamma}e^{-2a}\right],$$

$$a = 2Q\alpha R, \quad b = 2/(1+\gamma).$$

Thus, we have obtained the electron energy term as a function of the distance R, the charge Z, and the test charge Q. For $Q\alpha \ll 1$ ($\gamma \simeq 1$), expression (3) takes the form

$$E = Q^2\alpha^2F_1(a) + Q\alpha F_2(a), \tag{4}$$

where

$$F_1(a) = \frac{1}{2}\frac{1+e^{-a}(1+a-a^2/3)}{1+e^{-a}(1+a+a^2/3)},$$

$$F_2(a) = -Z\alpha\frac{1+2e^{-a}(1+a)+1/a-(1/a+1)e^{-2a}}{1+e^{-a}(1+a+a^2/3)}.$$

Expression (4) coincides with that which was obtained within the nonrelativistic LCAO method for the hydrogen molecular ion [2].

The charge Q is generally a function of R and Z; that is,

$$Q = Q(R, Z).$$

It is known from [2] that

$$Q|_{R\to 0} = 2Z, \tag{5}$$

$$Q|_{R\to\infty} = Z. \tag{6}$$

Figure 1 shows Q/Z as a function of R for the relativistic and nonrelativistic Er–Er systems, which have the charge of $Z = 68$. These results were obtained by numerically minimizing expressions (3) and (4) for the relativistic and nonrelativistic cases, respectively. It can be seen that, in the limiting cases of $R \longrightarrow \infty$ and $R \longrightarrow 0$, the effective charge tends to, respectively, the charge of the isolated atom and the charge of the combined one.

Figure 2 displays the relativistic and the nonrelativistic energy term for the charge value of $Z = 68$. We can see that relativistic corrections become sizable for small R.

Figure 3 presents the relativistic energy term for the system Br–Br ($Z = 35$) as calculated by our formula (3) (solid curve) and as obtained in [8] (dashed curve).

Evaluating the limit of expression (3) for $R \longrightarrow 0$ and taking into account (5), we obtain (combined atom)

$$E(R\longrightarrow 0) = \sqrt{1-4Z^2\alpha^2}.$$

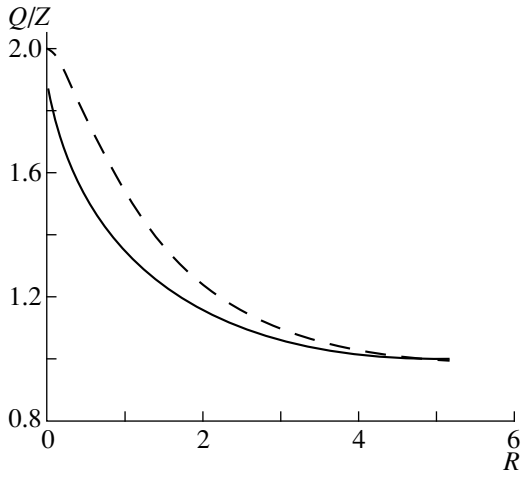

Fig. 1. Ratio Q/Z as a function of the center-to-center distance for the Er–Er system ($Z = 68$): (dashed curve) results obtained by minimizing expressions (4) for the nonrelativistic term and (solid curve) results obtained by minimizing expressions (3) for the relativistic term.

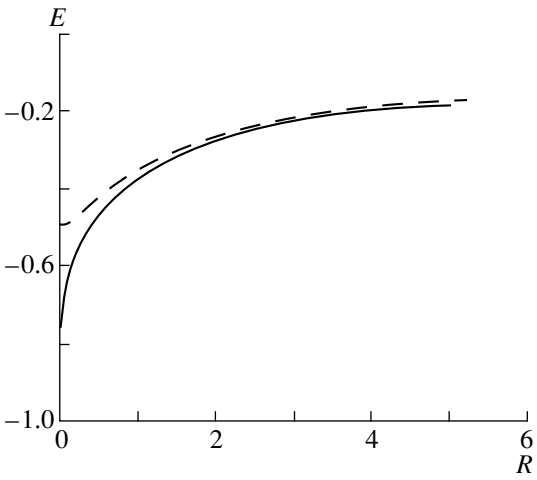

Fig. 2. Energy term for the case of $Z = 68$: (dashed curve) results for the nonrelativistic system and (solid curve) results for the relativistic system.

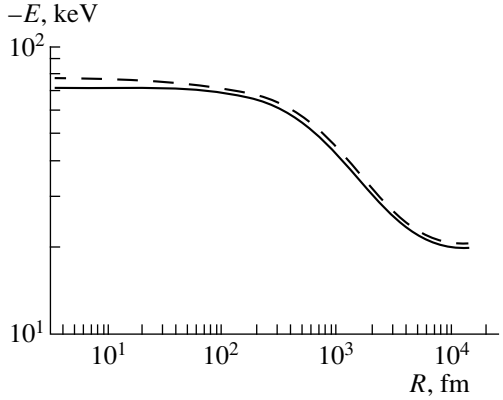

Fig. 3. Energy term for the Br–Br system ($Z = 35$): (solid curve) results obtained according to (3) and (dashed curve) results from [8].

A calculation for the limit $R \longrightarrow \infty$ with allowance for (6) yields (isolated atom)

$$E(R \longrightarrow \infty) = \sqrt{1 - Z^2\alpha^2}.$$

At $Z_1 + Z_2 \sim 170$, Popov's formula for the critical distance at which the ground-state level crosses the boundary of the lower continuum—in [5], this formula was derived by matching the asymptotic expressions at large distances from the nuclei—can be obtained directly from (3) under the same assumptions as in [5]. To demonstrate this, we consider that, in this case, $\gamma = ig = i\sqrt{4Z^2\alpha^2 - 1}$, $a \ll 1$, and $Q = 2Z$. From the condition

$$E(R_{cr}) = -1,$$

which corresponds to crossing the lower boundary of the continuum, we then obtain

$$[(1-\gamma)\cdot 4^{\gamma} + 2\gamma]a^{2\gamma} = -4\gamma\Gamma(2\gamma + 1),$$

or, equivalently,

$$(2R_{cr})^{-2\gamma}\frac{4\gamma}{(1-\gamma^2)^{\gamma}((\gamma-1)\cdot 4^{\gamma} - 2\gamma)}\Gamma(2\gamma+1) = 1 \equiv e^{2\pi i},$$

whence it follows that

$$R_{cr}^{-2\gamma} f(\gamma)\Gamma(1+2\gamma) = 1 \equiv e^{2\pi i},$$

where

$$f(\gamma) = \frac{4^{1-\gamma}\gamma}{(1-\gamma^2)^{\gamma}((\gamma-1)\cdot 4^{\gamma} - 2\gamma)}.$$

The above expression can be recast into the form

$$-2g\ln R_{cr} + \arg(f(ig)) + \arg\Gamma(1+2ig) = 2\pi,$$

or, equivalently, into the form

$$g\ln R_{cr} = -\pi + \frac{1}{2}(\arg(f(ig)) + \arg\Gamma(1+2ig)).$$

From the last equation, we obtain

$$R_{cr} = \exp\left(-\frac{\pi}{g} + \frac{1}{2g}[\arg(f(ig)) + \arg\Gamma(1+2ig)]\right). \quad (7)$$

Taking into account the asymptotic relations

$$\arg\Gamma(1+2ig) = 2g\Psi(1) + O(g^3) \approx 2g\Psi(1)$$

and

$$\arg(f(ig)) \approx 2.4g,$$

performing some simple transformations, and using (7), we find that the critical distance is given by

$$R_{cr} = C\exp\left(-\frac{\pi}{\sqrt{4Z^2\alpha^2 - 1}}\right),$$

where C is a constant. This formula coincides with that obtained previously in [9]. A calculation of the critical distance for the uranium nuclei according to (7) yields the value of $R_{cr} = 43.4$ fm; at the same time, this critical radius was estimated at 38.4 fm in [15] and at 34.7 fm in [8]. Upon the introduction of corrections for finite nuclear sizes, the value of $R_{cr} = 34.3$ fm was obtained in [16].

It should be noted that, at $Z = 92$, expression (3) is accurate to within 25%. For $Z = 35$, Fig. 3 shows that the computational errors amount to 10%.

In summary, we have derived the analytic formula (3) for the energy term of a relativistic electron moving in the field of two fixed Coulomb centers. This formula is correct over a wide range of the total nuclear charges and over a wide range of center-to-center distances. When the total nuclear charge is close to its critical value ($Z_1 + Z_2 \sim 170$), formula (3) reduces to Popov's well-known formula [5, 9] for the critical distance between the nuclei that corresponds to the crossing of the boundary of the lower continuum, in which case the generation of electron–positron pairs begins.

Currently, the properties of baryons containing two heavy quarks (QQq baryons) are widely discussed in the literature [17, 18]. These baryons are similar to the (Z_1, Z_2, e^-) system considered here: the Coulomb potential of interaction between the electron and the nucleus is replaced by the quark–quark interaction potential (it includes the Coulomb potential and a confining term). Hence, the method developed here can be used to solve the Dirac equation with a two-center quark potential for the motion of a light quark in the field of two heavy quarks.

ACKNOWLEDGMENTS

We are grateful to M.M. Musakhanov for stimulating discussions and enlightening comments.

REFERENCES

1. H. A. Bethe, Handbuch der Physik **B1**, 24/1: *Quantenmechanik der Ein- und Zwei-Electronenprobleme* (Berlin, 1933; ONTI, Moscow, 1935).
2. J. S. Slater, *Electronic Structure of Molecules* (McGraw-Hill, New York, 1963).
3. I. V. Komarov, L. I. Ponomarev, and S. Yu. Slavyanov, *Spheroidal and Coulomb Spheroidal Functions* (Nauka, Moscow, 1976).
4. S. S. Gershteĭn and Ya. B. Zeldovich, Zh. Éksp. Teor. Fiz. **57**, 654 (1969) [Sov. Phys. JETP **30**, 358 (1969)]
5. V. S. Popov, Yad. Fiz. **14**, 458 (1971) [Sov. J. Nucl. Phys. **14**, 257 (1971)].
6. A. A. Grib, S. G. Mamaev, and V. M. Mostepanenko, *Vacuum Quantum Effects in Strong Fields* (Énergoatomizdat, Moscow, 1988).
7. B. Müller, J. Rafelski, and W. Greiner, Phys. Lett. B **47**, 5 (1973).
8. B. Müller and W. Greiner, Z. Naturforsch. A **31**, 1 (1976).
9. V. S. Popov, Yad. Fiz. **17**, 621 (1973) [Sov. J. Nucl. Phys. **17**, 332 (1973)].
10. H. Wallmeier, Phys. Rev. A **29**, 2993 (1984).
11. D. N. Sambhu, Chem. Phys. Lett. **74**, 568 (1980).
12. J. Sucher, Phys. Rev. A **22**, 348 (1980).
13. J. D. Bjorken and S. D. Drell, *Relativistic Quantum Mechanics* (McGraw-Hill, New York, 1964).
14. M. Abramowitz and I. A. Stegun, *Handbook of Mathematical Functions* (Dover, New York, 1965).
15. V. I. Lisin, M. S. Marinov, and V. S. Popov, Phys. Lett. B **69**, 141 (1977).
16. V. D. Mur and V. S. Popov, Yad. Fiz. **31**, 617 (1980) [Sov. J. Nucl. Phys. **31**, 321 (1980)].
17. J. M. Richard, Phys. Rep. **212**, 1 (1992).
18. S. N. Mukherjee *et al.*, Phys. Rep. **231**, 203 (1993).

Translated by O. Chernavskaya